Fatigue & Fracture Mechanics

35th Volume

Richard E. Link
Kamran M. Nikbin
Editors

STP 1480

ASTM INTERNATIONAL

STP 1480

Fatigue and Fracture Mechanics: 35th Volume

Richard E. Link and Kamran M. Nikbin, editors

ASTM Stock Number: STP1480

ASTM International
100 Barr Harbor Drive
PO Box C700
West Conshohocken, PA 19428-2959

Printed in the U.S.A.

Library of Congress Cataloging-in-Publication Data
ISBN: 978-0-8031-3406-5
ISBN: 0-8031-3406-1

Copyright © 2007 AMERICAN SOCIETY FOR TESTING AND MATERIALS INTERNATIONAL, West Conshohocken, PA. All rights reserved. This material may not be reproduced or copied, in whole or in part, in any printed, mechanical, electronic, film, or other distribution and storage media, without the written consent of the publisher.

Photocopy Rights

Authorization to photocopy items for internal, personal, or educational classroom use, or the internal, personal, or educational classroom use of specific clients, is granted by the American Society for Testing and Materials International (ASTM) provided that the appropriate fee is paid to the Copyright Clearance Center, 222 Rosewood Drive, Danvers, MA 01923; Tel: 978-750-8400; online: http://www.copyright.com/.

Peer Review Policy

Each paper published in this volume was evaluated by two peer reviewers and at least one editor. The authors addressed all of the reviewers' comments to the satisfaction of both the technical editor(s) and the ASTM International Committee on Publications.

The quality of the papers in this publication reflects not only the obvious efforts of the authors and the technical editor(s), but also the work of the peer reviewers. In keeping with long-standing publication practices, ASTM International maintains the anonymity of the peer reviewers. The ASTM International Committee on Publications acknowledges with appreciation their dedication and contribution of time and effort on behalf of ASTM International.

Printed in Mayfield, PA
January, 2008

Foreword

The Fifth International ASTM/ESIS Symposium on Fatigue and Fracture (35th ASTM National Symposium on Fatigue and Fracture Mechanics) was held in Reno, Nevada on 18-20 May 2005. ASTM International Committee E08 on Fatigue and Fracture and the European Structural Integrity Society (ESIS) served as sponsors. The symposium chairmen and co-editors of this volume were Richard E. Link, United States Naval Academy, Annapolis, MD and Kamran Nikbin, Imperial College, London, England.

Kamran Nikbin
Imperial College

Richard Link
United States Naval Academy

Contents

Overview **vii**

SEDLOW LECTURE

Trends in High Temperature Structural Integrity Assessment—
G. A. WEBSTER 3

CREEP ASSESSMENT

European Code of Practice for Creep Crack Initiation and Growth Testing of Industrially Relevant Specimens—B. DOGAN, U. CEYHAN, K. M. NIKBIN, B. PETROVSKI, AND D. W. DEAN 23

Creep Crack Growth Predictions in Component Using a Damage Based Approach—M. YATOMI AND K. M. NIKBIN 43

Modelling the Redistribution of Residual Stresses at Elevated Temperature in Components—H. LEE AND K. M. NIKBIN 54

CREEP MODELING

Probabilistic Analysis of the Creep Crack Growth Rate of Type 316LN Stainless Steel by the Monte Carlo Simulation—W. G. KIM, S. J. KIM, W. S. RYU, AND S. N. YOON 71

Mechanistic Studies of High-Temperature Crack Initiation in Single Crystal Materials—E. P. BUSSO, N. P. O'DOWD, AND L. G. ZHAO 81

Creep Crack Growth Analysis of Welded Joints for High Cr Hear Resisting Steel—
M. TABUCHI, H. HONGO, T. WATANABE, AND A. T. YOKOBORI, JR. 93

Prediction of Scatter in Creep Crack Growth Data from Creep Failure Strain Properties—K. WASMER, K. M. NIKBIN, AND G. A. WEBSTER 102

Analysis of Creep Crack Initiation and Growth in Different Geometries for 316H and Carbon Maganese Steels—C. M. DAVIES, F. MUELLER, K. M. NIKBIN, N. P. O'DOWD, AND G. A. WEBSTER 115

FATIGUE DAMAGE AND ANALYSIS

Fatigue Strength in Presence of Inhomogeneities: Influence of Constraint—S. BERETTA, M. CARBONI, AND M. MADIA 137

Detection of Crack Initiation by Observations of Free Surface-Condition—K. GOMI, K. FUKUDA, K. TANIUCHI, AND S. S. YOSHIDA 148

Volumetric and Surface Position Annihilation Studies of Fatigue Damage Accumulation in a Steel Alloy—C. D. GLANCEY AND R. R. STEPHENS 158

Elasto-Viscoplastic Behavior of the Ferritic Stainless Steel AISI 441-EN 1.4509 from Room Temperature to 850 Degree Celsius—P. O. SANTACREU, L. BUCHER, A. KOSTER, AND L. REMY 168

Life Prediction of Fretting Fatigue of Ti-6AI-4V—O. JIN, J. CALCATERRA, AND S. MALL 174

Verification of the Analytical Models in a Fracture Mechanics Based Approach to Modeling Fretting Fatigue—S. A. POST-DOMASKY, L. BROOKS, AND N. YOUNG 185

The Effect of Large Strain Cycling on the Fatigue Strength of Welded Joint—K. OKUYA AND Y. KONDO 195

A Robust Structural Stress Parameter for Evaluation of Multiaxial Fatigue of Weldments—P. DONG AND J. K. HONG 206

FATIGUE CRACK GROWTH

Observations on Photo-Emission and the Process Zone of a Fatigue Crack—E. A. PATTERSON, F. A. DIAZ, AND J. R. YATES 225

Simulation on the Decrease in Threshold Stress Intensity Factor (SIF) Range due to High Maximum SIF—T. MESHII, K. ISHIHARA, AND T. ASAKURA 234

Anomalous Fatigue Crack Growth Data Generated Using the ASTM Standards—S. C. FORTH, J. C. NEWMAN, JR., AND R. G. FORMAN 244

Development of a Circumferentially Throughwall Cracked Tube Specimen for Fatigue Crack Growth Rate Tests—B. A. YOUNG, W. A. VAN DER SLUYS, AND P. J. KING 256

ENVIRONMENTAL FRACTURE

Effect of Microstructure on Pit-to-Crack Transition of 7075-T6 Aluminum Alloy—K. JONES AND D. HOEPPNER 271

The Role of Applied Potential on Environment-Assisted Cracking of Zirconium Alloys—A. K. ROY, U. VALLIYIL, AND E. GOVINDARAJ 281

FRACTURE MECHANICS ANALYSIS

Elastic T-Stress Solutions of Embedded Elliptical Cracks Subjected to Uniaxial and Biaxial Loadings—J. QU AND X. WANG 295

Asymptotic Stress Fields for Thermomechanically Loaded Cracks in FGMs—N. JAIN, R. CHONA, AND A. SHUKLA 309

Experimental Evaluation of the J or C Parameter for a Range of Crack Geometries—C. M. DAVIES, M. KOURMPETIS, N. P. O'DOWD, AND K. M. NIKBIN 321

FRACTURE TOUGHNESS AND CONSTRAINT

An Experimental and Numerical Study on the Fracture Strength Of Welded Structural Hollow Section X-Joints—T. BJORK, G. MARQUIS, V. PELLIKKA, AND R. ILVONEN 343

Constraint Corrected J-R Curve and Its Application to Fracture Assessment for X80 Pipelines—X. K. ZHU AND B. N. LEIS 357

Use of Miniaturized Compact Tension Specimens for Fracture Toughness Measurements in the Upper Shelf Regime—E. LUCON, M. SCIBETTA, R. CHAOUADI, AND E. VAN WALLE, 374

An Investigation of Specimen Geometry Effects on the Fracture Behavior of a Polytetrafluoroethylene Polymer—J. A. JOYCE AND P. J. JOYCE 390

Surface Roughness, Quasi-Static Fracture, and Cyclic Fatigue Effects on GFRP and CFRP-Concrete Bonded Interfaces—T. O. LAWRENCE AND D. BOYAJIAN 407

DUCTILE-BRITTLE TRANSITION

Temperature Dependence and Variability of Fracture Toughness in theTransition Regime for A508 Grade 4N Pressure Vessel Steel—T. R. LEAX 425

Application of the Reference Temperature to the Evaluation of Cleavage Fracture in HSLA-100 Steel—S. M. GRAHAM, G. P. MERCIER, AND B. P. L'HEUREUX 445

Prediction of the Shape of the K_J Ductile-to-Ductile Transition Temperature Curve for Ferritic Pressure Vessel Steels Using the Material's Resistance to Crack Extension K_J versus Δa Curve—G. WARDLE AND W. GEARY 457

DYNAMIC FRACTURE

Finite Element Simulation of Dynamic Crack Propagation for Complex Geometries without Remeshing—F. R. BIGLARI, A. REZAEINASAB, K. NIKBIN, AND I. SATTARIFAR 469

Analysis of Dynamic Fracture and Crack Arrest of an HSLA Steel in an SE(T) Specimen—R. E. LINK 485

Application of the Normalization Method to Dynamic Fracture Toughness Testing of Alloy 718—S. M. GRAHAM 511

Overview

This book is a presentation of work of several authors at the Fifth International ASTM/ESIS Symposium on Fatigue and Fracture, May 18–20, 2005, Reno, NV. Fatigue and fracture methodologies depend upon robust and accurate models of the damage accumulation and failure mechanisms that operate within the structures as well as an accurate characterization of the material response to the combined effects of loading, loading rate and environmental conditions. The combination of competing failure mechanisms and varying environmental conditions during the operational life of a component can make it a challenge to accurately predict its life. Hence the scope for this symposium captures the latest research covering state of the art work on fracture mechanics related topics such as fracture, fatigue, residual stress, creep, creep/fatigue, constraint and stress corrosion and links them to concepts used in structural integrity assessment. Furthermore the subject does not restrict itself to metallic materials but is applicable to polymers, composites as well as inhomogeneous materials. Papers and presentations delivered by nationally and internationally recognized authors were chosen to cover the general areas of modelling, testing and validation in crack dominant related research. It is felt that improvements in life assessment methods will only come about when validated fracture mechanics models are developed to produce verifiable predictions. Hence an emphasis on linking experimental and modelling techniques in the papers published in this volume should lead to the development of more accurate life assessment methods.

The papers contained in this publication represent the commitment of the ASTM Committee E-08 to providing the latest research information in the wide-ranging fracture mechanics field. The themes in the papers cover experimental results coupled to modelling techniques of linear, non-linear, time independent and dependant behaviour of cracked geometries of a range of materials. Papers relating to residual stress, crack tip constraint and probabilistic methods of analyses also highlight the importance of developing these fields for future improvements in life assessment methods.

Kamran Nikbin
Imperial College

Richard Link
United States Naval Academy

Sedlow Lecture

Journal of ASTM International, February 2006, Vol. 3, No. 2
Paper ID JAI13229
Available online at www.astm.org

George A. Webster[1]

Trends in High Temperature Structural Integrity Assessment

ABSTRACT: Failure in components that may contain defects and that operate at elevated temperatures can occur by creep, fatigue, or fast fracture, or some combination of these processes. Frequently, these components include welds and repairs to welds. Codes and standards are available for assessing the structural integrity of these types of components. This paper addresses the main issues of concern in making safety assessments and reliable lifetime predictions for situations where creep processes dominate. Emphasis is placed on the creep component of cracking. Initially, models of crack initiation and growth are reviewed. The creep fracture mechanics parameter C^* is used to make predictions. The influence of constraint on the mechanisms responsible for void nucleation and growth is considered and creep crack growth rate laws derived. Methods of calculating C^* in components from the plastic fracture mechanics parameter J or, approximately, from stress intensity factor K and limit analysis using reference stress concepts are described. A procedure for making remaining life assessments for cracking into progressively deteriorating material is considered. Techniques for dealing with an initial transient phase, or incubation period, during which damage builds up at a crack tip are presented. An indication of the scatter to be expected in creep crack growth data, for use in sensitivity studies, is provided. The role of residual stress on the early stages of cracking and subsequent crack propagation is discussed.

KEYWORDS: creep deformation, fracture mechanics, creep crack growth, incubation period, residual stress, lifetime assessment

Nomenclature

A = fatigue crack growth property
a = crack size
$\dot{a}$ = creep crack growth rate
$\dot{a}_1$, $\dot{a}_j$ = creep crack growth rate through element 1, element j
B = specimen thickness
B_n = specimen thickness between side grooves
B_r = creep rupture property
C, C_A = creep strain rate properties
C_t, $C(t)$, C^* = creep fracture mechanics parameters
D_o = creep crack growth rate property
E = elastic modulus
E' = E in plane stress, $E/(1-\nu^2)$ in plane strain
G = elastic strain energy release rate
H = plasticity property
h = nondimensional function
I_n = nondimensional factor
J = plastic fracture mechanics parameter
j = element number
K = stress intensity factor
K_{app}, K_{res} = applied load, residual stress intensity factors
m = index in fatigue crack growth law

Manuscript received April 18, 2005; accepted for publication September 8, 2005; published December 2005. Presented at ASTM Symposium on Fatigue and Fracture Mechanics: 35th Volume on 18–20 May 2005 in ; R. E. Link and K. M. Nikbin, Guest Editors.

[1] Dept. of Mechanical Engineering, Imperial College, London, SW7 2BX, UK.

Copyright © 2006 by ASTM International, 100 Barr Harbor Drive, PO Box C700, West Conshohocken, PA 19428-2959.

N = number of cycles
n = index in creep strain rate law
n_p = index in plastic strain relation
P, P_{LC} = load, collapse load
Q^* = creep fracture mechanics parameter
r = distance ahead of crack tip
r_c = size of creep process zone
s = arc length around contour
T_i = component of traction vector
t, t_i, t_τ = time, incubation period, transition time
t_r, $t_{r\ \mathrm{ref}}$ = rupture life, rupture life at reference stress
t_r^* = multiaxial stress rupture life
$\dot{u}_i$ = component of creep displacement rate vector
W, w = specimen, plate widths
W_s^* = creep strain energy rate density
x, y = coordinates
Γ = contour around crack tip
δ_ι = crack opening displacement at initiation
$\dot{\varepsilon}$, $\bar{\dot{\varepsilon}}$ = creep strain rate, equivalent creep strain rate
$\dot{\varepsilon}_{\mathrm{ref}}$ = creep strain rate at reference stress
ε_f, ε_f^* = creep failure strain, multiaxial creep failure strain
ε_p = plastic strain
θ = angle at crack tip
υ = index in creep rupture law
σ, σ_{ij}, $\tilde{\sigma}_{ij}(\theta, n)$ = stress, stress tensor, nondimensional function
σ_o = property in creep strain rate relation
σ_{ref}, σ_Y = reference stress, yield stress
ν = Poisson's ratio
ϕ = index in creep crack growth rate law
ω, ω_j = damage fraction, damage fraction in element j

Introduction

With the increasing use and sensitivity of nondestructive inspection techniques resulting in the detection of smaller and smaller cracks, there is a growing need to provide methods of assessing the significance of defects in equipment. Defects can be introduced during fabrication and/or use. In order to make an assessment, the processes responsible for the development of cracking need to be established. Previously companies in, for example, the aerospace, chemical process, electric power, manufacturing and nuclear industries provided their own codes of practice for performing assessments. For economic reasons, and also to satisfy national (and maybe international) regularity authorities, there is a trend toward the adoption of national and international standards or codes of practice, such as the American API 597 [1], ASME [2], French A16 [3], European SINTAP [4], FITNET [5], Japanese WES 2805 [6], and British R5 [7], R6 [8], and BS 7910 [9] procedures, for making structural integrity assessments of equipment that contains cracks. The main requirement of these procedures is to determine the safety and fitness for further service of the equipment being investigated to establish whether it should be replaced, or repaired, or whether the operating conditions and frequency of inspection should be modified.

The procedures referred to can address several modes of failure from cracks; these include brittle fracture, ductile tearing, plastic collapse, creep and fatigue cracking (or combinations of these), and in some instances, environmental attack. In this paper attention is restricted to high temperature applications where creep, fatigue, or combined creep-fatigue processes dominate. Initially models of the cracking process will be reviewed and the influence of constraint local to a crack tip examined. The role of residual stress, which is often of particular importance in welded structures, will be considered. Ways of dealing with scatter in material properties data in sensitivity studies will be discussed. Finally some general

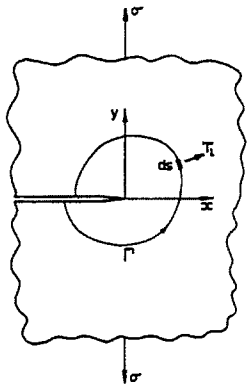


FIG. 1—*Integration contour around a crack tip for evaluating* C^*.

conclusions and guidelines for making assessments will be presented. Issues that need to be addressed in producing robust assessments include availability of materials properties data and knowledge of the operating conditions. Accurate information may not always be available.

Scope of Codes of Practice

All the procedures for making high temperature defect assessments apply similar fracture mechanics concepts to those that are used for describing brittle fracture and ductile tearing. Historically [10–12] several parameters have been employed for characterizing crack growth in the presence of creep; these include the stress intensity factor K, and the creep fracture parameters C_t, $C(t)$, Q^*, and C^*. For widespread creep conditions, all the creep parameters degenerate to C^*, which can be evaluated for a contour Γ surrounding a crack tip in a two-dimensional body of unit thickness from

$$C^* = \int_\Gamma W_s^* dy - T_i \frac{\partial \dot{u}_i}{\partial x} ds \tag{1}$$

where W_s^* is the creep strain energy rate density given by

$$W_s^* = \int \sigma_{ij} d\dot{\varepsilon}_{ij} \tag{2}$$

In these equations σ_{ij} and $\dot{\varepsilon}_{ij}$ are stress and creep strain rate tensors, respectively, T_i and $\dot{u}_i$ are components of the traction and creep displacement rate vectors, x and y are the coordinates along and perpendicular to the crack tip, and s is the arc length along Γ as shown in Fig. 1. This definition corresponds to that used for the J contour integral [13] in the presence of plasticity. For widespread creep conditions, C^* is path independent and can be used to describe the stress and creep strain rate distributions ahead of a crack tip. Prior to this situation being reached, it is more appropriate to describe the local stress state in terms of the $C(t)$ or C_t parameters [14,15]. When creep strain rate $\dot{\varepsilon}$ can be expressed in terms of stress σ by a relation of the form

$$\dot{\varepsilon} = \dot{\varepsilon}_0 \left(\frac{\sigma}{\sigma_0} \right)^n = C\sigma^n \tag{3}$$

where $\dot{\varepsilon}_0$, σ_0, C, and n are material constants, a conservative estimate of the time t_τ to reach widespread creep conditions is given by

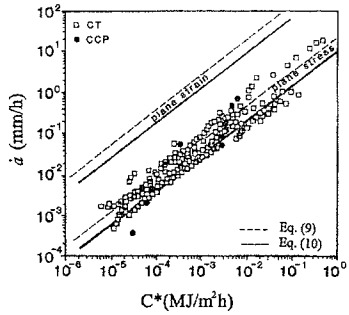


FIG. 2—*Dependence of creep crack growth rate on C^* for alloy 800 H at 800°C [18].*

$$t_T = \frac{G}{(n+1)C^*} = \frac{K^2}{E'(n+1)C^*} \tag{4}$$

where G is elastic strain energy release rate, E' is the elastic modulus E for plane stress, and $E/(1-\nu^2)$ for plane strain for a Poisson's ν.

The available experimental information suggests that, despite the introduction of the above fracture mechanics parameters, creep crack growth rate $\dot{a}$ can be interpreted most often in terms of C^* by an expression of the form

$$\dot{a} = D_o C^{*\phi} \tag{5}$$

where D_o and ϕ are material constants that are best determined experimentally. The recommended test procedure is given in ASTM E 1457 [16]. The procedure recommends the use of compact tension (CT) specimens to achieve high constraint at the crack tip. It is similar to that employed in ASTM E 647 [17] for measuring fatigue crack growth/cycle (da/dN) as a function of stress intensity factor range ΔK to obtain the material constants A and m in the Paris fatigue crack growth law

$$\frac{da}{dN} = A\Delta K^m \tag{6}$$

Typical results of creep crack growth rate against C^* obtained on tests performed in accordance with ASTM E 1457 are shown in Fig. 2 [18]. In this case, little difference is seen between the behavior of CT and center cracked plate (CCP) specimens because of the substantial ductility exhibited by the alloy. Usually, under conditions appropriate to those experienced by components during operation, fractures under creep dominating circumstances are predominantly intergranular and under fatigue loading are mainly transgranular as shown in Fig. 3 [19]. Under combined creep-fatigue loading mixed intergranular/

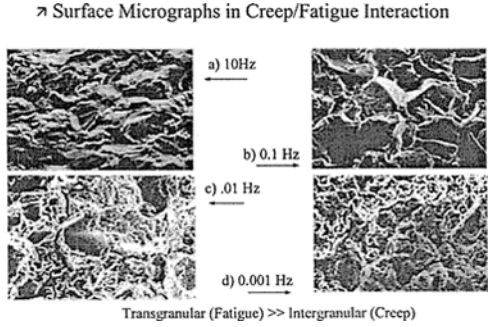


FIG. 3—*Transition from (a) transgranular fatigue failure at high frequency through (b) and (c) mixed mode failures to (d) intergranular cracking with decrease in frequency. (Magnification ×200).*

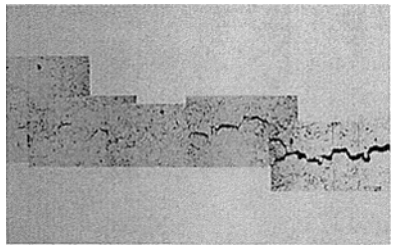


FIG. 4—*Section through a creep crack in a low alloy steel showing microcracking ahead of main crack tip. (Magnification ×80).*

transgranular fractures, as illustrated in Fig. 3, may be observed and it is common practice to obtain the total crack growth rate by summing the creep and fatigue contributions given by Eqs (5) and (6), respectively.

In order to be able to make predictions of crack growth in components that are subjected to creep and/or fatigue loading, it is necessary to know the appropriate material constants required by Eqs (3), (5), and (6) and to have available solutions for ΔK and C^*. Handbooks [20–22] exist for calculating K for a wide range of loading conditions and crack geometries, but not for estimating C^*. In the remainder of this paper, guidance is provided on how to make structural integrity assessments of cracked components that operate at high temperatures using these expressions. Situations where creep crack growth properties are available, and have not been measured, will each be examined. Methods of providing approximate estimates of C^* with the aid of limit analysis will be included. It may be that insufficient material properties data are available to justify use of finite element methods.

Steady State Models of Cracking Process

Microstructural evidence suggests, as seen in Fig. 4, that creep crack growth takes place intermittently by the linking up of microscracks and voids that are generated on grain boundaries ahead of the main crack tip, to the crack tip, in much the same way that creep damage develops in uniaxial creep specimens. The implication is that the same mechanisms that control failure by creep rupture also control failure by crack growth. Consequently, it may be expected that it should be possible to predict creep crack growth properties from uniaxial creep data. For a uniaxial creep law of the form of Eq (3), when widespread creep conditions are satisfied, it may be shown [14] that the stress field at (r,θ) ahead of the crack tip (as illustrated in Fig. 5) is given by

$$\sigma_{ij} = \left[\frac{C^*}{I_n C r}\right]^{1/(n+1)} \tilde{\sigma}_{ij}(\theta,n) + \cdots \tag{7}$$

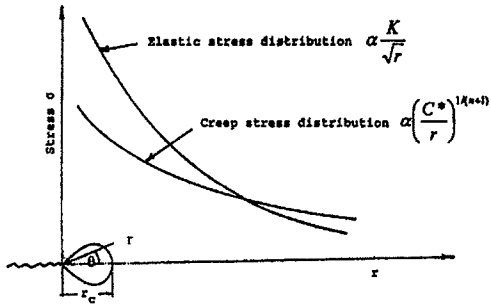


FIG. 5—*Creep process zone at a crack tip subjected to elastic and creep stress distributions.*

In this expression, I_n is a factor which is sensitive to n and state of stress (and has been tabulated by Riedel [23]) and the term $\tilde{\sigma}_{ij}(\theta, n)$ is a nondimensional function of n and θ, which is chosen in such a way that its maximum equivalent stress value is unity. Also it can be assumed that the additional terms in Eq (7), which take account of the influence of constraint and higher powers of r, can be ignored close to the crack tip where the first term dominates.

In these circumstances, by substituting Eq (3) into Eq (7) and taking the maximum equivalent value of $\tilde{\sigma}_{ij}(\theta, n)$ as unity to produce the highest strain rate, the equivalent creep strain rate $\bar{\dot{\varepsilon}}$ at distance r ahead of the crack tip becomes

$$\bar{\dot{\varepsilon}} = C\left[\frac{C^*}{I_n C r}\right]^{n/(n+1)} \tag{8}$$

By postulating that material will first experience creep damage when it enters the creep process zone, as shown in Fig. 5, at $r=r_c$ as crack advance takes place and that failure occurs when its available creep ductility ε_f^* is exhausted at the crack tip (where $r=0$), integration of Eq (8) gives [24–26]

$$\phi = \frac{n}{n+1} \tag{9a}$$

and

$$D_o = \frac{(n+1)}{\varepsilon_f^*}\left[\frac{C r_c}{I_n^n}\right]^{1/(n+1)} \tag{9b}$$

in Eq (5). It is evident from these equations, for typical values of n, that ϕ is a fraction close to unity and that cracking rate is inversely proportional to ε_f^* and relatively insensitive to C and the size of the creep process zone r_c.Since observations indicate that damage is usually confined to a few grains ahead of a crack tip, it is expected that r_c will be related to the grain size of a material. Typically it is found that r_c can be taken to be about 50 μm [24–26].

In Eq (9b), ε_f^* is the material creep ductility appropriate to the state of stress at the crack tip. Tests on circumferentially notched bars, of different notch root radius [27] to produced different states of triaxial tension (constraint) in the notch throat, suggest that ε_f^* decreases with increase in constraint. Estimates of its value can be obtained from this type of experiment [28] or from models [29–32] of the influence of maximum principal stress and hydrostatic stress on void nucleation and growth. These allow the ratio $\varepsilon_f^*/\varepsilon_f$ to be calculated for various states of stress, where ε_f is the uniaxial creep ductility of a material. Approximate bounds on this ratio for plane stress and plane strain are, respectively, 1 and 1/50. Since mostly $0.7 < \phi < 1$ and D_o is relatively insensitive to C and r_c, it is often satisfactory [24–26] to reduce Eq (5) to

$$\dot{a} = \frac{3C^{*0.85}}{\varepsilon_f^*} \tag{10}$$

with $\dot{a}$ in millimeter/hour, ε_f^* as a fraction of C^* in MJ/m^{2}h for scoping calculations when material crack growth properties are not available. Application of Eqs (9a), (9b) and (10) to experimental data on alloy 800H are shown in Fig. 2. It is apparent that close agreement is achieved with the plane stress predictions for this material which showed a substantial uniaxial creep ductility of 0.3 [18].

The creep law of Eq (3) assumes a constant creep strain rate (corresponding to secondary creep) throughout creep deformation. When primary, secondary, and tertiary creep are observed, it is possible to repeat the modeling of creep crack growth using an expression that describes this behavior. However, since all elements of material ahead of a crack tip must experience all stages of creep prior to fracture, and when only creep rupture data are available, it is possible to estimate an average creep rate $\dot{\varepsilon}_A$, as illustrated in Fig. 6(*a*), from

$$\dot{\varepsilon}_A = \varepsilon_f / t_r = C_A \sigma^n \tag{11}$$

where t_r is the creep rupture life at stress σ which can often be written in the form [Fig. 6(*b*)]

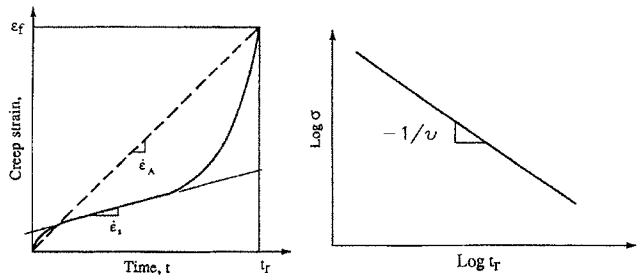


FIG. 6—*(a) Simplification of primary, secondary, and tertiary creep to an average creep strain rate* $\dot{\varepsilon}_A$ *and (b) typical stress rupture diagram.*

$$t_r = \frac{B_r}{\sigma^{\upsilon}} \tag{12}$$

In these two equations, C_A, B_r, and υ are material constants. When $n=\upsilon$, creep ductility is constant and D_o in Eq (9b) can be obtained by simply replacing C by C_A. However, insertion of C or C_A in Eq 9b will only have a small effect on D_o since in each case they are raised to a small fractional power and little effect on crack growth rate will be predicted. The main influence on cracking rate at a given value of C^* is ε_f^*.

When $n \neq \upsilon$, ε_f becomes dependent on stress and a constant creep ductility is not obtained. Often, for materials, ductility decreases with decrease in stress, giving $n > \upsilon$ and a slightly revised analysis of creep crack growth is required [11,12]. In this case, failure is predicted when each element ahead of a crack tip in Fig. 5 exhausts its available life fraction as it approaches the crack tip at $r=0$ as crack advance takes place, so that

$$\phi = \frac{\upsilon}{n+1} \tag{13a}$$

and

$$D_o = \left(\frac{n+1}{n+1-\upsilon}\right)\frac{t_r}{t_r^*}\left(\frac{1}{I_n C_A r_c}\right)^{\upsilon/(n+1)}\frac{r_c}{B_r} \tag{13b}$$

where t_r^* is the rupture life corresponding to a creep ductility of ε_f^*. For a creep rate law of the form of Eq (11), $t_r^*/t_r = \varepsilon_f^*/\varepsilon_f$ so that the ratio can be calculated from the same models [29–32] that are used for predicting the influence of state of stress on creep ductility.

Because of the influence of constraint on crack growth, ASTM E 1457 [16] recommends the use of side grooves along the crack plane in specimens to promote flat straight-fronted cracks. It is also recommended that sizes of specimens are tested that are consistent with the dimensions of components to be examined to produce the same level of constraint in each. Results on a range of sizes of specimens for a low alloy steel are shown in Fig. 7 [33]. These demonstrate that cracking in small specimens corresponds with the plane stress predictions of Eqs (9a), (9b) and (10) and that crack growth rate increases with increase in width W and thickness B in CT specimens of thickness B_n between side grooves. However, even for the largest specimens, the cracking rate does not approach the plane strain bound predictions of these equations. This can be explained as follows. It was assumed in making the predictions that the equivalent stress value of $\tilde{\sigma}_{ij}(\theta, n)$ was equal to its maximum value of one in Eq (7). This corresponds, for plane stress, with cracking progressing along the original crack plane $\theta=0$ but not for plane strain [23]. If this restriction on $\tilde{\sigma}_{ij}(\theta, n)$ is relaxed for cracking along $\theta=0$ for plane strain conditions, it can be shown [34,35] that the plane-strain crack growth rate predictions of Eqs (9b) (10) can be reduced by a factor of approximately 5 so that it becomes about ten times its plane stress estimate in approximate agreement with the experimental results for the largest specimens.

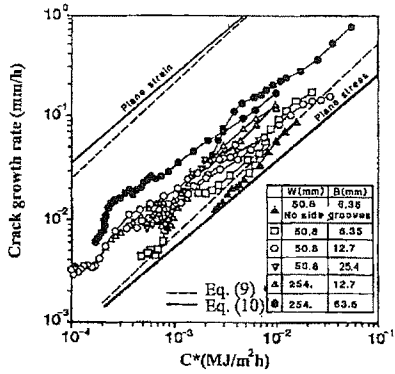


FIG. 7—*Increase in creep crack growth rate with increase in CT specimen size for $B_n/B=0.75$ for 1 % CrMoV steel at 538°C [33].*

Determination of C^* in Components

When making measurements of the creep crack growth properties of materials according to the ASTM E 1457 [16] procedure, C^* is determined from experimentally measured load line displacement rate. For components, C^* must be calculated from the applied loading conditions, crack geometry and component dimensions using uniaxial creep data. Solutions exist only in a few restricted circumstances [11,36]. However, it is always possible to write C^* in terms of some nominal stress σ, its corresponding creep strain rate $\dot{\varepsilon}$ and crack size a as

$$C^* = h\sigma\dot{\varepsilon}a \tag{14}$$

where h is a nondimensional function of crack size, component dimensions, state of stress, and n. Also, as $\dot{\varepsilon}$ is instantaneous creep strain rate, Eq (14) can be employed to incorporate primary, secondary, and tertiary creep when calculating C^*. When secondary creep prevails, substitution of Eq (3) into Eq (14) gives

$$C^* = hC\sigma^{n+1}a \tag{15}$$

Equation (14) is exactly the same form as the expression used in plasticity for J [37] except that plastic strain ε_p is replaced by creep strain rate. For power-law hardening materials which deform plastically in uniaxial tension according to

$$\varepsilon_p = H\sigma^{n_p} \tag{16}$$

where n_p and H are material constants

$$J = hH\sigma^{n_p+1}a \tag{17}$$

For the same loading conditions, crack geometry, component dimensions and when $n_p=n$, the same stress distribution is obtained ahead of a crack in a creeping material as in a work-hardening material and h will be the same in both cases so that C^* can be determined from Eqs (15) and (17) as

$$C^* = \left(\frac{C}{H}\right)J \tag{18}$$

Equation (18) enables estimates of C^* to be obtained when solutions for J only are available [37,38] provided J has been evaluated for $n_p=n$.

An alternative procedure for estimating C^* is to use limit analysis methods [3,7,9,11]. With this approach a reference stress σ_{ref} is defined across the uncracked ligament of a component in terms of applied load P as

$$\sigma_{ref} = \frac{P}{P_{LC}}\sigma_Y \tag{19}$$

where P_{LC} is the collapse load of the uncracked ligament for a material of yield stress σ_Y. Solutions for σ_{ref} for a number of applications are included in [3,7,9,11] and [39]. It has been found [40], when the nominal stress in Eqs (14), (15) and (17) is chosen as the reference stress, that h in these equations becomes relatively insensitive to n or n_p. This means that it can be evaluated from G, for which $n_p=1$ to give,

$$C^* = \sigma_{ref}\dot{\varepsilon}_{ref}\left(\frac{K}{\sigma_{ref}}\right)^2 \tag{20}$$

when G is expressed in terms of K. This equation provides estimates of C^* from solutions of K and σ_{ref} that are available in the codes of practice [1–9] and handbooks [20–22,39]. The reliability of the equation depends upon the accuracy with which K and σ_{ref} can be evaluated. When suitable solutions cannot be found C^* must be calculated by finite element methods.

Component Life Assessment

In order to determine the extent of creep crack growth in a component, it is necessary to apply Eq (5), (where, preferably, D_o and ϕ have been obtained experimentally from tests carried out according to ASTM E 1457 specifications), in conjunction with an expression for C^* such as Eq (20). When experimental values of D_o and ϕ are not available, Eqs (9a), (9b) and (10) or (13a) (13b) can be applied as appropriate. For a material that creeps according to Eq 3 and which exhibits a constant creep ductility, substitution of Eq (20) into Eqs (9a and 9b and) gives

$$\dot{a} = \frac{(n+1)}{\varepsilon_f^*}\dot{\varepsilon}_{ref}\left[\frac{K^2}{I_n\sigma_{ref}^2}\right]^{n/(n+1)} r_c^{1/(n+1)} \tag{21}$$

This equation illustrates that creep crack growth rate is proportional to the creep strain rate at the reference stress of the uncracked ligament. It is important therefore that accurate estimates of σ_{ref} are employed. For typical values of n, an error of 10 % in σ_{ref} could easily result in an error in cracking rate of a factor of about 2. Again for a constant creep ductility situation, if $\dot{\varepsilon}_{ref}$ is determined from rupture data, Eq (21) becomes

$$\dot{a} = \frac{(n+1)}{t_{r\,ref}}\frac{\varepsilon_f}{\varepsilon_f^*}\left[\frac{K^2}{I_n\sigma_{ref}^2}\right]^{n/(n+1)} r_c^{1/(n+1)} \tag{22}$$

where $t_{r\,ref}$ is the uniaxial creep rupture life at σ_{ref}. When creep ductility is not constant $n \neq v$ and Eqs (13a) and (13b) are used so that Eq (22) becomes

$$\dot{a} = \left(\frac{n+1}{n+1-v}\right)\frac{1}{t_{r\,ref}}\frac{\varepsilon_f}{\varepsilon_f^*}\left[\frac{K^2}{I_n\sigma_{ref}^2}\right]^{v/(n+1)} r_c^{(n+1-v)/(n+1)} \tag{23}$$

Equations (21) to (23) are appropriate for estimating creep crack growth rates in components from uniaxial creep data when experimental creep crack growth properties are not available.

Remaining Life Assessment

High temperature defect assessment procedures can be applied at the initial design stage to estimate the significance of postulated defects that could be missed during inspections and also to determine the acceptability of cracks that are detected during service. In the former case, it is relevant to employ virgin material properties. In the latter instance, it may be necessary to allow for material degradation during use. The ideal is to make an assessment based on degraded material properties data. When this information is not known an estimate can be made by making reference to Fig. 8 which shows a crack and its creep process zone growing into damaged material in the ligament ahead of the crack.

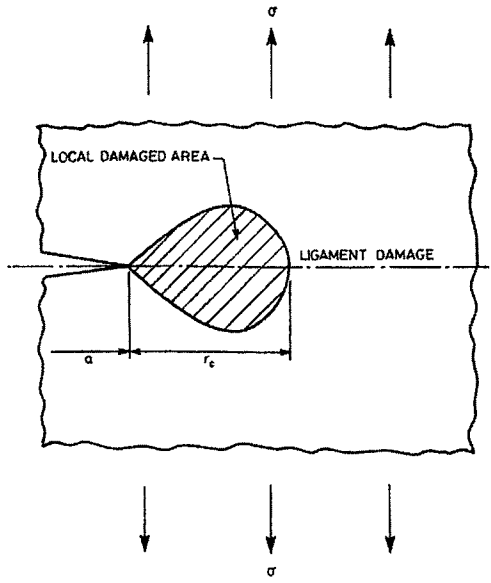


FIG. 8—*Regions of local and ligament damage ahead of a crack tip.*

The influence of ligament damage is to cause less ductility to be available to be exhausted in the creep process zone. The amount of damage accumulated in the ligament can be determined from the strain fraction or life fraction rules. When the life fraction rule, for example, is employed, the fraction of damage ω suffered in the ligament up to the present time t can be obtained from

$$\omega = \int_o^t \frac{dt}{t_{r\ \mathrm{ref}}} \tag{24}$$

where $t_{r\ \mathrm{ref}}$ is the rupture life at the reference stress of the uncracked ligament as previously. The remaining fraction of damage to be used up in the creep process zone at the crack tip is then only $(1-\omega)$). To allow for this deterioration Eq (5) must be modified to

$$\dot{a} = \frac{D_o}{(1-\omega)} C^{*\phi} \tag{25}$$

where D_o and ϕ can be obtained from any of the methods described previously.

Transient Crack Growth Analysis

The analysis undertaken so far has assumed that widespread creep conditions and a steady state distribution of damage have been developed at a crack tip. Under these circumstances a gradient of damage exists in the process zone. Elements of material closest to the tip, as illustrated in Fig. 9 [41], will have experienced most damage and will have almost exhausted their available ductility whereas those further away will have accumulated less damage. However, this situation does not exist immediately after loading as no damage will have had time to accumulate anywhere at the crack tip. The influence of buildup of damage in the process zone at the crack tip on the early stages of cracking is shown in Fig. 10 [42], where the arrows indicate the beginning of each test. It is apparent that each test exhibits a "tail" and it is not until crack growth is well established that steady-state conditions, as described by Eqs (5), (9a), (9b), (10) and (13a) (13b) are reached and all the data superimpose onto one line. The initial crack growth rate $\dot{a}_1$ on loading can be calculated from the time dt for element 1 in Fig. 9 distance dr from the crack tip to fail. For a material of variable creep ductility, using Eqs (7), (11), and (12)

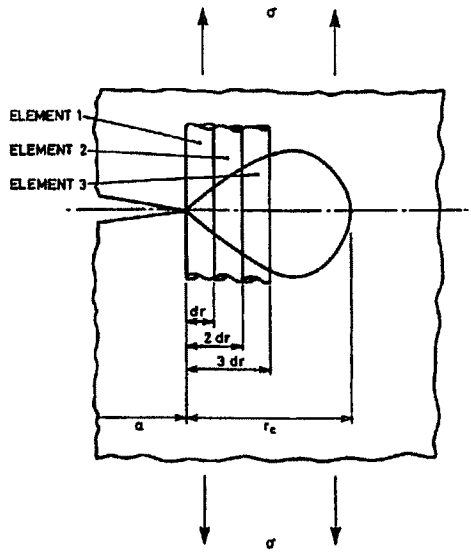


FIG. 9—*Elements in creep process zone in which damage builds up initially until a steady state is reached [41].*

$$\dot{a}_1 = \frac{dr}{dt} = \left(\frac{n+1-v}{n+1}\right)\left(\frac{dr}{r_c}\right)^{(n+1-v)/(n+1)} \dot{a} \tag{26}$$

where $\dot{a}$ is the steady-state crack propagation rate derived from Eqs (13a) and (13b). The element size dr can be chosen to be a suitable fraction of r_c but since $n \gg 1$ and $n \approx v$, dr/r_C will be raised to a small fractional power so that Eq (26) can be reduced to

$$\dot{a}_1 \approx \left(\frac{1}{n+1}\right)\dot{a} \tag{27}$$

Therefore, for most materials the initial crack growth rate will be expected to be approximately an order of magnitude less than predicted from a steady-state analysis. This is consistent with the experimental observations shown in Fig. 10 for a low alloy steel.

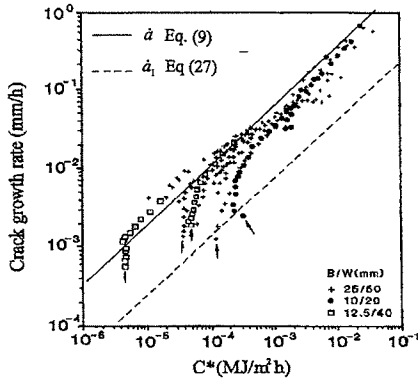


FIG. 10—*Creep crack growth in several sizes of CT specimen of 1 %CrMoV steel at 550°C showing "tails" [42].*

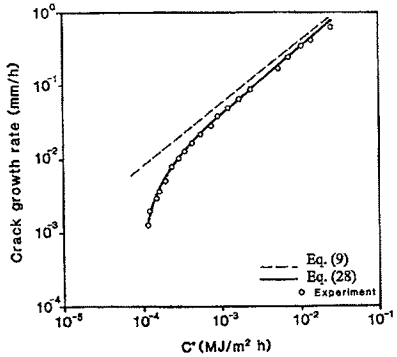


FIG. 11—*Prediction, using Eq (28), of transient crack growth in "tail" region of a test taken from Fig. 10.*

With each crack advance dr, each successive element in Fig. 9 will progressively accumulate more damage prior to fracture, and will have used up a larger fraction of its life prior to the crack reaching it, so that crack growth rate will increase. By considering element j ahead of the crack tip, the crack growth rate $\dot{a}_j$ in this element becomes (assuming that crack advance is so small that C^* can be taken as constant)

$$\dot{a}_j = \left(\frac{1}{1-\omega_j}\right)\dot{a}_1 \tag{28}$$

where ω_j is the fraction of creep damage incurred in element j prior to the crack reaching it. Numerical integration of Eq (28) enables the progression of crack growth prior to steady state to be determined as illustrated in Fig. 11 [11,12].

Prediction of Incubation Period

Materials accumulate damage at different rates depending on their creep properties. With ductile materials the build up of damage at a crack tip may be sufficiently slow, as indicated in Fig. 12 [43], that an incubation period, prior to the onset of cracking being detected, may be observed. The duration of this incubation period t_i will depend on the resolution of the equipment being employed to detect cracking. For fracture assessments of the onset of tearing, an engineering definition of the initiation of tearing is often

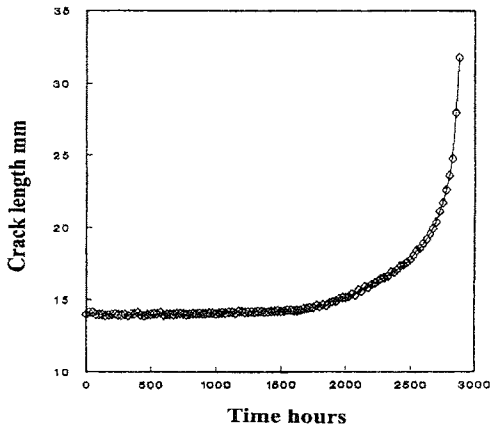


FIG. 12—*Example of an incubation period prior to the onset of creep crack growth in a SENT specimen of 2 1/4 % CrMo steel weld metal at 565°C [43].*

taken as 0.2 mm of crack extension [44]. This is also the crack advance employed in ASTM E 1457 for the onset of steady-state crack growth. If this criterion is adopted for the calculation of incubation periods, an upper bound on this time can be calculated from Eq (27) as

$$t_i < \frac{0.2}{\dot{a}_1} \tag{29}$$

for $\dot{a}_1$ in mm/h. This time can be reduced by about a half by numerical integration of Eq (28) if ϕ is taken to be typically 0.85 and the 0.2 mm of crack extension is split up into four increments of 50 μm. Because of Eq (27), this corresponds with an incubation time of approximately four to five times that predicted from Eq (5), assuming steady-state conditions for a crack advance of 0.2 mm. A lower bound on the incubation period is obtained by assuming steady-state conditions throughout so that for detection limit of 0.2 mm of crack extension

$$t_i > \frac{0.2}{\dot{a}} \tag{30}$$

Alternative procedures are included in R5 [7] for estimating incubation periods that are consistent with this approach when measurements of the crack opening displacement δ_t or the creep fracture toughness K^c_{mat} have been measured for a specified amount of crack extension, such as 0.2 mm. Thus calculation of creep crack growth in a component can be made by use of the steady-state creep crack growth law, Eq (5), in conjunction with numerical integration of Eq (28), to describe the "tail" of 0.2 mm of crack extension, or by estimation of an incubation period prior to the prediction of steady-state growth. It will always be conservative to ignore the initial transient phase of cracking and use the steady-state crack growth law throughout. In addition there is evidence [45] to suggest, in the presence of superimposed cyclic loading that the "tail" can be eliminated and BS 7910 [9] does not allow inclusion of an incubation period for this circumstance. However, for static loading alone, this transient phase (or incubation period) can exist over a considerable portion of life, as illustrated in Fig. 12. From the analysis presented here, this period for 0.2 mm of cracking can be estimated to be about four times the time taken to obtain 0.2 mm of crack growth assuming steady-state conditions.

Sensitivity Studies

Scatter exists in materials creep properties data. The sensitivity of crack growth predictions to this scatter can be estimated by drawing bounds to the data or by applying probabilistic methods [46] to determine probabilities of failure. When sufficient crack growth data are available this approach can be applied directly to Eq (5). When only uniaxial creep data are available, Eq (9a), (9b) or (13a) (13b) must be employed and it is evident from Eqs (21) to (23) that the scatter in creep crack growth data is expected to be the same as that measured in creep strain rate and rupture data. Final failure is taken to occur when either creep rupture of the uncracked ligament, based on the reference stress method, is reached or when fast fracture intervenes, whichever takes place first.

Role of Residual Stress

No allowance has been included so far in any of the analyses for the possible presence of residual stress in a component. Residual stresses can be introduced into components during fabrication by such processes as forging, bending, and welding. They can also be introduced during operation by the imposed loading conditions and steep thermal gradients. A characteristic of a residual stress distribution is that it must satisfy force and moment equilibrium. It will not, therefore, affect collapse and the value of σ_{ref}. However, a tensile residual stress distribution at a crack tip will tend to enhance early crack growth and a compressive stress distribution retard it, as illustrated in Fig. 13 [47], for tests carried out on precracked C-shaped specimens. Precompression results in tensile residual stress at the crack tip and pretension in compression. It is conservative to ignore the influence of compressive residual stress in the vicinity of a crack. However, a tensile residual stress, when combined with an applied tensile stress, will increase the stress local to a

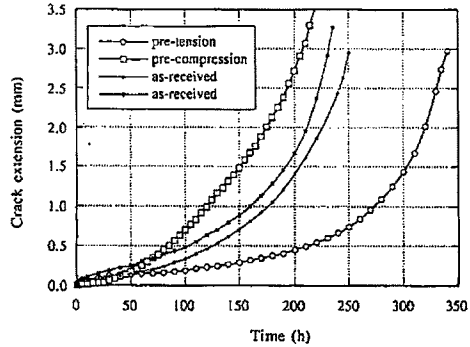


FIG. 13—*Influence of pretension and precompression on creep crack growth in a 1 % CrMoV steel at 550°C for the same applied loading [47].*

crack tip and add to the stress redistribution needed to reach widespread creep conditions through the use of Eq (4). As a consequence it is likely to affect the initial transient phase of cracking and the duration of an incubation period.

An approximate procedure for allowing for the influence of residual stress is to calculate a combined stress intensity factor K due to the applied loading K_{app} and that due to the residual stress distribution K_{res} such that

$$K = K_{app} + K_{res} \tag{31}$$

This enables a conservative estimate of the transition time to achieve widespread creep conditions at a crack tip to be determined from Eq (4) as

$$t_\tau = \frac{(K_{app} + K_{res})^2}{E'(n+1)C^*} \tag{32}$$

where C^* in this expression is its value once widespread creep conditions have been reached at the crack tip. It will be equal to the value from the applied loading only due to relaxation of the residual stress field. It can be obtained by substituting $K=K_{app}$ in Eq (20). Therefore from Eq (32), the presence of tensile residual stress at a crack tip will increase the duration of t_τ. For $t<t_\tau$ the stress local to a crack tip will be higher than predicted from using the steady-state value of C^* in Eq (7). This can be compensated for by calculating C^* for this period, when determining crack growth rates and incubation periods, from

$$C^* = \sigma_{ref}\dot{\varepsilon}_{ref}\left(\frac{K_{app} + K_{res}}{\sigma_{ref}}\right)^2 \tag{33}$$

It is expected that application of this formula will be conservative as K_{res} will relax by creep towards zero as t approaches t_τ.

A key feature of using this method is to have accurate estimates of residual stress distributions available so that reliable determinations of K_{res} can be obtained. Several procedures are available for measuring residual stress distributions in components [48–50]. Examples of measurements that have been made by neutron diffraction through a plate of thickness w at the toe of a T-butt weld in a low carbon ferritic steel are shown in Fig. 14 [51]. Lines representing an average through the data and an upper bound are included. The upper bound corresponds to the addition of a mean stress of $0.25\sigma_Y$ to the data. When a residual stress distribution is known, it can be incorporated into a failure assessment procedure. However, in most cases it is not known and normally codes of practice or standards [7–9] recommend the use of generic distributions, such as are shown in Fig. 15 [52] which can be considerably conservative and result in excessively pessimistic defect assessment predictions because of the over-estimate of the stress intensity factor K_{res} due to the residual stress field, as illustrated in Fig. 16 [52] for the case of the T-butt weld. It is important therefore that realistic estimates of residual stress fields are employed to obtain reliable predictions of their influence in structural integrity assessments.

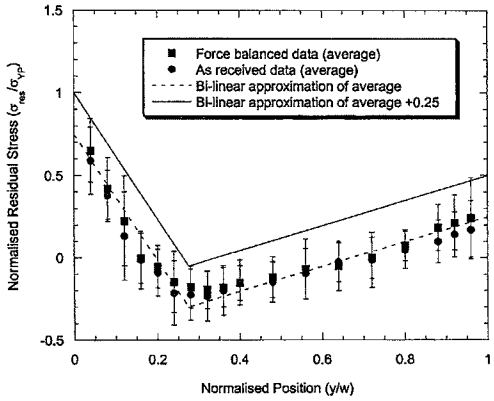


FIG. 14—*Bilinear approximations of average and upper bound transverse residual stress at distance y from the toe of a T-plate fillet weld [51].*

Conclusions

Procedures in codes of practice and standards for making predictions of crack growth under creep and/or fatigue loading conditions in components that operate at elevated temperatures have been reviewed. Emphasis has been placed on the creep component of cracking. The background to the procedures has been described. They all employ the creep fracture mechanics parameter C^* to make predictions. The ideal is to have available experimental creep crack growth properties for a material. When this information has not been collected, it is shown how it can be determined from uniaxial creep strain rate and rupture data for different states of stress using models of the influence of state of stress on creep ductility for the situation when widespread creep conditions and a steady-state distribution of damage has developed at a crack tip.

Methods of calculating C^* in conjunction with uniaxial creep data for components have been discussed. It is demonstrated how this term can be evaluated from the plastic fracture mechanics parameter J or, approximately, from stress intensity factor K and limit analysis using reference stress σ_{ref} concepts.

Methods for making component life assessments using the procedures described have been presented. It is shown that accurate estimates of σ_{ref} are needed for reliable predictions of creep crack growth rate to be obtained. A method is included for a crack propagating into predamaged material in making remaining life assessments for components in which cracks have been detected during an inspection. It is indicated

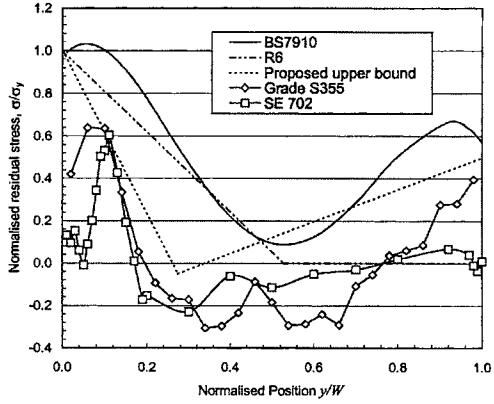


FIG. 15—*Comparison of measured transverse residual stress distributions at distance y from the toe of a T-plate fillet weld with code recommendations [52].*

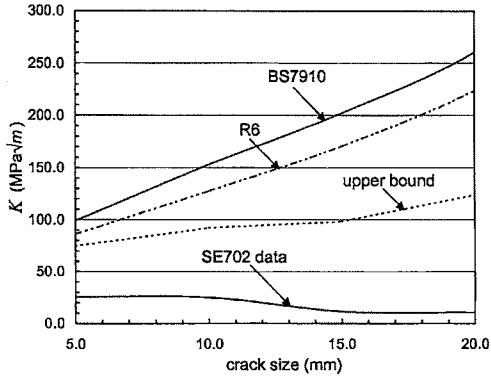


FIG. 16—*Estimated residual stress intensity factors for postulated residual stress distributions shown in Fig. 15 [52].*

that scatter in crack growth properties is expected to be the same as that in uniaxial creep data so that bounds on uniaxial data can be employed to provide bounds on creep crack growth predictions.

Procedures for dealing with an initial transient phase, or incubation period, during which damage builds up at a crack tip have been considered. The role of residual stress on this period and subsequent crack growth has also been examined. There is scope for further work to develop methods for dealing with residual stresses with less conservatism.

References

[1] *API RP 579*, "Standardized Fitness-for-Service Assessment Techniques for Pressurized Equipment Used in the Petroleum Industry," API, Washington, 2004.

[2] *ASME Boiler and Pressure Vessel Code*, Section XI, Division 1, "Rules for Inservice Inspection of Power Plant Components," ASME, New York, 2001.

[3] AFCEN "Design and Construction Rules for Mechanical Components of FBR Nuclear Islands," *RCC-MR, Appendix 16*, "Guide for Defect Assessment and Leak Before Break Analyses," AFCEN, Paris, 2002.

[4] SINTAP, "Structural Integrity Assessment Procedures for European Industry," Brite Euram Project no. BE 95-1426, Contract no BRPR-CT95-0024, Final Report, Nov. 1999.

[5] Kocak M., "Fitness for Service Analysis of Structures Using the FITNET Procedure; An Overview," *24th Int. Conf. on Offshore Mechanics and Artic Eng.*, Sponsored by ASME, paper no. OMAE 2005–67564, Halkidiki, Greece, June 12–17, 2005.

[6] *WES 2805-1997*, "Methods of Assessment for Defects in Fusion Welded Joints with Respect to Brittle Fracture and Failure Due to Fatigue Crack Growth," *Japan Welding Eng. Soc.*, Tokyo, 1997.

[7] *R5*, "Assessment Procedure for the High Temperature Response of Structures Containing Defects," Issue 2, British Energy Generation Ltd Barnwood, 1999.

[8] *R6*, "Assessment of the Integrity of Structures Containing Defects," *Revision 3*, British Energy Generation Ltd Barnwood, 2000.

[9] *BS 7910: 1999*, "Guide on Methods for Assessing the Acceptability of Flaws in Fusion Welded Structures"BSI, London, 1999.

[10] Saxena, A., "Analysis of Cracks Under Creep Conditions," in *Comprehensive Structural Integrity*," edited by I. Milne, R. O. Ritchie, and B. Karihaloo, 5, Elsevier, New York, 2003, pp. 201–240.

[11] Webster, G. A. and Ainsworth R. A., *High Temperature Components Life Assessment*, Chapman and Hall, London, 1994.

[12] Webster, G. A., "Creep Crack Growth" in *Comprehensive Structural Integrity*, edited by I. Milne, R. O. Ritchie, and B. Karihaloo), 5, Elsevier, New York, 2003, pp. 241–272.

[13] Rice, J. R., "A Path Independent Integral and the Approximate Analysis of Strain Concentrations by

Notches and Cracks," *J. Appl. Mech.*, 35, 379–386 (1968).
[14] Riedel, R. and Rice, J. R., "Tensile Cracks in Creeping Solids," in *Fracture Mechanics 12th Conf.*, ASTM STP 700, 1980, 112–130.
[15] Bassani, J. L., Hawk, D. E., and Saxena, A., "Evaluations of the C_t Parameter for Characterizing Creep Crack Growth Rates in the Transient Regime" in *Non-linear Fracture Mechanics*, ASTM STP 995, ASTM International, West Conshohocken, PA, 1987, 7–26.
[16] *ASTM Standard E 1457-00* "Standard Test Method for Measurement of Creep Crack Growth Rates in Metals," ASTM, 2001, West Conshohocken, PA **03-01**, 936–950.
[17] *ASTM Standard E 647-99*, "Standard Test Method for Measurement of Fatigue Crack Growth Rates," ASTM, West Conshohocken, PA, 2000, **03-01**, 591–630.
[18] Hollstein, T., Webster, G. A., and Djavanroodi, F., "Creep Crack Growth in a 1% CrMoV steel and a 32% Ni 20% Cr Alloy" in *EGF 8 Fracture Behaviour and Design of Materials and Structures*, edited by D. Firrao, EMAS Ltd., Halesowen, 1990, III, 1249–1256.
[19] Winstone, M. R., Nikbin, K. M., and Webster, G. A., "Modes of Failure Under Creep/Fatigue Loading of a Nickel-Based Superalloy," *J. Mater. Sci.*, 20, 2471–2476 (1985).
[20] Rooke, D. P. and Cartwright, D. J., *Compendium of Stress Intensity Factors*, HMSO, London, 1976.
[21] Murakami, Y., *Stress Intensity Factor Handbook*, Vols. 1 and 2, Pergamon, Oxford, 1987.
[22] Tada, H., Paris, P. C. and Irwin, G. R., *The Stress Analysis of Cracks Handbook*, 3rd Ed., ASME Press, New York, 2000.
[23] Riedel, H., *Fracture at High Temperatures*, Springer-Verlag, Berlin, 1987.
[24] Nikbin, K. M., Smith, D. J., and Webster, G. A., "Influence of Creep Ductility and State of Stress on Creep Crack Growth," in *Advances in Life Prediction Methods* edited by D. A. Woodford and J. R. Whitehead, ASME, New York, 1983, 249–258.
[25] Nikbin, K. M., Smith, D. J., and Webster, G. A., "Prediction of Creep Crack Growth from Uni-axial Creep Data," *Proc. R. Soc. London, Ser. A* 396, 183–197 (1984).
[26] Nikbin, K. M., Smith, D. J., and Webster, G. A., "An Engineering Approach to the Prediction of Creep Crack Growth," *J. Eng. Mater. Technol.* 108, 1986, 186–191.
[27] Al-Abed, B., Timmins, R., Webster, G. A., and Loveday, M. S., "Validation of a Code of Practice for Notched Bar Creep Rupture Testing: Procedures and Interpretation of Data for Design," *Mater. High. Temp.*, 16, (3), 143–158 (1999).
[28] Webster, G. A., Holdsworth, S. R., Loveday, M. S., Perrin, I. J., Nikbin, K., Purper, H., Skelton, R. P. and Spindler, M. W., "A Code of Practice for Conducting Notched Bar Creep Rupture Tests and for Interpreting the Data," *Fatigue Fract. Eng. Mater. Struct.*, 24, 319–342 (2004).
[29] Rice, J. R. and Tracey, D. M. "On the Ductile Enlargement of Voids in Triaxial Stress Fields,' ' *J. Mech. Phys. Solids*, 17, 201–217 (1969).
[30] Cocks, A. C. F and Ashby, M. F. "Intergranular Fracture During Power-Law Creep Under Multi-axial Stress," *Mater. Sci.*, 14, 395–402 (1980).
[31] Budiansky, B., Hutchinson, J. W. and Slutsly, S., "Void Growth and Collapse in Viscous Solids" in *Mechanics of Solids*, edited by H. G. Hokins and M. J. Sewell Pergamon Press, Oxford, 1982.
[32] Spindler, M. W., Hales, R., and Skelton, R. P., "The Multi-axial Creep Ductility of an Ex-Service Type 316H Stainless Steel," *9th Int. Conf. On Creep and Fracture of Eng. Mater. and Struct.*, April 2001, Swansea, publish. Inst. Materials, London, 2001, pp. 679–688.
[33] Tabuchi, M., Yagi, K., Kubo, K., and Tanaka, C., "Effect of Geometrical Constraint on Creep Crack Growth Behaviour of 1 Cr MoV Turbine Rotor Steel" in *Creep and Fracture of Engineering Materials and Structures*, edited by B. Wilshire and R. W. Evans, Inst. Metals, London, 1990, 729–738.
[34] Bettinson, A. D., O'Dowd, N. P., Nikbin, K. M., and Webster, G. A., "Experimental Investigation of Constraint Effects on Creep Crack Growth," *ASME Pressure Vessels and Piping Conference*, August 2002, Vancouver, Canada, ASME, West Conshohocken, PA 2002.
[35] Yatomi, M., Nikbin, K. M., O'Dowd, N. P., and Webster, G. A., "Theoretical and Numerical Modeling of Creep Crack Growth in a Carbon-Manganese Steel," submitted for publication.
[36] He, M. Y. and Hutchinson J. W., "Bounds on Fully Plastic Crack Problems for Infinite Bodies in Elastic-Plastic Fracture," ASTM STP 803, edited by C. F. Shih and J. P. Gudas, 1983, 1, 277–290
[37] Kumar, V., German, M. D., and Shih, C. F. "An Engineering Approach for Elastic-Plastic Fracture, *EPRI Report*, NP 1931, 1981

[38] Saxena, A., *Non-Linear Fracture Mechanics for Engineers*, CRC Press, Boca Raton, 1998.

[39] Miller A. G., "Review of Limit Loads of Structures Containing Defects," *Int. J. Pressure Vessels Piping*, 32, 197–327 (1988).

[40] Miller, A. G. and Ainsworth, R. A., "Consistency of Numerical Results for Power-Law Hardening Materials and the Accuracy of the Reference Stress Approximation, *J. Eng. Fract. Mech.*, 32, 233–247 (1989).

[41] Nishida, K., and Webster, G. A., "Interaction Between Build-Up of Local and Remote Damage on Creep Crack Growth," *Creep and Fracture of Engineering Materials and Structures*, edited by B. Wilshire and R. W. Evans, Inst. Metals, London, 1990, 703–713.

[42] Webster, G. A., "Methods of Estimating C^*," *Mater. High. Temp.*, 10, 74–78 (1992a).

[43] Holdworth, S. R., private communication, 1994.

[44] *ASTM Standard E 1820-99a* Standard Test Method for J_{IC}, a Measure of Fracture Toughness, ASTM, West Conshohocken, PA, 2000, **03-01**, 1000–1033.

[45] Chorlton, M. R., Nikbin, K. M., and Webster, G. A., "Investigation into the Early Stages of Crack Growth in Two Low Alloy Steels," in *Life Assessment and Life Extension of Engineering Plant, Structures and Components*, edited by J. H. Edwards et al., EMAS, Warley, UK, 1996, 117–124.

[46] Wasmer, K., Nikbin, K. M., and Webster, G. A., "Prediction of Scatter in Creep Crack Growth Data from Uniaxial Creep Properties," *5th Int. ASTM/ESIS Symposium on Fatigue and Fracture Mechanics*, May 2005, Reno (in press)

[47] Chorlton, M., Nikbin, K., and Webster, G. A., "Effects of Cyclic Loading and Residual Stresses on the Early Stages of Creep Crack Growth," *Lifetime Management and Evaluation of Plant, Structures and Components*, edited by J. H. Edwards et al., EMAS Publishing, UK, 1998, 47–57.

[48] Cheng, W. and Finnie, I., "Measurement of Residual Stress Distributions Near the Toe of an Attachment Welded on a Plate Using the Crack Compliance Method," *Eng. Fract. Mech.* 46, 79–91 (1993).

[49] Leggatt, R. H., Smith, D. J., Smith, S. D., and Faure, F., "Development and Experimental Validation of the Deep Hole Drilling Method for Residual Stress Measurement," *J. Strain Anal.* 31 (3), 177–186 (1996).

[50] Webster, G. A., "Development of a Standard for the Measurement of Residual Stress by Neutron Diffraction," *Proceedings ICRS-6*, July, 10–12 2000, Oxford, Institute of Materials, ISBN, I-86125-123-8 Vol. 1, 189–196.

[51] Wimpory, R. C., May, P. S., O'Dowd, N. P., Webster, G. A., Smith, D. J., and Kingston, E., "Measurement of Residual Stresses in T-Plate Weldments," *J. Strain Anal.* 38, 2003, 349–365.

[52] O'Dowd, N. P., Nikbin, K. M., Lee, H. Y., Wimpory, R. C., and Biglari, F. R., "Stress Intensity Factors Due to Residual Stresses in T-Plate Welds," *Trans. ASME* 126, 432–437 (2004).

Creep Assessment

Journal of ASTM International, February 2006, Vol. 3, No. 2
Paper ID JAI13223
Available online at www.astm.org

B. Dogan,[1] *U. Ceyhan,*[1] *K. M. Nikbin,*[2] *B. Petrovski,*[1] *and D. W. Dean*[3]

European Code of Practice for Creep Crack Initiation and Growth Testing of Industrially Relevant Specimens

ABSTRACT: The integrity and residual life assessment of high temperature components require information obtained from the material's mechanical, uniaxial creep, creep crack initiation (CCI), and growth (CCG) properties. The information derived from these material tests needs to be validated and harmonized following a Code of Practice (CoP) so that variability in data as well as in the analysis can be optimized between different institutions. The paper describes a CoP for creep crack growth testing of industrially relevant specimens, which was developed within the framework of the partially European Commission (EC) funded project called "CRETE." Novel aspects of the CoP include advice for testing different specimen geometries, which differ from the standard Compact Tension (C(T)) specimen proposed in the only available CCG testing standard ASTM E 1457. Recommendations for required number of tests, techniques for testing, treatment of test records, reduction of test data, and data analysis are presented. Associated specimen selection guidelines for industrial creep crack initiation and growth testing are also described. Validation tests carried out within the project on Type 316H steel at 550°C and a C–Mn steel at 400°C using relevant specimen geometries are also briefly described. The CoP contains recommended K and C^* solutions, Y functions, and η factors, which are used to determine values of the fracture parameters K and C^* for the specimen geometries considered, and these are summarized in this paper. Information from these new tests, together with a review of previous creep crack growth tests on nonstandard geometries, have been used in recommending the best method of analysis for the creep crack initiation (CCI) and creep crack growth (CCG) data for a range of creep brittle to creep ductile materials.

KEYWORDS: code of practice, fracture mechanics, creep crack initiation, creep crack growth, C^*, specimen geometry, η factor

Nomenclature

a = crack length
a_o, a_f = initial and final crack length measurements
Δa = amount of crack growth
$\dot{a}$, da/dt = crack growth rate
B, B_n, B_e = specimen thickness, net specimen thickness, effective specimen thickness
CCG, CCI = creep crack growth, creep crack initiation
CMOD = crack mouth opening displacement
C_o = compliance at time zero
CoP = code of practice
C(T) = compact tension specimen
CRETE = EC Project CRETE (Ref. [2])
CS(T) = C-shaped specimen in tension
C_t = crack tip parameter for transient to extensive creep
C^* = steady state creep fracture mechanics parameter
$C^*(t)$ = experimentally determined value of C^* at test time, t
DEN(T) = double edge notch tensile specimen
D', D'_i = material constant in $\dot{a}$ correlations with K

Manuscript received June 8, 2005; accepted for publication September 7, 2005; published December 2005. Presented at ASTM Symposium on Fatigue and Fracture Mechanics: 35th Volume on 18–20 May 2005 in Reno, NV; R. E. Link and K. M. Nikbin, Guest Editors.

[1] GKSS Research Center, Max-Planck-Str. 1 D-21502 Geesthacht, Germany.
[2] Imperial College, Exhibition Road, London, SW7 2AZ, UK.
[3] British Energy Generation Ltd., Barnwood, Gloucester, GL4 7RS, UK.

Copyright © 2006 by ASTM International, 100 Barr Harbor Drive, PO Box C700, West Conshohocken, PA 19428-2959.

D_c, D_i = material constant in $\dot{a}$ correlations with C^*
EDM = electric discharge machining
E = elastic modulus
E' = effective elastic modulus for plane strain
HAZ = heat affected zone
H = specimen height
H^{LLD} = geometric function to calculate C^* from load line displacement rate
H^{CMOD} = geometric function to calculate C^* from crack mouth opening displacement rate
J = J-integral crack tip parameter
K, K_n = stress intensity factor, stress intensity factor for net section thickness
K^c_{mat} = creep crack initiation toughness
L = half span length
LLD = load line displacement
LVDT = linear variable displacement transducer
M = bending moment
m' = material constant in $\dot{a}$ correlations with K
M(T) = middle crack tension specimen
N = plastic exponent
n = power-law creep stress exponent
P = applied load
PD = potential drop
R_i = inner radius of CS(T) specimen
R_0 = outer radius of CS(T) specimen
SEN(B) = single edge notch specimen in bending
SEN(T) = single edge notch specimen in tension
t_i = time for crack initiation (at Δa=0.2 and 0.5 mm)
t_T = transition time from primary to steady-state creep
U = area under load-displacement curve
V_i = value of the potential drop (PD) measurement at initiation
V_0, V_f = initial and final values of the potential drop (PD) measurement
W = specimen width or half width
$Y(a/W)$ = geometry factor to calculate K
$\dot{\Delta}_c$ = creep component of load line displacement rate
Δ^{LLD}, $\dot{\Delta}^{LLD}$ = load line displacement, load line displacement rate
$\dot{\Delta}^{LLD}_c$ = component of the load line displacement rate directly associated with the accumulation of creep strains
$\dot{\Delta}^{LLD}_i$ = component of the load line displacement rate directly associated with instantaneous (elastic and plastic) strains
$\dot{\Delta}^{LLD}_{i,e}$ = component of the load line displacement rate directly associated with instantaneous elastic strains
Δ^{CMOD}, $\dot{\Delta}^{CMOD}$ = crack mouth opening displacement, crack mouth opening displacement rate
ε^c_f = creep ductility
$\dot{\varepsilon}^c$ = creep strain rate
η^{CMOD} = geometric factor to calculate C^* from crack mouth opening displacement rate
η^{LLD} = geometric factor to calculate C^* from load line displacement rate
ϕ = material constant in $\dot{a}$ correlations with C^*
λ = nondimensional crack velocity
σ = stress
σ_b = nominal bending stress
σ_m = membrane stress
σ_{ref} = reference stress
ν = Poisson's ratio

Introduction

The industrial need for harmonized procedures for material testing and data analysis covers testing for materials development, design of components for engineering applications, and defect assessment of in-service components for lifing. The available codes for high temperature crack growth testing and characterization of materials are limited in scope and international acceptance. The most widely used standard for creep crack growth testing of metallic materials [1] is mainly addressing compact tension C(T) type specimens. Therefore, the outstanding need for characterization of creep crack growth in alternative industrial specimens has been the subject of a European project CRETE [2], which had the objective of harmonizing testing procedures for these specimens in order to obtain data for use in defect tolerance assessment of components. Recent reviews of high temperature defect assessment procedures [3] and the significance of creep in defect assessment procedures for low to high temperature [4] emphasize the need for reliable creep crack growth data. The British Standard document BS7910 [5] contains some indicative data for creep crack growth assessment, whereas, the R5 [6] procedure does not explicitly supply creep crack growth data, except where specifically used to validate the procedures. The present paper outlines the guidelines of a Code of Practice (CoP) for experimental determination and analysis of creep crack initiation (CCI) and creep crack growth (CCG) rate data. CCI can be defined as the extension of a pre-existing defect by a small amount of growth, typically 0.2 or 0.5 mm. Novel aspects of the CoP include interpretation of potential drop (PD) records, crack size determination and measurement on tested specimen surfaces, crack tip parameter (K, C^*) solutions, $Y(a/W)$ functions, and η factors for six specimen types. Validation tests carried out within the project on Type 316H steel at 550°C and a C–Mn steel at 400°C using relevant specimen geometries are presented.

European CoP for CCI and CCG Testing of Industrial Specimens

Scope and Use

The specific aim of the present CoP document is to provide recommendations and guidance for a harmonized procedure for measuring and analyzing CCI and CCG characteristics of metallic materials using a wide range of industrial fracture mechanics specimen geometries. It will allow laboratories with limited test material to carry out tests on different specimen geometries [7].

Specimens

The novel aspect of the presented CoP is the inclusion of component relevant industrial specimen geometries [7]. It covers testing and analysis of CCI and CCG in metallic materials at elevated temperature using six different cracked geometries (Fig. 1), for which validation tests have been conducted [2].

Specimen abbreviations and loading arrangements are as follows: compact tension C(T); C-shaped tension CS(T); double edge notched tension DEN(T); middle crack tension M(T); single edge notched tension SEN(T) in pin loading and single edge notched bend SEN(B), in three point bending.

Specimen Geometries

The dimensions of the specimen types shown in Fig. 1, which have been used for experimental and numerical validation in the CRETE project [2], are given in Table 1. These sizes were chosen to permit validation tests to be conducted on the Type 316H and C–Mn steels within the machine capacity available to the project. The CoP also permits geometrically similar specimens with different in-plane dimensions to be used and the thickness to width (B/W) ratio can also differ from the values given in Table 1, if required. The initial crack lengths used in the validation tests were with a_o/W ratio within a range of 0.2 to 0.4 for DEN(T), M(T), and SEN(T) specimens and 0.3 to 0.5 for the other specimens.

As shown in Table 1, H is the height of C(T), R_0 is the outer radius of CS(T), and L is the half span of the SEN(B) specimen and the half length (between loading points) of SEN(T), DEN(T), and M(T) specimens.

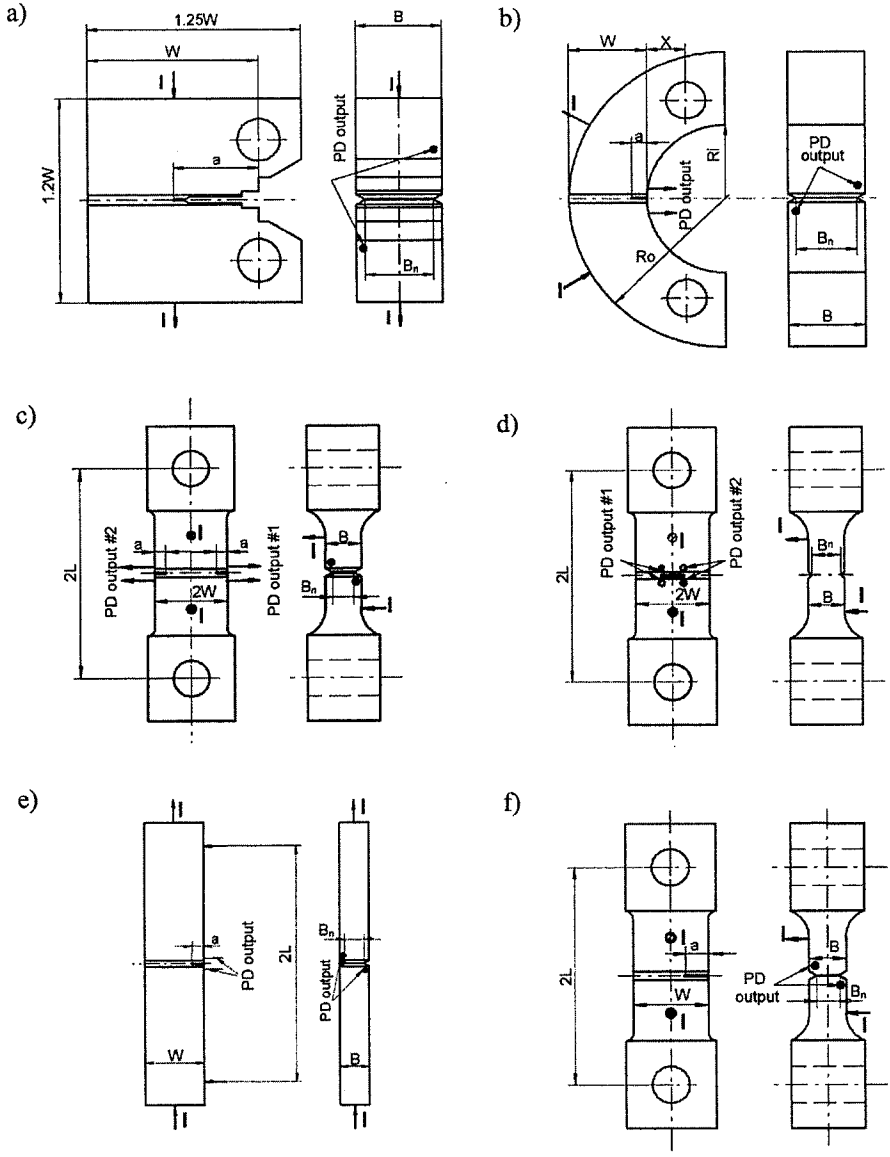


FIG. 1—*Specimen geometries (a) compact tension, C(T); (b) C-shaped tension, CS(T); (c) double edge notched tension, DEN(T); (d) middle cracked tension, M(T); (e) single edge notched bend, SEN(B); and (f) single edge notched tension SEN(T).*

Criteria for Specimen Selection

Attention should be given to the selection of the appropriate specimen geometry for the particular application being considered. This section outlines the main factors, which need to be considered in this process and summarizes the strengths and weaknesses of the standard C(T) specimen and the alternative industrial specimens.

TABLE 1—*CRETE Test specimen geometries.*

Specimen	Geometry	W (mm)	H, L, R_0 (mm)	B (mm)
C(T)	Compact tension	50	H=60	25
CS(T)	C-shape tension	25	R_0=50	25
DEN(T)	Double edge notched tension	12.5	L=37.5	12.5
M(T)	Middle tension	12.5	L=37.5	12.5
SEN(B)	Single edged notched bending	25	L=50	12.5
SEN(T)	Single edge notched tension	25	L=37.5	12.5

Material Availability

Material availability considerations influence the choice of specimen geometry. In many cases, the volume and dimensions of available material will be limited. This issue will be of particular concern when testing material obtained from components in both virgin and service exposed conditions. The shape of the material available can also influence the choice of specimen; for instance the CS(T) specimen is particularly suited to testing material from tubular components and the SEN(T) would be appropriate for blade type components.

Specimen Orientation

Components are not always made up of homogenous materials and may contain microstructural variations and even microvoids. Therefore, the orientation of the crack in the specimen should be chosen to be normal to the defect orientation, which might exist in the component being assessed. In addition the tensile and creep material properties in the direction of the defect orientation chosen should be available as they will be needed for the analysis of the CCI and CCG data. The required specimen orientation, together with the volume and dimensions of available material can significantly influence the choice of specimen geometry.

Machine Capacity

The machine capacity available for performing the creep crack growth tests will have a significant influence on the specimen geometry and dimensions which can be tested for a given material condition. The higher constrained C(T), SEN(B), and CS(T) specimens will require lower test loads for given ligament dimensions B_n, $(W\text{-}a)$ than the DEN(T), M(T), and SEN(T) geometries.

Component Geometry and Loading

Creep crack growth data are required for prediction of creep crack growth in service applications using procedures such as R5 [6]. It is important to be able to demonstrate that the creep crack growth data obtained are as follows:

1. Appropriate to the geometry and loading being considered.
2. Conservative for the geometry and loading being considered.

In the former case, if service loads are exclusively tensile, the DEN(T) or M(T) specimens may be most appropriate. However, if conservative creep crack growth data are required for a range of applications, it is more appropriate to test highly constrained geometries such as the C(T) or SEN(B).

Specimen Thickness

The specimen thickness should normally be chosen to be equal to, or exceed, the section thickness of the component being assessed. Table 1 gives the range of thicknesses that have been validated within CRETE. However this does not exclude the testing of other thicknesses as long as the tests are checked for validity.

Suitability for Initiation/Creep Crack Growth Testing

If it is required to introduce a fatigue precrack as the initial defect (e.g., if creep crack initiation data are required), this may influence the choice of specimen geometry. Planar specimens with single defects [e.g.,

C(T), CS(T), SEN(B), SEN(T)] are to be preferred in this respect as difficulties can arise with other types of specimen. It is difficult to achieve symmetrical initial defect sizes when fatigue precracking is utilized in DEN(T) and M(T) specimens which contain two crack tips. Planar specimens with single defects are also preferable for creep crack growth rate determination as nonsymmetrical creep crack growth is likely to occur from the two starter crack tips in DEN(T) and M(T) specimens.

Strengths and Weaknesses of Each Specimen Geometry

Compact Tension [C(T)]

Strengths—

- Highly constrained (for deep cracks, $a/W > 0.45$); can be used to generate conservative creep crack initiation and growth data for a range of applications.
- Low load capacity requirement (for a given ligament size).
- Compact; maximum/minimum dimension ratio is low (~2.5).
- Simple pin (or threaded) loading.
- Easy to fatigue precrack.
- Suitable for both creep crack initiation and growth testing.
- Best η factors and C^* estimates based on load-line displacements (for deep cracks, $a/W > 0.45$).

Weaknesses

- Cannot be used for shallow cracks (small a/W) as deformation spreads to the loading pins.

C-Shape Tension [CS(T)]

Strengths—

- Highly constrained for deeper cracks; can be used to generate conservative creep crack initiation and growth data for a range of applications.
- Low load capacity requirement (for a given ligament size).
- Relatively compact; maximum/minimum dimension ratio is relatively low (4).
- Particularly suited to testing tubular components.
- Simple pin loading.
- Easy to fatigue precrack.
- Suitable for both creep crack initiation and growth testing.

Weaknesses—

- Large specimen for a given area of defective section.
- Best η factors and C^* estimates require measurements of crack mouth opening rather than load-line displacements.

Single Edge Notch Bend [SEN(B)]

Strengths—

- Highly constrained (for deep cracks, $a/W > 0.5$); can be used to generate conservative creep crack initiation and growth data for a range of applications.
- Low load capacity requirement (for a given ligament size).
- Easy to fatigue precrack.
- Suitable for both creep crack initiation and growth testing.

Weaknesses—

- Maximum/minimum dimension ratio is high (~10).
- Requires a special loading fixture.
- Best η factors and C^* estimates require measurements of crack mouth rather than load-line displacements.

Double Edge Notch Tension [DEN(T)]

Strengths—

- Low constraint (for low values of a/W); can be used to generate creep crack initiation and growth data for low constraint applications involving tensile loading.
- Simple pin (or threaded) loading.

Weaknesses—

- Constraint can become high for very deep cracks.
- Maximum/minimum dimension ratio is high (~8).
- High load capacity requirement (for a given ligament size).
- Fatigue precracking can be problematic (due to asymmetry in the two cracks).
- Best η factors and C^* estimates require measurements of crack mouth rather than load-line displacements.

Single Edge Notch Tension [SEN(T)]

Strengths—

- Low constraint (for low values of a/W); can be used to generate creep crack initiation and growth data for low constraint applications involving tensile loading.
- Simple pin loading.
- Easy to fatigue precrack.
- Suitable for both creep crack initiation and growth testing.

Weaknesses—

- Constraint can vary significantly with a/W.
- Maximum/minimum dimension ratio is high (~8).
- Moderately high load capacity requirement (for a given ligament size).
- Best η factors and C^* estimates require measurements of crack mouth opening rather than load-line displacements.

Middle Cracked Tension [M(T)]

Strengths—

- Low constraint; can be used to generate creep crack initiation and growth data for low constraint applications involving tensile loading.
- Simple pin (or threaded) loading.
- Suitable for both creep crack initiation and growth testing.

Weaknesses—

- Maximum/minimum dimension ratio is high (~8).
- High load capacity requirement (for a given ligament size).
- Fatigue precracking can be problematic (due to asymmetric growth at the two crack tips).
- Best η factors and C^* estimates require measurements of crack mouth opening rather than load-line displacements.

Specimen Preparation

Prior to testing, specimen preparation consists of spot welding of thermocouples and potential drop (PD) wires and introduction of a sharp starter crack and side grooving. For positioning of the wires, advice should be sought from the PD equipment manufacturer. Current input wires should be placed remote from the crack tip and the potential output wires should be placed on the opposite face of the specimen, aligned near the crack tip, as shown on the specimen in Fig. 1. It is preferable to weld the current input leads to the specimen as this ensures good electrical contact, which is maintained throughout the test.

Starter Crack

Fatigue precracking is recommended for most situations although an electrodischarge machined (EDM) slit can also be used as a starter crack providing the crack tip radius is 0.05 mm or less. Both types of

starter crack can be used in CCG tests. However, if CCI information is required, fatigue precracking should be used to introduce the starter crack unless it can be demonstrated that equivalent initiation behavior is obtained using an EDM slit.

Side-Grooving

Side grooving (SG), 20 % in total, 10 % on each side, is generally required to obtain a straight crack front. However, for creep ductile materials, such as the C–Mn steel used in the CRETE validation tests, a total side-groove reduction of up to 40 % may be required to produce a straight crack front.

Tests and Measurement Techniques

Test techniques together with accuracy limits for measuring test variables will provide correct and repeatable test data that help to reduce data scatter. The type of testing and measurement equipment is left to the discretion of the users. The restrictions placed on the users are the limits of accuracies with respect to specimen dimensions, temperature, load, displacement, and crack length measurements. The limits proposed are the same as those used in ASTM E 1457 [1]. The Round Robin [2] work focused on constant load tests to determine CCI and CCG behavior. However, similar techniques can also be used to perform fixed displacement and fixed displacement rate tests. In some cases where the material is very creep brittle stress sensitive, or the industrial operational loading conditions are displacement controlled, it may be advisable to perform constant displacement or constant displacement rate tests. It is recommended, where possible, to compare data from these alternative types of test with that from constant load tests on C(T) specimens.

Test methods cover isotropic polycrystalline metallic materials. If significant material inhomogeneity exists, as in single crystals, directionally solidified materials and weldments [including cross-welds and heat affected zone (HAZ) tests], the testing techniques require further validation [8]. The energy method for deriving the experimental C^* parameter inherently takes into account that such inhomogeneities as the creep displacement rate measured is dependent on the type of material deforming local to the crack tip. However, caution should be exercised with the treatment of the data and its analysis since the correlation parameters have been validated only for homogeneous materials.

Environment

Aggressive environments at high temperatures can significantly affect the CCI and CCG behavior. Attention must, therefore, be given to the proper selection and control of temperature and environment in data generation. All relevant information should be fully logged for each test in order to identify diversions from the norm as specified in the CoP [7]. Tests are mostly carried out in laboratory air at test temperatures. Tests can also be carried out in vacuum or aggressive atmospheres in order to simulate the service conditions of the structural component to be assessed. Note that aggressive environments can enhance damage and hence affects the crack initiation and growth processes. Nevertheless, providing that creep is the dominant damage mechanism, the methods described here can be used although caution should be exercised in using the data to predict creep crack growth behavior for other environmental conditions.

Measurements During Tests

The load, potential drop, and displacement data are required to be logged starting from pre-load which is approximately 10 % of the full load all the way to the end of the test. This information is important for the subsequent analysis of the data using C^* and K. Any instantaneous deviation from the elastic loading condition prior to creep at or near zero time should be noted. In addition the load/displacement measurements give the specimen's elastic compliance for the initial crack length. The initial elastic displacement at full load and the final elastic displacement during the final unloading should be measured and logged. It is also possible to perform partial unloadings during the test of up to 15 % of the test load, as a means monitoring crack size development or if there is concern regarding premature failure of the specimen.

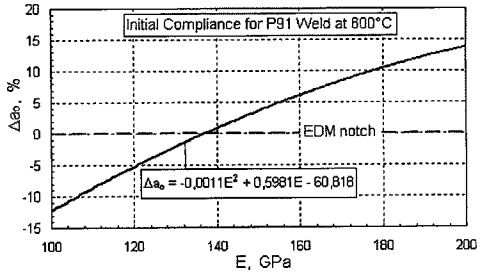


FIG. 2—*Variation of crack length Δa_o for a C(T) specimen determined by partial unloading compliance method with elastic modulus E of the material at test temperature.*

Crack Length Measurements

For crack length measurements, crack size monitoring equipment capable of reliably resolving crack extensions of at least ±0.1 mm at the test temperature is recommended. The selected crack size measurement technique must be capable of measuring the average crack size across the thickness. Since crack extension across the thickness of the specimen is not always uniform, surface crack length measurements by optical means are not considered to provide reliable estimates of the average crack size.

Partial unloading compliance may also be used for crack length estimation during the testing although the most commonly used method for crack length monitoring is the potential drop (PD) technique method using either direct current (DC) or alternating current (AC). The methods used are described in detail below.

Partial-Unloading Compliance

The measurement of compliance from load versus load-line displacement (LLD) data requires loading and unloading ΔP of a specimen at time $t=0$. The expression below is used for time zero compliance

$$C_0 = \Delta^{LLD}/\Delta P \tag{1}$$

The initial crack length is calculated from initial compliance at $t=0$, using formulas relating the crack size to the specimen compliance. For a fatigue precracked C(T) specimen [9]

$$a_o/W = 1.000196 - 4.06319U_{xo} + 11.242U_{xo}^2 - 106.043U_{xo}^3 + 464.335U_{xo}^4 - 650.677U_{xo}^5 \tag{2}$$

where $U_{xo}=1/[(B_eE'C_o)^{1/2}+1]$, effective thickness $B_e=B-[(B-B_n)^2]/B$, and $E'=E/[(1-\nu^2)]$ for plain strain and $E'=E$ for plain stress conditions.

There is a significant influence of elastic modulus E on crack length calculation accuracy and it is therefore important to have a reliable value of E data obtained at the test temperature. For E values ranging between 100 and 200 GPa the difference in predicted Δa for a C(T) specimen is depicted in Fig. 2, which shows that total errors of ±12 % can be introduced.

Potential Drop Method

Direct current potential drop (DCPD) and alternating current potential drop (ACPD) methods are often applied to monitor crack initiation and growth during testing. The crack size is determined from DCPD data using Johnson's formula given for C(T) geometry [1]. Correct use of PD data is particularly important when determining CCI as several possible types of PD-time behavior may be observed as shown schematically in Fig. 3.

The scatter in crack size using PD method is increased by the crack channeling with unbroken ligaments as observed on fracture surfaces. An accurate measurement of the initial (a_o) and final (a_f) crack size should be made when the specimen has been broken open outside the furnace after testing. The final measured crack length may be used to calibrate the crack lengths from potential data using Johnson's formula. Alternatively, linear interpolation between measured initial and final crack sizes determined on the broken open specimen surface may be used for crack length calculations.

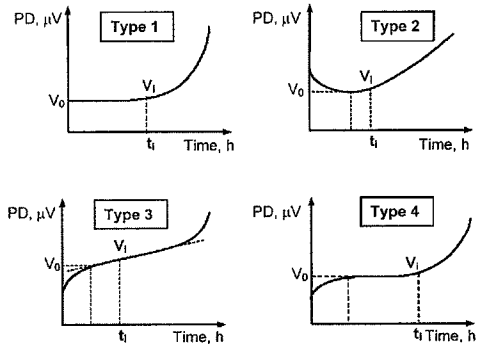


FIG. 3—*Types of potential drop (PD) vs time records in creep crack growth tests.*

From the complete data set, a sufficient number of data points (typically 30–50) were selected to describe the shape of the crack length, and Δ^{LLD} and Δ^{CMOD} versus time curves. When raw data are sparse or missing, interpolation should be performed without changing the trends in the overall data. In some cases, PD readings decrease after initial loading (which indicates an apparent decrease in the crack length), reach a minimum value and then start to increase (Type 2 in Fig. 3). For such cases, the value of V for all points of decreasing PD output should be taken to be the minimum value before the PD output again started to increase. The initial increase as seen in Types 3 and 4 in Fig. 3, recorded prior to crack tip opening is probably due to contacting pre-cracked faces and contacting debris. Therefore, it should not be accounted as the indication of CCG. Any jumps that occur in the PD or LVDT readings without an obvious explanation should be corrected by subtracting the magnitude of the jump in the LVDT or PD reading from the subsequent data points.

Test Interruption and Termination

Data logging and taking additional readings at the beginning of the test when rapid changes occur is important particularly for CCI studies. Also, when the test nears its final stage and CCG begins to accelerate additional readings should be taken. A decision must be made at some point to stop the test when CCG begins to accelerate toward rupture. It is ideal to stop the test just before failure or when the specimen has reached approximately 90–95 % of life. Alternatively, the test should be stopped as soon as both the potential drop and the displacement measurements show an acceleration in crack growth rates and displacement rates, indicating that final failure of the specimen is imminent. On-line crack length calculations using Johnson's formula [1] or unloading compliance measurements as described above may give guidance in deciding when to terminate the test.

Post Test Measurements and Metallographic Examination

An accurate measure of the initial (a_o) and final (a_f) crack front and crack size should be made when the specimen is broken open outside the furnace after testing. The total crack extension Δa_f is derived by subtracting the initial crack size a_o from the value of the final crack size a_f. The final crack size shall be determined from fracture surface measurements where possible. The initial and final measured crack lengths are used to compute the incremental crack length from PD measurements obtained during the tests. Post-test measurements are recommended to be carried out on the tested specimens. Any dimensional changes, necking, crack front shape, and fractured surface observations should be recorded. Detailed metallography to observe damage ahead of the crack tip, especially when crack initiation is of interest should be performed. Crack tip damage development is examined on completion of the test, on the sectioned half of the specimen, normal to the crack plane, using EDM the other half is broken open by a combination of fatigue and saw cutting, to reveal the fracture surface produced by creep crack growth [10]. If there is failure to stop the test before making the measurements the observations should make use of oxide surface markings using fractography to identify the crack tip profile. The crack size is measured on

half of the specimen at minimum of 8 (or 16 for the full specimen) equally spaced points centered on the specimen midthickness line and extending to 0.005 W from the roots of the side groove. The crack size used is the average between the measured lengths. If the ratio due to crack tip bowing between the crack tip center and the surface is >20 %, the longer final crack length a_f should be recorded. The measuring instrument shall have an accuracy of 0.025 mm. Alternatively, the fracture surfaces can be recorded using a digital imaging system and downloaded to provide a permanent electronic record. Measurements of mean values of a_o and a_f can then be made from the recorded data using an image analysis computer program based on crack area measurements.

Determination of Displacement Rates and CCG Rates

The crack length, load-line deflection, and time data need to be processed for determining the load-line displacement rate $d\Delta/dt$ and the creep crack growth rate da/dt. The data points are chosen consisting of crack length and the corresponding load-line displacement and time such that crack extension between successive data points is of the order of 0.005 W. If the crack growth is small, smaller Δa values should be chosen such that a minimum of ten data points will be determined for the total crack growth range.

Both the secant method and the incremental polynomial method can be used in determining the load-line displacement rate $d\Delta/dt$ and the creep crack growth rate da/dt [1]. Although the incremental polynomial method smoothes the data, reducing the scatter in rates, for the tests with small crack growth as in small size specimens of weldments, which usually have a small number of data points, the secant method is recommended for determining rates. It is also possible to fit alternative mathematical functions relating the load-line displacement and crack growth to time; these functions can then be differentiated to determine load-line displacement and creep crack growth rates. Different fitting functions may yield small difference in crack growth rate data only in CCI. Furthermore, the polynomial method may lead to artificial kinks in fit data at junction points of different functions.

Treatment of Creep Crack Growth

Creep Crack Growth (CCG) Rate Correlations

CCG rate is correlated with the crack tip parameter K or C^*. Background information on the rationale for employing the fracture mechanics approach in the analysis of creep crack growth data is presented in [7]. In order to correlate da/dt versus K or C^*, the required material properties may be obtained from uniaxial and CCG tests. The test conditions, in which the tests are performed, and the data reduction method and fitting may have a considerable influence on the test results. The da/dt values are determined from crack size data using a secant method or seven-point polynomial fit of crack length data. The da/dt versus time and da/dt versus C^* correlations may contain kinks due to high degree polynomial fit of crack length or load-line deflection that may be misinterpreted as material phenomena such as pop-in in crack growth. Therefore, a low degree of polynomial method of test data is recommended for data fitting procedure. The appropriate solutions for K and C^* are presented for crack growth rate correlations in an annex of [7]. These are valid for the size and specification of the test geometries given in Fig. 1. As recommended in the CoP, the applied load on a side grooved specimen will be acting over a shorter crack front, equal to the net section thickness B_n, and, therefore, the stress intensity will be higher by the following amount [7]:

$$K_n = K\left(\frac{B}{B_n}\right)^{0.5} \tag{3}$$

where B is the gross section thickness and

$$K = \sigma\sqrt{a}Y(a/W) \tag{4}$$

where $Y(a/W)$ is a function of geometry, crack length a, and width W, as shown in Fig. 1.

$Y(a/W)$ functions for stress intensity factors for various geometries are given in [7]. For specimens loaded under a tensile load P, the membrane stress, σ_m, is given by

$$\sigma_m = P/(BW) \tag{5}$$

[Replace W with $2W$ for DEN(T) and M(T) specimens], and for specimens subjected to a constant bending moment M the nominal bending stress at the outer fiber (surface) is given by

$$\sigma_b = 6M/(BW^2) \tag{6}$$

Creep Crack Growth Rate Correlations Using C^*

The choice of the appropriate crack growth rate correlation parameter depends mainly on the material behavior under service conditions, whether the material exhibits creep-ductile or creep-brittle behavior [1,11]. Steady-state creep crack growth rates in creep-ductile materials, exhibiting extensive creep, are correlated with C^*. In the small-scale creep region the parameter C_t [12] could also be used. However, for most practical examples in laboratory test pieces, it can be assumed that $C_t \cong C^*$ [2,11]. Therefore this procedure will adopt C^* for use in the correlation of the data for extensive creep conditions.

C^* can be determined experimentally or using numerical and limit analysis methods. The experimental procedure is applicable to the analysis of laboratory test specimens as in the CRETE project for generation of materials CCG data. The other two methods are generally employed for calculating C^* values for components.

The creep crack tip characterizing parameter C^* defined under widespread, steady-state creep conditions, is analogous to J_p for a nonlinear elastic material. Hence, for a power-law creeping material, C^* may be determined from the load displacement rate record during a creep crack growth tests using the relation

$$C^* = \frac{P\dot{\Delta}_c}{B(W-a)} H\eta \tag{7}$$

In Eq 7 the value of H and η for a power-law creep material, with creep exponent n, are the same as those for a power-law plastic material with exponent N when assumed $n=N$.

Determination of C^* from LLD and CMOD Rates

The experimental C^* parameter for a power-law material may be estimated from the creep components of load line displacement rate $\dot{\Delta}^{LLD}$ or crack mouth opening displacement rate $\dot{\Delta}^{CMOD}$ using Eqs 8 and 9, respectively [13],

$$C^* = \frac{P\dot{\Delta}_c^{LLD}}{B(W-a)} H^{LLD}\eta^{LLD} \tag{8}$$

$$C^* = \frac{P\dot{\Delta}_c^{CMOD}}{B(W-a)} H^{CMOD}\eta^{CMOD} \tag{9}$$

where P is the applied load, W is the specimen width [or half width for DEN(T) and M(T) specimens] and B_n is the net specimen thickness between the side grooves. Some of the solutions for the geometric functions H^{LLD}, H^{CMOD}, η^{LLD}, and η^{CMOD} for test specimens are given in Table 2. For all geometries examined, apart from M(T), DEN(T), and SEN(B), both H^{LLD} and H^{CMOD} are equal to $n/(n+1)$. The mean values of η^{LLD} and η^{CMOD}, have been used in the analysis for all geometries. The C^* values determined from experimental data using $\dot{\Delta}^{LLD}$ and $\dot{\Delta}^{CMOD}$ are correlated with crack growth rate, da/dt, for SEN(B) and SEN(T) specimens in Fig. 4. Although the difference is small, a tendency is observed for higher C^* values determined from $\dot{\Delta}^{LLD}$.

The total load-line displacement rate measured during the tests, $\dot{\Delta}^{LLD}$, can be partitioned into an instantaneous part, $\dot{\Delta}_i^{LLD}$, and a time-dependent part that is directly associated with the accumulation of creep strains $\dot{\Delta}_c^{LLD}$, such that

$$\dot{\Delta}_c^{LLD} = \dot{\Delta}^{LLD} - \dot{\Delta}_i^{LLD} \tag{10}$$

The instantaneous displacement rate $\dot{\Delta}_i^{LLD}$ can be further divided into an elastic and a plastic part, with the elastic part of the instantaneous load line displacement rate $\dot{\Delta}_{i,e}^{LLD}$ calculated as

TABLE 2—*Definitions of* η^{LLD}, η^{CMOD}, H^{LLD}, *and* H^{CMOD} *for each specimen [13].*

C(T)	$H^{LLD}=H^{CMOD}=n/(n+1)$	
	$\eta^{LLD}=\eta^{CMOD}=2.2\pm0.1$	$0.45\leq a/W\leq 0.7$
CS(T)	$H^{LLD}=H^{CMOD}=n/(n+1)$	
	$\eta^{LLD}=(7a/W-0.64)\pm0.6$	$0.2\leq a/W\leq 0.4$
	$\eta^{CMOD}=(4.6-1.6a/W)\pm0.2$	$0.2\leq a/W\leq 0.55$
DEN(T)	$H^{LLD}=H^{CMOD}=1/2(n-1)/(n+1)$	
	$\eta^{LLD}=(0.53a/W+0.42)\pm0.22$	$0.3\leq a/W\leq 0.7, 2\leq L/W\leq 4$
	$\eta^{CMOD}=(1.26-0.80a/W)\pm0.20$	$0.1\leq a/W\leq 0.5, 2\leq L/W\leq 4$
M(T)	$H^{LLD}=H^{CMOD}=1/2(n-1)/(n+1)$	
	$\eta^{LLD}=0.99\pm0.10$	$0.35\leq a/W\leq 0.7, 2\leq L/W\leq 4$
	$\eta^{CMOD}=(1.26-0.36a/W)\pm0.15$	$0.1\leq a/W\leq 0.7, 2\leq L/W\leq 4$
SEN(B)	$H^{LLD}=n/(n+1)$	
	$H^{CMOD}=2L/Wn/(n+1)$	
	$\eta^{LLD}=(0.56a/W+1.65)\pm0.07$	$0.3\leq a/W\leq 0.7$
	$\eta^{CMOD}=(0.92-0.46a/W)\pm0.06$	$0.1\leq a/W\leq 0.7$
SEN(T)	$H^{LLD}=H^{CMOD}=n/(n+1)$	
	$\eta^{LLD}=(5.0a/W-0.06)\pm0.38$	$0.1\leq a/W\leq 0.5, 1\leq L/W\leq 3$
	$\eta^{CMOD}=1.0\pm0.05$	$0.1\leq a/W\leq 0.7, 1\leq L/W\leq 4$

$$\dot{\Delta}_{i,e}^{LLD}=\frac{\dot{a}B_n}{P}\left[\frac{2K^2}{E'}\right] \tag{11}$$

where $\dot{a}$ is the crack growth rate and E' is the effective elastic modulus $[E/(1-\nu^2)$ for plane strain and E for plane stress]. ASTM E 1457 [1] also provides relations for the plastic instantaneous displacement rate. Inclusion of the plastic displacement rate in Eq 10 is particularly important in analyses of creep ductile materials such as C–Mn steel. However, it may lead to negative values of $\dot{\Delta}_c^{LLD}$ [14]. Similar problems have also been encountered when using Eq 11 to estimate elastic displacement rates [15]. In any case, for most practical situations of steady-state creep crack growth, the instantaneous displacement rate is insignificantly less than the total displacement rate and good correlation is found between crack growth rate and C^* evaluated using the total displacement rate $\dot{\Delta}^{LLD}$. There are currently no solutions corresponding to Eq 11 to allow a partition of the crack mouth opening displacement rate $\dot{\Delta}^{CMOD}$ into creep and instantaneous parts, though in principle such a partition is also possible [16].

Validity Criteria for the Use of C^*

Validity criteria are specified in ASTM E 1457 [1] for the use of C^* as a correlating parameter for CCG data determined by testing C(T) specimens. Firstly, the transition time t_T must be exceeded [17]. During a test t_T is estimated from [1]

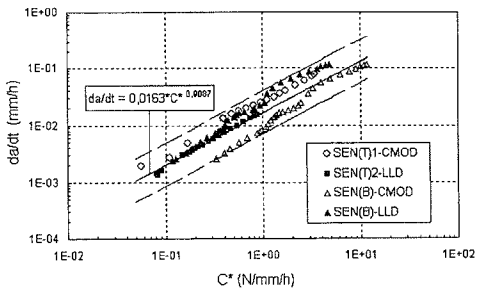


FIG. 4—*CCG rate as a function of* C^* *calculated using crack mouth opening displacement (CMOD) and load line displacement (LLD) SEN(T) and SEN(B).*

$$t_T = \frac{K^2(1-\nu^2)}{E(n+1)C^*(t_T)} \tag{12}$$

which assumes plane strain and elastic or small-scale yielding conditions. Although not specified in ASTM E 1457 and not performed here, it has been proposed in [17] that if there is significant plasticity on loading then K^2/E in Eq 12 may be replaced by total J [18].

Since the calculation of t_T depends implicitly on time through $C^*(t_T)$, its value is estimated by applying Eq 12, to each data point. Thus the value of t_T is given by the maximum value calculated in the test data set [1,17], i.e.,

$$t_T = \max\left[\frac{K^2(1-\nu^2)}{E(n+1)C^*(t)}\right] \tag{13}$$

In addition to satisfying the condition that $t > t_T$, if the C^* parameter is to be applied it is necessary to identify the material as "creep-ductile" in the test regime. Data are considered to be creep ductile if the creep load-line displacement rate, calculated using Eqs 10 and 11, constitutes at least half of the total load-line displacement, i.e., $\dot{\Delta}_c^{LLD}/\dot{\Delta}^{LLD} \geq 0.5$. For creep-brittle situations (i.e., $\dot{\Delta}_c^{LLD}/\dot{\Delta}^{LLD} \leq 0.25$) the stress intensity factor K may be used to describe the creep crack growth rate data [1].

Finally, following ASTM E 1457 [1], CCG rate data obtained prior to a crack extension $\Delta a = 0.2$ mm are assumed to comprise a part or the whole of the crack initiation and transient region, during which the damage distribution ahead of the crack tip reaches a steady state. Therefore, these data are not included when plotting crack growth rate against C^*. However, the early stage crack growth data may be correlated with K and/or C_t. The loading conditions and crack tip stress-strain state need to be analyzed and reported.

R5 Volume 4/5 [6] uses an additional criterion to establish that experimental creep crack growth rates are valid and governed by C^*; this requires that the nondimensional crack velocity λ is less than 0.5, where λ is defined by

$$\lambda = \frac{\dot{a}\sigma_{ref}^2}{EC^*} \tag{14}$$

where σ_{ref} is the reference stress. This criterion may also be used as further check and reported accordingly.

Treatment of Creep Crack Initiation

Creep crack initiation (CCI) could constitute a major portion of the time to failure. The collected data for initiation times to a crack extension of 0.2 mm and 0.5 mm can be correlated with K, C^* [19]. In most cases, initiation times are inversely proportional to the crack tip parameters. The experimental verification is shown in the section "Validation of CoP," below.

Recommended Minimum Number and Duration for Tests

Material property values are interpreted as constants, which can be used to help characterize the material in processing and design. If the calculations are based on "enough" data, the base values should be reproducible, to within engineering accuracy, across comparable data sets. The objective of the CoP is to highlight issues associated with the small-sample reproducibility and to provide guidance on how many data are necessary in base value calculations in order for these values to be approximately reproducible. How many data are "enough" depends on many factors, including:

- The statistical model which is used to approximate the population, from which the data is sampled.
- Accounting for the anisotropy of the material.
- The degree of reproducibility which is desired.
- The variability in the property being measured.
- Variability in measurements of the property due to the test method.
- Accuracy of the equipment.
- Cost and the capability of performing numerous tests.

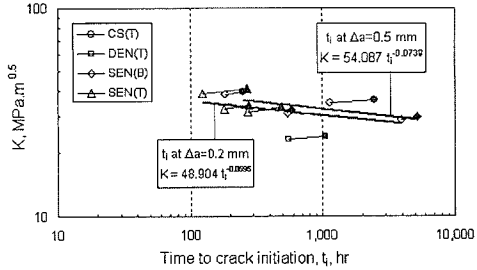


FIG. 5—*K vs time to crack initiation defined at crack growth* $\Delta a = 0.2$ *mm (hollow symbols) and 0.5 mm (solid symbols) for 316H steel at 550°C.*

It is suggested that a minimum of five tests at different loads should be performed. If the material exhibits such factors as irregular voids, large grains, and other inhomogeneities, or contains a weldment [e.g., cross weld and heat affected zone (HAZ) specimens], the minimum number of tests should be increased [8]. Also, more tests should be performed if the material CCG behavior exhibits increased scatter regardless of the reason for the variability. If there is insufficient material available or if there are other reasons, which would restrict multiple testing then the results should be considered with increased caution. Because of these factors, it is impossible to give firm recommendations. Batch to batch variation is more important in welds and cross-weld samples than in parent metallic materials. This is due to sensitivity of the properties on fabrication processes. Background information and guidelines about fabrication and test-piece preparation to assist the tester in making a sample size decision should be planned. It should be emphasized that differences and the stability of the material base values with respect to sample size and geometry need to be taken into account.

During testing the holding time at temperature prior to the start of the test should be governed by the time necessary to ensure that the temperature can be maintained within ±2°C [8]. This time will not be less than one hour per 25 mm of specimen thickness. The test duration may be estimated for guidance from applied load and materials data at test temperature, using K formulas for crack initiation. The calculated value will be revised after the first test for a more accurate test duration estimation. If failure of the specimen occurs prior to the stoppage of the test then measurements of the final crack size on the fractured surface may not be possible. In this case or when $\Delta a/a_o > 0.2$ an upper bound estimate of the final crack size should be made (i.e., $<0.75a/W$). However, a repeat test may also be needed.

Validation of the CoP

Extensive analyses have been carried out to validate the results from CRETE [2,7,13,16]. Essentially the experimental data are analyzed and correlated with predetermined crack tip parameters. CCI behavior for various geometries is characterized using both K and C^* parameters in Figs. 5–8. Thin lines in these

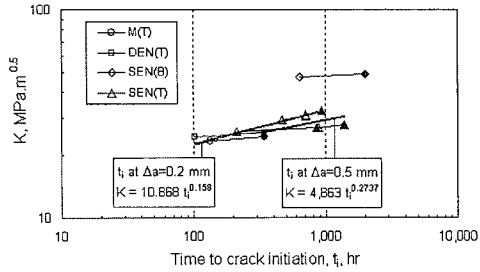


FIG. 6—*K vs time to crack initiation defined at crack growth* $\Delta a = 0.2$ *mm (hollow symbols) and 0.5 mm (solid symbols) for C–Mn steel at 400°C.*

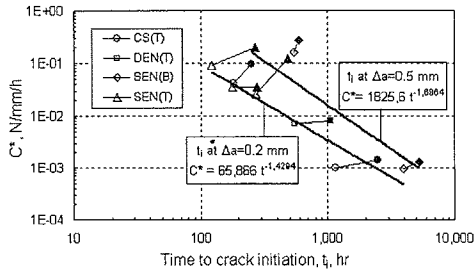


FIG. 7—*C^* vs time to crack initiation defined at crack growth $\Delta a = 0.2$ mm (hollow symbols) and $\Delta a = 0.5$ mm (solid symbols) for 316H steel at 550 °C.*

figures connect the data points for the same specimen, indicating the deformation and crack resistance of the material to grow a crack from 0.2 to 0.5 mm. A satisfactory correlation for CCI is observed in 316H steel for both K and C^* parameters for various geometries, as shown in Figs. 5 and 7. However, higher scatter with a particularly contradicting K-t correlation is seen in Fig. 6 for C–Mn steel. These observations direct attention to choice of load level and test conditions for high ductility C–Mn steel where plastic deformation may dominate at the crack tip.

The users of the CoP are advised, in any event, to correlate CCI and CCG data with K and C^* using the formulas given in [7,16] and report their findings.

The same condition regarding the validity of K or C^* will apply for CCG. The CCG data obtained from tests on different geometries are presented in Figs. 9–12. The presented data demonstrate the effects of specimen geometry and loading condition as well as lab-to-lab variation of data and its analysis, that further emphasize the need for harmonization of CCG testing and assessment. Note that the data received from the partners are assessed following the present CoP. It has been found that the method of data

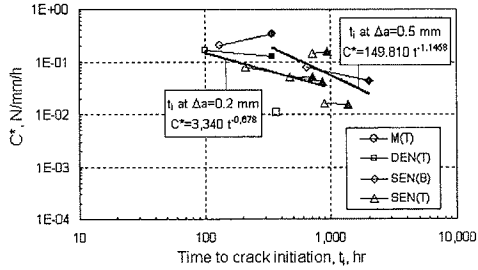


FIG. 8—*C^* vs time to crack initiation defined at crack growth $\Delta a = 0.2$ mm (hollow symbols) and 0.5 mm (solid symbols) for C–Mn steel at 400 °C.*

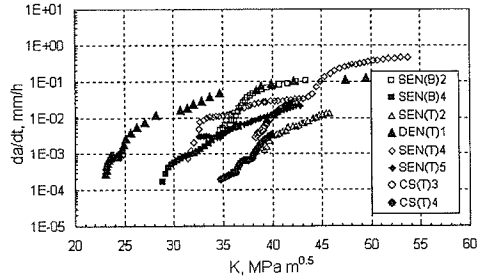


FIG. 9—*Crack growth rate vs K with data $\Delta a > 0.2$ mm for 316H steel at 550 °C.*

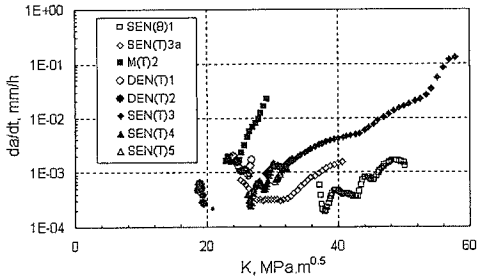


FIG. 10—*Crack growth rate vs K with data $\Delta a > 0.2$ mm for C–Mn steel at 400 °C.*

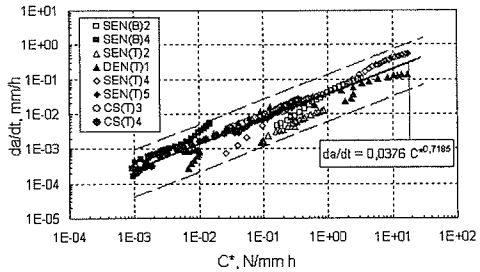


FIG. 11—*Crack growth rate vs C^* with data $\Delta a > 0.2$ mm for 316H steel at 550 °C.*

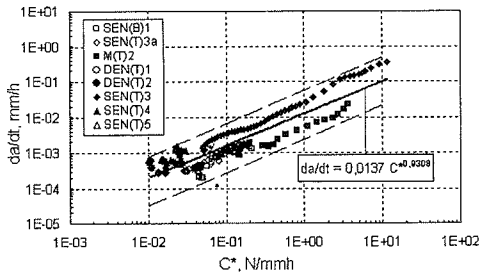


FIG. 12—*Crack growth rate vs C^* with data $\Delta a > 0.2$ mm for C–Mn steel at 400 °C.*

reduction slightly affects the scatter in the results. Generally, the figures show a high scatter in K correlation of CCG rate for both materials that is emphasized in K correlation and much improved correlation with C^* in the valid steady-state range. This demonstrates the applicability of the present CoP to industrially relevant specimens of different geometries for CCI and CCG since there is no effect observed due to geometry and size with the experimental scatter when the data are correlated with C^* for steady state crack growth. This is particularly important where the data are used for component assessment of utilities in high temperature service.

Application of Data for Assessment

The CoP [7] can be used to determine experimental crack initiation and crack growth rate correlations for assessment of components in high temperature service. The correlations of steady-state crack growth, CCI

and CCG rate with K and C^* can be represented by straight lines of different slopes on log/log plots and expressed by power laws of the form.

For CCI as

$$t_i = \frac{\Delta a}{\dot{a}} = \frac{D_i' \Delta a}{K^{m'}} \tag{15}$$

$$t_i = \frac{\Delta a}{\dot{a}} = \frac{D_i \Delta a}{C^{*\phi}} \tag{16}$$

For CCG as

$$\dot{a} = D' K^{m'} \tag{17}$$

$$\dot{a} = D_o C^{*\phi} \tag{18}$$

A steady-state relationship between crack growth rate and the parameters in Eqs 17 and 18 physically implies a progressively accelerating creep crack growth rate. For a conservative assessment the use of CCG data in the above equations are sufficient. However, CCI predictions using Eqs 15 and 16 can also be considered. There are also available models in existence [16,20] that can be used to predict these equations if insufficient experimental data are available.

Discussion and Conclusions

The recommendations for a CoP provide guidelines for specimen selection, testing, and data analysis that include novel aspects such as the use of new geometries for testing creep crack growth. The CoP has been validated using the tests on C–Mn and 316H steels conducted within the CRETE [2] project. The higher ductility of C–Mn steel requires special attention to be paid to test load level and the potential for significant plastic deformation; this can result in particular difficulties in correlating initiation times with K. These problems could be overcome by correlating initiation times with the creep toughness K^c_{mat}, as this parameter explicitly incorporates the effects of elastic, plastic, and creep deformation [15]. C^* correlations provide CCG rate information with minimum scatter for component assessment. The analysis using K and C^* solutions for CCI and CCG, $Y(a/W)$, and η factors for the geometries and type of loading covered by the CoP have been verified [13,16] using the tests conducted on C–Mn and 316H steels. These results suggest that for the range of geometries and dimensions tested, there are no significant size and geometry effects on CCI and CCG.

Certain conditions must be satisfied in the choice of laboratory specimens for testing in order to apply creep crack initiation and growth rate data to structural assessments. Machine capacity, material availability, and the volume and dimensions of usable material restrict the choice of geometry in many cases. This issue is of particular concern when testing material obtained from components in both virgin and service exposed conditions. The location and orientation of the crack in the specimen also need to be consistent with the defect orientation in the component being assessed.

Recommendations have been presented regarding the optimum choice of specimen geometry. Where loading capacity is limited, for example, the highly constrained C(T), SEN(B), and CS(T) specimens will require lower test loads for given ligament dimensions B_n $(W\text{-}a)$ than the DEN(T) and M(T) geometries. The stress state of the component and the mode of loading on the component could also influence the choice of specimen.

The crack growth rate value at a given C^* can vary as a result of inherent scatter in material response if all other variables such as geometry, specimen size, crack size, loading method, and temperature are kept constant. This scatter may be increased further by variables such as microstructural differences as in weldments, loading precision, environmental control, and data processing techniques. Therefore, it is good practice to conduct repeat tests at the same conditions. Confidence in the data will increase with the number of tests performed on any one batch of material. Using a reduced number of tests rather than a full set of available tests to characterize the CCG behavior of a material may yield unreliable results (Figs. 4 and 11). A valid set of data for use in subsequent structural analysis should include analysis of the data together with information from metallographic examination of the test specimens.

Short test durations (<5000 h) will influence the extent of plasticity and the level of crack tip blunting depending on the tensile strength of the material. It is therefore advisable to maximize test durations as far as possible. Otherwise, when using short-term data to assess long term component life the analysis should be treated with caution. It is commonly observed that creep rupture ductility decreases with increasing test duration [21]. Intergranular cavitation increasingly dominates the failure mechanism at longer times. In crack initiation and growth tests, the multiaxial stress state ahead of a crack promotes low displacement failures. For materials that cavitate readily, such mechanisms may be reproduced by testing at higher stress levels. However, in materials where the low stress mechanism is replaced by matrix deformation dominated failure at higher stresses, it may be necessary to accelerate tests by increasing temperatures rather than stresses. In either case, it is essential that the mechanisms operative in the test specimen lead to deformation resembling the service conditions.

Finally, it is concluded that for the specimen geometries and sizes proposed in the CoP, the CCI and CCG data can be reproduced for both creep brittle and creep ductile materials within an acceptable experimental range of scatter.

Acknowledgments

The CoP has been prepared with EC financial support within the FP5 "CRETE" Project Contract No. G6RD-CT-2001-00527, Project No. GRD2-2000-30021 (2001-2004). Contributions in drafting the document from other 'CRETE' Partners CESI—Centro Elettrotecnico Sperimentale Italiano, Italy; TU Darmstadt, Germany, CETIM—Centre Technique des Industries Mecaniques, France; and VTT Industrial Systems, Finland are gratefully acknowledged. This paper is published with permission of British Energy Generation Ltd.

References

[1] ASTM, Standard E 1457-00, "Standard Test Method for Measurement of Creep Crack Growth Rates in Metals," *Annual Book of ASTM Standards*, Vol. 3(1), ASTM International, West Conshohocken, PA, pp. 936–950.

[2] EC Project CRETE, "Development and Harmonization of Creep Crack Growth Testing for Industrial Specimens—A Root to a European Code of Practice," EC Project No: GRD2-2000-30021.

[3] Dogan, B., "High temperature defect assessment procedures," *Int. J. Pressure Vessels Piping*, 80, 149–156 (2003).

[4] Dogan, B., and Ainsworth, R., "Defect assessment procedure for low to high temperature," *ASME Conference PVP2003-2032*, 2003, Vol. 463, ASME, Cleveland, OH, pp. 105–111.

[5] British Standards Institution, "Guide on Methods for Assessing the Acceptability of Flaws in Metallic Structures," *BS 7910: 1999*, Incorporating Amendment No 1, 2000.

[6] R5 Issue 3, "An Assessment Procedure for the High Temperature Response of Structures," British Energy Generation Ltd. Procedure, 2003.

[7] Dogan, B., Nikbin, K., and Petrovski, B., "Code of Practice for European Creep Crack Growth Testing of Industrial Specimens. 2nd Version," EC Project CRETE, Deliverable 13, 2005.

[8] Dogan, B., "CoP for High Temperature Testing of Weldments," ESIS TC11, WG: on High Temperature Testing Weldments, 3rd Draft, 2005.

[9] ASTM, Standard E 1737-96, "Standard Test Method for J-Integral Characterization of Fracture Toughness," *Annual Book of ASTM Standards*, 1996, Vol. 3(1), ASTM International, West Conshohocken, PA, pp. 994–1017.

[10] Rinaldi, C., Dogan, B., Ceyhan, U., and Bicego, V., "Analysis of Creep Crack Growth Tests on Specimens with Different Geometries Made of AISI 316H and C–Mn steels," *Fifth International ASTM/ESIS Symposium on Fatigue and Fracture Mechanics*, Reno, NV, May 18–20, 2005, ASTM International, West Conshohocken, PA.

[11] Schwalbe, K. H., Ainsworth, R. A., Saxena, A., and Yokobori, T., Special Issue on Crack Growth in Creep-brittle Materials, *Eng. Fract. Mech.*, 62(1), 123–142 (1999).

[12] Saxena, A., "Creep Crack Growth under Nonsteady-State Conditions," *Fracture Mechanics ASTM STP 905*, 1986, Vol. 17, pp. 185–201.

[13] Davies, C. M., Kourbetis, M., O'Dowd, N. P., and Nikbin, K. M., "Experimental Evaluation of the J or C^* Parameter for a Range of Cracked Geometries," *Fifth International ASTM/ESIS Symposium on Fatigue and Fracture Mechanics*, Reno, NV, May 18–20, 2005, ASTM International, West Conshohocken, PA.

[14] Fookes, A. J., and Smith, D. J., "The Influence of Plasticity in Creep Crack Growth in Steels," *Int. J. Pressure Vessels Piping*, 80(7), 453–463 (2003).

[15] Dean, D. W., and Gladwin, D. N., "Characterization of Creep Crack Growth Behavior in Type 316H Steel Using Both C^* and Creep Toughness Parameters," *Proc 9th International Conference on Creep and Fracture of Engineering Materials and Structures*, Swansea, April 1–4, 2001, Institute of Materials, London, UK, pp. 751–761.

[16] Davies, C. M., Mueller, F., Nikbin, K., O'Dowd, N. P., and Webster, G. A., "Analysis of Creep Crack Initiation and Growth in Different Geometries for 316H and Carbon Manganese Steels," *Fifth International ASTM/ESIS Symposium on Fatigue and Fracture Mechanics*, Reno, NV, May 18–20, 2005, ASTM International, West Conshohocken, PA.

[17] Riedel, H., and Rice, J. R., "Tensile Cracks in Creeping Solids," *Fracture Mechanics Twelfth Conference*, 1980, St-Louis, ASTM STP 700, ASTM International, West Conshohocken, PA, pp. 112–130.

[18] European Structural Integrity Society, "ESIS Procedure for Determining the Fracture Behavior of Materials," ESIS P2-92, 1992.

[19] Dogan, B., Petrovski, B., and Ceyhan, U., "Significance of Creep Crack Initiation for Defect Assessment," *Proceedings of International Conference BALTICA VI on Life Management and Maintenance for Power Plants*, Espoo, Finland, 2004, VTT Symp. 234, Vol. 2, VTT Industrial Systems, Espoo, Finland, pp. 595–607.

[20] Webster, G. A., and Ainsworth, R. A., *High Temperature Component Life Assessment*, 1st ed., 1994, Chapman and Hall, London.

[21] EC Project Advanced Creep, WG1 on Guidelines and Procedures, European Creep Collaborative Committee (ECCC), Coordinator: A. Shibli, European Technology Development (ETD) Ltd., EC Project No: G1RT-CT-2001-05042, 2001–2005.

Journal of ASTM International, Vol. 3, No. 5
Paper ID JAI13198
Available online at www.astm.org

Masataka Yatomi[1] *and Kamran M. Nikbin*[2]

Creep Crack Growth Predictions in Component Using a Damage Based Approach

ABSTRACT: This paper presents a numerical study of simulated creep crack growth (CCG) prediction in a compact tension [C(T)] specimen and a pipe component containing cracks. The results are compared to experimental data of the same consisting of creep crack growth tests of a carbon-manganese steel (C-Mn) tested at 360°C. The constitutive behavior for this steel is described by a power law creep model and the uniaxial properties are used in a damage based model to predict CCG. For comparison between CCG properties of the pipe and C(T) specimens, different reference stress methods were used to derive appropriate C^* values. It has been shown that the global solution for collapse in the cracked pipes gives the best correlation with the C(T) data. On this basis CCG rates for pipe are higher than those for C(T) specimens at the same value of C^*. The damage-based approach combined with a crack tip constraint model based on void growth is also used to predict the crack propagation rates in the pipe component using a two-dimensional finite elements (FE) mesh. Elastic-plastic-creep analyses are performed using a node debonding criteria to simulate and predict crack extension under plane stress and plane strain conditions. It has been found that CCG against time predicted from the FE under plane stress conditions is almost the same as those for the experimental data. Comparing C^* derived from different reference stress methods to C^* from FE analysis it has been found that C^* from FE under plane strain condition correlates best with C^* from the global reference stress solution. Consequently the main CCG difference between the C(T) and the pipe component is found to be due to the method of estimating C^* and not due to constraint effects.

KEYWORDS: creep, crack growth rate, fracture mechanics, C^*, reference stress, C-Mn steel, high temperature, pipe, components, finite element, multiaxial

Introduction

Components used in power generation plant may be exposed to high temperatures over long periods of time. Because of a strong incentive to maximize component lifetimes and to keep them beyond their original design lifetimes improvements in life assessment techniques are needed. In addition, with advances in nondestructive examination (NDE), smaller defects and cracks can be detected. This would mean that improved fracture mechanics assessment to make estimates of remaining lifetimes is needed. Therefore validation of laboratory fracture mechanics data with component creep crack growth (CCG) data using both experimental and numerical modeling techniques will assist toward reaching an improved life estimation method.

Continuum damage methods have been used to predict failure at high temperatures [1–5]. Generally, these studies have focused on the prediction of crack initiation and rupture life. In this work, an uncoupled damage-based approach is used to simulate crack growth from the transient to the steady state regime. The node release method [6], whereby node is released when damage reaches a critical value, has been applied to the study of creep crack growth in a compact tension [C(T)] specimen for C-bMn steel at 360 °C. In this work, these methods are extended to pipe components which have been tested in the laboratory [7].

It has previously been reported [8–10] that CCG rates are normally correlated by the creep fracture parameter C^*. For C(T) specimen load-line displacement rate is usually used to determine the creep parameter, C^* [11]. While for components this term is estimated by reference stress methods [12–15]. It has also been reported that CCG rates for pipes are faster than those for C(T) specimen, which may be mainly due to the different methods of calculating C^* and constraint effect [16]. Therefore in this paper the

Manuscript received April 12, 2005; accepted for publication January 30, 2006; published online March 2006. Presented at ASTM Symposium on Fatigue and Fracture Mechanics: 35th Volume on 18–20 May 2005 in Reno, NV; R. E. Link and K. M. Nikbin, Guest Editors.

[1] Ishikawajima-Harima Heavy Industries Co., Ltd., 1, Shin-nakahara-cho, Isogo-ku, Yokohama, Japan, 235-8501.
[2] Department of Mechanical Engineering, Imperial College London, South Kensington Campus, London, UK, SW7 2AZ.

Copyright © 2006 by ASTM International, 100 Barr Harbor Drive, PO Box C700, West Conshohocken, PA 19428-2959.

comparison of C^* parameters for pipe determined from reference stress solutions and line integral definition is discussed.

Fracture Mechanics at High Temperature

For many materials, creep deformation can be considered to be composed of three regimes, namely, primary, secondary, and tertiary creep regimes. The secondary creep strain rate can be represented by a power law

$$\dot{\varepsilon}_s^c = A_s \sigma^{n_s} \tag{1}$$

where A_s and n_s are material constants. The use of an average creep rate obtained directly from creep rupture data has been proposed [17] to account for all three stages of creep.

$$\dot{\varepsilon}_A = \frac{\varepsilon_f}{t_r} = \dot{\varepsilon}_0 \left(\frac{\sigma}{\sigma_0} \right)^{n_A} = A_A \sigma^{n_A} \tag{2}$$

where ε_f is the uniaxial failure strain, t_r is the time to rupture, and σ is the applied stress. The variables $\dot{\varepsilon}_o$, σ_o, A_A, and n_A in Eq 2 are generally taken as material constants.

For a cracked body the stress field generated at a crack tip is characterized by J when plastic strains dominate [18]. When creep dominates it is characterized by C^* [10]. For a power law creeping material, the stress and strain rate in the vicinity of the crack tip are given by [10]

$$\sigma_{ij} = \sigma_0 \left(\frac{C^*}{\dot{\varepsilon}_0 \sigma_0 I_n r} \right)^{1/(n+1)} \tilde{\sigma}_{ij}(\theta, n)$$

$$\dot{\varepsilon}_{ij} = \dot{\varepsilon}_0 \left(\frac{C^*}{\dot{\varepsilon}_0 \sigma_0 I_n r} \right)^{n/(n+1)} \tilde{\varepsilon}_{ij}(\theta, n) \tag{3}$$

where r and θ measure distance and polar angle relative to the crack tip, I_n is a parameter which depends only on the creep exponent n, and $\tilde{\sigma}_{ij}$ and $\tilde{\varepsilon}_{ij}$ are dimensionless functions. The parameter C^* in Eq 3 may be obtained from a path independent integral and is analogous to the J integral for rate independent material behavior.

For the C(T) specimens ASTM standard E1457-01 [11] allows C^* to be calculated from creep load line displacement rate $\dot{\Delta}^c$ using the expression

$$C^* = \frac{P \dot{\Delta}^c}{B_n b} F \tag{4}$$

where P is the applied load, b is the remaining ligament ahead of the crack, B_n is the net thickness between side grooves when used, and F is a factor which depends on geometry and creep stress index n.

While in components it is difficult or impossible to measure load-line displacement rate, where a formula similar to Eq 4 is not available. Therefore for the components C^* must be determined by finite element methods or reference stress concepts [12,13]. When the reference stress approach is adopted, C^* can be expressed as

$$C^* = \sigma_{\text{ref}} \cdot \dot{\varepsilon}_{\text{ref}} \left(\frac{K}{\sigma_{\text{ref}}} \right)^2 \tag{5}$$

where K is the stress intensity factor and $\dot{\varepsilon}_{\text{ref}}$ is the uniaxial creep strain rate at the appropriate reference stress σ_{ref}. Ideally, $\dot{\varepsilon}_{\text{ref}}$ should be taken from uniaxial data obtained on the same batch of material.

Usually it is convenient to employ limit analysis [14,15,19] to obtain σ_{ref} from

$$\sigma_{\text{ref}} = \sigma_y \frac{P}{P_{\text{lc}}} \tag{6}$$

where P_{lc} is the collapse load of the cracked body and σ_y is the yield stress. The value of P_{lc}, and hence estimates of C^* in Eq 5, will depend on the collapse mechanism adopted and whether plane stress or plane strain conditions are assumed. Both "Global" and "Local" collapse mechanisms can be chosen [20,22].

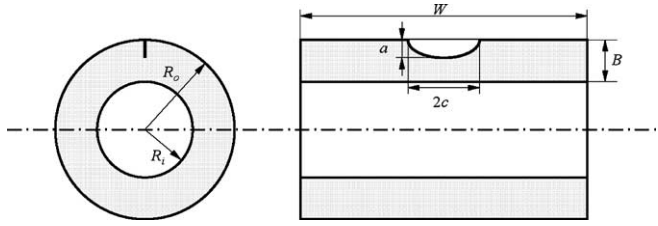


FIG. 1—*External surface crack in pipe oriented axially.*

Collapse load solutions are available for many geometries [8,9,21,22], but in some cases need to be derived numerically.

It is also important to note that the accepted procedure in the codes [8,9,21] is to estimate residual lives in components from "benchmark" data derived from C(T) specimens using the C^* approach. For situations where creep dominates, it has been found that [10] crack growth rate $\dot{a}$ can be described by

$$\dot{a} = DC^{*\phi} \tag{7}$$

where D and ϕ are material constants that can be measured experimentally or determined from uniaxial creep data [10–13].

Reference Stress for Axially Oriented External Crack in Pipe

R6 "Global" Solutions—The "Global" solutions [21,22] are based on collapse of the entire cross section at the site of a defect. For a semielliptical axial defect in a pipe subjected (see Fig. 1) to an internal pressure p, σ_{ref} can be expressed as

$$\sigma_{\text{ref Global 3D}} = \frac{p}{\dfrac{1}{R_o - a}\text{bate}(a,c) + \ln\left(\dfrac{R_o - a}{R_i}\right)} \tag{8}$$

where bate(a,c) is given by

$$\text{bate}(a,c) = \frac{a}{\sqrt{1 + 1.61\dfrac{c^2}{[(R_o - a)a]}}} \tag{9}$$

In these equations, a is crack depth, c is half crack length at the surface, and R_i and R_e are the internal and external radii of the pipe, respectively.

R6 "Local" Solutions—The "Local" solutions [21] are based on collapse in the ligament. σ_{ref} for "Local" solutions of a semielliptical axial defect in a pipe (see Fig. 1) can be expressed as

$$\sigma_{\text{ref 3D Local}} = \frac{g(\zeta)\dfrac{\sigma_b}{3} + \sqrt{g(\zeta)^2\left(\dfrac{\sigma_b}{3}\right)^2 + (1-\zeta)^2\sigma_m^2}}{(1-\zeta)^2} \tag{10}$$

where

$$g(\zeta) = 1 - 20\zeta^3\left(\frac{a}{2c}\right)^{0.75}, \quad \zeta = \frac{a \cdot 2c}{B \cdot (2c + 2B)} \tag{11}$$

While for long axial external surface defect (see Fig. 2), σ_{ref} can be expressed as

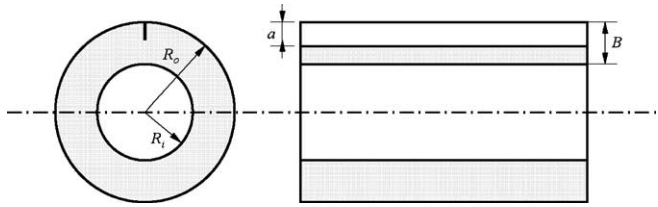


FIG. 2—*Long axial external surface crack in pipe.*

$$\sigma_{\text{ref 2D Local 1}} = \frac{\zeta\sigma_m + \frac{\sigma_b}{3} + \sqrt{\left(\zeta\sigma_m + \frac{\sigma_b}{3}\right)^2 + (1-\zeta)^2\sigma_m^2}}{(1-\zeta)^2} \tag{12}$$

where

$$\zeta = \frac{a}{B} \tag{13}$$

Solutions for BS 7910—In BS 7910, the reference stress for external surface flaw in cylinder (see Fig. 1) is given as

$$\sigma_{\text{ref BS7910 3D}} = 1.2M_s\sigma_m + \frac{2}{3}\frac{\sigma_b}{(1-a'')^2} \tag{14}$$

where σ_m and σ_b are the membrane and bending stress, respectively. M_s is calculated from

$$M_s = \frac{1 - \left(\frac{a}{B \cdot M_T}\right)}{1 - \left(\frac{a}{B}\right)} \tag{15}$$

and a'' is a nondimensional crack length represented by

$$a'' = \frac{a}{B\left[1 + \left(\frac{B}{c}\right)\right]}, \quad \text{for } W \geqslant 2(c+B) \tag{16}$$

and M_T is given by

$$M_T = \sqrt{1 + 1.6\left(\frac{c^2}{R_i B}\right)} \tag{17}$$

While for long external flaws in pipe (see Fig. 2), σ_{ref} can be expressed as

$$\sigma_{\text{ref BS7910 2D}} = 1.2M_s\sigma_m + \frac{2}{3}\frac{\sigma_b}{(1-a'')^2} \tag{18}$$

σ_m and σ_b are the membrane and bending stress, respectively. M_s is calculated from

$$M_s = \frac{1}{1 - \left(\frac{a}{B}\right)} \tag{19}$$

and a'' is a nondimensional crack length represented by

$$a'' = \frac{a}{B} \tag{20}$$

TABLE 1—*Chemical composition of C–Mn steel (in weight percent).*

	C	Si	Mn	P	S	Cr	Mo	Ni	Cu	Al	N	FN[a]
C-Mn steel	0.16	0.28	0.87	0.014	0.014	0.09	0.05	0.2	0.15	0.019	0.019	0.0110

[a]FN is calculated "free nitrogen" for 920 °C. This heat was categorized as high free nitrogen.

Experimental Data

Experimental data from three European collaborative projects [23,24] have been examined. The materials tested were a C-Mn steel with the compositions given in Table 1. They were tested at 360 °C. The material properties at the temperature are given in Table 2. Their corresponding creep strain rate data are shown in Table 3. The stresses applied during creep for the C-Mn steel were above the yield stress and significant plasticity occurred on loading. There was also appreciable primary and tertiary creep and average creep strain rate has been recorded for this material for Table 3.

In order to estimate C^* for pipe, three different kinds of reference stress solutions were used. In addition, two kinds of crack estimation (semielliptical crack and extended crack have been used. Table 4 shows five different reference stress solutions for C^* considered in this paper. For the semielliptical crack, it was assumed that the value of c (half length of surface crack) does not vary with crack growth, because it has been observed that in experiment the crack grew little in the axial direction.

Figure 3 shows the comparison of C^* obtained from the different solutions at each a/W (a =1–11 mm, W=13 mm). In the figure, geometry of Pipe E (see Table 3) is applied and applied pressure is 70 MPa. It is seen in Fig. 3 that for smaller values of a/W, the solution of R6 Local three-dimensional (3D) solution gives smaller values of C^* than the other solutions. As crack extends, R6 Local 2D solution gives much higher values of C^*, compared to the other solutions. The values of C^* obtained from BS7910 3D solution are almost the same as those from BS7910 2D solution throughout the range of a/W examined. Compared the values of C^* at the shallowest crack and the deepest crack, R6 global solution gives the narrowest band.

Figure 4 shows CCG rate against C^* prediction using the five different solutions for pipe with the data from the C(T) test [6] at 360 °C. The average creep strain rate for n_A=10.0 (see Table 2) is used to calculate the reference strain rate. It appears from Fig. 4 that each estimate gives quite different values of C^*. For all solutions, at high values of C^* (e.g., $C^*>$ about 15 J/m^2 h for R6 global 3D solution) the CCG rate is almost constant with increasing C^*. While at low values of C^*, the slope of the CCG rate versus C^* prediction curve obtained from the R6 global 3D solution is the closest to that for laboratory tests and the band of data for the pipe is close to the band of laboratory tests. Compared to the results estimated from

TABLE 2—*Material properties for C-Mn steel at* 360 °C *(for A_A and n_A, stress is in MPa and time in hours).*

Young's modulus (GPa)	σ_y (MPa)	UTS (MPA)	A_A	n_A	ε_f (%)
190	240	570	1.78×10^{-30}	10.0	18.1

TABLE 3—*Geometries and pressures applied to pipe.*

Materials	Specimen	Component geometry (mm)					Pressure (MPa)
		R_e	R_i	W	a_0	a_0/c_0	
C-Mn	Pipe D	32	25	7	1.0	0.04	73–85
	Pipe E	63.5	50.5	13	1.0	0.04	69–78
	Pipe F	57.7	45.5	12	1.0	0.04	69–78

Note: W=wall thickness, R_e-R_i.

TABLE 4—*Reference stress prediction of C^*.*

Methods	Crack shape	Method name
R6 global solutions	Semielliptical crack	R6 Global 3D solution
R6 local solutions	Semielliptical crack	R6 Local 3D solution
	Extended crack	R6 Local 2D solution
BS7910	Semielliptical crack	BS7910 3D
	Extended crack	BS7910 2D

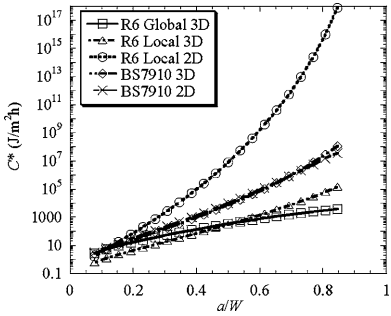


FIG. 3—*Dependence of C^* on a/W for axial external flaw in pipe.*

R6 Local 3D and 2D solutions (see Figs. 4(*b*) and 4(*c*)), the scatter of the results estimated from the extended crack are larger than that from the semielliptical crack, although the data band for the pipe estimated from the extended crack is closer to the band of the laboratory tests than that estimated from the semielliptical crack. Compared to the results from BS7910 3D and 2D solutions (see Figs. 4(*d*) and 4(*e*)), there is little difference between the two datasets, which corresponds to the result of Fig. 3. From the comparison of Figs. 4(*a*)–4(*e*)), it may be suggested that the R6 global 3D solution (Fig. 4(*a*) gives the best correlation, as the scatter of the data is the narrowest, the slope at the lower part of C^* is almost the same as that of C(T) data, and the part where CCG rates are constant is the smallest, compared to the other solutions. However it still does not give close agreement to the C(T) data.

Comparing the CCG rate for the pipe it is seen that they are higher than that for the C(T) data band regardless of the method of calculating C^*. It should be noted that in this case if laboratory data is used to predict CCG, the results become nonconservative. An interim solution for this treatment has been discussed in detail in Ref. [16].

Finite Element Modeling

Damage Accumulation Modeling Used in Numerical Calculations

A damage parameter ω is defined such that $0 \leqslant \omega \leqslant 1$ and failure occurs at a material point when $\omega = 1$. The rate of damage accumulation is related to the equivalent creep strain rate ($\dot{\varepsilon}_c$) by

$$\dot{\omega} = \frac{\dot{\varepsilon}^c}{\varepsilon_f^*} \tag{21}$$

where ε_f^* is the multiaxial creep ductility. Note that the evolution of damage is not coupled to the deformation, as in [1], so that the creep rate of the material is not enhanced due to the accumulation of damage.

Assuming that the mechanism of creep crack growth is void growth and coalescence, the Cocks and Ashby model [25] is the most appropriate for representing the multiaxial creep ductility of the material under study. From the Cocks and Ashby model the ratio of the multiaxial to uniaxial failure strain $\varepsilon_f^*/\varepsilon_f$ is given by

$$\frac{\varepsilon_f^*}{\varepsilon_f} = \sinh\left[\frac{2}{3}\left(\frac{n-1/2}{n+1/2}\right)\right] \Big/ \sinh\left[2\left(\frac{n-1/2}{n+1/2}\right)\frac{\sigma_m}{\sigma_e}\right] \tag{22}$$

where σ_m/σ_e is the ratio between the mean (hydrostatic) stress and equivalent (von Mises) stress.

Finite Element Model

In the section "Experimental Data" experimental data for internal pressurized shallow cracked pipe were presented. In this section a representative 2D model of a cracked pipe is examined. Specifically pipe E

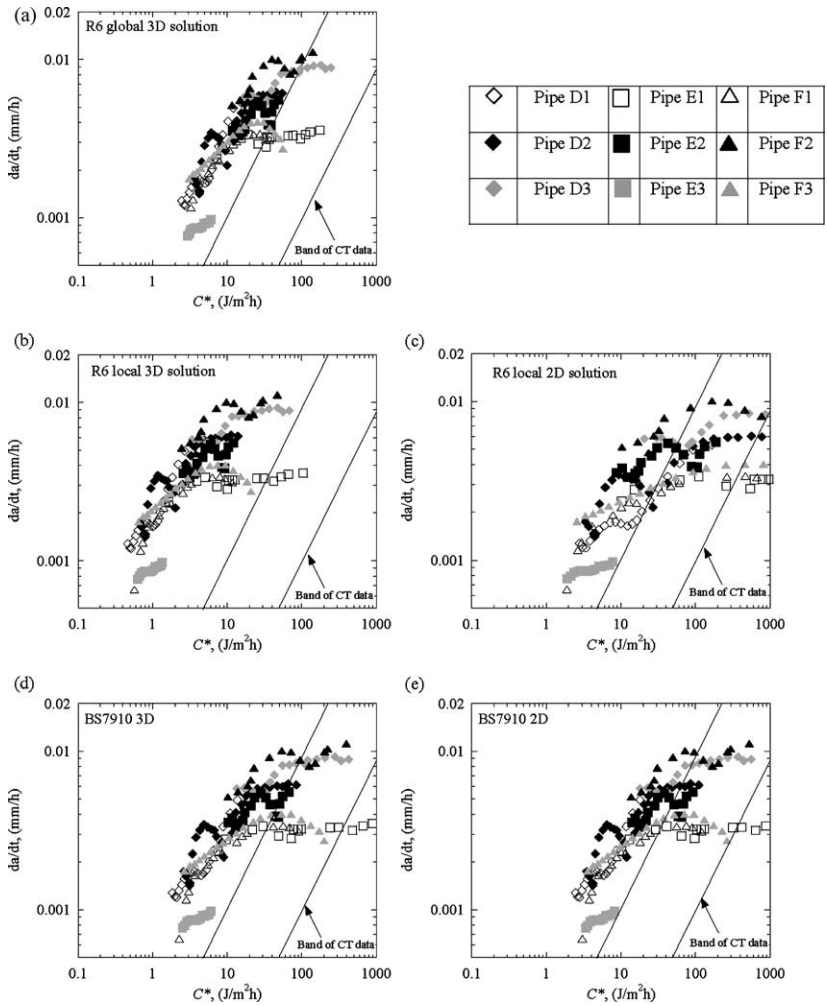


FIG. 4—*CCG rate versus C^* calculated from $n=10.0$ for a pipe compared with C(T) specimen. (a) R6 Global solution, (b) R6 Local 3D solution, (c) R6 Local 2D solution, (d) BS7910 3D solution, and (e) BS7910 2D solution.*

(see the section "Experimental Data") is examined, which is a pipe of $R_i=50.5$ mm, $R_o=63.5$ mm, crack depth $a_0=1$ mm, and crack length $c_0=25$ mm. Since the crack length-to-depth ratio of the crack (a_0/c_0) is 0.04, it is a reasonable condition to treat as an infinity long crack and to use 2D plane stress or the plane strain model to represent the crack geometry. The finite element (FE) model is shown in Fig. 5. All finite element analyses were conducted using ABAQUS 6.2 [26]. Crack growth was modeled using a nodal-release technique [6]—when damage ω reaches unity ahead of the crack tip, the node at the crack tip is released. Regular square elements were used in the vicinity of the crack tip so the crack grows through a region of uniform elements. It is assumed in the analysis that the crack grows in the plane of the initial crack front, i.e., along the symmetry plane. The model therefore assumes a sharp fronted flat crack, which idealizes the actual condition of microscopic multiple cracks linking up ahead of the main crack front. The mesh size at the crack tip is approximately 15 μm, which is close to the grain size of the C-Mn steels [6]. The mean

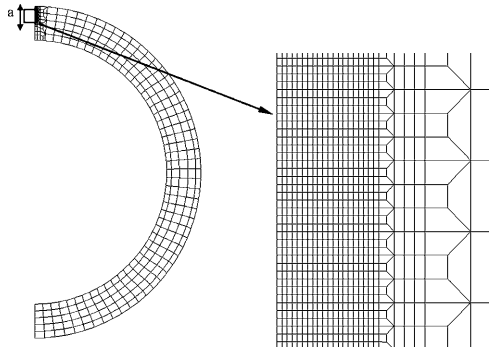


FIG. 5—*Finite element mesh of pipe for crack growth analysis.*

value of uniaxial failure strain $\varepsilon_f = 18$ %, the appropriate value of the creep exponent $n_A = 10$, were used in the analyses and elastic-plastic-creep analysis was also conducted.

Figure 6 shows CCG against time predicted under plane stress and strain conditions. The internal pressure (p) applied in this analysis is 70 MPa. Experimental data for $p = 69.3$ and 70 MPa are also plotted in Fig. 6. It is seen in Fig. 6 that the amount of the CCG predicted under plane stress conditions is close to the experimental data (slightly conservative), while under plane strain conditions the predicted amount of the CCG is less than that observed in the experiments, which is the same tendency as the prediction for the C(T) specimen [6].

Figure 7 shows the comparison of C^* at each a/W for the pipe. In this figure, C^* for the FE analysis is obtained directly from the line integral value of C^*, because Eq 4 is not appropriate for this geometry. For comparison C^* is also calculated using the reference stress solutions described in the section, "Reference Stress for Axially Oriented External Crack in Pipe." The internal pressure (p) applied in this analysis is 50 MPa, because it was possible to conduct the CCG analysis until longer crack length without numerical error for internal pressure of 50 MPa than 70 MPa. It is seen that under plane stress conditions (Fig. 7(a)) all reference stress solutions except for the R6 local 2D solution give a smaller value of C^* compared to the line integral C^* and the difference is weakly dependent on a/W. Thus the use of reference stress solutions would lead to an overestimate of CCG rate for this geometry. The R6 local 2D solutions give the lower value of C^* at small crack growth and as the crack grows, the value is close to the line integral C^*. Under plane strain conditions (Fig. 7(b)), the R6 global solution, the BS7910 3D solution, and the BS7910 2D solution give good agreement with the line integral C^* throughout the range of a/W calculated. In addition, it may be suggested that the R6 global solution gives the closest agreement with the line integral C^*. The value of C^* obtained from the R6 local 2D solution is close to the line integral C^* at a small amount of crack growth and as the crack grows, the value becomes higher than the line integral C^*. The

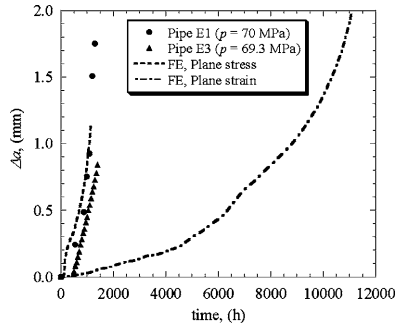


FIG. 6—*Predicted CCG against time with experimental data.*

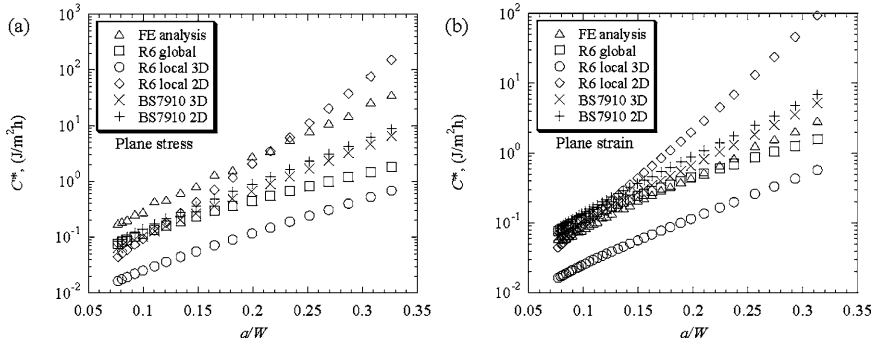


FIG. 7—*Comparison of C^* predicted from different solutions (a) plane stress and (b) plane strain conditions.*

R6 local 3D solution gives smaller value of C^* than the line integral C^* throughout the range of a/W. Thus the use of this reference stress solutions would lead to a nonconservative prediction.

Figure 8 shows the predicted CCG rate against C^* obtained from the R6 global solutions. For comparison, the experimental data for the pipes (see Fig. 4(*a*)) is also plotted in the figure. In the experimental data, the R6 global solutions are also used to calculate C^*. The FE results from the internal pressure (p) of 70 MPa are plotted in this figure, because this pressure is applied to the experimental data. It is seen that the predicted CCG rates for plane stress conditions are located in the experimental data, while the predicted CCG rates for plane strain conditions are lower than those of the experimental data. Therefore it might be suggested that the experimental conditions for these pipe are close to plane stress conditions.

Figure 9 shows the predicted CCG rate versus C^* for the pipe with the experimental data for the C(T) specimen and the pipe. The line integral value of C^* directly from the FE analysis is used to plot the FE data. For the experimental data of the pipes, the R6 global 3D solution (see Fig. 4(*a*)) was also applied. It is seen in Fig. 9 that at the same value of C^*, the predicted CCG rate under plane stress conditions is slightly higher than that under plane strain conditions. In addition the divergence of the predicted CCG rate between plane stress and plane strain conditions seen for the C(T) specimens (see [6]) is not observed. The numerical predictions for the pipe are within the band of the experimental data for the C(T) specimen but fall significantly below the experimental data for pipe.

Under plane stress conditions the R6 global solution gives about ten times smaller value of C^* than the line integral C^* in FE analysis (see Fig. 7(*a*)) and the predicted CCG rates are almost the same as those for the experimental data (see Fig. 6). Therefore in Fig. 9 the value of C^* shifts in horizontal axis from the data of R6 global solutions (see Fig. 8) and is located in the experimental data of C(T) specimens. While under plane strain conditions the R6 global solution gives almost the same values of C^* as the line integral C^*

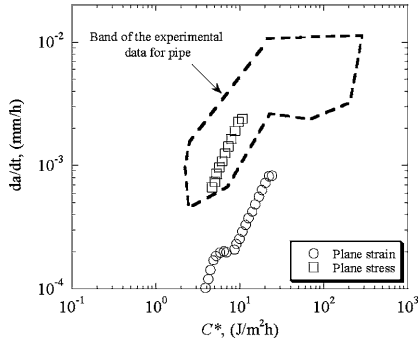


FIG. 8—*CCG rate against C^* predicted from R6 global solutions with the experimental data.*

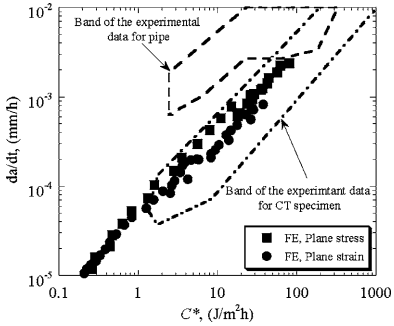


FIG. 9—*Comparison of predicted CCG rate with experimental data of pipe and C(T) specimens.*

(see Fig. 7(*b*)) and the predicted CCG rate are almost ten times lower than the experimental CCG rate (see Fig. 6). Consequently the predicted CCG rates shift in vertical axis and again are located in the experimental data of C(T) specimens.

Discussion and Conclusions

This paper presents the comparison of the reference stress solutions for pipe geometries with C(T) creep crack growth (CCG) data. Under steady state, CCG rates for the pipe are faster than those of the C(T) data at the same value of C^*. It is found that the extent of this difference depends on the reference stress solution used. The R6 Global solution gives the best correlation to the C(T) data for C-Mn steel at 360 °C.

In addition, creep crack growth in pipe is predicted numerically using a damage variable to quantify time dependent crack tip degradation under multiaxial stress conditions. A power law creep model is used to describe the constitutive behavior of the steel and both plane stress and plane strain conditions are examined using the finite element method. The amount of the CCG predicted under plane stress conditions is close to the experimental data, which is the same result for C(T) specimen [6]. The values of C^* obtained from the R6 Global solutions are also found to give the closest agreement to the FE line integral C^* under plane strain conditions within the range of $a/W=0.1-0.35$. While the values of C^* obtained from reference stress solutions is smaller than the line integral C^* under plane stress conditions. Consequently it has been found that the major differences between the CCG data for pipe and C(T) geometries is mainly due to the difference in the way C^* is derived and not due to effects of crack tip constraint.

References

[1] Hayhurst, D. R., Dimmer, P. R., and Morrison, C. J., "Development of Continuum Damage in the Creep Rupture of Notched Bars," *Philos. Trans. R. Soc. London, Ser. A*, 311, 103–129 (1984).

[2] Hyde, T. H., Sun, W., and Becker, A. A., "Creep Crack Growth in Welds: A Damage Mechanics Approach to Predicting Initiation and Growth of Circumferential Cracks," *Int. J. Pressure Vessels Piping*, 78, 765–771 (2001).

[3] Bellenger, E. and Bussy, P., "Phenomenological Modelling and Numerical Simulation of Different Modes of Creep Damage Evolution," *Int. J. Solids Struct.*, 38, 577–604 (2001).

[4] Perrin, I. J. and Hayhurst, D. R., "Continuum Damage Mechanics Analyses of Type IV Creep Failure in Ferritic Steel Cross-Weld Specimens," *Int. J. Pressure Vessels Piping*, 76, 599–617 (1999).

[5] Bassani, J. L. and Hawk, D. E., "Influence of Damage on Crack-Tip Fields Under Small-Creep Conditions," *Int. J. Fract.*, 42, 155–172 (1990).

[6] Yatomi, M., Nikbin, K. M., and O'Dowd, N. P., "Creep Crack Growth Prediction Using a Damage Based Approach," *Int. J. Pressure Vessels Piping*, 80, 573–583 (2003).

[7] BRITE/EURAM Collaborate Project, "Creep Crack Growth in Carbon Manganese at 320–400°C," 1994–1998.

[8] BS7910, "Guide on Methods for Assessing the Acceptability of Flaws in Fusion Welded Structures," BSI, London, 2000.
[9] R5-British Energy, "Defect Assessment Code of Practice for High Temperature Metallic Components," British Energy Generation Ltd., 2000.
[10] Webster, G. A. and Ainsworth, R. A., *High Temperature Component Life Assessment*, Chapman and Hall, London, 1993.
[11] ASTM Standard E1457-01, "Standard Test Method for Measurement of Creep Crack Growth Rates in Metals," ASTM International, West Conshohocken, PA, 2002.
[12] Ainsworth, R. A., "Some Observations on Creep Crack Growth," *Int. J. Fract.*, 20, 147–159 (1982).
[13] Ainsworth, R. A., "The Assessment of Defects in Structure of Strain Hardening Materials," *Eng. Fract. Mech.*, 19, 633–642 (1984).
[14] Penny, R. H. and Marriott, D. L., *Design for Creep*, McGraw-Hill, London, 1971.
[15] Miller, A. G., "Review of Limit Loads of Structures Containing Defects," *Int. J. Pressure Vessels Piping*, 32, 197–327 (1988).
[16] Nikbin, K. M., Yatomi, M., Wasmer, K., and Webster, G. A., "Probabilistic Analysis of Creep Crack Initiation and Growth in Pipe Components," *Int. J. Pressure Vessels Piping*, 80, 585–595 (2003).
[17] Nikbin, K. M., Smith, D. J., and Webster, G. A., "Prediction of Creep Crack Growth from Uniaxial Creep Data," *Proc. R. Soc. London, Ser. A*, 396, 183–197 (1984).
[18] Rice, J. R., "Mathematical Analysis in the Mechanics of Fracture," in *Treatise on Fracture*, edited by H. Liebowitz, Vol. 2, Academic Press, New York, 1968.
[19] Sim, R. G., "Evaluation of Reference Parameter for Structures Subject to Creep," *J. Mech. Eng. Sci.*, 13, 47–50 (1971).
[20] Miller, A. G., "Review of Limit Loads of Structures Containing Defects," *Int. J. Pressure Vessels Piping*, 32, 197–327 (1988).
[21] R6, Assessment of the integrity of structures containing defects, Revision 3, British Energy Generation, 2000.
[22] Wasmer, K., Nikbin, K. M., and Webster, G. A., "Creep Crack Initiation and Growth in Thick Section Steel Pipes Under Internal Pressure," *Int. J. Pressure Vessels Piping*, 80, 489–498 (2003).
[23] Results from the "Creep Crack Growth in Carbon-Manganese," Brite/Euram Collaborative Project, European Commission 1994–1998.
[24] Maskell, R. V., Fleming, A., Crawford, P. J., and Buchanan, L. W., "Creep Crack Growth in Internally Pressurised Tubes," *Mater. High. Temp.*, 15(3/4), 151–158 (1998).
[25] Cocks, A. C. F. and Ashby, M. F., "Intergranular Fracture During Power-Law Creep Under Multiaxial Stress," *Met. Sci.*, 14, 395–402 (1980).
[26] *ABAQUS version 6.2*, Hibbitt, Karlsson & Sorensen, Inc., 2002.

Journal of ASTM International, January 2006, Vol. 3, No. 1
Paper ID JAI13411
Available online at www.astm.org

Hyeong-Yeon. Lee[1] *and Kamran M. Nikbin*[2]

Modelling the Redistribution of Residual Stresses at Elevated Temperature in Components

ABSTRACT: In this study the effects of high temperature relaxation on the residual stresses has been examined for T-plate and tubular T-joint geometries by numerical analysis using elasto-plastic-creep finite element modelling. It is shown that residual stresses are important, especially at the early stages of lifetime before the residual stresses relax rapidly. A sensitivity analysis was carried out by varying the creep properties and geometric constraint under plane stress and plane strain conditions. A comprehensive residual stress profile derived from measured residual stresses of a range of steels and different geometries that have been welded, cold bent, repair welded, or overloaded, was used as a 'Master curve' of the residual stresses. In all cases compared, it has been shown that the transverse measured residual stresses were tensile at the surface The stress intensity factor (SIF) estimates using the master curve profile for the T-Plate, and tubular T-joint geometries are lower compared to current case specific residual stress profiles used in R6 and BS7910 procedures but is still sufficiently conservative when compared with experimental measured residual stress data. It has also been shown that the numerically calculated residual stresses induced by overload in this study compare well at the surface with the master curve but decrease more rapidly with respect to crack depth compared to experimental values. Furthermore, by considering creep stress relaxation rates from the present FE calculations, it is shown that the peak surface residual stresses drop rapidly to about 50 % at the relatively short duration of the first 1000 h. The SIF values of the predicted residual stresses are found to be lower than the experimentally measured data, and they are also found to be insensitive to stress relaxation in the through depth of the T-plate and tubular T-joint geometries. It was shown that the master curve gives an overall conservative SIF, though reduced, for the weld residual stresses as well as for residual stresses derived from overload. Furthermore, where redistribution of the residual stresses is concerned, it is shown that present profiles may all be unduly conservative in their SIF estimations.

KEYWORDS: Residual stress, Redistribution, Creep, Stress intensity factors, Overload, T-plate, Tubular T-joint, R6, BS7910

Introduction

The effect of residual stresses on component life needs to be accounted for within the life assessment procedures. If the operating temperature of the component is in the creep regime, the redistribution effect of the residual stresses should be taken into account in the assessment. It is important that such stresses are considered in safety assessment procedures such as the UK structural integrity procedures, R6 [1] and BS7910 [2]. Since information on residual stress distributions often is not directly available, compendia with recommended (upper-bound) residual stress profiles for use in an integrity assessment are included in R6 and BS7910.

A comprehensive residual stress profile was proposed [3,4] derived from a range of steels and different geometries that have been welded [5], cold bent [6], repair welded, or overloaded.

Manuscript received 15 April 2005; accepted for publication 22 June 2005; published January 2006. Presented at ASTM Symposium on Fatigue and Fracture Mechanics: 35th Volume on 18-20 May 2005 in Reno, NV.
[1] Mechanical Engineering Division, Korea Atomic Energy Research Institute Dukjindong 150 Yuseong 305-606 Daejeon, South Korea, hylee@kaeri.re.kr.
[2] Department of Mechanical Engineering, Imperial College London, South Kensington Campus, London, SW7 2AZ United Kingdom, k.nikbin@imperial.ac.uk.

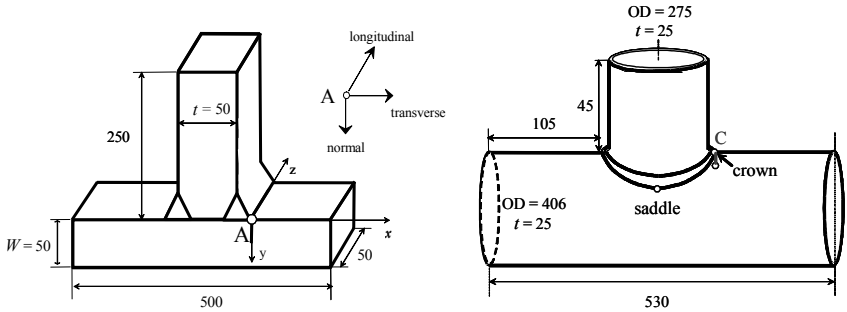
Copyright © 2005 by ASTM International, 100 Barr Harbor Drive, PO Box C700, West Conshohocken, PA 19428-2959.

Stress profiles collated from data available in the public domain for various types of weld geometries [5] were also examined in this study. The measured data cover a range of conditions such as materials, measurement methods, plate thicknesses, weld heat input, and boundary restraints. The materials included in the present geometries are ferritic, austenitic, C-Mn, and Cr-Mo steels. The measurement methods used include neutron diffraction, X-ray diffraction, hole-drilling and sectioning, block removal, trepanning, and slotting [5].

In this study, the redistribution behaviors of the residual stresses at high temperatures for a T-plate and tubular T-joint have been modelled numerically and compared to experimental measurements. The residual stresses were generated by modelling overload using material properties of 316H stainless steel exposed at 550°C in two components (a T-plate and a tubular T-joint). Subsequent relaxation analyses were performed for periods of up to 10 000 h.

Comprehensive Residual Stress Profile for Welded Joints

The two geometries used for the stress intensity factor (SIF) calculations are T-plate and tubular T-joint as shown in Fig. 1. In addition to the two weld geometries, five more cases – tubular Y, tube-on-plate, bent pipe, pipe butt weld, and repair weld – were taken into account in derivation of a comprehensive residual stress profile.

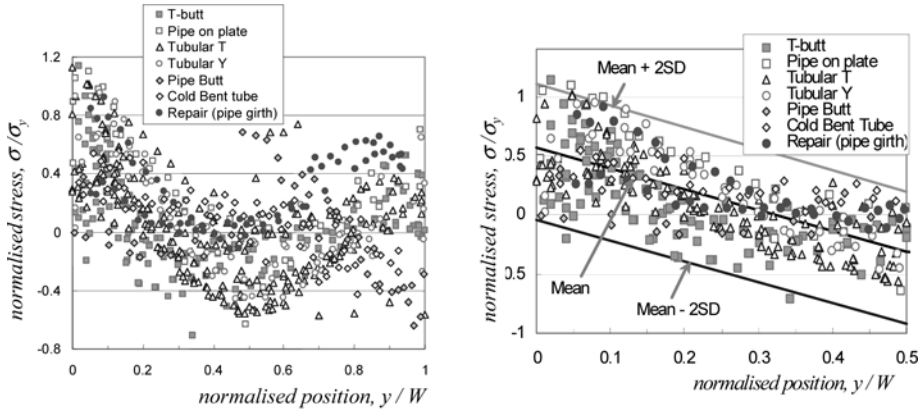


a) T-plate b) tubular T-joint

FIG. 1—*Geometry of welded components, all dimensions in mm.*

Measured Residual Stresses

Data from the geometries described above have been compared and presented in Fig. 2*a*, which includes the transverse residual stresses for a range of geometries and materials [5–7] normalized with their respective yield stresses. It may be seen that when the measured data are considered for up to y/W=0.5 (half of specimen thickness), the stress distributions are well represented using a straight line as shown in Fig. 2*b*. The region of interest for life assessment is the short crack region starting at the surface, and therefore y/W=0.5 is usually well beyond safety margins that will be considered in any life assessment procedure.



a) Dataset for full thickness b) Dataset for half thickness

FIG. 2—*Transverse residual stresses measured for a range of weld geometries and other cases.*

Statistical Analysis of the Measured Data

For the region of $y/W \leq 0.5$ shown in Fig. 2*b* it can be seen that all the data can be conveniently described by a linear regression line which contains a relatively large scatter. The variability of the data can be attributed to the differences in the geometry and materials as well as to a great extent to the scatter in the measurements of residual stresses, which in some cases could be as much as ±30 %. Given the wide variability, it would therefore be feasible to simplify the data to a linear relationship as shown in Fig. 2*b*. Figure 2*b* shows the best fit mean values for all the data and the upper/lower bound lines at two standard deviations (2SD). The SD value in Fig. 2*b* was calculated to be 0.26. The normalized linear mean line, for all the data shown in Fig. 2*b* is given by:

$$\hat{\sigma} = -1.76x + 0.57 \tag{1}$$

where $\hat{\sigma} = \sigma/\sigma_y$ and $x = y/W$, and σ is the stress, and σ_y is the yield stress.

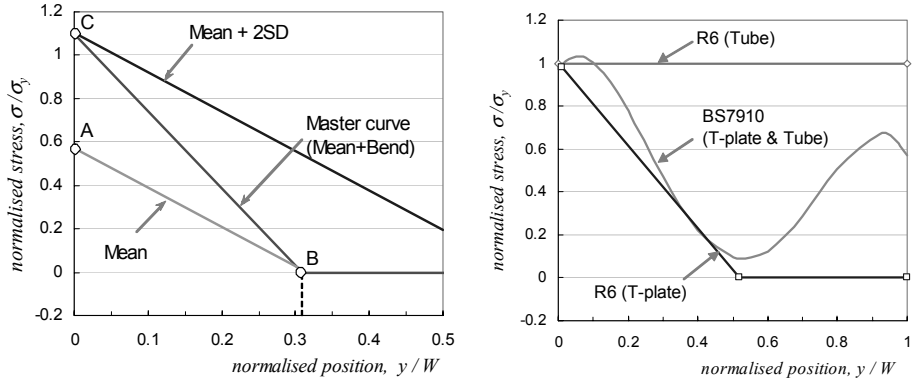
Derivation of 'Master Curve'

The mean fit form of Eq 1 indicates that the normalized mean curve is composed of a membrane (uniform) stress component of 0.57 and a bending (linear) stress with a slope of 1.76. So Fig. 3*a* can represent Fig. 2*b* using Eq 1 to derive two profiles. These consist of the linear fits of 'Mean + 2SD (standard deviation)' and 'Mean + Bend' as shown in Fig. 3*a*. The first line of 'Mean + 2SD' is obtained by shifting the membrane stresses as much as 2SD from the mean regression line of Eq 1. The second line of 'Mean + Bend' is obtained by rotating the bending stress from pivot point 'B' of Fig. 3*a* so that surface residual stress (point 'A') may be shifted as much as 2SD to point 'C' in Fig. 3*a* at the surface. It means that shifting of membrane stress as much as 2SD was given for 'Mean + 2SD' line, while shifting of bending stress as much as 2SD at the surface was given for 'Mean + Bend' profile. In the present study, this 'Mean + Bend' line

is termed as 'Master curve' for weld residual stresses. In 'Master curve' profile, any negative stress after point B in Fig. 3*a* is set as zero. The coordinate of point B in Fig. 3*a* is (0.31, 0). This profile was determined from a sensitivity analysis on changing the membrane and bending components and the corresponding SIFs.

The residual stress profiles for T-plate and tubular T-joint in the assessment procedures of R6 and BS7910 are shown in Fig. 3*b*. When R6 profile is compared with that of the present 'Master curve' for T-plate, they seem to be similar. However, it should be noted that the R6 profile is function of material properties (yield strength, thermal expansion coefficient, Young's modulus, density, specific heat, etc.) and welding conditions (weld travel speed and process efficiency), whereas the present 'Master curve' is only function of coordinate (y-axis in Fig. 1*a*) along the thickness direction. 'Master curve' was derived from a range of geometries, materials, and other sources of residual stress such as machining or metal forming. Therefore, this simple 'Master curve' is applicable to those cases.

BS7910 profile expressed as summation of polynomials of coordinate [2] is also only function of coordinates, but it is very conservative as shown in Fig. 3*b* because it is an upper bound fit to experimental data [8–10]. In addition, it should be noted that the residual stresses at the surface are always equal to yield stress, while those for 'Master curve' are be higher than yield stress.



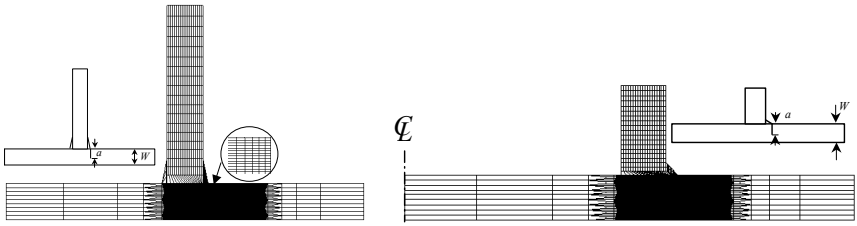
a) Master fits from statistical treatment b) Distribution of R6 and BS7910

FIG. 3—*Residual stress distributions for T-plate and tubular T-joint.*

Finite Element Model

The stress intensity factors for the two geometries in Fig. 1 have been determined using finite element (FE) analysis in conjunction with the superposition method as discussed in [7,10]. The FE meshes used in this work are illustrated in Fig. 4. A total of 13 540 linear elements and 14 094 nodes were used, and the smallest element size is 0.03 mm (6×10^{-4}W) for the T-plate mesh as shown in Fig. 4*a*. The tubular joint is a three dimensional geometry, but here it is represented by an axisymmetric, 'tube on disc' FE mesh as illustrated in Fig. 4*b*. A total of 13 534 linear elements and 14 091 nodes were used, and the smallest element size is 0.015 mm (6×10^{-4}W).

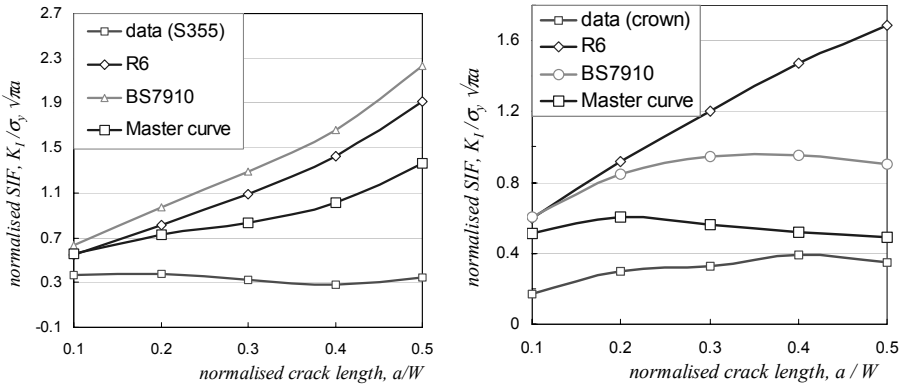
All FE analyses were carried out using ABAQUS [11]. As discussed in [7,10], only the crack surface stresses need to be considered as the loading condition in the calculation of the stress intensity factor (SIF) based on the superposition principle is assumed to be the same through thickness. Only transverse residual stresses are considered, and the mode I SIFs have been evaluated. The postulated crack is shown at weld toe 'A' for T-plate and 'C' for tubular T-joint as shown in Fig. 1.



a) T-plate b) Representation of tubular T- joint

FIG. 4—*Finite element meshes used in stress intensity factor calculation.*

The SIFs obtained using the recommended distributions of R6, BS7910, and 'Master curve' are shown in Fig. 5*a* for the T-plate and in Fig. 5*b* for the tubular T-joint. For the T-plate, the BS7910 distribution is the most conservative, and the 'Master curve' gives less conservative SIFs than BS7910 and R6 as shown in Fig. 5*a* when comparing with the SIF due to the measured distributions. For the tubular T-joint, 'Master curve' again gives less conservative SIFs than R6 and BS7910 as shown in Fig. 5*b*. From these results, it is clear that 'Master curve' is a simple profile for weld residual stresses but less conservative than existing distributions of R6 and BS7910.



a) T-plate b) tubular T-joint

FIG. 5—*Stress intensity factors due to residual stresses.*

Modelling the Residual Stresses at High Temperature

Figure 2 includes data from bent pipes as well as weld residual stresses. Hence, it can be argued that where there are tensile surface residual stresses (regardless of how they were produced) in the transverse direction of a range of components, then the in depth stress profiles will have a similar trend in the first half thickness of the specimen. Therefore, by modelling tensile residual stresses by plastically overloading the component, it could be comparable to residual stress distributions that are found in as welded components. Furthermore, the model can be used to estimate residual stress redistribution at high temperatures. The modelling for this procedure is shown below for a T-Plate for a range of conditions.

Generation of Residual Stresses by an Overload

Residual stresses may be generated due not only to welding but also to excessive plastic deformation under an overload, machining, or forming. As an example, Fig. 6 shows schematically the residual stresses that can be generated in the T-plate under a four point bend (4PB) beam overloading and unloading. When the T-plate is sequentially loaded and unloaded at high temperatures, residual stresses are developed, and when hold time is applied, the residual stresses will relax, and redistribution of the stresses will occur. In this work, ABAQUS [11] was used for an elasto-plastic-creep analysis, and a kinematic hardening model in combination with Norton's creep law was used. The tensile properties [12,13] used for the present 316H stainless steel are shown in Table 1. In this work, kinematic hardening model was used for elasto-plastic analysis, and the properties used in the kinematic hardening model are shown in Table 2. The model is known to be appropriate for the elasto-plastic simulation under cyclic load conditions of the 316H stainless steel structure which shows cyclic hardening or softening [14–16].

Residual stresses were generated for the T-plate using two models. One is four point bend (4PB) beam model, and the other is a simplified cantilever beam model as shown in Fig. 6. After applying overload at two points of the 4PB model, the loads were removed. Subsequent to this, the residual stresses for each model will be generated as shown in Fig. 7.

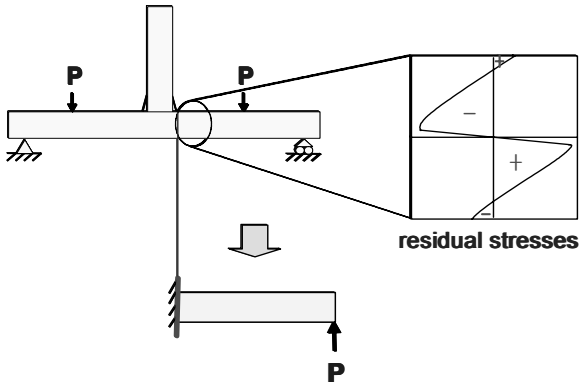


FIG. 6—*Modelling of T-plate as Four Point Bend(4PB) beam and Cantilever beam model.*

TABLE 1—*Tensile properties for ex-service 316 H at 550°C [13].*

E (GPa)	σ_Y (MPa): 0.2 %	σ_{UTS} (MPa)
130	190	595

TABLE 2—*Kinematic hardening model for ex-service 316 H at 550°C [13].*

Plastic Strain	True Stress (MPa)
0.0	190
0.296	589.2

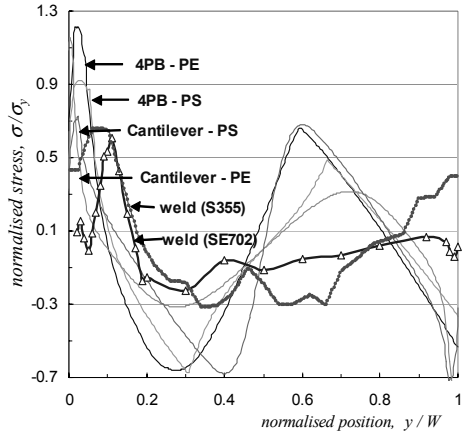


FIG. 7—*Residual stresses due to overload and welding.*

For the cantilever beam model, a concentric end load was applied and removed to obtain the residual stresses as shown in Fig. 6. For each model, the thickness effects were investigated for the cases of a plane strain (PE) and plane stress (PS) condition. The analysis results for 4PB model has shown that highest peak occurred in the case of 'plane strain' (4PB-PE) near the surface as shown in Fig. 7. The distributions for the 4PB plane stress (4PB-PS) were flatter with lower magnitudes than those for the 4PB-PE as shown in Fig. 7.

For the cantilever beam model, it was shown that its residual stress distribution tended to give lower values than those of the 4PB model. In Fig. 7, plane strain condition gave higher peaks with a narrower width (in through depth) than plane stress condition. In order to generate residual stress profiles (along y axis in Fig. 1) shown in Fig. 7, concentric forces of 3000 N at two points for 4PB model have been applied and concentric forces of 7000N as shown in Fig. 6 for the cantilever beam model (of T-plate) has been applied, which shows that the cantilever beam model requires higher concentric forces.

The calculated residual stress distributions, due to an overload, for the four cases (4PB-PE, 4PB-PS, cantilever-PE, cantilever-PS) shown in Fig. 7 are comparable to the experimental 'Master curve' in Fig. 2*b*. It is seen that the present residual stress distributions using overload are within the range of experimental scatter of the data in Fig. 2*b*.

Redistribution of the Residual Stresses

The redistribution analysis of the residual stresses due to an overload was carried out with a kinematic hardening model and the Norton's creep law. In this analysis the following power-law Norton's creep equation was used.

$$\dot{\varepsilon} = A\sigma^n \tag{2}$$

where the material constants A and n are given as A=5.3e-26, n=8.2 in the RCC-MR [12], A=7.23e-32, n=10.62, taken from the British Energy (BE) data [13], which were shown in Fig. 8.

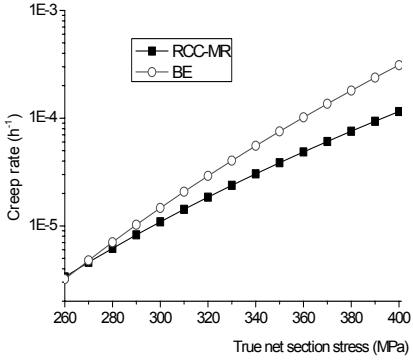


FIG. 8—*Power-law creep uniaxial creep rates for 316H SS [13].*

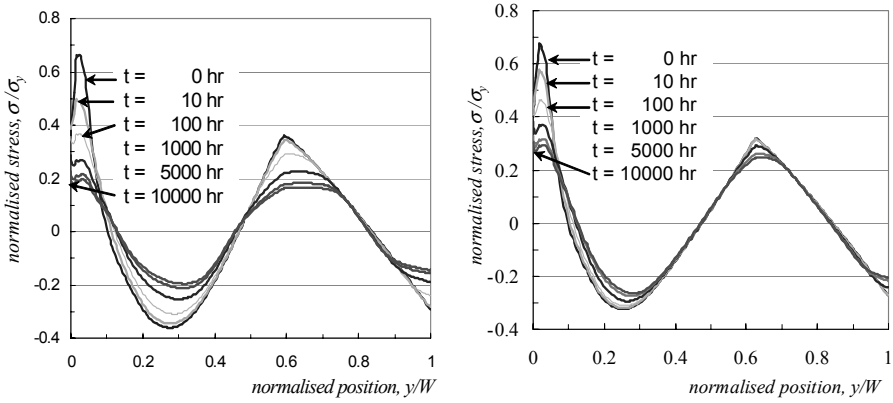
A sensitivity analysis with the above two creep properties for the type 316H stainless steel was carried out for the T-plate using the 4PB model and the cantilever beam model, and the tubular T-joint. The redistribution analysis of the T-plate using the 4PB model was carried out for the cases of plane strain (PE) and plane stress (PS). The hold time at the temperature of 550°C was up to 10 000 h (1.14 years).

For the 4PB-PE model, the peak residual stresses using the RCC-MR creep properties relaxed by as much as 70 % (from 226 to 68 MPa) while those for the British Energy (BE) data were relaxed by 56 % (from 234 to 102 MPa) for the PE condition after 10 000 h of hold time as shown in Fig. 9. It should be noted that 84 % of the total relaxation occurred during the first 1000 h for the PE condition of the 4PB model, which means the peak residual stresses drop rapidly at a relatively short time.

For the 4PB-PS model, it was shown that the peak residual stresses for the RCC-MR creep properties were relaxed by 68 % while those for the BE were relaxed by 54 % as shown in Fig. 10. The results show that the BE properties cause a lesser relaxation than those of the RCC-MR, and the plane strain condition causes a higher and narrower peak near the surface as shown in Figs. 9 and 10.

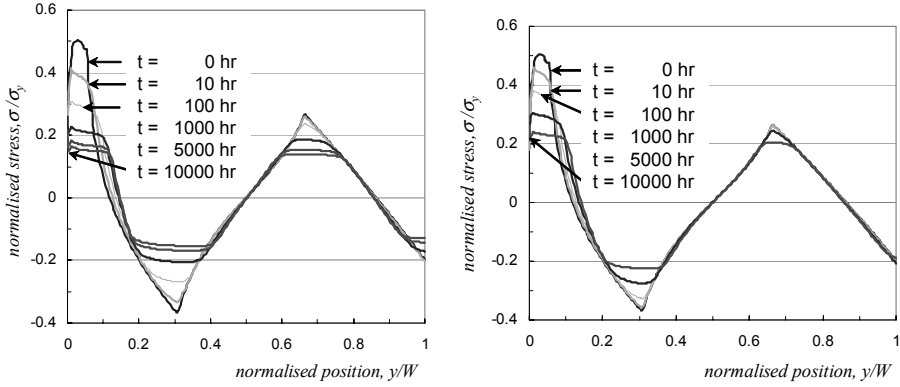
The redistribution analysis of the T-plate using cantilever beam model was also carried out for the PE and PS condition. The results showed that the peak residual stresses for the RCC-MR creep properties relaxed by as much as 71 % (from 219 to 62 MPa) for a plane strain as shown in

Fig. 11*a*, while those for a plane stress were relaxed by 65 % (from 137 to 47 MPa) after 10 000 h of a hold time. The redistribution analysis results for the tubular T-joint showed that the peak residual stresses near the surface were relaxed by 70 % (from 214 to 64 MPa) for the RCC-MR creep properties as shown in Fig. 11*b*, while those for BE creep properties were relaxed by 54 % after 10 000 h of a hold time. Figure 11 shows that a rapid redistribution occurs near the surface, and the stress distributions for cantilever model and tubular T-joint model are symmetric from the normalized position of a/W ≈0.50.



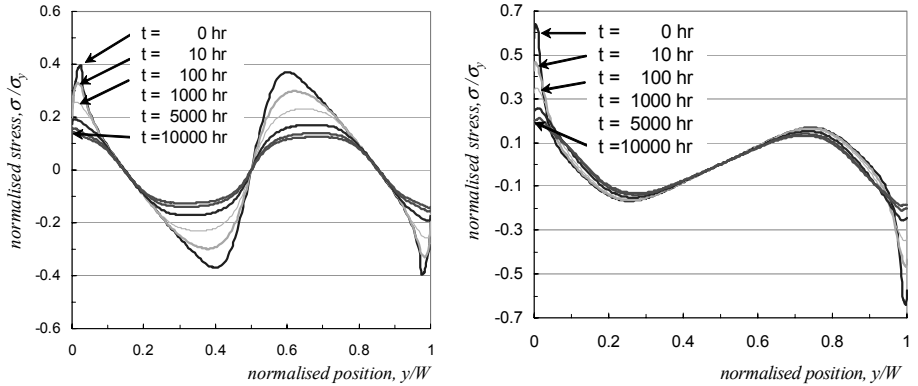
a) RCC-MR creep property b) BE creep property

FIG. 9—*Relaxation behavior of four point bend beam model in plane strain condition.*



a) RCC-MR creep property b) BE creep property

FIG. 10—*Relaxation behavior of four point bend beam model in plane stress condition.*



a) Cantilever beam model (plane stress) b) Tubular T-joint (RCC-MR)

FIG. 11—*Relaxation behavior.*

It should be noted that the data for S355 and SE702 are for ferritic steels, whereas the material properties used in the FE calculations are from 316H stainless steel. This should not be an important factor as it has been shown that the normalized stresses in the 'Master curve' taken from Fig. 2*b*, covers residual stresses due to welding and overload for a range of materials [3,4]. Hence, the same form of argument has been adopted for the numerical cases which disregard differences in geometry and material properties when the stresses are normalized with yield stress versus normalized crack length.

Statistical Treatment of the Numerical Residual Stress Data

It has been shown that material properties, boundary conditions, geometry, and loading will produce a 'scatter' of numerical data as shown in Fig. 7. Therefore, in much the same manner that the measured experimental data in Fig. 2 were treated, a statistical analysis has been carried out for all numerical results. The intersection point of 'A' in Fig. 12 was determined to be the point where the mean (best estimate) line enters compressive stress (zero stress axis) and the intersection points of the mean lines for '0', '1000,' and '10 000' h were located between y/W=0.145 and 0.146. So the intersection point 'A' was selected as a/W=0.15 in this work. This is the concept used in the determination of the intersection point 'B' for 'Master curve' of weld residual stress [3,4].

Since the data in Fig. 7 drop from a peak tensile stress up to around $y/W=0.3$, dataset up to $y/W \leq 0.3$ were sampled for statistical analysis of the numerical data. The analysis results are shown in Table 3, which shows that as hold time is increased, values of standard deviation (SD) decrease, suggesting a reduction in scatter. The mean fits of the numerical results for 0, 1000, and 10 000 h are shown in Fig. 12. The 'Mean+Bend' profiles with the hold time of 0, 1000, and 10 000 h were derived by adding 2SD as was done for 'Master curve' for experimental data. It is clear from Table 3 and Fig. 12 that the peak residual stresses at surface tend to decrease as hold time increases.

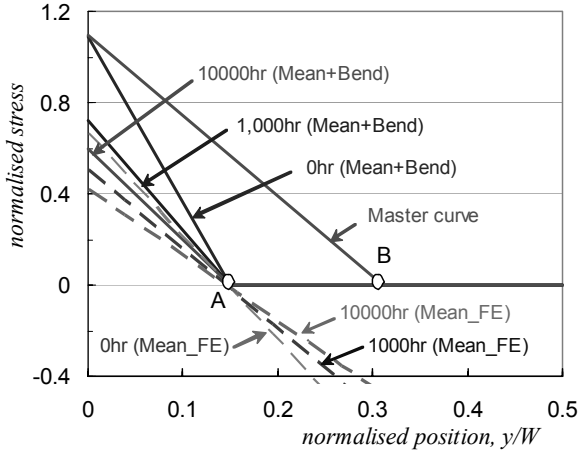


FIG. 12—*Comparison of experimental 'Master curve', and 'Mean+Bend' profiles for 0, 1000, and 10 000 hold-time at 550°C.*

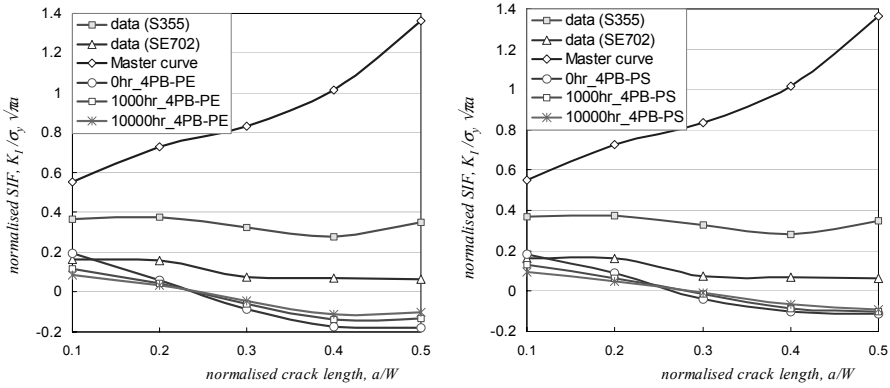
TABLE 3—*Statistical analysis of residual stress data.*

Hold time (h)	Standard Deviation (SD)	Normalized residual stress at surface (weld toe), σ / σ_y
0	0.21	1.09
1000	0.11	0.72
10 000	0.09	0.60
Master curve (Fig. 4*b*)	0.26	1.10

Analysis to Derive SIF from Stress Profiles

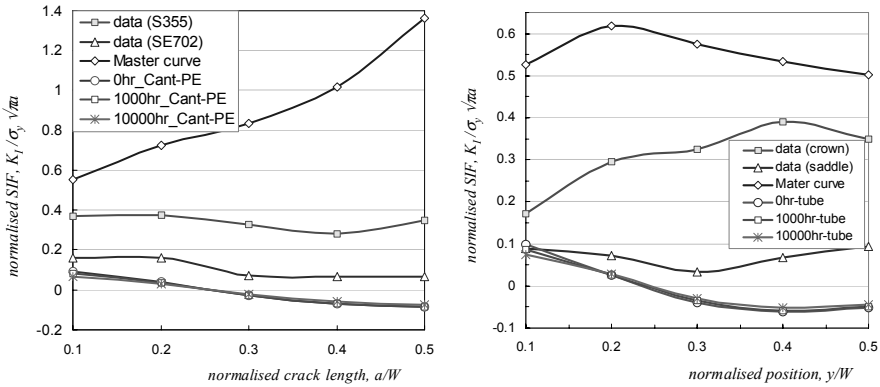
The stress intensity factors were calculated for the experimental 'Master curve' (Fig. 3*a*), each numerical residual stress distribution (Fig. 7), and 'Mean+Bend' lines at each stage of hold times (Fig. 12). The analysis results for 4PB-PS model show that the SIFs calculated for the hold time of 0 to 10 000 h were below the lines due to data (S355) and data (SE702) as shown in Fig. 13, which are the SIFs due to the measured residual stress distribution for the T-plate. S355 and SE702 are ferritic steels used for fabrication of the T-plates [7–9], of which residual stresses were measured. The SIF results for cantilever model of T-plate is similar to the 4PB model as shown in Fig. 14*a*, but the SIF results for tubular T-joint tend to decrease as crack length increases as shown in Fig. 14*b*.

Finally, as shown in Fig. 15, the residual stress profiles of the 'Mean+Bend' derived for the calculated overload at 0, 1000, and 10 000 h of hold time were used to calculate the SIF values for the four point bend beam model. When compared to the 'Master curve' based on the experimentally measured dataset, it was shown that the 'Master curve' is conservative as a whole but less conservative than the R6 or BS7910 profile for the present geometries.



a) plane strain b) plane stress

FIG. 13—*Calculated stress intensity factors due to redistributed residual stresses for four point bend beam model.*



a) Cantilever beam model b) tubular T-joint

FIG. 14—*Calculated stress intensity factors due to redistributed residual stresses for four point beam model.*

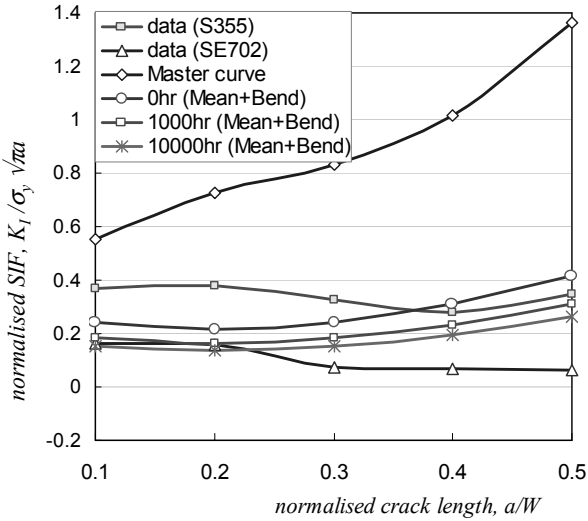


FIG. 15—*Calculated stress intensity factors due to 'Master curve' and 'Mean+Bend' profiles (at each stage of relaxation for four point bend beam model, plane strain condition).*

Discussions and Conclusions

The redistribution of the residual stresses due to overloading the specimen at an elevated temperature for a T-plate and tubular T-joint has been examined using numerical modelling. The results have been compared to a residual stress profile (called the 'Master curve') derived from the 'Mean+Bend' line of experimentally measured residual stress distributions for a range of geometries, materials, and fabrication processes. Essentially, it has been found where tensile transverse residual stress distributions exist in the geometry the trend for the stress profile in depth (normalized with yield stress) can be simplified in the first half depth of the geometry to a linear mean+bend stress combination. This is irrespective of the mode of inducing the residual stress. From the experimental measurements a statistically derived 'Master curve' is deduced, and the stress intensity factor (SIF) estimates for the T-plate and tubular T-joint geometries were derived. It has been shown that the SIF calculations using the 'Mater curve' are less conservative than current profiles proposed in the R6 and BS7910 and yet contain reasonable conservatism when compared to measured data. The use of this generic bi-linear profile is appropriate in the cases where there is insufficient information on weld procedures or residual stress profiles.

Based on the assumptions stated above, numerical overload predictions derived from the transverse residual stresses for the T-plate and tubular T-joint were examined. For the present study, they were found to show similar trends to the 'Master curve' at the surface but drop more rapidly with crack depth than experimental measurements. Furthermore, following the overload a creep redistribution analysis of the T-plate under the four point bend model was carried out for the cases of plane stress, plane strain, and different creep properties over the hold time of 0, 1000, and 10 000 h at the temperature of 550°C. It was shown that after 10 000 h, the peak residual stresses for the RCC-MR creep properties relaxed by 70 %, while those for the properties from

the British Energy data dropped by 56 % for the plane strain condition and four point bend (4PB) loading. It has also been shown that 84 % of total relaxation occurred during the first 1000 h in case of plane strain condition of the 4PB model, suggesting that the peak residual stress drops rapidly in a relatively short time.

The redistribution analysis of the T-plate using a cantilever beam model was also carried out for the cases of a plane stress and plane strain condition, and similar results to those for the 4PB model were obtained. It was shown that the residual stresses relaxed more rapidly for a plane stress condition. The redistribution analysis for the tubular T-joint was also carried out for a 0, 1000, and 10 000 h of hold time, and a similar trend in the relaxation behavior to those of the T-plate was obtained. It was found that the results were relatively insensitive to creep relaxation and hold times.

The SIF values due to the best fit stress profiles from the numerical predictions at different hold times were shown to be within the variations seen from experimentally measured profiles. Furthermore, the SIF values due to overloaded residual stresses were lower than those from the 'Master curve' based on the experimentally measured data. This suggests, for the present wide range of conditions considered, that the experimental 'Master curve' is less conservative when compared to the R6 and BS7910 case specific profiles but is, however, sufficiently conservative for life assessment predictions both for initial residual stresses resulting from welding or plastic overloading. Furthermore, it is suggested that if subsequent creep relaxation in the component is not accounted for, the present residual stress profiles are likely to be overly conservative.

References

[1] British Energy Generation Ltd, 2001, *Assessment of the Integrity of Structures Containing Defects*, R6 Rev. 4. British Energy Generation Ltd, UK.

[2] British Standard Institution, 2000, *Guide on methods for assessing the acceptability of flaws in metallic structures*, BS7910: 1999 (Rev. March 2000) British Standards Institution, London, UK.

[3] Lee,H.Y., Nikbin,K.M, 2004, "Simplified method for profiling residual stress distributions in plate and pipe components," Proceedings IPC 2004, International Pipeline Conference, Oct. 4-8, Calgary,Aberta,Canada.

[4] Lee,H.Y., Nikbin,K.M., D'Dowd, N.P., 2005, "A generic approach for a linear elastic fracture mechanics analysis of components containing residual stress," *International Journal of Pressure Vessel and Piping*, in press.

[5] Bate, S., Green, D., Buttle, D.,1995, "A review of residual stress distributions in welded joints for the defect assessment of offshore structures, " AEA Technology, OTH95-482.

[6] Kwon, O., Pathiraj, B., Nikbin, K.M., 2001, "Effects of residual stress in creep crack growth analysis of cold bent tubes under internal pressure," *International Journal of Pressure Vessel and Piping*, Vol. 78, pp.343-350.

[7] Lee,H.Y., Biglari, F., Wimpory, R., O'Dowd, N.P., Nikbin, K.M., 2004, "Treatment of residual stresses in life assessment procedures," Submitted to *ASTM International Journal*.

[8] Wimpory, R., May, P., O'Dowd, N.P. Webster, G., Smith, D., and Kinston, E., 2003, "Measurement of residual stresses in T-Plate Weldments" *Journal of Strain Analysis*, 38 (4), pp. 3469-365, 2003.

[9] May, P., 2002, *Effect of welding residual stresses on the fracture resistance of ductile steels,* PhD Thesis, Imperial College London.

[10] O'Dowd, N.P., Nikbin, K.M., Lee, H-Y., Wimpory, R. and Biglari, F., 2004, "Stress

Intensity Factors due to residual stresses in T-plate welds," *J PVT*, ASME, Vol. 126.
[11] Hibbitt, Karlsson and Sorensen Ltd., 2003, ABAQUS, *version 6.3*.
[12] RCC-MR, 1985, Design and construction rules for mechanical components of FBR nuclear islands, Technical Appendix A3, AFCEN.
[13] Bettinson, A.D., 2001, "The influence of constraint on the creep crack growth of 316H stainless steel," Ph.D Thesis, Imperial College London.
[14] Lemaitre, J., Chaboche, J-L., 1990, *Mechanics of Solid Materials*, Cambridge university press.
[15] Lee, H.Y., Kim,J.B., Lee,J.H., 2003, "Thermal ratcheting deformation for 316L stainless steel cylindrical structure under moving temperature distribution," *International Journal of Pressure Vessel and Piping*, Vol. 80, pp.41-48.
[16] Lee, H.Y., Kim,J.B., Lee,J.H., 2004, "Evaluation of Progressive Inelastic Deformation for the Welded Structure Induced by Spatial Variation of Temperature," *International Journal of Pressure Vessel and Piping*, vol. 81. No. 5, pp. 433-441.

Creep Modeling

Journal of ASTM International, January 2006, Vol. 3, No. 1
Paper ID JAI13375
Available online at www.astm.org

Woo-Gon Kim,[1] *Song-Nam Yoon,*[2] *Woo-Seog Ryu,*[1] *Seon-Jin Kim,*[3] *and Won Yi*[2]

Probabilistic Analysis of the Creep Crack Growth Rate of Type 316LN Stainless Steel by the Monte Carlo Simulation

ABSTRACT: This paper presents a probabilistic analysis for evaluating the creep crack growth rate (CCGR) of type 316LN stainless steel. The CCGR data was obtained from the creep crack growth tests, which are conducted under various applied loads at 600°C. The crack growth rate was characterized as a function of the C^* fracture parameter. In order to logically obtain the B and q values in the CCGR equation of $\dot{a} = B(C^*)^q$, three methods of the least square fitting method (LSFM), a mean value method (MVM), and a probabilistic distribution method (PDM) were adopted. Also, using the Monte Carlo simulation, a number of random variables was generated, and the CCGR lines were predicted probabilistically. The three methods did not show a large difference in the CCGR lines, but the PDM was most useful because the CCGR line can be evaluated with a probabilistic reliability. Both the B and q coefficients followed a lognormal distribution, even though the B ones were a little scattered for the points of the data. In the case of a standard deviation of 1σ for the probability variables, P (B,q), the results of the MCS and the PDM for the distribution ranges of the CCGR lines were compared and discussed.

KEYWORDS: creep crack growth rate, Type 316LN SS, probability, Monte Carlo simulation

Introduction

Type 316LN stainless steel (SS) is widely used as the structural material for liquid metal reactor (LMR) components, as a consequence of its good high temperature mechanical properties, compatibility with the coolant liquid sodium, and adequate weldability. Their components may be subjected to a non-uniform stress and temperature distribution during service. These conditions generate localized creep damage and propagate the cracks and ultimately cause a fracture. A significant portion of the component's life can be spent in a crack propagation. Most GEN-IV reactors are also operated at the high temperature creep range above 500°C [1–3]. Thus, it is very important to evaluate the creep crack growth rate (CCGR) from a design concern and in predicting the residual life of the components during the high temperature service [4–6]. In addition, for ensuring the safety and integrity of the components, it is necessary to assess the CCGR from the probabilistic viewpoint which defines the probability of a fracture. However, until now, the design and/or evaluation of the components have been conducted mostly by deterministic fracture mechanics (DFM). This method may bring about an overly conservative evaluation by applying highly upper limit values in the material properties. So the crack propagation is reasonable to evaluate probabilistically using probabilistic fracture mechanics

Manuscript received 7 April 2005; accepted for publication 22 June 2005; published January 2006. Presented at ASTM Symposium on Fatigue and Fracture Mechanics: 35th Volume on 18-20 May 2005 in Reno, NV.
[1] Principal Researcher, Dept. of Nuclear Material Technology Development, Korea Atomic Energy Research Institute (KAERI), 150 Deogjin-dong,Yuseong-gu, Daejeon, 305-353, Korea (South).
[2] Graduate Student and Professor, respectively, Soong-sil University, 1-1 Sangdo-dong, Dongjak-gu, Seoul, 156-743, Korea.
[3] Professor, Pukyong National University, 599-1 Daeyon-dong, Nam-gu, Busan, 608-737, Korea.

Copyright © 2005 by ASTM International, 100 Barr Harbor Drive, PO Box C700, West Conshohocken, PA 19428-2959.

(PFM).

In this paper, the CCGR data were dealt with from probabilistic viewpoints in order to logically evaluate the CCGR in type 316LN SS. The creep crack growth data were obtained from several experimental CCGR tests under different applied loads at 600°C and characterized in terms of the C^* parameter. The CCGR equations were compared with the least square fitting method (LSFM), a mean value method (MVM), and a probability distribution method (PDM). Also, using the Monte Carlo simulation (MCS), a number of random variables was generated, and the CCGR lines were predicted probabilistically. For an application of the PDM and the MCS, in the case of a standard deviation of 1σ for the probability variables, P (B, q), the CCGR lines were predicted and discussed.

Experimental Method

Chemical compositions of type 316LN SS are given in Table 1. Laboratory ingots were prepared by a vacuum induction melting (VIM) and were homogenized at 1150°C for 2 h in an argon atmosphere and shaped to 15 mm plates by the hot rolling processes. The type 316LN plates were solution annealed for 1 h at 1100°C and water quenched.

Tension testing specimens were machined to be cylindrical with a 25.4 mm gauge length and 6.35 mm in diameter. And a creep test specimen was machined to be cylindrical with a 30 mm gage length and 6 mm diameter. All the specimens were taken along the rolling direction. The gage sections of the creep specimens were polished using #1000 grit sand papers with strokes along the specimen axis. In order to obtain the material properties of the type 316LN SS, tension and creep tests were conducted at 600°C. Creep tests were carried out using dead weight machines with a lever ratio of 20/1. The experimental procedures for the creep tests followed the recommendations of the ASTM standard E 139. Creep data were automatically collected through a personal computer. The mechanical properties of D_1, m, A, and n, which are obtained from the tension, and creep tests at 600°C are listed in Table 2.

Creep crack growth tests were carried out at a constant load with applied load ranges of 5500 N to 7000 N at 600°C. Compact tension (CT) specimens were a width (W) of 25.4 mm, a thickness (B) of 12.7 mm, and side grooves of a 10 % depth. Initial crack ratio (a/W) was about 0.5. Load-line deflection was measured using a linear gauge assembly attached to the specimen, and the crack length was determined by the direct current potential drop (DCPD) method. Crack extension data were continuously collected using a data acquisition system. The test temperature was constantly maintained to within 2°C during the test. The test was continued until a sufficient crack growth occurred. After testing, the CT specimens were cooled down in a liquid nitrogen solution and fractured to measure the final crack length.

The crack length was calculated using the Johnson's formula from the results of the DCPD. All the experimental procedures followed the ASTM standard E 1457. The results of the crack size measurement in each condition are given in Table 3. As seen in Table 2, the results between the predicted and measured crack sizes are well within the 5 % of the requirements in the ASTM E 1457 [7].

TABLE 1—*Chemical composition of type 316LN SS.*

Fe	C	Si	Mn	P	S	Cr	Ni	Mo	N	B
Bal.	0.022	0.70	1.01	0.029	0.005	17.15	12.30	2.35	0.094	0.003

TABLE 2—*Material properties at 600°C of type 316LN SS.*

E (GPa)	σ_{YS} (MPa)	σ_{UTS} (MPa)	Plastic constants, $\varepsilon_p = D_1\sigma^m$		Creep constants, $\dot{\varepsilon}_{ss} = A\sigma^n$	
			D_1	m	A	n
149	104	420	6E-4	2.54	6.35E-33	11.8

TABLE 3—*CCGR test conditions and crack size measurement at 600°C of type 316LN SS.*

S.P –I.D.	Test conditions & transition time				Results of crack size measurement				
	Load (N)	Applied K ($MPa\sqrt{m}$)	Test time (hr)	t_T (hr)	a (mm)	a_o (mm)	a_{pf} (mm)	a_{mf} (mm)	Error (%)
K1	7000	34.9	526.3	245	10.19	12.11	13.52	13.41	0.80
K2	6500	32.7	667.9	221	10.29	12.18	14.52	14.65	-0.88
K3	6000	30.0	884.9	428	10.18	12.13	13.04	13.33	-2.26
K5	5500	28.5	1284.0	423	10.59	12.43	14.90	15.00	-0.64
K6	6000	29.8	749.8	245	10.28	12.08	22.50	23.64	-4.81
K7	6000	29.9	811	301	10.12	12.02	25.27	24.68	-2.31
KR	6500	31.9	662.6	331	10.13	12.03	14.06	14.28	1.52

- a : initial crack size(at sharp notch), a_o: pre-cracked size by fatigue
- a_{pf} : predicted final crack size, a_{mf} : measured final crack size
- t_T : transition time

Results and Discussion

Calculation of the C^* values

Fracture mechanics parameter, C^*-integral has been widely used to characterize the CCGR in metals undergoing a steady state creep. The general form between the CCGR (da/dt) and the C^* can be expressed as the following [8, 9]:

$$da/dt = B[C^*]^q \tag{1}$$

In this expression, the B and q coefficients are material constants, which are generally obtained from a regression line of the CCGR data. They are related to the intercept and slope, respectively, of the da/dt versus C^* relationship on a log-log plot [5,10]. For calculating the da/dt in Eq 1, the material constants, D_1, m, A, and n were obtained from the tension and creep tests at 600°C, as described in Section 2. Material properties of Table 2 were used to calculate the C^* values. The relationship between the da/dt and the C^* was obtained for all the seven samples. Calculating procedures of the C^* values followed the ASTM E 1457.

The CCGR Lines for Regression Methods

The values of the B and q coefficients are very important because the CCGR behavior depends on them. Their values change from material to material and may change with regression methods. Therefore, to logically obtain the CCGR line of the type 316LN SS, the three methods of the LSFM, the MVM, and the PDM are applied and compared. Here, the MVM is to take a mean value which is obtained by the total sum of each B and q value of the CCGR lines. The PDM is obtained by a statistical distribution of the CCGR data. Figure 1 shows the results of the CCGR lines obtained from the LSFM, the MVM, and the PDM, respectively. The three methods are found to have a little difference in the CCGR lines.

At first, the CCGR equation in the LSFM was obtained as

$$da/dt = 3.84\times10^{-2}[C^*]^{0.89} \tag{2}$$

It is shown that the slope, q of a regression line was the lower than the other two methods and was not in full accord with the experimental data points. Although the LSFM has been generally used as a good method for obtaining the best fitting of the CCGR data so far, it obtains only the best regression line of the y-axis for all the data points, regardless of the C^* ranges of the x-axis for each applied condition. It has been known that the LSFM estimates an independent regression for the data of the x-axis and of the dependent one for the data of the y-axis [11]. In reality, each range of the C^* values for the CCGR lines are different with the applied load conditions. The numbers of data points is also different with the C^* values. Owing to this reason, the q value in the LSFM is low with 0.89. As a consequence, the LSFM may generate some error in the regression line.

Secondly, the conception of a mean value was adopted for obtaining the CCGR line. The MVM line showed a good agreement with the experimental data, as shown in Fig. 1. Because the MVM line takes a mean value of each B and q of all the CCGR lines, this method equally reflects the individual characters of each experimental line. The q value in the MVM was 0.93 higher than that in the PDM, and the CCGR equation in the MVM was obtained as

$$da/dt = 5.32\times10^{-2}[C^*]^{0.93} \tag{3}$$

Finally, the conception of a probability distribution was applied to obtain the CCGR line from a probabilistic viewpoint. For using this method, it is necessary to investigate the probability distribution of the B and q coefficients. Figures 2 and 3 show the results of the B and q distributions obtained from seven experimental CCGR data. Probability distribution of lognormal distribution on paper follows a linear relationship, even though the B distribution was a little scattered for the data points. Thus, the B and q data are shown to follow a lognormal distribution. Standard deviation, σ_{L10} (subscript L means log) and mean value, μ_{L10} for the lognormal distributions of the B and q can be obtained using the results of Figs. 2 and 3. The standard deviation for the q is low with $\sigma_{L10} = 0.056$, while the one for the B is a little bit high with $\sigma_{L10} = 0.324$. The CCGR equation in the PDM was obtained as

$$da/dt = 4.64\times10^{-2}[C^*]^{0.92} \tag{4}$$

The CCGR line of the PDM shows a good result when compared with that of the LSFM because the PDM line closely approaches the MVM one. Thus, the PDM can be used as a reasonable method for estimating the CCGR of high temperature materials. Especially using this

method, we can predict the CCGR with a probabilistic reliability. For the usability of the three methods, each method may have an advantage or disadvantage. The MVM is not convenient because each CCGR line should be obtained for each applied condition.

Meanwhile, the LSFM is very convenient because the CCGR line is easily obtained by a fitting at a time for all the data points. The PDM is superior from the probabilistic viewpoints to the other two methods.

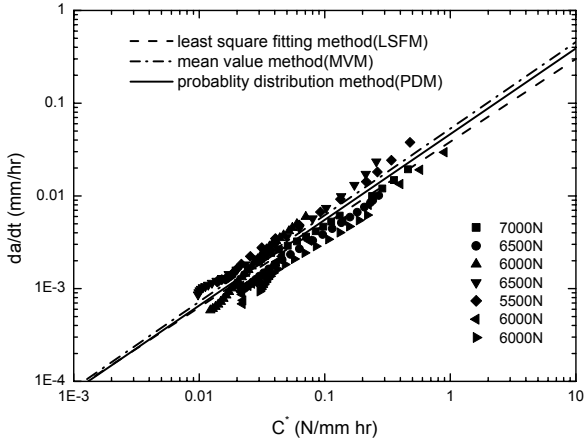


FIG. 1—*Comparison of the CCGR lines for the three methods.*

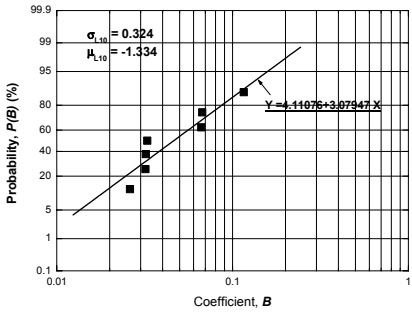


FIG. 2—*Lognormal distribution of the B data.*

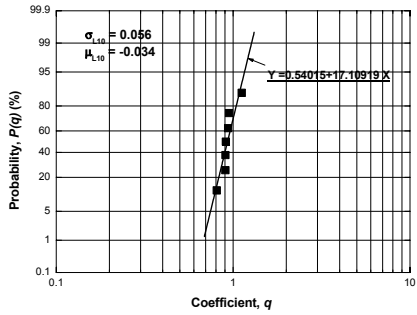


FIG. 3—*Lognormal distribution of the q data.*

Probabilistic Prediction of the CCGR Line

By knowing the probabilistic distributions of the B and q, the CCGR line can be predicted probabilistically. As described above, the B and q data followed a lognormal distribution. Thus, the B and q values at any probability can be calculated from Figs. 2 and 3. As an example for an application, in the case of 1σ in which the probability variable, $P(B, q)$, is [15.87 % ≤ $P(B, q)$ ≤ 84.13 %], the distribution ranges of the CCGR line are plotted in Figs. 4 and 5.

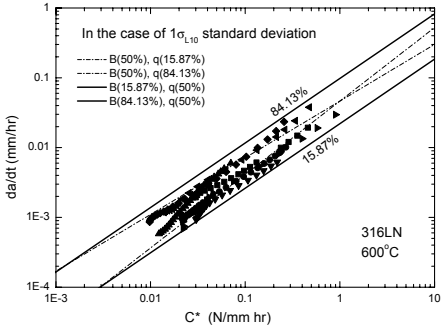


FIG. 4—*Probability line in the 1σ of the B.*

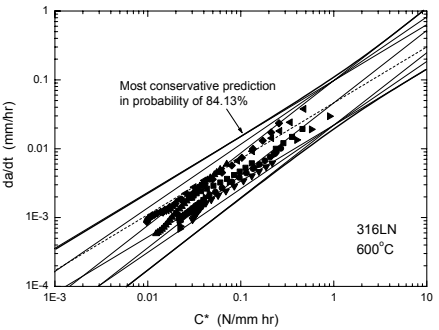


FIG. 5—*Probability line in the 1σ of the B and q.*

Figure 4 shows the results of the CCGR lines in the case that the *B* and *q* ranges are changed with 1σ for *B* and *q* of 50 %, respectively. In the 1σ range of *B* (15.87–84.13 %) for *q* of 50 %, all data are included. Meanwhile, in the 1σ range of *q* (15.87–84.13 %) for *B* of 50 %, all the data are not included perfectly. Thus, the *B* and *q* coefficients should be considered with the wider probability to predict more conservatively the CCGR line.

Figure 5 shows the results of the CCGR lines which are considered for all the eight cases. The values of the *B* and *q* are freely changed with 15.87 %, 50 %, and 84.13 %, respectively. Probability lines of 84.13 % and 15.87 % were calculated using the results of the lognormal distribution as shown in Figs. 2 and 3, respectively. In this case, the upper and lower prediction band is wider than that of Fig. 4. The upper prediction line of 84.13 % will be the most conservative prediction, because the fastest CCGR is predicted here. On the contrary, the lower prediction line of 15.87 % will be the most non-conservative prediction, because the lowest CCGR is predicted here. It indicates that by knowing the probability distribution for the *B* and *q*, the CCGR can be predicted probabilistically. The PDM can be utilized usefully for predicting a design life and a remaining life of cracked components under a high temperature creep condition.

Monte Carlo Simulation (MCS) for the B and q

For engineering purposes, a simulation may be applied to predict the performance and response of a system. For problems involving random variables with known or assumed probability distributions, the MCS has been commonly used. In this study, the MCS is applied to generate the appropriate values of random variables (i.e., random numbers) for the *B* and *q* coefficients. Box and Muller [12] have proposed that random variables (*S*) with a standard normal distribution can be represented as

$$S = (-2 \ln U_1)^{0.5} \cos 2\pi U_2 \tag{5}$$

In this expression, the U_1 and U_2 are standard uniform variables, which have a uniform probability density function (PDF) between 0 and 1.0. Thus, random variables (x) with a normal distribution $N(\mu, SD)$ can be given as [13]

$$x = \mu + SD \cdot S = \mu + SD(-2 \ln U_1)^{0.5} \cos 2\pi U_2 \tag{6}$$

For a lognormal random variable x', the distribution of $x = \log(x')$ is a normal distribution. Thus, if x is a value generated from Eq 6

$$x' = 10^{x} \tag{7}$$

Equation 7 becomes a random number for the lognormal distribution with a mean μ and standard deviation *SD*. Equations 6 and 7 were used to generate the values of the B and q, which were shown to be a lognormal distribution, as shown above.

Figures 6 and 7 show the results of the MCS for the lognormal distribution of the B and q. Standard uniform variables of the U_1 and U_2 were generated using Eq 6. The numbers of the random variables were 100 for each B and q. The B and q data follow the lognormal distribution because the data plots a linear relationship. The B and q values are almost similar to those of the experimental data obtained in Figs. 2 and 3. It means that the random variables of the B and q were well realized by the MCS.

Figure 8 is the typical results of the MCS showing the variations of the da/dt at various C^* values. The probability distribution of the da/dt was calculated using Eq 1 from the B and q distributions of Figs. 6 and 7. Probability distributions of 50 numbers were generated for the wide ranges of the C^* values from 0.001 to 100. From these distributions, the CCGR lines can be predicted probabilistically. The results are shown in Figs. 9 and 10, respectively. Figure 9 presents the results of the probability line obtained from the MCS for the 1σ of the B value, as shown in Fig. 4. However, as clearly shown in Fig. 9, in the lower and upper values of the C^*, several data points are out of the boundaries. So the q coefficient should be considered probabilistically.

Figure 10 presents the results of the probability line obtained from the MCS in the 1σ of the B and q ones, as noted in Fig. 5. The probability lines of 84.13 % and 15.87 % were calculated using the results of the MCS obtained in Figs. 6 and 7, respectively. In this case, the band of the upper and lower prediction lines is wider than that of Fig. 9. All the data are included in the 1σ range of 15.87 % and 84.13 %. The upper prediction line of 84.13 % will be the most conservative prediction. Meanwhile, the lower prediction line of 15.87 % will be the most non-conservative prediction. The bands of the upper and lower lines in the PDM and the MCS are a little different, as shown in Figs. 11 and 12. The comparative results are discussed below.

Figs. 11 and 12 show the comparative results of the PDM and the MCS for the predicted CCGR lines. In the 1σ of the B value and in the 1σ of the B and q ones, the two methods showed a little difference in the bands of the predicted CCGR lines. It is found that the PDM line is wider than the MCS one. It means that the PDM line was faster than the MCS one, because the upper prediction line is only considered in the design of the CCGR. Thus, the PDM will make a more conservative design than the MCS. Contrarily, the MCS will make an economic and reasonable design. However, the PDM and the MCS do not generate a large difference in the predicted lines, so both methods are used for predicting the creep crack growth of type 316LN SS. It is also regarded that the MCS of this study were successfully performed without an error.

Consequently, by using the lognormal distribution investigated for type 316LN SS, a number of random variables, $P(B, q)$ with the various C^* values can be generated by the MCS. Then, the CCGR lines can be predicted with a probabilistic reliability by using the generated random variables.

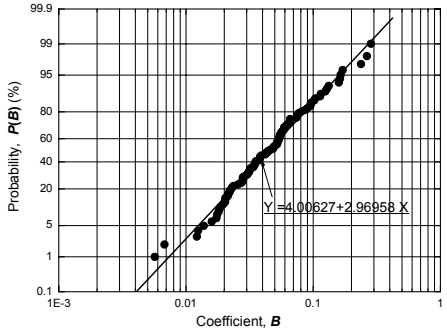


FIG. 6—*Result of the MCS for the B distribution.*

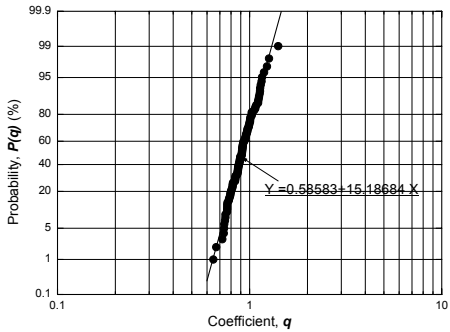


FIG. 7—*Result of the MCS for the q distribution.*

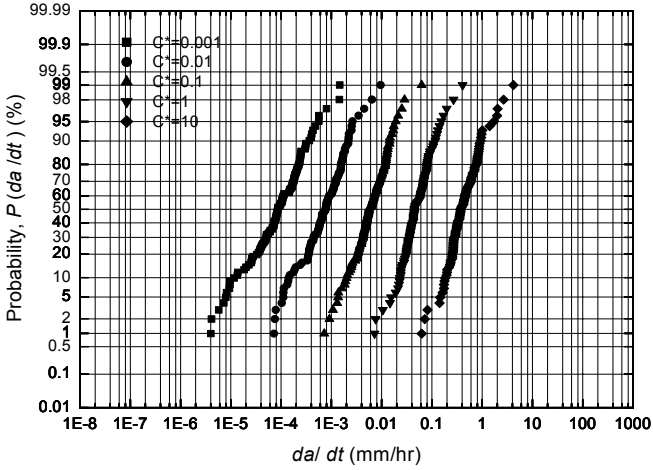


FIG. 8—*The MCS of the CCGR with the C^* values.*

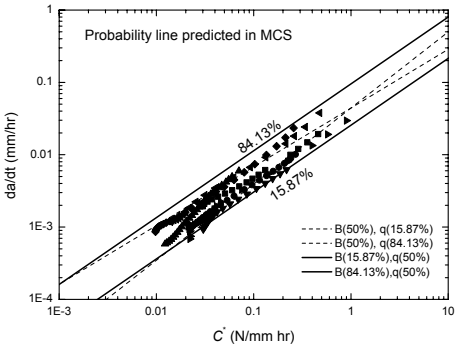


FIG. 9—*Probability line obtained in the MCS.*

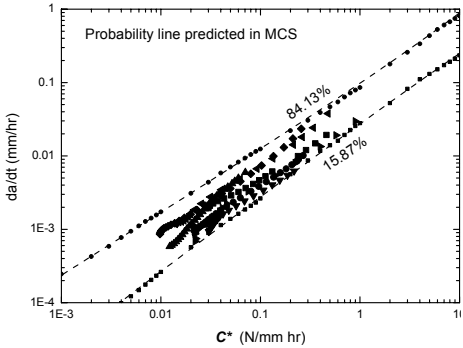


FIG. 10—*Probability line obtained in the MCS in the 1σ of the B in the 1σ of the B and q.*

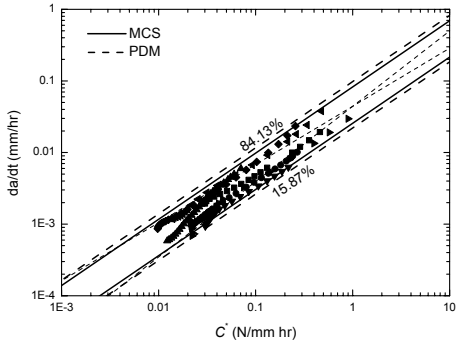


FIG. 11—*Comparison of CCGR lines for MCS and MCS PDM in the 1σ of the B.*

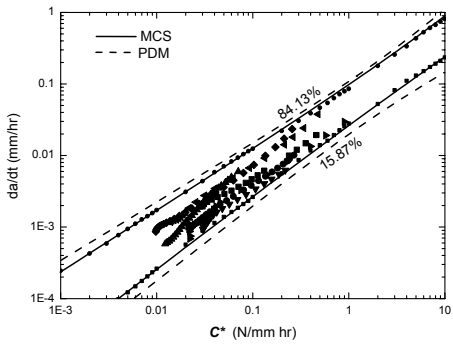


FIG. 12—*Comparison of CCGR lines for and PDM in the 1σ of the B and q.*

Conclusions

In order to logically obtain the creep crack growth rate (CCGR) of type 316LN stainless steel, the CCGR lines were obtained by the three methods of the least square fitting method (LSFM), the mean value method (MVM), and the probability distribution method (PDM), and the CCGR lines were analyzed probabilistically by the Monte Carlo simulation (MCS). The three methods did not show a significant difference in the CCGR lines, but, above all, the PDM was most useful because the CCGR line can be predicted probabilistically. It was found that both the *B* and *q* coefficients of the CCGR data of type 316LN stainless steel followed a lognormal distribution, even though the *B* ones were a little scattered in the CCGR data. By using the lognormal distribution, the CCGR lines were predicted with a probabilistic reliability. In addition, by applying the Monte Carlo simulation, a number of random variables for the *B* and *q* was generated, and the CCGR lines were successfully predicted without an error. As an example for application, the results of the CCGR line between the PDM and the MCS, in the case of the 1σ

of the B value and of the B and q ones, did not show a significant difference. It is thus regarded that the MCS is useful in the probabilistic evaluation of the CCGR for type 316LN stainless steel, and especially for new and emerging class of high-temperature materials where the CCGR data is lacking.

Acknowledgments

This work was performed under the Long-term Nuclear R&D Program sponsored by the Korean Ministry of Science and Technology.

References

[1] Kim, D.W., Lee, Y.K., Kim, W.G. and Ryu, W.S., "Effect of Nitrogen on Creep Properties of Type 316L(N) Stainless Steel," *Journal of Korean Institute Metal & Material*, Vol. 39, 2001, pp.1241-1248.
[2] Kim, W.G., Kim, S.H. and Ryu, W.S., "Creep Characterization of Type 316LN and HT9 Stainless Steels by the K-R Creep Damage Model," *KSME International Journal*, Vol. 15, 2001, pp. 1463-1471.
[3] Jang, J., Ryu, W.S. and Hong, J.H., "Material-Related Issues for Gen IV Supercritical Water-Cooled Reactor," *Proc. of Sixteenth Conference on Mechanical Behaviors of Materials*, Cheju, Korea, Nov. 8, 2002, pp. 425-431.
[4] Nikbin, K.M., Smith, D.J. and Webster, G. A., "An Engineering Approach to the Prediction of Creep Crack Growth," *Transactions of the ASME*, Vol. 108, 1986, pp. 186-191.
[5] Saxena, A., "Nonlinear Fracture Mechanics for Engineers," *CRC Press*, New York, 1997, pp. 363-377.
[6] Yagi, K., Tabuchi, M., Kubo, K., Kim, J.J. and Huk Y.H., "The Influence of Fracture Mechanisms on the Creep Crack Growth Behavior of 316 Stainless Steel," *Engineering Fracture Mechanics*, Vol. 57, 1997, pp. 463-473.
[7] ASTM E1457-00, "Standard Test Method for Measurement of Creep Crack Growth Rates in Metals," ASTM Standard, 2000.
[8] Anderson, T.L., "Fracture Mechanics," Second Edition, *CRC Press*, Boca Raton, Ann Arbor, London, Tokyo, 1995, pp. 226-228.
[9] Ryu, W.S., Kim, W.G. and Lee, K.Y., "Evaluation of Creep Crack Growth Behavior of Type 316LN Stainless Steel, SMiRT-17, Paper No. F05-4, 2003.
[10] Kim, W.G., Kim, H.H., Yoon, K.B., Ryu, W.S., "Application of Creep Ductility Model for Evaluating Creep Crack Growth Rate of Type 316SS Series," *Materials Science Forum*, Vols. 475-479, 2005, pp. 1433-1436.
[11] Microcal Software, Inc, Origin User Manual, Version 5, 1997, pp. 460-463.
[12] Box, G.E.P. and Muller, M.E. "A Note on the Generation of Random Normal Deviates," *Annals of Math. Stat*., Vol. 29, 1958, pp. 610-611.
[13]Yatomi, M., "Factors Affecting the Failure of Cracked Components at Elevated Temperature," Ph.D. Thesis, Imperial College, 2003, pp. 58-59.

Journal of ASTM International, Vol. 3, No. 7
Paper ID JAI13219
Available online at www.astm.org

E. P. Busso,[1] *N. P. O'Dowd,*[2] *and K. Nikbin*[2]

Mechanistic Studies of High-Temperature Crack Initiation in Single Crystal Materials

ABSTRACT: In this work, the results of mechanistic studies of surface crack initiation due to the coalescence of microcracks from casting defects are presented. Two approaches are considered; namely, a continuum damage (CD) one and another where a microvoid is explicitly introduced in the vicinity of a notch. In both cases, a rate-dependent crystallographic theory is relied upon to describe the visco-plastic behavior of the single crystal. The numerical studies are conducted on a notched compact tension (CT) specimen with and without a single casting defect, idealized as a cylindrical void close to the notch surface. CD predictions of the formation of surface cracks under constant far-field loading, linked to the nucleation and coalescence of microcracks from internal porosities, are obtained from a recently proposed mechanistic anisotropic void growth model. In the explicit-void modeling approach, the time to crack initiation under constant load has been predicted using a strain-based failure criterion. Finite element analysis of the CT specimen revealed that, due to the strong localization of inelastic strain at the void, a microcrack will initiate in the vicinity of the void rather than at the notch surface. The numerical results have also shown that the time to crack initiation depends strongly on the applied load level and the void location. These results and those obtained from the CD predictions are compared and discussed. The applicability of a failure assessment approach, based on the linear elastic stress intensity factor to predict the crack initiation time under creep loading, is also considered.

KEYWORDS: nickel base superalloy, fracture, surface diffusion, creep, finite elements

Introduction

An important contributing factor to failure in single-crystal superalloys is the localization of the inelastic deformation caused by the heterogeneity of the material microstructure. In two-phase single crystals, heterogeneities exist at both the microscopic (i.e., γ' precipitates) and mesoscopic (i.e. casting-related porosities) levels [8]. Furthermore, high-temperature superalloy component life is generally dominated by short-crack initiation and growth. Observations of fracture surfaces in nickel superalloy creep specimens, loaded in a $\langle 001 \rangle$ crystallographic direction, have revealed multiple $\{001\}$ facets, resulting from the propagation of microcracks, which appear to have initiated from casting porosities [1,2]. Due to localized deformation in the vicinity of a notch root, microcracks are expected to initiate, either at the notch, or at a neighboring microvoid (e.g., see Fig. 1). Under increasing load, these microcracks propagate and coalesce, leading to the growth of the mesoscopic crack and eventual fracture of the specimen. Further evidence of the initiation of microcracks at casting porosities in Ni-base single-crystal superalloys has been obtained in the low cycle fatigue tests on RR2000 and CMSX4 at 750°C and on directionally solidified Ni-base superalloys at 650°C by MacLachlan and Knowles [3] and Okazaki et al. [4] respectively.

The aim of this work is to conduct a detailed comparison between recent contrasting mechanistic studies conducted to understand the initiation of microcracks in single-crystal superalloy components operating under typical service conditions. Two approaches were considered to study the crack initiation phenomena. First, a continuum damage (CD) approach whereby the initiation of microcracks was assumed to be controlled by an evolving continuum damage variable linked to the local deformation around individual microvoids, driven by the local stress state. This approach is based on the work of Dumoulin et al. [5], which incorporates a continuum damage model based on the initiation of microcracks from the

Manuscript received June 14, 2005; accepted for publication March 31, 2006; published online June 2006. Presented at ASTM Symposium on Fatigue and Fracture Mechanics: 35th Volume on 18–20 May 2005 in Reno, NV; R. E. Link and K. M. Nikbin, Guest Editors.

[1] Centre des Matériaux, Ecole des Mines de Paris, B.P. 87-91003 Evry, France.

[2] Department of Mechanical Engineering, Imperial College London, London, SW7 2AZ, UK.

Copyright © 2006 by ASTM International, 100 Barr Harbor Drive, PO Box C700, West Conshohocken, PA 19428-2959.

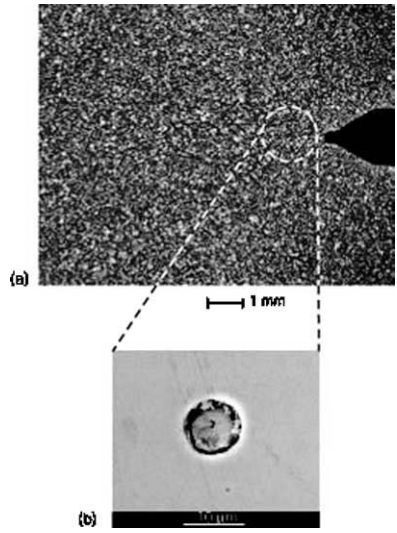


FIG. 1—*Relevant material length scales: (a) notch in a compact tension specimen (macroscale), and (b) micrograph of a typical casting defect (mesoscale) [3].*

surface of internal voids at the mesoscale (20 μm). Thus, the interaction between the void and crack is not accounted for as the void is not modeled explicitly. In this approach, cracks are assumed to initiate once the fully damage region extends over a microstructure-related length scale. In the second approach, the deformation fields when a microvoid is present in the vicinity of a relatively sharp notch in a single-crystal nickel alloy, were examined.

An idealized cylindrical microvoid, representing a material casting defect in a notched compact tension specimen, was considered and a strain-based failure criterion used to predict the crack initiation time under creep (Zhao et al. [6]) and fatigue (Busso et al. [7]) loadings. In both approaches, the constitutive behavior of the single-crystal material is described by a rate-dependent multiscale crystallographic continuum framework.

The structure of the paper is as follows. In Sec. II, the crystallographic theory for the Ni-based superalloy single crystal is described. In Sec. III, the two different theoretical approaches to predict crack initiation phenomena are introduced, including the micromechanics void growth formulation used to predict the critical void volume associated with the initiation of microcracks (i.e., damage) from the voids surface. For simplicity, only creep loading conditions will be considered. In Sec. IV, an outline of the finite element (FE) procedures and details of the finite element models of a compact tension (CT) specimen and the failure criteria are given. The results of the finite element analyses are given in Sec. V, including the effects of load level and void location on the time to crack initiation. Finally, concluding remarks are presented in Sec. 6.

Crystallographic Single-Crystal Material Model

The macroscopic mechanical constitutive behavior of the superalloy of interest, CMSX4, is described by a finite deformation, multiscale rate-dependent crystallographic formulation (Busso et al. [8]) which extends the physically based model of Busso [9] (e.g., see also Busso and McClintock [10]). The formulation relies on the multiplicative decomposition of the total deformation gradient, $\mathbf{F}=\mathbf{F}^e\mathbf{F}^p$, where $\mathbf{F}^e$ is the component which accounts for elastic deformation and rigid-body rotations and $\mathbf{F}^p$ is the inelastic component associated with pure slip. $\mathbf{F}^p$ is calculated from the plastic velocity gradient:

$$\mathbf{L}^p = \dot{\mathbf{F}}^p \mathbf{F}^{p^{-1}} = \sum_{\alpha=1}^{n} \dot{\gamma}^\alpha (\mathbf{m}^\alpha \otimes \mathbf{n}^\alpha) \tag{1}$$

where $\dot{\gamma}^\alpha$ is the shear strain rate on the slip system α and $\mathbf{m}^\alpha$ and $\mathbf{n}^\alpha$ are the slip direction and the slip plane normal, respectively.

Based on a stress-dependent activation energy, the flow rule is expressed in terms of two scalar state variables per slip system (α): a macroscopically average slip resistance S^α and an internal or back stress B^α. Thus

$$\dot{\gamma}^\alpha = \dot{\gamma}_o \exp\left[-\frac{F_o}{k\theta} \left\langle 1 - \left\langle \frac{|\tau^\alpha - B^\alpha| - S^\alpha \mu/\mu_0}{\hat{\tau}_0 \mu/\mu_0} \right\rangle^p \right\rangle^q \right] \mathrm{sgn}(\tau^\alpha - B^\alpha) \tag{2}$$

where k is the Boltzmann constant; τ^α is the resolved shear stress on the system α; θ the absolute temperature; μ, μ_0 the shear moduli at θ and 0 Kelvin, respectively; and F_o, $\hat{\tau}_0$, p, q, and $\dot{\gamma}_o$ are material constants.

In this work, the slip resistance in each slip system (S^α) is related to the overall dislocation density for that system (ρ^α) by the relationship

$$S^\alpha = \lambda \mu b^\alpha \left(\sum_{\beta=1}^{N} \delta_S^{\alpha\beta} \rho^\beta \right)^{1/2} \tag{3}$$

where λ is a parameter that accounts for the nature of the dislocation distributions, b^α is the magnitude of the Burgers vector, $\delta_S^{\alpha\beta}$ the cross-hardening or interaction matrix, and N is the number of slip systems.

The evolutionary behavior of the overall dislocation density and the associated back stress for the slip system α are expressed as

$$\dot{\rho}^\alpha = \frac{1}{b^\alpha} \left(\frac{1}{l_{\mathrm{app}}^\alpha} - d_D \rho^\beta \right) |\dot{\gamma}^\alpha| \tag{4}$$

$$\dot{B}^\alpha = h_B \dot{\gamma}^\alpha - r_D B^\alpha |\dot{\gamma}^\alpha| \tag{5}$$

In Eq 4, l_{app}^α is the dislocation mean free path and d_D is a dynamic recovery coefficient. In Eq 5, h_B is a hardening coefficient and r_D is a dynamic recovery function that depends on the current state given by ρ^α. The multiscale nature of the formulation is incorporated into Eqs 4 and 5 by making an explicit link between the initial dislocation density ρ_0^α and the dislocation mean free path l_{app}^α, with the features of the microstructure at a lower scale, i.e., at the microscale. Thus, for the most general case, the functional forms for ρ_0^α and l_{app}^α are defined in terms of the size D and volume fraction v_f of the γ' precipitate population (see, e.g., Dumoulin et al. [5] for details).

The crystallographic formulation has been implemented numerically as a user-defined material subroutine within the commercial finite element code ABAQUS [11]. The numerical implementation relies on an implicit algorithm to update the stress and the internal slip system variables (see Busso et al. [12]; Meissonnier et al. [13]). The calibration of the material model was carried out under the assumption that twelve octahedral ($\{111\}\langle 011\rangle$) and six cubic ($\{100\}\langle 011\rangle$) slip systems are potentially active. Furthermore, the reference stress-strain data required was that corresponding to the initial precipitate volume fraction; viz., v_f=68 %. When changes in precipitate volume fraction linked to high-temperature oxidation processes need to be accounted for, then data for lower precipitate volume fractions are required (see, e.g. Dumoulin et al. [5]; Zhao et al. [6]). Typical predictions of uniaxial monotonic and steady-state cyclic response in the $\langle 001\rangle$ direction at 950°C are shown in Figs. 2(*a*) and 2(*b*), respectively.

Crack Initiation Approaches

Critical Damage Approach

Here, the approach proposed in Dumoulin et al. [5] will be summarized. It relies on a void growth formulation and a crack initiation criterion to describe the evolution of a suitable damage variable. A

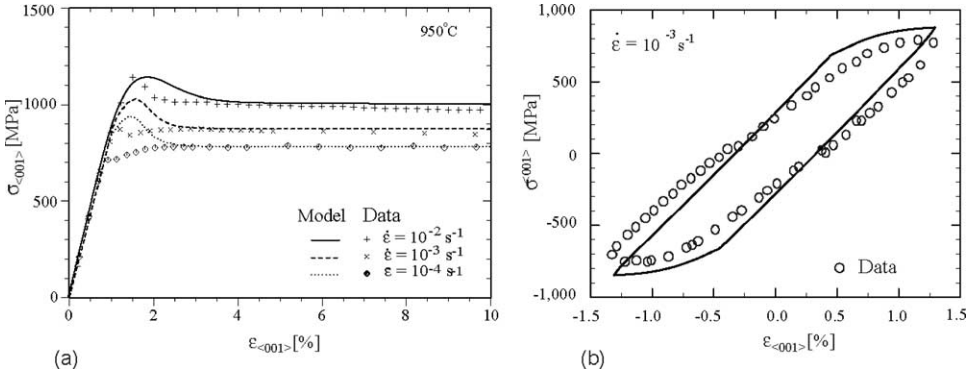


FIG. 2—*Predicted and measured (a) ⟨001⟩ uniaxial monotonic response and (b) ⟨001⟩ steady-state uniaxial cyclic response at* 950°C *and at constant strain rates (the experimental data, indicated by the symbols, are from Dumoulin et al. [6], and Busso et al. [9]).*

critical value of this variable is then used to predict microcrack initiation in the CT specimen. The effect of the void is incorporated through the damage variable, and thus the interaction between the void and the notch is not accounted for.

To formulate and calibrate the void growth model, the multiscale rate-dependent crystallographic formulation was used to quantify the behavior of a representative volume element or unit cell of the single crystal containing an initially spherical void (Busso et al. [8]). An extensive FE parametric study was undertaken to determine the effect of stress state, temperature, relative crystallographic orientation, and characteristic length scale (here defined as the ratio between the distance from a free surface L_v to the void diameter D) on the void growth rate.

The void growth formulation, first introduced in Busso et al. [9], is an extension of that used by Budiansky for isotropic materials. The total volumetric void growth rate $\dot{V}$ is assumed to be controlled by slip and defined as

$$\frac{\dot{V}}{V} = \left[a_1 \left(\frac{\dot{V}_{\text{oct}}}{V} \right)^r + a_2 \left(\frac{\dot{V}_{\text{cub}}}{V} \right)^r \right]^{1/r} \tag{6}$$

where V is the current void volume, and $\dot{V}_{\text{oct}}$ and $\dot{V}_{\text{cub}}$ are the contributions to the void growth rate from slip on the octahedral and cubic slip systems, respectively, and r, a_1, and a_2 are parameters calibrated numerically from the FE void growth calculations.

Expressions for $\dot{V}_{\text{oct}}$ and $\dot{V}_{\text{cub}}$ are:

$$\frac{\dot{V}_{\text{oct}}}{V\dot{\varepsilon}_{\text{oct}}} = \hat{\alpha}_{\text{oct}}(n) \left| \frac{\sigma_m}{\sigma_e} \right|^{w_{\text{oct}}} \tag{7}$$

$$\frac{\dot{V}_{\text{cub}}}{V\dot{\varepsilon}_{\text{cub}}} = \hat{\alpha}_{\text{cub}}(n) \left| \frac{\sigma_m}{\sigma_e} \right|^{w_{\text{cub}}} \tag{8}$$

where $\dot{\varepsilon}_{\text{oct}}$ and $\dot{\varepsilon}_{\text{cub}}$ are the equivalent inelastic strain rates due to octahedral and cubic slip, respectively, σ_m is the mean stress, and σ_e is an equivalent stress defined as

$$\sigma_e = \sqrt{\frac{3}{2} S_{ij} S_{ij}} \tag{9}$$

and where S_{ij} are the deviatoric components of the stress tensor. In Eqs 7 and 8, w_{oct}, w_{cub}, $\hat{\alpha}_{\text{oct}}(n)$, and $\hat{\alpha}_{\text{cub}}(n)$ are functions calibrated from the FE unit cell void calculations (Dennis [3], Busso et al. [9]) and n is the instantaneous material strain rate sensitivity defined as

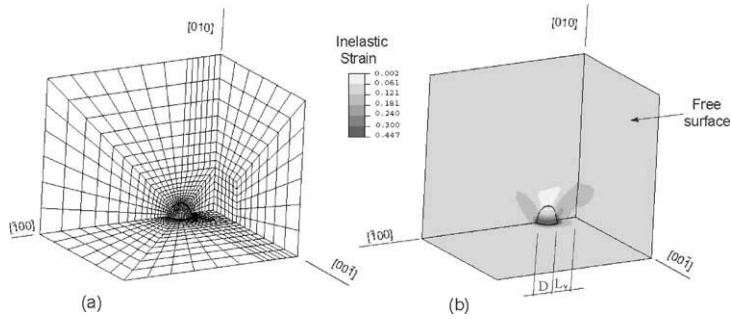


FIG. 3—*(a) Typical finite element model for the void-free surface interaction studies, and (b) contour plot of accumulated inelastic strain around a void* ($L_v/D=1$) *after* 830 h *at* 850°C *under a uniaxial far-field* ⟨*010*⟩ *applied stress of* 600 MPa *(Busso et al. [9]).*

$$n = \frac{\partial \log \dot{\varepsilon}}{\partial \log \sigma_e} \tag{10}$$

Here, $\dot{\varepsilon}$ is the equivalent strain rate.

A typical finite mesh, made up of 4000 three-dimensional (3D) linear isoparametric elements, used in the calibration of the void growth model, is shown in Fig. 3(*a*). In addition, the contour plot of Fig. 3(*b*) shows the predicted distribution of the accumulated uniaxial equivalent inelastic strain in a unit cell containing a void with $L_v/D=1$. The localization of the deformation around the void can be clearly seen—note that the maximum accumulated inelastic strain in the vicinity of the void (i.e., 45 %) is approximately five times greater than the far-field value.

Figure 4 shows a comparison between the predictions given by Eq 6 for different triaxialities, L_v/D ratios, and applied equivalent stresses, and the FE reference solutions obtained from unit cell FE analyses similar to that illustrated in Fig. 3.

In this work, it is assumed that microcracks initiate when a critical value of the equivalent inelastic strain is reached at the void surface. For convenience, this condition can be equivalently expressed in

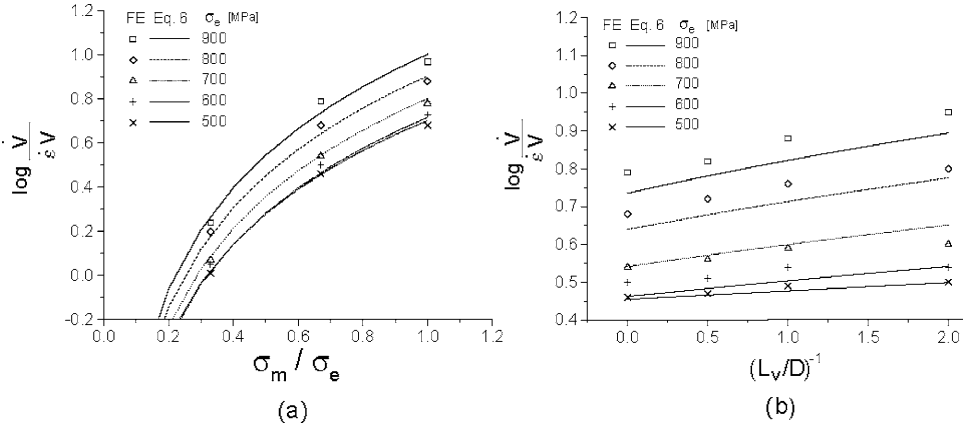


FIG. 4—*Effect of (a) the mean triaxiality normalized by the equivalent stress,* $\sigma_m/\tilde{\sigma}_e$*, and (b) the void diameter relative to the distance from the free surface* (D/L_v) *on the void growth rate* $\dot{v}$.

terms of a corresponding critical void volume. The unit cell FE studies (Busso et al. [9]) revealed that, for a fixed critical microstrain, the corresponding critical void volume depends on the global triaxiality σ_m/σ_e. The normalized critical void volume may then be expressed as

$$\frac{V_c}{V_0} = 1 + b \exp\left(c\frac{\sigma_m}{\sigma_e}\right) \tag{11}$$

where V_c and V_0 are the critical and initial void volumes, respectively. Thus, the criterion for crack initiation (at the microscale) is given when $V \geqslant V_c$, where V is obtained explicitly by integrating Eq 6. The parameters b and c in Eq 11 were calibrated from notched bars loaded under creep conditions in conjunction with 3D FE simulations of the actual test. For further details, see Dennis [2], Busso et al. [8].

Following the above definition of the void growth rate and critical normalized void volume, one can define a corresponding macroscopic damage variable D:

$$D = \frac{V - V_0}{V_C - V_0} \tag{12}$$

This definition of damage ensures that $D=0$ for $V=V_0$ and that $D=1$ for $V=V_C$. The above void growth formulation, initiation criterion, and corresponding damage variable have been implemented numerically into a FE material subroutine for the CMSX4 superalloy.

Explicit-Void Approach

In this approach, the void is modeled explicitly, thus, the void-notch interaction and the effect of void distance from the notch on the deformation are examined directly. We note in passing that the treatment of fatigue-induced microcrack initiation from spherical defects generally requires a probabilistic approach, e.g., see Busso et al. [7]. Under noncyclic loading, crack initiation is deemed to occur when the equivalent inelastic strain $\tilde{\varepsilon}^p$ reaches the critical value $\tilde{\varepsilon}^p_{\text{critical}}$. Due to the relatively large strain gradients in the vicinity of the notch and void, the failure strain must be associated with a representative distance d^*. Here, d^* is chosen to be 1.5 μm, which is on the order of the size of the γ' precipitate. Hence, failure at the microscale can be associated with the cracking of one or more γ' precipitates. The distance of 1.5 μm also corresponds to the size of one element adjacent to the void in the FE mesh, as discussed in Zhao et al. [6]. There, it is shown that the results are not very sensitive to the value of d^*.

The value of the local critical failure strain ($\tilde{\varepsilon}^p_{\text{critical}}$) for CMSX4 was found to be 0.38 through a combination of FE analyses and experimental measurements of a notched bar specimens under creep loading (Dennis, [2]). This value is assumed to be a material property independent of the stress state.

Finite Element Procedure

A typical two-dimensional finite element (FE) mesh for the compact tension specimen containing a single void is shown in Fig. 5. The specimen contains a semicircular notch with radius, $R=0.1$ mm, specimen width, $W=26$ mm, and the notch length to specimen width ratio a/W is 0.5. As indicated in Fig. 5(*a*), the plane of the specimen is normal to the [001] crystallographic axis and the crack lies on the (010) plane. Due to the symmetries of the specimen and the crystallographic lattice, only half of the specimen is modeled. The void density of the alloy is low, with typical void spacing on the order of 100 μm. Therefore, in this work, void interaction is ignored and only the interaction of a single microvoid with the notch is examined. The void, indicated in Fig. 5(*b*), has a diameter $d=15$ μm and is located a distance $L/d=10$ from the notch.

A fine mesh is generated around the notch and the void as shown in Fig. 5(*b*). The whole mesh consists of 3500 four-node elements. A typical finite element is shown in Fig. 5. A similar level of mesh refinement was used to model the CT specimen without the presence of a void. For details, refer to Dumoulin et al. [5].

The analyses were conducted at 950°C and for values of load, $P=2$, 3, 4, 5.5, 7, 8.5, and 10 kN, corresponding to stress intensity factors for the notched specimen of $K=10$, 15, 20, 27, 35, 42, and

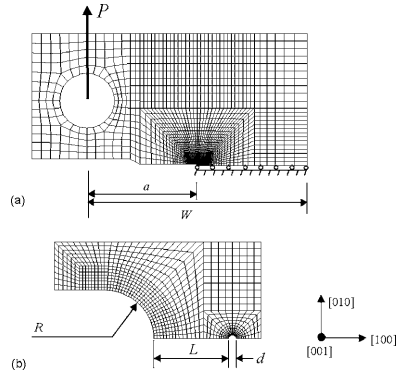


FIG. 5—*(a) Finite element mesh for the voided CT specimen. (b) Refined mesh around the notch and the void.*

50 MPa$\sqrt{\text{m}}$, respectively. The load P is applied to the specimen through a rigid pin with the pin and specimen modeled as a pair of contact surfaces. A constant load P is applied to the specimen (see Fig. 5(*a*)) over typically 1000 h.

Results and Discussion

The results of the FE analyses will be discussed next. The notch analyses without interacting with a void will be shown in terms of stresses, strains and damage at the mesoscale. Similar results will be discussed taking into account the explicit interaction between the notch root and a nearby void and the implications of these findings in relation to time to crack initiation will be discussed.

Analyses With No Notch-Void Interaction—The profile of the normal stresses σ_{010} as a function of distance from the notch root at different times is shown in Fig. 6(*a*). It can be observed that the peak stress drops by more than 50 % in the first 50 h, from ~1650 MPa to ~800 MPa, due to stress relaxation. The stress decreases by a further 30 % over the next 950 h, which is close to the steady state stress distribution. The position of the peak stress also moves from 20 μm from the notch root at $t=0$, to approximately 260 μm at 1000 h.

Figure 6(*b*) shows the profile for the normal stress versus distance from the notch root for the notch-void interaction case. Here the point position (r) is normalized by the distance between the void and notch root. This figure will be discussed in the next section.

In Figs. 7(*a*) and 7(*b*), contours of the accumulated inelastic strain around the notch region due to

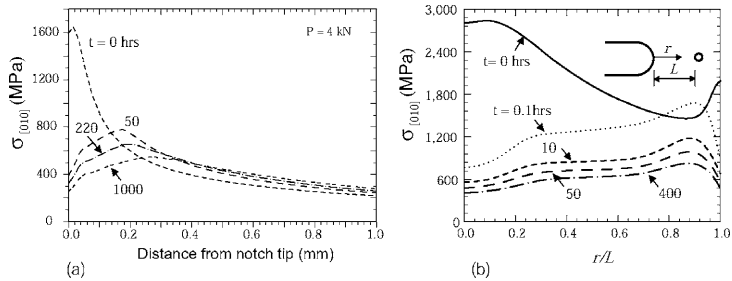


FIG. 6—*Distribution of the [010] stress component along the specimen symmetry line at different times in (a) the void-free CT specimen under a constant* $K=20$ MPa m$^{1/2}$ *load and (b) the voided case with* $L/d=10$ *at* $K=35$ MPa $m^{1/2}$.

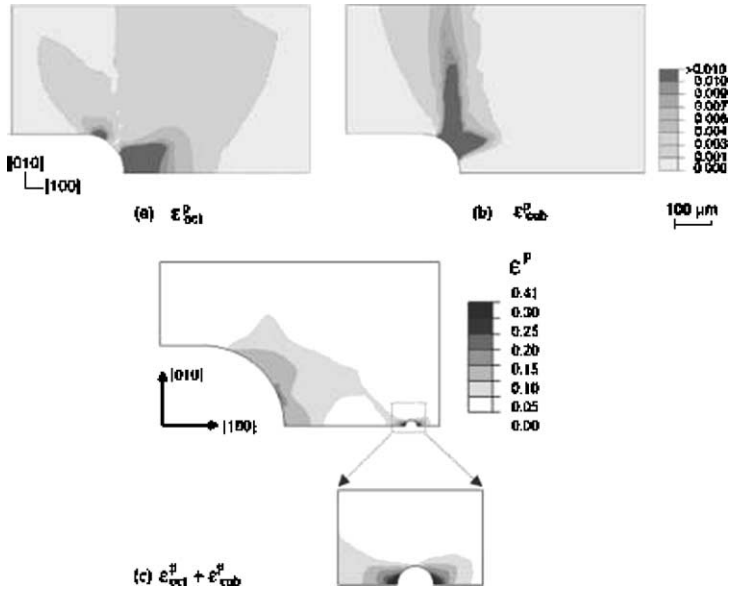


FIG. 7—*Contour plots of equivalent inelastic strain near the notch root in the void-free and voided CT specimens due to (a) octahedral and (b) cubic slip, for an applied* $K = 20$ MPa $m^{1/2}$ *after 1000 h, and (c) octahedral and cubic slip after* 400 h *with an applied* $K = 35$ MPa $m^{1/2}$ *at 950°C.*

octahedral (ε^p_{oct}) and cubic (ε^p_{cub}) slip are presented. The contours are plotted on the deformed configuration. Here, the uniaxial equivalent strain measures ($\varepsilon^p_{oct}, \varepsilon^p_{cub}$) are calculated from

$$\varepsilon^p_{oct,cub} = \sqrt{\frac{2}{3}(\mathbf{F}^p_{oct,cub} - 1)(\mathbf{F}^p_{oct,cub} - \mathbf{1})} \tag{13}$$

where $\mathbf{F}^p_{oct,cub}$ are obtained by integrating Eq 1 for the octahedral and cubic slip families, and **1** is the second-order identity tensor.

It can be seen in Figs. 7(*a*) and 7(*b*) that the peak strains at the notch root are highly localized (over distances less than 250 μm) and range between 1 % and approximately 10 %. The strain patterns are typical of glide on these systems: the peak octahedral strains lie on {111} planes (intersecting the (001) plane at ±45° in Fig. 7(*a*)) while the peak cubic strains lie on {100} planes (90° in Fig. 7(*b*)). It is also worth noting that, although octahedral slip systems are dominant under <001> uniaxial loading, there is a significant contribution to the inelastic strain from cubic slip since the resolved shear stress on these slip systems is no longer zero due to the presence of the notch.

Figure 8 shows contours of damage as defined by Eq 12 at two different times. The size of the

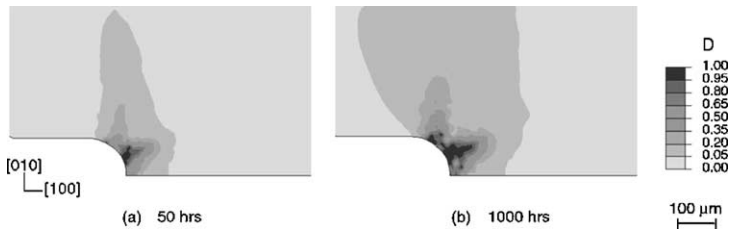


FIG. 8—*Contours of damage after (a) 50 h and (b) 1000 h under a* $K = 20$ MPa $m^{1/2}$ *applied load.*

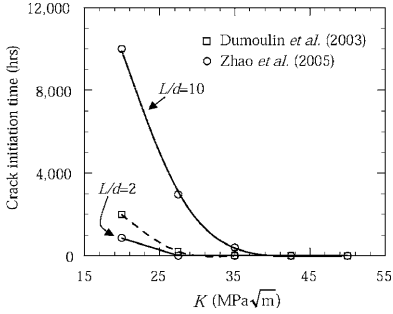


FIG. 9—*Effect of loading level* (K) *and void location* (L/d) *on the time to crack initiation at 950°C. The solid lines indicate the current results; the dashed lines the results from the damage analysis of Dumoulin et al. [6].*

damaged region increases with time as the critical strain for crack initiation is reached in elements further ahead of the notch. Regions where damage reaches a value of 0.99 are taken to have failed, which are identified as the darkest regions in Fig. 8 shown as 0.95–1. The damage patterns suggest that damage is strongly influenced by the accumulated inelastic strains (see Fig. 7) and that crack growth may not occur straight ahead of the notch but rather at a ±45° to 60° angle. This is consistent with experimental observations on fatigue tests on CMSX4 notched bars (Boubidi [14]). It was also found that the peak hydrostatic stress σ_m occurs directly ahead of the notch tip while the peak inelastic strains are at an angle to the notch, as shown in Fig. 7. However, the magnitude of the triaxiality (σ_m/σ_e) in the notch region ranges from $0.6 < \sigma_m/\sigma_e < 2.5$. Over this triaxiality range the failure strain is relatively independent of triaxiality (Dumoulin et al. [5]). Therefore, the magnitude and extent of damage is expected to depend more strongly on the localization of inelastic strain in this region.

Analyses With Notch-Void Interaction—For the notch-void interaction case, crack initiation time has been determined using the criterion defined earlier in the text for different load levels, quantified by the stress intensity factor K and varying distance of the void from the notch (L/d).

The redistribution of stress in the vicinity of the notch as a result of the presence of the microvoid was previously shown in Fig. 6(*b*) for $L/d=10$. Here, stress is plotted as a function of distance r from the notch root; a distance $r/L=1$ corresponds to the void surface (see inset to Fig. 6(*b*)). Note that the peak stress is initially located close to the notch root ($r/L=0$), but following the redistribution of stress due to creep (in Fig. 6(*b*)), the peak stress shifts towards the void ($r/L=1$). The peak inelastic strain is always found in the vicinity of the void, and crack initiation is thus predicted to occur at the void.

Figure 7 shows contours of equivalent inelastic strain after 400 h for a CT specimen with $K=35$ MPa $m^{1/2}$ and a representative void distance of $L/d=10$. It can be seen that significant inelastic strain accumulates at the void surface, indicating that crack initiation is expected to occur near the void.

The predicted crack initiation time for CMSX4, with $\tilde{\varepsilon}^p_{\text{critical}}=0.38$, is plotted in Fig. 9, as a function of the applied loading level. The critical strain is reached at a location adjacent to the void and one or two elements away from the specimen symmetry line. It may be seen that the predicted life reduces significantly with increasing load. It is found that if $K>40$ MPa $m^{1/2}$, fracture initiation occurs during loading; that is, when $t<100$ s.

The effect of the void spacing (L/d) is also shown in Fig. 9. For $L/d=2$, the void is very close to the notch and the time to crack initiation is significantly reduced. This is due to the strong interaction between the notch and the void as seen in Fig. 7(*c*)—a concentrated shear band emanates from the notch and amplifies the strain at the void. At $K=20$ MPa $m^{1/2}$, an approximately ten-times reduction in the time to crack initiation is predicted when the void location is changed from $L/d=10$ to $L/d=2$.

The predictions from the CD analysis are also included in Fig. 9. In the work of Dumoulin et al. [5], the time to crack initiation was taken as the time when the fully damaged region extended 50 μm ahead of the notch. A damage region of 50 μm in that work can be considered to be equivalent to a void spacing

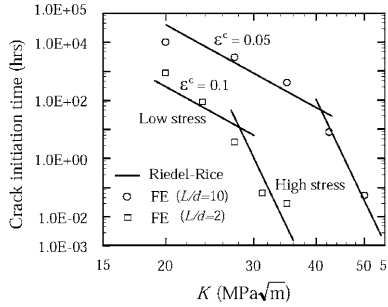


FIG. 10—*Comparison between Riedel-Rice equation (Eq 14) and FE analysis for crack initiation time under creep loading conditions (Zhao et al. [7]).*

of $L=50$ μm for the explicit-void analysis. It can be seen in Fig. 9 that the results from the CD analysis (dashed line) are located between those for $L/d=2$ ($L=30$ μm) and $L/d=10$ ($L=150$ μm), and are therefore consistent with those obtained with the explicit-void approach.

K-Based Creep Failure Assessment

Relative to the specimen dimensions, the creep zone in Fig. 7 is very limited in size and thus the problem falls into the small-scale creep regime. Under small-scale creep conditions, Riedel and Rice [15] proposed a relation to predict the initiation of a stationary crack in an isotropic, power-law creep material, based on the linear elastic stress intensity factor K. It was assumed that initiation occurs when the critical equivalent inelastic strain ε^c is reached at a small distance r ahead of the crack tip. The time to crack initiation t_i is then given by

$$t_i = \frac{(\varepsilon^c)^{n+1}}{E^n B(n+1)}\left[\frac{E^2 I_n r}{K^2(1-\nu^2)}\right]^n \tag{14}$$

where E is the (isotropic) Young's modulus, ν is Poisson's ratio, and B and n are parameters of the isotropic power-law creep relation

$$\dot{\varepsilon} = B\sigma^n \tag{15}$$

measured in uniaxial tension creep tests. The value of I_n depends on the creep exponent n (see, e.g., [16], Eq 14) has been derived for an isotropic material with a simple power law creep dependence. The applicability of the approach to the more complex material response of a single-crystal alloy has been examined in Zhao et al. [6] and will be discussed here.

In most superalloy single crystals, the steady-state creep deformation in the <001> direction at 950°C exhibits distinctive high- and low-stress regimes, where the strain rate sensitivity is approximately constant. Thus, creep parameter values can be obtained from a least-squares curve fitting of the test data in each region. For CMSX4, one finds $B=1.88\times10^{-20}$ MPa^{-n} s^{-1} and $n=4.72$ in the low-stress regime, and $B=2.12\times10^{-56}$ MPa^{-n} s^{-1} and $n=17.93$ in the high-stress regime. The corresponding values of I_n are 5.1 and 4.2 for the low- and high-stress regimes, respectively [16]. Equation 14 can be used to determine the crack initiation time for the CT specimen. The Young's modulus E and Poisson's ratio ν are the <001> values for CMSX4 at 950°C and r is the distance of the void from the notch root. The predicted crack initiation times from the Riedel-Rice (R-R) model are compared with the result from the FE analyses in Fig. 10, where the assumed critical strain values ε^c are approximately 0.05 for $L/d=10$ and approximately 0.1 for $L/d=2$. Note that the failure strain in Eq 14, which is determined here by fitting to the FE results, is a macroscale quantity and thus is not expected to be equal to the mesoscale failure strain $\bar{\varepsilon}^p_{\text{critical}}$, which includes the effect of the void at the meso/microscale.

A good correspondence between the Riedel-Rice relation and the FE result is demonstrated in Fig. 10. It is also interesting to note that when plotted in the form of Fig. 10, distinct low-stress and high-stress regimes can be identified in the FE predictions of the crack initiation time. However, note that the good

agreement between the FE prediction and Eq 14 was obtained by using different critical strains corresponding to the different void locations. The requirement for different macroscale failure strain values to match the FE predictions for different void locations may be related to changes in stress triaxiality at the different locations.

Conclusions

The FE studies have shown that the crack initiation time for the nickel superalloy depends strongly on the applied loading level, on the interaction between a microvoid and a notch, and on the critical distance over which failure is assumed to occur in a continuum damage approach. When the microvoid and the notch are close enough, concentrated shear bands form between the two which can lead to considerable reductions in crack initiation times. Predictions of crack initiation times obtained from the CD analysis under the assumption that cracks initiate from the notch once the fully damaged region extends to approximately one void spacing from the notch were found to be consistent with those obtained with the void-notch localization study.

It has also been found that the results can be described with the Riedel-Rice small-scale creep crack initiation model and the linear elastic stress intensity factor K. The applicability of the R-R model provides the potential for a probabilistic-based framework for the prediction of initiation time for CMSX4, which incorporates the strong sensitivity to void location. Such an approach has been proposed in a separate publication [16].

Acknowledgment

This work was jointly funded by the UK Engineering and Physical Research Council (UK) through grant GR/N12313 and by ALSTOM Power (UK).

References

[1] Douglas, J. P., "The Effect of Multiaxial Stress States on the Deformation of a Single-Crystal Nickel Based Superalloy at High Temperatures," PhD thesis, Imperial College London, 1999.

[2] Dennis, R. J., "Mechanistic Modelling of Deformation and Void Growth Behaviour in Superalloy Single Crystals," PhD thesis, Imperial College London, 2000.

[3] MacLachlan, D. W. and Knowles, D. M., "Fatigue Behaviour and Lifting of Two Single Crystal Superalloys," , Vol. 24, 2001, pp. 503–521.

[4] Okazaki, M. R., Tabata, T., and Nohmi, S., "Intrinsic Stage I Crack Growth of Directionally Solidified Ni-Base Superalloys During Low-Cycle Fatigue at Elevated Temperature," *Metall. Trans. A*, Vol. 21A, 1990, pp. 2201–2208.

[5] Dumoulin, S., Busso, E. P., and O'Dowd, N. P., "A Multiscale Approach for Coupled Phenomena in fcc Materials at High Temperatures," *Philos. Mag.*, Vol. 83, 2003, pp. 3895–3916.

[6] Zhao, L. G., O'Dowd, N. P., and Busso, E. P., "A Coupled Kinetic-Constitutive Approach to the Study of High Temperature Crack Initiation in Single Crystal Nickel-Base Superalloys," *J. of the Mechanics and Physics of Solids*, 2005, Vol. 54, 2006 , pp. 288–309.

[7] Busso, E. P., Cailletaud, G., and Quilici, S., "A Multiscale Micromechanics Approach to Describe Environmental Effects on Surface Crack Initiation Under Cyclic Loading," *Proc. of the IUTAM Symposium on Multiscale Modelling of Engng. Materials*, Marrakesh, Oct. 2002, S. Ahzi et al., Eds., Kluver Academic, pp. 49–57.

[8] Busso, E. P., O'Dowd, N. P., and Dennis, R. J., "A Rate Dependent Formulation for Void Growth in Single Crystal Materials," *Proceedings of the Fifth IUTAM Symposium on Creep in Structures*, 2001, S. Murakami and S. Ohno, Eds., pp. 41–50.

[9] Busso, E. P., "Cyclic Deformation of Monocrystalline Nickel Alluminide and High Temperature Coatings," PhD thesis, Department of Mechanical Engineering, Massachusetts Institute of Technology, Cambridge, MA, USA, 1990.

[10] Busso, E. P. and McClintock, F. A., "A Dislocation Mechanics-Based Crystallographic Model of a

B2-type Intermetallic Alloy," *Int. J. Plast.*, Vol. 12, 1996, pp. 1–28.
[11] *ABAQUS, V.6.2.8*, Hibbitt, Karlsson and Sorensen Inc., Providence, R.I., USA, 2003.
[12] Busso, E. P., Meissonnier, F., and O'Dowd, N. P., "Gradient-Dependent Deformation of Two-Phase Single Crystals," *J. Mech. Phys. Solids*, Vol. 48, 2000, pp. 2333–2361.
[13] Meissonnier, F., Busso, E. P., and O'Dowd, N. P., "Finite Element Implementation of a Generalised Non-Local Rate Dependent Crystallographic Formulation for Finite Strains," *Int. J. Plast.*, Vol. 17, 2001, p. 601.
[14] Boubidi, P., PhD thesis, Centre des Materiaux, Ecole des Mines de Paris, France, 2000.
[15] ASTM Standard STP 700, Riedel, H. and Rice, J. R., "Tensile Cracks in Creeping Solids," *Annual Book of ASTM Standards*, ASTM International, West Conshohocken, PA, 1980, pp. 112–130.
[16] ASTM Standard STP 560, Shih, C. F., "Small-Scale Yielding Analysis of Mixed Mode Plane-Strain Crack Problems," *Annual Book of ASTM Standards*, ASTM International, West Conshohocken, PA, 1974, pp. 187–210.

Journal of ASTM International, Vol. 3, No. 5
Paper ID JAI13226
Available online at www.astm.org

M. Tabuchi,[1] *H. Hongo,*[1] *T. Watanabe,*[1] *and A. T. Yokobori, Jr.*[2]

Creep Crack Growth Analysis of Welded Joints for High Cr Heat Resisting Steel

ABSTRACT: The creep strength of weldment for high Cr ferritic steels decreases due to Type IV damages in the heat affected zone during long-term services at high temperatures. It is important to predict initiation and growth of creep voids and cracks in weldment. This paper clarified the Type IV crack initiation and growth properties in fine-grained HAZ of weldments for tungsten strengthened high Cr steels. On the basis of experimental results, the computational simulation for Type IV crack growth behavior was conducted. The effect of multiaxial stress condition on vacancy diffusion and crack initiation was discussed.

KEYWORDS: high Cr heat resisting steel, welded joint, Type IV fracture, creep crack growth, FEM

Introduction

In consideration of reduction of CO_2 emissions and energy saving for thermal power plants, the steam pressure and temperature conditions of boiler components is tending to increase. The tempered martensitic P91 steel strengthened by Nb and V addition is widely used at around 873 K. The 9-12 %Cr steels strengthened by replacing Mo with W, P92 and P122 steels have higher creep strength than P91 steel. These steels are now applied to the boiler components of the ultra-supercritical (USC) power plants operating at around 893 K. The creep strength of weldment of these steels, however, decreases at above 873 K due to the Type IV creep damages formed in the ne-grained heat affected zone (HAZ) [1,2]. The lower creep strength of ne-grained HAZ structure is considered as the primary cause of Type IV fracture [3]. It is important to predict initiation and growth of creep crack in ne-grained HAZ of weldment. The creep crack growth properties of these tungsten strengthened steels [4] and their weldment [3], however, are scarcely investigated.

The present paper has investigated the creep crack initiation and growth properties of base metal and welded joints for W strengthened P122 and P92 steels. The computational analysis for Type IV crack growth behavior has been conducted. The effect of multiaxial stress condition on vacancy diffusion and crack initiation was investigated.

Material and Welding

The materials tested are 11Cr-0.4Mo-2W-CuVNb steel (ASME P122) and 9Cr-0.5Mo-1.8W-VNb steel (ASME P92) plates with the thickness of 27 and 30 mm, respectively. The chemical compositions of these steels are given in Table 1. The P122 steel was normalized at 1323 K for 100 min and tempered at 1043 K for 360 min. The P92 steel was normalized at 1323 K for 120 min and tempered at 1053 K for 120 min.

TABLE 1 *Chemical composition of the present steels (wt. %).*

	C	Si	Mn	P	S	Cu	Cr	Mo	W	V	Nb	B	N
P122	0.12	0.28	0.61	0.018	0.001	0.97	10.5	0.36	2.05	0.21	0.06	0.003	0.069
P92	0.09	0.16	0.47	0.010	0.001		8.72	0.45	1.87	0.21	0.06	0.002	0.050

Manuscript received April 12, 2005; accepted for publication January 30, 2006; published online February 2006. Presented at ASTM Symposium on Fatigue and Fracture Mechanics: 35th Volume on 18 20 May 2005 in Reno, NV; R. E. Link and K. M. Nikbin, Guest Editors.

[1] Group Leader and Senior Researchers, respectively, National Institute for Materials Science, High Temperature Materials Group, 1-2-1 Sengen, Tsukuba, 305-0047; Japan.

[2] Professor, Tohoku University, Department of Nano Mechanics, Aoba01, Aramaki, Aoba-ku, Sendai, 980-8579; Japan.

Copyright © 2006 by ASTM International, 100 Barr Harbor Drive, PO Box C700, West Conshohocken, PA 19428-2959.

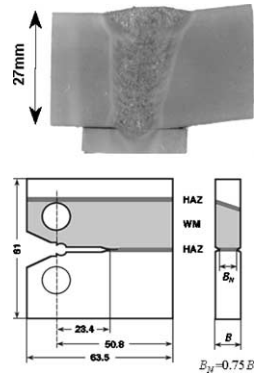


FIG. 1—(*a*) *Cross-sectional view of the GTAW joint and* (*b*) *CT specimen.*

The A_{c1} and A_{c3} temperatures were estimated to be 1093 and 1193 K for the P122 steel and 1123 and 1193 K for the P92 steel, respectively.

Welded joints were fabricated using multi-layer gas tungsten arc welding (GTAW) with single bevel groove as shown in Fig. 1(*a*). Welding consumable used for GTAW was matching filler wire developed recently for welding this class of steel. Laser beam welded (LBW) joints were also prepared in order to investigate the effect of HAZ width. The width of HAZ was about 2.5 mm for GTAW and 0.5 mm for LBW. The welded joints were subjected to the post weld heat treatment (PWHT) at 1013 K for 260 min.

The tensile test and creep tests for weld metal (WM), base metal (BM), simulated coarse-grained and fine-grained HAZ were conducted at 923 K using standard creep specimen with a 6-mm diameter and a 30-mm gage length. The simulated fine-grained HAZ specimens were produced heating up to 1223 K and cooling down [3]. The material properties obtained are Young's modulus E, yield stress σ_{ys} and Norton's creep law $\dot{\varepsilon}=A\sigma^n$ of P122 steel at 923 K shown in Table 2.

Creep Crack Growth Test Procedure

Creep crack growth tests were conducted according to the standard of ASTM E 1457 [5]. The creep crack growth tests for base metal, welded joints, and simulated fine-grained HAZ were conducted using CT specimen at 923 K. The specimen thickness B was 10 and 17 mm. The notch tip of welded joint specimen was located in HAZ as shown in Fig. 1(*b*). The specimens were fatigue precracked with 3 mm in length, and then side-grooved with 25 % of specimen thickness. Creep crack length was measured by D-C electrical potential method. The crack growth tests were stopped when the final fracture of specimens were imminent. The crack length was corrected by comparing the actual final crack length with the measured one by electrical potential. The crack opening displacement was measured.

Creep Crack Growth Behavior of Welded Joints

Figure 2 shows the examples of creep crack propagation profile of welded joint specimen. Propagation of a very sharp creep crack in fine-grained HAZ, i.e., the Type IV crack, was observed for all the welded joint specimens tested at 923 K. It is difficult to machine the notch tip in the center of HAZ in some cases, but

TABLE 2—*Material properties of P122 steel weldment at 923 K.*

	E (GPa)	σ_{ys} (Mpa)	A (MPa^{-n}h^{-1})	n
Weld metal	106	91	2.45×10^{-36}	14.8
Coarse-grained HAZ	99	135	4.86×10^{-22}	8.4
Fine-grained HAZ	77	82	4.58×10^{-20}	7.7
Base metal	103	104	1.35×10^{-25}	10.0

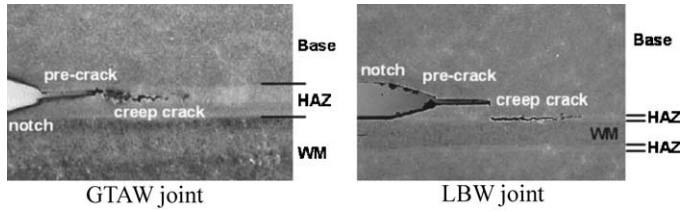


FIG. 2—*Creep crack propagation profile of welded joint specimens of P122 steel.*

creep crack propagated in fine-grained HAZ. Creep void formation was observed around the main crack for both GTAW and LBW joints.

Figure 3 shows the obtained creep crack growth curves of welded joints, base metal, and simulated fine-grained HAZ for P122 steel tested at the same loading conditions; initial stress intensity factor K_{in} =18 and 16 MPam$^{1/2}$. The crack growth lives of the welded joints and simulated fine-grained HAZ are about one-third of base metals independent of HAZ width. Here the crack growth life means the time when the final fracture of specimen is imminent and the test is stopped. For the welded joints, the incubation period, during which the crack scarcely grows, exists and then the crack grows rapidly in the accelerating stage. The amount of crack extension during incubation period is about 0.25 mm for welded joints. The effect of specimen thickness between B=10 and 17 mm on creep crack growth behavior was very small as shown in Fig. 3(*a*). The creep crack growth test results for P92 steel was shown in Fig. 4. Nearly the same tendency of crack growth behavior was observed for both P122 and P92 steels.

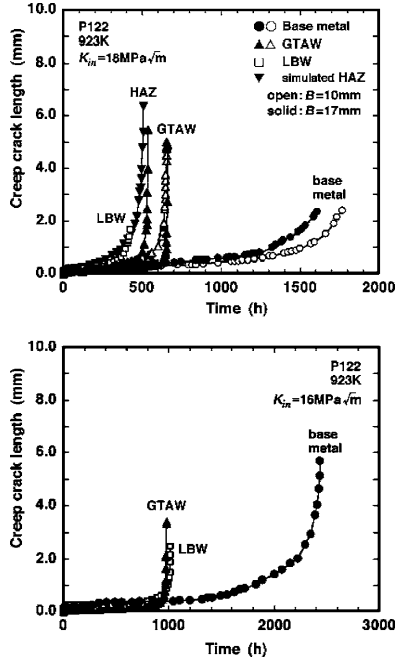


FIG. 3—*Creep crack growth curves of base metal, welded joints, and simulated HAZ of P122 steel at 923 K for the loading conditions for (a)K_{in}=18MPam$^{1/2}$ and (b) K_{in}=16MPam$^{1/2}$.*

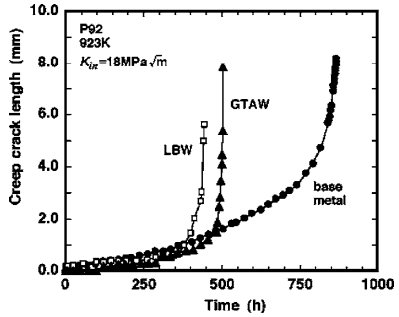


FIG. 4—*Creep crack growth curves of base metal and welded joints of P92 steel at 923 K for the loading conditions for* $K_{in}=18MPam^{1/2}$.

Creep Crack Initiation and Growth Properties

Because the incubation period for crack growth was observed, evaluation of crack initiation is important. The evaluation method for creep crack initiation time by using C^* value at crack initiation was proposed based on a model of the build-up of damage in the process zone at the crack tip [6]. The C^* line integral at initial crack length was calculated by FEM using two-dimensional mesh of CT specimen under plane stress condition. Norton's creep law of fine-grained HAZ and base metal of P122 steel in Table 2 is used for FEM analysis. Figure 5 shows the computed C^* value for base metal, GTAW, LBW, and simulated fine-grained HAZ plotted against loading time. For this computation, only the width of fine-grained HAZ was changed as 1.2 and 0.2 mm for GTAW and LBW joint, respectively. The computed C^* value for the fine-grained HAZ is about one order higher than that of base metal. The C^* value of welded joints is decreased as the width of HAZ is decreased. From the computed C^* value, decreasing of HAZ width is expected to improve the crack growth life, while the experimental results of Figs. 3 and 4 are different.

The computed C^* approaches to a constant value as the loading time increases. The experimental incubation time of crack growth is plotted against this constant C^* value at initial crack length in Fig. 6. Here we plotted the onset time of accelerating stage as the incubation time. Although the crack initiation time could be evaluated from the initial C^* value, the scattering of data due to the effect of HAZ width, which seemed to be related to the mechanical constraint effect [6], was observed in the relations of Fig. 6. For the same C^* value, decreasing HAZ width decreased the crack initiation time.

The creep crack growth rate was evaluated by C^* parameter calculated as follows [7]

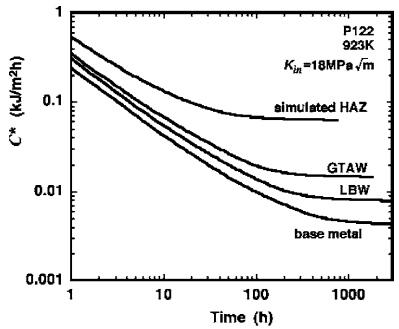


FIG. 5—*Computed* C^* *line integral at initial crack length by FEM for P122 steel.*

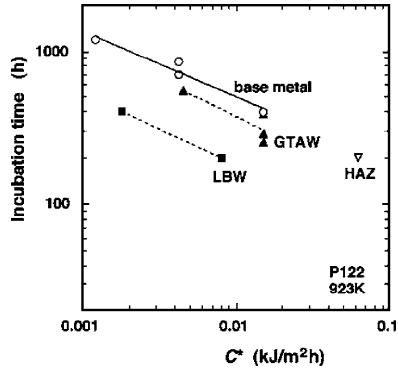


FIG. 6—*Relationship between experimental incubation time versus computed C^* at initial crack length for P122 steel at 923 K.*

$$C^* = \frac{n}{n+1}\frac{Pd\delta/dt}{B_N(W-a)}\left(\gamma - \frac{\beta}{n}\right) \tag{1}$$

where W is the specimen width, a is the crack length, P is the load, B_N is the net thickness, $d\delta/dt$ is the crack opening displacement rate, n is the creep exponent in Norton's law. β and γ are given as follows

$$\gamma = \frac{2(1+\alpha)(1+a/W)(1+\alpha^2)+\alpha(1-a/W)}{(1+a/W)+\alpha(1-a/W)} \tag{2}$$

$$\beta = \frac{\alpha}{\alpha+(1+a/W)/(1-a/W)} \tag{3}$$

$$\alpha = \sqrt{\{2a/(W-a)+1\}^2+1} - \{2a/(W-a)+1\} \tag{4}$$

The relations between creep crack growth rate da/dt versus C^* parameter of welded joints and base metal for P122 and P92 steels are indicated in Figs. 7 and 8, respectively. The data points before incubation time were removed in these figures. The data band of P91 steel [8] is also given in this figure. The creep crack growth rate of base metal of P92 and P122 steels strengthened by tungsten were higher compared to the data band of P91 steel. While the creep crack growth rate of welded joints were higher than the base metal at higher C^* region, the differences of da/dt between welded joints and base metal were small for the present high Cr steels.

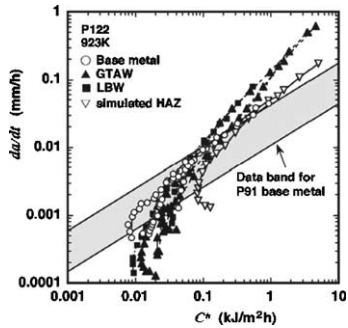


FIG. 7—*Relations between creep crack growth rate versus C^* parameter of the base metal and welded joints for P122 steel at 923 K.*

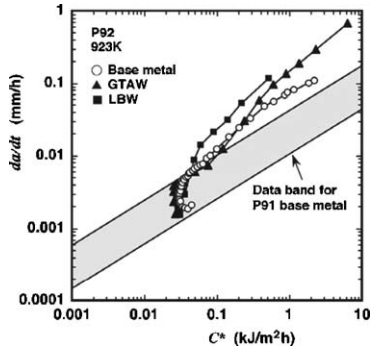


FIG. 8—*Relations between creep crack growth rate versus C^* parameter of the base metal and welded joints for P92 steel at 923 K.*

While the differences of da/dt between welded joints and base metal was negligible, the crack initiation times and crack growth lives of welded joints were shorter than that of base metals as shown in Figs. 3 and 4. From the present results, the prediction of crack initiation time was considered to be important for the evaluation of fracture life of the welded joints.

Simulation for Type IV Creep Crack Growth

Based on the experimental results, we have conducted computational simulation for Type IV creep crack growth. The FEM analyses were conducted for the three-dimensional CT specimen model shown in Fig. 9 using material constants in Table 2. Although the mesh size effect exists for crack growth simulation, here we use a comparatively coarse mesh by reason of CPU times for three-dimensional simulation. Based on the model that creep crack growth occurs at the crack tip when the available creep ductility of the material is exhausted there, creep crack growth rate can be characterized by creep ductility ε_f^* [9]. Therefore, when the equivalent strain ahead of the crack tip reached to fracture strain, the coordinate of crack tip node was moved and the fixed boundary condition of the crack tip was removed [10,11].

The lines of Fig. 10 indicate the computed crack growth curves of welded joints and base metal. For this computation, the same creep ductility of $\varepsilon_f^*=0.1$ was used for base metal and weldment and only the width of HAZ was changed. Because the creep fracture strain is influenced by the stress triaxiality, the value of smaller fracture strain than that under uniaxial condition should be used. The effect of CT specimen thickness on creep fracture strain value, however, is not clear, so we indicate the computed examples obtained by using 0.1 for the critical strain in Fig. 10. The uniaxial creep ductility of the round bar specimen for this material was about 0.6. The tendency of crack growth lives of welded joints and base metal can almost be simulated. From the computed curve, decreasing of HAZ width is considered to increase crack growth life, while the experimental results show the different tendency. Here we used the same creep ductility for welded joints and base metal, but it should be changed dependent on stress multiaxiality [11].

For the welded joints, the narrow fine-grained HAZ with lower creep strength was mechanically constrained by base metal and weld metal with higher creep strength. Therefore, the Type IV crack grew

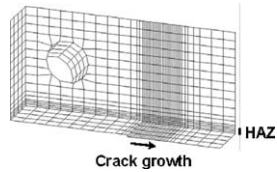


FIG. 9—*Three-dimensional CT specimen model.*

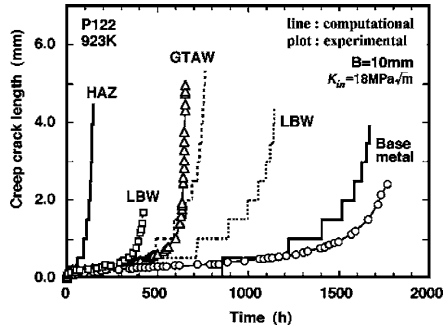


FIG. 10—*Computed crack growth curve against time for welded joint and base metal of P122 steel.*

accompanying with creep voids ahead of the crack tip. It has been proposed that under creep conditions the diffusion of vacancies towards a crack or a void would contribute to crack growth [12]. The vacancy diffusion, void formation and crack initiation would be accelerated under multiaxial stress field. Here we evaluate the vacancy diffusion according to the following equation [12,13]

$$\frac{\partial C}{\partial t} = \alpha_1 D \nabla^2 C + \alpha_2 \frac{D}{RT} \nabla C \nabla \nu \tag{5}$$

$$\nu = -\sigma_p \Delta V \tag{6}$$

where C is the vacancy concentration, D is the diffusion coefficient, R is the gas constant, T is the absolute temperature, σ_P is the hydrostatic stress, ΔV is the change of molar volume by vacancy diffusion. The α_1 and α_2 are weight coefficient [13]. In this equation the vacancy diffusion is controlled by hydrostatic stress gradient. The vacancy diffusion equation is solved for three-dimensional CT specimen model using the hydrostatic stress gradient computed by FEM. The boundary conditions for vacancy diffusion analysis used here is $\partial C/\partial x = C - C_0$ at the crack tip and free for other specimen surfaces.

Figure 11 shows the computed result of changes in vacancy concentration ahead of the crack tip during creep using $\alpha_2/\alpha_1 = 300$, $\Delta V = 2.0 \times 10^{-6} (\mathrm{m}^3/\mathrm{mol})$ and $D = 1.5 \times 10^{-9} (\mathrm{m}^2/\mathrm{s})$ for welded joints. The vacancy concentration increases faster as the width of HAZ is decreased, because the multiaxiality in fine-grained HAZ is increased. The increase of vacancy concentration is considered to be related to the formation of creep damage zone. This means that the decreasing width of HAZ cannot improve the Type IV crack initiation time or growth life.

In order to reflect the vacancy concentration to the crack growth analysis here, we assume the following computational procedure. When the vacancy concentration increases, which means the formation of creep damage, the stiffness matrix $[K]$ around the crack tip is decreased linearly dependent on the vacancy

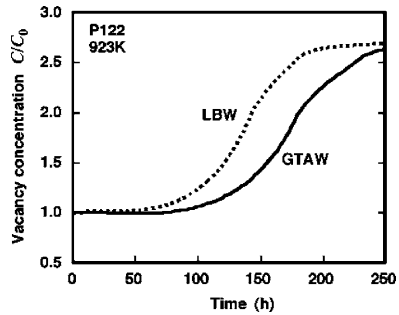


FIG. 11—*Changes of vacancy concentration ahead of the crack tip for the welded joints during creep.*

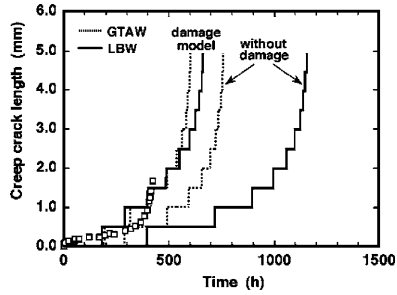


FIG. 12—*Example of crack growth simulation taking damage zone into account.*

concentration. The computed result of Fig. 12 shows that the crack initiation time and crack growth life is accelerated by taking the damage formation into account. From these results, the effect of multiaxial stress condition in HAZ on damage formation and crack initiation is considered to be important for life evaluation of welded joints.

Summary

The creep crack initiation and growth properties of welded joints and base metals for tungsten strengthened high Cr heat resisting steels were investigated. The results can be summarized as follows:

1. Creep crack growth properties of welded joints and base metal of P122 and P92 steels were clarified. Creep crack propagation in the fine-grained HAZ, i.e., Type IV crack growth, was observed for all welded joints at 923 K.
2. The differences in creep crack growth rate between welded joints and base metal were small for the present high strengthened steels, whereas the crack initiation time was shorter for welded joints than base metal.
3. The crack initiation time could be correlated with initial C^* value computed by FEM, while the effect of mechanical constraint was observed.
4. A three-dimensional analysis program for vacancy diffusion and crack growth under creep condition has been developed in order to simulate Type IV fracture.
5. The effect of multiaxial stress condition in HAZ of weldment on damage formation and crack initiation is considered to be important for the life prediction of welded joints.

Acknowledgments

A part of this study was financially supported by the Budget for Nuclear Research of the Ministry of Education, Culture, Sports, Science and Technology, based on the screening and counseling by Atomic Energy Commission.

References

[1] Bell, K., "Elevated Temperature Midlife Weldment Cracking (Type IV) - A Review," TWI Report 597/1977, The Welding Institute, Abington, Cambridge, 1997.

[2] Masuyama, F., Matsui, M., and Komai, N., "Creep Rupture Behavior of Advanced 9-12 %Cr Steel Weldment," *Key Eng. Mater.*, Vols. 171–174, 2000, pp. 99–107.

[3] Tabuchi, M., Watanabe, T., Kubo, K., Matsui, M., Kinugawa, J., and Abe, F., "Creep Crack Growth Behavior in the HAZ of Weldments of W Containing High Cr Steel," *Int. J. Pressure Vessels Piping*, Vol. 78, Nos. 11 and 12, 2001, pp. 779–784.

[4] Yokobori, Jr. A. T., Takamori, S., Yokobori, T., Hasegawa, Y., Kubota, K., and Hidaka, K., "Mechanical Behavior and Strengthening Mechanism of W Containing 9-12 %Cr Steels Under Creep

Condition for a Cracked Specimen," *Key Eng. Mater.*, Vols. 171–174, 2000, pp. 131–138.

[5] Standard Test Method for Measurement of Creep Crack Growth Rates in Metals, ASTM Standard E 1457-00, ASTM International, West Conshohocken, PA, 2000.

[6] Webster, G. A. and Ainsworth, R. A., "High Temperature Component Life Assessment," Chapman & Hall, London, 1994.

[7] Ernst, H. A., "Unified Solution for J Ranging Continuously from Pure Bending to Pure Tension," ASTM STP 791, 1983, pp. 499–519.

[8] Shibli, I. A. and Hamata, N. LeMat, "Creep Crack Growth in P22 and P91 Welds—Overview from SOTA and HIDA Projects," *Int. J. Pressure Vessels Piping*, Vol. 78, Nos. 11 and 12, 2001, pp. 785–793.

[9] Nikbin, K. M., Smith, D. J., and Webster, G. A., "An Engineering Approach to the Prediction of Creep Crack Growth," *Trans. ASME, J. Eng. Mater. Tech.*, Vol. 108, No. 2, 1986, pp. 186–191.

[10] Hsu, T. R. and Zhai, Z. H., "A Finite Element Algorithm for Creep Crack Growth," *Eng. Fract. Mech.*, Vol. 20, No. 3, 1984, pp. 521–533.

[11] Yatomi, M., Nikbin, K. M., and O'Dowd, N. P., "Creep Crack Growth Prediction Using a Damage Based Approach," *Int. J. Pressure Vessels Piping*, Vol. 80, Nos. 7 and 8, 2003, pp. 573–583.

[12] Leeuwen, H. P., "The Application of Fracture Mechanics to Creep Crack Growth," *Eng. Fract. Mech.*, Vol. 9, No. 4, 1977, pp. 951–974.

[13] Yokobori, Jr., A. T., Nemoto, T., Satoh, K., and Yamada, T., "Numerical Analysis on Hydrogen Diffusion and Concentration in Solid with Emission Around the Crack Tip," *Eng. Fract. Mech.*, Vol. 55, No. 1, 1996, pp. 47–60.

Journal of ASTM International, February 2006, Vol. 3, No. 2
Paper ID JAI13227
Available online at www.astm.org

K. Wasmer,[1] *K. M. Nikbin,*[2] *and G. A. Webster*[2]

Prediction of Scatter in Creep Crack Growth Data from Creep Failure Strain Properties

ABSTRACT: Procedures are available for determining the creep crack growth (CCG) properties of materials experimentally in terms of the creep fracture mechanics parameter C^*. When these properties have not been measured, predictions can be made from models of the cracking process. These models show that creep crack growth rate at a given value of C^* is most sensitive to the creep ductility ε_f^* appropriate to the state of stress at a crack tip. For plane stress conditions, it is found that ε_f^* can be taken to be equal to the uniaxial creep ductility ε_f of a material and for plane strain to be given by $\varepsilon_f/30$. Hence, in this paper, uniaxial creep properties on type 316 L(N) austenitic stainless steel and two 9 %Cr steels, designated P91 and P92, in the temperature range 500–750°C are reported and scatter in the data identified from statistical analysis. For each steel, the dependence of creep ductility on stress and temperature is determined. It has been found that none of the rupture time (t_R), creep strain rate ($\dot{\varepsilon}$), and net section stress (σ_{net}), parameters has a better relationship with the creep failure strain. Hence, none of these parameters characterizes better than the other the creep ductility's behavior. Additionally, it has been observed that although the creep failure strain of 316 L(N) is independent of these parameters, it increases with temperature. In contrast, the creep failure strain of P91 is slightly sensitive to σ_{net} but is overcompensated by the scatter and so can be assumed stress independent. The creep failure strain of P91 is seen to be also insensitive to temperature. For P92, ε_f goes from a lower to an upper shelf through a transition region. Thus the best solution to characterize the failure strain behavior is to use a polynomial solution. Creep crack growth properties obtained on cracked compact tension and C-shaped specimens are also presented. Probabilistic analysis, based on Monte Carlo simulation methods, is employed to predict scatter in the creep crack growth data from scatter in the uniaxial creep properties. In most instances, close agreement is found between the experimentally measured scatter in the cracking results and that predicted from the scatter obtained from creep ductility data.

KEYWORDS: uniaxial creep properties, creep ductility, creep crack growth, probabilistic methods

Nomenclature

A, A_{ave} = constants in creep strain rate laws
H = constant in creep rupture law
I_n = nondimensional function of n
r_c = size of creep damage zone
$\dot{a}$ = creep crack growth rate
C^*, C^*_{Exp} = steady-state creep fracture mechanics parameter and experimental C^* value
D = constant in creep crack growth law
e_{ε_f} = error in creep failure strain
K = stress intensity factor
n, n_{ave}, n_s = stress indices in power-law creep equations
r_{STAT}, r^2_{STAT} = statistical correlation, coefficient of determination
SD = standard deviation of the errors

Manuscript received May 7, 2005; accepted for publication September 7, 2005; published December 2005. Presented at ASTM Symposium on Fatigue and Fracture Mechanics: 35th Volume on 18–20 May 2005 in Reno, NV; R. E. Link and K. M. Nikbin, Guest Editors.

[1] Project manager, Swiss Federal Laboratories for Materials Testing and Research (EMPA–Thun), Laboratory for Materials Technology, Feuerwerk-strasse 39, 3602 Thun, Switzerland.

[2] Principal Reseach Fellow and Professor, respectively, Department of Mechanical Engineering, Imperial College, London, SW7 2BX, United Kingdom.

t_R = uniaxial rupture time
W = width of the specimen
ϕ = index in creep crack growth law
ε_f, $\bar{\varepsilon}_f$ = uniaxial creep failure strain, mean creep failure strain
ε_f^* = creep ductility appropriate to state of stress
$\dot{\varepsilon}_{\text{ref}}$ = creep strain rate at the reference stress
$\dot{\varepsilon}$, $\dot{\varepsilon}_{\text{ave}}$ = secondary (or minimum) strain rate, average creep strain rate
$\sigma, \sigma_{\text{ref}}, \sigma_{\text{net}}$ = stress, reference stress, and net section stress
ν = stress index in creep rupture law

Introduction

In order to predict the lifetimes of components that operate at high temperatures reliably, it is essential to determine their creep rupture and creep crack growth (CCG) behavior accurately. Several design and assessment procedures are available for dealing with this situation. These include the French A16 [2,3], British Energy R5 [4], and BS 7910 [5] codes. Each of these procedures adopts the same basic principles by describing creep strain rate $\dot{\varepsilon}$ and crack growth rate $\dot{a}$ by the power-law relations

$$\dot{\varepsilon} = A \cdot \sigma^n \tag{1}$$

and

$$\dot{a} = D \cdot C^{*\phi} \tag{2}$$

where A, n, D, and ϕ are material constants, σ is stress, and C^* is the creep fracture mechanics parameter [6,7]. In laboratory tests this term is determined experimentally based on the ASTM E 1457 [8] procedure. In components, it is usually estimated from reference stress methods [9,10]. A deterministic approach is employed most often to make assessments and decisions have to be made about whether to choose upper or lower bound material properties to achieve conservative predictions. A worst case combination of bounds may result in excessive conservatism.

Although D and ϕ are best obtained experimentally from tests carried out according to ASTM E 1457 [8], models are available for predicting their values from uniaxial creep data [11,12]. For a creep law of the form of Eq 1 these give

$$\phi = \frac{n}{n+1} \tag{3}$$

and

$$D = \frac{(n+1)}{\varepsilon_f^*}\left[\frac{A \cdot r_c}{I_n^n}\right]^{1/n+1} \tag{4}$$

where r_c is the size of the creep zone at the crack tip in which damage accumulates, I_n is a non-dimensional function of n and state of stress, and ε_f^* is the creep ductility of the material appropriate to the state of stress at the crack tip. For plane stress conditions ε_f^* can be taken as the uniaxial creep ductility ε_f of a material and for plane strain as $\varepsilon_f/30$. Since for most practical purposes $0.7 < \phi < 1$ and the terms in square brackets in Eq 4 are raised to a small fractional power, Eq 2 can often be simplified to

$$\dot{a} = \frac{3 \cdot C^{*0.85}}{\varepsilon_f^*} \tag{5}$$

where $\dot{a}$ is in mm/h, C^* in MPa/m^2·h and ε_f^* as a fraction.

Replacing ε_f^* by either ε_f or $\varepsilon_f/30$ in Eq 5, it is evident that D in Eqs 2 and 4, and so CCG predictions, are most sensitive to the creep ductility of a material. Consequently, it may be expected that it should be possible to predict the scatter in creep crack growth data from that recorded in the creep ductility data. To enhance the CCG predictions, it is imperative to have a characterization of the failure strain as close as possible to the reality. In this investigation scatter in uniaxial creep strain rate, rupture and creep ductility data are examined to establish the scatter to be expected in cracking properties. Data on austenitic stainless

steel type 316 L(N) [13,14] and two advanced 9% Cr steels designated P91 [15–23] and P92 [19–24] are considered. The results of the characterization will then be used in a probabilistic method in a latter section.

Materials and Experiments

The data used in this study come mainly from European HIDA, LICON, and CRETE collaborative projects (See Acknowledgment section). Based on these databases, sufficient data were available to allow them to be examined separately as individual batches as well as using them all as one dataset. The nominal chemical compositions of these steels are shown in Table 1. The uniaxial creep data were collected at temperatures in the range 500 to 750°C in accordance with ASTM E 139 [25]. The tests were performed on several casts of the steels. The materials were selected on the basis that they are used in the fabrication of some of high temperature power plant components. Emphasis has been placed on the analysis of creep ductility, secondary, and average creep strain rates defined in Eq 6. Large datasets have been analyzed and the statistical results given in this paper in order to be used as benchmark for CCG predictions.

$$\dot{\varepsilon}_{\text{ave}} = \frac{\varepsilon_f}{t_R} = A_{\text{ave}} \cdot \sigma^{n_{\text{ave}}} \tag{6}$$

with rupture life t_R expressed as

$$t_R = H \cdot \sigma^{-\nu} \tag{7}$$

where A_{ave}, n_{ave}, H, and ν are material constants and creep crack growth rate. In these equations when $n=\nu$, creep failure strain is independent of stress. When $n_{\text{ave}}>\nu$ creep ductility decreases with decrease in stress.

By combining Eqs 6 and 7, ε_f can be expressed in the form of

$$\varepsilon_f = A_{\text{ave}} \cdot H \cdot \sigma^{n_{\text{ave}}-\nu} \tag{8}$$

Equation 8 does not predict ε_f of each data point but only its means value as well as the sensitivity of the failure strain according to the applied stress. When $n_{\text{ave}}=\nu$, ε_f is constant and is equivalent to the mean creep failure strain $\bar{\varepsilon}_f$, whereas when $n_{\text{ave}}>\nu$, ε_f increases as σ increases. Therefore, two types of creep failure strain behavior are expected and have been reported by R5 [4]. These are (i) a trend of increasing ductility with increasing net section stress from a lower shelf to an upper shelf and (ii) no clear trend of increasing ductility with stress.

The recommendations of ASTM E 1457 [8] were followed for performing the crack growth tests and in interpreting the results. The results of CCG tests of two types of geometries are presented here which are the compact tension (CT) and c-shape (C). Statistical analysis routines were employed for determining the scatter in the data.

Uniaxial Results

Results of statistical analyses that have been performed on the entire uniaxial creep data are presented in Tables 2–5 for the 316 L(N), P91, and P92 steels, respectively. These tables include information on a wide range of tests on several batches of material. In Table 6 additional results are provided for batches of material on which CCG studies were performed. These tables contain mean values of n, n_{ave},ν, $\bar{\varepsilon}_f$, and standard deviation in ductility SD ε_f at each temperature for all the batches of material combined. Also included in Table 6 are the mean values of D and ϕ obtained from the cracking data in addition to the standard deviation in crack growth rate.

The dependence of creep ductility on secondary creep rate and stress for three batches of 316 L(N) steel at 650°C, from which CCG tests were performed, are shown in Fig. 1. First, it has been found that none of the following parameters, the rupture time (t_R), the creep strain rate ($\dot{\varepsilon}$), and the net section stress (σ_{net}), has a better relationship with ε_f. Hence, none of these parameters characterizes better than the other the creep ductility's behavior and evidence of this is illustrated in Fig. 1 and Table 2 with the statistical correlation value r_{STAT}. Second, it is difficult to establish a clear trend between different casts. This behavior was expected since it has been observed from Table 2, that $n_{\text{ave}} \approx n_s \approx \nu$ for 316 L(N)–PM. Since

ε_f is not stress dependent and that no cast influence is perceived (see Fig. 1), it is possible to analyze all creep failure ductility results regardless their cast and origin. This is supported further in Fig. 2 where the creep failure strain is plotted on a normal probability diagram for all the 316 L(N) tests at 650°C. The visual examination of this figure demonstrates that, except for a few points, the data are normally distributed and this is corroborated by a r_{STAT}=0.98. This proves that creep failure strain data can be assumed to be insensitive to the stress and normally distributed. The dependence of creep ductility on stress for the entire dataset is presented in Fig. 3 together with the upper and lower two standard deviation (2*SD*) bounds. It is apparent, within the range of scatter observed, that creep failure strain can be regarded as independent of stress for this temperature. Similar trends were observed for the other temperatures examined. The mean, standard deviations, and correlation coefficients obtained for each temperature are listed in Table 2. This table and Fig. 4 indicate that the mean creep ductility and the standard deviations for each temperature for 316 L(N) stainless steel increase with temperature. The ±2 standard deviation (±2*SD*) bounds for the average creep strain rate at 650°C are shown in Fig. 5 as a function of net section stress. These approximate to a range of about times 22.

The creep failure strain behavior of the two 9 %Cr steels are different as those obtained on the 316 L(N) stainless steel as indicated in Tables 3 and 4. Illustrations of the scatter obtained in creep ductilities are shown in Figs 6–9 for the P91 steel. Based on Fig. 6, the P91 creep ductility seems to increase with the net section stress. This is consistent with Eq 8 in conjunction with the results given in Table 3 where $n_{Ave} > \nu$. However, this trend disappears when all individual batches of material are combined into one

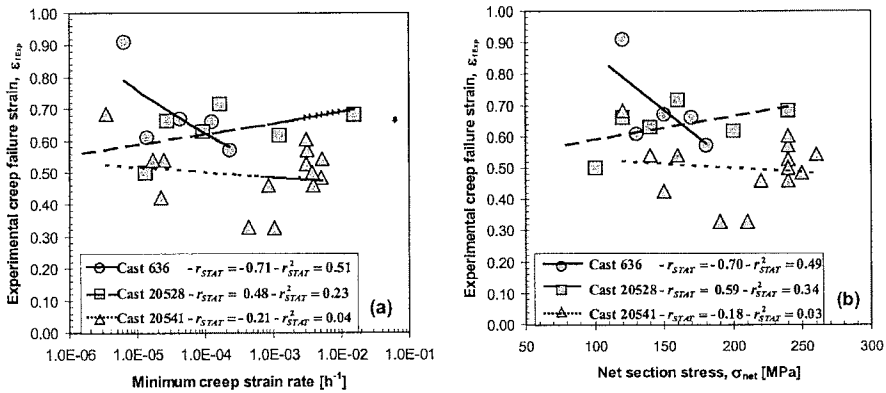


FIG. 1—*The effect of (a) secondary creep rate and (b) stress on the creep failure strain for three casts of 316 L(N) steel at 650°C.*

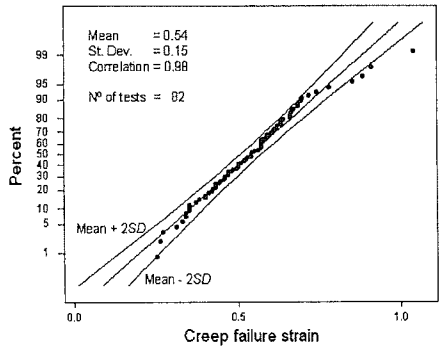


FIG. 2—*Normal probability plot of creep failure strain for all tests on 316 L(N) steel at 650°C.*

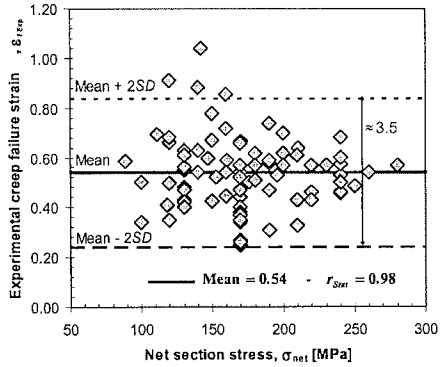


FIG. 3—*Creep failure strain as a function of stress for all tests on 316 L(N) steel at at 650°C.*

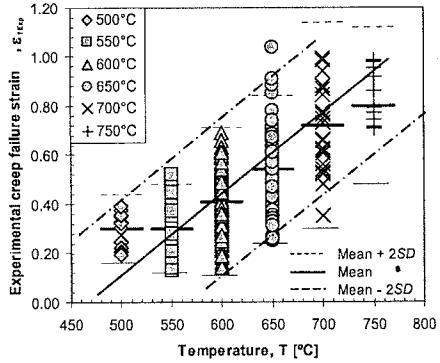


FIG. 4—*Effect of temperature on the creep failure strain for all tests on 316 L(N) steel.*

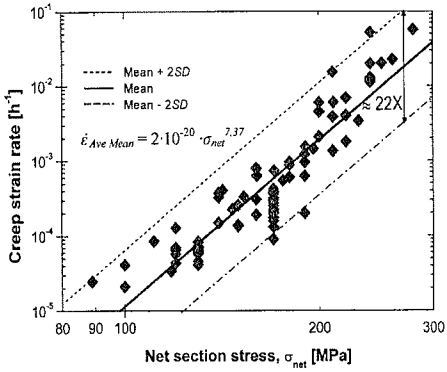


FIG. 5—*Average creep strain rate for all tests on 316 L(N) steel at 650°C.*

dataset as evidence from Figs. 7–9. Based on these figures, it is evident that, for the P91 steel, ε_f can be regarded as independent of stress, and so normally distributed. This is demonstrated by making this assumption and testing with the normal probability plot as in Fig. 7. Figure 8 illustrated the results of the complete dataset available for P91 including the mean and ±2 standard deviations. Furthermore, P91 is, in contrast to 316 L(N), insensitive to temperature, and evidence of this is in Fig. 9. Also dissimilar to 316 L(N) stainless steel, its scatter for the total dataset rises with an increase in temperature only between 500 and 550°C. This may be due to the small number of tests available at 500°C.

The scatter in ε_f for P92 is presented in Figs 10–12. These figures show that ε_f increases with both stress and temperature. The stress dependence can be interpreted in terms of a lower and upper shelf ductility, with a transition region, as reported in R5 - British Energy [4] and seen in Fig. 10, or by a polynomial expression as indicated in Figs 11 and 12. The fitting coefficients to a fifth degree polynomial fit are listed in Table 5. The purpose of the table is to be used as benchmark when no P92 uniaxial data are available for CCG predictions. Even if r^2_{STAT}, the coefficient of determination, in Table 5 are not high, the polynomial expression is by far the simplest method to represent the creep ductility behavior since determining the lower and upper shelves linked by the transition only on a statistical basis is not viable. In all cases, it has been found that results on individual batches of material can be combined into one dataset for statistical analysis.

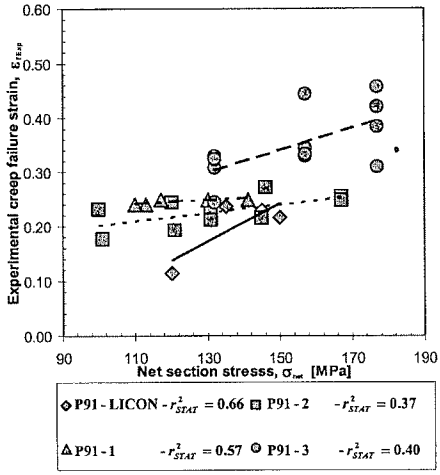


FIG. 6—*The effect of net section stress on the creep failure strain for of P91 steel at 600°C.*

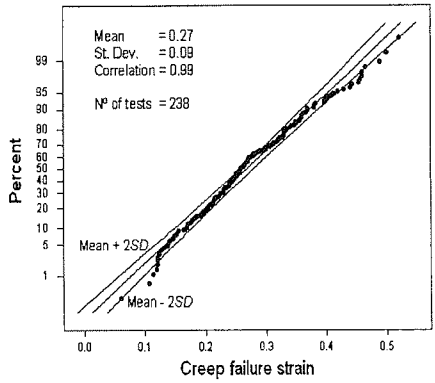


FIG. 7—*Normal probability plot of creep failure strain for all tests on P91 steel at 600°C.*

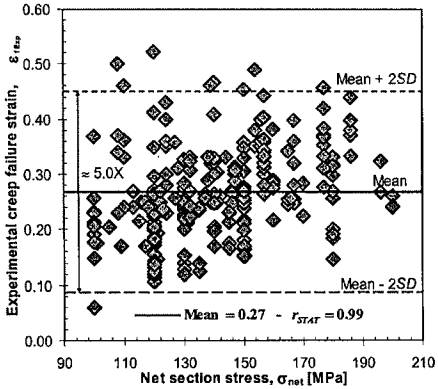


FIG. 8—ε_f *dependence on* σ_{net} *for all P91 casts at 600°C assuming normal distribution.*

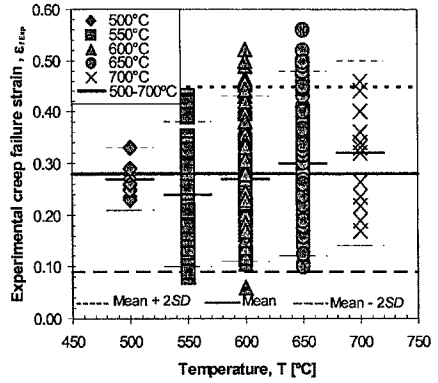


FIG. 9—*Effect of temperature on creep failure strain for all casts of P91 steel.*

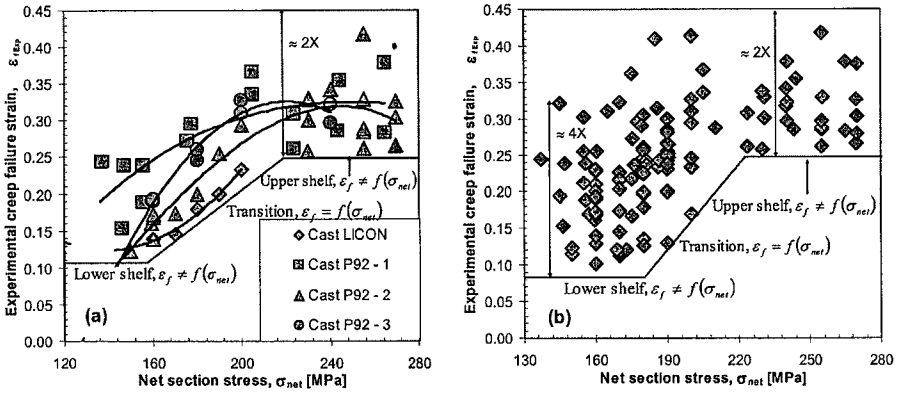


FIG. 10—*Effect of* ε_f *on* σ_{net} *for (a) specific casts and (b) all casts of P92 steel at 600°C.*

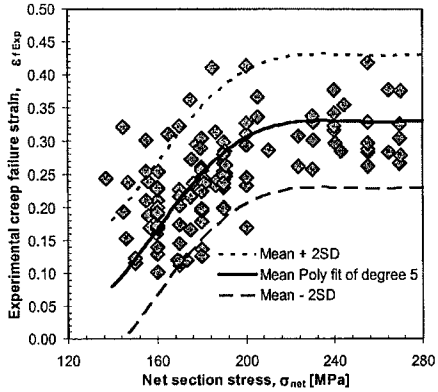


FIG. 11—*Fit of polynomial of degree five to all creep ductility data on P92 steel at 600°C.*

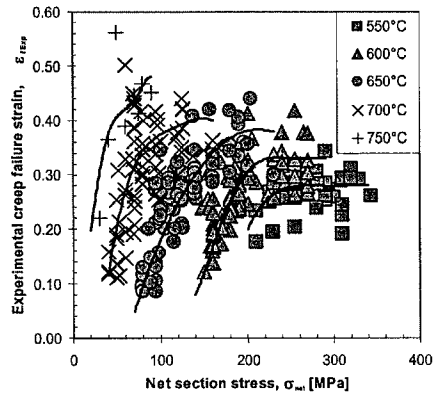


FIG. 12—*Effect of temperature on creep failure strain for all tests on P92 steel.*

Creep Crack Growth Results

The results of statistical analysis that have been carried out on the experimental creep crack growth data are given in Table 6 and in Fig. 13. These results will be used in the prediction of creep crack growth section. Also included in Table 6 are the uniaxial material properties obtained on individual batches of the steels used to make the probabilistic calculations based on Monte Carlo simulations (MCS). Figure 13(*a*) shows that the scatter in CCG rate results for the 316 L(N) stainless steel is similar to that of the multicast uniaxial creep data of Fig. 5 although only two batches of the material were tested for the cracking experiments. However, in addition, two sizes of CT specimens were examined. In contrast, in Fig. 13(*b*) for the more creep brittle 9 %Cr steel, only one cast of material and one size of the c-shaped specimen were examined and the scatter is found to be much lower.

TABLE 1—*Chemical compositions of 316 L(N), P91 and P92 (in weight percent).*

Mat.	C	Si	Mn	P	S	Cr	Cu	Mo	N	Nb	Ni	V	W
316 L(N)	0.040	0.310	1.830	0.036	0.020	17.30	0.030	2.460	0.070	-	11.90	-	-
P91	0.106	0.320	0.470	0.016	0.001	8.930	0.110	0.940	0.065	0.067	0.300	0.210	-
P92	0.114	0.190	0.410	0.020	0.008	9.370	0.090	0.470	-	0.055	0.230	0.190	1.720

TABLE 2—*Statistical results of creep analysis for multicasts 316 L(N)-PM steel.*

Material	Temp. (°C)	No. of tests	n_{Ave}	n_s	ν	$\bar{\varepsilon}_f$	$SD\ \varepsilon_f$	r_{STAT} for ε_f
316 L(N)	500	11	11.63	16.59	8.78	0.30	0.07	0.97
316 L(N)	550	127	11.74	10.15	10.79	0.30	0.09	0.95
316 L(N)	600	124	8.96	8.76	9.38	0.41	0.15	1.00
316 L(N)	650	82	7.37	8.27	7.42	0.54	0.15	0.98
316 L(N)	700	24	5.98	6.63	6.26	0.72	0.21	0.99
316 L(N)	750	15	5.78	5.78	5.47	0.80	0.16	0.90

TABLE 3—*Statistical results of creep analysis for multicasts P91-PM steel.*

Material	Temp. (°C)	No. of tests	n_{Ave}	n_s	ν	$\bar{\varepsilon}_f$	$SD\ \varepsilon_f$	r_{STAT} for ε_f
P91	500	11	20.81	N / A	21.22	0.27	0.03	0.95
P91	550	110	13.87	N / A	12.89	0.24	0.07	0.99
P91	600	238	9.41	13.51	8.73	0.27	0.08	0.99
P91	650	145	7.98	N / A	7.37	0.30	0.09	0.99
P91	700	13	6.71	N / A	6.48	0.32	0.09	0.98
P91	500–700	668	N / A	N / A	N / A	0.27	0.09	0.99

TABLE 4—*Statistical results of creep analysis for multicasts P92-PM steel.*

Material	Temp. (°C)	No. of tests	n_{Ave}	n_s	ν	$SD\ \varepsilon_f$
P92	550	49	18.97	18.62	18.63	0.03
P92	600	125	16.15	14.88	14.76	0.06
P92	650	130	11.81	11.56	10.40	0.05
P92	700	70	8.13	8.53	7.46	0.06
P92	750	8	6.74	7.35	6.23	0.08

TABLE 5—*Statistical results of multicasts creep failure strain for P92a.*

Material	Temp. (°C)	No. of tests	$\sigma_{net\ Max}$ (MPa)	$\sigma_{net\ Min}$ (MPa)	σ^5_{net}	σ^4_{net}	σ^3_{net}	σ^2_{net}	σ^1_{net}	σ^0_{net}	r^2_{STAT} for polynomial expression
P92	550	56	210	350	$5.57\cdot10^{-13}$	$-9.98\cdot10^{-11}$	$6.44\cdot10^{-7}$	$-3.69\cdot10^{-4}$	$8.14\cdot10^{-2}$	−6.15	0.65
P92	600	125	135	280	$-2.92\cdot10^{-11}$	$3.30\cdot10^{-8}$	$-1.45\cdot10^{-3}$	$3.10\cdot10^{-3}$	$-3.15\cdot10^{-1}$	12.30	0.76
P92	650	130	70	250	$5.78\cdot10^{-12}$	$-4.51\cdot10^{-9}$	$1.37\cdot10^{-6}$	$-2.18\cdot10^{-4}$	$2.12\cdot10^{-2}$	−0.74	0.90
P92	700	70	40	160	$-1.81\cdot10^{-11}$	$4.68\cdot10^{-9}$	$3.92\cdot10^{-8}$	$-2.35\cdot10^{-4}$	$2.62\cdot10^{-2}$	0.60	0.77
P92	750	8	30	70	$-1.28\cdot10^{-9}$	$3.34\cdot10^{-7}$	$-309\cdot10^{-5}$	$-1.13\cdot10^{-3}$	$6.57\cdot10^{-3}$	0.07	0.65

TABLE 6—*Experimental creep crack growth results and uniaxial data used in MCS.*

			Experimental creep crack growth results							Experimental uniaxial creep results							
Material[a]	Batch	Temp. (°C)	Spec.	No. of tests/ points	Log(D)	ϕ	SD $\hat{a}$	Ratio $\pm2SD$	r^2_{STAT}	No. of tests	$Ratio_D$	A_{ave}	n_{ave}	$\bar{\varepsilon}_f$	$SD\varepsilon_f$	Ratio $\pm2SD$	r_{STAT} for ε_f
316 L(N)	HIDA	650	CT	7/89	0.44	0.83	0.30	16.0	0.95	5	2.74	1.9E-22	8.35	0.54	0.15	3.5	0.99
P91	LICON	600	C-shape	6/109	0.69	0.70	0.16	4.4	0.93	8	1.33	1.2E-32	13.30	0.27	0.09	5.0	0.99
P92	LICON	625	C-shape	2/47	0.92	0.75	0.11	2.8	0.98	6	1.49	7.4E-34	13.59	0.18	0.05	3.5	0.99

[a]Dataset for 316 L(N)-PM-CT specimens comes from the HIDA project. In contrast, the dataset for P91 and P92-C-shaped specimens comes from the LICON project.

$$\sigma_{ref} = \frac{P}{P_{LC}}\sigma_Y \tag{19}$$

where P_{LC} is the collapse load of the uncracked ligament for a material of yield stress σ_Y. Solutions for σ_{ref} for a number of applications are included in [3,7,9,11] and [39]. It has been found [40], when the nominal stress in Eqs (14), (15) and (17) is chosen as the reference stress, that h in these equations becomes relatively insensitive to n or n_p. This means that it can be evaluated from G, for which $n_p=1$ to give,

$$C^* = \sigma_{ref}\dot{\varepsilon}_{ref}\left(\frac{K}{\sigma_{ref}}\right)^2 \tag{20}$$

when G is expressed in terms of K. This equation provides estimates of C^* from solutions of K and σ_{ref} that are available in the codes of practice [1–9] and handbooks [20–22,39]. The reliability of the equation depends upon the accuracy with which K and σ_{ref} can be evaluated. When suitable solutions cannot be found C^* must be calculated by finite element methods.

Component Life Assessment

In order to determine the extent of creep crack growth in a component, it is necessary to apply Eq (5), (where, preferably, D_o and ϕ have been obtained experimentally from tests carried out according to ASTM E 1457 specifications), in conjunction with an expression for C^* such as Eq (20). When experimental values of D_o and ϕ are not available, Eqs (9a), (9b) and (10) or (13a) (13b) can be applied as appropriate. For a material that creeps according to Eq 3 and which exhibits a constant creep ductility, substitution of Eq (20) into Eqs (9a and 9b and) gives

$$\dot{a} = \frac{(n+1)}{\varepsilon_f^*}\dot{\varepsilon}_{ref}\left[\frac{K^2}{I_n\sigma_{ref}^2}\right]^{n/(n+1)} r_c^{1/(n+1)} \tag{21}$$

This equation illustrates that creep crack growth rate is proportional to the creep strain rate at the reference stress of the uncracked ligament. It is important therefore that accurate estimates of σ_{ref} are employed. For typical values of n, an error of 10 % in σ_{ref} could easily result in an error in cracking rate of a factor of about 2. Again for a constant creep ductility situation, if $\dot{\varepsilon}_{ref}$ is determined from rupture data, Eq (21) becomes

$$\dot{a} = \frac{(n+1)}{t_{r\,ref}}\frac{\varepsilon_f}{\varepsilon_f^*}\left[\frac{K^2}{I_n\sigma_{ref}^2}\right]^{n/(n+1)} r_c^{1/(n+1)} \tag{22}$$

where $t_{r\,ref}$ is the uniaxial creep rupture life at σ_{ref}. When creep ductility is not constant $n \neq v$ and Eqs (13a) and (13b) are used so that Eq (22) becomes

$$\dot{a} = \left(\frac{n+1}{n+1-v}\right)\frac{1}{t_{r\,ref}}\frac{\varepsilon_f}{\varepsilon_f^*}\left[\frac{K^2}{I_n\sigma_{ref}^2}\right]^{v/(n+1)} r_c^{(n+1-v)/(n+1)} \tag{23}$$

Equations (21) to (23) are appropriate for estimating creep crack growth rates in components from uniaxial creep data when experimental creep crack growth properties are not available.

Remaining Life Assessment

High temperature defect assessment procedures can be applied at the initial design stage to estimate the significance of postulated defects that could be missed during inspections and also to determine the acceptability of cracks that are detected during service. In the former case, it is relevant to employ virgin material properties. In the latter instance, it may be necessary to allow for material degradation during use. The ideal is to make an assessment based on degraded material properties data. When this information is not known an estimate can be made by making reference to Fig. 8 which shows a crack and its creep process zone growing into damaged material in the ligament ahead of the crack.

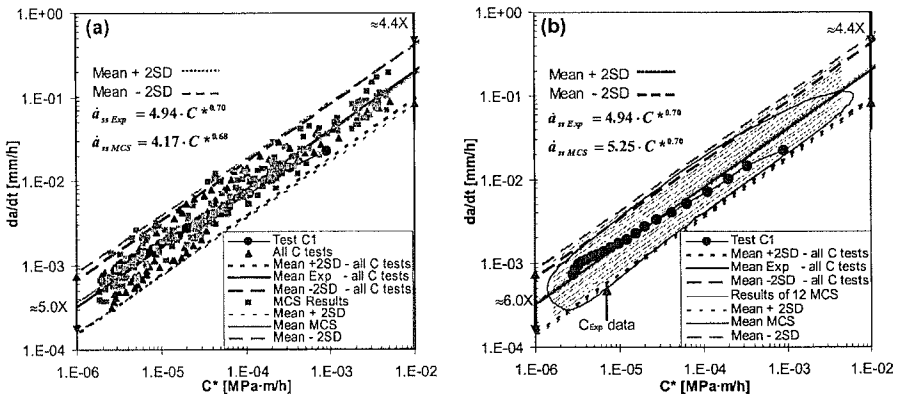


FIG. 14—*Comparison between experimental and predicted scatter in crack growth data for P91 steel at 600°C when (a) C^* is determined experimentally and (b) C^* is calculated from reference stress methods.*

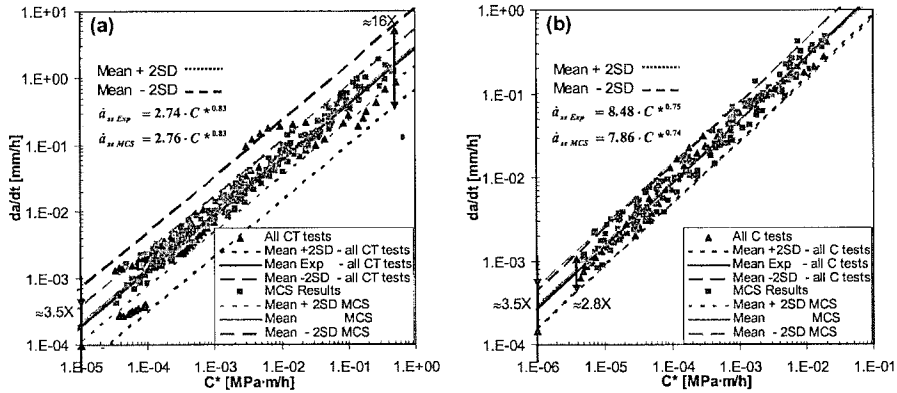


FIG. 15—*Comparison between experimental and predicted scatter in creep crack growth data and C^* determined experimentally for (a) 316 L(N) steel at 650°C and (b) P92 steel at 625°C.*

experimental data are included in the figures. It is apparent, in all cases, that the cracking data can be correlated by an expression of the form of Eq 2.

Comparisons were also made using the alternative procedure for predicting scatter in crack growth data. In this instance, C^* was determined by reference stress methods [9,10] from

$$C^* = \sigma_{ref} \cdot \dot{\varepsilon}_{ref} \cdot \left(\frac{K}{\sigma_{ref}}\right)^2 \tag{11}$$

where K is stress intensity factor and $\dot{\varepsilon}_{ref}$ is the creep strain rate at reference stress σ_{ref}. It has already been shown that creep crack growth predictions are sensitive to the reference stress formula and creep strain rates [1] and [28,29]. Consequently, the Monte Carlo simulation procedure was employed as previously except in this case C^* was calculated from Eq 11. To avoid the influence of the reference stress and materials properties, these parameters were selected to give the best approximation of the experimental C^*, C^*_{Exp}. For the test C1-PM, the best σ_{ref} is taken from plane strain—Von Mises (Pε–VM). The mean average creep rate, obtained from rupture data, was used in the calculations to determine $\dot{\varepsilon}_{ref}$, without taking into account its scatter to only investigate the influence of variation in ε_f, to allow approximately for all stages of creep. The material properties employed are based on the average strain rate and are given in Table 6.

The results are presented in Fig. 14(*b*). Again a virtually identical spread in the data is predicted to that measured experimentally. It is evident, whichever method of determining C^* is adopted, that similar overall predictions of experimental scatter can be replicated by the MCS method. The analysis demonstrates that experimental scatter in creep crack growth data can be predicted from the scatter in uniaxial creep rupture strain when $\bar{\varepsilon}_f > 0.5$ and $SD\ \dot{a} > 10$.

Conclusions

The scatter in uniaxial creep data on type 316 L(N) stainless steel and two 9 %Cr steels designated P91 and P92 has been analyzed statistically. It has been found that none of the rupture time (t_R), the creep strain rate ($\dot{\varepsilon}$), and the net section stress (σ_{net}), has a better relationship with the ε_f. Hence, none of these parameters characterizes better than the other the creep ductility's behavior. Additionally, the results from different batches of one material can be treated individually but that a clear trend can be established only when they are treated as one large dataset with the variability in creep ductility exhibiting a normal distribution with a bigger standard deviation to that of an individual batch of material. It has also been established that the creep failure strains of the 316 L(N) stainless steel and the P91 steel are independent of stress whereas, for the P92 steel, creep failure strain increases with stress. In addition it has been shown for all the steels that the standard deviation in creep ductility tends to increase with an increase in temperature. However, this does not necessarily implie an increase in scatter since the ratio between $\pm 2SD$ is strongly dependent on $\bar{\varepsilon}_f$. A probabilistic approach has been adopted, using Monte Carlo simulation methods, to predict the expected scatter in creep crack growth data from that experienced by the creep failure strain. It is demonstrated for each material that close agreement is achieved, in most instances, with the experimental scatter observed in crack growth tests for conditions where $\bar{\varepsilon}_f > 0.5$ and $SD\ \dot{a} > 10$. The results of this investigation indicate, that when only sparse creep crack growth information is available, the scatter in the data can be predicted from the scatter in creep ductility irrespective of whether C^* is determined experimentally or by reference stress methods. Due to the increase in scatter observed in creep failure strain with an increase in temperature, it is anticipated that, for materials where $\bar{\varepsilon}_f$ is insensitive to the temperature, as for P91, the spread in creep crack growth data should also get larger as the test temperature rises.

Acknowledgments

The authors would like to acknowledge the provision of data from the European Brite/Euram "HIDA" (1996–2000), "LICON" (1997–2001), and CRETE (2001–2004) project partners.

References

[1] Wasmer, K., "Prediction of Creep Crack Growth for a Range of Steels," Ph.D. Thesis, Mechanical Engineering Department, Imperial College, London, 2003.

[2] Commissariatà l'Energie Atomique. A16, "Guide for Defect Assessment and Leak Before Break Analysis," 3rd ed., Saclay, CEA, 1995.

[3] Commissariatà l'Energie Atomique. A16, "Guide for Defect Assessment and Leak Before Break Analysis," 4th ed., Saclay, CEA, 2002.

[4] R5-British Energy, "Defect Assessment Code of Practice for High Temperature Metallic Components," British Energy Generation Ltd., 1999.

[5] BS 7910, "Guide on Methods for Assessing the Acceptability of Flaws in Fusion Welded Structures," London, BSI, 2000.

[6] Nikbin, K. M., Webster, G. A., and Turner, C. E., *Relevance of Non-Linear Fracture Mechanics to Creep Cracking, Cracks and Fracture*, ASTM STP 601, Pittsburgh, pp. 47–62, 1976.

[7] Webster G. A. and Ainsworth R. A., *High Temperature Components Life Assessment*. Chapman & Hall, London, 1993.

[8] ASTM Standard E 1457-00, "Standard Test Method for Measurement of Creep Crack Growth Rates in Metals," Annual Book of ASTM Standards, Vol. 3, No. 1, ASTM International, West Consho-

hocken, 936–950, (2001).
[9] Ainsworth, R. A., "Some Observations on Creep Crack Growth," *Int. J. Fract.*, 20, 147–159 (1982).
[10] Ainsworth, R. A., "The Assessment of Defects in Structure of Strain Hardening Materials," *Eng. Fract. Mech.*, 19, 633–642 (1984).
[11] Nikbin, K. M., Smith, D. J., and Webster, G. A. "Influence of Creep Ductility and State of Stress on Creep Crack Growth," *Advances in Life Prediction Methods at Elevated Temperatures*, ASME International Conference, New York edited by D. A. Woodford and J. R. Whitehead 1983, 249–258 (1983).
[12] Nikbin, K. M., Smith, D. J., and Webster, G. A. "Prediction of Creep Crack Growth from Uniaxial Creep Data," *Proc. R. Soc. London, Ser. A* 396, 183–197 (1984).
[13] Lehmann, D., "Final Report: Evaluation of the Stress to Rupture and Creep Properties of Type 316 L(N) Steel for Design Use," European Commission: Nuclear Science and Technology, EUR-16168, 1995.
[14] Hyde, T. H., "Creep of 316 Stainless Steel at 500° and 600°C and the Effects of Short Duration Overloads on Creep at 550°C," *Mater. High. Temp.*, 14,(1), 27–35 (1997).
[15] NRIM Creep Data Sheet No. 43, "Data Sheets on the Elevated Temperature Properties of 9Cr-1Mo-V-Nb Steel Plates for Boilers and Pressure Vessels (ASME SA-387/SA-387M Grade 91), 1996.
[16] Bendick, W., "*Damage Assessment on P91 Specimens from Uniaxial Creep Tests: Final Report*," Mannesmann Forschunginstitut, LICON/MFI 016/TR07, 1999.
[17] Prunier, V., Gampe, U., Nikbin, K. M., and Shibli, A., "HIDA Activity on P91 Steel," *Mater. High. Temp.*, 15, 35–42 (1998).
[18] Schuster, F. A. and Hanus, R., "Foundry Experience in Large Turbine Casings and Valve Bodies made of Steel Castings P91 and G-X12 CrMoWVNbN 10 11," Paper presented at the *Creep and Fatigue*, London, 1999, 11–22.
[19] Hald, J., "Creep Strength and Ductility of 9 to 12% Chromium Steels," *Mater. High. Temp.* 21(1), 41–46 (2004).
[20] Ricci, N. and Bontempi, P., "Metallographic Examination of P91, P92 and E911 Specimens Tested in the Frame of the LICON Task 3," *Centro Elettrotecnico Sperimentale Italiano*, LICON/CESI011/PR08, 2000.
[21] Taylor, N., Lucon, E., Bicego, V., and Bontempi, P., "Crack Stability Assessment of Advanced 9CR Steels in Boilers Components," Paper presented at the *Advanced Steam Plant*, London, 1997, pp. 201–210.
[22] Verelst, L., "Creep Test Results of Accelerated Damage Enhancement (ADE) Testing," LABORELEC, LICON/LE 007/TR03, 1998.
[23] Holdsworth, S. R. and Davies, R. B., "A Recent Advance in the Assessment of Creep Rupture Data," *Nucl. Eng. Des.*, 190,(3), 287–296 (1999).
[24] NRIM Creep Data Sheet No. 48 Data Sheets on the Elevated-Temperature Properties of 9Cr-0.5Mo-1.8W-V-Nb Steel Pipe for High Temperature Service (ASME SA-335/SA-335M Grade P92), 2002.
[25] ASTM Standard E 139-00, "Standard Test Method for Conducting Creep, Creep-Rupture and Stress-Rupture Tests of Metallic Materials," *Annual Book of ASTM Standards*, Vol. 3(1), West Conshohacken, PA, pp. 270–281, 2001.
[26] Nikbin, K. M., Yatomi, M., Wasmer, K., and Webster, G. A., "Probabilistic Analysis of Creep Crack Initiation and Growth in Pipes Components," *Int. J. Pressure Vessels Piping*, 80(7-8), 585–595 (2003).
[27] Wasmer, K., Nikbin, K. M., and Webster, G. A., "Sensitivity of Creep Crack Initiation and Growth in Plates to Material Properties Variations," *J. Am. Inst. Electr. Eng.*, 2(1) (2005).
[28] Wasmer, K., Nikbin, K. M., and Webster, G. A. "A Sensitivity Study of Creep Crack Growth in Pipes," PVP Vol. 438, *New and Emerging Computational Methods: Applications to Fracture, Damage and Reliability*, ASME, New York, 2002, pp. 17–24.
[29] Wasmer, K., Nikbin, K. M., and Webster, G. A., "Creep Crack Initiation and Growth in Thick Section Steel Pipes under Internal Pressure," *Int. J. Pressure Vessels Piping*, 80(7-8), 489–498 (2003).

Journal of ASTM International, February 2006, Vol. 3, No. 2
Paper ID JAI13220
Available online at www.astm.org

C. M. Davies,[1] *F. Mueller,*[2] *K. M. Nikbin,*[1] *N. P. O'Dowd,*[1] *and G. A. Webster*[1]

Analysis of Creep Crack Initiation and Growth in Different Geometries for 316H and Carbon Manganese Steels

ABSTRACT: Results obtained from a European collaborative project aimed at producing a draft code of practice for creep crack growth testing are presented. The tests were performed on an Austenitic Type 316H Stainless Steel at 550°C and a carbon manganese steel at 400°C. A range of specimen test geometries has been examined. These are the single edge notched specimen in tension and bending, the double edge notched specimen in tension, the middle cracked specimen in tension, and the C-shaped specimen in tension. The results obtained are compared to those obtained using the standard compact tension specimen following the ASTM Standard Test Method for Measurement of Creep Crack Growth Rates in Metals (E 1457). Creep crack creep growth rates and initiation times have been correlated with the fracture mechanics parameter C^*. The applicability of the stress intensity factor K to describe the creep cracking behavior is also assessed. Recommendations are made to support the use of different geometries in creep crack growth and/or creep crack initiation testing.

KEYWORDS: Fracture mechanics, Creep crack growth, Creep crack initiation, C*, Specimen geometry, Code of Practice, Constraint

Nomenclature

a = crack length
a_0, a_f = initial and final crack length measurements
Δa = amount of crack growth
$\dot{a}$ = crack growth rate
$\dot{a}^{\mathrm{NSW}}$ = crack growth rate prediction from the Nikbin, Smith and Webster (NSW) model
$\dot{a}^{\mathrm{NSWA}}$ = crack growth rate prediction from approximate NSW model
$\dot{a}^{\mathrm{NSW\text{-}MOD}}$ = crack growth rate prediction from the modified NSW model
$\dot{a}_0$ = initial crack growth rate (at $\Delta a = 0$)
$\dot{a}_s$ = crack growth rate during steady state conditions
n = power-law creep stress exponent
r = radial distance from the crack tip
r_c = creep process zone size
t_T = transition time
$t_{0.2}$, $t_{0.5}$ = time to reach 0.2 mm and 0.5 mm of crack growth
A = coefficient in the power-law creep strain rate expression
B, B_n = specimen thickness and (net) thickness between side grooves
C^* = steady state creep fracture mechanics parameter
$C^*(t)$ = experimentally determined value of C^* at test time t
D, ϕ = material constants in $\dot{a}$ correlations with C^*
D', m = material constants in $\dot{a}$ correlations with K
E = elastic (Young's) modulus

Manuscript received May 2, 2005; accepted for publication September 7, 2005; published December 2005. Presented at ASTM Symposium on Fatigue and Fracture Mechanics: 35th Volume on 18–20 May 2005 in Reno, NV; R. E. Link and K. M. Nikbin, Guest Editors.
[1] Department of Mechanical Engineering, Imperial College London, South Kensington Campus, Exhibition Road, London, SW7 2AZ, e-mail: catrin.davies@imperial.ac.uk
[2] Institute of Materials Technology, Darmstadt University of Technology, Germany.
Copyright © 2006 by ASTM International, 100 Barr Harbor Drive, PO Box C700, West Conshohocken, PA 19428-2959.

E' = effective elastic modulus $= E/(1-\nu^2)$ for plane strain and E for plane stress
H^{LLD} = geometric function to calculate C^* from load line displacement rate
H^{CMOD} = geometric function to calculate C^* from crack mouth opening displacement rate
I_n = dimensionless function of n in the Riedel-Rice (RR) stress field distribution
K = stress intensity factor
P = applied load
V_0, V_f = initial and final measurements of the potential difference (PD)
W = specimen width or half width
Δ^{LLD}, $\dot{\Delta}^{LLD}$ = load line displacement, load line displacement rate
$\dot{\Delta}_c^{LLD}$ = component of the load line displacement rate directly associated with the accumulation of creep strains
$\dot{\Delta}_i^{LLD}$ = component of the load line displacement rate directly associated with instantaneous (elastic and plastic) strains
$\dot{\Delta}_{i,e}^{LLD}$ = component of the load line displacement rate directly associated with instantaneous elastic strains
Δ^{CMOD}, $\dot{\Delta}^{CMOD}$ = crack mouth opening displacement, crack mouth opening displacement rate
ε_f, ε_f^* = uniaxial and multiaxial creep ductility
$\dot{\varepsilon}^c$ = creep strain rate
η^{CMOD} = geometric factor to calculate C^* from crack mouth opening displacement rate
η^{LLD} = geometric factor to calculate C^* from load line displacement rate
ν = Poisson's ratio
σ = stress
σ_e, σ_h = equivalent stress and hydrostatic stress
$\tilde{\sigma}_{ij}$, $\tilde{\varepsilon}_{ij}$ = dimensionless functions of n and θ.
θ = crack tip angle

Introduction

Currently the creep crack growth testing standard ASTM E 1457 [1] restricts testing to the use of the compact tension specimen C(T). However, alternative geometries may be more suitable under certain circumstances, due to, e.g., material or equipment availability or the need for comparability of specimen crack tip constraint with in-service conditions. As part of a collaborative European program CRETE [2], tests on a variety of specimen geometries have been performed to establish their applicability in creep crack initiation (CCI) and creep crack growth (CCG) testing. These results will contribute toward a code of practice for high temperature testing of fracture specimens, that is being developed by the CRETE partners [3].

Two materials have been tested, an austenitic type 316H stainless steel at 550°C and a low free nitrogen CMn steel at 400°C. In this work the test data generated from the CRETE project are analyzed and compared to previously collected C(T) specimen data for the same materials. Trends between the creep crack initiation and growth behavior of the various test geometries are examined. Predictions from existing CCI and CCG models are evaluated and compared to the data. The main aim is to verify the testing and data analysis methods employed, enabling recommendations to be made for the determination of creep crack growth rates from different specimen geometries.

Deformation and Fracture at High Temperatures

For many materials under steady-state conditions, the creep strain rate $\dot{\varepsilon}^c$ may be related to the stress σ by a power-law expression,

$$\dot{\varepsilon}^c = A\sigma^n, \tag{1}$$

where n and A are the power-law creep stress exponent and coefficient, respectively. For such a material the stress and strain fields near a stationary crack tip may be represented by the well-known Riedel-Rice (RR) distribution [4]

TABLE 1—*Material properties for steels 316H at* 550°C *and CMn at* 400°C.

	316H	CMn
E	140 GPa	195 GPa
σ_y	170 MPa	199 MPa
A[a]	1.56×10^{-35}	4.80×10^{-49}
n	11.95	18.2
ε_f[b]	21 %	67 %

[a]Stress in MPa, time in hours.
[b]Creep failure strain, determined from reduction of area in a uniaxial creep test.

$$\sigma_{ij} = \left(\frac{C^*}{AI_n r}\right)^{1/(n+1)} \tilde{\sigma}_{ij}(\theta, n) \tag{2}$$

$$\dot{\varepsilon}_{ij} = A\left(\frac{C^*}{AI_n r}\right)^{n/(n+1)} \tilde{\varepsilon}_{ij}(\theta, n), \tag{3}$$

where r is the radial distance from the crack tip and θ the crack tip angle. In Eqs 2 and 3 the amplitude of the crack tip fields C^* may be determined analytically by an integral around the crack tip [5] or estimated from the remote displacement rate; I_n is a nondimensional function of n, and $\tilde{\sigma}_{ij}$ and $\tilde{\varepsilon}_{ij}$ are dimensionless functions of n and θ. Under steady-state conditions, when Eqs 2 and 3 prevail, it is expected that the time to crack initiation from a sharp defect and the rate of crack growth will be uniquely determined by the parameter C^* for a given material and temperature. The creep crack growth (CCG) rate $\dot{a}$ may then be described by the relationship

$$\dot{a} = DC^{*\phi}, \tag{4}$$

where D and ϕ are material constants, which may be temperature and stress state dependent [6].

At short times and/or low loads the stresses in the vicinity of the crack may be represented by the linear elastic stress intensity factor K and it is expected that crack initiation and growth will be controlled by K. Under such conditions, the rate of crack growth can be represented as

$$\dot{a} = D'K^m, \tag{5}$$

where, again, D' and m are material constants which may depend on temperature and stress state.

Experimental Procedure

The procedures used in the CRETE test program followed the ASTM E 1457 [1] test standard as far as possible. Since the majority of the tests were performed using geometries not included in ASTM E 1457, additional recommendations were made throughout the test program to ensure that the same procedures were carried out by all the laboratories carrying out measurements. This section highlights the important issues that were addressed in the testing program.

Material and Test Specimen Geometries Details

The materials tested are an austenitic type 316H stainless steel at 550°C and a ferritic, low free nitrogen CMn steel at 400°C, for which materials data are available from [7] and [8], respectively. The relevant material properties of the CMn and 316H steel are given in Table 1. The test specimen geometries are shown in Fig. 1, and relevant dimensions are provided in Table 2. Each specimen type is identified by an acronym as follows: single edge notched specimen in tension [SEN(T)] and bending [SEN(B)], the double edge notched specimen in tension, [DEN(T)], the middle cracked specimen in tension [M(T)], the compact tension specimen [C(T)], and the C-shaped specimen in tension [CS(T)]. The individual tests details for specimens produced from 316H and CMn steel are given in Tables 3 and 4, respectively. All the 316H steel specimens have a prefatigued starter crack and possess 20 % side grooves (10 % each side). Most of the CMn steel specimens have an Electro-Discharge Machine (EDM) slit starter crack with a notch tip radius of 0.075 mm, and are side grooved by 40 % (20 % each side). Specimens that were side grooved by 20 % or given a prefatigue starter crack are identified in Table 4.

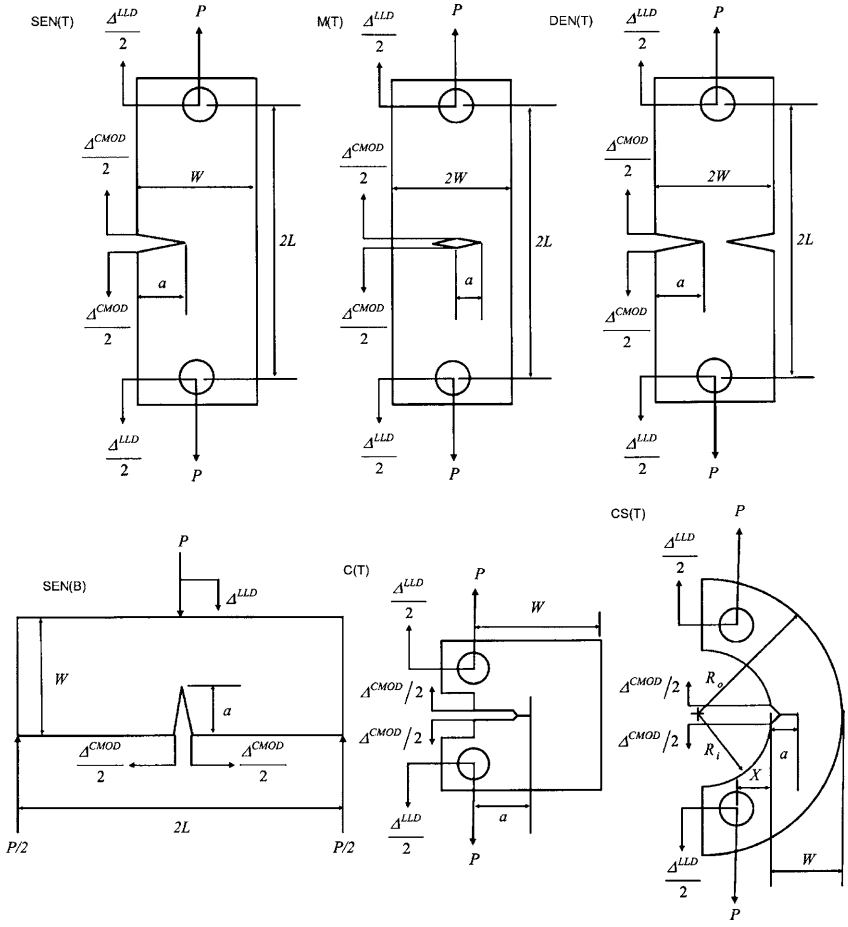


FIG. 1—*Specimen geometry definitions.*

No significant differences were found in the CCG data using either EDM notches or prefatigue cracks. However, for specimens containing two crack fronts, [DEN(T) and M(T) specimens] following fracture, it was observed that the prefatigue crack had developed to unequal lengths along the two crack fronts. The amount of creep crack growth was therefore much larger for the crack front with the longer prefatigue crack. The effect on the DEN(T) specimen is believed to be more severe than on the M(T) specimen, since the DEN(T) specimen is subjected to an increasing amount of bending during the creep test, due to the increasingly asymmetric crack growth.

TABLE 2—*CRETE test specimen geometry.*

Specimen geometry	*B* (mm)	*W* (mm)	*L* (mm)	R_o (mm)	R_i (mm)
SEN(T)	12.5	25	37.5	…	…
DEN(T)	12.5	12.5	37.5	…	…
M(T)	12.5	12.5	37.5	…	…
SEN(B)	12.5	25	50	…	…
CS(T)	25	25	…	50	25
C(T)	25	50	…	…	…

TABLE 3—*316H steel specimen details.*

Test code	Specimen geometry	a_0/W	a_f/W	Δa (mm)	Load, P (kN)	Test duration, t_f (h)	t_T/t_f (%)	$t_{0.2}/t_f$ (%)
316/DT1	DEN(T)	0.39	0.93	6.7	45	7609.6	2.0	31.2
316/DT3	DEN(T)	0.32	0.43	1.4	43	13600	1.6	37.3
316/ST2	SEN(T)	0.38	0.44	1.3	30	379	2.4	32.9
316/ST4	SEN(T)	0.31	0.51	5.0	35	601	6.3	63.3
316/ST5	SEN(T)	0.35	0.43	2.0	32	525	4.1	7.7
316/SB2	SEN(B)	0.33	0.43	2.4	9	641	9.2	84.2
316/SB4	SEN(B)	0.33	0.43	2.5	7.6	6522	10.4	52.6
316/CS4	CS(T)	0.23	0.30	1.6	16.5	3830	14.1	29.8
316/CT1	C(T)	0.53	0.56	1.4	20	1221	13.7	27.9

Crack Length Monitoring

The ac or dc potential drop (PD) technique was used to measure the crack length. At the end of the test, the specimens were fractured to identify the initial and final crack lengths and the linear correlation method, relating crack extension directly to the output PD, was used for all geometries. Thus, the crack length a during the test was calculated following ASTM E 1457 [1]

$$a = \left[(a_f - a_0)\frac{V - V_0}{V_f - V_0} \right] + a_0, \tag{6}$$

where a_0 and a_f are the initial and final measured crack length, respectively, V is the instantaneous PD reading and V_0 and V_f are the initial and final PD readings, respectively. For the DEN(T) specimen, which has two crack fronts, PD outputs were available for both crack fronts and the crack which showed the greatest amount of crack growth was analyzed. For the M(T) specimens, only a single PD output was available, so the final crack length a_f in Eq 6 was taken to be the average of the two crack lengths in the specimen and the calculated crack length a is considered to be an "average" crack length for the specimen.

Load Line Displacement and Crack Mouth Opening Displacements

Figure 1 identifies the recommended positions for measuring load line displacement (Δ^{LLD}) and the crack mouth opening displacement (Δ^{CMOD}) for each specimen type. Both displacements have been measured for the majority of the SEN(T) and SEN(B) tests.

Displacement and CCG Rate Determination

In accordance with ASTM E 1457 [1] the displacement rates and creep crack growth (CCG) rates for all geometries have been determined by the incremental polynomial method. The initial and final crack lengths and displacement measurements reported are those measured at the end of the test.

TABLE 4—*CMn steel specimen details.*

Test code	Specimen geometry	a_0/W	a_f/W	Δa (mm)	Load, P (kN)	Test duration, t_f (h)	t_T/t_f (%)	$t_{0.2}/t_f$ (%)
CMn/CC2[a]	M(T)	0.3	0.45	5.6	55	673	0.1	19.3
CMn/ST3[b]	SEN(T)	0.28	0.41	3.2	29	6642	0.1	2.3
CMn/ST4	SEN(T)	0.3	0.43	3.2	30	8279	1.1	0.7
CMn/SENT4[c]	SEN(T)	0.3	0.36	1.4	32	2338	0.6	31.0
CMn/SENT5[c]	SEN(T)	0.3	0.32	0.6	37	904	0.6	65.7
CMn/SENB1[a]	SEN(B)	0.3	0.42	2.9	10.6	5902	0.2	8.0

[a]20 % side grooved (10 % each side).

[b]Prefatigue starter crack.

[c]Test stopped significantly prior to the onset of failure.

Data Reduction and Correction

Following each test the crack length a and the displacements Δ^{LLD} and Δ^{CMOD} (where available) are obtained as a function of time. From the complete data set, a sufficient number of data points (typically 30–50) were selected to describe the shape of the crack length, Δ^{LLD} and Δ^{CMOD} curves versus time, while ensuring that there is no decrease in any of the measurements with time due to scatter and noise in the recorded data. Where raw data was sparse or missing, interpolation was performed without changing the trends in the overall data. In some cases the PD readings decreased after initial loading (which indicates an apparent decrease in the crack length), reached a minimum value, and then started to increase. For cases such as this, the value of V used in Eq 6 for all points of decreasing PD output were taken to be the minimum value before the PD output again started to increase. Any jumps that occurred in the PD or displacement readings without obvious explanation were corrected by subtracting the magnitude of the jump in the displacement or PD from the subsequent data points.

Analysis of Creep Crack Initiation and Growth Data

ASTM E 1457 [1] details the procedures to determine correlating parameters for the C(T) specimen. In [9] corresponding methods to evaluate C^* for geometries other than the C(T) specimen have been presented. A summary of these results are presented here.

Determination of Experimental C^* Parameter

Under steady-state conditions, the experimental C^* parameter for a power-law material may be estimated from the load line displacement rate $\dot{\Delta}^{LLD}$ or crack mouth opening displacement rate $\dot{\Delta}^{CMOD}$ using Eqs 7 and 8, respectively,

$$C^* = \frac{P\dot{\Delta}^{LLD}}{B_n(W-a)} H^{LLD}\eta^{LLD} \tag{7}$$

$$C^* = \frac{P\dot{\Delta}^{CMOD}}{B_n(W-a)} H^{CMOD}\eta^{CMOD} \tag{8}$$

where P is the applied load, W the specimen width [or half width for DEN(T) and M(T) specimens] and B_n is the (net) specimen thickness between the side grooves. Solutions for the geometric functions H^{LLD}, H^{CMOD}, η^{LLD}, and η^{CMOD} for test specimens are given in [9]. The mean values of η^{LLD} and η^{CMOD}, reported in [9], have been used in the analysis for all geometries.

The total load line displacement rate measured during the tests $\dot{\Delta}^{LLD}$ can be partitioned into an instantaneous part $\dot{\Delta}_i^{LLD}$ and a time-dependent part that is directly associated with the accumulation of creep strains $\dot{\Delta}_c^{LLD}$ such that

$$\dot{\Delta}_c^{LLD} = \dot{\Delta}^{LLD} - \dot{\Delta}_i^{LLD}. \tag{9}$$

The instantaneous displacement rate $\dot{\Delta}_i^{LLD}$ can be further divided into an elastic and a plastic part, with the elastic part of the instantaneous load line displacement rate $\dot{\Delta}_{i,e}^{LLD}$ calculated as

$$\dot{\Delta}_{i,e}^{LLD} = \frac{\dot{a}B_n}{P}\left[\frac{2K^2}{E'}\right], \tag{10}$$

where $\dot{a}$ is the crack growth rate and E' is the effective elastic modulus [$E/(1-\nu^2)$ for plane strain and E for plane stress]. ASTM E 1457 [1] also provides relations for the plastic instantaneous displacement rate. However, inclusion of the plastic displacement rate as defined in ASTM E 1457 [1] may lead to negative values of $\dot{\Delta}_c^{LLD}$ (see, e.g., [10]). In any case, as will be seen, good correlation has been found between the crack growth rate and C^* evaluated using the total displacement rate $\dot{\Delta}^{LLD}$. There are currently no solutions corresponding to Eq 10 to allow a partition of the crack mouth opening displacement rate $\dot{\Delta}^{CMOD}$ into creep and instantaneous parts, though, in principle, such a partition is also possible.

Validity Criteria for the Use of C^*

Validity criteria are specified in ASTM E 1457 [1] for the use of C^* as a correlating parameter for CCI and CCG data [for a C(T) specimen]. First, the transition time t_T must be exceeded [4]. During a test t_T is estimated following ASTM E 1457 [1]

$$t_T = \frac{K^2(1-\nu^2)}{E(n+1)C^*(t_T)}, \tag{11}$$

which assumes plane strain and elastic or small scale yielding conditions. Since the calculation of t_T depends implicitly on time through $C^*(t_T)$, its value is obtained by applying Eq 11, to each data point. Thus the value of t_T is given by the maximum value calculated from the test data set, i.e.,

$$t_T = \max\left[\frac{K^2(1-\nu^2)}{E(n+1)C^*(t)}\right]. \tag{12}$$

In addition to satisfying the condition that $t > t_T$, if the C^* parameter is to be applied it is necessary to identify the material as "creep ductile" in the test regime. Data are considered to be creep ductile if the creep load line displacement rate, calculated using Eq 9, constitutes at least half of the total load line displacement, i.e., $\dot{\Delta}_c^{LLD}/\dot{\Delta}^{LLD} \geq 0.5$. For creep-brittle situations ($\dot{\Delta}_c^{LLD}/\dot{\Delta}^{LLD} \leq 0.25$) ASTM E 1457 [1] suggests that the stress intensity factor K may be used to describe the creep crack growth rate data. Finally, following ASTM E 1457 [1], CCG data obtained prior to a crack extension $\Delta a = 0.2$ mm are assumed to comprise a part or the whole of the transient crack growth region, during which the damage distribution ahead of the growing crack tip has not yet reached a steady state. Therefore these data are not included when plotting crack growth rate against C^*.

Small Scale Creep Conditions

The C_t parameter has been proposed [11] to describe crack growth during the small-scale creep regime, where $t < t_T$. In the extensive creep regime ($t \geq t_T$) the value of C_t becomes identical to that of C^*. An approximate estimate of C_t for small scale and extensive creep conditions may be obtained from the expression [12]

$$C_t = \left[1 + \left(\frac{t_T}{t}\right)^{(n-3)/(n-1)}\right] C^*. \tag{13}$$

The use of the C_t parameter may be necessary for tests where there is significant crack growth prior to the transition time.

Experimental Determination of Initiation Time

The creep crack initiation (CCI) time t_i is defined as the time to achieve a measurable small amount of crack extension. A crack extension of 0.2 mm is recommended in ASTM E 1457 [1] to describe CCI for laboratory tests. In the current set of experiments, the time for 0.2 mm crack extension $t_{0.2}$ has been determined by linearly interpolating between the test times of two consecutively recorded data points where $\Delta a \leq 0.2$ mm and $\Delta a \geq 0.2$ mm, respectively. The time for 0.5 mm crack extension has also been obtained, as current crack detection techniques for components may not be sufficiently precise to detect reliably 0.2 mm of crack growth.

Creep Crack Initiation and Growth Models

Current testing procedures do not include predictive models. However, models are useful tools to assist the experimenter in optimizing the testing procedure and reducing the number of tests required to completely describe the material response.

An outline of the appropriate models for CCI and CCG are presented here and used to assist in the interpretation of the data. The models used to estimate CCI time are based on the time for a slowly growing crack to grow a certain distance (either 0.2 or 0.5 mm). Therefore, models for CCG are first presented.

TABLE 5—*NSW-MOD model values used for 316H at* 550°C *and CMn at* 400°C.

	316H		CMn	
	Plane stress	Plane strain	Plane stress	Plane strain
θ for $\dot{a}_{\max}$	0	50	0	85
$\tilde{\varepsilon}_{eq}(\theta,n)$	1	0.3	1	0.9
$\varepsilon_f^*(\theta,n)/\varepsilon_f$	0.5	0.03	0.5	0.09
$\varepsilon_f(\tilde{\varepsilon}_{eq}/\varepsilon_f^*)_{\max}$	2	10	2	10
I_n	3.1	4.4	2.9	4.2
$\dot{a}_{\max}^{P\varepsilon}/\dot{a}_{\max}^{P\sigma}$	3.54		3.48	

NSW Model

A model for CCG, known as the Nikbin, Smith and Webster (NSW) model, was proposed in [13] which assumed that crack advance occurs when the creep ductility is exhausted at the growing crack tip. Assuming that stress redistribution has taken place so that the crack tip stress and strain are described by Eqs 2 and 3, the creep crack growth rate under steady-state conditions, may be written as [13]

$$\dot{a}^{\text{NSW}} = \frac{n+1}{\varepsilon_f^*}(Ar_c)^{1/(n+1)}\left[\frac{C^*}{I_n}\right]^{n/(n+1)}, \tag{14}$$

where r_c is the size of the creep process zone (usually related to the grain size of the material) and ε_f^* is the appropriate (multiaxial) crack tip creep ductility. It has been found that CCG data for ductile steels approach the plane stress prediction of this model [6].

Approximate NSW Model

It has been found that for a range of steels the CCG rate is most sensitive to the multiaxial creep ductility ε_f^*. Therefore, the steady-state CCG rate may be approximated as [14]

$$\dot{a}^{\text{NSWA}} = \frac{3C^{*0.85}}{\varepsilon_f^*}, \tag{15}$$

where $\dot{a}$ and C^* have the units of millimetres per hour (mm/h) and megapascal metres per hour (MPam/h), respectively and ε_f^* is taken as the uniaxial failure strain ε_f for plane stress conditions and $\varepsilon_f/30$ for plane strain [15]. This model is henceforth referred to as the approximate NSW (NSWA) model.

Modified NSW Model

In the NSW model the maximum value of the equivalent strain, $\tilde{\varepsilon}_{eq}(\theta,n)$, in Eq 3 is used (which is unity) and thus the implicit assumption is that failure occurs at the angle θ, where the equivalent creep strain reaches its maximum value. A more general expression can be obtained that considers the dependence of $\tilde{\varepsilon}_{eq}(\theta,n)$ on crack angle θ. Furthermore, the dependence of the multiaxial ductility ε_f^* on stress state and crack tip angle may be considered by obtaining values of triaxiality σ_h/σ_e from Eq 2, where σ_h and σ_e are hydrostatic and equivalent stress, respectively. By incorporating the level of triaxiality into an appropriate model for the failure strain ratio $\varepsilon_f^*/\varepsilon_f$, (e.g., [16]) an additional dependence on θ and n enters the NSW equation. The NSW model may then be modified to give the NSW-MOD equation, [17,18]

$$\dot{a}^{\text{NSW-MOD}} = (n+1)(Ar_c)^{1/(n+1)}\left[\frac{C^*}{I_n}\right]^{n/(n+1)}\left|\frac{\tilde{\varepsilon}_{eq}(\theta,n)}{\varepsilon_f^*(\theta,n)}\right|_{\max}. \tag{16}$$

Crack growth is thus assumed to occur along the direction where the ratio of equivalent strain to multiaxial failure strain $\tilde{\varepsilon}_{eq}/\varepsilon_f^*$ reaches a maximum.

The form of Eq 16 is essentially the same as that of Eq 14 except that the angular and n dependence on $\tilde{\varepsilon}_{eq}$ and ε_f^* is included [in Eq 14, $\tilde{\varepsilon}_{eq}$ is taken to be unity].

Results for $\tilde{\varepsilon}_{eq}(\theta,n)$ and the ratio $\varepsilon_f^*/\varepsilon_f$ are reported in [17,18]. The appropriate values used for the materials examined here are given in Table 5, from which it may be seen that for 316H at 550°C a factor of just over 33 is predicted between $\varepsilon_f^*/\varepsilon_f$, under plane strain conditions, in conjunction with the Cocks and Ashby multiaxiality model [16], which is close to the factor 30 used in the NSWA model. For the CMn

steel this factor becomes 11, which is around a third of that assumed in the NSWA model. Incorporating the effect of multiaxiality on the failure strain and the variation of equivalent strain with angle θ, the creep crack growth rate predicted from the NSW-MOD model under plane strain conditions is approximately 3.5 times that under plane stress conditions for both the 316H steel at 550°C and CMn steel at 400°C (see Table 5).

Initial CCG Rates

In the previous sections estimates of the steady state crack growth rate have been presented. In [6], it was shown that, provided the crack tip fields are described by Eqs 2 and 3, the initial crack growth rate $\dot{a}_0$ defined as the crack growth rate at $\Delta a = 0$, is on the order of $1/(n+1)$ times slower than the steady state CCG rate

$$\dot{a}_0 \approx \frac{\dot{a}_s}{n+1}. \tag{17}$$

Thus, from the approximate NSW model [Eq 15], the initial creep crack growth rate may be approximated as

$$\dot{a}_0^{\text{NSWA}} \approx \frac{\dot{a}^{\text{NSW}}}{n+1} = \frac{3C^{*0.85}}{(n+1)\varepsilon_f^*}. \tag{18}$$

Similarly, if the modified NSW model is used

$$\dot{a}_0^{\text{NSW-MOD}} \approx \frac{\dot{a}^{\text{NSW-MOD}}}{n+1} = (Ar_c)^{1/(n+1)} \left[\frac{C^*}{I_n}\right]^{n/(n+1)} \left|\frac{\tilde{\varepsilon}_{\text{eq}}}{\varepsilon_f^*}\right|_{\max}. \tag{19}$$

In the transient regime, as steady-state crack growth conditions are approached, the crack growth rate is expected to vary between $\dot{a}_0$, estimated by Eqs 18 and 19, and the steady-state crack growth rate, estimated by Eqs 14–16.

Prediction of CCI Times

An expression for initiation time is derived in [4], which is based on the attainment of a critical strain at a critical distance ahead of a stationary crack tip and relies on the RR fields, Eqs 2 and 3. In this work, as stated previously, the CCI time t_i is defined as the time to achieve a measurable small amount of crack extension. If the minimum crack extension that can be measured reliably is Δa and it is assumed that crack growth is a continuous process, which begins immediately on loading, then, following [19], the initiation time t_i may be obtained from

$$t_i = \int_{a_0}^{a_0+\Delta a} \frac{da}{\dot{a}}. \tag{20}$$

The integration in Eq 20 cannot be simply performed as the dependence of $\dot{a}$ on time is not generally available. However, estimates of initiation time may be obtained by assuming a constant crack growth rate over Δa, i.e. Eq 20 becomes,

$$t_i \approx \frac{\Delta a}{\dot{a}}. \tag{21}$$

Upper and lower bound estimates for t_i may be obtained by substituting appropriate estimates of $\dot{a}_0$ or $\dot{a}_s$, respectively, into Eq 21 for $\dot{a}$, i.e.

$$\frac{\Delta a}{\dot{a}_s} \leqslant t_i \leqslant \frac{\Delta a}{\dot{a}_0}. \tag{22}$$

If the approximate NSW equations are used to estimate the crack growth rates in Eq 22 and if it is assumed that C^* remains constant during the small amount of crack growth from a_0 to $a_0+\Delta a$, we obtain

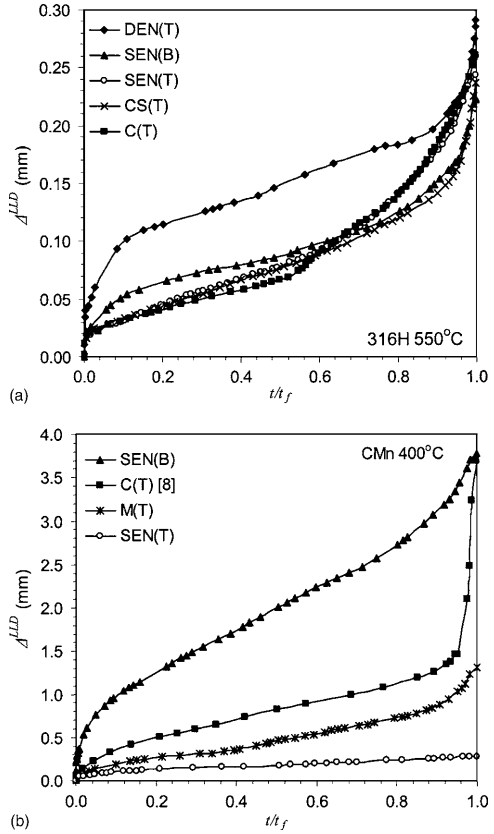


FIG. 2—*Example of creep load line displacement* Δ^{LLD} *with normalized time for each type of specimen tested in (a) 316H and (b) CMn steel.*

$$\frac{\Delta a \varepsilon_f^*}{3C^{*0.85}} \leqslant t_i \leqslant \frac{\Delta a (n+1)\varepsilon_f^*}{3C^{*0.85}}. \tag{23}$$

Similarly, if the NSW-MOD equations are used Eq 22 becomes

$$\frac{\Delta a}{(n+1)(Ar_c)^{1/(n+1)}}\left(\frac{I_n}{C^*}\right)^{n/(n+1)}\left|\frac{\varepsilon_f^*}{\tilde{\varepsilon}_{\mathrm{eq}}}\right|_{\max} \leqslant t_i \leqslant \frac{\Delta a}{(Ar_c)^{1/(n+1)}}\left(\frac{I_n}{C^*}\right)^{n/(n+1)}\left|\frac{\varepsilon_f^*}{\tilde{\varepsilon}_{\mathrm{eq}}}\right|_{\max}. \tag{24}$$

Predictions from Eqs 23 and 24 will vary under conditions of plane stress and plane strain, due to the influence of stress state on ε_f^*, $\tilde{\varepsilon}_{\mathrm{eq}}$, and I_n. The two extreme predictions of initiation time are then provided by the lower bound model (based on $\dot{a}_s$) from Eq 24 under plane strain conditions and the upper bound model (based on $\dot{a}_0$) from Eq 23 under plane stress conditions. The former prediction is the more conservative (i.e., shorter initiation times predicted).

Experimental Results

The results for both the 316H and CMn materials are described in this section. Load line displacement data (Δ^{LLD}) are plotted against test time normalized by test duration t/t_f for each type of specimen in Figs. 2(*a*) and 2(*b*) for 316H and CMn steel, respectively. An initial period of decreasing displacement rate, follow-

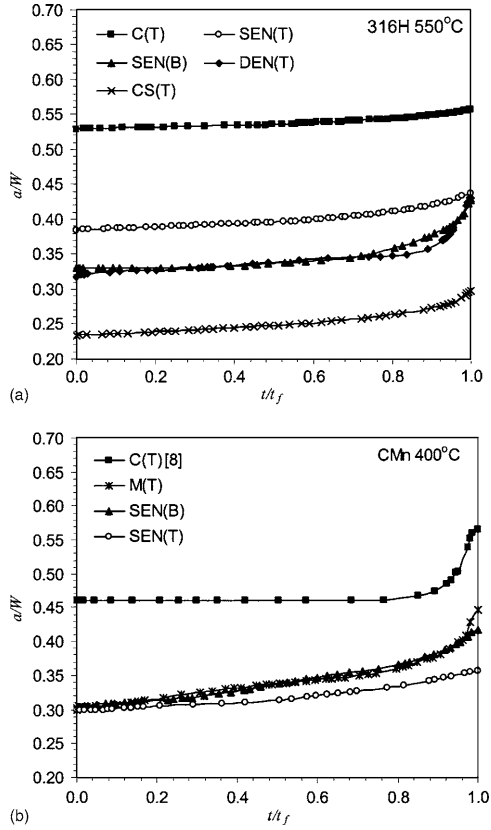


FIG. 3—*Example of normalized crack length with time for each type of specimen tested in (a) 316H and (b) CMn steel.*

ing crack tip stress relaxation due to creep, followed by an approximately linear region, where the displacement rate is constant, is displayed for most geometries. The majority of tests were stopped in the region where the load line displacement increases rapidly, which is assumed to be close to the point of failure of the specimen. However, two tests (as noted in Table 4) were stopped in the early stages of crack growth and thus the test duration t_f does not represent the failure time for these tests and the region of increasing displacement rate is not observed.

In Fig. 3 the crack length normalized by specimen width a/W is plotted against test time normalized by test duration t/t_f for the same specimens as in Fig. 2. For many specimens a significant portion of the test time is associated with little or no crack growth, highlighting the importance of the CCI period (note also the values $t_{0.2}/t_f$ in Tables 3 and 4).

A comparison of the displacement measured at the load line (Δ^{LLD}) and at the crack mouth (Δ^{CMOD}), for one of the SEN(B) and SEN(T) tests is shown in Figs. 4(*a*) and 4(*b*) for the 316H and CMn steel, respectively. For the SEN(T) specimen, Δ^{CMOD} is greater than Δ^{LLD} indicating the effect of remote bending on the load line displacement. Finite element analysis [9] has indicated that for the SEN(T) specimen under uniform stress (representative of a pin loading condition) Δ^{CMOD} is larger than Δ^{LLD}, which is consistent with these measurements. For the SEN(B) specimen Δ^{LLD} is greater than Δ^{CMOD}, particularly for the CMn steel.

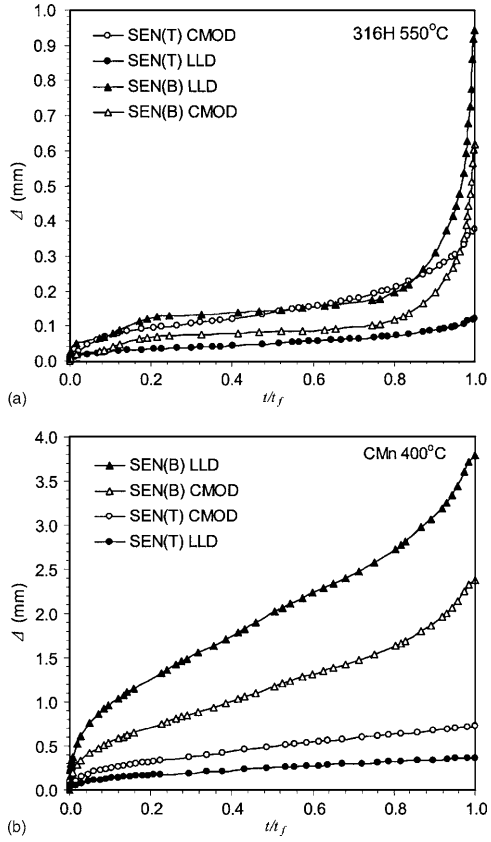


FIG. 4—*An example comparison of creep load line displacement* Δ^{LLD} *and crack mouth opening displacement* Δ^{CMOD} *with normalized time in (a) 316H and (b) CMn steel.*

Validity of CCG Data According to ASTM E 1457

The values of the transition time t_T calculated using Eq 11, and the time to reach 0.2 mm crack growth $t_{0.2}$ obtained from the PD output, are given in Tables 3 and 4 for the CRETE specimens, and Table 6 for the C(T) specimens of CMn steel. As stated previously, the use of the C_t parameter may be necessary for tests where significant crack growth occurs prior to the transition time. Since, for the cases examined here, the amount of crack growth that occurs for $t < t_T$, is negligible (in Tables 3 and 4 $t_T \ll t_{0.2}$ for the majority of tests) the use of the C_t parameter does not require consideration.

The validity criteria for the application of the C^* parameter to describe CCG rate are examined in Fig. 5, where the ratio of the creep to total load line displacement rates $\dot{\Delta}_c/\dot{\Delta}$ calculated using Eqs 9 and 10, is

TABLE 6—*CMn steel C(T) test specimen details.*

Test code	W (mm)	a_0/W	a_f/W	Δa (mm)	Load, P (kN)	Test duration, t_f (h)	t_T/t_f (%)	$t_{0.2}/t_f$ (%)
C7A_9	25	0.45	0.58	3.2	7.8	10 022	0.2	31.6
C7b_5_15W	15	0.46	0.66	3.0	2.3	11 170	0.5	61.0
C7b_7_15W	15	0.46	0.56	1.56	2.7	4730	0.1	89.5
C7b_15_50W	50	0.45	0.59	7.1	26	13 812	0.3	52.4

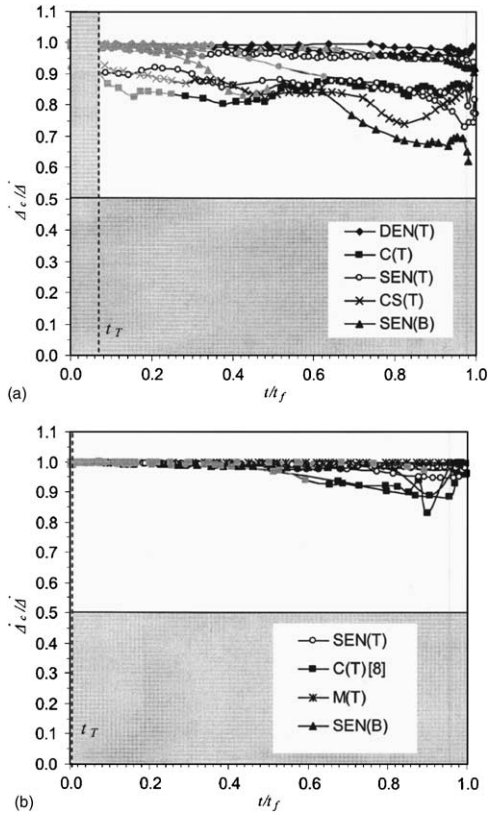


FIG. 5—*Analysis of validity criteria for CCG rate $\dot{a}$, correlation with C^* for (a) 316H and (b) CMn steel.*

shown for all tests of 316H and CMn steel. (Note that the instantaneous plastic displacement rate has not been included in the calculation of $\dot{\Delta}_i$.) Also indicated in this figure is the average value of the transition time t_T from all tests on the same material.

As discussed previously, data points obtained for $t < t_T$ or $t < t_{0.2}$ are considered invalid. Data points where $\dot{\Delta}_c/\dot{\Delta} < 0.5$ are also invalid, but note that all data points in Fig. 5 are outside this region (assuming $\dot{\Delta}_i = \dot{\Delta}_{i,e}$). Data points that are considered invalid are shown shaded in Fig. 5. Since the instantaneous plastic displacement rate has not been included in the estimation of $\dot{\Delta}_i$, there is a possibility that $\dot{\Delta}_c/\dot{\Delta} < 0.5$ for some of the data in this figure. However, as will be seen subsequently, good correlation between the crack growth rate $\dot{a}$ and C^* is observed with these data indicating that provided $t > t_{0.2}$, t_T and $(\dot{\Delta} - \dot{\Delta}_{i,e})/\dot{\Delta} > 0.5$, data are likely to be valid.

Estimation of C^* using $\dot{\Delta}^{\mathrm{LLD}}$ and $\dot{\Delta}^{\mathrm{CMOD}}$

As mentioned previously, for the SEN(B) and the majority of the SEN(T) specimens both $\dot{\Delta}^{\mathrm{LLD}}$ and $\dot{\Delta}^{\mathrm{CMOD}}$ are available. In Figs. 6(*a*) and 6(*b*) the value of C^* obtained for 316H using $\dot{\Delta}^{\mathrm{LLD}}$ and $\dot{\Delta}^{\mathrm{CMOD}}$ from Eqs 7 and 8, respectively, are compared for SEN(B) and SEN(T), respectively. Similar results have been obtained for the CMn steel. It may be seen in Fig. 6(*a*) that for the SEN(B) specimen the C^* values obtained from the two displacement rates are very close and in places are almost indistinguishable. However, a clear

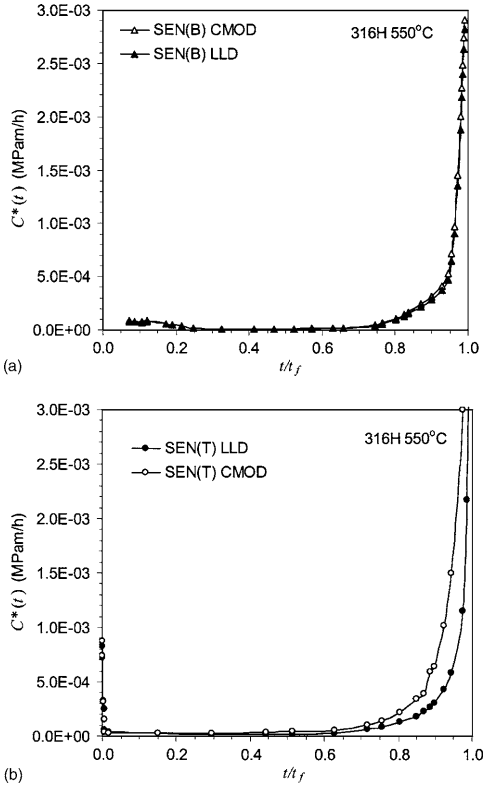


FIG. 6—*An example comparison of C^* values based on Δ^{LLD} and Δ^{CMOD} with normalized time for tests in (a) SEN(B) and (b) SEN(T) specimen of 316H stainless steel.*

separation between the C^* values calculated by the two displacement measurements is seen for the SEN(T) specimen in Fig. 6(*b*). Some of this difference may be due to the variability in the values of η^{CMOD} and η^{LLD} used to estimate C^* for the SEN(T) specimen. For the SEN(T) specimen the uncertainty in the C^* measurement associated with variability in η^{LLD} and η^{CMOD} can be up to ±26 % and ±5 %, respectively, within the range of a/W examined [9]. This cannot fully account for the difference observed between these two estimates of C^* suggesting that differences between the two C^* estimates for the SEN(T) specimen may be due to other unquantified experimental uncertainties.

Correlation of Creep Crack Growth (CCG) Rate

The creep crack growth rate is plotted against stress intensity factor K in Figs. 7(*a*) and 7(*b*) for 316H and CMn steel, respectively. All data are included in the figure, including that for $t < t_T$, following ASTM E 1457 [1]. The majority of these data have been generated as part of the CRETE program apart from two C(T) tests, indicated by open square symbols in Fig. 7(*a*), which have been supplied by British Energy Generation Ltd (BE) [20]. Figure 7 indicates that there is no unique relationship between CCG and K for these data and thus K is an unsuitable correlating parameter under these conditions. This result is expected as most of the data fall outside the small scale creep regime (as specified in ASTM E 1457 [1]) where K is an appropriate characterizing parameter.

In Figs. 8(*a*) and 8(*b*) the CCG rate $\dot{a}$ is plotted against C^*, calculated from $\dot{\Delta}^{LLD}$, for 316H and CMn steel, respectively. Following ASTM E 1457 [1] data points for $t < t_{0.2}$ and $t < t_T$ have been removed. It

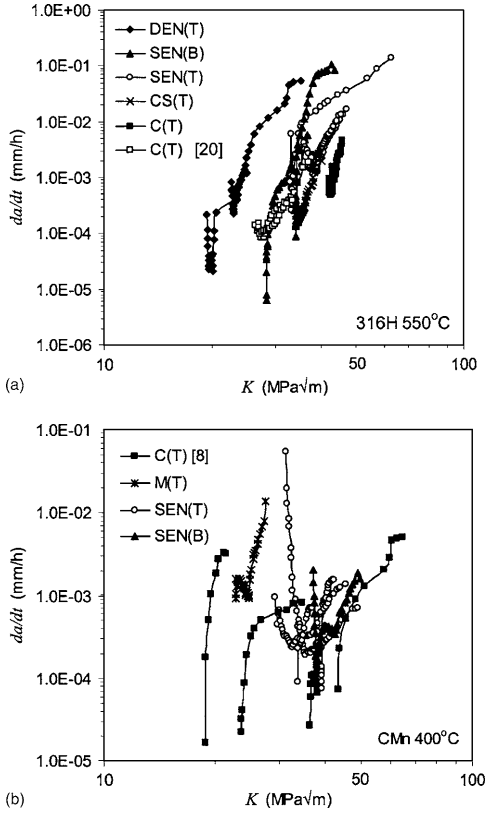


FIG. 7—*Creep crack growth rates correlated with K for all tests in (a) 316H and (b) CMn steel.*

may be seen that for the 316H data there is near linear correlation between $\dot{a}$ and C^* on a log-log scale [following Eq 4], with some variation between the different specimen types. It may also be seen that the data from the SEN(T), SEN(B), CS(T), DEN(T), and C(T) for $C^* > 1 \times 10^{-5}$ MPam/h lie within a relatively tight data band. The significance of the higher creep rates experienced by the C(T) specimen at low C^* (from [20]) will be discussed further in subsequent sections. Also included in Fig. 8(*a*) is a set of test data from C(T) specimens of different size [7], shown as an outlined region in the figure. It is seen that most of the new data fall within the C(T) data band with one of the SEN(T) data sets falling slightly below.

The correlation between CCG rate, $\dot{a}$ and C^* is somewhat less good for the CMn specimens, as seen in Fig. 8(*b*). In addition to the CRETE specimens, C(T) data from [8] have been included for comparison (solid squares). Although all data fall outside the region, $t < t_{0.2}$ and $t < t_T$ and $(\dot{\Delta} - \dot{\Delta}_{i,e})/\dot{\Delta} > 0.5$ for all data points, a linear correlation with C^* is not seen for much of the data. In particular, for the C(T) data at low C^* there is not a unique relationship between $\dot{a}$ and C^*. Thus the ASTM E 1457 [1] recommendations for valid data may not be appropriate for all materials.

Comparison of CCG Rate Data with Theoretical Models

In Fig. 9 the data are compared with the theoretical CCG models discussed previously. Only the approximate NSW model (NSWA) and the modified NSW model (NSW-MOD) are included in the figure as they cover the extremes of the model predictions. The failure strain ε_f used in both models is the uniaxial failure strain based on the reduction of area measurement in all cases (see Table 1). In the NSWA model

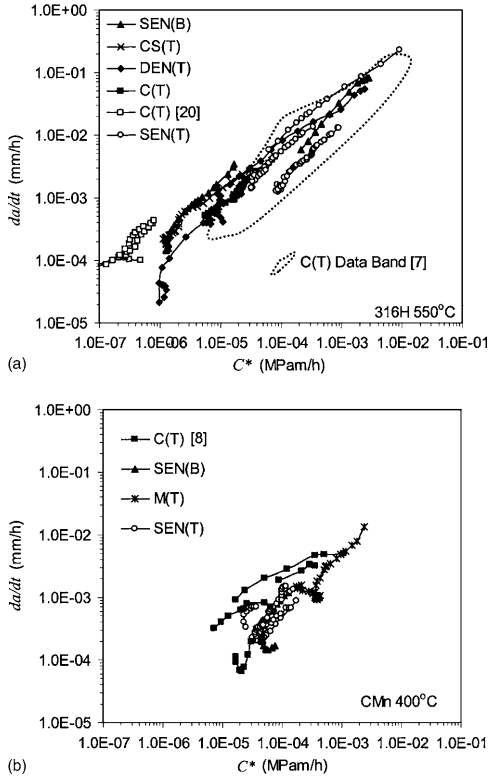


FIG. 8—*Comparison of the creep crack growth rates with C^* for alternative geometries with the C(T) geometry, for $\Delta a \geq 0.2$ mm, in (a) 316H stainless steel (b) CMn Steel.*

the multiaxial failure strain ε_f^* is taken to be equal to ε_f, under plane stress conditions and $\varepsilon_f/30$ for plane strain. The value of r_c has been taken to be the average grain size of the material (0.05 mm for 316H and 0.015 mm for CMn).

All of the data in Fig. 9(*a*), except the long term C(T) data (open squares), fall close to the plane stress lines (the NSWA and NSW-MOD estimates provide similar predictions). The long term C(T) test data lie close to the plane strain NSW-MOD line, suggesting that these tests more closely represent plane strain conditions than the short term tests. The factor of 30 applied to the multiaxial failure strain under plane strain conditions, used in the NSWA model, is seen to be overly conservative for these data, as the plane strain NSWA prediction significantly overestimates the experimental CCG rates. The NSW-MOD plane strain line provides a conservative prediction for most of the data [slightly nonconservative for the long term C(T) data].

In Fig. 9(*b*) the results for the CMn steels are shown, though fewer tests are available for comparison. The CCG rates for the SEN(T), SEN(B), and M(T) specimen are generally less than that of the C(T) specimens at the same value of C^*. All data lie close to or below the plane stress NSW-MOD prediction and the NSW-MOD plane stress line provides a conservative prediction.

Correlation of Creep Crack Initiation (CCI) Times

The measured initiation times t_i are shown plotted against the C^* parameter, calculated at the point of initiation, $C^*(t)$, in Figs. 10 and 11 for 316H and CMn steel, respectively. The individual data points from the C(T) tests reported in [7] are also shown in Fig. 10. Two crack extensions $\Delta a = 0.2$ and 0.5 mm, have

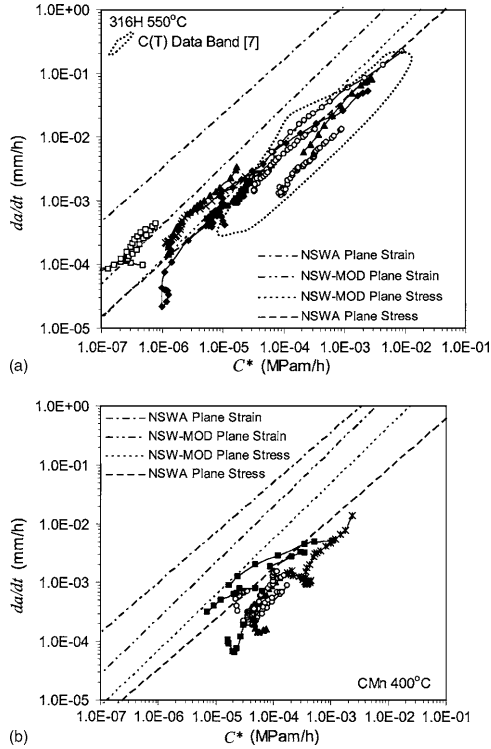


FIG. 9—*Comparison of the creep crack growth rates with C^* for alternative geometries with the C(T) geometry, for $\Delta a \geq 0.2$ mm, including NSW bounds, in (a) 316H steel and (b) CMn steel. The symbols used for the individual data sets are the same as in Fig. 8.*

been examined. Also included in the figures are the lower bound plane strain initiation time predictions, based on $\dot{a}_s$, and the upper bound plane stress predictions, based on $\dot{a}_0$, given by Eqs 23 and 24. Figure 10 shows that the upper bound plane stress and lower bound plane strain NSW-MOD solution, provide a reasonable estimate of the scatter in the 316 data at both $\Delta a = 0.2$ and 0.5 mm. No clear trends between the initiation times of the different specimen geometries can be deduced.

Figure 11 provides the result for the CMn steel. In Fig. 11(*b*), it may be seen that for a crack extension of 0.5 mm, three of the four points from the SEN(T) specimens form a straight line relation (on a log-log plot) between t_i and $C^*(t)$, suggesting that C^* may be an appropriate correlating parameter for creep crack initiation under these conditions. As was seen for the 316H data, the plane strain NSWA or NSW-MOD model, based on the steady-state crack growth rate, provides a conservative estimate of the time to crack initiation, and the region between the upper bound plane stress and lower bound plane strain NSWA lines includes most of the initiation data for $\Delta a = 0.2$ and 0.5 mm.

Discussion

For the range of specimen geometries and sizes the CCG data correlate quite well with C^* and, as expected for these creep-ductile tests, the stress intensity factor does not characterize CCG. No influence on the results has been found due to the starter crack type-prefatigue crack or an EDM slit, confirming the result in [7]. The influence of side grooving on the CCG rates in the CMn specimens is not considered, since, due to the limited number of tests, no firm conclusions may be reached.

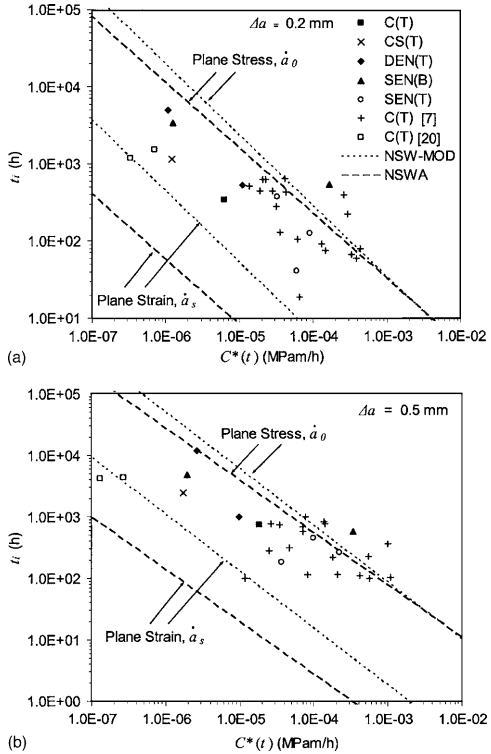


FIG. 10—*Comparison of the initiation times for alternative geometries of 316H steel with the C(T) geometry, including NSW bounds, in (a)* $\Delta a = 0.2$ mm, *(b)* $\Delta a = 0.5$ mm.

The estimated time for stress redistribution to a C^* controlled crack tip stress field is typically a small portion of the total test time for these tests, whereas the time for a creep crack extension of only 0.2 mm has been found to occupy a significant fraction of the test time for some tests. A power-law correlation between CCG rate and C^* is not always exhibited after a crack extension of 0.2 mm, even when the necessary validity criteria are met. This is observed in particular for the CMn data, Fig. 9(*b*), and indicates that 0.2 mm may not be an absolute measure of crack extension to ensure steady state creep crack growth.

Noticeably different behavior has been exhibited for the long term C(T) tests on 316H though relatively few data are available for these conditions. Comparison of the data with theoretical models for creep crack growth suggests that these long term tests are more closely representative of plane strain conditions while the short term tests appear to be closer to plane stress. This may indicate a significant influence from loss of constraint for the short term tests, leading to reduced CCG rates at the higher loads. The implications of using short term test data for the prediction of industrial high temperature components may therefore require further consideration. The experimental data presented here suggests that such an approach may be nonconservative, as the CCG rates for long term tests will be underestimated.

When defined as the time to attain a detectable amount of crack extension, either 0.2 or 0.5 mm of crack extension, the initiation time t_i is not uniquely characterized by C^* for the materials examined. For a given C^*, t_i can vary by up to an order of magnitude for two different tests on 316H with $\Delta a = 0.2$ mm [Fig. 10(*a*)]. Such a strong variation may be associated with difficulties in detecting accurately small amounts of crack growth in laboratory tests. The variability is somewhat less for $\Delta a = 0.5$ mm for 316H. Theoretical models based on estimates of initial crack growth rate provide conservative predictions of crack initiation time for both materials.

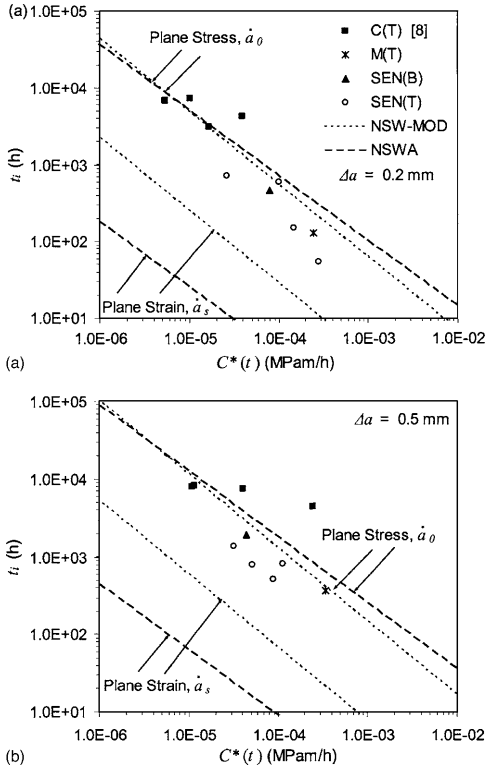


FIG. 11—*Comparison of the initiation times for alternative geometries of CMn steel with the C(T) geometry, including NSW bounds, in (a)* $\Delta a = 0.2$ mm, *(b)* $\Delta a = 0.5$ mm.

Conclusions

Tests have been performed on two steels operating in the creep regime, an austenitic Type 316H stainless steel at 550°C and a carbon manganese steel (CMn) at 400°C. A range of specimen geometries including the single edge notched specimen in tension and bending, the double edge notched specimen in tension, the middle cracked specimen in tension, and the C-shaped specimen in tension, have been examined and measured creep crack growth rates have been compared with those obtained from standard compact tension specimens, following ASTM E 1457 [1]. In order to characterize the creep crack growth rate data $\dot{a}$, the stress intensity factor K and creep fracture mechanics parameter C^* have been considered. Creep crack growth rates have been successfully correlated with the fracture mechanics parameter C^* for 316H and with less success for the CMn steel. No clear trend has been found between the CCI and CCG behavior of the various specimen geometries, suggesting that constraint effects may not be very important for the conditions examined. The approximate NSW CCG model has been found to provide adequate predictions for creep crack growth rates and initiation times, though overly conservative in cases. A closer prediction of the CCG rate is provided using the modified NSW model.

Different behavior has been observed between long and short term test data from C(T) specimens, suggesting that care must be taken when attempting to predict the lifetimes of components from short term test data.

References

[1] ASTM Standard E 1457-00, “Standard Test Method for Measurement of Creep Crack Growth Rates

in Metals," *Annual Book of ASTM Standards*, Vol. 3(1), ASTM International, West Conshohocker, PA. pp. 936–950.

[2] CRETE, *Development and Harmonisation of Creep Crack Growth Testing for Industrial Specimens—A Route to a European Code of Practice*, EU Framework 5 Project, GRD2-2000-30021, 2001–2004.

[3] Dogan, B., Ceyhan, U., Nikbin, K. M., Petrovski, B., and Dean, D. W., *European Code of Practice for Creep Crack Initiation and Growth Testing of Industrial Specimens*, submitted for publication, 2005.

[4] Riedel, H. and Rice, J. R., *Tensile Cracks in Creeping Solids*, in *Fracture Mechanics: Twelfth Conference*, 1980, ASTM STP 700, American Society for Testing and Materials, Philadelphia, PA, pp. 112–130.

[5] Rice, J. R., "A Path Independent Integral and the Approximate Analysis of Strain Concentration by Notches and Cracks," *Trans. ASME, J. Appl. Mech.*, 35, 379–386 (1968).

[6] Webster, G. A. and Ainsworth, R. A., *High Temperature Component Life Assessment*, 1st ed., 1994, Chapman and Hall, London.

[7] Bettinson, A. D., *The Influence of Constraint on the Creep Crack Growth of 316H Stainless Steel*, Ph.D. thesis, Department of Mechanical Engineering, Imperial College London, 2002.

[8] Kwon, O., *Failure and Fracture at Low Creep Temperatures*, Ph.D. and D.I.C thesis, Department of Mechanical Engineering, Imperial College London, 1998.

[9] Davies, C. M., Kourmpetis, M., O'Dowd, N. P., and Nikbin, K. M., "Experimental Evaluation of the J or C^* Parameter for a Range of Cracked Geometries," submitted for publication 2005.

[10] Fookes, A. J. and Smith, D. J., "The Influence of Plasticity in Creep Crack Growth in Steels," *Int. J. Pressure Vessels Piping*, 80(7), 453–463 (2003).

[11] Saxena, A., *Creep Crack Growth under Nonsteady-State Conditions*, in *Fracture Mechanics: Seventeenth Volume*, ASTM STP 905, 1986, American Society for Testing and Materials, Philadelphia, PA, pp. 185–201.

[12] Bassani, J. L., Hawk, D. E., and Saxena, A., "Evaluation of the C_t Parameter for Charaterising Creep Crack Growth Rates in the Transient Regime," in *Nonlinear Fracture Mechanics: Time-Dependent Fracture Mechanics*, Vol. I, ASTM STP 995, 1989, American Society for Testing and Materials, Philadelphia, PA, pp. 7–29.

[13] Nikbin, K. M., Smith, D. J., and Webster, G. A., "Influence of Creep Ductility and State of Stress on Creep Crack Growth," in Advances in Life Prediction Methods at Elevated Temperatures ASME, New York, pp.249–258 (1983).

[14] Nikbin, K. M., Smith, D. J., and Webster, G. A., "An Engineering Approach to the Prediction of Creep Crack Growth," *J. Eng. Mater. Technol.*, 108, 186–191 (1986).

[15] Tan, M., Célard, N. J. C., Nikbin, K. M., and Webster, G. A., "Comparison of Creep Crack Initiation and Growth in Four Steels Tested in HIDA," *Int. J. Pressure Vessels Piping*, 78(12), 737–747 (2001).

[16] Cocks, A. C. F. and Ashby, M. F., "Intergranular Fracture During Power-Law Creep under Multi-Axial Stress," *Met. Sci.*, 14, 395–402 (1980).

[17] Yatomi, M., "Factors Affecting the Failure of Cracked Components at Elevated Temperature," Ph.D., and D.I.C. thesis, Department of Mechanical Engineering, Imperial College London, 2003.

[18] Yatomi, M., Nikbin, K. M., O'Dowd, N. P., and Webster, G. A., "Theoretical and Numerical Modelling of Creep Crack Growth in a Carbon-Manganese Steel," *Eng. Fract. Mech.*, (to be published).

[19] Austin, T. S. P. and Webster, G. A., "Prediction of Creep Crack Growth Incubation Periods," *Fatigue Fract. Eng. Mater. Struct.*, 15(11), 1081–1090 (1992).

[20] Dean, D. W., and Gladwin, D. N., *Creep Crack Incubation and Growth Behaviour of Type 316H Steels*, British Energy Generation Ltd Report, E/REP/BDBB/0040/GEN/03 Revision 000, April 2004.

Fatigue Damage and Analysis

Journal of ASTM International, April 2006, Vol. 3, No. 4
Paper ID JAI13199
Available online at www.astm.org

Stefano Beretta,[1] *Michele Carboni,*[1] *and Mauro Madia*[1]

Fatigue Strength in Presence of Inhomogeneities: Influence of Constraint

ABSTRACT: The effect of defects on the entity of the fatigue limit is nowadays well known and is demonstrated to be equivalent to the nonpropagating condition of short cracks. The influence of constraint at the defect tip has been addressed in the present paper considering a mild steel whose mechanical behavior has been experimentally determined together with the propagation threshold values for long cracks. The activity has first dealt with the determination of the Kitagawa diagram by means of fatigue limit tests using specimens containing micro-notches with different shapes (drilled holes and narrow slits). Experimental results showed a significant influence of the defect shape on the fatigue limit and thresholds. In order to understand the reasons, defects have then been analyzed by elasto-plastic FEM analyses. Computational results have confirmed a significant difference in the global constraint factor at the crack tip between round and narrow defects.

KEYWORDS: fatigue, constraint factor, defect shape, fatigue thresholds

Introduction

Fatigue assessment of mechanical steel components has to deal with the presence of defects [1,2], whose main sources are the steel production process (inclusions) or the manufacturing process (e.g., surface micro-folds and oxide entrapments for forging, gas pores, and shrinkage cavities for casting). In these cases, it is very useful to estimate the size of the largest inhomogeneity that can be found in a material volume or in a batch of components [2] and then to assess the fatigue strength.

The behavior of materials containing defects has been explained by Murakami et al. [1], who clearly showed that the fatigue limit is the threshold stress for nonpropagation of the small cracks which emanated from the original defects. From this point of view, the relationship between fatigue strength and defect or crack size (the so-called Kitagawa-Takahashi diagram) can be predicted by a model able to describe the relationship between ΔK_{th} and defect or crack size. The experiments have shown that the fatigue strength is not related to the shape of defects but to their size [1,3]. This kind of result can be explained on the basis of theoretical ndings of Murakami who showed that SIF at the tips of cracks with very different shapes can be estimated with the very simple and precise relationships [4]:

$$\Delta K = 0.65 \cdot \Delta\sigma \cdot \sqrt{\pi \cdot \sqrt{area}} \quad \text{surface defects} \tag{1}$$

$$\Delta K = 0.5 \cdot \Delta\sigma \cdot \sqrt{\pi \cdot \sqrt{area}} \quad \text{internal defects} \tag{1b}$$

One could eventually expect that there are no effects on fatigue strength other than the crack size. However, a number of sources suggest that the fatigue life of internal and surface defects is different (see for example [5]) and considering the thresholds of metallic materials Murakami and Endo [3] propose the following equations derived from experimental results:

$$\Delta K_{th} = 3.3 \cdot 10^{-3} \cdot (Hv + 120) \cdot (\sqrt{area})^{1/3} \quad \text{surface defects} \tag{2}$$

$$\Delta K_{th} = 2.77 \cdot 10^{-3} \cdot (Hv + 120) \cdot (\sqrt{area})^{1/3} \quad \text{internal defects} \tag{2b}$$

Manuscript received April 13, 2005; accepted for publication January 26, 2006; published online February 2006. Presented at ASTM Symposium on Fatigue and Fracture Mechanics: 35th Volume on 18 20 May 2005 in Reno, NV; R. E. Link and K. M. Nikbin, Guest Editors.

[1] Professor, Researcher, and Ph.D. Student, respectively, Politecnico di Milano, Department of Mechanical Engineering, Via La Masa 34, I-20156 Milano, Italy.

Copyright © 2006 by ASTM International, 100 Barr Harbor Drive, PO Box C700, West Conshohocken, PA 19428-2959.

TABLE 1—*Basic mechanical behavior of the considered mild steel.*

Monotonic Properties		Cyclic Properties	
E [MPa]	203 000	E_{cyclic} [MPa]	204 000
$R_{p0.2}$ [MPa]	585	$R_{p0.05cyc}$ [MPa]	365
UTS [MPa]	685	$R_{p0.2cyc}$ [MPa]	450

where ΔK_{th} (MPa$\sqrt{m}$) is the threshold SIF range, Hv (kgf/mm^2) is the Vickers hardness of the metal matrix, and $\sqrt{area}$ (μm) is the defect (or crack) dimension. Equations 2 and 2b are valid for a variety of materials (especially steels and cast irons) for defect sizes in the range 100 to 1000 μm.

This kind of effect can be intuitively explained in terms of constraint at the defect tip. In order to investigate this aspect, which can be relevant both for the fatigue strength estimation and for ΔK_{th} experiments on small cracks [6], in this research a number of fatigue tests in the presence of different surface defects have been carried out onto a mild steel. Experimental evidences, which definitely show a lower fatigue strength for 2D-like narrow defects, have then been analyzed by elasto-plastic FEM analyses. Computational results have confirmed a significant difference in the global constraint factor at the crack tip between round and 2D-like narrow defects.

Basic Experimental Characterization of the Mechanical Behavior of the Mild Steel Under Investigation

The material under investigation is a mild steel [7] used in the production of tubes for mechanical applications. In order to characterize the basic mechanical behavior of the considered material, monotonic and low cycle fatigue tensile tests were carried out. Details about the experimental procedures and instrumentation are reported elsewhere [8], while a summary of the results is presented in Table 1. The comparison between the monotonic curve and the cyclic one (the latter in terms of the Ramberg-Osgood relationship) showed the softening behavior of the material subjected to cyclic loading.

Dedicated experimental tests were also carried out (see again [8] for details) in order to characterize the crack propagation behavior of the considered material. Particularly, in order to determine the threshold of long cracks at different stress ratios, the ΔK-decreasing technique was applied to SE(B) specimens according to ASTM Standard Test Method for Measurement of Fatigue Crack Growth Rates (E 647). The two tests ($R=-1$ and $R=0.1$) were stopped when a crack rate of 10^{-11} m/cycle was achieved. The obtained results in terms of threshold SIF range will be used in the following as normalizing values.

Fatigue Tests on Smooth and Micro-notched Specimens

Fatigue tests were carried out on hourglass smooth and micro-notched specimens in order to define the fatigue limit of the considered material and its sensibility to defects and inclusions. Two different specimens were adopted in these tests: test pieces with a circular cross section (Fig. 1(*a*)) and pieces with a

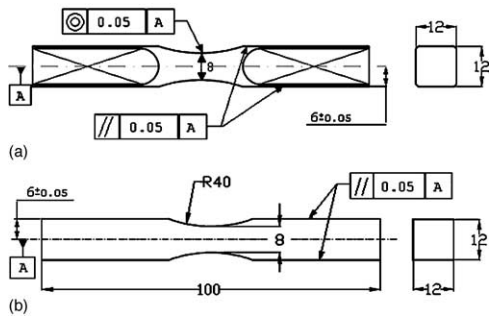


FIG. 1—*Geometry of specimens for fatigue tests: (a) circular cross section; (b) rectangular cross section.*

rectangular cross section (Fig. 1(*b*)). Round specimens were used for tensile tests, while square specimens were used for plane bending tests.

Preparation of the specimens consisted, first, in a mechanical polishing by emery papers up to a 1000# grit. Eventually, in order to remove the work hardened layer and to minimize residual stresses, the specimens were electro-polished (solution of 96 % acetic acid, 4 % perchloric acid) removing a 30 μm layer. X-ray measurements of surface residual stresses on six specimens showed a reduction to −40 MPa of the original residual stress equal to −200 MPa.

Fatigue Tests on Smooth Specimens

In order to define the fatigue limit of the considered mild steel, fatigue tests were carried out on smooth hourglass circular cross section specimens (Fig. 1(*a*)), at a frequency equal to 20 Hz and by means of a SCHENCK Hydropuls® servo-hydraulic axial machine with nominal maximum load equal to 250 kN.

Fatigue limit tests were carried out at stress ratios equal to −1 and 0.1 using "stair-case" sequences. Specimens were considered "run-out" if they survived 12×10^6 fatigue cycles. Results of stair-case sequences were analyzed by the Hodge and Rosenblatt method [9].

The fatigue limit on smooth specimens at R=−1 resulted to be $\sigma_{wo,R=-1}=355$ MPa. It is of some importance to remark that $\sigma_{wo,R=-1}$ is very close to $R_{p0.05,cyc}$ in accordance to Miller's definition [10] that fatigue limit on smooth specimens at R=−1 corresponds to the "cyclic yield stress."

Fatigue Tests on Micro-notched Specimens

The second part of fatigue tests was carried out using both types of specimen (Figs. 1(*a*) and 1(*b*)): in the case of round specimens, the tests were carried out at a frequency equal to 20 Hz using the SCHENCK facility already described, while, in the case of square specimens, the tests were carried out at a frequency equal to 120 Hz using a resonant bending machine RUMUL Cracktronic® with nominal maximum load equal to 160 Nm. Moreover, artificial defects of given size (expressed in term of Murakami's parameter $\sqrt{area}$ [3]) were introduced onto the surface of the specimens. Particularly, two different geometries of defects were adopted: micro-holes and narrow slits.

The former, in the following named "round defects," were used on the circular cross section specimens for obtaining defects characterized by a $\sqrt{area}$ value in the range 100–600 μm, while the latter, in the following named "narrow defects," were used on the rectangular cross section specimens for obtaining defects characterized by a $\sqrt{area}$ value in the range 600–1000 μm.

In the case of circular cross section specimens, two adjacent micro-holes (i.e., separated by a small diaphragm, Fig. 2) were machined by means of a high speed electric drilling machine. Two different dimensions of round defects were considered (Fig. 2(*a*)): (i) twin holes having a diameter of 100 μm, depth of 100 μm, and a diaphragm width of 20 μm, giving a $\sqrt{area}$ value equal to 150 μm; (ii) twin holes having a diameter of 300 μm depth of 300 μm, and a diaphragm width of 30 μm, giving a $\sqrt{area}$ value equal to 390 μm. As an example, Fig. 2(*b*) shows the electronic microscope picture of a defect having $\sqrt{area}=390$ μm.

In the case of rectangular cross section specimens, defects were obtained by means of the Electro Discharge Machining (EDM). Two different dimensions of narrow defects were considered (Fig. 2(*c*)): (i) prismatic hole having dimensions $2 \times 0.2 \times 0.12$ mm with a $\sqrt{area}$ value equal to 630 μm; (ii) prismatic hole having dimensions $3 \times 0.3 \times 0.12$ mm with a $\sqrt{area}$ value equal to 950 μm. As an example, Fig. 2(*d*) shows the electronic microscope picture of a defect with $\sqrt{area}=630$ μm.

Fatigue limit tests on micro-notched specimens were carried out using stair-case sequences considering run-out specimens at 12×10^6 fatigue cycles. Tests were planned in order to determine the dependence of fatigue limit on defect size at R=−1 and R=0.1. Particularly, two stair-case sequences were applied at R=−1 ($\sqrt{area}$ equal to 150 and 630 μm) and four at R=0.1 ($\sqrt{area}$ equal to 150, 390, 630 and 950 μm). Fatigue tests results were again analyzed by the Hodge and Rosenblatt method [9] and are summarized in Table 2, in terms of fatigue stress amplitudes normalized to $\sigma_{wo,R=-1}$.

Fatigue Thresholds and Threshold Model

According to Murakami's concepts [11], at the tip of micro-notches in run-out specimens it was, in general, possible to observe nonpropagating cracks. Figure 3 shows some examples of nonpropagating

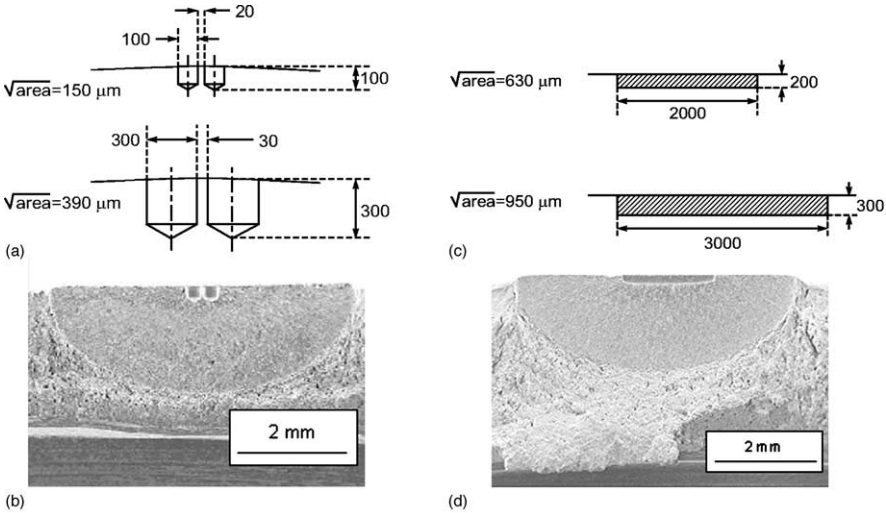


FIG. 2—*Round defects and narrow defects: (a) dimensions of the introduced round defects (*$\sqrt{area}$ =150 μm *and* $\sqrt{area}$=390 μm*); (b) SEM image of a round defect fracture surface (*$\sqrt{area}$=390 μm*); (c) dimensions of the introduced narrow defects (*$\sqrt{area}$=630 μm *and* $\sqrt{area}$=950 μm*); (d) SEM image of a narrow defect fracture surface (*$\sqrt{area}$=630 μm*).*

cracks observed by the Scanning Electron Microscope (SEM) on micro-notched specimens which survived 12×10^6 cycles in the fatigue limit tests. In particular, the two micro-holes were always connected by a crack at the bottom of holes and therefore can be treated as a single small crack.

It is then possible to assimilate micro-notches to small cracks [3] and to reconsider the results of fatigue limit tests in terms of propagation thresholds of the corresponding small cracks. The ΔK_{th} value corresponding to each test series was determined by introducing in Eq 1 the fatigue limit range $\Delta\sigma_w$ and the considered $\sqrt{area}$ parameter: Table 3 shows the fatigue threshold values for all the carried out fatigue tests. The reported values are normalized in terms of the threshold values for long cracks ($\Delta K_{th,LC}$) at R =−1 and R=0.1 obtained from the previously described crack propagation tests.

With the aim of obtaining a simple model able to describe the dependence of ΔK_{th} on defect size, a modified version [12] of the El-Haddad model can be applied:

$$\Delta K_{th} = \Delta K_{th,LC} \cdot \sqrt{\frac{\sqrt{area}}{\sqrt{area} + \sqrt{area_o}}} \tag{3}$$

where $\sqrt{area_o}$ is the El-Haddad's parameter in terms of the Murakami's parameter $\sqrt{area}$. In particular, at a given stress ratio, $\sqrt{area_o}$ can be written as [12]:

TABLE 2—*Normalized fatigue limit values for micro-notched specimens at R=−1 and R=0.1.*

Size of Defect $\sqrt{area}$ [μm]	Defect Type	Normalized Average Fatigue Limit Value $\sigma_w/\sigma_{wo,R=-1}$	Stress Ratio R
Smooth	…	1	−1
150	*round*	0.84	−1
630	*narrow*	0.52	−1
Smooth	…	0.78	0.1
150	*round*	0.68	0.1
390	*round*	0.5	0.1
630	*narrow*	0.34	0.1
950	*narrow*	0.28	0.1

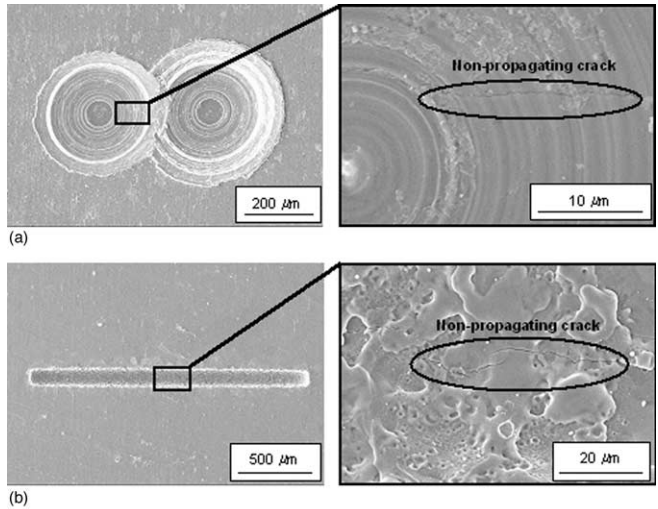


FIG. 3—*Examples of SEM observations on run-out specimens: (a) a nonpropagating crack at the tip of round defect with* $\sqrt{area}$=390 μm *tested at* R=0.1*; (b) a nonpropagating crack at the bottom of narrow defect with* $\sqrt{area}$=630 μm *tested at* R=0.1.

$$\sqrt{area}_{o} = \frac{1}{\pi} \cdot \left(\frac{\Delta K_{th,LC}}{0.65 \cdot \Delta \sigma_{wo}} \right)^2 \tag{4}$$

Figure 4 shows the threshold models at R=−1 and R=0.1 compared with the experimental evidences.

It is worth noting that experimental evidences of Fig. 4 suggest a different behavior for round and narrow defects. In particular, experimental results could be interpolated with Eq 3 considering different threshold values in accordance with Eqs 2 and 2b by Murakami and Endo.

It is so suggested that, together with the $\sqrt{area}$ parameter, also the defect shape can play an important role, particularly in terms of constraint at the crack tip. In order to check this assumption, FEM analyses were carried out on both kinds of defects.

FEM Analyses of Constraint Factor of Round and Narrow Defects

In order to evaluate the differences between the fatigue limits of round and narrow defects, FEM analyses were carried out. Particularly, the finite-element approach has been applied in order to evaluate these differences in terms of the global constraint factor α_g [13]. This parameter is usually adopted to characterize the "plasticity induced crack closure" phenomenon [14] in well known life prediction softwares, such as NASGRO [15] and AFGROW [16], where Strip-Yield analytical models [13] are implemented in

TABLE 3—*Normalized fatigue threshold values for micro-notched specimens at R=−1 and R=0.1.*

Size of Defect $\sqrt{area}$ [μm]	Defect Type	Normalized Fatigue Threshold Value $\Delta K_{th}/\Delta K_{th,LC}$	Stress Ratio R
150	*round*	0.65	−1
630	*narrow*	0.82	−1
Long cracks	…	1	−1
150	*round*	0.77	0.1
390	*round*	1.04	0.1
630	*narrow*	0.91	0.1
950	*narrow*	0.9	0.1
Long cracks	…	1	0.1

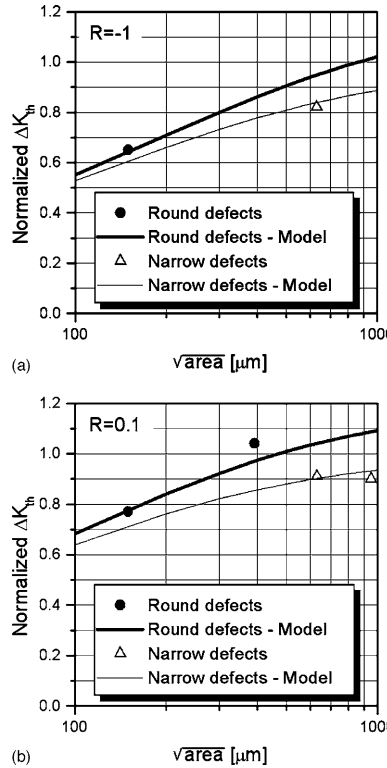


FIG. 4—*Threshold models for the mild steel under investigation: (a)* R=−1*; (b)* R=0.1.

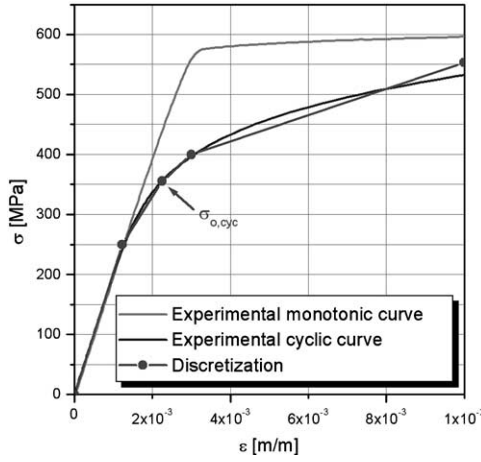


FIG. 5—*Discretization of the cyclic behavior of the considered material.*

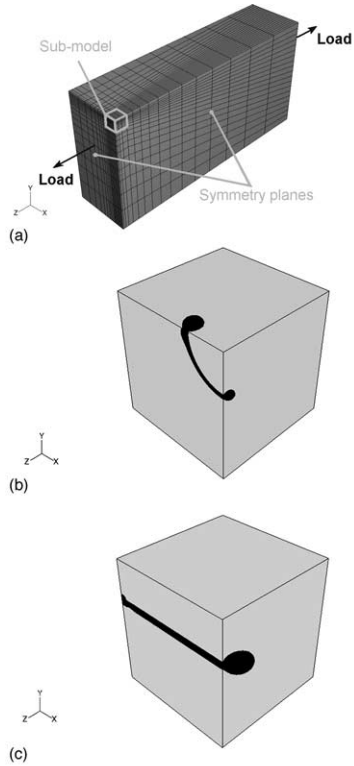


FIG. 6—*FEM analyses of round and narrow defects: (a) global model showing also the position of submodels; (b) and (c) plastic zone in the submodels at the tip of the round and the narrow defect in terms of von Mises stresses* ($\sigma_{max}/\sigma_{o,cyc}$=0.55).

order to simulate load interaction and stress ratio effects on crack propagation. One critical point in this kind of model is the adopted constitutive law, on which the definition of the constraint factor and, consequently, a reliable simulation of the plastic wake are based. From this point of view, in the case of structural mild steels, it has been demonstrated [17–19] that the best choice, for flow properties at the crack tip, considers the cyclic properties of the material.

Model Description and FE Results

The FEM analyses were carried out by means of ABAQUS® software v.6.4 [20]. Brick elements with 20 nodes were chosen and advantage was taken of all the possible symmetries of the models.

As mentioned above, the material behavior was modeled by means of a fine discretization (Fig. 5) of the experimentally derived Ramberg-Osgood relationship. The yield stress for this characterization of the material will be assumed to be $\sigma_{o,cyc}$ equal to the experimental $R_{p0.05}$, in accordance with [17–19] and instead of the monotonic properties.

A semicircular crack and a rectangular crack, both having a depth equal to 0.3 mm (Fig. 6(*a*)), were considered in order to model round and narrow defects, respectively. The submodeling technique was applied to the cracked zone of the modeled specimens (Figs. 6(*b*) and 6(*c*)) in order to reduce computational times. In particular, the submodel regarding the narrow defect represented only the central region of the defect itself because, in that zone, nonpropagating cracks could be observed (Fig. 3(*b*)).

Three different tensile stress levels were applied to both defects. These stress values, in terms of

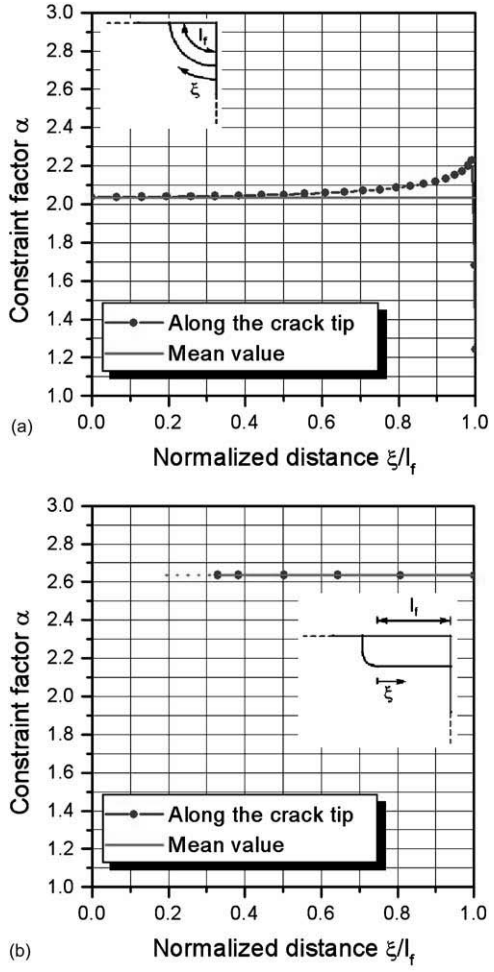


FIG. 7—*Trend of the constraint factor along the crack front* ($\sigma_{max}/\sigma_{o,cyc}$=0.27)*: (a) round defect; (b) narrow defect.*

$\sigma_{max}/\sigma_{o,cyc}$, were 0.27, 0.41 and 0.55 which correspond to the stress levels of fatigue limits at R=−1 for $\sqrt{area}$ values greater than 500 μm. Figures 6(*b*) and 6(*c*) show the plastic zones of both the defects in the case of $\sigma_{max}/\sigma_{o,cyc}$ equal to 0.55. It is important to add that the refinement of the mesh was studied so that, also in the case of the lowest applied load, at least six or seven elements could be included in the plastic zone.

Considering the round defect, it is possible to remark the different extension of the plastic zones in the internal part of the specimen and in the external one where the stress state is supposed to be close to a plane stress condition.

Considering, instead, the narrow defect, the extension of the plastic zone remains quite constant along the crack front. Moreover, in the region closer to the longitudinal symmetry plane of the specimen, where plane strain can be assumed, a higher stress pattern can be observed in respect to the corresponding one of the round defect, so suggesting that the crack has a higher possibility to nucleate and grow.

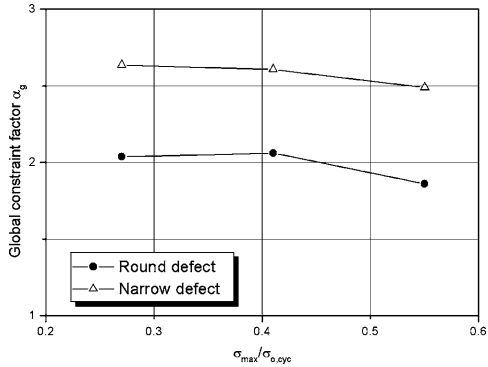


FIG. 8—*Global constraint factors for round and narrow defects.*

Analysis of the Constraint Factors

The global constraint factor assessment has been made according to Newman's method [21]:

$$\alpha_g = \frac{\int_{A_o} \sigma_n dA_n}{\sigma_{o,cyc} A_o} \tag{5}$$

where α_g is the global constraint factor, σ_n is the stress in the nth yielded element of the plastic zone, A_n is the projected area of the same element on the ligament, $\sigma_{o,cyc}$ is the cyclic yield stress of the material and A_o is the projected area of the whole plastic zone on the ligament.

In order to understand the trend of the constraint factor along the crack front, several slices were considered ahead of the crack tip: the global constraint factor can so be defined as the average value of all the chosen slices along the crack front.

Figure 7(*a*) shows the variation of the constraint factor along the crack front of the round defect for $\sigma_{max}/\sigma_{o,cyc}=0.27$: α can be assumed constant for all the crack lengths except in the region near the specimen free surface where a high drop can be noted. Consequently, the mean (global) value of the constraint factor is really close to the values in the inner part of the specimen where a plane strain state is present. Figure 7(*b*) shows the same analysis for the case of the narrow defect: it is possible to note a systematic higher value of the constraint factor in respect to the round defect.

The results of the systematic application of the method to all the applied stresses are summarized in Fig. 8. It is useful to add that, for the theoretical conditions of pure plane stress and plane strain, the values of the global constraint factor are 1 and 3, respectively [13].

Newman suggested [22] that a higher constraint factor value implies a lower opening load for crack surfaces which, in turn, means a lower fatigue threshold and a lower fatigue limit. This fact supports the differences in the fatigue limit values between round and narrow defects and it is thus in accordance with Eqs 2 and 2b.

Concluding Remarks

In the present paper, the fatigue strength in presence of inhomogeneities in a mild steel used in the production of tubes for mechanical applications has been analyzed. Particularly, the influence of defects shape has been considered and the results can be summarized as follows:

- Fatigue tests on smooth and micro-notched specimens were used to obtain the Kitagawa diagrams of the material for two different stress ratios;
- The adopted defects were characterized by two different shapes (micro-holes and narrow slits) which showed a significant influence on the experimental fatigue limits; and
- FEM analyses demonstrated that the influence of defect shape on fatigue limit and threshold must be attributed to the different constraint factor at the crack tip.

Acknowledgments

The present paper has been developed in the frame of a Research Contract between POLITECNICO DI MILANO and TENARIS-DALMINE. The authors wish to thank Tenaris Industrial & Automotive Product Development Division, directed by Dr. Mario A. Rossi, for permission to publish the results presented here.

References

[1] Murakami, Y., *Metal Fatigue: Effects of Small Defects and Nonmetallic Inclusions*, Elsevier, Oxford, 2002.
[2] Murakami, Y. and Beretta, S., "Small Defects and Inhomogeneities in Fatigue Strength: Experiments, Models and Statistical Implications," *Extremes*, Vol. 2, 1999.
[3] Murakami, Y. and Endo, M., "Effect of Defects, Inclusions and Inhomogeneities on Fatigue Strength," *Int. J. Fatigue*, Vol. 16, 1994.
[4] Murakami, Y., "Analysis of Stress Intensity Factors of Modes I, II, and III for Inclined Surface Cracks of Arbitrary Shape," *Eng. Fract. Mech.*, Vol. 22, 1985.
[5] Chai, G., "Fatigue Behaviour of Duplex Phase Alloys in Very High Cycle Regime," *Proceedings of the International Conference "Very High Cycle Fatigue" (VHCF3)*, Japan, 2004.
[6] Beretta, S., Giglio, M., Mariani, U., and Vicario, M., "Flaw Tolerance Evaluation of Helicopter Rotor Parts," *Proceedings ICAF 2003*, EMAS, Sheffield, 2003.
[7] *Steel Tubes for Precision Applications—Technical Delivery Conditions—Part 1: Seamless Cold Drawn Tubes*, EN 10305–1, 2003.
[8] Beretta, S., Carboni, M., Desimone, H., Madia, M., and Sapienza, A., "Defect Tolerance of Mechanical Components Obtained From Tubes," Final Report of the Research Contract #19/2003, Politecnico di Milano, 2004.
[9] Brand, A., *Donneès technologiques sur la fatigue*, CETIM, France, 1989.
[10] Miller, K. J., "The Short Crack Problem," *Fatigue and Fracture of Engineering Materials and Structures*, Vol. 5, 1982.
[11] Murakami, Y. and Endo, M., "Effects of Hardness and Crack Geometries on ΔK_{th} of Small Cracks Emanating from Small Defects," in *The Behavior of Short Fatigue Cracks*, K. J. Miller and E. R. De Los Rios, Eds., MEP, London, 1986.
[12] Beretta, S., "Propagation of Short Cracks in a High Strength Steel for Railway Axles," in *Fracture Mechanics Beyond 2000*, A. Neimitz, I. V. Rokach, D. Kocanda, and K. Golos, Eds., EMAS, Sheffield, 2002.
[13] Newman, J. C., Jr., "A Crack Closure Model for Predicting Fatigue Crack Growth Under Aircraft Spectrum Loading," *ASTM STP 748*, ASTM International, West Conshohocken, PA, 1981.
[14] Elber, W., "The Significance of Fatigue Crack Closure," in *Damage Tolerance in Aircraft Structure*, *ASTM STP 486*, ASTM International, West Conshohocken, PA, 1971.
[15] Anon, "Fatigue Crack Growth Computer Program 'NASGRO' version 3.0—Reference Manual," JSC-22267B, NASA Technical Report, 2001.
[16] Harter, J. A., "AFGROW Users Guide and Technical Manual," AFRL-VA-WP-TR-2002-XXXX, U. S. Air Force Research Laboratory Technical Report, 2002.
[17] Beretta, S., Carboni, M., Machniewicz, T., and Skorupa, M., "Correlation Between Experiments and Strip Yield Model Results on Fatigue Crack Growth in Structural Steel," *Proceedings of the 14th European Conference on Fracture*, Krakow, Poland, 2002.
[18] Skorupa, M., Machniewicz, T., Skorupa, A., Beretta, S., and Carboni, M., "Application of the Strip-Yield Crack Closure Model to Crack Growth Predictions for Structural Steel," *Proceedings of the 11th International Conference on Fracture (ICF XI)*, Torino, 2005.
[19] Beretta, S. and Carboni, M., "A Strip-Yield Algorithm for the Analysis of Closure Evaluation Near the Crack Tip," *Eng. Fract. Mech.*, Vol. 72, 2005.
[20] ABAQUS® 6.4., *Reference Manual*, 2004.
[21] Newman, J. C., Jr., Bigelow, C. A., and Shivakumar, K. N., "Three-dimensional Elastic-plastic Finite-element Analyses of Constraint Variations in Cracked Bodies," *Eng. Fract. Mech.*, Vol. 46,

1993.
[22] Newman, J. C., Jr., "A Crack Opening Stress Equation for Fatigue Crack Growth," *Int. J. Fatigue*, Vol. 24, 1984.

Journal of ASTM International, Vol. 3, No. 6
Paper ID JAI13189
Available online at www.astm.org

Kensuke Ichinose,[1] *Sanichiro Yoshida,*[2] *Kenji Gomi,*[3] *Kiyoshi Taniuchi,*[4] *Katsumi Fukuda,*[5] *and Hideyuki Ishii*[6]

Detection of Crack Initiation by Observations of Free Surface Condition

ABSTRACT: A simple method to detect crack initiation is presented. By polishing the surface of carbon steel structure properly and using the Lüders bands and orange peel as indicators for damage, it is possible to predict crack initiation with the naked eye. The initiation of the Lüders bands is the yellow light of the crack initiation, for instance, in the traffic signal, and orange peel is the red light. The relationship between the observed surface condition and the cyclic stress-strain characteristics is discussed.

KEYWORDS: fatigue damage, cyclic stress-strain diagram, low cycle fatigue, fatigue crack initiation, Lüders band, orange peel

Introduction

It is widely known that the existence of a crack causes structures or members to break. Various methods have been developed to detect or monitor fatigue cracks [1]. Examples of these methods include acoustic emission techniques, eddy current techniques, and ultrasonic methods. However, these methods commonly require sophisticated instrument and are usually expensive. If a simple method is available to predict the initiation of cracks, it will be useful for many applications. It will also work as an auxiliary method for the above-mentioned well-developed techniques. From the viewpoint of low cycle fatigue, we consider a simple method to detect the initiation of cracks.

A number of reports have been published concerning the initiation and propagation of cracks [2,3]. Discussions have been made on the underlying mechanism from various viewpoints. However, there is no report that describes visualization of the continuous change in the material's surface condition during the process of crack initiation. The starting point of crack initiation has not been clarified. Therefore, when one tries to evaluate crack initiation life, it is not clear which point to define as the beginning of the crack initiation life.

On a stress-strain diagram, the yield point is always located before the fracture point. This indicates that materials necessarily experience yielding before it fractures. From the viewpoint of nondestructive testing, while it is not generally considered seriously, the change in the surface condition under cyclic loading after the yield point is quite important for analysis of the metal fatigue.

Fundamental properties of materials can be obtained from the stress-strain diagrams. For metal fatigue, it is necessary to analyze the cyclic stress-strain diagram. As for the method to obtain information con-

Manuscript received April 7, 2005; accepted for publication August 12, 2005; published online May 2006. Presented at ASTM Symposium on Fatigue and Fracture Mechanics: 35th Volume on 18–20 May 2005 in Reno, NV; R. E. Link and K. M. Nikbin, Guest Editors.

[1] Professor, Department of Mechanical Engineering, Tokyo Denki University, 2-2 Kanda Nishiki-cho, Chiyoda-ku, Tokyo, Japan, 101-8457.

[2] Associate Professor, Department of Chemistry and Physics, Southeastern Louisiana University, SLU 10878, Hammond, LA 70402.

[3] Assistant Professor, Department of Mechanical Engeering, Tokyo Denki University, 2-2 Kanda Nishiki-cho, Chiyoda-ku, Tokyo, Japan, 101-8457.

[4] Former Professor, Meiji University, 5-10-12, Wakamatsu, Sagamihara-shi, Japan 229-0014.

[5] Professor, Department of Mechanical Engineering, Tokyo National College of Technology, 1220-2 Kunugida-machi, Hachioji-shi, Tokyo, Japan, 193-0997.

[6] Graduate Student, Department of Mechanical Engneering, Tokyo Denki University, 2-2 Kanda Nishiki-cho, Chiyoda-ku, Tokyo, Japan, 101-8457.

Copyright © 2006 by ASTM International, 100 Barr Harbor Drive, PO Box C700, West Conshohocken, PA 19428-2959.

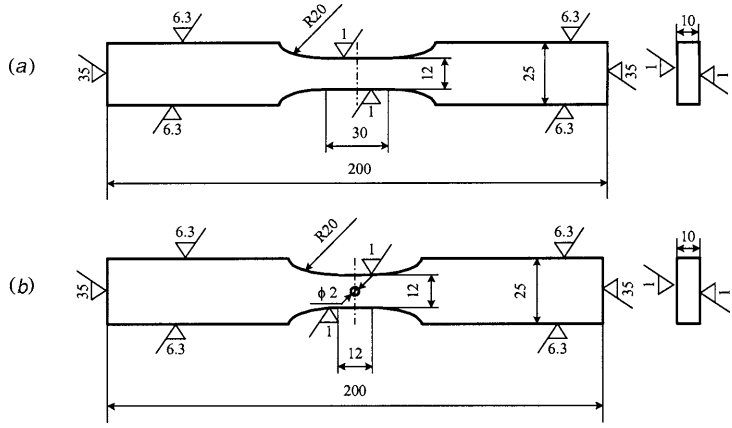


FIG. 1—*A schematic diagram of the specimen configuration.*

cerning cyclic stress-strain diagrams, the report by Landgraf et al. [4] is widely known. However, this report does not deal with observation of the specimen surface. From the viewpoint of nondestructive testing, we cannot ignore the change in the surface condition in connection with the stress-strain diagram. However, there is no report that deals with this problem.

It is well known that when carbon steel yields, the stripe pattern known as the Lüders band propagates on the specimen. It is also known that when the specimen is about to break under tension testing the specimen experiences local narrowing effect at the location where it eventually breaks and that the surface around this local region shows roughness known as the orange peel. By using the Lüders band and the orange peel as indicators for damage, it is possible to find the yielded region and fracturing location on a real time basis [5,6]. In this study, we observed the surface condition of low-carbon steel specimens by cyclic loading and clarified the relationship between the surface condition and the cyclic stress-strain diagram.

Specimens and Experimental Procedures

Figure 1 shows the shape and dimension of the specimen used in this study. The dimension conforms to ASTM E606. The material is commercially available SS400. Table 1 shows the chemical composition of this material. Prior to machining, we annealed the material at 900°C, and after the machining we vacuum annealed at 650°C. The surface of each specimen was polished with emery paper (No. 2000). Immediately before the test, the surface profile Ra was 0.05 μm, the hardness value (HV) value was 124, and the grain size was 12 μm. Using an electrohydraulic-servo fatigue-testing machine, we applied cyclic loads in the strain-controlled mode with load ratio R of −1. We increased the strain at every two cycles at a frequency of 1 Hz. The strain increment was 0.02 % for the strain-controlled mode. These increments were determined empirically. The strain was measured with axial extensometers (MTS Model Number 634.31F-24). A video camera continuously recorded the striped pattern, which appears on the surface of the specimen. All experiments were carried out at room temperature.

TABLE 1—*Chemical composition in weight percentage.*

C	Si	Mn	P	S	Ni	Cr	Cu
0.090	0.220	0.580	0.020	0.007	0.009	0.230	0.070

Surface Condition of Specimen for Direct Observation

On the analysis of fatigue, observation of the surface condition provides important information. Fatigue damage is accompanied by plastic deformation, and therefore, in the case of mild steel flat bar, dull lines known as the flow, strain figures, or Lüders bands normally appear on its surface.

Nadai [7] proposes the use of the Lüders bands to study slips on specimens. He explains the Lüders bands as a stripe pattern visible when the specimen surface is mirrorlike polished. At the same time, he lists three methods for observing the flow figures; etching method by Fry, Schlieren method, and stress coat method. He mentions that the etching method is suitable for studying the distribution of the surface of slip in the interior of mild steel specimens, and that the other two methods are conveniently used to make the slips visible on the surface of stressed pieces. It is now a common practice to visualize the Lüders bands by one of these three methods. Examples of such studies include the observation of the yielded zone near crack tips by the etching method [8] and the observation of Lüders bands by the stress coating method [9].

On the other hand, in Ref. [10] there is a description: "The plastic deformation that occurs within yield point elongation is accompanied by the formation of visible bands of deformation on the product surfaces. These bands are called stretcher strains or the Lüders bands, and they can be aesthetically undesirable." This description is inconsistent with the above-mentioned Nadai's description. It is interesting to note that on one hand, efforts are made to visualize the stripe pattern with the etching method or other technique and on the other hand it is characterized as an undesirable pattern and measures are considered to prevent the formation.

There is a reason behind this inconsistency. Most material tests use a rod specimen. In the case of a rod specimen, even if the Lüders bands are formed inside the material, they are invisible from the surface [11]. In the case of plate test specimens, the Lüders bands are not visible unless the surface is polished to be as good as Ra:0.15 μm; if the surface is rough, the Lüders bands are buried in the bumpy surface pattern [12]. It is unlikely that the surface is polished to this level in material tests. Thus in most material tests, the condition is such that either the Lüders bands are invisible or extremely hard to observe.

The surface profile of press-processed, low-carbon steel plates usually shows Ra values around 0.15 μm. This range of Ra values indicates that the accompanying stretcher strains or Lüders bands ought to be visible to the naked eye.

The visible band on the surface can be observed with the naked eye if the surface is flat and polished to be Ra=0.15 μm or better. Surface treatment such as the etching method or stress coatings is unnecessary. Note that Lüders bandlike stripe patterns have been observed in silicon steel, ferrite stainless steel, aluminum-magnesium alloys, and molybdenum [7,13,14,15]. Therefore, this idea is applicable in various real-world situations.

Unlike the Lüders bands, the orange peel is visible on the surface of a rod specimen.

Experimental Results and Discussion

Cyclic Stress-Strain Diagram

It is known that, when a static load is applied, the reaction of the material can be characterized by referring to the stress-strain diagram of the material. Extending this concept, it is expected that the fatigue process, which is caused by a cyclic load, should be characterized by referring to the cyclic stress-strain diagram of the material. Therefore, it is worth comparing the cyclic stress-strain diagram and the stress-strain diagram for the same material. Moreover, it is expected that through such a comparison we can deepen our understanding of the characteristic of the material and the mechanism of the fatigue process.

Here the cyclic stress-strain diagram is defined as the loci of the tips of stable hysteresis loops from tests at reversed constant strain amplitudes [4]. Figure 2 shows a cyclic stress-strain diagram under strain control mode with a load ratio R of -1, strain increment of 0.02 %, and loading rate 1 Hz. The horizontal axis represents the number of cycle, which corresponds to plastic strain. For comparison, the stress-strain diagram recorded under tension testing with a crosshead speed of 0.5 mm/min is shown in Fig. 3.

Figures 2 and 3 are similar to each other in the sense that the diagram consists of a linear part representing the regime where the stress is proportional to the strain, and a nonlinear part representing strain hardening. However, there is a considerable difference in the range where the nonlinear part extends.

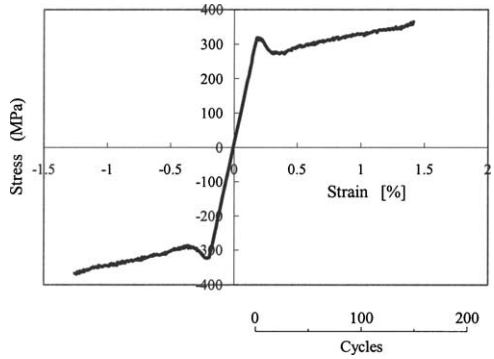


FIG. 2—*Cyclic stress-strain diagram, Load ratio R:1. Frequency:1 Hz.*

The nonlinear part in Fig. 2 extends from about 0.15 % for about 1.4 %, and this is much smaller than the corresponding part in Fig. 3, which extends from about 1 % for about 22 %. This leads to the fact that the maximum strain under cyclic loading is generally much lower than monotonic loadings. In this particular case, the maximum strain observed in Fig. 2 is 1.4 % whereas that in Fig. 3 is 22 %. This tendency is generally observed. In Fig. 2, the strain hardening regime corresponds to fatigue. Therefore, judging from the amount of total strain, it is inappropriate to substitute this regime by the strain hardening obtained under a monotonic loading like Fig. 3. It is thus concluded that fatigue analysis must be based on a cyclic stress-strain diagram, not a stress-strain diagram under monotonic loading.

Figure 2 indicates that there is yield point elongation under cyclic loading, as discussed by previous reports [12,16], but its extent is much shorter than that typically observed under monotonic loading. Careful observation of Fig. 2 near the yield point reveals that while the upper yield point is a sharp peak, the lower yield point extends flat parallel to the horizontal axis. Along with the fact that the specimen surface of this stage shows a Lüders bandlike stripe pattern, this observation indicates that the stress-strain diagram under cyclic loading has a flat regime that can be considered as the yield point elongation. Note that the extent of the yield point elongation under cyclic loading is much shorter than that typically observed under monotonic loading. In this particular case, the total strain in the yield point elongation in Fig. 2 is about 0.15, which is much smaller than the corresponding total strain of about 0.75 observed in Fig. 3.

Figure 2 indicates that the cyclic stress-strain diagram recorded under strain-controlled testing shows the upper yield point at the beginning of the yield point elongation. Historically, the existence of upper yield point has been overlooked under cyclic loading. This is mainly because the yield point elongation under cyclic loading extends much shorter than monotonic loading, as Fig. 2 indicates. Also, it is usually the case that in a low cycle fatigue test for steady state analysis a high load is applied from the beginning, and therefore the yield point tends to be overlooked.

This difference in the stress-strain diagram is thought to be due to the difference in the way the load is applied to the specimen. In the case of the cyclic loading with $R=-1$, a load of the same magnitude and

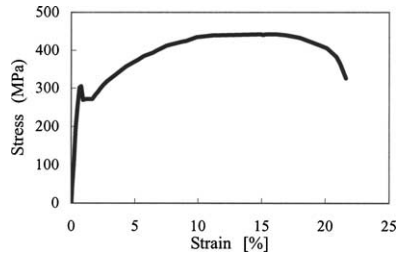


FIG. 3—*Stress-strain diagram, Crosshead speed; 0.5 mm/min.*

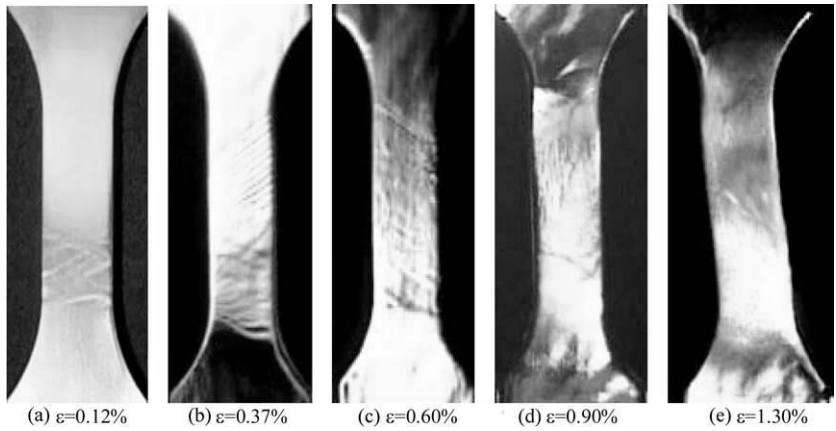


FIG. 4—*Striped patterns on specimen surface caused by cyclic loading. Load ratio* $R: -1$.

opposite directions are applied to the specimen alternatively. Consequently, the resultant strain varies as a function of time and shows hysteresis. In contrast, under monotonic loading, the same positive load is applied continuously. It is very unlikely that the material responds in the same fashion to these completely different patterns of load application. Thus, naturally, the stress-strain diagrams are different between the cyclic and monotonic loading. Landgraf [4] points out that the stress-stain diagrams of cyclic loading and monotonic loading can be drastically different. The comparison of Figs. 2 and 3 support the Landgraf's observation.

In the case of $R=-1$, when the negative load increases as the magnitude of the load increases. Consequently, the specimen experiences a buckling unless it is hourglass configuration. On the other hand, in the case of monotonic loading, the specimen experiences local narrowing as the load increases. This difference can be related to the difference in the strain hardening observed in Figs. 2 and 3.

Surface Conditions of Specimen due to Cyclic Loading

If the surface state is understood in connection to the cyclic stress-strain diagram, it is useful for nondestructive testing as well as analysis of fatigue phenomena. We made an attempt to understand the relationship between the surface state and cyclic loading. Figure 4 is the surface condition of the specimen recorded concurrently with Fig. 2. As the total strain increased, the stripe patterns were initiated and propagated as shown in Figs. 4(*a*)–4(*e*). The number shown below the figure denotes the total strain at which each pattern was observed. When the strain reaches a certain level, a stripe pattern was initiated at a location of the specimen, and then the whole surface was covered by the same pattern. As the strain further increases, the stripe pattern gradually changes. The initial pattern is apparently the Lüders bands, and they change to the pattern known as orange peel. The change in the surface condition observed in Fig. 4 is similar to usually observed under tension testing. However, the pattern of the Lüders band are different between tensile loading and cyclic loading. In the case of the former, the Lüders bands appear to be a straight line, as opposed to a somewhat wavy line as seen in Fig. 4 for the latter. The orange peel pattern is the same in the cyclic load and the tensile load.

Comparison of Figs. 2 and 4 indicates that the strip pattern (*a*) in Fig. 4 corresponds to the upper yield point in Fig. 4. In monotonic loading, Lüders bands appear at the upper yield point. From this and the appearance seen in Fig. 4(*a*), this stripe pattern can be interpreted as a Lüders band. In other words, it can be said that specimens under cyclic loading show yield point elongation, and correspondingly, a Lüders band appear as monotonic loading.

The yield point elongation and the appearance of Lüders band indicate that the material deforms plastically at the location of the Lüders band. In the case of cyclic loading, it means that the fatigue process

has started in the material. In other words, when a Lüders band appears, the material starts fatigue at that location, and it is reasonable to say that the moment at which a Lüders band begins to appear is the starting point of fatigue life.

It is shown in the cyclic stress-strain diagram that there is little possibility of low cycle fatigue when maximum of the repeated loads lies in the elastic region. The plastic deformation, or permanent deformation, occurs under the repeated load above the yield point which is the boundary between elasticity and plasticity.

According to ASTM E1823, fatigue is the process of progressive localized permanent structural change occurring in a material. Thus, the fatigue must be considered to start with plastic deformation due to the yield of the material. Since Lüders bands appear at the yield point, its stripe pattern is the mark when the fatigue starts.

An orange peel is observed in Fig. 4(*e*). This corresponds to the right end of the stress-strain diagram, which corresponds to the initiation of a crack in monotonic loading. In other words, an orange peel appears right before a crack is initiated, and therefore the orange peel can be used as an indicator for prediction of crack initiation. Figures 4(*b*)–4(*d*) show the transitional stage from the Lüders band to the orange peel, and it is possible to know the stress-strain relationship corresponding to the transitional stage from Fig. 2. Figures 2 and 4 provide important data to examine the fatigue process.

The change from the Lüders bands to the orange peel, which the specimen showed as the load increased, was easily observed with the naked eye. In other words, the change in the condition of free surface due to fatigue is easily recognized with the naked eye.

Surface Profile, Vickers Hardness

To evaluate the stripe pattern observed on the surface of specimen under cyclic loading quantitatively, we measured the surface profile and the Vicker's hardness value (HV). Figures 5(*a*)–5(*e*) show the surface profile measured for the same conditions as Figs. 4(*a*)–4(*e*), respectively. Note that (*a*) is the stage where the Lüders band is visible, (*b*)–(*d*) is the stage when the Lüders band is changing to the orange peel, and (*e*) is when only the orange peel is visible. In Fig. 5(*e*), the fact that on either side of the curve has a slope is thought to be due to the warp of the surface by buckling.

Figure 5 indicates that there is a clear difference in the surface profile between the Lüders band and orange peel. It is seen that the Ra value for the Lüders band is higher than that of the orange peel, whereas the HV value at the Lüders band is lower than that at the orange peel. It is thought that the main factor that the value of Ra changes is due to the progress of multiple slip and the forming of cell structure. The difference in the HV value seems to be caused by the work hardening of material in deuced by the repeated load application.

The surface roughness curve shows a wavy pattern while the Lüders bands is visible, as opposed to the finer fluctuation when the orange peel is visible.

Microstructure of Specimen Surface

As is clear from Figs. 4 and 5, the stripe pattern observed on the free surface changes its appearance as the load increases and also changes the Ra value. Figure 6 shows crystallographic pictures that represent the changes. Figures 6(*a*) and 6(*b*) correspond to Figs. 4(*a*) and 4(*d*), respectively.

A remarkable difference is observed in the pattern of slip bands between the regions where the Lüders band is formed and the orange peel is formed.

Free Surface Condition around a Circular Hole under Cyclic Loading

It has been observed that the stripe pattern appears and propagates on the free surface of the specimen under cyclic loading, and that the pattern changes as the load increases. This phenomenon indicates it is possible to analyze the fatigue process of structures through direct observation of the free surface with the naked eye. As an example, we attempted to observe the fatigue process near a small hole with the naked eye. Note that in this type of study, it is essential that the observed fatigue process includes a fatigue-induced crack. However, in the case of the specimen shown in Fig. 1(*a*), it is likely that the specimen experiences buckling under $R=-1$ before a crack is initiated. Therefore, we used a specimen having a

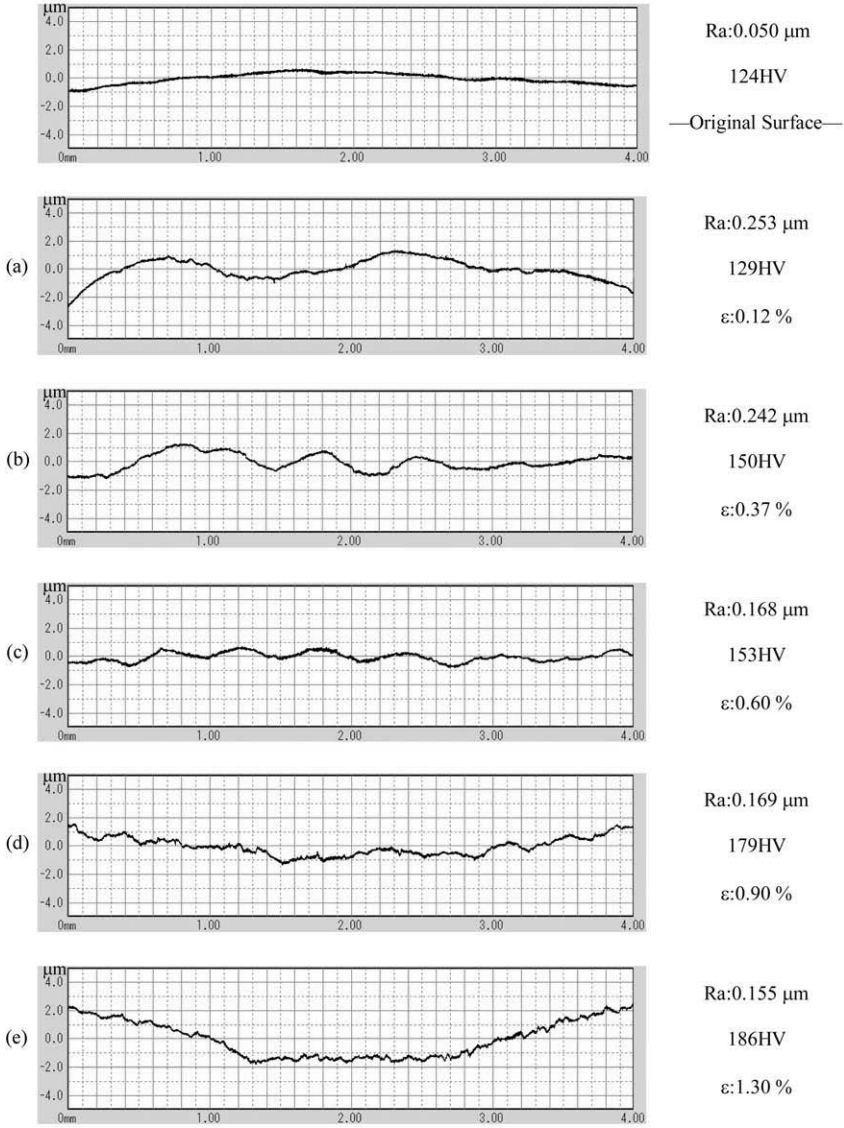


FIG. 5—*Surface profile and Vickers hardness.*

small hole at the center as shown in Fig. 1(*b*). Figure 7 shows the change of the free surface near the small hole of 2 mm in diameter that we recorded continuously. The cyclic condition for this experiment was strain increment of 0.01 % at a cycle frequency of 1 Hz.

As the load increased, the surface state changed as Figs. 7(*a*)–7(*d*). Note that in (*a*) a Lüders band is observed and in (*d*) a crack surrounded by an orange peel is observed. Figures 7(*b*) and 7(*c*) show the transitional stage in which the Lüders bands changes into an orange peel in the vicinity of the circular hole. The crack is observed when the transition from the Lüders bands to the orange peel has completed.

When an orange peel is observed, a crack is initiated shortly. So, the orange peel can be interpreted as

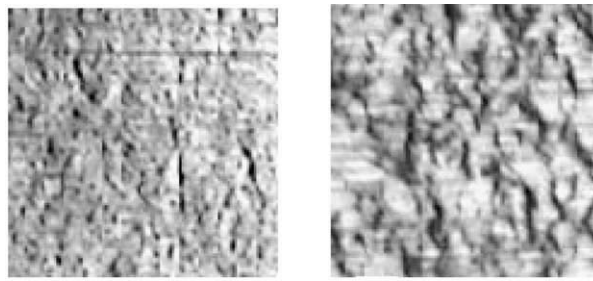


FIG. 6—*Microstructure of specimen surface.*

the red light of crack initiation. As is clear from the continuous observation of the surface state, the orange peel is transformed from the Lüders bands as a result of an increase in the load. So, the Lüders bands can be interpreted as the yellow light of crack initiation. It can be said that this yellow light indicates the initiation of the fatigue life.

The initiation of a crack can be predicted with the naked eye by simply polishing the specimen surface and observe it properly. Polishing with No. 2000 emery paper by hand is easy in most field applications.

In Fig. 7(*a*), the Lüders bands are inclined at about 45° to the load axis indicating that it is caused by the shear stress. On the other hand, the stripe in Fig. 7(*d*) indicates that the stripe pattern in this stage is associated with the normal stress. This observation indicates that the fatigue process is initiated by the shear stress and finalized by the normal stress.

The striped pattern of Lüders band or Stretcher strains is influenced by the applied stress and, in particular, the surface of the pressed product becomes flamboyant. Figure 7(*a*) shows that Lüders band appears as a thick line, about 45° inclined, in the neighborhood of the hole. This suggests that the shearing stress acts remarkably under the influence of the stress concentration.

Figure 8 is the cyclic stress-strain diagram recorded concurrently with Fig. 7. Here (*a*)–(*d*) in Fig. 8 correspond to (*a*)–(*d*) in Fig. 7. Figure 8(*a*) indicates that at this point the specimen experiences yield point elongation, confirming the above interpretation that the stripe pattern observed in Fig. 7(*a*) is a Lüders band. Figure 8(*d*) represents the cyclic stress-strain relationship when an orange peel appears around the crack initiated near the circular hole.

The stress is at the maximum at point (*c*) on the diagram shown in Fig. 8. It is expected that corresponding to this maximum stress, a certain phenomenon take place in the vicinity of the small hole. Therefore, we enlarged Fig. 7(*c*) and obtain Fig. 9. In Figure 9, slip lines are observed on the free surface

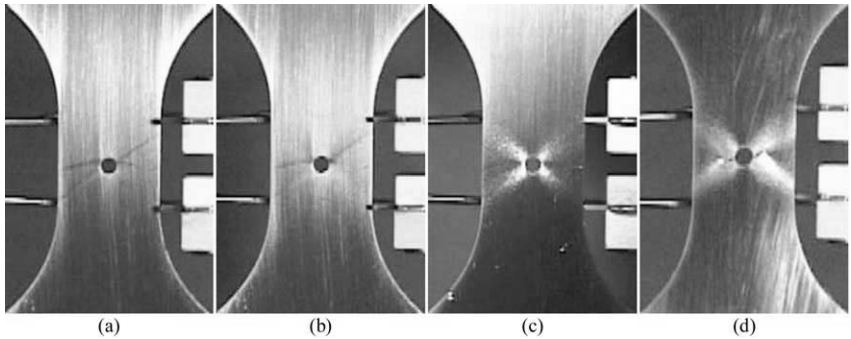


FIG. 7—*Surface condition around a circular hole under cyclic loading.*

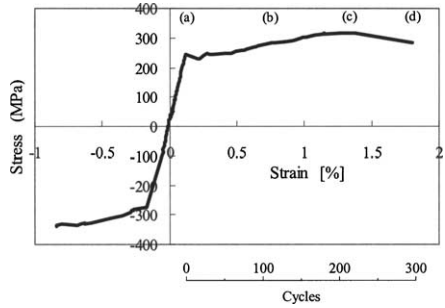


FIG. 8—*Cyclic stress strain diagram of specimen with a hole. Load ratio R: −1. Frequency: 1 Hz.*

near the small hole. Considering this, the small bump observed in the inner rim can be interpreted as the precrack initiation stage. In other words, corresponding to the maximum stress on the stress-strain diagram, a bump is initiated in the inner rim of the small hole of the specimen, which leads to the initiation of a crack.

The starting point of the fatigue life is not clearly defined. Figures 7(*a*)–7(*d*) indicate that the material experiences plastic deformation in the region where the crack is initiated. From this observation, it is reasonable to define the moment when the specimen enters the plastic regime as the start of crack initiation life. The above-mentioned yellow light is the starting point of fatigue life.

Usually, the crack initiation life is expressed in terms of the repetition number of cyclic loads that the specimen has experienced until the crack grows to a specified length. In such a practice, it is not clear how to define the starting point of the crack initiation life. Moreover, there is uncertainty in the accuracy of the measurement of the crack length. As opposed to this, the prepetition number between the initiation of the yield in Fig. 8, i.e., the yellow light, and the maximum stress point is clearly defined, and therefore can be a better definition of the crack initiation life.

From Fig. 8 and based on the above-mentioned argument, the crack initiation life can be estimated to be 215 for this particular experiment.

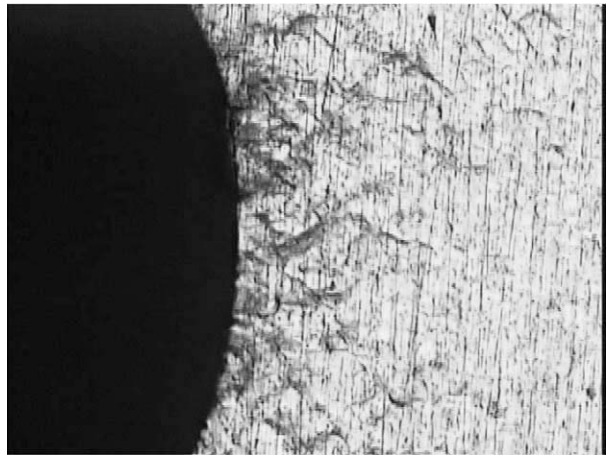


FIG. 9—*Magnified figure of Fig. 7(c). (X300).*

Conclusions

Applying strain-controlled, cyclic loads to low carbon steel specimens at load ratios of −1, we recorded the cyclic stress-strain diagram. At the same time, we observed the surface condition with the naked eye and compared it with the cyclic stress-strain diagram

It has been confirmed that by polishing part of a structure appropriately and observing it with the naked eye, it is possible to predict crack initiation. If the surface is polished to the level of Ra:0.2 μm, the diagnosis can be made by the naked eye and no other instrument is needed. As the load increased, the strip pattern turned to the orange peel. The surface showed the orange peel immediately before the crack was initiated like the case of tension testing, the stress-strain diagram under the cyclic loading showed the yield point elongation. Moreover, during the yield point elongation, the Lüders bands were formed.

We also applied a similar load to a specimen with a circular hole of 2 mm in diameter, and observed the surface state near the hole. Consequently, we clarified that the initiation of fatigue life is appropriately defined by the moment when the deformation enters the plastic regime. This is a method to estimate the fatigue crack initiation life. The results of this study provide basic data concerning the relationship between the load and change in the surface state, which can be used in fatigue process analysis.

References

[1] ASM Handbook, Vol. 19, "Fatigue and Fracture Section 2", ASM International Handbook Committee, 1997, pp. 210–223

[2] Barsom, J. M. and Rolfe, S. T., *Fracture and Fatigue Control in Structures: Applications of Fracture Mechanics*, 3rd ed., Chapter 8, ASTM International, West Conshohocken, PA, 1999, pp. 163–193.

[3] Larsen, James M. and Allison, John E., "*Small-Crack Test Methods, ASTM STP 1149*," ASTM International, West Conshohocken, PA, 1992, pp. 34–80.

[4] Landgraf, R. W., Morrow, JoDean, and Endo, T., "Determination of the Cyclic Stress-Strain Curve," *J. Mater.*, JMLSA, 4, No. 1, 1969, pp. 176–188.

[5] Taniuchi, K., "*Simple Stress Sensor: Utilizing of Stretcher Strain, ASTM, STP 1025*," ASTM International, West Conshohocken, PA, 1989, pp. 217–232.

[6] Taniuchi, K., "Visual Stress Sensor," *Proc., Smart Structures and Materials 1995 Smart Sensing, Processing, and Instrumentation*, Vol. 2444, SPIE, San Diego, 1995, pp. 438–446.

[7] Nadai, A., *Theory of Flow and Fracture of Solids*, Vol. 1, 2nd ed., McGraw-Hill Co. Inc., New York, 1950, pp. 275, 279–281, 282.

[8] Hahn, G. T., and Rosenfield, A. R., "Local Yielding and Extension of a Crack Under Plane Stress", *Acta Metall.*, 13, 1965, pp. 293–306.

[9] Kyriakides, S., and Miller, J. E., "On the Propagation of Lüders Bands in Steel Strips, " *Trans. ASME, J. Appl. Mech.*, 67, 2000, pp. 645–654.

[10] ASTM, *Metals Handbook* 10th ed., Vol. 1, ASTM International, West Conshohocken, PA, 1990, p. 204.

[11] Nishihara, T. and Kawamoto, M., "The Detection of the Fatigued Zone by a Corrosion Method," *Trans. Jpn. Soc. Mech. Eng.*, 5 [20, No. 1)], 1939, pp. 43–50, (in Japanese).

[12] Ichinose, K., Kosaka, Y., Fukuda, K., and Taniuchi, K., "Detection of the Failure Zone Caused by Cyclic Loading," *J. Intell. Mater. Syst. Struct.*, 10, 1999, pp. 214–220.

[13] Randak, V. A., Chemisch bestandige Stahle, besonders fur kalt gewalztes Blech und Band, Stahl u. Eisen, Nr. 19, 22.September, 86, 1966, pp.1239–1254.

[14] Phillips, V. A., Swain, A. J., and Eborall, R., "Yield-Point Phenomena and Stretcher-Strain Markings in Aluminum-Magnesium Alloys," *J. Inst. Met.*, 81, 1952–1953, pp. 625–647.

[15] Carreker, R. P. and Guard, R. W., "Tensile Deformation of Molybdenum as a Function of Temperature and Strain Rate," *J. Met.*, 1956, pp. 178–184.

[16] Ichinose, K., Fukuda, K., Gomi, K., Taniuchi, K., and Sano, M., "Yield Strength in Relation to Cyclic Loading," *J. Test. Eval.*, JTEVA, 29, No. 6, 2001, pp. 529–534.

Journal of ASTM International, Vol. 3, No. 5
Paper ID JAI13181
Available online at www.astm.org

Christopher D. Glancey[1] *and Robert R. Stephens*[1]

Volumetric and Surface Positron Annihilation Studies of Fatigue Damage Accumulation in a Steel Alloy

ABSTRACT: Fatigue crack nucleation comprises a significant portion of the fatigue life for many structures. The ability to inspect and quantify damage before significant cracks appear could improve safety while allowing components to be retired only when they have reached the end of their useful life. Positron annihilation is one technique that allows for observation of damage accumulation on a much smaller scale than traditional nondestructive evaluation techniques. As-polished and shot-peened 300M steel specimens were fatigued under constant amplitude. Tests were interrupted at several fatigue life ratios between the as-received and failed conditions, and damage was measured with positron annihilation techniques. Positron annihilation was sensitive to both induced residual stresses and fatigue damage build up, but measurement uncertainty was high and sensitivity was low. Positron annihilation presents a potentially revolutionary nondestructive evaluation technique that could give a quantitative measure of early fatigue damage.

KEYWORDS: fatigue crack nucleation, nondestructive evaluation, positron annihilation, 300M steel

Introduction

Despite decades of research in the area of fatigue crack nucleation and early fatigue damage, the exact mechanisms and processes involved are still not well understood or measurable [1–3]. Most theories for fatigue crack nucleation are based on models of dislocation and slip behavior in materials. In many structures, a majority of the fatigue life is spent nucleating a fatigue crack. Typically, a safe-life approach to fatigue design must be adopted in these structures, and retirement is often based on calculated lifetime rather than the actual damage accumulated in the structure. Many components are retired early in their lives and at considerable cost.

Damage tolerant design approaches are dependent on the sensitivity of the nondestructive evaluation (NDE) techniques used for inspection of a particular component or part. The smallest flaw detectable by NDE is assumed to exist and a lifetime to failure is calculated by fracture mechanics techniques. Using this lifetime, a suitable maintenance schedule can be established such that cracks can be observed and monitored in a structure before failure and the part can be retired at the end of its useful life. In structures where the majority of life is consumed nucleating a crack or at crack lengths too small to be observed by traditional NDE methods, damage tolerant design methods are not practical due to the frequency of inspections required. NDE techniques exist, however, that can quantify damage before significant cracks or flaws exist in a structure. One of these techniques is positron annihilation. Positron annihilation in material defects has been studied in detail and several reviews have been published [4–6].

Positron annihilation techniques use positrons, the antimatter equivalent of electrons, to study atomic scale defects in solids. When a highly energized positron is first injected or generated in a material, it is quickly slowed in a process called thermalization. When the positron is slowed to thermal velocities (10^5 m/s), it begins to wander through the lattice in a process called diffusion. Diffusion is the useful part of the positron life cycle, as a positron can travel a total distance of 20 μm, visiting up to 10^5 lattice sites before annihilation [6]. This means a wandering positron has a reasonable chance of encountering a vacancy or defect. Because of their positive charge, positrons are repelled from the nucleus of an atom reducing interaction with tightly bound core electrons. Atomic defects and dislocations, however, often

Manuscript received April 21, 2005; accepted for publication January 30, 2006; published online April 2006. Presented at ASTM Symposium on Fatigue and Fracture Mechanics: 35th Volume on 18–20 May 2005 in Reno, NV; R. E. Link and K. M. Nikbin, Guest Editors.

[1] Graduate Research Assistant and Professor, respectively, Mechanical Engineering Department, University of Idaho, Moscow, ID 83844-0902.

Copyright © 2006 by ASTM International, 100 Barr Harbor Drive, PO Box C700, West Conshohocken, PA 19428-2959.

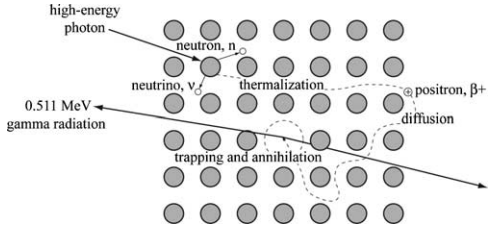


FIG. 1—*Typical positron life cycle in a crystalline solid.*

contain the slower moving conduction electrons and have a net negative charge. Positrons are thus attracted to defects and become trapped in them, essentially eliminating their kinetic energy. While annihilation can occur during any of the stages in a positron's lifetime, it typically happens during the diffusion and trapping stage. When a positron encounters an electron, the net kinetic energy and mass of the particles are typically converted into two detectable gamma (γ) rays. The energy and direction of the gamma rays depends on the momentum of the positron and electron before annihilation, but is generally around 0.511 MeV. This radiation gives a measure of the annihilation momentum and therefore the defect density in the solid. Figure 1 illustrates a typical positron life cycle.

While positron annihilation has been used to study material defects for decades, its use as an NDE tool has been limited [6–8]. This has been largely due to the fact that natural positron emitters limit studies to the outer surface of a specimen. As such, natural positron emitters only have application in carefully controlled laboratory studies. Recently, a unique technique has been developed that generates positrons deeper in a sample or component so that information can be obtained below the surface [8]. This technique, called photon-induced positron annihilation (PIPA), uses high-energy photons or γ-rays to generate short-lived positron emitters in the bulk of many materials. High-energy photons can knock neutrons out of the nucleus of an atom making it proton-rich and unstable. The proton then decays into a neutron (n), a positron (β^+) and a neutrino (ν). An example of this decay is given by:

$$ {}_{26}\mathrm{Fe}^{54} + \gamma(11 - 19\ \mathrm{MeV}) \rightarrow {}_{26}\mathrm{Fe}^{53} + n $$

$$ {}_{26}\mathrm{Fe}^{53} \rightarrow {}_{25}\mathrm{Mn}^{53} + \beta^+ + \nu \tag{1} $$

Using this concept, positron emitters can be generated through photo-nuclear reactions deep in the bulk of a sample. While positrons cannot travel very far in a sample, photons can. Photons can be used to generate positron emitters at depths of up to 5 cm in steel [8]. This means parts of nearly any geometry and surface condition can be studied with this technique. The emitted gamma radiation from positron annihilations can be detected with a Germanium crystal detector and analyzed with a digital signal processor and PC. The PIPA process is shown in Fig. 2.

PIPA can be used to generate positron-emitting probes for surface studies of components. This process is called Distributed Source Positron Annihilation (DSPA). A positron emitting source material like copper foil can be activated via PIPA and then attached to or placed near the component of interest. Highly energetic positrons are then ejected from the foil into the first few millimeters of the surface and gamma radiation is examined in the same way as PIPA.

PIPA and DSPA techniques can be used to measure fatigue damage accumulation throughout the fatigue life for many components and in many materials. While the nucleation and early propagation of fatigue cracks are nearly indistinguishable processes, both involve significant amounts of localized dislocation build up, which is detectable with positron annihilation. The ability to measure damage on this scale will improve understanding of early fatigue mechanisms and improve design methodologies for structures where this stage of the total fatigue life is significant. This study was performed to investigate the ability of both volumetric (PIPA) and surface (DSPA) positron annihilation techniques to distinguish and quantify damage in shot-peened and as-polished samples of the steel alloy 300M.

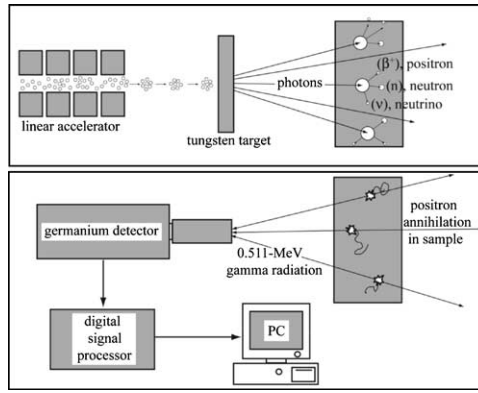


FIG. 2—*Schematic of photon-induced positron annihilation (PIPA).*

Experimental Procedure

Specimen Preparation

A medium carbon, low-alloy steel, 300M, that can be heat-treated to strengths of 2140 MPa. The chemical composition of 300M is given in Table 1. For this study, 300M was vacuum melted to produce a cleaner microstructure and improve toughness and ductility; 300M is typically heat treated by oil quenching from about 870°C and tempering at about 315°C [9]. Specimens were machined from rod stock and ground to final shape. Specimens were polished in the longitudinal direction to a final finish of 8 Ra or finer. Half of the specimens studied were shot-peened to an Almen intensity of 10 with 200 % coverage. The mechanical properties for the alloy studied are given in Table 2. Specimen geometry is given in Fig. 3.

The residual stress profile for a shot-peened specimen was obtained with X-ray diffraction. A compressive residual stress of 837 MPa was recorded at the specimen surface, while a maximum compressive residual stress of 1022 MPa was measured at a depth of 0.05 mm. Beyond 0.2 mm, the residual stresses were no longer compressive. The residual stress profile for a shot-peened 300M sample is shown in Fig. 4.

TABLE 1—*Chemical composition of 300M steel [9].*

Component	C	Mn	Si	Cr	Ni	Mo	V	Fe
Wt. (%)	0.4-0.46	0.65-0.9	1.45-1.8	0.7-0.95	1.65-2	0.3-0.45	0.05 min	bal

TABLE 2—*Mechanical properties for 300M steel.*

Material	Yield Strength [MPa]	Ultimate Strength [MPa]	Percent Elongation [%]
300M	1613	1958	10

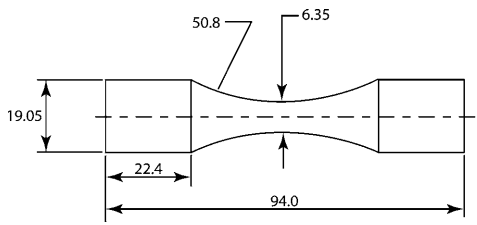


FIG. 3—*Fatigue specimen geometry. All dimensions in mm.*

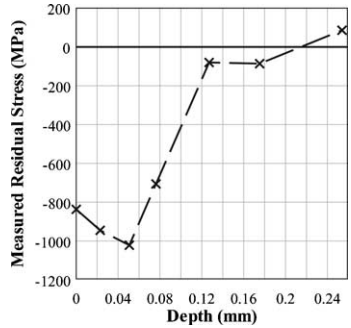


FIG. 4—*Measured residual stress profile for shot-peened 300M specimen.*

Fatigue Testing

The samples were cycled at a maximum stress, S_{max}, of 1270 MPa and load ratio, R, of −0.33. Fatigue tests were performed at room temperature at a frequency of 4 Hz using a 100 kN servo-hydraulic load frame. Tests were interrupted for PIPA/DSPA analysis at nominally 0, 10, 25, 50, 75, and 100 % of the average fatigue lives of the first few tests cycled to failure. Extreme care was taken to maintain consistent specimen alignment and orientation when specimens were removed for positron annihilation analysis and then reinserted for additional fatigue cycling. The nominal percentage of fatigue life changed as more specimens were cycled to failure. The fatigue life ratio (N/N_f) is presented as the number of cycles at interruption (N) divided by the number of cycles to failure (N_f) for the given specimen.

Positron Annihilation Analysis

For photon-induced positron annihilation (PIPA) analysis, specimens were irradiated by 19 MeV photons for 15 min to activate positron emitters within the sample through photo-nuclear reactions. Photons were generated with a linear accelerator. The iron isotope, ^{54}Fe, was the primary positron emitter activated by the photons. For distributed-source positron annihilation (DSPA) analysis, copper foil pieces were activated with the same technique and then attached to the surface of the specimens. The isotope, ^{63}Cu, was the primary emitter activated in the copper foil for the DSPA technique. After specimens (or foil sources) were activated, they were moved from the linear accelerator chamber into a background free measurement area where the annihilation radiation could be measured and analyzed. PIPA was initially carried out with a 12.7 mm collimator on a Germanium crystal detector. In the last sequence of positron annihilation measurements, a smaller 9 mm collimator was used to improve sensitivity.

Although several analytical techniques can be used for positron annihilation analysis [6], the measurement technique used in this project was the Doppler broadening technique. Doppler broadening gives a measure of the gamma ray energy distribution around the 0.511 MeV positron annihilation peak and allows defect concentrations to be determined by measuring differences in the shape of the peak. These changes can give a measure of the defect density and provide indications about defect type. Higher momentum annihilations lead to a broadening of the annihilation radiation response, while lower momentum annihilations sharpen the Doppler broadened peak. Therefore, damaged materials will exhibit a sharper peak than undamaged. This response is quantified using the line shaping parameter, referred to as the S-parameter, which is the number of counts at the center of an annihilation spectrum over the total counts. Figure 5 shows Doppler broadened positron annihilation spectra for as-polished 300M normalized to a smoothed spectrum and illustrates the S-parameter.

Experimental Results

Fatigue Testing

Fatigue tests were repeatable in both the as-polished and shot-peened 300M. The average fatigue life results are shown in Table 3. This table presents the averages for six specimens tested to failure in the

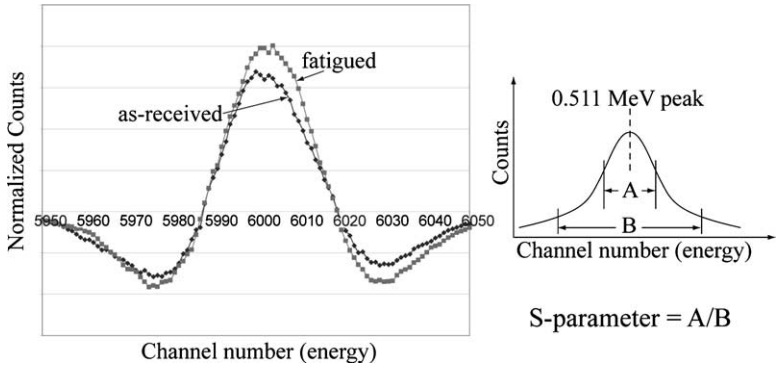


FIG. 5—*Sample annihilation spectra and S-parameter definition. Spectra are normalized to the same smoothed line to show differences between as-received and fatigued spectra.*

as-polished condition, and nine specimens in the shot-peened condition. As-polished 300M had an average life of 528 000 cycles and a standard deviation of 133 000 cycles. The average fatigue life in as-polished 300M was significantly longer than expected and will be discussed later. The average life for shot-peened 300M was shorter at 379 000 cycles with a standard deviation of 115 000 cycles.

Fracture surfaces of representative specimens for each surface condition were observed with scanning electron microscopy. Figures 6(*a*) and 6(*b*) show the fracture surface of an as-polished specimen that failed after 637 556 cycles. Figures 7(*a*) and 7(*b*) show the fracture surface of a shot-peened specimen that failed after 524 646 cycles. Both as-polished and shot-peened specimens exhibited subsurface crack nucleation at depths greater than 0.6 mm, as shown in Figs. 6(*a*) and 7(*a*). The cracks nucleated well below the surface and grew from initial flaws of about 10 μm, as shown in Figs. 6(*b*) and 7(*b*). Subsurface crack nucleation was observed in all of the samples tested.

Subsurface crack nucleation in the as-polished specimens was not initially expected. Extended lives were attributed to the finely polished surface and grinding procedures associated with specimen preparation. Studies [10,11] have shown grinding can introduce significant residual stresses in the surface of hardened materials. With the similar subsurface crack nucleation locations for both the shot-peened and as-polished specimens, an improved fatigue life could be expected in the as-polished specimen due to the tensile residual stresses that exist below the surface in shot-peened components at depths greater than 0.2 mm, as shown in Fig. 4.

Photon-Induced Positron Annihilation

PIPA showed some success in identifying both fatigue damage build-up and surface residual stresses in the 300M. It should be noted that measurements were performed on several samples of each condition rather than looking at a single sample at several fatigue levels. Some differences in microstructure and surface conditions between specimens could account for some of the discrepancies in measurements. Actual fatigue life ratio data were used to account for different total fatigue lives in specimens, but some variation in fatigue damage accumulation can be expected between specimens.

Figure 8 presents the PIPA results in as-polished 300M. The spread in S-parameter can be large even in the same specimen at the same fatigue level as shown by the measurements taken at N/N_f of 0.27, 0.46, and 0.58. Data at these fatigue levels represent repeat measurements taken in the same sample on different days without additional fatigue cycling. These errors become significant when not averaged out as can be

TABLE 3—*Average fatigue life results for 300M steel.*

300M Steel	Average Fatigue Life, N_f (cycles)	Standard Deviation (cycles)
As-polished	528 000	133 000
Shot-peened	379 000	115 000

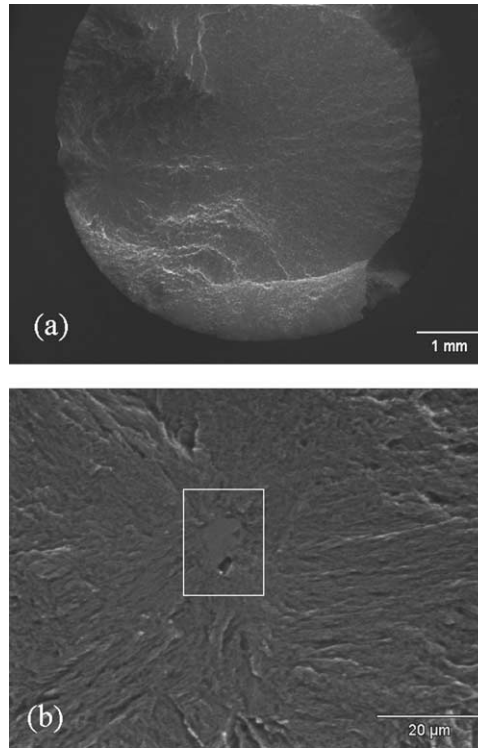


FIG. 6—*As-polished 300M specimen: (a) fracture surface, and (b) nucleation site.*

seen in the data. Average S-parameter values where measurements were performed at similar fatigue ratios are shown as lines. A definite increase in S-parameter with increasing damage level can be seen when looking at this averaged data. The 12.7 mm collimator, which was used for most of the positron annihilation analysis, was not sensitive enough to provide a unique trend. This is due to the fact that in an hourglass specimen like that used in this research, the maximum stresses, strains, and damage all occur at a localized region at the minimum diameter. If the collimator is too large, the less damaged material away from the minimum gage section is averaged in with the damaged material. It can be seen that using a smaller 9 mm collimator, which essentially looks at a smaller portion of the sample, greatly increases sensitivity to damage although the data is limited and does not allow specific conclusions to be drawn.

Figure 9 presents the shot-peened PIPA data. A general increase in S-parameter with increase in fatigue level was observed with the exception of the data at a fatigue life ratio of 0.34. This spike represents a single specimen in the test program. Several specimens would need to be analyzed at this particular fatigue life ratio to determine whether the spike is significant. Only a general trend can be drawn from this data. The 12.7 mm collimator was not very sensitive in distinguishing levels of fatigue damage. Again, the 9 mm collimator showed greatly improved sensitivity to fatigue damage, but the dataset is limited.

Figure 10 presents the averaged PIPA data for both the as-polished and shot-peened 300M specimens for comparative purposes. The increased S-parameter response in the shot-peened specimens compared to the as-polished specimens is attributed to the plastic deformation and thus increased dislocation density associated with the shot-peened surface. PIPA was sensitive to both the fatigue damage and the surface residual stresses in 300M.

PIPA provides a volumetric analysis meaning a relatively large volume is studied with each measurement. This can lead to difficulties in focusing the analysis on a particular point in a structure, as seen with the larger collimator on the relatively simple geometry in this study. The volumetric capability of PIPA has

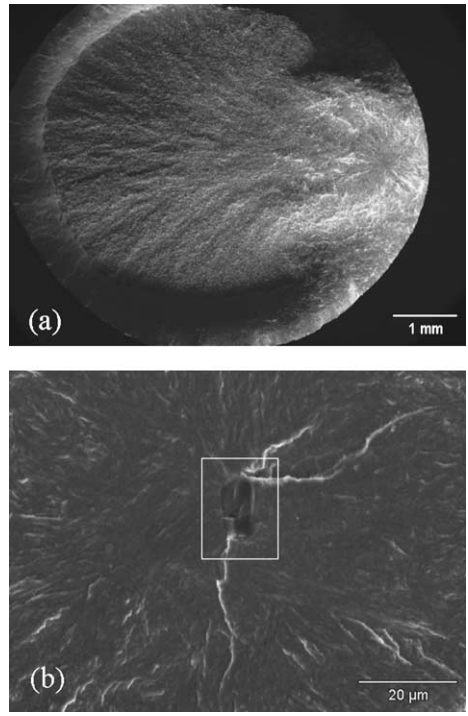


FIG. 7—*Shot-peened 300M specimen: (a) fracture surface, and (b) nucleation site.*

some advantages over surface techniques, however. As seen in this study, PIPA was able to detect both surface (shot-peening) and volumetric (fatigue) types of damage. PIPA allows studies to be performed that are relatively insensitive to surface preparation which is key to the use of positron annihilation as an NDE technique.

Distributed-Source Positron Annihilation

DSPA was performed only in the initial round of positron annihilation to determine whether primarily surface (DSPA) or volumetric (PIPA) techniques were to be performed throughout the remainder of this

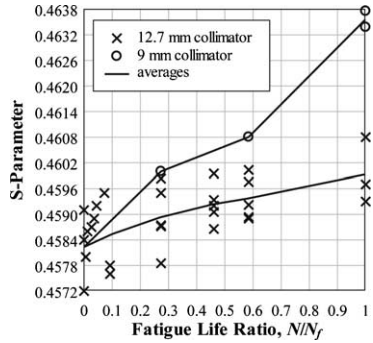


FIG. 8—*PIPA results in as-polished 300M.*

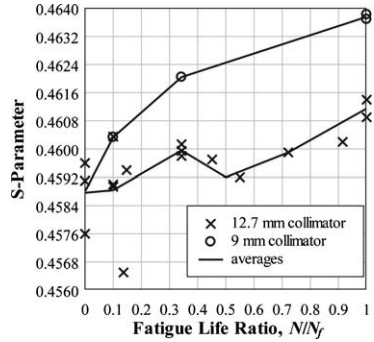


FIG. 9—*PIPA results in shot-peened 300M.*

project. In this initial round, DSPA data seemed to be sensitive to the surface residual stresses associated with the shot-peening in the steel, but did not show an increase with increasing fatigue damage level.

Figure 11 presents the DSPA data for both as-polished and shot-peened 300M. Note that each of these data points represents only one measurement on one specimen. The DSPA data from the shot-peened samples show an increase in the S-parameter compared to the as-polished samples. DSPA is clearly

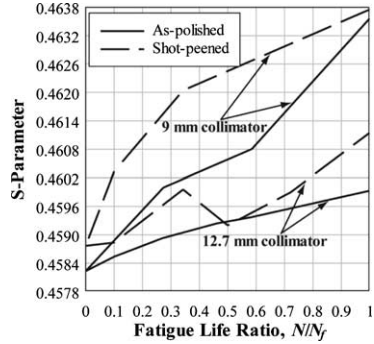


FIG. 10—*Comparison of averaged PIPA results for as-polished and shot-peened 300M.*

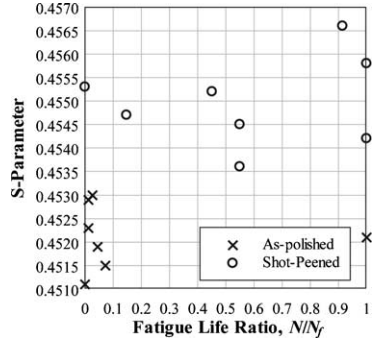


FIG. 11—*DSPA results in as-polished and shot-peened 300M.*

sensitive to the surface damage induced by shot-peening. Sensitivity to fatigue damage, however, was much lower with DSPA than with PIPA. In fact, no differentiation could be made between an as-received and fatigue cycled specimen as shown in Fig. 11.

Positron implantation depth is directly related to the positron energy level and the density of the solid. A method for obtaining the mean positron implantation depth was suggested by Brandt and Paulin [12], where the mean implantation depth, R_+, is given by:

$$R_+ = \frac{E_+^{1.43}}{17\rho} \text{ [cm]} \tag{2}$$

where E_+ is the positron energy level in MeV and ρ is the density of the material being studied in g/cm^3. Given the energy level of ^{63}Cu positrons (2.93 MeV) [8] and the density of steel (7.83 g/cm^3), a mean implantation depth of 0.35 mm is calculated. This suggests that a majority of the positrons are likely being trapped and annihilated before reaching depths where fatigue crack nucleation was observed. This explains why DSPA was sensitive to the surface residual stresses and not fatigue damage in the material studied.

As DSPA is a surface positron annihilation technique, it is more sensitive to damage that accumulates or is present near the surface. For the specimens studied, the majority of fatigue damage accumulated below the mean implantation depth for ^{63}Cu positrons generated for DSPA analysis. Although DSPA implants positrons to depths of up to 1 mm in steel, a majority of them are likely thermalized, trapped, or annihilated before reaching this depth. However, in studies where fatigue crack nucleation and growth are expected or observed at the surface, DSPA may prove to be the more sensitive positron annihilation technique.

Conclusions

1. Fatigue testing data were repeatable, but the subsurface crack nucleation and the subsequently longer fatigue lives in the as-polished samples were not initially expected. Subsurface nucleation in the as-polished specimens was likely due to grinding procedures associated with specimen preparation. The shorter lives in the shot-peened specimens compared to the as-polished specimens were attributed to the tensile residual stress that is present at depths below 0.2 mm in the shot-peened specimens.
2. A smaller 9 mm collimator showed much higher sensitivity to fatigue damage using PIPA in 300M than a 12.7 mm collimator. The 9 mm collimator was only used on the last sequence of positron annihilation testing, so there is limited data with the smaller collimator size. An improvement in sensitivity of roughly three-fold allowed fatigue levels to be more clearly determined and reduced uncertainty in positron annihilation measurements.
3. PIPA was sensitive to both the surface compressive residual stresses and fatigue damage in 300M. An increase in S-parameter was observed with increased fatigue damage. A clear offset is observable between shot-peened and as-polished PIPA data, which was attributed to the shot-peened layer.
4. In this study, fatigue crack nucleation and growth did not occur at the surface. As such, the surface technique (DSPA) was not very sensitive to fatigue damage, but did detect the residual stresses due to shot-peening. This is seen in the offset between as-polished and shot-peened DSPA data. It is possible that DSPA may be a more applicable technique in cases where surface cracking is expected or observed.
5. PIPA and DSPA positron annihilation techniques are experimental in nature and not yet mature enough to take a single measurement in a component and determine its damage level. Averages of several measurements generally provided a clearer picture of damage accumulation in the sample. Without averaging, data were very scattered. Specimen positioning techniques led to some measurement error due to the geometry of the samples. Refined positioning techniques would likely reduce the error seen in measurements made on the same sample with the same damage level.
6. Promising results with the 9 mm collimator warrant further investigation. Improved sensitivity and reduced uncertainty are necessary before useful life predictions can be made.

Acknowledgments

The authors would like to thank General Atomics and the NASA Idaho Space Grant Consortium for providing material and financial support for this project. We would also like to thank Positron Systems, Inc., for the positron annihilation testing performed in this study.

References

[1] Gough, H. J. and Hanson, D., "The Behaviour of Metals Subjected to Repeated Stresses," *Proceedings of the Royal Society of London. Series A, Containing Papers of a Mathematical and Physical Character*, Vol. 104, No. 727, 1923, pp. 538–565.

[2] Laird, C. and Duquette, D. J., "Mechanisms of Fatigue Crack Nucleation," *Corrosion Fatigue: Chemistry, Mechanics, and Microstructure*, O. F. Devereux, A. J. McEvily, R. W. Staehle, Eds., National Association of Corrosion Engineers, Houston, TX, 1972, pp. 88–117.

[3] Lukas, P. and Kunz, L., "Small Cracks—Nucleation, Growth and Implication to Fatigue Life," *Int. J. Fatigue*, Vol. 25, 2003, pp. 855–862.

[4] Hautojarvi, P. and Vehanen, A., "Introduction to Positron Annihilation," *Positrons in Solids*, P. Hautojarvi, Ed., Springer-Verlag, Berlin, 1979, pp. 1–23.

[5] West, R. N., "Positron Studies of Lattice Defects in Metals," *Positrons in Solids*, P. Hautojarvi, Ed., Springer-Verlag, Berlin, 1979, pp. 89–144.

[6] Coleman, C. F. and Hughes, A. E., "Positron Annihilation," *Research Techniques in Nondestructive Testing, Volume III*, R. S. Sharpe, Ed., Academic Press, London, 1977, pp. 355–394.

[7] Kawaguchi, Y., Nakamura, N., and Yusa, S., "Non-Destructive Evaluation of Fatigue Damage in Type 316 Stainless Steel Using Positron Annihilation Lineshape Analysis," *Mater. Trans., JIM*, Vol. 43, No. 4, 2002, pp. 727–734.

[8] Akers, D. W., Denison, A. B., and Harmon, F., "In situ Positron Annihilation Analysis Produced by High Energy Photon-induced Neutron Deficient Positron Emitting Nuclei," *Applied Surface Science*, Vol. 194, 2002, pp. 245–249.

[9] Philip, T. V. and McCaffrey, T. J., "Ultrahigh-Strength Steels," *Metals Handbook: Tenth Edition, Volume 1, Properties and Selection: Irons, Steels, and High-Performance Alloys*, ASM International, Materials Park, OH, 1990, pp. 434–436.

[10] Grum, J., "A Review of the Influence of Grinding Conditions on Resulting Residual Stresses After Induction Surface Hardening and Grinding," *J. Mater. Process. Technol.*, Vol. 114, 2001, pp. 212–226.

[11] Balart, M. J., Bouzina, A., Edwards, L., and Fitzpatrick, M. E., "The Onset of Tensile Residual Stresses in Grinding of Hardened Steels," *Mater. Sci. Eng., A*, Vol. 367, 2004, pp. 132–142.

[12] Brandt, W. and Paulin, R., "Positron Implantation-profile Effects in Solids," *Phys. Rev. B*, Vol. 15, No. 5, 1977, pp. 2511–2518.

Journal of ASTM International, Vol. 3, No. 7
Paper ID JAI13197
Available online at www.astm.org

Laurent Bucher,[1] *Pierre-Olivier Santacreu,*[2] *Alain Köster,*[1] *and L. Remy*[1]

Elasto-Viscoplastic Behavior of the Ferritic Stainless Steel AISI 441-EN 1.4509 from Room Temperature to 850°C

ABSTRACT: In order to predict the thermomechanical fatigue (TMF) damage of stainless steel parts submitted to thermal loading, the elasto-viscoplastic behavior has to be described accurately in a wide range of temperature, strain, and strain rate levels. The study is done on a stabilized ferritic stainless steel grade equivalent to AISI 441 or EN 1.4509 standard which is used more and more in high temperature application up to 950°C, for example, in exhaust manifolds, heat exchanger, burners, or water-boiler device. The elasto-viscoplastic model proposed by Chaboche is chosen and identified on the basis of isothermal cyclic tests including relaxation and graduated cyclic strain tests performed under air at 300, 650 and 850°C. The validation procedure was performed afterward by comparison with stabilized behavior under nonisothermal conditions, especially in-phase, out-of-phase, and diamond TMF cycles. Results of simulation show very good fitting with the experimental curves which would lead to a more accurate fatigue life prediction.

KEYWORDS: thermomechanical fatigue, elasto-viscoplastic behavior, ferritic stainless steel, behavior model

Nomenclature

T = Temperature
$\underline{\underline{\varepsilon}}_{sub}$ = Strain tensor where subscripts *el*, *th*, *vp* and *m* indicated elastic, thermal, viscoplastic, or mechanical strain
$\underline{\underline{\sigma}}$ = Stress tensor
E, υ, α = Young modulus, Poisson ratio and coef cient of thermal expansion
R, R_0, Q, b = Isotropic hardening variable and parameters
$\underline{\underline{X}}, C, D$ = Kinematic hardening variable and parameters
K, n = Viscous parameters

Introduction

Stainless steels are now widely used for high temperature (HT) applications such as automotive exhaust manifold, heat exchanger, burner, and probably in the future for turbo-charger and as fuel cell components. The main reasons for this evolution are an increase of the temperature of use up to 1000 C in such systems and in parallel to the demand to improve their durability. These components are generally submitted to severe thermal cyclic loads, which generate strain and stress in the most constrained zones. In a numerical fatigue design approach, it appears important to predict possible failure or lifetime of the component before its prototyping. To this aim, the behavior of the material has to be described accurately in a wide range of temperatures strain level, and strain rate. In fact, the behavior of such steel for temperatures above 500 C around the third of the melting temperature is mainly viscoplastic.

Manuscript received April 11, 2005; accepted for publication March 27, 2006; published online May 2006. Presented at ASTM Symposium on Fatigue and Fracture Mechanics: 35th Volume on 18 20 May 2005 in Reno, NV; R. E. Link and K. M. Nikbin, Guest Editors.
[1] Centre des Mat riaux de l Ecole des Mines de Paris, URA-CNRS, Evry, France.
[2] Ugine&Alz Research Center, Isbergues, France.
Copyright © 2006 by ASTM International, 100 Barr Harbor Drive, PO Box C700, West Conshohocken, PA 19428-2959.

TABLE 1—*Chemical composition (wt%).*

Cr	C	Si	Mn	Ti	Nb	N
17.8	<0.02	0.5	0.3	0.16	0.5	<0.02

Experimental Procedure

Material

The F17TNb® is a 17 %Cr stabilized ferritic stainless steel corresponding to AISI 441 or EN 1.4509 grades. Its typical chemical composition is given in Table 1. Both titanium and niobium prevent against a chromium carbide precipitation during heat treatment or welding and therefore provide a very good corrosion resistance. Also, an excess of niobium leads to a precipitation of Laves phases at grain boundaries which improves greatly the creep behavior of the grade. Finally, because of its complete ferritic structure from room temperature to around 1000°C, and therefore a lower coefficient of thermal expansion close to those of its oxide layer, the cyclic oxidation resistance of the grade is excellent compared to the austenitic refractory grade [1]. For these many reasons and despite its low mechanical yield strength at high temperature, F17TNb can be used up to 950°C if mechanical loadings on the component are acceptable for the material.

Thermomechanical Fatigue Tests

All thermomechanical fatigue (TMF) tests have been performed using hydraulic or mechanical testing machines equipped with a lamp furnace. Tests are basically strain-controlled and at a low frequency cycle using a 10 mm gage extensometer. Stress is measured using a load cell of 10 or 50 kN. In TMF tests, temperature is measured continuously by using a thermocouple fixed at the center of the sample. In the present study, the two types of cylindrical samples with M18 extremities were machined from a hot rolled slab with a thickness of around 30 mm.

Isothermal Tests at 300, 650, and 850°C—To identify the material behavior, different isothermal cyclic tests were performed on LCF specimen of 6-mm diameter and of 12-mm gage length and with a polished surface (Fig. 1). The tests consist of (i) cyclic hardening tests in air under strain control, using a triangular symmetric strain cycle with zero mean strain, (ii) in the same way as (i) but with tests which included dwell periods in tension and some in compression, (iii) graduated cyclic strain, and (iv) classical LCF tests (see Fig. 2).

TMF Tests—The specimen geometry is a 11-mm diameter hollow tube with 1-mm thickness to avoid any thermal gradient and has a 25-mm gage length. The surfaces of test specimens were also polished to a high degree (Fig. 3). A computer is used to generate two signals at the same time, the first being mechanical strain ϵ_m (total strain minus thermal strain), and the second the temperature range that the specimen will be put through. From the input-output board, the computer records the load, the measured temperature and the total strain are collected.

Thermomechanical tests were performed in air in the range 250–850°C with both *in-phase* (IP) and *out-of-phase* (OP) strain loading. It was chosen to perform the test with a thermal variation of $5\,^{\circ}Cs^{-1}$ for both 2×10^{-3} and 4×10^{-3} mechanical strain amplitude under *in-phase* strain-temperature cycle (maximum of the strain at the maximum of the temperature and same at minimum) and *out-of-phase* strain-

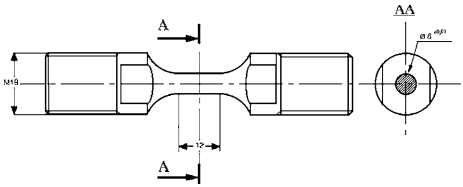


FIG. 1—*LCF specimen.*

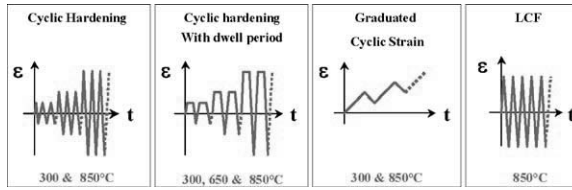


FIG. 2—*Different isothermal tests performed for model identification: total strain as function of time.*

temperature cycle (minimum of the strain at the maximum of the temperature and inversely). The cycle duration is 4 min and the strain rates investigated are thus in the range 3×10^{-5} s^{-1} to 6×10^{-5} s^{-1}. More complex Diamond TMF tests were also performed between 250 and 900°C with a strain amplitude of 0.4 % and a varying strain rate (Fig. 4).

Elasto-Viscoplastic Model and Identification Procedure

Constitutive Model

The elasto-viscoplastic behavior of a metal subjected to cyclic loading at HT is well described using a nonlinear kinematic and isotropic hardening coupled with a Norton creep model like the unified model proposed by Lemaitre and Chaboche [2].

Strain partitioning in thermal (*th*), elastic (*el*), and viscoplastic (*vp*) parts gives

$$\underline{\underline{\epsilon}} = \underline{\underline{\epsilon}}_{th} + \underline{\underline{\epsilon}}_{el} + \underline{\underline{\epsilon}}_{vp} \quad \text{and} \quad \underline{\underline{\epsilon}}_{m} = \underline{\underline{\epsilon}} - \underline{\underline{\epsilon}}_{th} \tag{1}$$

where the thermo-elastic part of the strain is expressed by

$$\underline{\underline{\epsilon}}_{el} = \frac{(1+\nu)}{E}\underline{\underline{\sigma}} - \frac{\nu}{E} \cdot Tr(\underline{\underline{\sigma}})\underline{\underline{\mathbf{I}}} \tag{2}$$

$$\underline{\underline{\epsilon}}_{th} = \alpha \cdot \Delta T \cdot \underline{\underline{\mathbf{I}}} \tag{3}$$

The yield criterion including both isotropic and kinematic hardening is defined by

$$J_2(\underline{\underline{\sigma}} - \underline{\underline{X}}) - R \geqslant 0 \tag{4}$$

where J_2 is the second stress invariant following von Mises criterion.

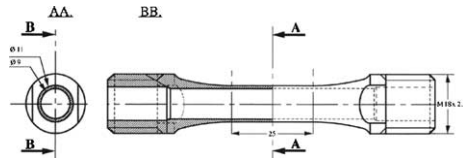


FIG. 3—*TMF specimen.*

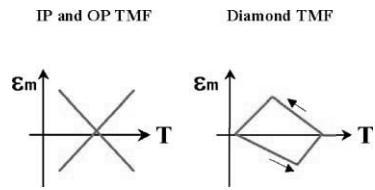


FIG. 4—*Different TMF tests performed for the validation of the model: mechanical strain as function of temperature.*

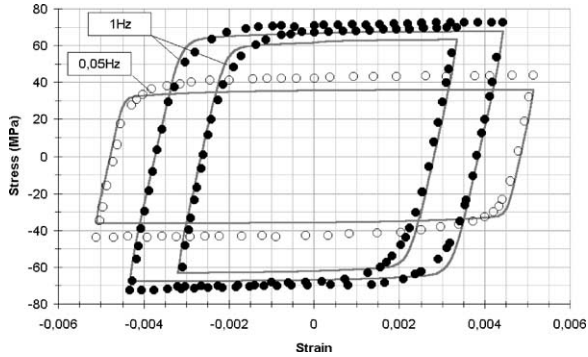


FIG. 5—*LCF at 850°C, experimental (dot) and simulation (line).*

Viscoplastic strain rate is deduced

$$\underline{\underline{\dot{\epsilon}}}_{vp} = \frac{3}{2} \cdot \dot{p} \cdot \frac{\underline{\underline{\sigma}}' - \underline{\underline{X}}'}{J_2(\underline{\underline{\sigma}} - \underline{\underline{X}})} \quad \text{where} \quad \dot{p} = \left\langle \frac{J_2(\underline{\underline{\sigma}} - \underline{\underline{X}}) - R}{K} \right\rangle^n \tag{5}$$

where superscript ($'$) indicates deviatoric part of the tensors, and dot () indicates the time derivative.

The nonlinear back stress X and isotropic hardening are expressed by

$$\dot{\underline{\underline{X}}} = \frac{2}{3} C \dot{\underline{\underline{\epsilon}}}_{vp} - D \underline{\underline{X}} \dot{p} \tag{6}$$

$$\dot{R} = b(Q - R)\dot{p} \tag{7}$$

Theoretically, the kinematic and isotropic hardening terms of the model would have to be extended by some other terms for varying temperature conditions. On the other hand, the identification will be conducted in isothermal condition—temperature by temperature. Therefore we assume that the model will be able to describe correctly nonisothermal situations, and that will be verified later.

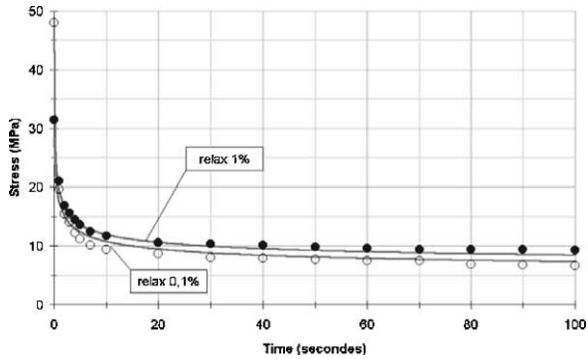


FIG. 6—*Relaxation at 850°C experimental (dot) and simulation (line).*

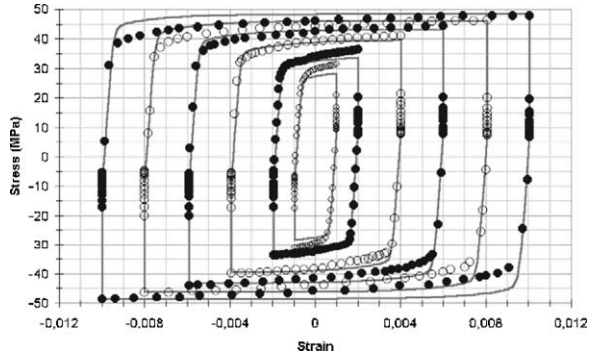


FIG. 7—*Cyclic hardening at 850°C experimental (dot) and simulation (line).*

TABLE 2—*Parameters of the Chaboche model.*

T (°C)	E(GPa)	K(MPa.s^{-1})	n	R_0(MPa)	Q(MPa)	b	C(MPa)	D(–)
300	169	85.3	12	96	119	5	69400	885
650	132	159	5	70	64	113	43560	786
850	102	171	4	3.5	0	0	1000	515

Results

Identification Coefficients of the Model

From the different isothermal fatigue tests at 300, 650, and 850°C, the eight coefficients of the model—E, n, K, C, D, R_0, Q and b—have been determined. Coefficient derivation is based on stabilized cycle in order to simulate the stabilized behavior of the material. However, some grades could not exhibit any clear stabilization at a certain temperature due to the precipitation or aging phenomenon. The coefficient of thermal expansion α was already known. Poisson ratio ν is assumed to be independent to the temperature and equal to 0.3. An optimization software dedicated to nonlinear model identification was used to fit the experimental curves. Figures 5–7 show the model regarding the experimental curves used for the identification at 850°C for three different fatigue tests: LCF, relaxation, and cyclic hardening. Identification for the two other temperatures was done in the same way.

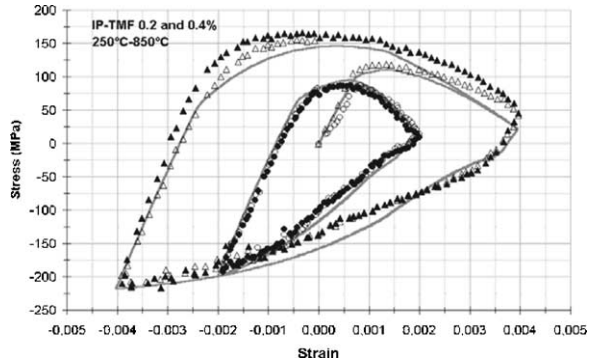


FIG. 8—*In-phase TMF between 250–850°C test comparison of experimental loops (dot) with simulation (line).*

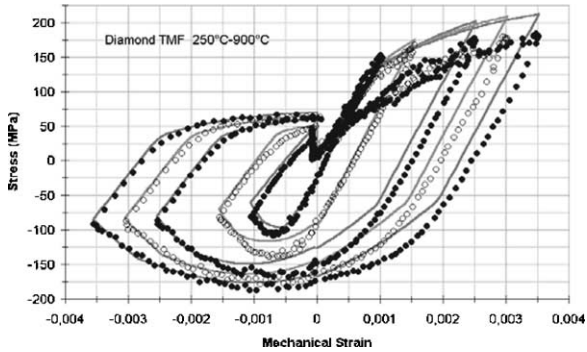


FIG. 9—*Diamond TMF test between 250–900°C comparison of experimental (dot) with simulation (line).*

Validation Tests

In order to validate the use of Chaboche model (Table 2) for nonisothermal conditions and prove the accuracy of the identified parameters numerical simulations of the in-phase, out-of-phase, and diamond TMF experimental cycles were done using the proposed model. The coefficients for unchecked temperatures were extrapolated or interpolated. Finally, it is confirmed that the simulation of such complex thermaomechanical tests fit quite well with the experimental curves. Figures 8 and 9 show two examples of in-phase TMF cycles between 250°C–850°C for 0.2 and 0.4 % of mechanical strain, and the second, diamond TMF cycles between 250°C and 900°C.

Conclusion

The present work leads to the identification of the cyclic behavior of a ferritic stainless steel grade—F17TNb AISI 441—in a wide range of temperature and strain rate. This grade is used more and more in high temperature application because of its very good cyclic oxidation and thermal fatigue resistance. Because of the studied range of temperature an elasto-viscoplastic model is necessary to accurately describe the behavior. In this paper the Chaboche model has been proposed and presented. Its identification was achieved on the basis of isothermal cyclic hardening, relaxation, and graduated cyclic tests were performed at 300, 650, and 850°C. Different nonisothermal experimental tests including in-phase, out-of phase, and diamond TMF tests were used to validate the model and a quite good fit was evidenced between the simulated loop and experimental results. Finally, the Chaboche model is applied successfully today in the thermal fatigue finite element analysis of real parts, in particular the automotive exhaust manifold where an accurate computation of the viscoplastic strain—the main parameter to evaluate the damage—is needed to predict the lifetime of such a part [3].

References

[1] Antoni, L. and Herbelin, J.-M., EFC Working Party Report on Cyclic Oxidation of High Temperature Materials: Mechanisms, Testing Methods, Characterization and Lifetime Estimation, M. Schütze, and W. J. Quadakkers, Eds., Publication No. 27 in European Federation of Corrosion Series, Institute of Materials, 1999, p. 187.

[2] Lemaitre, J. and Chaboche, J.-L., *Mécanique des Solides*, Dunod Eds., Paris, 1985.

[3] Santacreu, P.-O., Simon, C., and Coleman, A., "Thermomechanical Fatigue Behavior of Stainless Steel Grades for Automotive Exhaust Manifold Applications," *Thermomechanical Fatigue Behavior of Material: 4th Volume, ASTM STP 1428s*, M. A. McGaw, S. Kalluri, J. Bressers, and S. D. Peteves, Eds., ASTM International, West Conshohocken, PA, 2002.

Journal of ASTM International, Vol. 3, No. 7
Paper ID JAI100346
Available online at www.astm.org

Ohchang Jin,[1] *Jeffrey Ronald Calcaterra,*[2] *and Shankar Mall*[3]

Life Prediction of Fretting Fatigue of Ti-6Al-4V

ABSTRACT: The present study was aimed towards improving the prediction capability of fretting fatigue life of Ti-6Al-4V. Incremental and interrupted fretting fatigue tests were conducted. Based on the crack propagation pattern observed on the fractured surface fretting fatigue life was predicted. The disappearance of contact stresses was evidenced by the change in crack growth direction from oblique to perpendicular path to the loading direction. Thus, fatigue crack initially propagated under the influence of the contact stress, and then it grew due to the applied stress amplitude to the substrate. The transition crack length between these two conditions varied between 20 to 30 μm and depended on the contact load. This enabled the prediction of short and long crack propagation life. There was good correlation between the predicted fretting fatigue life and the experimental life.

KEYWORDS: fretting fatigue, life prediction, Ti-6Al-4V

Nomenclature

b = Fatigue strength exponent
c = Fatigue ductility exponent
CM = Cof n-Manson parameter
d = Empirical constant
E = Elastic modulus
K_c = Fracture toughness
K_{eff} = Effective stress intensity factor
$K_{\max}$ = Maximum stress intensity factor
$K_{\min}$ = Minimum stress intensity factor
K_{th} = Threshold stress intensity factor
K' = Cyclic strength coef cient
n' = Cyclic strain hardening exponent
N_f = Number of reversal to failure
m = Paris constant
P = Empirical constant
Q = Empirical constant
SWT = Simth-Watson-Topper parameter ($\sigma_{max}\varepsilon_a$)
$\sigma_{\max}$ = Maximum normal stress
σ'_f = Fatigue strength coef cient
ε_a = Normal strain amplitude
ε'_f = Fatigue ductility coef cient
$\Delta\epsilon$ = Total normal strain range
$\Delta\epsilon_p$ = Local plastic tensile strain range
$\Delta\gamma_t$ = Total shear strain range

Manuscript received May 2, 2005; accepted for publication April 5, 2006; published online May 2006. Presented at ASTM Symposium on Presented at ASTM Symposium on Fatique and Fracture Mechanics: 35th Volume on 18 20 May 2005 in in Reno, NV; and R. E. Link and K. M. Nikbin, Guest Editors.

[1] Assistant Professor, School of Engineering, Mercer University, 1400 Coleman Ave, Macon, GA 31207.
[2] Senior Materials Engineer, Materials & Manufacturing Directorate, U.S. Air Force Research Laboratory, Wright-Patterson AFB, OH 45433.
[3] Professor, U.S. Air Force Institute of Technology, Wright-Patterson AFB, OH 45433.

Copyright © 2006 by ASTM International, 100 Barr Harbor Drive, PO Box C700, West Conshohocken, PA 19428-2959.

$\Delta\gamma_p$ = Local plastic shear strain range
ρ_{max} = Maximum plastic zone size
υ = Poisson's ratio

Introduction

Fretting fatigue cracks can nucleate as early as during 2–5 % of the total life. This premature crack nucleation is caused by highly localized stresses at or near the contact surface. The early crack propagation occurs at an angle between 30 and 50 deg relative to the applied loading direction to the substrate. This initial crack propagation continues in a shearing mode up to a certain depth. It then changes its direction along a normal direction to the applied load where it propagates under opening tensile mode. Endo and Goto [1] observed that the length of shear crack in 0.34C steel varied with contact pressures and that the crack growth rate after the change in crack growth direction was identical among different specimens. This observation suggests that the transition from shear to tensile crack occurs when the effect of fretting disappears. Thus, the fretting damage is saturated in very early life and thereafter the propagation results solely from the applied cyclic stress.

The fretting fatigue crack initiation has been studied extensively. In general, there are two approaches to model the crack initiation: multi-axial stress model and critical plane model. The former has been used since the stress state in fretting contact region is of the multi-axial nature. Szolwinski and Farris [2] modified Smith-Watson-Topper (SWT) model [3] to account for multi-axial state of stress and assumed that crack nucleation occurs on the plane where product of normal strain amplitude and maximum normal stress is the maximum. Neu et al. [4] found that SWT parameter predicted well the location of crack initiation in PH-13-8Mo. On the other hand, the crack growth from the critical plane models is predicted using shear stress or a combination of normal and shear stresses on critical plane. One of the authors proposed a shear stress based critical plane parameter and found that this was effective in characterizing fretting fatigue crack initiation in terms of location as well as its orientation on the contact surface [5]. This shear stress-based model was later modified to take into account the effect of normal stress on the critical plane that contributes towards opening of the crack [6].

Short fatigue cracks, which would be usually nonpropagating in the absence of fretting fatigue load, propagate in the region near the contact surface due to the highly localized contact stresses. Alic and Hawley [7] suggested in their study of fretting fatigue of Al 7075 that the higher crack growth rates in early stages of fretting fatigue resulted from the combined effects of small crack size and the fretting stresses. Sato et al. [8] also observed that the crack growth rate in the early stage decreased due to the decrease in fretting effect. Therefore, to characterize the effects of fretting on crack propagation, it is necessary to examine the early stages of fatigue crack growth. The present study is focused on the investigation of short crack propagation behavior under contact stress distribution in order to improve the prediction capability of fretting fatigue life of Ti-6Al-4V which is used in dovetail joint for disk/blade attachment in gas turbine engines.

Materials and Experimental Procedures

Both specimens and fretting pads were made of titanium alloy, Ti-6Al-4V. The material was heat-treated prior to machining: solution heat-treatment at 935°C for 1.75 h, cooling in air, annealing at 700°C for 2 h in vacuum, and cooling in argon. These heat-treatments resulted in a duplex microstructure, consisting of 60 % primary α (hcp) phase and 40 % transformed β (bcc) phase. The α platelets nucleated inside β phase and average grain size was approximately 20 μm as shown in Fig. 1. The material properties are listed in Table 1.

Dog-bone type of specimen was used in the present study (Fig. 2). The width and thickness of the reduced area were 6.4 mm and 3.8 mm, respectively. The specimen was first cut by the wire electrical discharge method. It was then subjected to low stress grinding to reduce the residual stress due to machining. Finally, they were polished using 600 grit silicon carbide paper. The pad with cylindrical end was also made of Ti-6Al-4V. The dimensions of the pad were 9.5 mm $\times$ 9.5 mm. The radii of the cylindrical end of the pad were either 50.8 mm or 104 mm.

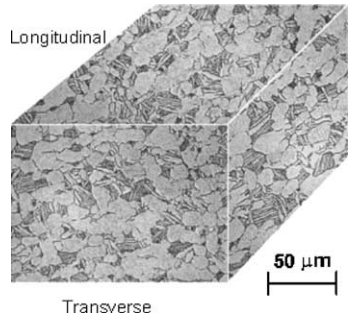


FIG. 1—*Microstructure of* Ti-6Al-4V.

A specially designed fretting fatigue system was used to apply shear and normal contact loads on each side of the specimen through a pair of pads along with axial fatigue load on the specimen to simulate fretting fatigue loading condition. The test frame is capable of applying maximum force of 22 kN at cyclic frequencies as high as 200 Hz. The normal load is applied through lateral spring, and tangential force is measured using a load cell on top grip and a force link on the bottom grip. Details on the fretting fixture and test procedure can be found in a previous study [6].

Constant amplitude loading tests were conducted at various stress amplitudes 121 MPa–302 MPa, with stress ratios of 0–0.5, test frequency of 50 Hz, and normal load on fretting pads of 1334 N–4000 N. All tests were conducted under the ambient laboratory condition. To characterize crack growth under fretting fatigue, a series of incremental and interrupted tests were also conducted at the stress amplitude of 217 MPa and normal contact load of 3558 N. The average fretting fatigue life was determined from the tests where specimens were tested until their failure. For the incremental tests fretting specimen was subjected to a given percentage of the average fretting fatigue life, which ranged from 10 to 70 %. Then, the specimen tested under incremental test condition, was heated to 420°C for 2 h. This heat-treatment (i.e., heat-tinting) changed the color of existing crack surface (if any), which allowed us to measure the crack length as well as crack shape. During the interrupted fretting tests, the test was stopped at an increment of 5000 cycles and the pads were removed to examine the fretted region. A plastic replication technique was used to measure crack length, if any. Then the test was continued, and the test procedure was repeated for every 5000 cycles.

Results and Discussion

Early Crack Growth Details

Incremental fretting fatigue tests showed overall crack growth shape after a given percentage of the average fretting fatigue life, N_f, which was measured to be 83 000 cycles, an average of four constant

TABLE 1—*Mechanical properties of* Ti-6Al-4V *at room temperature.*

E (GPa)	σ_y(MPa)	σ_{UTS} (MPa)
126	930	978

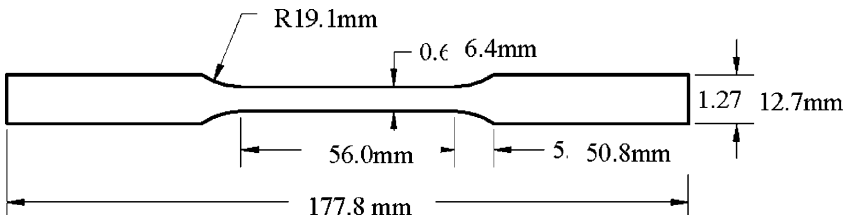


FIG. 2—*Schematic drawing of specimen.*

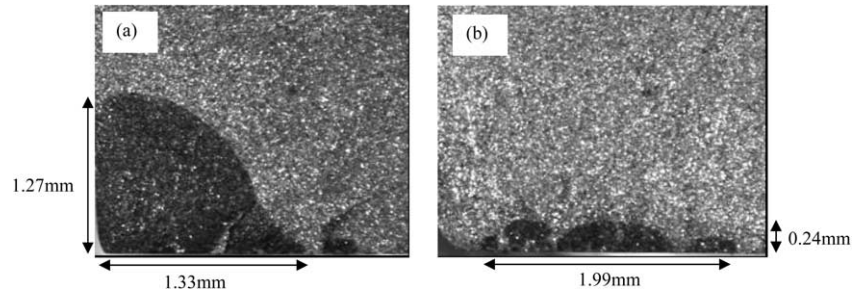


FIG. 3—*Fracture surface after* 2 h *of heat-tinting at* 420°C *after: (a)* 40 % N_f *and (b)* 60 % N_f.

amplitude tests. No cracks were found up to 30 % N_f. Figure 3 shows the fracture surfaces of the specimens subjected to 40 and 60 % of N_f after 2 h of heat-tinting at 420°C. Corner crack with semicircular shape was shown in the 40 % specimen (Fig. 3(*a*)) whereas elliptical crack with large crack aspect ratio (c/a, ratio of half crack length to crack depth) of 4.2 was evident in the 60 % specimen (Fig. 3(*b*)). Even though corner crack was observed in a few tests, typical crack geometry under fretting fatigue was elliptical with large aspect ratios. In general, fretting fatigue induces multiple crack nucleation and these small cracks join to form a single crack. This is evident in Fig. 3(*b*) where three cracks were independently nucleated and they were in the process of coalescence. Further, this single crack was initially surface cracked and then it eventually became a through-the-thickness crack leading to failure of the specimen.

Interrupted tests did not produce consistent crack length measurements due to the difficulty in the repositioning of fretting pads exactly at the original fretting location after plastic replication. Subsequent fatigue cycles resulted in damage accumulation in a new area, leading to a fresh fretting effect. Figure 4 shows the fracture surface of specimen subjected to interrupted fretting fatigue test up to cycles equal to 60 % N_f. The crack shape was elliptical with a crack aspect ratio of 1.5. Two cracks are evident in Fig. 4, which may have resulted from the difficulty in repositioning the pads exactly at the same location once they were removed to observe the crack growth.

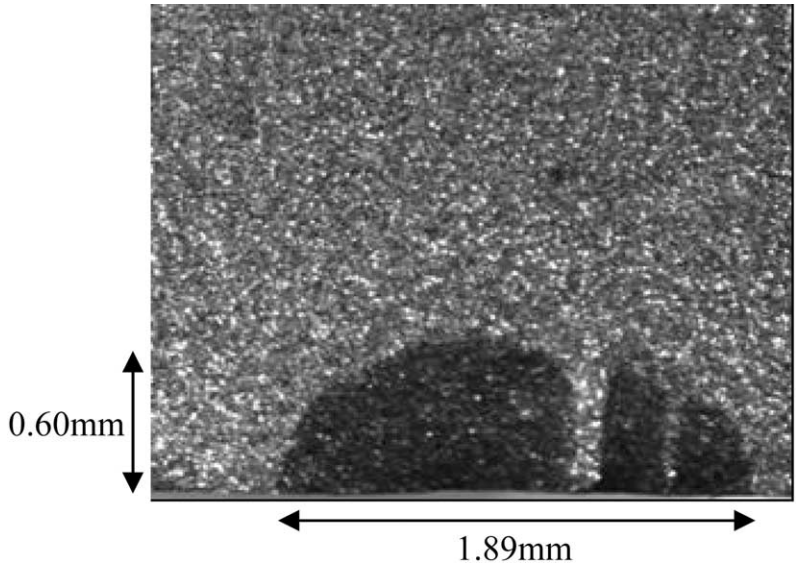


FIG. 4—*Crack shape after an interrupted test and* 2 h *of heat-tinting at* 420°C.

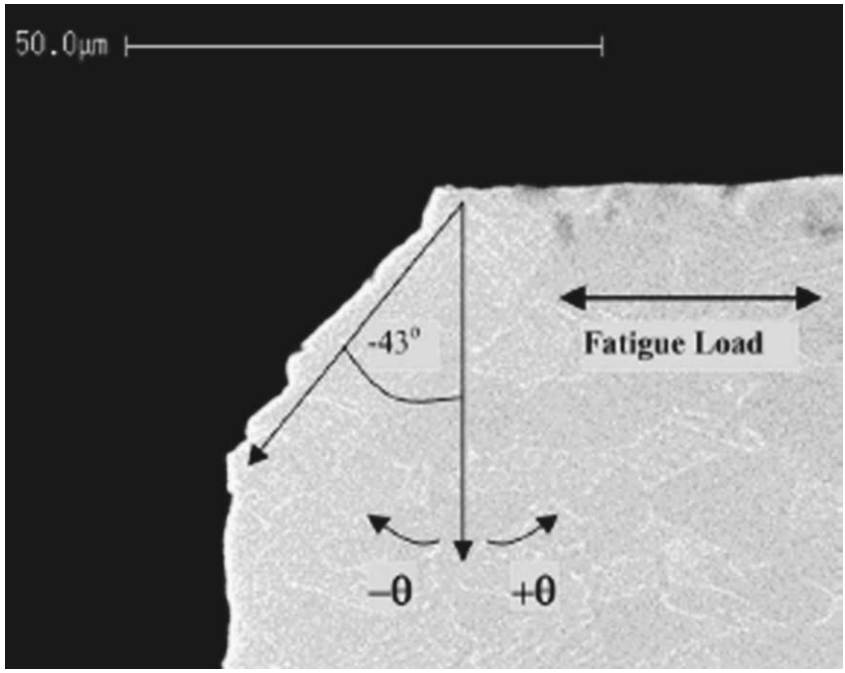


FIG. 5—*Crack growth pattern during early crack propagation.*

To examine crack growth pattern in fretting fatigue, several specimens were cycled and sectioned. Typical fretting fatigue crack propagation during its early stage of growth is shown in Fig. 5. The crack nucleated and grew at approximately 45° from the applied loading direction. The initial shear crack length (i.e., inclined part) was about 22 μm in the horizontal direction in the case shown. However, the size of shear crack ranged from 20 μm to 50 μm depending on the loading conditions (i.e., normal pressure and applied stress). Thereafter, the crack grew perpendicular to the loading direction in the opening tensile mode. From this crack growth pattern, it can be reasonably assumed that the change in crack growth direction resulted due to the disappearance of fretting induced stresses and due to the presence of stress state induced by the applied fatigue load only. This is illustrated in Fig. 6 which shows a schematic drawing of crack regime versus stress field. When the crack changed its growth direction, the crack was exposed to the applied stress only. In other words, the nucleated crack grew under shear mode due to contact stresses, and after transition from shear mode to normal mode it was subjected to the applied stress amplitude only. Since short crack regime lasts up to 3–5 grain size (~100 μm in the present study since grain size of test material was ~20 μm, Fig. 1), the part of the short crack grew under the influence of contact stresses and the rest under the applied stress amplitude. After this, the crack became a long crack and its propagation life can be estimated using long crack growth models.

Life Prediction—Fretting fatigue life consists of crack nucleation, short and long crack propagation lives. For the crack nucleation and short crack propagation lives, it is necessary to find contact stress distribution. The contact stress state can be estimated from either analytical solution [9] or finite element analysis (FEA). Both results in similar contact stress distribution (Fig. 7) with about 5 % difference in maximum normal stress on the contact surface. In the present study, the analytical solution was used to obtain the contact stress state to reduce computational time.

Crack Nucleation To predict the crack nucleation life Smith-Watson-Topper (SWT) model and Coffin-Manson (CM) equations were used:

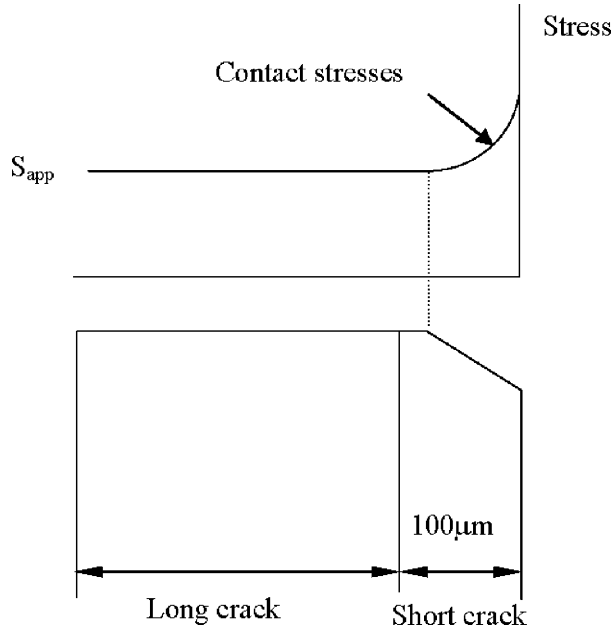


FIG. 6—*Schematic drawing of crack regime and corresponding local stress.*

$$\sigma_{\max} \cdot \varepsilon_a = \frac{\sigma_f'^2}{E}(2N_f)^{2b} + \sigma_f' \cdot \varepsilon_f'(2N_f)^{b+c} \tag{1}$$

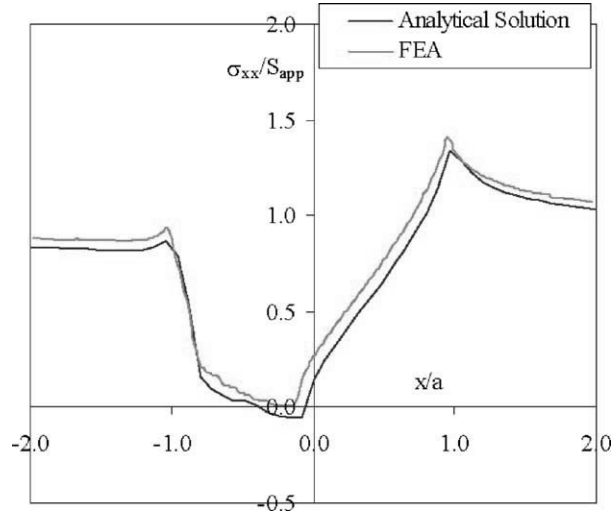


FIG. 7—*Normal contact stress distribution along the contact length.*

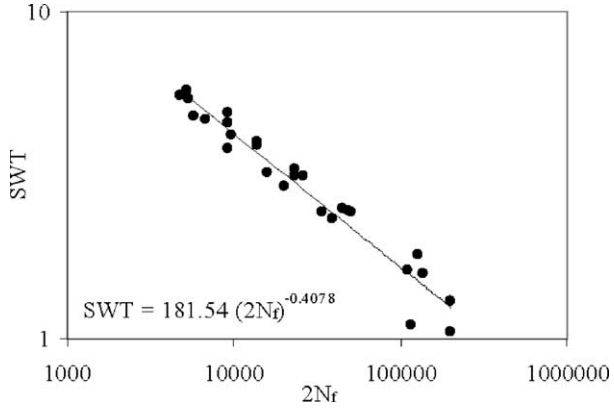


FIG. 8—*Plot of SWT parameter versus plain fatigue life.*

$$\varepsilon_a = \frac{\sigma_f'}{E}(2N_f)^b + \varepsilon_f'(2N_f)^c \tag{2}$$

where σ_{max} is the maximum normal stress, ε_a is normal strain amplitude on the critical plane. It is to be noted that only elastic component of Eqs 1 and 2 was used because the contact stresses are within the elastic limit in all cases of this study. The constant b was determined using plain fatigue test data obtained under the Air Force High Cycle Fatigue (HCF) program [10] using the same test material as this study. Figures 8 and 9 show SWT parameter ($\sigma_{max}\varepsilon_a$) versus fatigue life ($N_f$) and CM parameter ($\varepsilon_a$) versus fatigue life ($N_f$) for plain fatigue condition, respectively. For fretting fatigue, the parameters in Eqs 1 and 2 were determined at all locations on all planes at orientation ranging $-90° \leq \theta \leq 90°$ from a vertical to the applied loading direction in step of 0.1° by using the computed stresses and strains obtained from the analytical solution.

Short Crack Propagation Short crack propagation life was estimated by using Wang model [11]. This model was chosen since it is simple to use and capable of simulating oscillatory short crack growth behavior. Wang model assumes that when slip initiates within a grain, the whole grain undergoes slip and the grain boundaries provide a barrier to dislocation movement. The crack growth law is expressed as:

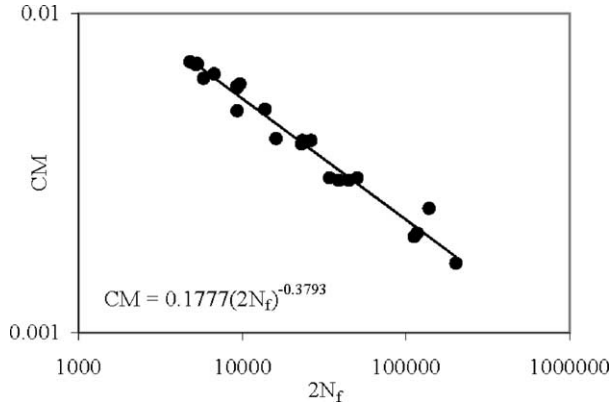


FIG. 9—*Plot of Coffin-Mason parameter (normal strain amplitude) versus plain fatigue life.*

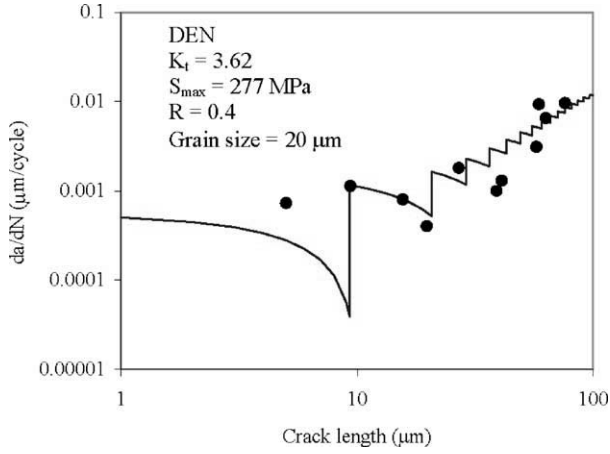


FIG. 10—*Comparison of Wang model with experimental short crack growth rate under plain fatigue.*

$$\frac{da}{dN} = \Delta\gamma_p \cdot \rho_{\max} \tag{3}$$

$$\frac{da}{dN} = B \cdot \Delta\gamma_t \cdot \rho_{\max} \tag{4}$$

In Eq 3, $\Delta\gamma_p$ is the local plastic shear strain range and is related to the local plastic tensile strain range, $\Delta\epsilon_p$ by this relationship: $\Delta\gamma_p = 1.5 \cdot \Delta\epsilon_p$ [12]. When the plastic strain is small, Eq 4 is used where $\Delta\gamma_t = (1 + \upsilon) \cdot \Delta\varepsilon$. The value of B was determined by setting Eqs 3 and 4 equal to each other at just above the fatigue limit, which resulted to be 0.113. The cyclic plastic strain can be determined by a power law:

$$\Delta\varepsilon_p = \left(\frac{\Delta\sigma}{K'}\right)^{(1/n')} \tag{5}$$

The measured short crack growth behavior of Ti-6Al-4V under plain fatigue condition is shown in Fig. 10 along with its prediction from the Wang model. The grain size was assumed to be 20 μm (see Fig. 1). As the crack approaches the grain boundaries its growth rate decelerates and when the crack passes through the grain boundary its growth rate accelerates. Wang model captures average short crack growth behavior well. A similar procedure was used in the fretting fatigue case except for that the average contact stress over a distance was used to calculate short crack growth life since contact stress state changes (i.e., decreases) with distance from the contact surface.

Long Crack Propagation Crack was assumed to be a through-the-thickness type of crack with a length of 100 μm. In the present work, crack interaction was not considered even though multiple cracks were found. A long crack growth model from the U.S. Air Force HCF program [10] was used, which is expressed as:

$$\frac{da}{dN} = F(K_{\max}, K_{\min}) \tag{6}$$

$$F(K_{\max}, K_{\min}) = 3.5 \cdot 10^{-7} \left(\frac{K_{eff}}{K_{th}}\right)^P \left[\ln\left(\frac{K_{eff}}{K_{th}}\right)\right]^Q \left[\ln\left(\frac{K_c}{K_{eff}}\right)\right]^d \tag{7}$$

TABLE 2—*Mechanical properties of* Ti-6Al-4V *at room temperature.*

K_{th} (MPa $m^{1/2}$)	K_c (MPa $m^{1/2}$)	P	Q	d	m
3.82	60	3.71	0.235	−0.0066	0.275

$$K_{eff} = K_{\max}^{1-m} \cdot (K_{\max} - K_{\min})^m \tag{8}$$

where $K_{\max}$ and $K_{\min}$ are maximum and minimum stress intensity factors, K_{eff} is effective stress intensity factor, K_{th} is threshold stress intensity factor, K_c is fracture toughness, and P, Q, d and m are constants. Empirical constants used in Eqs 6 and 7 are given in Table 2. Simpson's rule was used to compute fatigue cycles corresponding to a crack extension:

$$N = \tfrac{1}{3}\sum_{i=0}^{m} \Delta a(F_i^{-1} + 4F_{i+1}^{-1} + F_{i+2}^{-1}) \tag{9}$$

where F^{-1} is inverse of the right-hand equation of Eq 7.

Figure 11 shows a plot of predicted fretting fatigue life versus experimental life using both SWT and Coffin-Manson. The latter provides a better correlation between predicted and experimental lives. Further, it was observed that the Coffin-Manson model resulted in an excellent prediction in tests conducted at low stress ratios (<0.2). However, as the stress ratio increased the predicted fretting fatigue life deviated from the experimental life. This may have resulted from highly random nature of fatigue process at the lower applied stress amplitudes. Crack nucleation life estimated by the Coffin-Manson equation was at least 27 % of the total life. This matches with the results of the incremental fretting fatigue tests which showed no crack nucleation up to 30 % of the average fatigue life. Percent lives spent in the short and long crack regimes are shown in Fig. 12. Short crack propagation life was very short, approximately 5–18 % of the total fatigue life. However, it was 10–35 % of the total crack propagation life. This is substantial considering that short crack propagation life under plain fatigue is 50–90 % of the total fatigue life. Therefore, the short fatigue life in fretting fatigue cannot be ignored in the fatigue life prediction. This phenomenon has not been considered or reported in the fretting fatigue literature so far, where either crack nucleation and long crack propagation or both, has been considered only to estimate the life. This study thus provides a procedure not only to improve the prediction capability of fretting fatigue life but also it provides insight about the early crack growth details in fretting fatigue case.

Conclusion

The crack growth behavior in titanium alloy, Ti-6Al-4V, under the fretting fatigue loading condition investigated. The main results of the investigation are as follows.

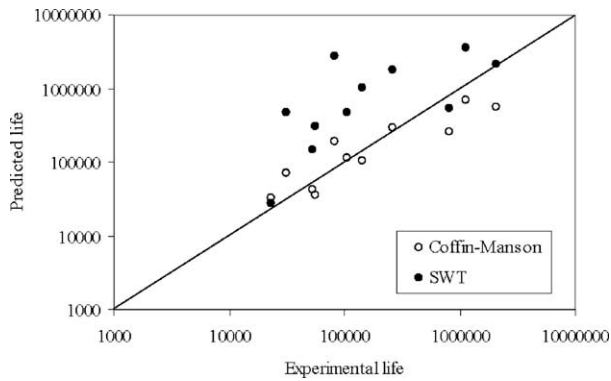


FIG. 11—*Comparison of the predicted life with the experimental life.*

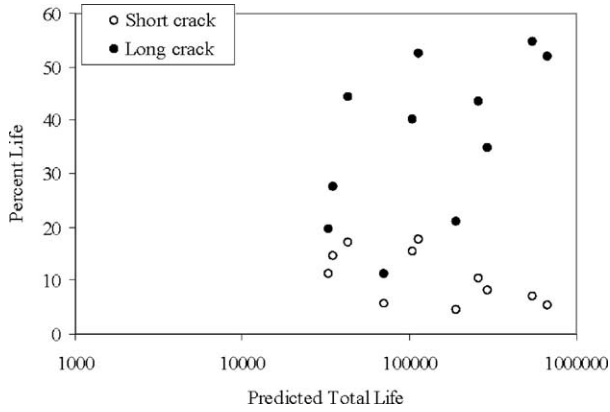


FIG. 12—*Percent life of short and long crack.*

1. Crack nucleation was not observed up to 30 % of the total fretting fatigue life. In most specimens, multiple short cracks were nucleated and they joined to form a major crack, resulting in a surface crack with high aspect ratio. Once the crack nucleated it grew approximately at 45 deg from the applied loading direction and this shear crack became an opening mode crack at 90 deg to the applied fatigue loading direction (i.e., normal to load direction) within 50 μm length due to the disappearance of contact stress effects.

2. Short crack propagation life was predicted using a microstructural fracture mechanics approach. It was assumed that short to long crack transition occurs at 100 μm (i.e., after a length equal to five grains) and short crack propagates under the influence of contact stress from fretting action. The prediction showed that short crack growth life constituted 10 to 35 % of the total fatigue propagation life.

3. Crack nucleation life was estimated to be at least 27 % of the total life. This observation was evidenced and supported from the result of the incremental fretting fatigue tests which showed no crack nucleation up to 30 % of the failure life.

References

[1] Endo, K., and Goto, H., "Initiation and Propagation of Fretting Fatigue Cracks," *Wear*, Vol. 38, 1976, 311–324.

[2] Szowinski, M., and Farris, T., "Mechanics of Fretting Fatigue Crack Formation," *Wear*, Vol. 198, 1996, pp. 93–107.

[3] Smith, R. N., Watson, P., and Topper, T. H., "A Stress-Strain Function for the Fatigue of Metals," *J. Mater.*, Vol. 5, 1970, pp. 767–778.

[4] New, R., Pape, J., and Swalla-Michaud, D., "Methodologies for Linking Nucleation and Propagation Approaches for Predicting Life Under Fretting Fatigue," *Fretting Fatigue: Current Technology and Practices, ASTM STP 1367*, D. Hoeppner, V. Chandrasekaran, and C. Elliot, Eds., ASTM International, West Conshohocken, PA, 2000.

[5] Lykins, C. D., Mall, S., and Jain, V. K. "A Shear Stress Based Parameter for Fretting Fatigue Crack Initiation," *Fat. Fract. Engng Mater Struct.*, Vol. 24, 2001, pp. 461–473.

[6] Namjoshi, S. A., Mall, S., Jain, V. K., and Jin, O., "Fretting Fatigue Crack Initiation Mechanism in Ti-6Al-4V," *Fat. Fract. Engng Mater Struct.*, Vol. 25, 2002, pp. 955–964.

[7] Alic, J. A. and Hawley, A. L., "On The Early Growth of Fretting Fatigue Cracks," *Wear*, Vol. 56, 1979, pp. 377–389.

[8] Sato, K., Fujii, H., and Kodama, S., "Crack Propagation Behavior in Fretting Fatigue," *Wear*, Vol. 107, 1986, pp. 245–262.

[9] Nowell, D., and Hills, D. A., *Mechanics of Fretting Fatigue*, Kluwer Academics, The Netherlands,

1994, pp. 41–64.
[10] Improved High Cycle Fatigue Life Prediction, AFRL-ML-WP-TR-2001-4159, Materials and Manufacturing Directorate, Air Force Research Laboratory, WPAFB, OH 45433-7750, January 2001.
[11] Wang, C. H., "Effect of Stress Ratio on Short Fatigue Crack Growth," *Trans. ASME*, Vol. 118, 1996, pp. 362–366.
[12] Babbantine, J. A., Comer, J. J., and Handrock, J. L. "*Fundamentals of Metal Fatigue Analysis*," Prentice-Hall Inc., 1990, p. 250.

Journal of ASTM International, Vol. 3, No. 8
Paper ID JAI13206
Available online at www.astm.org

Scott A. Prost-Domasky,[1] *Craig L. Brooks,*[1] *and Nichole Young*[1]

Verification of Analytical Models in a Fracture Mechanics Based Approach to Modeling Fretting Fatigue

ABSTRACT: A fracture mechanics-based approach which uses Mode I Stress Intensity Factor (SIFs) to estimate the influence of fretting fatigue loads (which can consist of normal and shear contact loads, as well as bulk or far-field loads) has been proposed by Rooke and Jones ("Stress Intensity Factors in Fretting Fatigue," Journal of Strain Analysis, Vol. 14, No. 1, 1979, pp. 1–6), who proposed a cracking scenario in which a single edge crack propagates to failure under the influence of the contact and bulk stress damage drivers. A major shortcoming of this approach is that the underlying analytical method and closed form integral equations assume that the single edge crack propagates into a semi-infinite domain or half-space. Significant differences in the stress states for finite width domains have been postulated by Fellows et al. ("Contact Stresses in a Moderately Then Strip (with Particular Reference to Fretting Experiments," Wear, Vol. 185, 1995, pp. 235–238) among others. SIFs can be roughly correlated with stress; therefore variations in the stress states normally result in variations in the SIFs. Variations in the SIFs due to shear and normal contact loads, and due to finite width effects are quantitatively evaluated with the finite element method (FEM). Results with the finite element approach are compared to those using the Rooke and Jones method, as well as other results from the open literature.

KEYWORDS: fretting fatigue, holistic models

Nomenclature

a = crack length
b = plate semithickness
E^* = effective stiffness
E_i = Young's modulus of material i
K_{I} = Mode I Stress Intensity Factor
P' = pad normal load, per unit width
p_0 = maximum contact normal traction (pressure)
Q' = pad shear load, per unit width
R = pad radius
α = contact area semiwidth
μ = friction coefficient
ν_i = Poisson ratio of material i
σ_0 = bulk stress
σ_{xx} = normal stress in x-direction
σ_{yy} = normal stress in y-direction

Introduction

Fretting is a wear phenomenon that occurs between two mating surfaces: It is adhesive in nature, and vibration is its essential causative factor. In general, fretting occurs between two tight fitting surfaces that are subjected to a cyclic, relative motion of extremely small amplitude. Fretted regions are highly sensitive to fatigue cracking. Under fretting conditions, fatigue cracks can nucleate at stress levels in the fretted

Manuscript received April 8, 2005; accepted for publication June 8, 2006; published online August 2006. Presented at ASTM Symposium on Fatigue and Fracture Mechanics: 35th Volume on 18–20 May 2005 in Reno, NV; R. E. Link and K. M. Nikbin, Guest Editors.
[1] APES, Inc., St. Louis, MO
Copyright © 2006 by ASTM International, 100 Barr Harbor Drive, PO Box C700, West Conshohocken, PA 19428-2959.

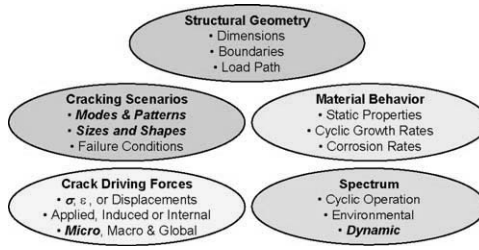


FIG. 1—*Robust structural life prediction methodology accommodates fretting fatigue methodology. Points of emphasis in fretting are cracking scenarios (modes and patterns, sizes and shapes), crack driving forces (microstresses), and load spectra.*

structure that are lower than the endurance limit, often resulting in structural failure that occurs at many fewer cycles than anticipated. Nucleation of fatigue cracks in fretted regions depends mainly on the state of stress on the surface and particularly on the stresses superimposed on the cyclic stress. The time to nucleation of cracks can be significantly reduced as a result of fretting. Common sites for fretting are in joints that are bolted, keyed, pinned, press fitted, and riveted. These sites are common in the assembly of most air vehicles, ground vehicles, power plants, equipment, and machinery.

Fretting damage is differentiated by three distinct modes: fretting wear, fretting fatigue, and gross sliding wear. Fretting wear, which occurs for relatively small vibratory motion, normally results in relatively little damage and rarely causes premature structural failure. Gross sliding wear, which occurs for relatively large vibratory motion, normally results in visual surface damage, but rarely causes premature structural failure. Fretting fatigue, the subject of this paper, is caused by intermediate vibratory motion and is often the most damaging, causing cracks and often resulting in premature structural failure.

Reliable (verified and validated) life prediction methods are needed to account for the deleterious effects of fretting fatigue on structure's damage tolerance. Holistic life assessment methods can be used to assess structural integrity under cyclic and time dependent damage drivers such as fretting, which is rarely constant over time, [1]. Two fracture mechanics based methods that account for fretting fatigue damage drivers, incorporated into a holistic life assessment framework [2], will be investigated: An analytical approach that requires the stresses due to contact and bulk stress be known prior to completing the numerical integration, and a finite element based approach. "Holistic life" prediction methods require description of a structure's physical state in the following areas: geometry, cracking scenarios, material behavior, crack driving forces, and spectra (which includes stress, environment, and dynamics), Fig. 1. This paper will discuss efforts to adequately describe the stress states in a simple fretting fatigue test, in which two opposing cylinders are held at a constant normal load against a flat dog bone coupon, which itself has a cyclic bulk stress applied to it, Fig. 2. Sufficiently accurate descriptions of the contact stress state due to normal and shear stress must be obtained; efforts to acquire accurate stress states are the subject of this paper.

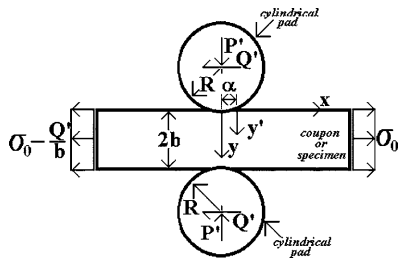


FIG. 2—*Fracture mechanics method models the fretting pad with normal and shear contact on stress intensity factors for an edge crack in a fatigued coupon. Pad can be flat or cylindrical. Coordinate system used in later analysis shown.*

An analytical approach first proposed by Rooke and Jones [3] will be the one evaluated. The method as proposed by Rooke and Jones offers an efficient method for estimating the influence of contact tractions (normal and shear) on a flat surface on the Modes I and II Stress Intensity Factors for a single edge through crack whose origin is on the flat surface (only the Mode I will be investigated). The method appears to work well for this particular crack scenario. To demonstrate the utility of the method, T. Hattori and colleagues at Hitachi have applied the Rooke and Jones approach to the modeling of fretting fatigue experiments [4–7].

Analytical Models

Two methods for computing fracture mechanics parameters such as the Mode I Stress Intensity Factor K_I. will be compared by application to a fretting fatigue experiment in which cylinder pads are held with constant normal force up against a finite width coupon. The contact normal force on the pad varied from 420.3 kPa/m (2.4 kips/in.) to 560.4 kPa/m (3.2 kips/in.), and the bulk stress from 110.3 MPa (16 ksi) to 193.0 MPa (28 ksi). Analysis of this fretting fatigue experiment requires accurate descriptions of the stress states and a reliable method for "converting" the stress state into fracture mechanics parameters such as Mode I Stress Intensity Factors (SIFs) K_I. A *p*-version finite element method software will be used to validate stress states and SIFs when needed.

Normal Contact of a Cylinder

The classical solution for a cylinder indenting a flat body in two-dimensional (2D) plane strain is found in Johnson [8], who theorized that even though the fundamental equations are coupled shear and normal contact tractions, these contact tractions are independent, if the bodies are elastically similar. The normal contact traction (or pressure) $p(x)$ has the following closed form:

$$p(x) = \frac{2P'}{\pi\alpha^2}\sqrt{\alpha^2 - x^2} \tag{1}$$

where $\alpha = (4P'R/\pi E^*)^2 = 2P'/\pi p_0$ is the contact semiwidth and $1/E^* = ((1-\nu_1^2)/E_1 + (1-\nu_2^2)/E_2)$ is the effective Young's modulus, a function of the Young's moduli and Poisson ratios of the two bodies, E_1, ν_1 and E_2, ν_2.

This solution is limited by the key assumption that the flat body is semi-infinite. Such a body is also known as a "half space." The half-space assumption was relaxed in a paper by Fellows et al. [9], which demonstrated the use of Fourier integrals to estimate the effect of application of the pressure solution derived for the cylinder contacting a half-space to a finite width flat plate. Fellows assumed that the pressure solution is close to the Johnson half space for all plate thickness, but that stress internal to the plate is significantly affected by the thickness. Using the same Fourier transform technique as Fellows et al. used, Fett and Munz [10] explicitly described the integral equations needed to compute the internal stress fields for the same opposing cylindrical contact of flat plates, and extended this work by using the stress fields in a weight function method that they used to calculate the Modes I and II Stress Intensity Factors for a single edge crack which origins are located at the surface of contact (Fett and Munz made no mention of the Fellows et al. work, though their description of the method used to derive the integral stress fields appears to be identical to the method used in the earlier Fellows et al. work).

In principle, the half-space assumption is not limiting, as the effect of the normal contact stress on the overall stress state dies off fairly quickly as distance from the contact surface increases. A key result in this paper will be a determination of how important this limiting assumption is for a range of experimental parameters.

Rooke and Jones Influence Functions

A fracture mechanics based approach that can be used to calculate Mode I Stress Intensity Factors (SIFs) K_I from contact stress uses the analytical method developed by Rooke and Jones [3]. This approach estimates the influence of normal and shear point forces on the SIF for an edge crack of length "*a*" located some distance "*x*" away from the point force application and has generalized to account for variable pressure distributions that result from the contact of two bodies, Fig. 3. The method by Rooke and Jones

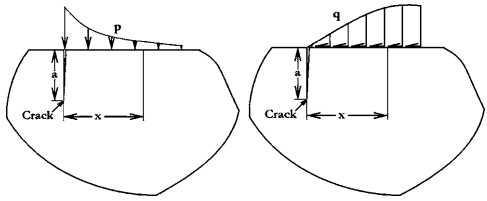


FIG. 3—*Fracture mechanics method extends the Rooke and Jones Mode I Stress Intensity Factor solutions (for point forces) to spatially varying amplitude normal and shear tractions.*

assumes that the edge crack is straight, through, and perpendicular to the surface as shown in Fig. 3. The Rooke and Jones estimated stress intensity factor (SIF) solutions for distributed normal and shear tractions located as indicated in Fig. 3 have the following forms:

$$K_I(p) = \int \frac{p}{\sqrt{\pi a}}(1-\xi^2)[0.824 + 0.0637\xi - 0.843\xi^2 + 15.41\xi^3 - 53.38\xi^4 + 59.74\xi^5 - 21.83\xi^6]dx \quad (2)$$

$$K_I(q) = \int \frac{q}{\sqrt{\pi a}}(1-\xi^2)[1.2943 + 0.0044\xi + 0.128\xi^2 + 10.89\xi^3 - 22.14\xi^4 + 10.96\xi^5]dx \quad (3)$$

$$\xi = \frac{x}{x+a} \quad (4)$$

Note that these equations are derived with the assumption that the flat body is "semi-infinite," that is, the body is flat on one side, but extends to infinity in all other directions. In general, $K_I(p)$ is negative in Eq 2 for most crack lengths, but is dominated by the K_I due to the far-field loading. The reader is advised to always keep in mind that the Rooke and Jones method was demonstrated for straight edge through cracks, while it is well-known that fretting cracks that form during tests of the configuration of Fig. 2 normally grow immediately from the surface at an angle, "turning" to perpendicular after a short distance from the surface.

The actual mechanical system being modeled is comprised of two opposing fretting pads (of the same geometry, either flat or cylindrical cross sections), with an elastic *finite thickness* coupon or substrate in between, Fig. 2. A single edge through crack with origin at the leading edge of the contact surface is introduced into the model. The Mode I Stress Intensity Factor due to the far-field applied stress σ_0 (also know as "bulk stress") is calculated from the single edge through crack [11]

$$K_I(\sigma_0, \alpha, b) = \beta(\alpha/b)\sigma_0\sqrt{\pi a} \quad (5)$$

The total Mode I Stress Intensity Factor due to the fretting and the far-field applied stress is calculated from a superposition of Eqs 2, 3, and 5 to model the mechanical system of Fig. 2

$$K_I(\sigma_0, p, q) = K_I(p) + K_I(q) + K_I(\sigma_0) \quad (6)$$

Note that this superposition, depicted in Fig. 4 below, works well only if the bulk stress used in the $K_I(\sigma_0)$ term is $\sigma_0 - Q'/b$, instead of σ_0; the reason for this is that the derivation of the Rooke and Jones equations of the stress intensity factors assume far-field stresses are evenly distributed (for instance, on the right and left boundaries of Fig. 3).

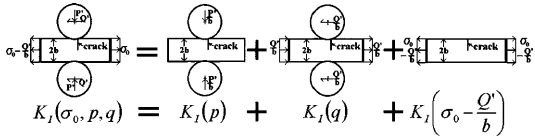


FIG. 4—*The superposition of the stress intensity factors calculated by the Rooke and Jones method.*

The advantage of this approach is that if the contact stress distribution is known, a robust fracture mechanics based prediction can be made, and crack growth analysis tools such as the U.S. Air Force's (AFGROW) that can be driven by an Excel spreadsheet with Visual Basic©[2] coding can be used. The disadvantages of this approach are (1) three-dimensional effects are not modeled well (however, by using compounding, the stress intensity $K_I(p)$ and $K_I(q)$ can be used to adjust the stress intensity factors K_I in Eq 6) for a surface elliptical crack, (2) slant cracks cannot be modeled directly yet, and (3) Mode II crack propagation is so far ignored.

Contact Algorithm

If the contacting bodies do not have the same geometry as one of the few analytical solutions that exist, an alternate method for estimating contact tractions must be used. Recently, the commercial *p*-version finite element method software STRESSCHECK©[3] (ESRD, Inc., St. Louis, Missouri), Ref. [12], has added a contact mechanics capability which can compute normal contact tractions in two- and three-dimensional domains. The details of the contact algorithm [13] will not be discussed here; however, the analyst does have direct control over one algorithm parameter, the "contact spring stiffness," which will be fixed for all finite element solutions.

Results

Numerical Convergence Issues

The goal of any finite element analyses should be stated up front, along with the accuracy and reliability requirements for the computed engineering data. For example, the goal of the analysis might be "obtain the maximum contact pressure within 5 %." There are two types of solution convergence that are important to consider in these contact problem models: contact pressure convergence and numerical error. Because contact is mechanically nonlinear (that is, the contact areas and stress are not known a priori), the STRESSCHECK© contact algorithm, like other contact algorithms, requires an iterative numerical method to reach a numerically converged solution; iterations continue until the maximum contact pressure does not change much from iteration to iteration (to within 0.01 %) or until the maximum number of iterations as specified the analyst is reached. If the maximum number of iterations is reached, more mesh refinement is usually indicated. In no case was the contact iteration error larger than 0.05 % in the analyses reported in this paper.

The numerical error is also evaluated. The contact problem modeled in these analyses, a cylinder in contact with a finite thickness flat plate, does not have an exact solution, therefore the finite element analyst can only attempt to minimize numerical error with extensions, defined as "systematic changes of discretization so that the number of degrees-of-freedom is increased at each change," Ref. [14]. The numerical error is quantified by using extensions whereby that the degrees-of-freedom (DOFs) are increased until no changes in the numerical solution are apparent. Convergence theory requires a minimum of three extensions (or finite element solutions) of the discretization—that is, the convergence can be characterized by a simple three parameter equation. The three unknown constants in this equation can be solved with three equations based on engineering data computed in three finite element solutions. In each finite element solution reported in this document, a minimum of three discretizations for each combination of geometry, loads, and boundary conditions were analyzed, and the computations of these three discretizations checked for convergence.

Every finite element (FE) result presented herein was checked and has excellent numerical convergence—typical results representative of all numerical results reported in this document are shown in Fig. 5 below. This figure illustrates the magnitude of the numerical error, which is always within 1 % of estimated exact solution (a few procedures for estimating the exact solution are described in [14]).

[2]AFGROW is fracture mechanics software and is copyrighted by the U.S. Air Force Research Laboratories, Air Vehicles Directorate (AFRL/VASM, Wright–Patterson Air Force Base, Dayton, Ohio, USA).
[3]STRESSCHECK® is a *p*-version finite element analysis software and is a registered trademark of Engineering Software Research and Development, Inc. (ESRD, Inc., St. Louis, Missouri, USA).

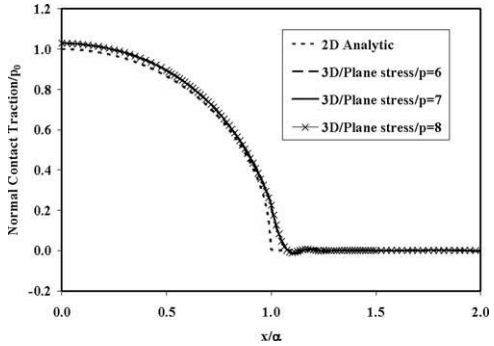


FIG. 5—*Convergence of the contact traction with p extension. The phrase "3D/plane stress" signifies a 3D analysis, with one edge stress free. Stresses normalized by analytical* p_0.

Validation of Contact Model

The new contact capability will be validated for the case of an elastic cylinder indenting a finite width flat elastic plate, Fig. 2. For convenience, the material properties of the flat plate and the cylinder are elastically similar, with Young's modulus of 68.93 GPa (10,000 ksi) and Poisson's ratio 0.3. The 2D contact analysis will vary the flat plate thickness from 4.64 mm (0.182 in.) to 15.5 mm (0.609 in.), while the 3D contact analysis will fix the plate thickness to 12.7 mm (0.5 in.). Both the 2D and 3D contact analysis fix the pad radius to 127 mm (5 in.) and fix the pad normal load at 560.4 kN/m (3.2 kips/in.).

Two-Dimensional Contact of Cylinder and Flat Plate

2D plane strain models of a cylinder in contact with finite thickness flat plates are modeled with STRESSCHECK© finite element (FE) software and comparing the FE results to the analytical results of Fellows et al. [9]. The pad has a constant normal load applied, no friction (therefore no shear) between the cylinder and flat plate, and the bulk stress (perpendicular to the normal load) is 0. Due to the symmetry of the geometry and loads, the finite element domain was only 1/4th of the entire model domain. The contact spring stiffness in the FE model was fixed at 8143.4 GPa/m (30000 ksi/in.). The normal tractions computed with the FE contact algorithm are compared to the Johnson analytical solution (labeled "half space") [1] and the Fellows et al. analytical solutions [9] for finite width plates, Fig. 6, which shows the normal stress σ_{xx} (normalized by the analytic p_0=230.7 MPa) into the depth of the flat plate, at the edge of contact (coordinate y' in Fig. 5).

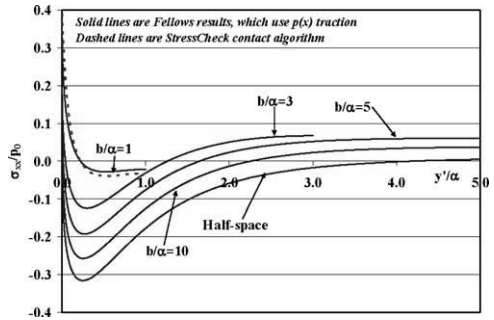


FIG. 6—*Thickness effect significant for thickness ratio* $b/\alpha \geq 3$ *for in-depth normal stress. Fellows =solid lines; finite element method=dashed lines.*

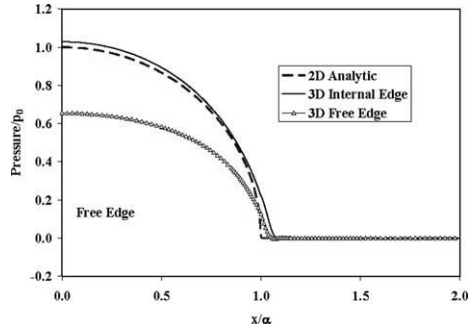


FIG. 7—*Variation of contact tractions of 3D body along the centerline of contact, from interior to free edge.*

Three-Dimensional Contact of Cylinder and Flat Plate

A 3D model of a cylinder in contact with a finite thickness flat plate is modeled with STRESSCHECK©. The pad has a constant normal load applied, and the bulk stress (perpendicular to the normal load) is 0.0. Due to the symmetry of the geometry and loads, the finite element domain was only 1/8th of the entire model domain. The contact spring stiffness was fixed at 8143.4 GPa/m (30,000 ksi/in.). The contact normal tractions are compared to the Johnson analytical solution, which assumes a 2D plane strain model, Fig. 7. The negative of the stress σ_{yy} has been normalized by the analytic p_0=230.7 MPa.

A significant effect of the free edge is the variation of contact surface and resulting contact normal traction along the axis of the cylinder; the shape of this contact surface has been variously called a "race track" or an "oval." This effect is demonstrated well in the 3D finite element method solution, Fig. 8.

Two conclusions are obvious from these results: (1) there is a substantial Poisson's effect on the contact pressure for the configurations simulated—the peak pressure drops 33 % from the center to the free edge, while the contact area drops only 2 %; and (2) while there can be a substantial finite thickness effect on the interior stress states, the difference between the analytical contact traction from Johnson (which assumes a half space) and the finite element computed results that simulated the contact of a cylindrical body with a finite thickness flat plate is substantial only for "thin" flat plates, on the order of three contact area widths and smaller, $b/\alpha \leqslant 3$. If $b/\alpha \geqslant 3$, there is substantially no difference in the interior stress state between using the "half-space" contact pressure and simulating the contact with the contact algorithm—as a practical matter, this trend will allow greater efficiency in computing the finite element solutions, as the two-body contact will not have to be simulated with the reliable but computationally expensive contact algorithm.

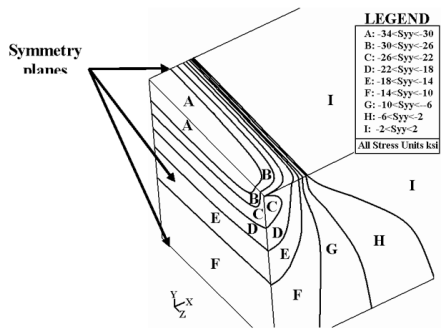


FIG. 8—*The contact area pressure contours vary along the pad axis (aligned with z axis), demonstrating a clear "plane stress" effect.*

TABLE 1—*Fixed parameters for stress intensity factor calculations. Parameters magnitudes are representative of experimental values cited in Ref [1].*

Parameter	Symbol	Value
Effective stiffness	$\mathbf{E}^*$	37883 MPa (5495 ksi)
Friction coefficient	$\boldsymbol{\mu}$	0.80
Pad radius	**R**	127 mm (5.0 in.)
Plate semithickness	**b**	12.7 mm (0.5 in.)
Bulk stress	$\boldsymbol{\sigma_0}$	193 MPa (28 ksi)

Comparisons of Computed Stress Intensity Factors

Mode I Stress Intensity Factors are computed from two methods: the Rooke and Jones model and finite element models. The contact of a cylinder with a finite thickness flat plate is simulated. *In contrast to previous sections*, one small edge through crack is introduced at the edge of contact of the two cylinders of Fig. 2, closest to the applied load σ_0 in the plane stress finite element models. Contact again is simulated by the Johnson [1] analytical expressions for contact of a cylindrical pad. In addition to the contact pressure simulated in the previous sections, shear between the cylinders and the flat plate is modeled by applying shear traction, Eq 7. Geometry, pad normal and shear loads, friction coefficients, and bulk stresses representative of the proposed experimental program in Ref. [1] are used, Table 1.

The results of the previous sections demonstrated that if the flat plate is thick enough, $b/\alpha \geqslant 3$, there is little difference in the stress states that result from modeling the contact directly with a contact algorithm or from modeling the contact with contact normal tractions (pressure) that were derived for the half space. The contact semiwidth a is estimated to be 0.00155 m (0.0609 in.); $b/\alpha \geqslant 4$, therefore the plate is thick enough to use the half-space contact normal tractions, Eq 1. The contact shear tractions were simulated with the half-space analytical solution, again found in Johnson [8]

$$q(x) = \begin{bmatrix} \mu \dfrac{2P'}{\pi\alpha^2}\sqrt{\alpha^2 - x^2} & c \leqslant |x| \leqslant \alpha \\ \mu \dfrac{2P'}{\pi\alpha^2}\left(\sqrt{\alpha^2 - x^2} - \sqrt{c^2 - x^2}\right) & |x| \leqslant c \end{bmatrix} \tag{7}$$

where $c = \alpha\sqrt{1 - Q'/\mu P'}$ is the stick region semiwidth and Q' is the contact shear load.

Normal stress perpendicular to the crack front, σ_{xx} plotted in Fig. 6, is the principal contributor to the Mode I Stress Intensity Factor (SIF) for these edge through cracks: If this normal stress is positive, it is expected the SIF would be positive, and vice versa. In Fig. 6, it is clear that if the flat plate has "finite" thickness, the normal stress close to the surface will be positive, suggesting that the SIF for an edge through crack would be positive for "small" crack lengths. However, for a half space, since the normal stress σ_{xx} is negative deep into the body, we expect the SIFs to also be negative deep into the body. Two load cases are analyzed, Table 2. The pad shear loads, which depend on the stiffness of the fretting pad holder in the experiment, are fixed to 50 % of the pad normal loads for both cases. First, only the effect of the contact normal traction (for two values of the normal load, 420.3 kN/m and 560 kN/m) on the edge through crack SIF was calculated with the Rooke and Jones and finite element models, Fig. 9.

The SIFs are positive for small cracks in the finite element models, while the Rooke and Jones SIFs are negative for all crack lengths shown, consistent with the trends in the normal stress in Fig. 6. Is this difference in sign for the small cracks significant? To answer this question, two additional loads were added to the modeling: contact shear traction and bulk stress, Fig. 10, using the parameters indicated in Tables 1 and 2. The results from the two load cases in Table 2 are compared.

TABLE 2—*Contact load cases for stress itensity factor calculations. Parameters magnitudes are representative of experimental values cited in Ref. [1].*

Load case	Bulk stress	Pad normal load	Pad shear load
1	193 MPa	420.3 kN/m	210 kN/m
	(28 ksi)	(2.4 kips/in.)	(1.2 kips/in.)
2	193 MPa	560.4 kN/m	280.2 kN/m
	(28 ksi)	(3.2 kips/in.)	(1.6 kips/in.)

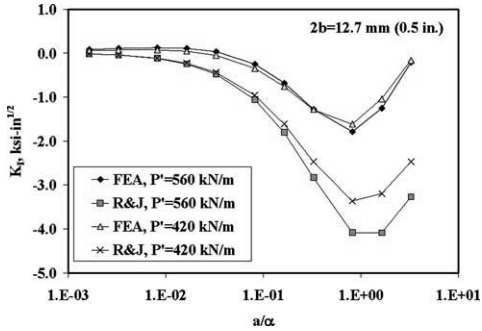


FIG. 9—*Distribution of stress intensity factors for an edge through crack, contact normal only. R&J* =Rooke *and Jones models;* FEA=finite *element models.*

The positive normal stress σ_{xx} in the small region shown in Fig. 6 results in positive SIF due to the contact normal traction for small cracks, as shown in Fig. 9. However, as Fig. 10 shows, the magnitudes of the SIFs for small cracks were small relative to other crack driving stresses such as contact shear tractions and bulk stress (Table 2 loads), suggesting that for the order of the contact and bulk loads modeled here, the contact normal traction has a nearly insignificant effect on the SIFs and therefore might not have to be modeled at all in a crack growth analysis.

Conclusions

The classical contact solutions for a cylinder in contact with a flat surface found in Johnson [8] are derived using the assumption that the flat surface is part of a body that is infinite in all directions except for one; the body is often called a "half space" or a "semi-infinite" plate. The merits of this assumption were tested by comparing engineering data calculated by a finite element method computer code that has two-body contact mechanics capabilities, as well as fracture mechanics capabilities.

- The normal stress located at the edge of the contact area between a cylinder and the flat surface of an elastic body and perpendicular to the contact surface becomes positive for progressively larger distances into the depth of the body as the thickness of the body decreases relative to the contact width. While this behavior leads to positive Mode I Stress Intensity Factors for "small" edge through cracks located at the edge of contact, the magnitudes of these SIFs were small relative to other crack driving stresses such as contact shear tractions and bulk stress.

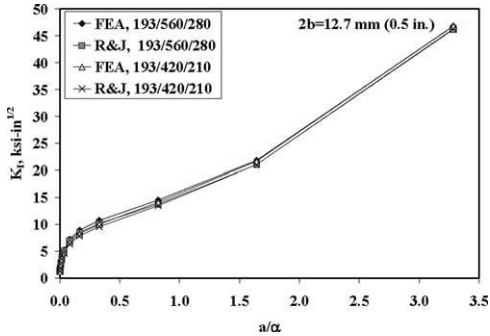


FIG. 10—*Distribution of stress intensity factors for an edge through crack, two load cases. In the legend,* 193/560/280 *signifies* σ_0=193 MPa, P'=560 kN/m, Q'=280 kN/m, *etc.*

- The 3D contact simulations demonstrated that there is a substantial Poisson's effect on the contact pressure for the configurations simulated—the peak pressure drops 33 % from the center to the free edge, while the contact area drops only 2 %.
- While there can be a substantial finite thickness effect on the interior stress states, the difference between the half-space contact traction and the finite element results that simulated the contact of a cylindrical body with a finite thickness flat plate is substantial only for "thin" flat plates, on the order of three contact area widths and smaller, $b/\alpha \leqslant 3$. If $b/\alpha \geqslant 3$, there is substantially no difference in the interior stress state between using the "halfspace" contact pressure and simulating the contact with the contact algorithm.
- The differences between the Rooke and Jones solutions and the FEA solutions for Model I Stress Intensity Factors (SIFs) due to normal contact forces, while they appear to be substantial when compared against each other, in reality have a minimal effect on the overall crack growth life of the examined fretting fatigue coupons since the overall SIFs are dominated by the bulk and the fretting shear stress terms, *for the magnitude of the fretting contact and normal loads simulated*.

Acknowledgments

The efforts described in this paper were funded in part by U.S. Department of Defense, Office of the Secretary of Defense's (OSD) Small Business Innovative Research (SBIR), U.S. Air Force Contract No. F33615-02-M-3204. This paper is approved for public release, Document No. AFRL-WS 05-1029.

References

[1] Brooks, Craig L., Prost-Domasky, Scott A., Honeycutt, Kyle T., and Mills, Thomas B., "Predictive Modeling of Structure Service Life," ASM Handbook, Vol. 13A, *Corrosion: Fundamental, Testing and Protection*, 2003, pp. 946–958.

[2] Brooks, C. L., Prost-Domasky, S. A., Honeycutt, K. T., Mills, T. B., and Young, N., "Fretting Fatigue Model," U.S. Air Force SBIR Phase I Final Report, AFRL-VA-WP-TR-2003-3012, Air Force Research Laboratories, February 2003.

[3] Rooke, D. P., and Jones, D. A., "Stress Intensity Factors in Fretting Fatigue," *J. Strain Anal.*, Vol. 14, No. 1, 1979, pp. 1–6.

[4] Hattori, T., Nakamura, M., Sakata, H., and Watanabe, T., "Fretting Fatigue Analysis using Fracture Mechanics," *Japan Society of Mechanical Engineers International Journal—Series*, Vol. 1, No. 31, 1988, pp. 100–107.

[5] Hattori, T., and Watanabe, T., "Fracture Mechanics Analyses of Fretting Fatigue Cracks Considering Propagation Directions," *Proc. Eur. Conf. EUROMAT 2000 on Advances in Mechanical Behavior, Plasticity and Damage*, 2000, pp. 1015–1020.

[6] Hattori, T., Nakamura, M., and Watanabe, T., "A New Approach to the Prediction of the Fretting Fatigue Life that Considers the Shifting of the Contact Edge by Wear," *Fretting Fatigue: Current Technology and Practices*, ASTM STP 1367, 2000, pp. 19–30.

[7] Hattori, T., Nakamura, M., and Watanabe, T., "Fretting Fatigue Life Simulation using Stress Singularity Parameters and Fracture Mechanics," *Materials Science Research International*, STP-1, 2001, pp. 208–215.

[8] Johnson, K. L., *Contact Mechanics*, Cambridge University Press, Malta, 1994.

[9] Fellows, L. J., Nowell, D., and Hills, D. A., "Contact Stresses in a Moderately Thin Strip (with Particular Reference to Fretting Experiments)," *Wear*, Vol. 185, 1995, pp. 235–238.

[10] Fett, T., and Munz, D., "Influence of Stress Gradients on Failure in Contact Strength Tests with Cylinder Loading," *Eng. Fract. Mech.*, Vol. 69, No. 12, 2002, pp. 1353–1361.

[11] Tada, H., Paris, P. C., and Irwin, G. R., *The Stress Analysis of Cracks Handbook*, ASTM Press, 2000.

[12] STRESSCHECK© Master Guide, Engineering Software Research and Development, Inc. (ESRD, Inc.), St. Louis, Missouri, www.esrd.com

[13] Páczelt, I., Szabó, B., and Szabó, T., "Solution of Contact Problem Using the *hp*-Version of the Finite Element Method," *Comput. Math. Appl.*, Vol. 39, 1999, pp. 49–69.

[14] Szabó, B., and Babuška, I., *Finite Element Analysis*, John Wiley & Sons, Inc., New York, 1991.

Journal of ASTM International, April 2006, Vol. 3, No. 4
Paper ID JAI13232
Available online at www.astm.org

Kazuhiko Okuya[1] *and Yoshiyuki Kondo*[2]

The Effect of Large Strain Cycling on the Fatigue Strength of Welded Joint

ABSTRACT: Earthquakes sometimes create damages to steel structures. The structures which have not been seriously damaged are still used after an earthquake. The fatigue strength of these structures, however, might have been decreased due to the cyclic loads during an earthquake. In order to clarify the effect of seismic loading on the fatigue strength of the welded joint of a steel structure, a high cycle fatigue test of welded joint after large straining was performed. Although a large residual tensile stress induced by plastic deformation caused little effect on the fatigue limit even in gross plasticity condition, the cyclic application of large strain substantially decreased the fatigue limit. An application of large straining for a small number of cycles initiated a short crack at the weld toe in the low cycle fatigue manner, which acted as a trigger for high cycle fatigue failure after seismic loading. The reduction of fatigue limit depended on the size of the crack. The linear elastic fracture mechanics was used to evaluate the fatigue strength of welded joint. Although the short crack was initiated by cyclic application of plastic straining and the crack was in gross plasticity, the ΔK_{th} of the small crack determined the fatigue limit of small-cracked welded joint after seismic loading.

KEYWORDS: welded joint, cyclic large strain, fatigue strength, fatigue limit, pre-crack, crack closure

Introduction

Steel structures, such as buildings and bridges, are subjected to uctuating loads. In countries where earthquakes frequently occur, steel structures sometimes collapse during a large-sized earthquake. An example of fracture of a steel structure was reported in the damage investigation of the South Hyogo earthquake in Japan [1,2]. In these reports, it was shown that brittle fracture was triggered by fatigue crack which was initiated by very low cycle fatigue at the stress concentration of a welded joint. Steel structures which did not collapse even after a large earthquake are still currently used. Among them, some structures are used with reduced strength than that before the earthquake. Many investigations have been done and reported on the effect of variable loading on the fatigue strength of structures and various factors which affect the fatigue behavior were pointed out [3]. However, few investigations have been done on the residual fatigue strength after large strain cycling which enters into gross plasticity. The peculiar characteristics of seismic loading is the application of extremely large strain cycling which exceeds the yield point with a relatively small number of cycles. These strain cycles initiate small fatigue cracks at a notched part, which reduces the fatigue strength.

The objective of this study is to clarify the integrity evaluation method of steel structures which experienced seismic loading. The high cycle fatigue test of a welded joint which had been subjected to a large cyclic strain as a simulation of a seismic loading was conducted and the residual fatigue strength was investigated.

Manuscript received May 23, 2005; accepted for publication September 25, 2005; published online March 2006. Presented at ASTM Symposium on Fatigue and Fracture Mechanics: 35th Volume on 18 20 May 2005 in ; R. E. Link and K. M. Nikbin, Guest Editors.

[1] Professor, Department of Residential and Architectural System Engineering, Kyushu Polytechnic College, Fukuoka, 802-0985, Japan.

[2] Professor, Department of Intelligent Machinery and Systems, Kyushu University, Fukuoka, 819-0395, Japan.

Copyright © 2006 by ASTM International, 100 Barr Harbor Drive, PO Box C700, West Conshohocken, PA 19428-2959.

TABLE 1—*Chemical compositions of materials (wt %).*

Material	C	Si	Mn	P	S	Ceq
SN400B(12 mm)	0.14	0.13	0.71	0.018	0.008	0.27
SN400B(32 mm)	0.11	0.24	1.22	0.013	0.003	0.33

Experimental Procedures

Test Specimen and Test Material

The material used was a rolled steel for architectural construction designated as SN400B in the Japan Industrial Standard. This steel is often used for welded joints in steel structures. The chemical composition and mechanical properties are shown in Tables 1 and 2, respectively. The configuration of the test specimen is shown in Fig. 1.

Two steel plates with thicknesses of 32 and 12 mm were welded by the automatic CO_2 gas shielded welding. The welding method was the both-side fillet welding with one layer. The welded plate was machined into the shape shown in Fig. 1. The welding wire designated as JIS Z 3312, YGW18, with a 1.4 mm diameter was used. The welding conditions were as follows: welding current of 300 A, welding voltage of 31 V, welding velocity of 245 mm/min, distance of 20 mm between the tip base material, gas flow rate of 20 L/min, and wire electrode extension of 15 mm with downward position welding.

Testing Apparatus

The fatigue testing machine is shown in Fig. 2. One side of the specimen was fixed to the bed and a cyclic uniform bending moment was applied at the other end. The cyclic bending moment was given to the specimen by the arm and the deflection generated by motors at its end. The large cyclic strain simulating seismic loading was given by the up and down movement generated by the stepping-motor. The high frequency cyclic bending moment was generated by the cyclic displacement by the eccentric cam. The high cycle fatigue test was done at a frequency of 28 Hz. The control condition was the displacement control at the cam location. The loading condition was adjusted based on the strain measured by a strain gage pasted on each specimen. The loading condition of the high cycle fatigue test was expressed by $E\varepsilon_a$ using the measured strain amplitude ε_a and Young's modulus E. 206 GPa was used for E. The nominal strain was measured by the strain gage pasted 20 mm from the weld toe. In the case of testing apparatus in this study, the distribution of the bending moment was uniform in the longitudinal direction of the specimen. The stress distribution calculated using the finite element method showed that the stress 20 mm away from the weld toe was not affected by the stress concentration of the weld toe, which confirmed that the strain measured at this location gives a nominal strain.

Considering the capability of nondestructive inspection in steel frame structures, such as penetrant test or ultrasonic test, the definition of fatigue life in this test was determined as the point when the fatigue

TABLE 2—*Mechanical properties of materials.*

Material (Thickness)	Yield Stress (MPa)	Tensile Strength (MPa)	Elongation (%)
SN400B(12 mm)	288	431	29
SN400B(32 mm)	302	440	31

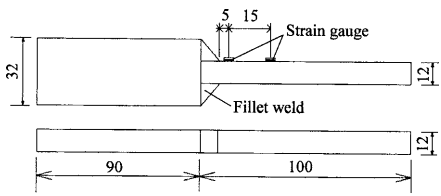


FIG. 1—*Fatigue test specimen (dimensions are in mm).*

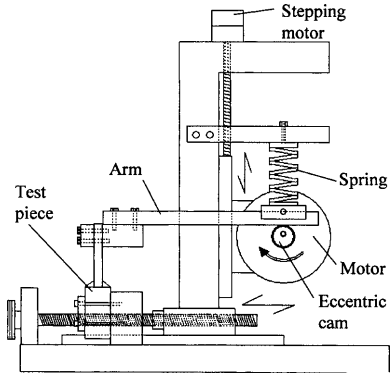


FIG. 2—*Fatigue testing machine.*

crack became 1 mm deep. Since the measurement of crack initiation by visual inspection was difficult, a compliance method was used. Another strain gage was pasted 5 mm from the weld toe to measure the compliance change due to the crack growth. As the crack depth increased, the strain near the crack was released. The relation between the reduction ratio of strain amplitude and the crack depth was determined in calibration tests. A 6 % reduction of the strain amplitude corresponded to the crack depth of 1 mm. The actual crack depth was measured on each fracture surface which was opened after the test. The fatigue limit was defined as the run-out at 10^7 cycles. The fatigue test was done at an ambient temperature in air.

Constant Amplitude Fatigue Test Results

Test Method

A large-sized earthquake may induce plastic deformation in structure components. Some components deform and are constrained at the deformed position. The others deform and then return to the original position. In both cases, a large residual stress plastically can be generated. Therefore, the knowledge about the effect of residual strain on the fatigue strength is important for the evaluation of integrity after an earthquake. A constant amplitude high cycle fatigue test was conducted under four levels of mean strains, i.e., 0, 1, 3, and 5 %.

Effect of Mean Strain in Constant Amplitude Fatigue

Figure 3 shows the results of high cycle fatigue tests at four levels of mean stains. The *S-N* curve of 0 % mean strain is usually used as a standard in fatigue design. The welded joint used in this study is classified

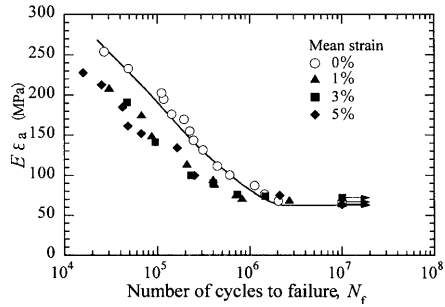


FIG. 3—*Effect of mean strain on the S-N behavior.*

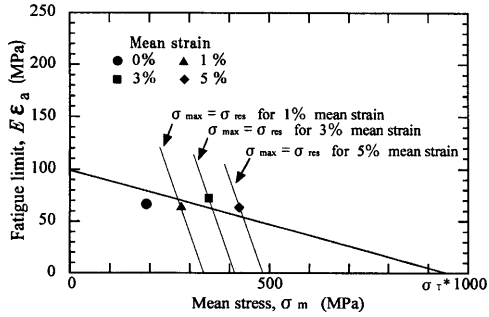


FIG. 4—*Effect of mean strain on fatigue limit.*

as a fillet welded joint without surface finish, load transfer type, and toe failure type according to the fatigue design guideline of the Japanese Association of Steel Structure [4]. In the guideline, the allowable stress amplitude $\Delta\sigma_f/2$ at 2×10^6 cycles is 32.5 MPa. The test result showed that the specimen in this study satisfied the guideline. As shown in the figure, the fatigue limits were not influenced even by large mean strains exceeding the yield point. However, the fatigue life was reduced by the existence of 1–5 % mean strain.

The reason why mean strains had little effect on the fatigue limit was examined in the fatigue limit diagram. Residual stresses were measured near the weld toe as follows. At first, each specimen was loaded at 0, 1, 3, and 5 % static strain and the strain gage was pasted 1 mm apart from the weld toe. The residual stress was released by cutting the specimen close to the strain gage. The measured residual stress was regarded as the mean stress and plotted in the fatigue limit diagram in Fig. 4. High residual stress existed even in 0 % mean strain specimen. Higher residual stress was detected in the specimen with higher mean strain. However, since the slope of the fatigue limit diagram was not so steep, mean strain had little influence on the high cycle fatigue limit. Figure 5 shows the macro-structure near the weld toe. The crack initiated at the weld toe and propagated into the base metal. Vickers hardness Hv (0.5 N) before the fatigue test was 180 at the weld toe, 220 at the heat affected zone and 125 at the base metal, respectively. Figure 6 shows an example of 1 mm deep crack observed in a fatigue test. The crack was almost two-dimensional.

Fatigue Strength after Large Cyclic Straining

Test Method

The effect of large strain cycling simulating seismic loading on the residual fatigue strength of a welded joint was investigated. A high cycle fatigue test was conducted on specimens which were initially sub-

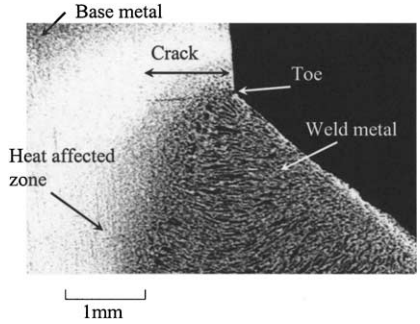


FIG. 5—*Fatigue crack shape of constant amplitude test.*

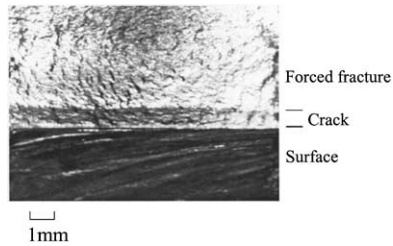


FIG. 6—*Crack shape of high cycle fatigue after large straining.*

jected to the large cyclic strains for a given number of cycles. Two types of mean strain conditions were used in the following high cycle fatigue test. The pattern A is shown in Fig. 7(*a*). The mean strain was chosen as the maximum strain in the large strain cycling by assuming that the strain after the earthquake is constrained at the maximum value in the earthquake. In pattern B shown in Fig. 7(*b*), the strain was constrained at zero.

Crack Growth Behavior in Large Strain Cycling

The fatigue crack propagation behavior in large strain cycling was examined. The relation between crack depth and number of cycles is shown in Fig. 8. Multiple specimens were used and each plot in the figure corresponds to each specimen. The crack depth was measured on the fracture surface. A few hundred cycles of 1 % strain generated a few tenths mm deep crack.

The stress state in the large straining was in elasto-plastic condition. It was examined whether existing fracture mechanics can predict the crack growth behavior under large cyclic straining shown in Fig. 8. The use of *J*-integral in real engineering application is not easy for the welded joint. Therefore, the applicability of $\Delta\varepsilon(\pi a)^{1/2}f(a)$ was examined considering the easy application to variable loadings. The result is shown in Fig. 9. It gave a sufficiently good result for a crack emanating at the notch root of the welded joint even in elasto-plastic condition.

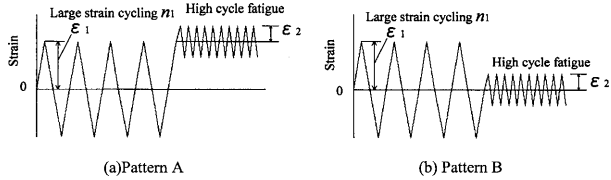


FIG. 7—*High cycle fatigue test after cyclic large straining.*

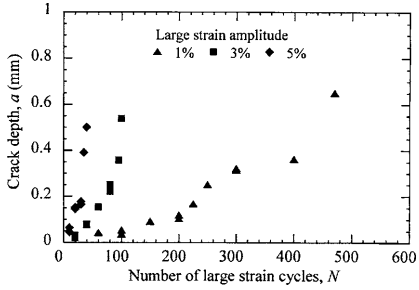


FIG. 8—*Fatigue crack growth by large straining.*

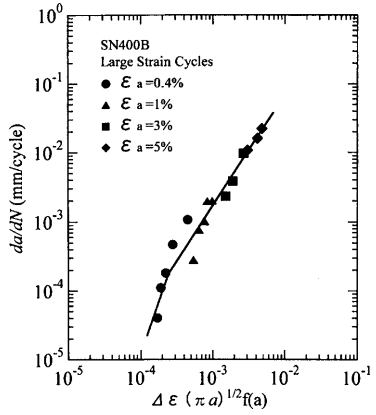


FIG. 9—*Fatigue crack propagation rate under large straining.*

The accuracy of prediction on the crack growth behavior was examined. Assuming the initial crack depth a_i as 0.02 mm, the crack growth was calculated on the basis of linear accumulation of cycle-by-cycle crack growth amount as shown in Fig. 10. Each symbol shows the experimental result. The prediction accuracy was within a factor of two. Using this tool, we are now able to estimate the fatigue crack growth behavior in the welded joint even for the large scale yielding condition.

Effect of Cyclic Large Strain in Strain Pattern A

A fatigue test on the strain pattern A was performed. An example of crack surface in this test is shown in Fig. 11. A few tenths mm deep fatigue crack was generated in the low cycle manner by the large strain cycling, which acted as a pre-crack for the following high cycle fatigue. Both cracks propagated as a two-dimensional crack.

Figure 12 shows the *S-N* curves for specimens of strain pattern A in which the large cyclic strain amplitude was 1 % and the mean strain of the high cycle fatigue was 1 %. The application of several hundreds of cycles of 1 % strain substantially decreased the residual fatigue strength, which did not satisfy the permissible stress amplitude.

Figures 13 and 14 show the results for other strain amplitudes 3 % and 5 %, respectively. As shown in the figures, the fatigue strength as well as fatigue life decreased as the number of cycles of large straining increased. This is because the depth of the crack generated by the cyclic large straining increased as the number of cycles increased.

The depths of nonpropagating cracks were measured on the specimens that run-out 10^7 cycles. The relation between the depth of nonpropagating crack and the fatigue limit is shown in Fig. 15. For cracks

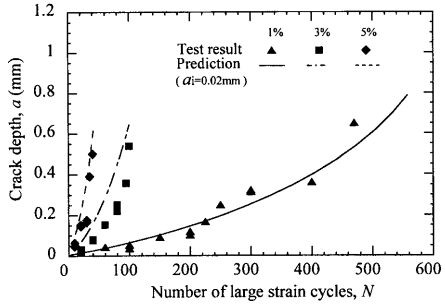


FIG. 10—*Prediction and the test results of fatigue crack propagation.*

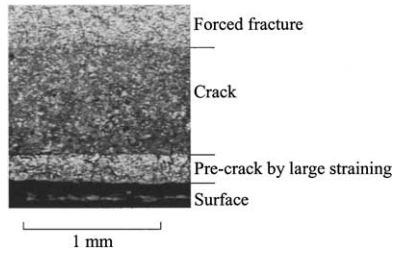


FIG. 11—*Example of crack in high cycle fatigue after large straining.*

deeper than 0.2 mm, the slope was −1/2, which means that the fatigue strength after large straining is governed by the stress intensity factor range of the crack initiated by the large straining. Although the crack was in gross plasticity condition, the fatigue strength could be evaluated using the elastic fracture mechanics parameter. On the other hand, the slope was smaller for crack shallower than 0.2 mm. It was suggested that the characteristic of a short crack appeared in a shallow crack.

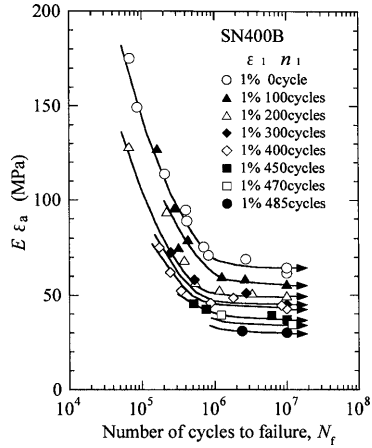


FIG. 12—*High cycle fatigue behavior of 1 % cyclically strained specimen in pattern A.*

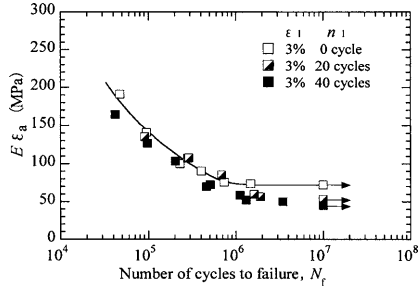


FIG. 13—*Fatigue behavior of 3 % cyclically strained specimen in pattern A.*

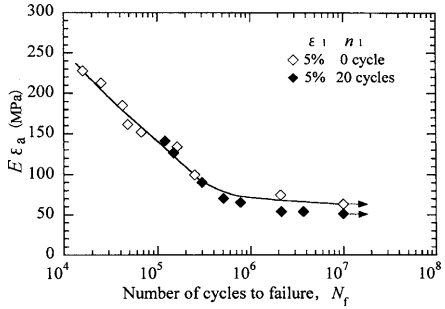


FIG. 14—*Fatigue behavior of 5 % cyclically strained specimen in pattern A.*

Effect of Cyclic Large Strain in Strain Pattern B

Fatigue tests for strain pattern B shown in Fig. 7(*b*), in which the strain after an earthquake returns to the original position, were done. Fatigue test results are shown in Fig. 16, in which the previous fatigue test results with a positive mean strain were also plotted for comparison. Little difference was observed. In Fig. 17, the relation between fatigue limit and nonpropagating crack depth obtained in both tests were plotted. Little difference can be seen. It is noted that the mean strain has little influence on the high cycle fatigue limit.

To make clear the reason why there was little influence of mean strain in the high cycle fatigue limit, the residual stress and the crack closure behaviors were measured. The residual stress at the weld toe for the condition in which the strain of large strain cycling was returned to zero was measured. The residual stress was 377 MPa. It was found that the positive residual stress at the weld toe after cyclic straining was almost equal to the yield stress.

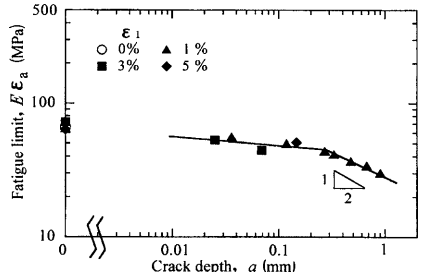


FIG. 15—*Relation between nonpropagating crack depth and fatigue limit in pattern A.*

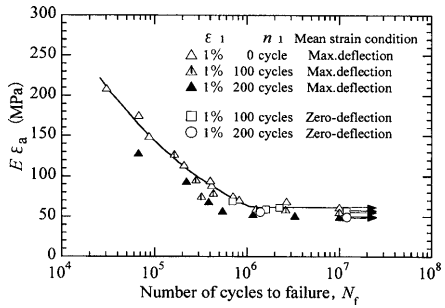


FIG. 16—*Fatigue behavior of 1 % cyclically strained specimen in pattern B.*

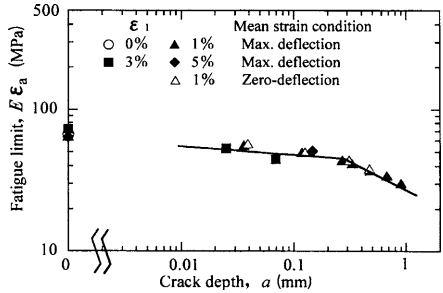


FIG. 17—*Relation between nonpropagating crack depth and fatigue limit in pattern B.*

The crack closure behavior was measured using the unloading elastic compliance method [5]. The strain gage was attached as shown in Fig. 18. Figure 19 shows the hysteresis loops measured by the unloading elastic compliance method by changing the mean strain to search the crack closure point. It was found that the offset hysteresis curve began to bend at the nominal strain of 1600×10^{-6} in compressive side and that the crack was fully open down to the compressive yield stress. These observations indicated that the crack generated by the large straining was fully open for high cycle loading in both strain pattern A and B. The same high cycle fatigue strength after large cyclic straining with different mean strain was attributed to the fact that the crack was fully open due to the high tensile residual stress in both cases.

Evaluation of the Fatigue Limit of Cracked Materials by Fracture Mechanics

The fatigue limit of the specimen with a small crack was evaluated based on fracture mechanics. The stress intensity factor of the cracked specimen was calculated using the finite element method. Figure 20 shows the crack model. NASTRAN was used as the FEM code. Since the shape of the crack was two-dimensional as experimentally confirmed in Fig. 12, two-dimensional elastic analysis was done. The quadrilateral plane stress element was used. The notch radius of the weld toe was also modeled. The minimum distance between nodes near the crack tip was 0.002 mm. Calculated results are shown in Fig. 21. The correction factor of the stress intensity factor of a crack emanating at the weld toe was affected by the stress concentration of the weld toe in short crack region. It was decreased and tended to level off in cracks longer than 0.5 mm.

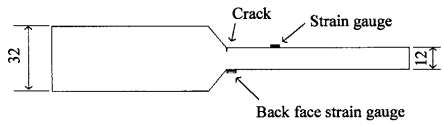


FIG. 18—*Strain gage arrangement.*

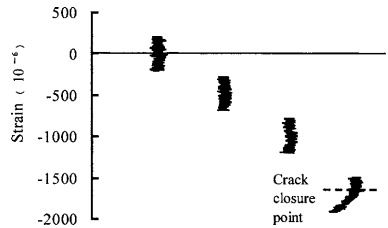


FIG. 19—*Crack closure behavior of zero strain specimen measured by unloading elastic compliance method.*

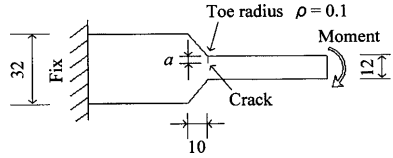


FIG. 20—*FEM model (dimensions are in mm).*

The threshold stress intensity factor $\triangle K_{th}$ calculated using the nonpropagating crack depth and the fatigue limit is shown in Fig. 22. ΔK_{th} was almost constant and equal to the long crack data for cracks deeper than 0.2 mm. ΔK_{th} decreased for cracks shallower than 0.2 mm. The hatched zone indicates the effective threshold stress intensity factor range $(\Delta K_{eff})_{th}$ obtained in the previous study [6–8]. The crack initiated by large cyclic straining was always open in the high cycle fatigue due to the large positive residual stress at the weld toe. This is the reason why the threshold stress intensity factor ΔK_{th} of crack at the weld toe agreed with the effective threshold intensity factor $(\Delta K_{eff})_{th}$ of base material shown by hatched zone. Since the data obtained in this experiment on the welded joint are within the range of the previous data, it can be said that the threshold stress intensity factor including the short crack characteristic was the governing factor of the residual high cycle fatigue limit after large cyclic straining.

Conclusions

The structures which have not been seriously damaged are still used after earthquakes. The fatigue strength of these structures might have been decreased due to the seismic loading. In order to clarify the effect of large cyclic straining by seismic loading on the fatigue strength of the welded joint, high cycle fatigue tests after large cyclic straining was conducted using a low strength steel SN400B which is used in architectural construction. Obtained results are as follows.

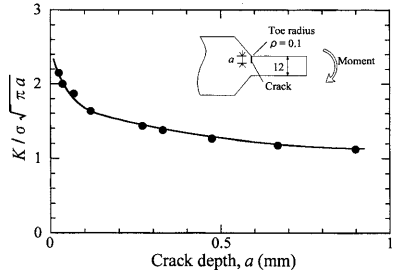


FIG. 21—*Correction factor of stress intensity factor for a crack in welded joint.*

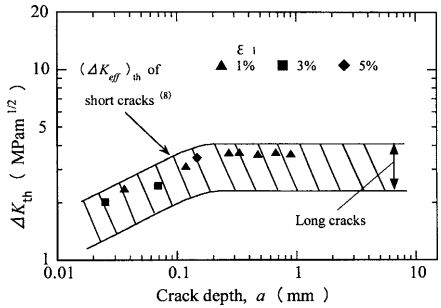


FIG. 22—*Relation between crack depth and threshold stress intensity factor range* ΔK_{th}.

1. The large residual tensile stress induced by plastic deformation due to seismic loading had little effect on the fatigue limit even in gross plasticity condition.
2. The cyclic application of large strain substantially decreased the fatigue limit of the welded joint. Application of large straining for a small number of cycles initiated short crack at the weld toe in the low cycle fatigue manner, which acted as a trigger for the high cycle fatigue failure after seismic loading. The reduction of fatigue limit depended on the depth of fatigue crack.
3. Although the short crack was generated by the cyclic application of large plastic strain and the crack was in gross plasticity condition, it was shown that the ΔK_{th} of small crack determined the fatigue strength of small-cracked welded joint after seismic loading.
4. Effect of mean strain on the fatigue limit after large cyclic straining was not remarkable. The reason for this effect was attributed to the fact that the cracks were fully open because of tensile residual stress.

References

[1] Architectural Institute of Japan, The Japan Society of Mechanical Engineers, Report on the Hanshin-Awaji Earthquake Disaster, 1997, pp. 13–19, pp. 22–50, pp. 68–99.
[2] Architectural Institute of Japan, 1995HYOUGOKEN Southern Earthquake of an Investigation News Flash of Accident, 1995, pp. 63–65.
[3] The Society of Materials Science, Japan, *Fatigue Design Manual*, 1995, pp. 204–240, pp. 408–412.
[4] Japanese Society of Steel Construction, "Fatigue Design Pointer of Steel Structure and Commentaries," 2001, pp. 5–11, pp. 21–38.
[5] Kikukawa, M., Jono, M., Tanaka, K., and Takatani, M., *Proceedings of ICM-II*, Boston, special volume, 1976, pp. 254–277.
[6] Kashiwagi, M., Kudou, T., Kubota, M., Sakae, C., and Kondo, Y., *Journal of the Society of Materials Science, Japan* (in Japanese), Vol. 52, 2003, pp. 1345–1350.
[7] Kondo, Y., Sakae, C., Kubota, M., and Kudou, T., *Fatigue and Fracture of Engineering Materials and Structures*, Vol. 26, 2003, pp. 675–682.
[8] Kondo, Y., *Materials Science Forum*, Vol. 482, 2005, pp. 89–94.

Journal of ASTM International, Vol. 3, No. 7
Paper ID JAI100348
Available online at www.astm.org

P. Dong[1] *and J. K. Hong*[2]

A Robust Structural Stress Parameter for Evaluation of Multiaxial Fatigue of Weldments

ABSTRACT: In this paper, the applicability of a new mesh-insensitive structural stress method is examined for the evaluation of multiaxial fatigue behaviors in welded joints. The mesh-insensitive structural stress method proves to be effective in characterizing stress concentration effects in multi-axial fatigue of welded components. In seeking an effective structural stress based fatigue parameter, some well-known published test data were analyzed. These include those published by researchers, e.g., from the Electric Power Research Intitute (EPRI), the Fraunhofer-Institute for Structural Durability (LBF), the University of Illinois at Urbana-Champaign (UIUC), and the Welding Institute (TWI) under bending, torsion, and in-phase and out-of-phase loading combinations. An effective structural stress parameter has then been formulated in a form of a proposed modified Gough's ellipse for considering both in-phase and out-of-phase multiaxial loading conditions. The aforementioned multiaxial fatigue data from a total of five independent sources can be effectively correlated with a structural stress based parameter presented in this paper, without introducing any other material-related empirical parameters. The present method is rather simple to use for day-to-day finite element based fatigue evaluation of welded joints in actual structures subjected to multiaxial loading conditions.

KEYWORDS: multiaxial fatigue, mesh-insensitive structural stress method, modified Gough's ellipse, finite element analysis, welded joint

Introduction

The effectiveness of a new mesh-insensitive structural stress method has been demonstrated in a series of recent publications [1–5] for consistently capturing stress concentration effects on fatigue behaviors of welded joints. With the mesh-insensitive structural stress method, a single master S-N curve has been developed for assessing a large number of joint types, loading modes, and plate thicknesses [2], which otherwise are typically characterized by a family of a large number of S-N curves in weld classification approach [6]. As a result, the method has been adopted by ASME Div 2 Rewrite [2] for fatigue evaluation of welded piping and vessel components.

A natural question to pose here is, "Can the mesh-insensitive structural stress method can be used to evaluate multiaxial fatigue behaviors of welded joints?" Along this line, a large amount of multiaxial fatigue test data published in the literature was investigated in this study, including the multiaxial fatigue data published by LBF [7], University of Illinois [8], TWI [9], and EPRI [10], etc. All these tests were conducted using tube-to-flange welded specimens with circumferential fillet welds. The loading conditions were mostly bending/torsion combinations, except that TWI used tension/torsion combinations [9].

Through a detailed review of the published data on weldments and associated fatigue damage models in the literature, as far as weld toe cracking is concerned, some of the important observations regarding multiaxial fatigue issues associated with welded joints may be summarized as follows, including proportional loading (in-phase) or nonproportional loading (out-of-phase):

1. Fatigue crack tends to originate from a weld toe (e.g., in full penetration welds) and propagates into the base plate thickness in approximately the same plane as typically observed under uniaxial dominated loading conditions, at least for the majority of the life. This fact that failure of welded joints tends to follow a distinct failure mode (both location and orientation) further illustrates the fundamental difference between fatigue of welds and that of plain metals (or base

Manuscript received April 22, 2005; published online June 2006. Presented at ASTM Symposium on Fatigue and Fracture Mechanics, 35th Volume on 18–20 May 2005 in Reno, NV; R. E. Link and K. M. Nikbin, Guest Editors.
[1] Center for Welded Structures Research, Battelle, 505 King Avenue, Columbus, OH 43201, e-mail: dongp@battelle.org
[2] Center for Welded Structures Research, Battelle, 505 King Avenue, Columbus, OH 43201.
Copyright © 2006 by ASTM International, 100 Barr Harbor Drive, PO Box C700, West Conshohocken, PA 19428-2959.

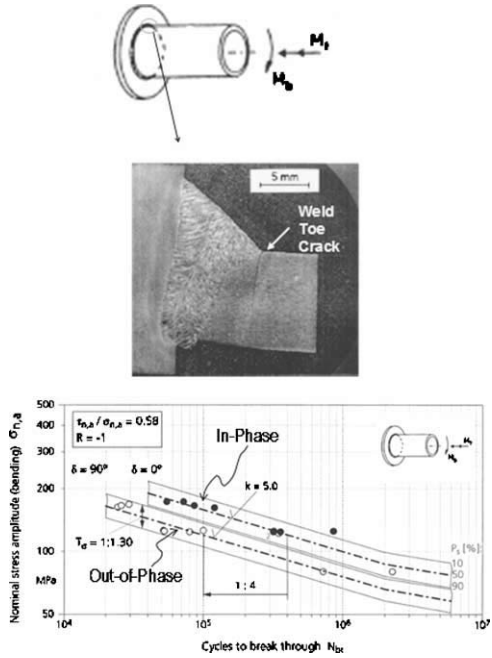


FIG. 1—*Typical test specimens and fatigue failure observations on multiaxial fatigue behavior in welded joints [7].*

materials) without welds. For dealing with applications without welds, there are a number of well-known multiaxial fatigue damage models available in the literature, including those by Dang Van et al. [11], Papadopoulos [13], and others. The former [11] represents the classical critical plane method on crack initiation due to multiaxial stress state. However, the method does not calculate fatigue lives, but determines if a component will have infinite life. The method by Papadopoulos [13] is representative of the more recent integral-based approaches of the critical plane type on crack initiation. As discussed above in the context of welded joints, fatigue failures investigated in this paper are best described by through-thickness failures, which is propagation-dominated fatigue phenomenon [6]. Therefore, further discussions on existing multiaxial fatigue approaches in the literature will be focused upon those more relevant to fatigue failures associated with welded joints, such as those by Sonsino and Kueppers [7] and those reviewed recently by Backstrom and Marquis [14,15], etc.

2. Another well-known observation is that in-phase bending plus torsion loading seems more damaging than bending only, as shown in Fig. 1 in which nominal stress amplitude versus cycles to failure is shown in log-log scale. Note that under combined loading (bending plus shear), the largest nominal stress amplitude of the two is used by Sonsino and Kueppers [7] in Fig. 1. In addition, out-of-phase loading is more damaging than in-phase under bending (or tension) combined with torsion, as shown in Fig. 1.

In what follows, we start with a brief introduction to the mesh-insensitive structural stress method, which is provided with respect to the joint types and multiaxial loading conditions of interest in this investigation. Then, some of the typical effective stress definitions used in the literature for characterizing multiaxial fatigue of welded joints are examined to compare their abilities in correlating the multiaxial fatigue data. In-phase loading is considered first. Out-of-phase loading is then investigated by introducing a modified Gough's ellipse. An effective structural stress parameter is then formulated based on the modified Gough's ellipse with consideration of both multiaxial in-phase and out-of-phase loading. Finally,

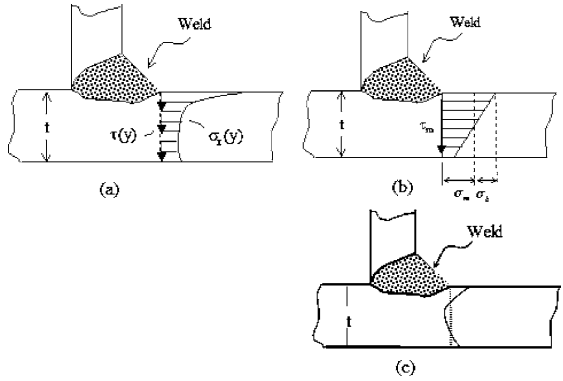


FIG. 2—*Through-thickness structural stresses definition: (a) local stresses from FE model; (b) structural stress or far-field stress; (c) self-equilibrating stress.*

the effectiveness of the structural stress based parameter in correlating the existing multiaxial fatigue data from a total of five independent sources available in the open literature will be demonstrated.

The Structural Stress Method

It has been a typical practice in performing finite element analysis of welded structures for fatigue evaluation that a sharp weld toe (i.e., with a zero toe radius) is assumed in finite element based idealization of a welded joint [2,6]. As a result, the stresses at the weld toe become singular, resulting in so called mesh-size sensitivity. To overcome such a difficulty, various national or international bodies such as the International Institute of Welding (IIW) have introduced surface extrapolation based hot spot stress procedures (e.g., see [6]). However, all these surface-stress based extrapolation procedures suffer a similar mesh-size sensitivity in stress concentration calculations at welded joints, as demonstrated by a large number of publications in the literature, as cautioned in the IIW recommendations in [6] and summarized recently in [2–6,16]. The mesh-insensitive structural stress method developed by the authors follows a different approach and its effectiveness has been validated over a thousand joint types and geometries from more than five industries [2–6]. A brief summary on how the mesh-insensitive structural stress method works is given below. Further details can be found in [1–6].

The Formulation

The essence of the new structural stress method was based on the following considerations for fatigue evaluations of welded joints [1–4]:

1. It was postulated that stress concentration at a fatigue prone location, such as a weld toe as shown in Fig. 2(*a*), can be represented by an equilibrium-equivalent simple stress state [as shown in Fig. 2(*b*)] and self-equilibrium stress state [as shown in Fig. 2(*c*)]. The former describes a stress state corresponding to an equivalent far field stress state in fracture mechanics context [3], or simply, a generalized nominal stress state at the same location, while the latter can be estimated by introducing a characteristic depth, as shown in detail in [3].
2. Within the context of displacement-based finite element methods, the balanced nodal forces and moments within each element or a group of elements always satisfy the equilibrium conditions at every nodal position. Stresses, however, do not have to satisfy the equilibrium conditions at nodes or across element boundaries, particularly at notch locations. Therefore, the equilibrium-equivalent structural stress state in the form of membrane and bending can be calculated by using the nodal forces/moments at a location of concern from a finite element model, instead of using stresses directly.

The application of the nodal force based structural stress method [1–4] is straight forward in dealing with

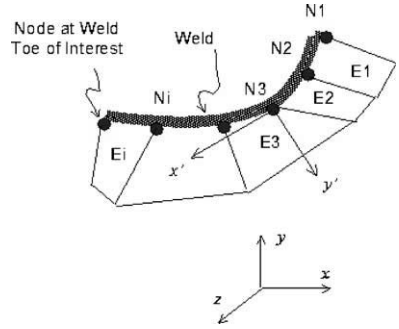


FIG. 3—*Mesh-insensitive structural stress calculation procedure for an arbitrarily curved weld using shell/plate element models.*

both uniaxial [3,4] and multiaxial loading conditions in structures where plate and shell theory is applicable. As shown in Fig. 3 for an arbitrarily curved weld in space, with respect to the local x'-y'-z' coordinate system (note that the balanced nodal forces from a finite element model are retrieved with respect to a fixed global x-y-z coordinate system), the nodal forces (F_i) at the nodal positions along a weld line can be related to the line forces (f_i) in the form of the following matrix equations [1–4] for linear element models

$$\begin{Bmatrix} F_1 \\ F_2 \\ F_3 \\ \vdots \\ \vdots \\ F_{n-1} \end{Bmatrix} = \begin{bmatrix} \frac{(l_1+l_{n-1})}{3} & \frac{l_1}{6} & 0 & 0 & \cdots & \frac{l_{n-1}}{6} \\ \frac{l_1}{6} & \frac{(l_1+l_2)}{3} & \frac{l_2}{6} & 0 & \cdots & 0 \\ 0 & \frac{l_2}{6} & \frac{(l_2+l_3)}{3} & \frac{l_3}{6} & 0 & \vdots \\ 0 & 0 & \ddots & \ddots & \ddots & 0 \\ \vdots & \ddots & 0 & \frac{l_{n-3}}{6} & \frac{(l_{n-3}+l_{n-2})}{3} & \frac{l_{n-2}}{6} \\ \frac{l_{n-1}}{6} & \cdots & 0 & 0 & \frac{l_{n-2}}{6} & \frac{(l_{n-2}+l_{n-1})}{3} \end{bmatrix} \begin{Bmatrix} f_1 \\ f_2 \\ f_3 \\ \vdots \\ \vdots \\ f_{n-1} \end{Bmatrix} \quad (1)$$

Equation 1 represents the relationship between the balanced nodal forces along a line of nodes (i.e., weld line) and line forces at these nodes, which satisfies both work-equivalent and traction continuity conditions. For normal structural stress (normal to the weld line in the y' direction) calculations (Fig. 4), the nodal force vector on the left-hand side of Eq 1 is to be substituted by nodal force F_i in the y' direction (Fig. 3) to obtain the line force in y' and by nodal moment M_i with respect to x' to obtain the line moment m_i. Then, the normal structural stress is expressed in the context of elementary structural mechanics theory as

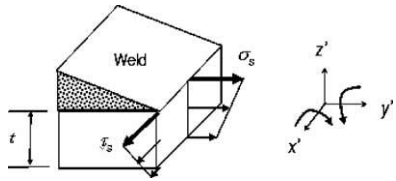


FIG. 4—*Structural stress definitions with respect to the local coordinate (x'-y'-z') for both normal and in-plane shear components corresponding to weld toe failure.*

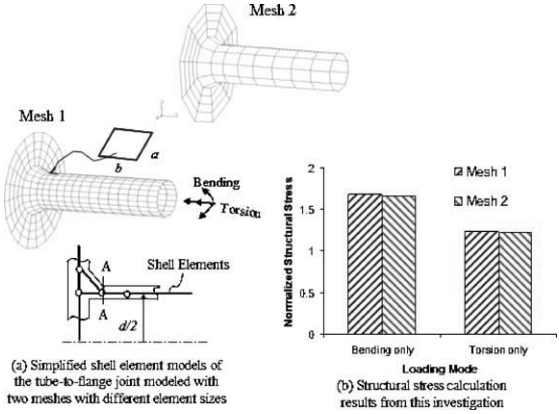


FIG. 5—*Mesh-insensitivity demonstration in the structural stress calculation using the present calculation procedure for the flange-to-tube fillet weld specimens tested by Sonsino and Kueppers [7]. (a) Simplified shell element models of the tube-to-flange joint modeled with two meshes with different element sizes. (b) Structural stress calculation results from this investigation.*

$$\sigma_s = \sigma_m + \sigma_b = \frac{f_{y'}}{t} - \frac{6m_{x'}}{t^2} \tag{2}$$

By the same token, the nodal shear forces along x' and nodal twisting moments with respect to y' can be used to obtain the corresponding shear line force and twisting line moments for all nodes along the weld line. Then, the in-plane shear structural stress (Fig. 4) can be simply expressed as

$$\tau_s = \tau_m + \tau_b = \frac{f_{x'}}{t} + \frac{6m_{y'}}{t^2} \tag{3}$$

The corresponding structural stress state in terms of both the normal components (σ_m, σ_b) and in-plane shear components (τ_m, τ_b) are illustrated in Fig. 4 for evaluating weld toe fatigue cracks. Other failure modes, e.g., weld root cracking, can be evaluated in a similar manner with respect to their respective hypothetical crack planes. In most shell or plate structures, the transverse shear (in the z' direction in Fig. 3) can be ignored.

Calculation Examples

The structural stress method described in Eqs 1 and 2 for calculating the normal structural stress component (Eq 2) has been extensively validated for many joint types and loading conditions [2–5]. For a validation of the mesh insensitivity of the structural stress calculation procedure for multiaxial loading conditions, two relevant calculation examples are given below.

Tube to Flange Joint—The tube-to-flange joint described in Fig. 1 is used here to demonstrate the effectiveness of the present structural stress method in characterizing stress concentration characterization under both simple pure bending and pure shear loading conditions. As shown in Fig. 5, two three-dimensional (3D) shell models of rather different element sizes [see Fig. 5(*a*)] were used to compute the structural stress states under pure bending and pure torsion for the same component geometry and conditions investigated by Sonsino and Kueppers [7]. By all FE modeling standards, the mesh designs shown in Fig. 5(*a*) are rather coarse. The normal (bending) and in-plane shear structural stresses (normalized by their respective nominal stresses) are calculated according to Eqs 1–3 and summarized in Fig. 5(*b*). With a uniform element size of about $a \times b = 1t \times 1t$ and $2t \times 2t$ (t is the tube thickness, about 10 mm), the resulting structural stresses at the weld toe are essentially the same from the two different models with the mesh size varying from $1t \times 1t$ and $2t \times 2t$. It is worth noting that in [7], where a fine finite element model

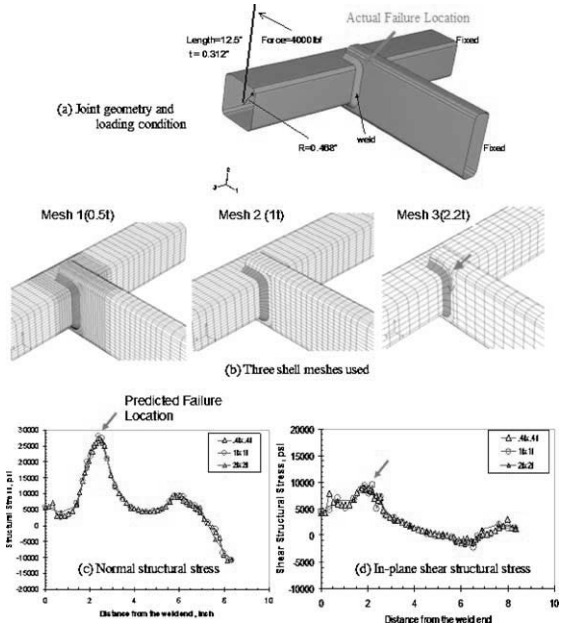


FIG. 6—*Mesh-insensitivity demonstration in the structural stress calculation—a rectangular hollow section (RHS) joint under both bending and torsion.*

with a mesh size in the order of less than 1 mm, was used for calculating surface extrapolated hot spot stress at weld toe [7], the stress calculated became the nominal stress for bending and torsion loading, respectively.

SAE FD&E RHS Joint—Figure 6(*a*) shows a rectangular hollow section (RHS) joint under complex loading conditions tested for the 2003 Society of Automotive Engineers Fatigue Design and Evaluation Committee (SAE FD&E) "weld challenge" for soliciting blind life predictions by various participants, in which the mesh-insensitive structural stress method won the Best Prediction among all participants [16]. The structural stress results shown in Figs. 6(*a*)–6(*c*) were directly taken directly from the blind life prediction contest by the authors (from the original presentation before the test results being disclosed) using the structural stress method discussed in the above. The mesh insensitivity of the structural stress calculations can be clearly seen in Fig. 6(*c*) as the shell model mesh size varies from $0.5t \times 0.5t$ to $2.2t \times 2.2t$. In this investigation, the in-plane shear structural stresses are calculated using the same models [Fig. 6(*b*)] as used in [16] and are plotted in Fig. 6(*d*) for the same weld toe line. The in-plane shear structural stress distribution shows that the peak stress location occurs exactly at the same peak location as that in Fig. 6(*c*), but of a much smaller magnitude location. In this example, the weld is subjected to both bending and shear, as shown in Fig. 6(*a*). The mesh insensitivity is obvious in both the normal and in-plane shear structural stresses along the entire weld line [Figs. 6(*c*) and 6(*d*)]. More detailed discussions on this example and life predictions using the mesh-insensitive structural stress procedure can be found in [16].

Treatment of Multiaxial Fatigue

Numerous theories and fatigue correlation parameters have been proposed in the literature, including the publications cited in the above. For instance, Sonsino and Kueppers [7] proposed a local stress based approach referred to as an equivalent effective stress hypothesis (EESH) which requires rather fine finite element (FE) mesh to determine local stresses with an assumed notch radius. The Siljander et al. [8] approach falls into a similar category, referred to as a critical plane approach. Maddox and Razmjoo [9]

TABLE 1—*Structural stress based SCFs calculated for specimens tested by five organizations as documented in the literature.*

Source	Loading mode	SS-based SCF membrane	SS-based SCF bending	SS-based SCF total
Sonsino (Stress relieved)	Bending	0.887	0.755	1.642
	Torsion	0.897	0.201	1.098
UIUC (Stress relieved)	Bending	0.795	0.624	1.419
	Torsion	0.844	0.251	1.095
Yousefi (Stress relieved)	Bending	0.905	0.819	1.724
	Torsion	0.912	0.205	1.117
EPRI (As-welded)	Bending	0.946	0.553	1.499
	Torsion	0.949	0.129	1.078
TWI (As-welded)	Torsion	0.877	0.247	1.124

and Backstrom and Marquis [14,15], recognizing that for engineering applications a local stress or strain based method may not be practical, examined both nominal stress and hot spot stress based approaches recognized by some of the existing fatigue evaluation procedures in various Codes and Standards. However, the resulting scatter bands [8,14,15] in S-N representations of the available literature data seem too large for reliable fatigue assessment.

In this investigation, the aim was to investigate the feasibility of using the mesh-insensitive structural stress parameter presented so far to correlate the existing multiaxial fatigue test data available from literature. The mesh-insensitive structural stresses calculated using Eqs 1–3 are global in nature without the need to model actual local notch geometries. From a practical application point of view, such a global stress based approach can be attractive for dealing with complex structures.

Structural Stress Characterizations

By reviewing the specimen geometries and testing conditions published in [7–10,17], the structural stress calculations by applying Eqs 1–3 for both normal and in-plane shear components are summarized in Table 1. Note that in some of the multiaxial fatigue tests, such as those by Sonsino and Kueppers [7], the stress concentration factor (SCF) can be rather sensitive to the detailed mounting conditions between the flange and "rigid support" [7]. Without such detailed information, best judgments were exercised to impose a consistent interpretation of the boundary and loading conditions based on the information provided by the publications from the four sources.

Treatment of In-Phase Loading

As a reference case, the nominal stress ranges (bending stress under bend loading and shear stress under torsion) are used to present the in-phase fatigue data from [7,10] in Fig. 7. The corresponding structural stress based SCFs are summarized in Table 1 for single loading modes. Naturally, under in-phase torsion and bending, an effective stress measure in terms of the structural stress components need to introduced. Typical effective stress definitions reported in the literature are von Mises, Tresca, or maximum principle stress definitions. Recognizing that stress range is typically typical welded joints in fatigue evaluation [6],

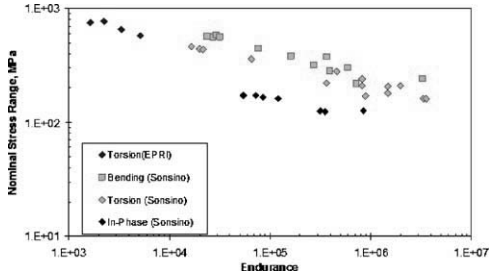


FIG. 7—*In-phase fatigue data from EPRI and LBF—nominal stress range versus cycles to failure.*

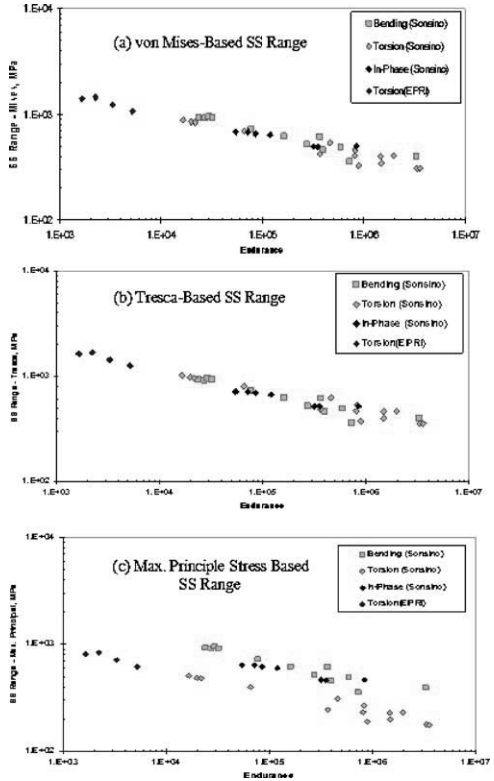


FIG. 8—*Comparison of three effective stress definitions using structural stress parameters—in-phase fatigue data from EPRI and LBF.*

one can express an effective stress range parameter according to von Mises, Tresca, and maximum principle stress definitions using the normal structural stress range $\Delta\sigma_s$ and in-plane shear structural stress range $\Delta\tau_s$ as

$$\Delta\sigma_e = \sqrt{(\Delta\sigma_s)^2 + 3(\Delta\tau_s)^2} \quad \text{(von Mises)} \tag{4}$$

$$\Delta\sigma_e = \sqrt{(\Delta\sigma_s)^2 + 4(\Delta\tau_s)^2} \quad \text{(Tresca)} \tag{5}$$

$$\Delta\sigma_e = \frac{1}{2}(\Delta\sigma_s + \sqrt{(\Delta\sigma_s)^2 + 4(\Delta\tau_s)^2}) \quad \text{(Maximum Principle)} \tag{6}$$

Obviously, for a given pair of $\Delta\sigma_s$ and $\Delta\tau_s$, the difference between the von Mises and Tresca based effective stress definitions is small. Once the structural stress based SCFs are calculated (tabulated in Table 1), the effectiveness of three effective stress definitions above can be tested in terms of their abilities to collapse the data shown in Fig. 7. The results are summarized in Fig. 8. Both von Mises and Tresca based stress range definitions are seen to be effective. However, the maximum principle stress range parameter (Eq 6) fails to provide any reasonable correlation of the same data, as shown in Fig. 8(*c*).

Treatment of Out-of-Phase Loading

In a recent publication [18], the same authors presented a feasibility study by introducing Miner's rule by considering both in-phase and out-of-phase loading as two separate events by deriving an equivalent cycle

definition for representing the out-of-phase data. Although the results in [18] showed a reasonable correlation for the data analyzed, the approach has a number of deficiencies. Chief among them is that the approach in [18] cannot differentiate the effects of the phase angle. In this investigation, the efforts were focused upon the development of an effective multiaxial fatigue parameter with the following important attributes:

1. Relying upon a global stress based parameter which can be readily computed from typical engineering finite element models used in day to day design and analysis activities by industry.
2. Offering consistency in the fatigue evaluation procedure for treating single loading mode (e.g., either bending or torsion), combined in-phase, and out-of-phase loading with explicit dependency on phase angle.
3. Requiring a minimum number of empirical parameters required in correlating test data under various joint geometries and combined in-phase and out-of-phase loading conditions.

Among various plausible hypotheses investigated, Gough's ellipse [19], typically written in the form of

$$\left(\frac{\Delta\sigma_s}{\Delta S_e}\right)^2 + \left(\frac{\Delta\tau_s}{\Delta T_e}\right)^2 = 1 \tag{7}$$

by substituting the normal and in-plane shear structural stress components $\Delta\sigma_s$ and $\Delta\tau_s$ defined in Eqs 1–3 in place of nominal bending and shear stress components. In addition, ΔS_e and ΔT_e in Eq 7 represent the fatigue limits under pure $\Delta\sigma_s$ and pure $\Delta\tau_s$ actions, respectively [19]. However, it is well known that the fatigue limits ΔS_e and ΔT_e are typically not well defined for welded joints. For instance, IIW recommendations [6] suggest that the stress range corresponding 2×10^6 cycles may be treated as the fatigue limit for a give joint type, beyond which, the same stress range does not cause damage. However, recent test data as summarized in [4] showed the S-N slope continues beyond 10^7 and 10^8 cycles.

Recognizing the effectiveness of Eq 4 in correlating the S-N data shown in Fig. 8 (the same effectiveness has also been observed for other sources of the multiaxial S-N data under both uniaxial and combined in-phase loading), one can assume the following relationship exists:

$$\left(\frac{\Delta S_e}{\Delta T_e}\right)^2 = 3 \tag{8}$$

Then, Eq 7 takes a von Mises form of Eq 4 in relating fatigue strengths between that under pure bending and that under pure torsion, as validated in Fig. 8(*a*).

For out-of-phase loading, one can hypothesize that a modified Gough's ellipse similar to Eq 7, but expressed as

$$\left(\frac{\Delta\sigma_s}{\Delta S_e}\right)^2 + \left(\frac{\Delta\tau_s}{\Delta T_e}\right)^2 = [F(\delta)]^2 \tag{9}$$

could be used to correlate both in-phase and out-of-phase multiaxial fatigue damage process. In Eq 9, $F(\delta)$ is a dimensionless parameter as a function of out-of-phase angle δ. If $F(\delta)$ becomes unity, the original Gough's ellipse (Eq 7) is realized for in-phase loading. Note that for out-of-phase loading, it has already been shown that the von Mises stress definition (Eq 4) as well as Eq 7 is not capable of correlating existing S-N data available in the literature, as discussed in [7–9,14,15,18,20].

In seeking various plausible expressions for $F(\delta)$, von Mises form of an effective stress range is again considered here. With the consideration of a given phase angle δ, the von Mises expression (or "SEQA") used in ASME Boiler and Pressure Vessel Code [21,22] can be expressed as

$$\sigma_{VM}(\delta) = \frac{1}{\sqrt{2}}\sqrt{[(\Delta\sigma_s)^2 + 3(\Delta\tau_s)^2] + \sqrt{[(\Delta\sigma_s)^2 + 3(\Delta\tau_s)^2]^2 - 12(\Delta\sigma_s)^2(\Delta\tau_s)^2\sin^2\delta}} \tag{10}$$

For in-phase loading, $\delta = 0$, Eq 10 becomes Eq 4. Thus, one simple definition of $F(\delta)$ may be expressed as

$$F(\delta) = \frac{\sigma_{VM}(\delta)}{\sigma_{VM}(\delta = 0)} = \frac{1}{\sqrt{2}}\sqrt{1 + \sqrt{1 - \frac{12(\Delta\sigma_s)^2(\Delta\tau_s)^2\sin^2\delta}{[(\Delta\sigma_s)^2 + 3(\Delta\tau_s)^2]^2}}} \tag{11}$$

With a zero phase angle δ, the original Gough's ellipse definition [19] in the form of Eq 7 is recovered from Eq 9 with $F(\delta)$ taking on unity. When $\delta \neq 0$, $F(\delta)$ is always smaller than unity. Substituting Eq 8 into

TABLE 2—*Test out-of-phase loading conditions analyzed.*

Test data source	Bending/shear ratio (nominal stress)	Out-of-plane angle
LBF [7]	0.58	90°
UIUC [8]	0.42	90°
Yousefi et al. [16]	0.6	90°

Eq 9, one obtains the following effective structural stress range parameter with respect to normal stress component:

$$\Delta S_e = \frac{1}{F(\delta)} \sqrt{(\Delta\sigma_s)^2 + 3(\Delta\tau_s)^2} \tag{12}$$

or, with respect to the in-plane shear structural stress component

$$\Delta T_e = \frac{1}{F(\delta)} \sqrt{\frac{1}{3}(\Delta\sigma_s)^2 + 3(\Delta\tau_s)^2} \tag{13}$$

The out-of-phase parameter $F(\delta)$ given by Eq 11 is applicable for any given phase angle δ. The adequacy of Eq 12 or 13 for correlating out-of-phase multiaxial fatigue data is to be demonstrated next with existing test data from literature. For easy reference, all out-of-phase multiaxial testing conditions in Table 1 analyzed are summarized in detail in Table 2 in terms of their nominal bending and nominal shear stress ratios and associated out-of-phase angles.

Analysis of Sonsino and Kuepper's Data—Sonsino and Kuepper [7] of LBF proposed a local stress based EESH parameter for correlating multiaxial fatigue data collected from flange to tube joints (see Fig. 5). The EESH based local equivalent stress amplitude versus cycles to failure plot was digitized from the same figure in [7] and replotted in Fig. 9(*a*). The data points correspond to pure bending, pure torsion, in-phase combined bending and torsion, and out-of-phase ($\delta = 90°$) combined bending and torsion. The square of correlation coefficient R^2 for the data shown in Fig. 9(*a*) is about 0.86 based on the MS Excel spread sheet calculation. Once all the nominal stress based S-N data reported in [7] were analyzed using the mesh-insensitive structural stress procedure, Fig. 9(*b*) was generated using Eq 12. The corresponding correlation coefficient R^2 is about 0.89 using the modified Gough's ellipse approach presented in this paper. It is worth noting that the global stress based parameter (Eq 12), without resorting to detailed local stress calculation or any additional empirical parameters, provides a rather good correlation of the multiaxial fatigue data, by comparing Fig. 9(*b*) (current approach) with Fig. 9(*a*) (EESH local approach [7]).

It should be noted that the data points in Fig. 9(*a*) (directly taken from [7]) contain a few additional data points which could not be located in the nominal stress based plots reported in [7] [but included in Fig. 9(*b*)], while a few data points given in terms of nominal stress versus cycles to failure, shown in Fig. 9(*b*), cannot be located in Fig. 9(*a*). This may be in part attributed to the digitization process in converting the print figure [shown in Fig. 9(*a*)] from [7]. However, the overall data trends observed in both Figs. 9(*a*) and 9(*b*) would not have been noticeably changed even if all the data points in the questions discussed above were considered in both plots in Fig. 9.

Analysis of Multiaxial S-N Data from Other Sources—Any good fatigue parameter must withstand the test of a large amount of S-N data under different geometric and loading conditions. All test data collected in this investigation, except those by EPRI [10], were collected using component geometries very similar to the tube-to-flange fillet weld component tested by Sonsino and Kueppers [7], as illustrated in Figs. 1 and 5. All used cantilever bending conditions with the flange side being fixed to a support fixture. The tube thickness varies from 6 mm to 10 mm and flange thickness varies from 10 mm to 25 mm. The tests performed by EPRI [10] were based on girth welded straight pipes. All these test data are summarized in Fig. 10(*a*) using the von Mises based effective stress definition as described in Eq 10, but using nominal stress range given by the respective authors.

Note that Eq 10 is exactly the same as the "SEQA" parameter [20–22]. As expected, the correlation coefficient R in Fig. 10(*a*) indicates the overall data correlation is rather poor. As discussed by Dong and

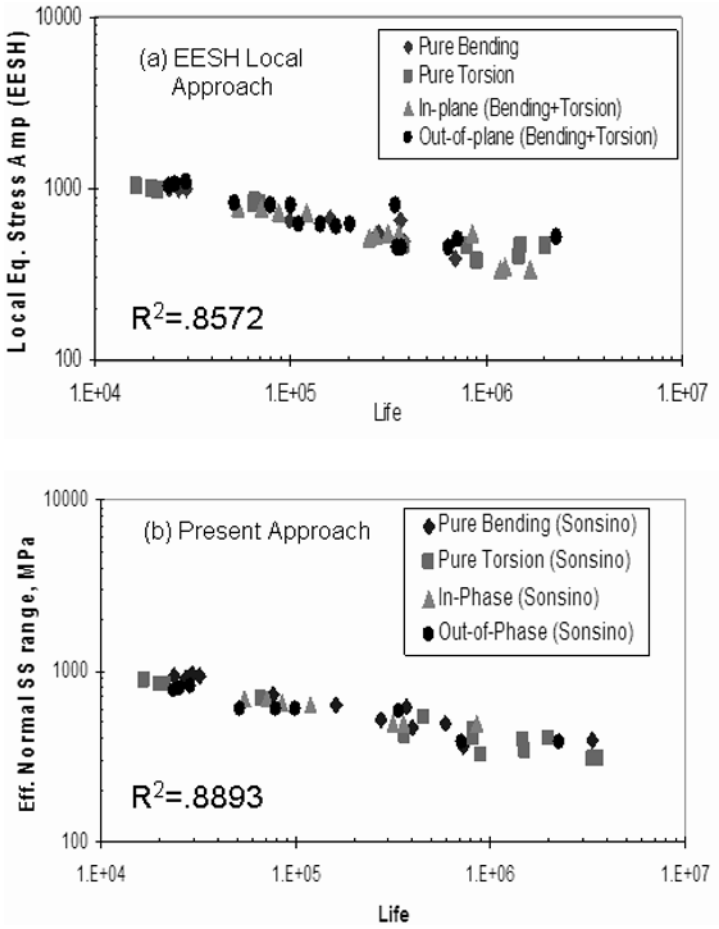


FIG. 9—*Comparison of multiaxial S-N data correlation of test data by Sonsino and Kueppers [7] using: (a) EESH based local equivalent stress amplitude and (b) present structural stress based approach using the modified Gough's ellipse.*

Hong [18], the maximum principle stress based parameter does not correlate with multiaxial fatigue data and is not further discussed in this paper. By using the same effective structural stress range parameter (i.e., Eqs 11 and 12) as that for Fig 9(*b*), Fig. 10(*b*) shows a significant improvement of the overall data correlation, given the fact that a total of five independent sources of the test data are used and that some testing and specimen geometry details required for a more detailed analysis are not available from some of the publications cited above.

Implications of Out-of-Phase Parameter $F(\delta)$

Up to this point, all data correlations [see Figs. 9(*b*) and 10(*b*)] involved with out-of-phase loading have been based on the expression given in Eqs 11 and 12, which do not contain any material related parameters, nor were any empirical-based parameters introduced to achieve further improved data correlation. There are numerous publications in the literature on the sensitivity of different materials to out-of-phase loading induced damage [e.g., [7–9,14,15,20]] and more recently by Kueppers and Sonsino [12] on welded

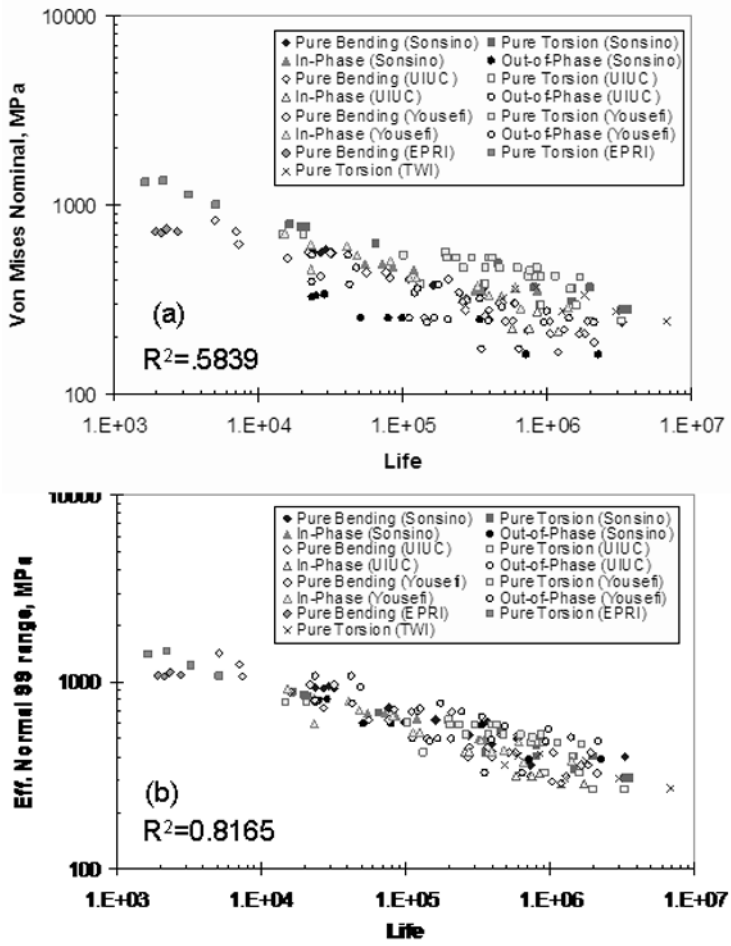


FIG. 10—*Correlation of existing multiaxial fatigue date from five sources: (a) using von Mises stress based nominal stress range Eq 10; (b) Using the present effective structural stress range based on the modified Gough's ellipse (Eqs 11 and 12).*

aluminum component tests under both in-phase and out-of-phase loading conditions. It should be noted that most of the observations on material effects are reported based on investigations into a specific group of fatigue tests performed by various researchers. To our best knowledge, a generalized approach for incorporating material effects on multiaxial fatigue damage seems still not available in the literature.

Based on the present formulation of the out-of-phase parameter $F(\delta)$ as expressed in Eq 11, the fatigue damage induced by the presence of out-of-phase loading is solely described by the term containing $\sin^2 \delta$, $\Delta\sigma_s$, and $\Delta\tau_s$ in Eq 11. It then follows that any material effects on the out-of-phase loading induced damage could be simply represented by inserting a material-related parameter μ (ranging from 0 to 1) in front of this term, which can be referred to as material's sensitivity parameter to out-of-phase loading induced damage. Equation 11 then becomes

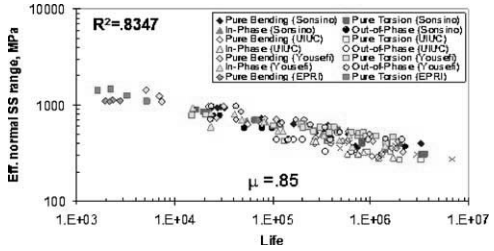


FIG. 11—*Correlation of all steel weld data (shown in Fig. 9(b)) by introducing the best-fit material sensitivity paper* $\mu = 0.85$ *in Eq 14.*

$$F(\delta) = \frac{1}{\sqrt{2}} \sqrt{1 + \sqrt{1 - \mu \frac{12(\Delta\sigma_s)^2(\Delta\tau_s)^2 \sin^2 \delta}{[(\Delta\sigma_s)^2 + 3(\Delta\tau_s)^2]^2}}} \tag{14}$$

The introduction of the material sensitivity parameter μ in the above equation was first suggested by Radaj [23] after his review of the modified Gough's ellipse approach discussed so far in this paper. The material sensitivity parameter μ in Eq 14 can be determined by examining a given set of fatigue data by searching for the value yielding the best fit under all combinations of δ, $\Delta\sigma_s$, and $\Delta\tau_s$. If $\mu = 0$, $F(\delta) = 1$, the modified Gough's ellipse described by Eq 9 becomes the original Gough's ellipse (Eq 7). This implies that the material may be said to be insensitive to out-of-phase loading induced damage. If $\mu = 1$, Eq 14 becomes Eq 11, as used for generating Figs. 9(*b*) and 10(*b*). The use of the parameter μ will be demonstrated for all steel weld data in Fig. 10(*b*) and a recent set of aluminum alloy weld data in [12] in the next section.

Use of Parameter μ *for All Steel Weld Data*

If Eq 14 is used to reevaluate the data shown in Fig. 10(*b*) by introducing the material sensitivity parameter μ, the results are summarized in Fig. 11, showing an improved correlation when $\mu = 0.85$ after a few iterations. The correlation coefficient R^2 increases to 0.83 in Fig. 11 from 0.81 in Fig. 10(*b*).

Use of Parameter μ *for Aluminum Weld Data*

Kuppers and Sonsino [12], based on their recent test data on aluminum weldments tested under both in-phase and out-of-phase multiaxial loading conditions, proposed a rather different multiaxial damage parameter in order to correlate the aluminum weld data from the one used for steel weld data [7] [also see Fig. 9(*a*)]. The approach they proposed was referred to as KoNoS hypothesis [12], which may be viewed as a local stress based critical plane approach. The specimen geometry used for performing these multiaxial fatigue tests on the aluminum alloy welds is identical to the specimens used by them for conducting steel weld tests [7], shown in Figs. 1 and 5(*b*). The failure modes in these tests are also the same as those in [7], i.e., weld toe failure into the tube thickness. The fatigue test conditions and specimen geometry details are shown in Fig. 12, as reported in [12].

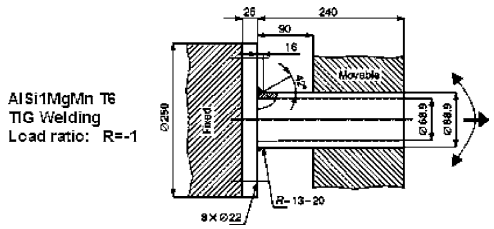


FIG. 12—*Multiaxial fatigue tests of welded aluminum alloy component by Kueppers and Sonsino [12].*

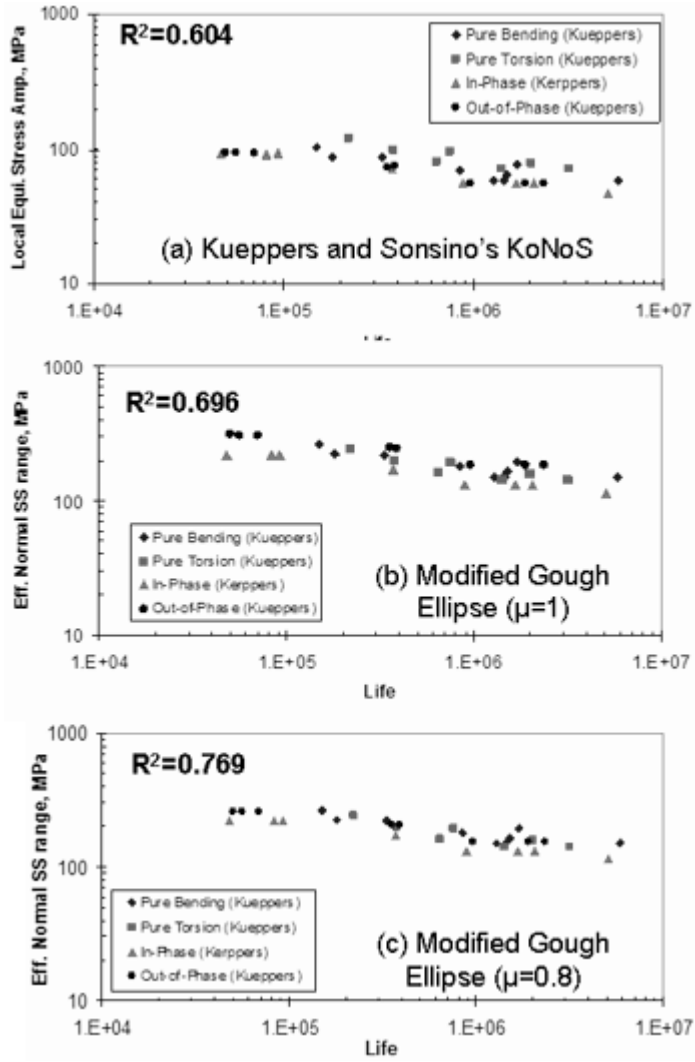


FIG. 13—*Comparison of the Kueppers and Sonsino KoNoS hypothesis (a) and the proposed modified Gough's ellipse approach with (c) and without using material sensitivity parameter* μ *(b).*

By digitally scanning a final summary figure generated using the KoNoS approach by Kueppers and Sonsino as given in [12], Fig. 13(*a*) shows the S-N plot according to KoNoS hypothesis in [12]. The ordinate of Fig. 13(*a*) stands for "local equivalent stress amplitude" as given in [12]. The corresponding correlation coefficient $R^2=0.6$ was calculated using MS Excel, also shown in Fig. 13(*a*) for comparison purposes. By using Eq 14 with $\mu=1$ and Eq 12, i.e., without considering material-related sensitivity to out-of-phase loading, Fig. 13(*b*) shows the results for the same data given in Fig. 13(*a*). The correlation coefficient becomes about $R^2=0.7$. If the material sensitivity parameter μ is introduced, Fig. 13(*c*) shows the results corresponding to $\mu=0.8$ after a few iterations in seeking the best fit. The correlation coefficient now becomes $R^2=0.8$. It should be emphasized that for both all steel weldments and the recent aluminum

weldments reported in [12], the same out-of-phase parameter $F(\delta)$ described by Eq 14 is used throughout this investigation to arrive at Figs. 11 and 13(*c*). The simplicity and effectiveness of the proposed approach is evident as indicated in Figs. 9(*b*), 10(*b*), 11, and 13(*c*).

The Minimum $F(\delta)$

In various practical applications, an accurate tracking of the out-of-phase angle may be difficult, if not impossible. Under those circumstances, the formulation of the out-of-phase parameter $F(\delta)$ as embodied in Eq 14 indicates that there exists a minimum possible value regardless of μ, i.e.,

$$F(\delta)_{\min} = \frac{1}{\sqrt{2}} \tag{15}$$

among all combinations of the out-of-phase angle, δ, $\Delta\sigma_s$, and $\Delta\tau_s$. This was first observed by Radaj [23] after reviewing a draft version of this paper. Therefore, if an accurate tracking of the out-of-phase angle for a given arbitrary loading history is difficult, Eq 15 can be directly used to provide a conservative estimation of the maximum possible fatigue damage due to the presence of any out-of-phase loading combinations.

Concluding Remarks

In this paper, the applicability of the mesh-insensitive structural stress method in characterizing stress concentrations in welded joints due to multiaxial loading is investigated using various test specimens or joint geometries documented in the open literature. A total of five sources of multiaxial fatigue data from welded components documented in the literature has been investigated in detail. The major findings include:

1. The mesh-insensitive structural stress method is proven to be robust for consistently capturing the stress concentration characteristics in welded joints under multiaxial loading conditions. As a result, the structural stress based stress concentration factor at a failure location so calculated can be viewed as a property of joint geometry and loading mode.
2. An effective structural stress parameter in von Mises form is proven effective in correlating fatigue data tested under both single loading mode (bending or torsion) and in-phase multiaxial loading conditions. The Tresca form of the effective structural stress range definition also serves as an effective fatigue parameter. The maximum principle stress criterion is not effective, as least for the test data investigated in this study.
3. For out-of-phase loading, the proposed modified Gough's ellipse incorporating the out-of-phase parameter $F(\delta)$ expressed in a form of von Mises stress form as a function of the out-of-phase angle provides a simple and robust approach to the consolidation of multiaxial fatigue data from a total of five independent sources reported in the literature. The method does not require any local stress analysis using fine finite element models, not does it require any additional empirical parameters.
4. Comparing with uniaxial dominated fatigue data for welded joints (over 1000 tests), as reported [2,4], the amount of well-documented multiaxial test data (about a total of 200 fatigue tests) analyzed in this paper should not be considered as comprehensive, particularly for test specimens with drastically different thicknesses and joint geometries. Research efforts are currently under way to collect additional multiaxial test data from the literature and future research programs. After additional data become available, the effective structural stress parameter presented in this paper can be further refined. In addition, some data sets reported in this paper require further analysis once their testing and specimen details are further clarified. However, the results presented in this paper clearly suggest the applicability of the present mesh-insensitive structural stress method in both stress concentration characterizations and in the final correlation of the existing multi-axial S-N data in the literature.
5. The proposed approach in the form of the modified Gough's ellipse not only provides a simple and effective form for incorporating material's sensitivity to out-of-phase loading induced damage, but also provides a clearly defined maximum possible damage due to out-of-phase loading

or the minimum value of the out-of-phase parameter. For example, $F(\delta)_{\min}=1/\sqrt{2}$, which is convenient to use for taking into account the maximum possible out-of-phase loading induced damage, if out-of-phase angle for complex loading histories cannot be easily tracked in practice.

Acknowledgments

The authors would like to express their gratitude to Professor D. Radaj for his insightful comments and suggestions during their preparation of the draft manuscript. The authors would also like to thank all reviewers for their valuable suggestions and comments which were essential for the improved presentation of the relevant technical background and final results in the revised manuscript.

References

[1] Dong, P., Zhang, J., and Hong, J. K., "Structural Stress Analysis," Patent No. US 6,901,809 B2, 2005.
[2] Dong, P., Hong, J. K., Osage, D., and Prager, M., "Master S-N Curve Method for Fatigue Evaluation of Welded Components," *WRC Bulletin*, No. 474, August, 2002, Welding Research Council, New York.
[3] Dong, P., Hong, J. K., and Cao, Z., "Stresses and Stress Intensities at Notches: 'Anomalous Crack Growth' Revisited," *Int. J. Fatigue*, Vol. 25, Nos. 9–11, 2003, pp. 811–825.
[4] Dong, P. and Hong, J. K., "The Master S-N Curve Approach to Fatigue Evaluation of Offshore and Marine Structures," *Proceedings of OMAE04, 23rd International Conference on Offshore Mechanics and Arctic Engineering*, June 20-25, 2004, Vancouver, Canada.
[5] Healy, B., "A Case Study Comparison of Surface Extrapolation and Battelle Structural Stress Methodologies," Paper No. OMAE2004-51228, *Proceedings of the 23rd OMAE International Conference*, Vancouver, Canada, June 2004.
[6] Hobbacher, A., *Fatigue Design of Welded Joints and Components: Recommendations of IIW Joint Working Group XIII-XV*, Abington Publishing, Abington, Cambridge, 1996.
[7] Sonsino, C. M. and Kueppers, M., "Multaxial Fatigue of Welded Joints under Constant and Variable Amplitude Loadings," *Int. J. Fatigue*, Vol. 24, 2001, pp. 309–327.
[8] Siljander, A., Kurath, P., and Lawrence, F. V., Jr., "Nonpropotional Fatigue of Welded Structures," Carter, R. G., *Advances in Fatigue Lifetime Predictive Techniques*, ASTM STP 1122, M. R. Mitchell and R. W. Landgraf, eds., ASTM, Philadelphia, PA, 1992, pp.319–338.
[9] Maddox, S. J., and Razmjoo, G. R., "Interim Fatigue Design Recommendations for Fillet Welded Joints under Complex Loading," *Fatigue Fract. Eng. Mater. Struct.*, Vol. 24, 2001, pp.329–337.
[10] Wais, E. A., Dodabaugh, E. C., and Carter, R., "Investigation of Torsional Stress Intensity Factors and Stress Indices for Girth Butt Welds in Straight Pipe," *Design and Analysis of Piping, Vessel and Components*, ASME PVP-Vol. 440, 2002, pp. 83–89.
[11] Dang Van, K., Griveau, B., and Message, O., "On a New Multiaxial Fatigue Limit Criterion: Theory and Application," *Biaxial and Multiaxial Fatigue*, EDF 3, M. W. Brown and K. J. Miller, eds. 1989, pp. 479–496.
[12] Kueppers, M., and Sonsino, C. M., "Critical Plane Approach for the Assessment of the Fatigue Behavior of Welded Aluminum under Multi-Axial Loading," *Fatigue Fract. Eng. Mater. Struct.*, Vol. 26, 2003, pp. 507–513.
[13] Papadopoulos, I. V., "Long Life Fatigue under Multiaxial Loading," *Int. J. Fatigue*, Vol. 23, 2001, pp. 839–849.
[14] Backstrom, M., and Marquis, G., "A Review of Multiaxial Fatigue of Weldments: Experimental Results, Design Code, and Critical Plane Approach," *Fatigue Fract. Eng. Mater. Struct.*, Vol. 24, 2001, pp. 279–291.
[15] Backstrom, M., and Marquis, G., "Interaction Equations for Multi-Axial Fatigue Assessment of Welded Structures," *Fatigue Fract. Eng. Mater. Struct.*, Vol. 27, 2004, pp. 991–1003.
[16] Kyuba, H., and Dong, P., "Equilibrium-Equivalent Structural Stress Approach to Fatigue Analysis of a Tubular Joint," IIW Doc. XIII - 1993-03, June, 2003.
[17] Yousefi, F., Witt, M., and Zenner, H., "Fatigue Strength of Welded Joints under Multiaxial Loading:

Experiments and Calculations," *Fatigue Fract. Eng. Mater. Struct.*, Vol. 24, 2001, pp. 339–355.
[18] Dong, P. and Hong, J. K., "An Effective Structural Stress Parameter for Evaluation of Multi-Axial Fatigue," International Institute of Welding (IIW) Doc. No. IIW Doc. XIII-2036-04/XV-1133-04, IIW Annual Assembly, July 2004, Osaka, Japan.
[19] Gough, H. J., Pollard, H. V., and Clenshaw, W. J., *Some Experiments on the Resistance of Metals to Fatigue under Combined Stresses*, Aeronautical Research Council, R&M, 2522, 1951.
[20] Park, J., and Nelson, D. V., "In-Phase and Out-of-Phase Combined Bending-Torsion Fatigue of a Notched Specimens," *Multiaxial Fatigue and Deformation: Testing and Prediction*, ASTM STP 1387, S. Kalluri and P. J. Bonacuse, Eds., American Society for Testing and Materials, West Conshohocken, PA, 2000, pp. 246–265.
[21] ASME Boiler and Pressure Vessel Code, Sec. III Div. 1, Class 1 Component, Subsection NB, rules for Construction of Nuclear Power Plant Components, ASME, New York, 1988.
[22] ASME Boiler and Pressure Vessel Code, Sec. III Div. 1, Code Case N-47-23, Class 1 Component in Elevated Temperature Service, Appendix T, ASME, New York, 1988.
[23] Radaj, D., private communication, 2005.

Fatigue Crack Growth

Journal of ASTM International, Vol. 3, No. 6
Paper ID JAI13222
Available online at www.astm.org

Eann A. Patterson,[1] *Francisco A. Diaz,*[2] *and John R. Yates*[3]

Observations on Photo-Emission and the Process Zone of a Fatigue Crack

ABSTRACT: Cyclic loading of a solid material induces a cyclic temperature fluctuation. The thermal cycle is asynchronous with the loading cycle when the strains are elastic. This is commonly known as the thermoelastic effect. In differential thermography, a sensitive infrared camera is used to measure this temperature variation; typically of the order of a few tens of milliKelvin. Since the magnitude of the temperature variation is proportional to the dilational strain, values of the surface elastic stress can be derived. Recent advances in infrared camera technology and data processing algorithms have enabled values of effective stress intensity factor ranges and the location of fatigue cracks to be determined from temperature fluctuations around the crack tip on the specimen surface. Careful observation in the region near a crack tip reveals deviations from the asynchronous behavior of the photon signal relative to the load cycle. Phase shifts up to $\pi/8$ are commonly observed. The spatial distribution of these phase shifts exhibits characteristic features which are described and discussed. The features in this distribution appear to be associated with high elastic strain gradients, regions of plasticity and contact between the crack faces. Interpretation of the phase shift and its spatial distribution may lead to a better understanding of the mechanics of fatigue crack growth.

KEYWORDS: thermoelasticity, fatigue crack, plastic zone

Nomenclature

Symbol	=	Interpretation Units
E	=	Energy level, J
h	=	Planck's constant (6.63×10^{-34}), J s
m	=	Particle mass, kg
n	=	Positive integer
r	=	Distance from crack tip, m
R	=	Temperature range, Kelvin
s	=	Particle speed, m/s
X, Y	=	Vector components of R, Kelvin
ΔK_I	=	Range of stress intensity factor, Pa$\sqrt{}$m
$\varepsilon_1, \varepsilon_2$	=	Maximum, minimum principal strains
λ	=	Photon wavelength, m
ρ	=	Radius of orbit, m

Introduction

When a material is subject to cyclic strain under adiabatic conditions, an asynchronous cyclic temperature variation occurs on its surface which is directly proportional to the first strain invariant. In thermoelastic

Manuscript received April 11, 2005; accepted for publication April 7, 2006; published online May 2006. Presented at ASTM Symposium on Fatigue and Fracture Mechanics: 35th Volume on 18–20 May 2005 in Reno, NV; R. E. Link and K. M. Nikbin, Guest Editors.

[1] Professor, Department of Mechanical Engineering, Michigan State University, 2555 Engineering Building, East Lansing, MI 48824.

[2] Assistant Professor, Departamento de Ingeniería Mecánica y Minera, Universidad de Jaen, Edificio A-3, Despacho 021, Campus Las Lagunillas, 23071- Jaén, Spain.

[3] Professor, Department of Mechanical Engineering, University of Sheffield, Mappin Street, Sheffield, S1 3JD, UK.

Copyright © 2006 by ASTM International, 100 Barr Harbor Drive, PO Box C700, West Conshohocken, PA 19428-2959.

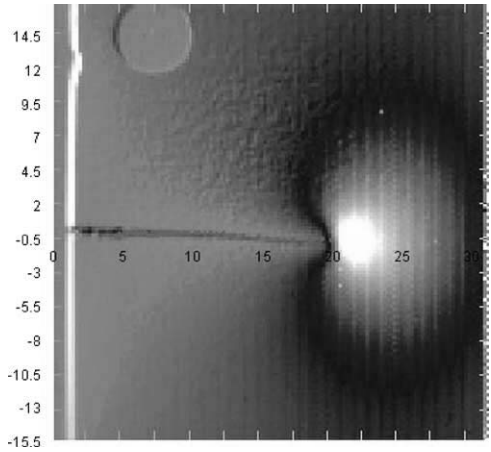


FIG. 1—*Thermoelastic data from a crack approximately 20 mm long in a compact tension specimen with the locations of the crack tip obtained by the new algorithm [7] superimposed on the image.*

stress analysis, this temperature variation is measured using very sensitive infrared detectors and processed to provide a map of the surface stress distribution. When the stress field around a fatigue crack is examined, the temperature data from the elastic field around the crack tip can be used to evaluate the range of stress intensity factor ΔK which is useful in predicting the fatigue life using the Paris law. A number of methodologies for calculating the stress intensity factor are available and have been reviewed by Tomlinson and Olden [1]. All of these methods require knowledge of the location of the crack tip and an initial estimate of the stress intensity factor. Further, they do not utilize the information immediately adjacent to the crack tip. The aim of the work described below was to develop means of tracking the location of the crack tip during a fatigue event using the cyclic temperature data and to explore the interpretation of the near field temperature data.

The technique of thermoelastic stress analysis has been reviewed by Dulieu-Barton and Stanley [2] and the theory underlying the technique has been reviewed by Pitarresi and Patterson [3]. However, a phenomenological explanation is rarely provided and is necessary in order to develop an interpretation of the temperature data from the field adjacent to the crack tip such as that shown in Fig. 1.

For a body in equilibrium with its surroundings the energy content of the photon flux arriving at its surface is equal to the energy content of the photon flux being emitted from the surface. In thermoelastic stress analysis, only infrared photons are detected in one of the two wavelength intervals in which the atmosphere transmits them. These are 3 to 5 μm and 8 to 12 μm so that the photons of interest have a relatively low energy level, E as result of Planck's law [4]:

$$E = \frac{h}{\lambda} \tag{1}$$

where λ is the wavelength of the photon and h is Planck's constant (6.63×10^{-34} Joule seconds).

In the material of the body electrons occupy certain orbits around the nucleus in their atom. The location of these orbits relative to the nucleus correspond to the radii at which the electrons can form standing or stationary waves around the nucleus. De Broglie [4] proposed that particles could form waves with a wavelength, λ governed by:

$$\lambda = \frac{h}{ms} \tag{2}$$

where m is the mass of the particle, s is its speed and hence the orbits correspond to electron paths around the nucleus for which the circumference is an exact multiple of the electron wavelength, i.e.,

$$\rho = \frac{n\lambda}{2\pi} \tag{3}$$

and for the nth orbit

$$\rho_n = 0.53 \times 10^{-10} n^2 \tag{4}$$

where ρ is the radius of the orbit in metres and n is a positive integer. As a consequence, electrons inhabit orbits that occur in distinct steps, in other words they are quantized and the energy level of electrons in these orbits is also quantized such that for the nth orbit the energy level E_n is given by:

$$E_n = \frac{-2.2 \times 10^{-18}}{n^2} \text{ Joules} \tag{5}$$

Electrons prefer to inhabit a low energy orbit and will spontaneously fall from outer to inner orbits moving away from the repulsive effects of electrons in neighboring atoms and towards the positive charge of protons in their own nucleus. To fall to an inner or lower orbit an electron must release energy corresponding to the difference in the energy levels between the two orbits and this difference can be found using Eq 5. This energy is released in the form of photons whose energy levels will be quantized and their wavelength can be evaluated using Eq 1.

There are many transitions between orbits which an electron can undergo leading to an emission spectrum for a particular atom. When a photon is incident on a material and enters an atom, if its energy level corresponds exactly to the difference between the energy levels for two electron orbits in an atom then the photon will be absorbed by an electron in the lower orbit and the electron will move or be promoted to the higher orbit; however, if the energy of the photon does not correspond to a difference between two electron orbits then the photon passes straight through the atom. For a material in equilibrium with its surroundings, the energy content in photons released due to electrons falling back equals the energy content of photons absorbed when electrons are promoted.

When heat is applied to a material, the heat energy causes electrons to be promoted and hence more will spontaneously fall back emitting photons so that the net photon flux from the material goes up. When a large amount of heat is applied then higher energy photons at wavelengths in the visible spectrum are released whereas at lower levels of heat the photons released are in the infrared spectrum. The promotion of electrons to outer orbits increases the effective radius of the negative charge in the atom and thus increases the repulsive forces between the atoms. The increased repulsive forces cause atoms to move away from one another in order to maintain equilibrium and thus the volume of the material increases.

When a tensile strain is applied to a material the volume increases which decreases the repulsive forces between atoms and increases the probability of electrons occupying outer orbits. However, in order to occupy the outer orbits electrons need to absorb energy from incident photons which decreases the net photon flux from the material. This decrease in photon flux from the material is detected as an apparent drop in temperature. Similarly, when a compressive strain is applied to the material, the repulsive forces between the atoms are increased shifting the probability distribution so that more electrons prefer to inhabit lower orbits and spontaneously release photons as they fall back to achieve this state which increases the net photon flux from the material and is detected as an apparent temperature rise.

In thermoelastic stress analysis, strain is applied cyclically causing a cyclic variation in the net photon flux which is 180° out-of-phase with the applied strain. Since this effect is related to volume change or dilatory strain the photon signal is proportional to first strain invariant, $(\varepsilon_1 + \varepsilon_2)$. Recent developments in photon detectors have lead to staring array cameras capable of detecting very small changes in the photon flux equivalent to a temperature range of a few tens of milliKelvin and of capturing many images per second. These advances have made it possible to continuously monitor the photon emissions in the vicinity of a fatigue crack. These arrays can be used with conventional infrared lenses allowing fields of view from about 3 mm square to the order of 1 m to be examined.

Experimental Procedure

Fatigue cracks were grown in compact tension specimens (Fig. 2) made from aluminum alloy (2024) and sprayed with matt black paint (type RS 496-782) to provide a uniform emissivity. The material was

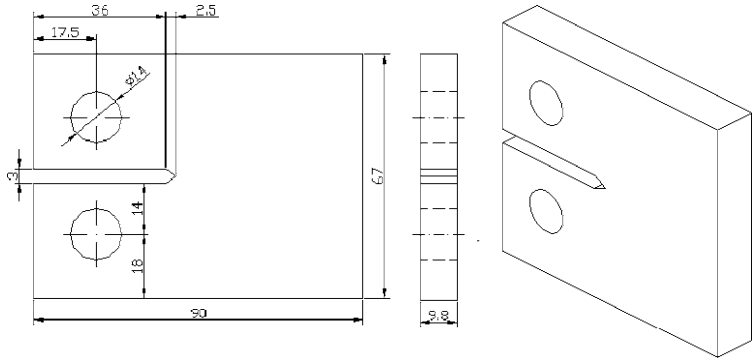


FIG. 2—*Notched aluminum compact tension specimen used in the tests.*

calibrated using a tensile dog-bone specimen which was sprayed with the same matt black paint on one side and had a strain gage rosette (Tokyo Sokki Kenkyujo Co., Ltd., type FPA-2-11, 2 mm, 120±0.5Ω) mounted on the other side.

The specimen had a machined notch as shown in Fig. 2 from which a fatigue crack was grown at a frequency of 12 Hz and an R-ratio of 0.1 while the stress field around the crack tip was continuously monitored using a Deltatherm system (StressPhotonics Inc., DT1500) with a 320×256 Indium-Antimonide detector operating in the 2 to 5 μm wavelength range and cooled to 77 K using a Stirling cycle heat pump. The system had an adjustable framing rate of up to 158 frames/s with maximum thermal and spatial resolutions of 2 mK and 25 μm, respectively. The data supplied from the Deltatherm system were a map of the range, R of the temperature or photon flux variation over the field of view and a map of the phase difference or angle between the applied loading and the temperature signal. These data could also be considered as a vector of magnitude, R at the given phase angle from which the system could generate maps of the components of the vector, X and Y. In purely elastic and adiabatic conditions the phase difference and Y components should be zero and $X=R$ such as in Figs. 1 and 3. In Figs. 1 and 3, the color scale relates to the amplitude of the temperature or photon emission produced by the cyclic strain experienced in the material. The crack was initiated near the center of the left edge and has propagated to approximately the center of the image so that its tip is roughly at (20,0) in Fig. 1 and (100, 127) in Fig. 3.

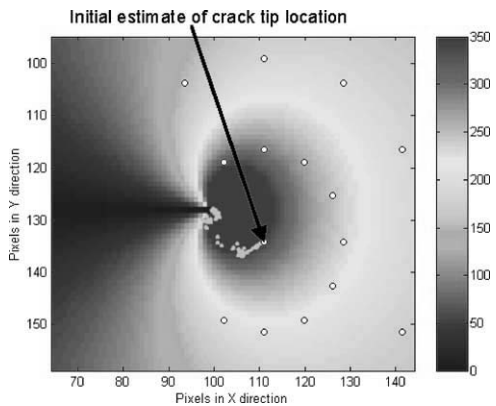


FIG. 3—*Map of the thermoelastic signal around a crack growing from center left to the right showing the relatively rapid convergence to the actual crack tip from a remote and arbitrary initial value. The gray points are the series of iterative solutions for the location of the crack tip at approximately (100, 127) and the black circles with white centers are the array of data points employed.*

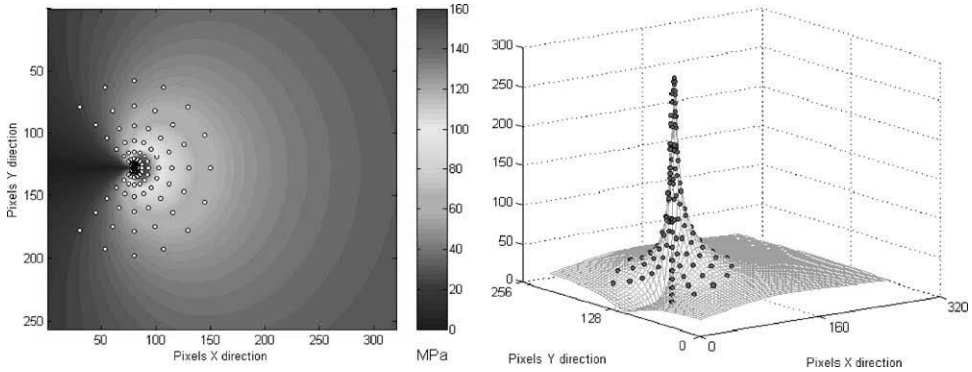


FIG. 4—*Thermoelastic data around a crack tip (left) with the array of data points used to solve for the stress intensity factor and a three-dimensional representation of the data (right).*

The flanks of the crack are free of strain and hence appear blue/black corresponding to a zero amplitude of temperature while ahead of the crack the strain field declines in a classical $(1/r^2)$ manner where r is the distance from the crack tip.

Data Processing

Crack Tip Location

The array of data from the Deltatherm was supplied to a specially written MatLab program which evaluated the stress intensity factor from the data field in a number of steps [5]. First an arbitrary point in the array was selected as the crack tip together with an array of points around it. If a point remote from the actual crack tip was selected initially then the array needed to cover a large area as shown in Fig. 3. However, it was found that if the phase angle between the thermoelastic signal and the applied load was plotted along a line ahead of the crack tip then the point of inflexion provided a close estimate of the actual crack tip location. The characteristics of this phase map are discussed in a later section. If the initial estimate of the crack tip location was close to the actual crack tip then a more tightly defined array could be used as shown in Fig. 4. The type of array shown in Fig. 4 was necessary to evaluate the stress intensity factor and so once the solution had converged on a crack tip location using the type of array shown in Fig. 3 it was necessary to redefine the array.

Valid Data Zone

The polar array in Fig. 4 contains about 80 points within an annulus around the crack tip. The inner and outer radii of the annulus were selected to provide data only within the elastic stress field dominated by the crack tip. This zone was defined using a technique based on the work of Stanley and Chan [6] in which the maximum values of the temperature range, R along lines parallel to the crack flanks were plotted as a function of distance of the line from the crack tip in the form $1/r^2$. This plot is linear in the elastic zone but becomes nonlinear as the crack tip is approached and the stress field is strongly influenced by the crack tip plasticity and triaxiality in the stress field and also at a distance from the crack tip where the stress field is no longer dominated by the crack tip. These two limits define the annulus and the valid data as shown in Fig. 5 where linear elasticity dominates from about $r=0.5$ mm and the dominance of the crack tip strain field is lost at about $r=4$ mm.

Stress Intensity Factor

It was assumed that the stress field within the region where linear elastic fracture mechanics was valid could be described by a pair of Fourier series based on the approach of Muskhelishvili [7]. The constants

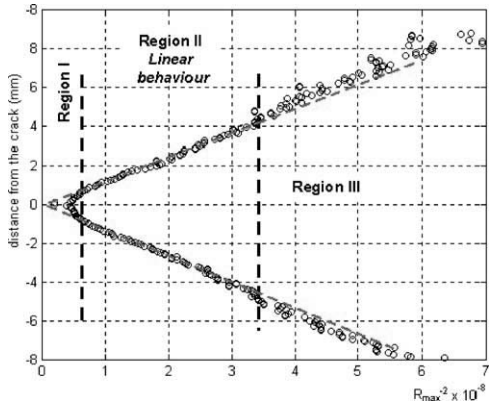


FIG. 5—*Plot of the maximum thermoelastic signal* (R) *along lines parallel to the crack flanks plotted as a function of distance from the crack flank. Data for the array in Fig. 4 was taken only from region II where the plot is linear.*

in the series were initially unknown and when evaluated can be used to calculate the stress intensity factor. Thus, the coefficients in the Fourier series and the coordinates of the crack tip are taken as the unknowns and a genetic algorithm used to minimize the difference between the stress field described by the array of points and the strain field described by the pair of Fourier series. The genetic algorithm required no *a priori* knowledge of the crack tip stress field and hence could be applied to a very large search space. A limited number of iterations or generations of the genetic algorithm were allowed in the interests of time and the downhill simplex method was used for a local search seeded from the result of the genetic algorithm in order to refine the solution. This technique has been described in more detail previously by the authors [7] and by Pacey et al. [8,9] who originally developed it for use with data from digital photoelasticity. In practice the solution process was repeated in order to find the crack tip and an example of the iterative solution from a remote initial value of the crack tip is shown in Fig. 3. The quality of the solutions was assessed by monitoring the mean and standard deviation of the least square differences between the solution and the data at points in the array. The final step was to calculate the stress intensity factor from the Fourier description of the crack tip stress field. The speed of data collection and processing made it possible to monitor a fatigue crack continuously as it propagated without needing to interfere with the fatigue test. Typical results for the crack path computed from the thermoelastic data by repeatedly evaluating the crack tip location from the new Deltatherm images is shown in Fig. 1 superimposed on the image of the crack. Figure 6 shows the corresponding results for the stress intensity factor range, ΔK_I

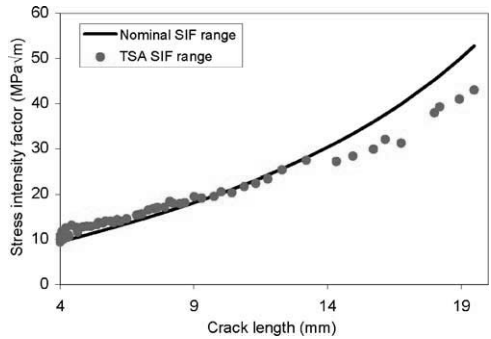


FIG. 6—*Stress intensity factors determined from thermoelastic data for the propagating fatigue crack shown in Fig. 1.*

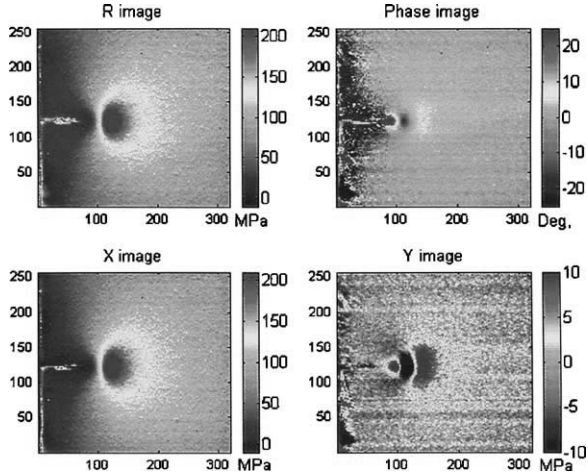


FIG. 7—*Set of images generated by the Deltatherm 1500 for a crack growing from left to right. When the temperature signal is considered to be a vector of magnitude R in a direction relative to the forcing signal given by the phase then the mutually perpendicular components of the vector are given by the X and Y images where X is the component parallel to the force vector.*

which increases linearly to about $a = 16$ mm.

Discussion

Figure 6 shows the range of the stress intensity factor, ΔK_I obtained from experiment (symbols) plotted together with the nominal value (solid line) calculated from the applied load and geometric or shape factor. The correlation is good at shorter crack lengths but beyond about $a = 13$ mm the results from experiments are lower than the nominal values. This difference probably arises from the presence of crack closure effects at the longer crack lengths. This phenomenon would raise the minimum stress intensity factor during the unloaded portion of the loading cycle without affecting the maximum in the loaded portion; thus decreasing the range. Such behavior is not accounted for in the calculation of the nominal value and is likely to be more prevalent at longer crack lengths where the plastic zone is larger.

The data processing described above represents a recent advance through the use of a crack tip search algorithm and the application of a genetic algorithm to remove the requirement for *a priori* knowledge. However, in common with previous analyses, no use was made of the near field information, i.e., the data from immediately adjacent to the crack tip. Figure 7 shows a complete set of phase difference, *R*, *X*, and *Y* component data maps for a propagating fatigue crack.

There is a significant quantity of information in the phase map and *Y* image in the near field. A plot through the phase map along a line ahead of the crack tip is shown in Fig. 8. Four distinct regions, A through D, can be identified in the figure based on the features in the plot, principally zero-intercepts, and different mechanisms postulated for the material behavior in each region. At a distance from the crack tip in region A assumptions of linear elastic fracture mechanics apply and the temperature signal is asynchronous with the applied load so the phase difference is uniform and taken to be zero although strictly it is 180° but it is the convention to ignore the sign reversal. In region B as the crack tip is approached, the stress gradient becomes very steep producing a steep temperature gradient and as a consequence heat transfer occurs within a cycle so that adiabatic conditions are not achieved. The loss of adiabatic conditions is manifested in a positive phase difference in region B. Heat will transfer down the temperature gradient so that additional heat arrives at a location after its indigenous peak causing a smearing or apparent shift in temperature-time response which is detected as a phase difference. In tension-tension loading, heat transfer in the elastic region will be towards the crack tip, i.e., up the stress gradient. In the

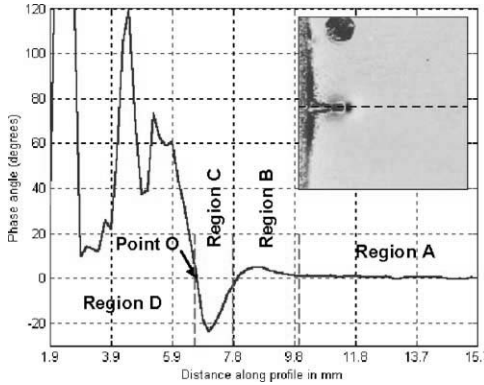


FIG. 8—*Phase difference (deg) between the forcing signal applied to the specimen and the temperature signal detected by Deltatherm as a function of distance along the crack path which is shown as a black dashed line in the inset. The inset shows the phase difference on the surface of the specimen with the crack growing from a free edge on the left with loading applied vertically.*

example in Fig. 8 the loss of adiabatic conditions causes a positive phase shift with a maximum value of about 5 deg.

In region C the phase difference changes sign and has a maximum value of about −22 deg in Fig. 8. Region C corresponds to the cyclic plastic zone since based on linear elastic fracture mechanics the radius of the plastic zone is about 0.13 mm. For a stationary crack, Rabiei et al. [10] have shown that heat is generated in the cyclic plastic zone due to hysteresis until the crack closes while for a growing crack during extension temperature rises of several tens of degrees may occur immediately ahead of the crack [11]. In fatigue this heat generation will be cyclical and of a magnitude that will completely swamp the thermoelastic effect and result in heat transfer away from the crack tip towards the elastic zone, i.e., in tension-tension loading this transfer is in the opposite sense to the one occurring in region B which goes someway to explain the reversal in the phase shift between regions B and C seen in Fig. 8. These observations are corroborated by the work of Beghi et al. [12] who used thermocouples to monitor the variation of temperature with applied load in stainless steel CT specimens. In monotonic tests, they observed that when plasticity occurred in a region the temperature signal as a function of load was inverted relative to regions where elastic conditions prevailed. Tests using cyclic loading revealed a phase shift between temperature signals coming from the plastic and elastic regions.

Two forms of plastic behavior are believed to generate heat in the vicinity of the crack tip. In the monotonic plastic zone dislocations will move and extend the plastic zone ahead of the crack, as the crack propagates and this is in-phase with the loading. The second is the movement of a much smaller number of dislocations close to the crack tip on unloading. This creates the reversed, or cyclic, plastic zone. This also extends as the crack propagates, but the photon emissions will be out of phase.

In region D in Fig. 8 huge phase shifts are observed as a consequence of heat generated by the contact of the crack flanks when the crack is closed and of background radiation reflecting from the flanks when the crack is open. The crack tip lies somewhere between regions C and D and point O where the phase difference crossed the axis forms a reliable initial estimate of the crack tip location. The notation of the crack tip is only relevant in linear elastic fracture mechanics, i.e., in this context for the purpose of solving for the stress intensity factor. In reality, a precise crack tip does not exist and instead there will be a process zone where nucleation of voids ahead of the crack occurs.

The identification of the various zones remains open to discussion and is proposed here as a plausible explanation based on current understanding of crack growth mechanisms [13] and observations of the movement of these regions with crack growth, i.e., these regions track the growth of the crack.

Conclusions

The use of thermoelastic stress analysis for quantifying the stress intensity factor for fatigue cracks has been established for some time. However, the capital cost of the equipment has inhibited its widespread use although new high-speed sensors combined with more robust algorithms offer the possibility of real-time crack monitoring at an acceptable cost. The real-time monitoring of the location of the crack tip is viable and provides an easy-to-use and objective method of monitoring crack growth without *a priori* knowledge. These capabilities have been demonstrated and validated and provide the potential to obtain substantially more information about cracks growing in the real engineering artifacts since the instrumentation is not dependent on laboratory conditions. There is a substantial quantity of additional data available in the maps of phase difference and the magnitude of the out-of-phase temperature signal that can be supplied by modern staring array sensors; however, the interpretation of this data is rather speculative at the moment although connections to fatigue crack growth mechanisms can be made.

References

[1] Tomlinson, R. A. and Olden, E. J., "Thermoelasticity for the Analysis of Crack Tip Stress Field—A Review," *Strain J. Brit. Soc. Strain Measurement*, Vol. 35, No. 2, 1999, pp. 49–55.

[2] Dulieu-Barton, J. M. and Stanley, P., "Development and Applications of Thermoelastic Stress Analysis," *J. Strain Anal.*, Vol. 33, No. 2, 1998, pp. 93–104.

[3] Pitarresi, G. and Patterson, E. A., "A Review of the General Theory of Thermoelastic Stress Analysis," *J. Strain Anal.*, Vol. 38, No. 5, 2003, pp. 405–417.

[4] Davies, P. C. W., *The Forces of Nature*, Cambridge University Press, Cambridge, 1979.

[5] Diaz Garrido, F. A., "Development of a Methodology for Thermoelastic Investigation of the Stress Intensity Factor," Ph.D. Thesis, The University of Sheffield, 2004.

[6] Stanley, P. and Chan, W. K., "The Determination of Stress Intensity Factors and Crack Tip Velocities from Thermoelastic Infrared Emissions," Proc. IMechE., Vol. C262, 1986, pp. 105–114.

[7] Diaz, F. A., Patterson, E. A., Tomlinson, R. A., and Yates, J. R., "Measuring Stress Intensity Factors During Fatigue Crack Growth Using Thermoelasticity," *Fatigue Fract. Eng. Mater. Struct.*, Vol. 27, No. 7, 2004, pp. 571–584.

[8] James, M. N., Pacey, M. N., Wei, L-. W., and Patterson, E. A., "Characterisation of Plasticity-Induced Closure-Crack Flank Contact Force Versus Plastic Enclave," *Eng. Fract. Mech.*, Vol. 70, No. 17, 2003, pp. 2473–2487.

[9] Pacey, M. N., James, M. N., and Patterson, E. A., "A New Photoelastic Model for Studying Fatigue Crack Closure," *Experimental Mechanics*, Vol. 45, No. 1, pp. 42–52.

[10] Rabiei, A., Evans, A. G., and Hutchinson, J. W., "Heat Generation During the Fatigue of Cellular Al Alloy," *Metall. Mater. Trans. A*, Vol. 31A, 2000, p. 1129.

[11] Flores, K. M. and Dauskardt, R. H., "Local Heating Associated with Crack Tip Plasticity in Zr-Ti-Ni-Cu-Be Bulk Amorphous Metals," *J. Materials Research*, Vol. 14, No. 3, 1999, pp. 638–643.

[12] Beghi, M. G., Bottani, C. E., Caglioti, G., and Fazzi, A., "Spectral Analyzer for the Thermoelastic and Thermoplastic Response of Solids to Low Frequency Dynamic Loads," Stress Analysis by Thermoelastic Technique, Proc. SPIE, Vol. 731, 1987, pp. 2–16.

[13] Bathias, C., "Retrospective View on the Role of the Plastic Zone at a Fatigue Crack Tip," *Fatigue Fract. Eng. Mater. Struct.*, Vol. 19, No. 11, 1996, pp. 1301–1306.

Journal of ASTM International, February 2006, Vol. 3, No. 2
Paper ID JAI13195
Available online at www.astm.org

Toshiyuki Meshii,[1] *Kenichi Ishihara,*[2] *and Toshiyuki Asakura*[3]

Simulation on the Decrease in Threshold Stress Intensity Factor (SIF) Range due to High Maximum SIF

ABSTRACT: In this paper, a method is proposed to quantitatively estimate the decrease in threshold stress intensity factor (SIF) range due to high maximum SIF, that is observed for some materials in constant maximum SIF fatigue crack growth tests. The parameters for the simulation were inversely determined from the experimental data of carbon steel, Al and Ti alloys with the aid of genetic algorithm. The set of candidate parameters named as a "generation" were repeatedly generated and evaluated until the experimental data were reproduced by the simulation. A very interesting fact was that though the test conditions for these three materials were different, the obtained simulation parameters seemed to be independent of material. Finally, the proposed method was validated by comparing predictions with experimentally determined values of the decrease in threshold on an embrittled carbon steel.

KEYWORDS: fracture mechanics, fatigue crack growth, threshold stress intensity factor range, static fracture mode, simulation, genetic algorithm

Nomenclature

a = average of the crack length measured at the CT specimen surfaces; $a=(a_1+a_{n\text{column}})/2$
a_0 = initial crack length
a_j = crack length of the jth column (Fig. 2)
a_{END} = crack length for terminating simulation
b = column size of a cell; $=B/n_{\text{column}}$
da/dN = fatigue crack growth rate in mm/cycle; $=C_{\text{Paris}}\cdot(\Delta K)^m$
$fit(k)$ = fitness of $k(=1\sim k_{\text{END}})$-th $\Delta K_{\text{th,sim}}$; Eq (9)
g = average grain size; used as the width of a cell
i, j = row and column index of a cell ($i=1\sim n_{\text{row}}$, $j=1\sim n_{\text{column}}$)
k_j = local crack driving force of the jth column corresponding to the static failure mode (Fig. 4)
k_{Cij} = material resistance of the (i,j)-th cell corresponding to the static failure mode
l = index to distinguish the $K_{\max}$=constant FCG test condition in Fig. 1 ($l=1\sim2$)
z = number of $\Delta K_{\text{th,sim}}$ (for $k=1\sim k_{\text{END}}$) that satisfied $|fit(k)|\leq0.1$
B = CT specimen thickness
C = ΔK gradient in Eq 1
E = Young's modulus
$F_{\max}$ = nominal maximum load in the Nth cycle
K_C = basic material resistance corresponding to the static failure mode; set as K_{IC}: fracture toughness
M = index that specifies the generation
N = number of load cycles

Manuscript received April 9, 2005; accepted for publication August 24, 2005; published December 2005. Presented at ASTM Symposium on Fatigue and Fracture Mechanics: 35th Volume on 18–20 May 2005 in Reno, NV; R. E. Link and K. M. Nikbin, Guest Editors.

[1] Professor, , Faculty of Graduate School of Engineering, University of Fukui, 3-9-1 Bunkyo, Fukui, Fukui, Japan.
[2] Graduate Student, Graduate School of Engineering, University of Fukui, 3-9-1 Bunkyo, Fukui, Fukui, Japan.
[3] Professor Emeritus, University of Fukui, 3-9-1 Bunkyo, Fukui, Fukui, Japan.

Copyright © 2006 by ASTM International, 100 Barr Harbor Drive, PO Box C700, West Conshohocken, PA 19428-2959.

RAND = uniform random number of 0 ~ 1 for a "seed" $RI(RI=RI_{start} \sim RI_{end})$
W = width of a CT specimen
α_1, β_1, α_2, β_2 = simulation parameters to consider scatter in cell material resistances; Eq 2
γ = decrease rate of ΔK_{th} obtained under constant K_{max} FCG test, due to increase in K_{max}; Fig. 1
λ_j = compliance of the jth slice (Fig. 4)
ν = Poisson's ratio
ϕ_j = load distribution coefficient of the jth slice; Eq 6
ξ = $=a_j/W$
ψ_{ij1}, ψ_{ij2} = uniform random number of 0 ~ 1
Δk_j = local crack driving force of the jth column corresponding to the cyclic failure mode (Fig. 4)
Δk_{Sij} = material resistance of the (i,j)-th cell corresponding to the cyclic failure mode cyclic
ΔF = nominal load range in the Nth cycle
ΔK = SIF range; Eq 2
ΔK_{th} = threshold SIF range
$\Delta K_{th,sim}$ = threshold SIF range obtained by simulation
ΔK_S = basic material resistance corresponding to the cyclic failure mode; set as ΔK_{th}: threshold SIF range

Introduction

The applied stress intensity factor (SIF) range ΔK has been known to be a major controlling parameter in fatigue crack growth (FCG) rate da/dN and its threshold ΔK_{th} under small scale yielding conditions [1]. Almost without exception, existing data show that the ΔK_{th} tends to decrease with increasing load ratio R [2]. Schmidt and Paris rationalized this behavior solely on the basis of the crack closure concept [3]. According to their model, the ΔK_{th} obtained by the maximum SIF (K_{max})-constant test method (that ensures closure free conditions) is expected to be independent of K_{max} and constant. However, this does not happen for all the materials [2,4]. In this paper, the interesting behavior (Fig. 1) that some materials experience under K_{max}-constant FCG tests that show a decrease in ΔK_{th} due to an increase in K_{max} (hereafter called as "the decrease in ΔK_{th} due to high K_{max}") was considered and simulated. This phenomenon is reported to be independent for crack closure and environment [2,4].

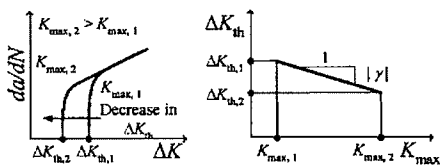


FIG. 1—*Decrease in* ΔK_{th} *due to high* K_{max} *for* K_{max}*-constant tests.*

In the previous work, an assessment diagram to assess whether a material will experience this decrease in ΔK_{th} due to high K_{max} was proposed and a possible mechanistic explanation of the behavior (Fig. 2) was considered [5]. The FCG mechanism was considered the same regardless of ΔK or K_{max} on the point that macroscopic crack front growth was observed as a coalescence of microscopic cracks in grains (modeled as cells in Fig. 2). Another assumption was that microscopic crack growth is selectively determined as cyclic or static mode failure, depending on the direction of the slip plane of the grain. The subject of this paper is to propose a quantitative method to estimate the decrease rate γ in Fig. 1. To accomplish the object, the conceptual FCG model that was proposed in the previous work (Fig. 2) was evolved to a concrete simulation algorithm using minimal experimental data for the purpose. The proposed method was

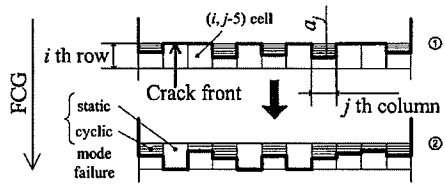


FIG. 2—*The simplified microscopic crack coalescence FCG model [5].*

validated by comparing predictions with experimentally determined values of γ on an embrittled carbon steel.

Proposal of γ Estimation Method

Simulation Algorithm

In this section, the qualitative FCG model (Fig. 2) [5] that can explain the mechanism of the decrease in ΔK_{th} due to high K_{max} was evolved to a concrete simulation algorithm. The FCG mechanism was considered the same regardless of ΔK and K_{max}, based on the standpoint that microscopic cracks grow locally (such as in crystal grain) due to cyclic or static mode failure and that the macroscopic crack front growth is observed as coalescences of microscopic cracks. The microscopic crack growth in all directions will therefore contribute to macroscopic crack growth, because the grains are separated. In Fig. 2, the grains are simplified to be square (hereafter named as a cell) and the cells are fractured in the same plane. Another simplification is that the microscopic crack growth direction coincides with the macroscopic FCG direction. The fundamental idea of the proposed simulation is to compare the local crack driving forces (cyclic and static) with the cell material resistances at the crack tip, and then evaluate the local crack growth due to the corresponding failure mode. The step-by-step algorithms of the simulation (flow chart: Fig. 3) are explained in the following.

Initial Setting—First, the compact tension (CT) specimen dimensions (B: thickness, W: width, a_0: initial crack length, a_{END}: crack length for forced termination of the simulation), the cell dimensions (g: size of a cell in the FCG direction, b: size of a cell in the CT specimen thickness direction set as $b \approx g$), fundamental material properties (E: Young's modulus, ν: Poisson's ratio, C_{Paris}, m: material constants of Paris law) are specified and load control parameters ΔK_0 (initial SIF range) and the C (ΔK gradient) in

$$\Delta K = \Delta K_0 \exp[C(a - a_0)], \tag{1}$$

defined in the standard ASTM FCG test [6] are specified.

Then the microscopic cell material resistances are specified. In order to specify these microscopic material resistances, the location of a cell by the ith row and the jth column ($i = 1 \sim n_{row}$, $j = 1 \sim n_{column}$) is specified. Here the material resistances for cyclic and static mode failure are specified as Δk_{Sij} and k_{Cij}, respectively. There is no one way rule to specify these quantities, so it was decided to generate these microscopic material resistances based on the two basic material resistances ΔK_S and K_C, corresponding to cyclic and static failure mode. And then consider the scatter by introducing simulation parameters α,β and uniform random number ψ_{ij} as follows:

$$\Delta k_{Sij} \equiv (\alpha_1 + \beta_1 \cdot \psi_{ij1})\Delta K_S, \quad k_{Cij} \equiv (\alpha_2 + \beta_2 \cdot \psi_{ij2})K_C, \tag{2}$$

The way to select the two basic material resistances from experimental data will be discussed later.

Local Crack Driving Force Calculation—The second step is to calculate the local crack driving forces of the jth row from the nominal maximum SIF K_{max} and SIF range ΔK that is controlled in a constant-K_{max} FCG test. The nominal load in the simulation is controlled so that the maximum SIF is equal to the specified K_{max} and so that the relationship between the SIF range ΔK and the average crack length a

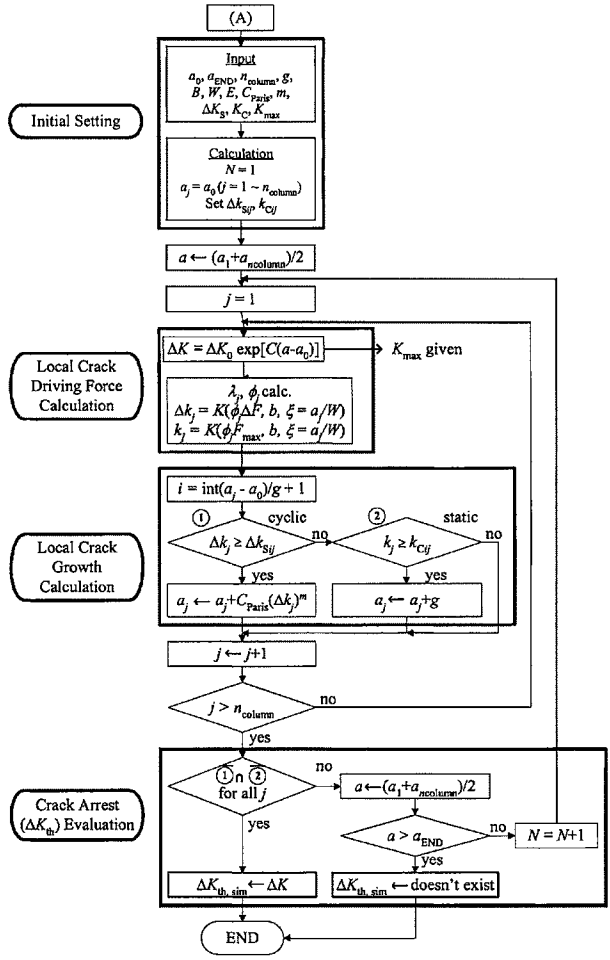


FIG. 3—*Flow chart of FCG simulation.*

$=(a_1+a_{n\text{column}})/2$ relationship for CT specimen satisfies Eq 1 in agreement with ASTM E-647 [6]. The nominal maximum load F_{max} and the load range ΔF corresponding to K_{max} and ΔK is calculated backward from the SIF equation for the ASTM CT specimen [6].

$$K(F,B,W,\xi = a/W) = \frac{F}{B\sqrt{W}}\left[\frac{(2+\xi)}{(1-\xi)^{1.5}}(0.886 + 4.64\xi - 13.32\xi^2 + 14.72\xi^3 - 5.6\xi^4)\right]. \quad (3)$$

Then, in order to calculate the local maximum crack driving force k_j and the range Δk_j in the crack tip of the jth column, the load distribution coefficient ϕ_j is introduced as

$$f_j = \phi_j \cdot F_{max}, \quad \Delta f_j = \phi_j \cdot \Delta F, \quad (4)$$

where f_j and Δf_j is the maximum and the range of the force corresponding to k_j and Δk_j. This ϕ_j is calculated by modeling the CT specimen with n_{column} CT slices of width W, thickness $b=B/n_{column}$, crack length a_j, and compliance λ_j as shown in Fig. 4. Since the displacement at the load point (Fig. 4, left) is uniform for thickness, the slice model (Fig. 4, right) is considered as n_{column} parallel springs and ϕ_j is deduced as

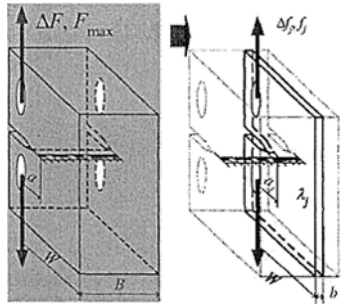


FIG. 4—*Slice model for stress redistribution.*

$$\phi_j = 1 \Big/ \left(\lambda_j \sum_{l=1}^{n_{\text{column}}} \frac{1}{\lambda_l} \right) \tag{5}$$

Here ASTM's following equation [6] is used for the plane stress condition to evaluate the compliance of the sliced (thin) CT specimen $\lambda_j(\xi = a_j/W)$,

$$\lambda_j = \frac{1-\nu^2}{Eb}\left[\frac{19.75}{(1-\xi)^2}(0.5 + 0.192\xi + 1.385\xi^2 - 2.919\xi^3 + 1.842\xi^4) \right]. \tag{6}$$

Though there was a choice to include the effect of plane stress/strain by varying E along the specimen thickness, it was decided to be simple because the slice model itself is a simplified engineering model.

Finally, the local crack driving forces are calculated by using this ϕ_j, nominal loads and Eq 3 as follows:

$$k_j = K(\phi_j \cdot F_{\max}, b, W, \xi_j = a_j/W), \quad \Delta k_j = K(\phi_j \cdot \Delta F, b, W, \xi_j = a_j/W). \tag{7}$$

Local FCG Evaluation—Once the local crack driving force of the jth column is obtained, the local crack growth is evaluated for each column. First, the row index i of the crack tip cell for the jth column is identified by

$$i = \text{int}[(a_j - a_0)/g] + 1, \tag{8}$$

where "int" stands for the integer function.

Then the local crack growth is evaluated by comparing the local crack driving force range Δk_j and maximum k_j with the corresponding material resistances of this cell Δk_{Sij} and k_{Cij}, respectively, for all the columns. Naturally, in this evaluation, the local crack growths by cyclic and static modes cannot be evaluated at the same time. If the load cycle is simulated faithfully, one might consider the idea to evaluate the crack growth first from a static mode, followed by a cyclic mode to be reasonable. However, there is a report that damage due to static mode failure does not necessarily occur in case that slip occurs early in a load cycle [7]. Thus, it was chosen to first evaluate the occurrence of cyclic mode failure and, in case of no cyclic mode failure, then evaluate the occurrence of static mode failure. In sucession, the amount of local crack growth in a certain cycle is evaluated as follows:

1. In the case of $\Delta k_j \geq \Delta k_{Sij}$, the amount of local crack growth in the jth column is evaluated as $C_{\text{Paris}} \cdot (\Delta k_j)^m$ according to the Paris law.
2. In the case of $k_j \geq k_{Cij}$, the amount of local crack growth is assumed to be g, the size of a cell. [Note: There is a possibility that crack growth due to static failure mode is smaller than g, as a result of $k_j \geq k_{Cij}$ becomes not satisfied due to load redistribution. However, change in load distribution factor ϕ_j due to local crack growth calculated by Eq 5 is small, so the amount of growth was simply evaluated as g].

Crack Arrest Evaluation—The last step is crack arrest evaluation. It is evaluated whether a macroscopic crack front growth is continuing or not, after local crack growth evaluation is performed for all the columns.

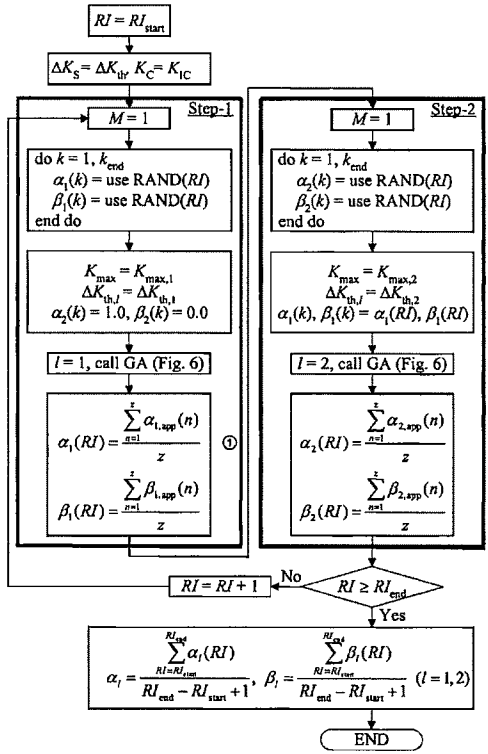


FIG. 5—*Procedure to presume simulation parameters* α *and* β.

1. In case $\Delta k_j < \Delta k_{Sij}$ and $k_j < k_{Cij}$ are satisfied for all the columns, it is defined that the crack has arrested. The nominal SIF range ΔK at this time is the desired ΔK_{th}.
2. In case $a \geq a_{END}$ is satisfied as a result of FCG, it is defined that there is no ΔK_{th}.

If these conditions are not satisfied, local crack driving force calculation and the local FCG evaluation is repeated for the next cycle.

Presuming Simulation Parameters by Genetic Algorithm

Now the conceptual FCG model in Fig. 2 has been evolved to a concrete simulation algorithm. However, some more challenges are necessary to estimate γ quantitatively. That is, the method to select the basic material resistances ΔK_S, K_C and the simulation parameters α_1, β_1, α_2, and β_2 stated previously has to be proposed and validated. The proposal in this paper is to select ΔK_S as ΔK_{th} obtained for low K_{max} FCG test, and K_C as the fracture toughness K_{IC}. Then it is proposed to find these simulation parameters by first assuming some initial values, run simulation until the past experimentally obtained γ is fitted. For this fitting, genetic algorithm (GA) [8] was applied.

It was considered that fitting the experimentally obtained γ is in other words to reproduce by the simulation some $\Delta K_{th,1}$ obtained for FCG test under some low $\Delta K_{max,1}$ held constant (without static failure), and to simulate $\Delta K_{th,2}$ obtained under FCG test under some high $K_{max,2}$ held constant (with static failure), with the same simulation parameters α_1, β_1, α_2, and β_2. Because simulation of $\Delta K_{th,1}$ is not affected by static failure mode, it was considered possible to presume simulation parameters α_1 and β_1 from this simulation, independently of α_2 and β_2. Thus, simulation parameters were set as $\alpha_2 = 1$ and $\beta_2 = 0$ and α_1 and β_1 were presumed by reproducing $\Delta K_{th,1}$ with the simulation (Step 1 in Fig. 5).

After presuming simulation parameters α_1 and β_1, α_2 and β_2 were presumed by reproducing $\Delta K_{th,2}$

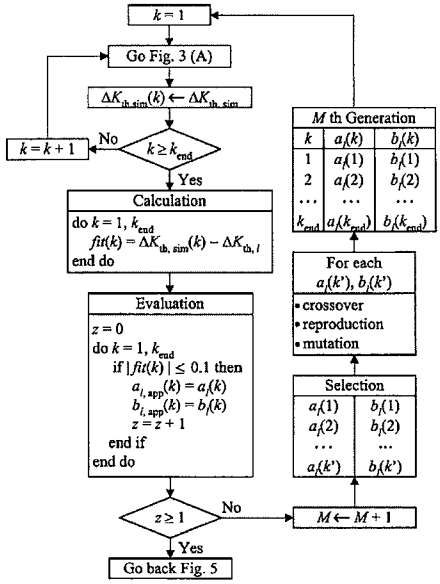


FIG. 6—*GA algorithm for Mth generation.*

with the simulation (Step 2 in Fig. 5). In this process, α_1 and β_1 obtained in Step 1 are used. The procedure in Fig. 5 and the GA algorithm (Fig. 6) is explained in detail in the following.

Concrete Procedure to Presume Simulation Parameters—Step 1. In Fig. 5, *RI* is an index to distinguish CT test specimens (i.e., scatter in material) or in words of computer programs, a seed for generating uniform random numbers ψ_{ij1} and ψ_{ij2}. Simulation is started with a CT specimen numbered as $RI = RI_{start}$. The basic material resistances throughout the following procedures are set as $\Delta K_S = \Delta K_{th,1}$ and $K_C = K_{IC}$. k_{end} candidates are considered, or in GA terminology "individual," for the simulation parameters designated as $\alpha_1(k)$ and $\beta_1(k)$ ($k = 1 \sim k_{end}$). As an initial value, or in GA terminology "generation $M = 1$" for $\alpha_1(k)$ and $\beta_1(k)$, random uniform numbers generated with seed $RI = RI_{start}$ are assigned. Then the test condition K_{max} is set as $K_{max,1}$ and the result desired to reproduce by simulation ΔK_{th} as $\Delta K_{th,1}$. As mentioned previously, $\alpha_2(k) = 1$ and $\beta_2(k) = 0$ were applied for this step and the GA subroutine summarized in Fig. 6 was called. Here, l is a parameter to formally distinguish the step number, set as 1 in this step.

In the GA subroutine, the FCG simulation explained previously for kth candidate ($k = 1 \sim k_{end}$) with the simulation parameters $\alpha_1(k)$, $\beta_1(k)$, $\alpha_2(k)$, and $\beta_2(k)$ is run and the obtained ΔK_{th} is saved as $\Delta K_{th,sim}(k)$. After $\Delta K_{th,sim}(k)$ is obtained for all k, the validity of the assumed α and β, or in GA terminology "fitness," is evaluated by the function $fit(k)$ defined as

TABLE 1—*(a) K_{max}-const ΔK_{th} test data (CT specimen configuration and material properties).*

	Material	W (mm)	B (mm)	a_0 (mm)	E (GPa)	ν	K_{IC} (MPam$^{1/2}$)	g (μm)
	S55C [5]	50.0	12.5	18.00	206	0.3	80	30
	Al7050 [4]	30.5	2.5	12.15	70	0.3	29	60
	Ti-6Al-4V [2]	25.0	8.0	9.00	116	0.3	67	30

(b) K_{max}-const ΔK_{th} test data (loading condition and results).

Material	ΔK_0 (MPam$^{1/2}$)	C (mm^{-1})	$K_{max,1}$ (MPam$^{1/2}$)	$\Delta K_{th,1}$ (MPam$^{1/2}$)	$K_{max,2}$ (MPam$^{1/2}$)	$\Delta K_{th,2}$ (MPam$^{1/2}$)	γ	C_{Paris}	m
S55C [5]	12	−0.7	18	2.6	70	2.0	−0.0115	1.35×10^{-9}	3.77
Al7050 [4]	3	−0.8	5.5	1.1	22	0.73	−0.0224	4.00×10^{-7}	2.93
Ti-6Al-4V [4]	3	−0.08	26.5	2.33	56.5	2.04	−0.0097	7.00×10^{-9}	3.77

TABLE 2—*Simulation parameters for GA.*

Material	a_{END} (mm)	n_{row}	ncolumn	k_{end}	RI_{start}	RI_{end}
S55C	21.1	138	400	10	1001	1010
Al7050	14.3	54	40	10	1001	1010
Ti-6Al-4V	20.8	428	250	10	1001	1010

$$fit(k) = \Delta K_{th,sim}(k) - \Delta K_{th}. \tag{9}$$

It is considered that the assumptions for $\alpha_1(k)$ and $\beta_1(k)$ were valid when $|fit(k)| \leq 0.1$. The number of the candidates satisfying this condition is designated as z. In case $z \geq 1$, then it is considered that valid $\alpha_1(k)$ and $\beta_1(k)$ were found, and return to the main routine in Fig. 5. Finally, the desired α_1 and β_1 are set for the CT specimen (a case of $RI=RI_{start}$) as the average of z candidates.

On the other hand, in case $z=0$, the $M=2$ generation candidates $\alpha_1(k)$ and $\beta_1(k)$ are generated by applying the GA methodology such as elite selection, one point crossover with corssover probability =0.8, and usual mutation with probability=0.1. Then the procedure in Fig. 6 is repeated until $\alpha_1(k)$ and $\beta_1(k)$ that satisfy $|fit(k)| \leq 0.1$ are found.

Step 2. The second step is to presume α_2 and β_2 to reproduce $\Delta K_{th,2}$ corresponding to $K_{max,2}$. The procedure explained in Step 1 is applied faithfully, after the test condition K_{max} is set as $K_{max,2}$ and the result to be reproduced by simulation ΔK_{th} is set as $\Delta K_{th,2}$. In addition, $\alpha_2(k)$ and $\beta_2(k)$ are treated as unknowns, and α_1 and β_1 as given.

After simulation parameters α_1, β_1, α_2, and β_2 are obtained for a specific CT specimen (a case of $RI=RI_{start}$), the above-mentioned simulation parameters presuming procedure for cases of $RI=RI_{start} \sim RI_{end}$ is repeated to optimize the obtained simulation parameters in a statistical sense.

Numerical Example of Presuming Simulation Parameters by GA—Simulation parameters α_1, β_1, α_2, and β_2 were presumed for Ti-6Al-4V [2], Al7050 [4], and carbon steel S55C [5], that experienced the decrease in ΔK_{th} due to high K_{max}, using the above-mentioned procedure. The experimental data used for the presumption is summarized in Tables 1(a) and 1(b). Here W, B, and a_0 are width, thickness and initial crack length of an ASTM CT specimen [6]. E, ν, K_{IC} is Young's modulus, Poisson's ratio, and fracture toughness, respectively. g is the average grain size and was read from the photograph in the references. ΔK_0 and C are the load control parameters of K_{max}-constant ΔK_{th} test [Eq 1], and $(K_{max,l}, \Delta K_{th,l})$ $(l=1,2)$ are the data set used for compilation of γ. Moreover, C_{Paris} and m are the constants of Paris law $da/dN=C_{Paris} \cdot (\Delta K)^m$ mm/cycle. Other parameters in Figs. 3, 5, and 6 are summarized in Table 2. Finally, a_{END} was set as the value corresponding to $\Delta K=\Delta K_S/2$ in Eq 1.

The results are shown in Table 3. Although the test specimen configuration, material constants, grain size, load control parameters, and the γ were different, it can be seen from Table 3 that the presumed α_1, β_1, α_2, and β_2 are independent of material in an engineering sense. Though these results are limited to the materials under consideration, and thus a further verification might be necessary in the future, it seems that the results as the microscopic grain material resistances having some unique relationship with the macroscopic material resistances in a statistical sense, in case a material experiences the decrease in ΔK_{th} due to high K_{max}.

Proposal of a Method to Quantitatively Estimate γ

In summary, though further discussion might be necessary, the method proposed to estimate γ is as follows. First, select basic material resistance ΔK_S as ΔK_{th} obtained for a low K_{max} constant FCG test, and K_C as fracture toughness K_{IC}. Note that the constants in Paris law are obtained through this FCG test. Then run the FCG simulation described in Fig. 3 with the recommended simulation parameters in Table 4, which

TABLE 3—*GA results* (mean±standard *deviation).*

Material	α_1	β_1	α_2	β_2
S55C	0.29±0.02	0.87±0.02	0.31±0.02	0.69±0.05
Al7050	0.32±0.06	0.88±0.03	0.28±0.04	0.69±0.11
Ti-6Al-4V	0.26±0.06	0.81±0.05	0.31±0.04	0.68±0.09

TABLE 4—*Recommended simulation parameters.*

α_1	β_1	α_2	β_2
0.29	0.86	0.30	0.69

are the average of three materials summarized in Table 3. Thus, the decrease in ΔK_{th} due to high K_{max} can now be estimated quantitatively once a single low K_{max}-constant FCG test and a fracture toughness test are run.

Validation of the Proposed Method

The proposed γ estimation method was validated by applying it to a case for an embrittled carbon steel S55C (hereafter named as S55C-E. Composition in wt %: 0.53C, 0.17Si, 0.62Mn, 0.023P, 0.018S, 0.12Cr, balance Fe. 1100°C × 1 h, air cooling: σ_B=814 MPa, σ_Y=413 MPa), which also experienced the decrease in ΔK_{th} due to high K_{max}. S55C-E's average grain size g=100 μm and the fracture toughness measured by the tested CT specimen was 64 MPam$^{1/2}$. Thus, $K_{max,2}$ was selected as 50 MPam$^{1/2}$. $K_{max,1}$ was set as 18 MPam$^{1/2}$, same with that for the un-embritteled S55C [5]. FCG test result for this S55C-E and unembrittled S55C [5] are summarized in Figs. 7(*a*) and 7(*b*), respectively.

Table 5 compares the simulated and experimental results for S55C-E. In this simulation, the basic material resistances were selected as $\Delta K_S = \Delta K_{th,1}$=3.29 and K_C=64 MPam$^{1/2}$. The recommended simulation parameters in Table 4 were used. For comparison, simulation of the normal S55C was run with the simulation parameters in the same table. The results for the unembrittled S55C were also summarized in Table 5.

It is seen in Table 5 that, naturally, experimental γ for the unembrittled S55C is simulated well also with the recommended simulation parameters in Table 4. It is also seen in Table 5 that the γ for embrittled S55C was more than doubled compared with that of unembrittled S55C in experiment, and that the proposed simulation predicted this tendency. When the scatter in experimental ΔK_{th} is considered, it seems that the estimation was acceptable in an engineering sense.

Discussion

A very interesting result was obtained that the simulation parameters α and β in the proposed FCG simulation seem to be independent for materials, under assumptions that the materials experienced the decrease in ΔK_{th} due to high K_{max} and that basic material resistances are chosen as proposed. It cannot be denied that there is still a possibility that the materials chosen for numerical examples were very special. For example, though the CT specimen configuration, material constants, grain size, load control parameters, and the γ were different, the $\Delta K_{th}/K_{IC}$ were in the range of 0.03–0.04 for all the materials considered. However, $\Delta K_{th}/K_{IC}$ for stainless steel SUS304, high tension steel HT60, and carbon steel SS400 (that did not experience the decrease in ΔK_{th} due to high K_{max}) were all less than 0.02 [5]. Thus, though further validation might be necessary, it is considered that the materials selected in this paper are special in the

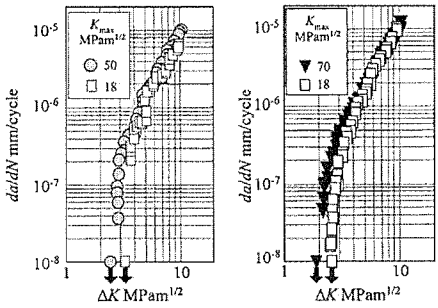


FIG. 7—*FCG behavior of (a) embrittled S55C(S55C-E) and (b) S55C [5].*

TABLE 5—*Comparison of* γ *by simulation and experiment.*

Material	γ by simulation	γ by experiment
S55C	−0.0117	−0.0115
Embrittled S55C (S55C-E)	−0.0230	−0.0268

meaning that they experienced the decrease in ΔK_{th} due to high K_{max}, and that the $\Delta K_{th}/K_{IC}$ might present some information on whether a material would experience the decrease in ΔK_{th} due to high K_{max}.

There might be an opinion that the linear elastic fracture mechanics (LEFM) concept is applicable to the continuum media where material is linear and homogeneous, and in microscopic level, this is not the case as in the FCG model in Fig. 2. However, assumptions for the proposed method were that (1) a very thin CT specimen with thickness approximately equal to the grain size (plane stress) is considered and (2) the quantity of the crack growth considered in one load cycle is smaller than the range the material is assumed to be uniform (the grain size). Because the crack length of this sliced CT specimen is large enough to apply the LEFM concept, it was thought that if attention is paid to the region close to the crack tip, the LEFM methodology might be valid in an engineering sense. The simulation results seemed to support the assumptions made for the proposed method.

Conclusions

In this paper, a quantitative method to estimate the decrease in ΔK_{th} due to high K_{max} (γ in Fig. 1), that is observed for some materials in constant K_{max} FCG tests, is proposed. The FCG mechanism is considered the same regardless of ΔK or K_{max} on the point that macroscopic crack front growth was observed as a coalescence of microscopic cracks in grains. Another assumption is that microscopic crack growth is selectively determined as cyclic or static mode failure, depending on the direction of the slip plane of the grain. This conceptual FCG model (Fig. 2) was evolved to a concrete simulation algorithm applied to a CT specimen, using minimal experimental data (the ΔK_{th} from a single low K_{max} constant FCG test and the fracture toughness). The simulation algorithm consists of a method to assign the statistical microscopic material resistance distribution and a method to determine local (microscopic-)crack driving forces at the crack front. The parameters to give the scatter in microscopic material resistances were inversely determined from the experimental data of carbon steel, Al, and Ti alloys with the aid of genetic algorithm. Finally, the proposed method is validated by comparing predictions with experimentally determined values of the decrease in threshold on an embrittled carbon steel. As a result, the γ can be predicted once a single K_{max}-constant FCG test and a fracture toughness test are run.

References

[1] Paris, P. C. and Erdogan, F., "A Critical Analysis of Crack Propagation Laws," *Trans. ASME, J. Appl. Mech.* 85, 528–534 (1963).

[2] Boyce, B. L. and Ritchie, R. O., "Effect of Load Ratio and Maximum Stress Intensity on the Fatigue Threshold in Ti-6Al-4V," *Eng. Fract. Mech.*, 68(2), 129–147 (2001).

[3] Schmidt, R. A. and Paris, P. C., "Thresholds for Fatigue Crack Propagation and the Effects of Load Ratio and Frequency," *Progress in Flaw Growth and Fracture Toughness Testing, ASTM STP 536*, American Society for Testing and Materials, West Conshohocken. PA, 1973, pp. 79–94.

[4] Newman, J. A., Riddell, W. T., and Piascik, R. S., "Effects of Kmax on Fatigue Crack Growth Thresholds in Aluminum Alloys," *Fatigue Crack Growth Thresholds, Endurance Limits, and Design, ASTM STP 1372*, edited by J. A. Newman, W. T. Riddell, and R. S. Piascik, American Society for Testing and Materials, West Conshohocken. PA, 2000, pp. 63–77.

[5] Meshii, T., Ishihara, K., and Watanabe, K., "Assessment for Decrease in Threshold Stress Intensity Factor (SIF) Range due to High Maximum SIF," *J. ASTM Int.*, 2(6), 1–13 (2005).

[6] ASTM Standard E647-95a, "Standard Test Method for Measurement of Fatigue Crack Growth Rates," *Annual Books of ASTM Standards*, Section 3, Vol. 03.01, West Conshohocken, PA, 1999.

[7] Ritchie, R. O., and Knott, J. F., "Mechanisms of Fatigue Crack Growth in Low Alloy Steels," *Acta Metall.*, 21(5), 639–648 (1973).

[8] Kitano, H., *Genetic Algorithm (in Japanese)*, Sangyo Tosho, Tokyo, 1993, pp. 13–15.

Journal of ASTM International, March 2006, Vol. 3, No. 3
Paper ID JAI13180
Available online at www.astm.org

S. C. Forth,[1] *J. C. Newman, Jr.,*[2] *and R. G. Forman*[3]

Anomalous Fatigue Crack Growth Data Generated Using the ASTM Standards

ABSTRACT: The ASTM standard for fatigue crack growth, E 647, was co-developed by industry and government in the late 1970s to define a standard procedure for generating material crack growth behavior under a variety of loading conditions. The standard specifies tolerances on laboratory procedures, specimen configurations to generate material characterization information of a high integrity. Recent research developing fatigue crack growth rate data has uncovered significant issues with the standard test method and specimen configurations. The data generated has been largely dependent on specimen configuration, i.e., M(T) and C(T) specimens produce very different crack growth rate curves; C(T) specimens of different sizes do not generate the same material response; and finally, the development of steady-state, as defined using constant ΔK testing, does not agree with the data generated with the standard ASTM test method. Therefore, in this paper the authors present data that does not lend confidence in the integrity of the standard C(T) specimen tested using the ASTM standard method and investigate causes for the observed anomalous crack growth rate behavior.

KEYWORDS: fatigue crack growth, ASTM E 647, crack growth, crack closure

Introduction

The ASTM Standard Test Method for Measurement of Fatigue Crack Growth Rates (E 647) was co-developed by industry and government in the late 1970s to define a standard procedure for generating material crack growth behavior under a variety of loading conditions [1]. One of the primary motivations for a standard crack growth rate test method at the time was the United States Air Force damage tolerance initiative for aircraft fuselage and wing systems [2]. The operating environment for an aircraft fuselage or wing produces relatively few cycles per flight hour and the crack propagation rate is considered stable in thin-gage materials. Therefore, the standardized laboratory middle tension, M(T), specimens were designed to produce linear-elastic, stable, material-dependent crack growth properties similar to those observed in practice. Several years of testing using this specimen configuration produced reliable, repeatable data because little change was introduced into tolerances or procedures of the standard testing methodology. However, the aerospace industry desired crack growth information about thicker, smaller, more complex material systems, for applications such as engines, resulting in other specimen configurations and testing procedures being adopted into the ASTM E 647 standard [1]. The development of the compact tension, C(T), specimen [3] and the improvement in automated testing systems has led to the employment of the standard to a wide-range of material forms.

Recent research developing fatigue crack growth rate data has uncovered significant issues with the standard test specimens [4]. The data generated have been largely dependent on specimen configuration, i.e., M(T) and C(T) specimens produce very different crack growth rate curves [5]; C(T) specimens of different sizes do not generate the same crack growth rate curve [6]; and the development of steady-state, as defined using constant ΔK testing, does not agree with the data generated with the standard ASTM test method [7]. Therefore, in this paper, the authors discuss the standard ASTM test method; present fatigue

Manuscript received April 8, 2005; accepted for publication October 10, 2005; published December 2005. Presented at ASTM Symposium on Fatigue and Fracture Mechanics: 35th Volume on 18–20 May 2005 in Reno, NV; R. E. Link and K. M. Nikbin, Guest Editors.

[1] Materials Research Engineer, NASA Langley Research Center, MS 188E, 2 West Reid St., Hampton, VA 23681.

[2] Professor, Department of Aerospace Engineering, Mississippi State University, 330 Walker Engineering Lab, Hardy Street, Mississippi State, MS 39762.

[3] Senior Scientist, NASA Johnson Space Center, 2101 NASA Road 1, Mail Code EM2, Houston, TX 77058.

Copyright © 2006 by ASTM International, 100 Barr Harbor Drive, PO Box C700, West Conshohocken, PA 19428-2959.

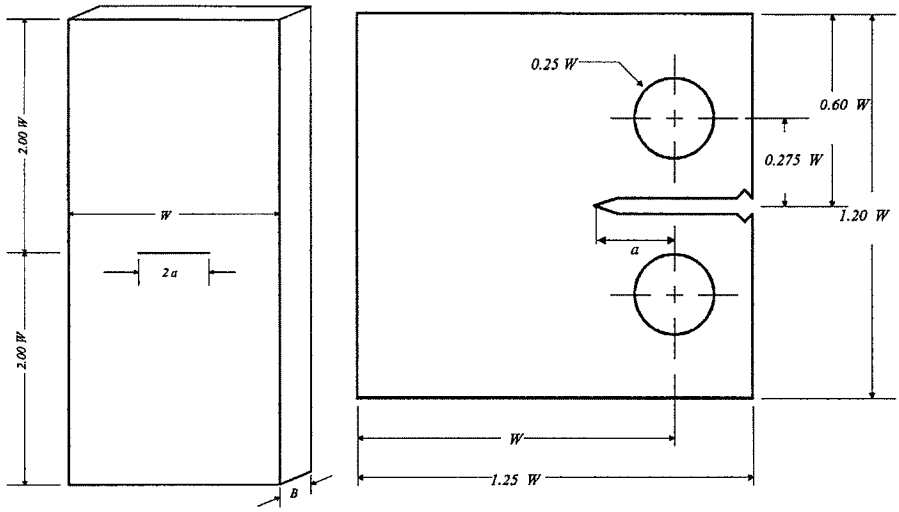


FIG. 1—*Schematic of middle tension, M(T) and compact tension, C(T), specimens.*

crack growth rate data that are dependent on specimen configuration and environment; and discuss causes for the observed anomalous material crack growth rate behavior.

Standard Fatigue Crack Growth Rate Data

The fatigue crack growth rate versus stress intensity factor range (da/dN versus ΔK) has long been deemed a material response curve [8] to be used in design, analysis, etc. The fatigue crack growth rate curve is used as a material property because fracture mechanics theory is fundamentally based on the assumption that the relationship between da/dN and ΔK is independent of geometric configuration, termed similitude [9]. Similitude of the stress intensity solution requires that any data generated using laboratory specimens can be directly applied to predicting crack growth in complex structural geometries. The only means for similitude to function as intended is if the laboratory data represents a physical steady-state condition, e.g., equilibrium. Steady-state is the condition where the crack growth rate data generated is solely dependent on the material response, not specimen configuration or laboratory environment. Therefore, ASTM E 647 specifically outlines experimental procedures, specimen geometries and crack configurations along with tight tolerances on dimensions and operating parameters to generate the steady-state fatigue crack growth response that will maintain similitude. ASTM E 647 defines the compact tension, C(T), and middle tension, M(T), specimens as suitable for maintaining steady-state and similitude conditions. Figure 1 is a graphic depiction of both specimens where the geometric tolerances on width are dictated by the material yield stress such that the uncracked ligament of the specimen is predominately elastic. The tolerance on thickness, B, is a function of the width, W, where a C(T) specimen is $W/20 < B < W/4$ and an M(T) is $W/8 < B < W/4$.

Fatigue crack growth rate data for 7075-T73 aluminum [10,11] are presented in Fig. 2 to be representative of typical data and to be used as a baseline for comparisons made in this paper. The data were generated in accordance with ASTM E 647 using 76-mm wide, 12.7-mm thick compact tension, C(T), and middle tension, M(T), specimens (depicted graphically in Fig. 1). The relationship between stress ratio, fatigue crack growth rate, specimen configuration and stress intensity factor range presented in Fig. 1 is considered typical because:

(1) the M(T) and C(T) data are similar because the theory of similitude in the stress intensity factor range, ΔK, states that different specimen configurations have similar fatigue crack growth rate properties, da/dN versus ΔK, and

(2) the R=0.1 data have slower crack growth rates than the R=0.7 data for any given ΔK, and the

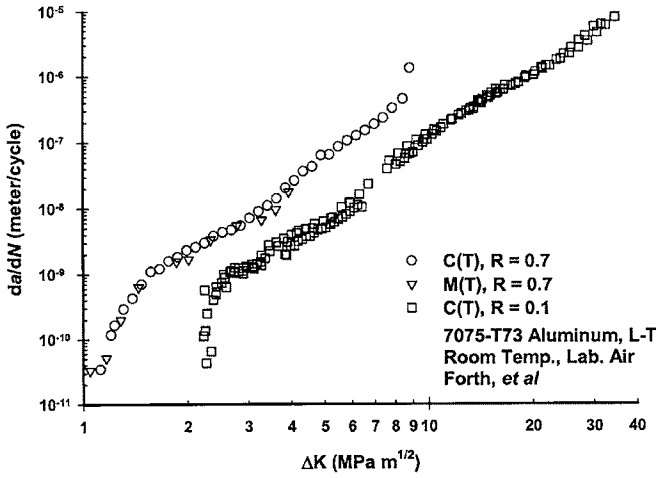


FIG. 2—*Baseline crack growth rate vs. stress intensity factor range data.*

curves run nearly in parallel over the entire range of ΔK, because the relationship of crack growth rate to stress ratio is an extrinsic crack closure effect having a different steady-state condition [12].

Anomalous Fatigue Crack Growth Rate Data

Fatigue crack growth rate data for D6AC steel are presented in this section that does not adhere to the conventions described as typical. First, the details of the ASTM E 647 standard experimental methods used to obtain the atypical data are discussed. Second, data generated using C(T) and M(T) specimens are presented that do not support similitude. Last, data are presented that does not support steady-state. The steel alloy D6AC was chosen for study because it is used extensively by the aerospace industry [13]. Constant stress ratio, R, of 0.1 and maximum stress intensity factor range, K_{max}, of 22 MPa $m^{1/2}$ fatigue crack growth rate data were generated using four different C(T) specimen configurations (W=76.2 mm, B=12.7 mm, W=76.2 mm, B=5.08 mm, W=50.8 mm, B=5.08 mm, and W=25.4 mm, B=5.08 mm) and one M(T) specimen configuration (W=76.2 mm, B=5.08 mm) in both laboratory and dry air.

Experimental Setup

Testing was conducted in accordance with ASTM E 647. The laboratory environment, denoted "room temp, lab air" varies between room temperatures of 20 to 30°C, with a mean of 23°C, and the laboratory air relative humidity varies between 24 to 38 %, with a mean of 28 %. Malfunctions in the air conditioning system have resulted in relative humidity levels approaching 60 % and the tests conducted during these times are discussed separately. A dry air environment (<3 % relative humidity) was set up locally around specific specimens, while maintaining the same temperature range, to assess the affect of humidity on the fatigue crack growth rate data being generated. The "dry air" environment was accomplished by plumbing filtered, compressed air into a plastic enclosure sealing the specimen. The air was deemed clean of oil particulates from the compressor by placing clean, white paper in front of the hose and periodically assessing the cleanliness of the paper over several months of operation.

All experiments were conducted in loading frames of 89 to 222 Newton capacity. The load cells were calibrated using ASTM Standard Practices for Force Verification of Testing Machines (E 4). Load path alignment was verified using ASTM Standard Practice for Verification of Specimen Alignment under Tension Loading (E 1012). Load range cards were used to improve resolution for lower applied forces to within 2 % of the expected force. In several cases an additional in-line 22 Newton load cell was used to resolve small forces. The tests were conducted in force control at a frequency of 20 Hz using an analog controller. A computer control system [14] was used for K control to adjust the forces based on compliance

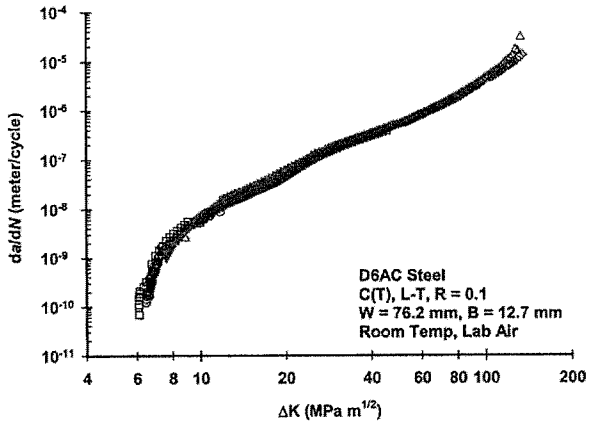


FIG. 3—*Representative variability of crack growth rate versus stress intensity factor range data.*

readings from strain or displacement gages and user input. Visual measurements of the crack length were taken throughout the test to verify the compliance based crack length used to control the test system. The middle tension, M(T), specimens were installed in hydraulically actuated wedge grips and force was shed manually using the step method described in ASTM E 647. The compact tension, C(T), specimens were installed in sized clevises for each width tested and force was shed using K control. Force was shed at a rate of −80/m with the exception of the 25.4 mm wide C(T) specimens where a shed rate of −240/m was used because fatigue crack growth rates below 10^{-9} m/cycle could not be physically obtained with a lower shed rate on this specimen. A minimum of one repeat was performed for all test data shown herein on a separate specimen and the scatter in the data between tests was less than 10 % on ΔK, for any given growth rate, *da/dN*, in all cases. Figure 3 is a representative plot of the amount of scatter observed in six tests conducted on six separate C(T) specimens at a stress ratio of 0.1. The fatigue crack growth rate data were reduced using software per the data reduction guidelines of ASTM E 647.

Similitude

Similitude is one of the fundamental theories of fracture mechanics where the stress intensity factor solution is transferable from a laboratory specimen to a complex structure. In other words, similitude means that the ΔK driving a crack in a C(T) specimen will propagate a crack in an aircraft fuselage at exactly the same rate, *da/dN*. Therefore, crack growth rate data generated on one laboratory specimen are directly applicable to any other laboratory specimen or a structure. However, recent research has shown that variations in the configuration of the ASTM E 647 laboratory specimens can give distinctly different crack growth rate curves [6].

Crack growth rate data were generated using M(T) and C(T) specimens of similar thickness and width at a stress ratio of 0.1. The tests were conducted concurrently; therefore, it is assumed that the temperature and humidity range of the laboratory environment for the two datasets are similar. Figure 4 plots crack growth rate, *da/dN*, versus stress intensity factor range, ΔK, for a stress ratio, R=0.1, condition. The differences between the M(T) and C(T) data at R=0.1 are large near threshold, e.g., at a ΔK of approximately five, the M(T) is propagating at a rate twice that of the C(T). Based on the results presented in Fig. 4, the fatigue crack growth rate data for D6AC steel is considered anomalous because similitude between M(T) and C(T) specimens does not hold.

Steady-State Crack Growth

The definition of a steady-state crack is given in ASTM Standard Terminology Relating to Fatigue and Fracture Testing (E 1823) as "a crack that has advanced slowly until the crack-tip plastic zone size and crack-tip sharpness remain constant with further crack extension." ASTM standard E 647 does not contain

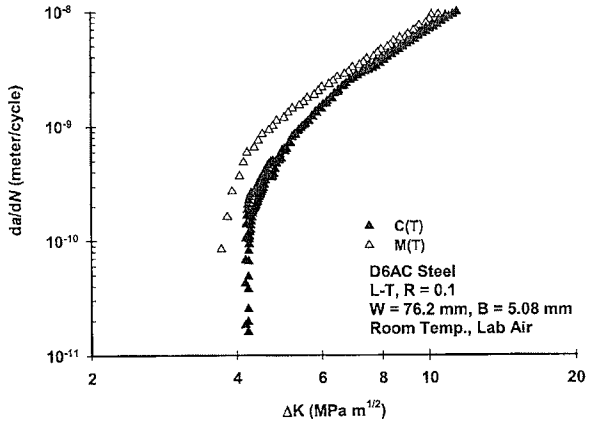


FIG. 4—*Comparison of M(T) and C(T) specimen crack growth rate vs. stress intensity factor range data.*

a definition of steady-state but uses the term freely in describing desirable characteristics of crack growth. Therefore, the authors adopted the above definition of steady-state as it is both reasonable and accurate for defining steady-state fatigue crack growth. It has been postulated in the literature [15] that there are three distinct mechanisms that affect crack-tip plastic zone size and sharpness: plasticity-, roughness-, and environment-induced closure. The full development of each of these closure mechanisms defines steady-state. Plasticity-induced crack closure is described by the development of a uniform plastic zone ahead of the crack tip and a well-defined crack wake [12]. The development of plasticity-induced closure is a function of both crack length and number of cycles, i.e., a cyclic phenomenon. Roughness-induced closure is described as the contact of crack wake asperities behind the crack tip [16]. The development of roughness-induced closure is a function of crack length and loading level, i.e., a physical phenomenon. Finally, environment-induced crack closure is described as the build-up of debris in the crack wake and blunting of the crack tip from chemical modification of the material due to environment [17–19]. The development of environment-induced closure is a function of time, i.e., a progressive phenomenon. The authors will look at each of these mechanisms to describe steady-state behavior.

Figure 5 is a plot of crack growth rate, da/dN, versus stress intensity factor range, ΔK, for the 76.2-mm wide C(T) specimens tested. The 12.7-mm thick specimen data are plotted as circles and the 5.08-mm thick as triangles, with the filled symbols representing the data generated in laboratory air. The

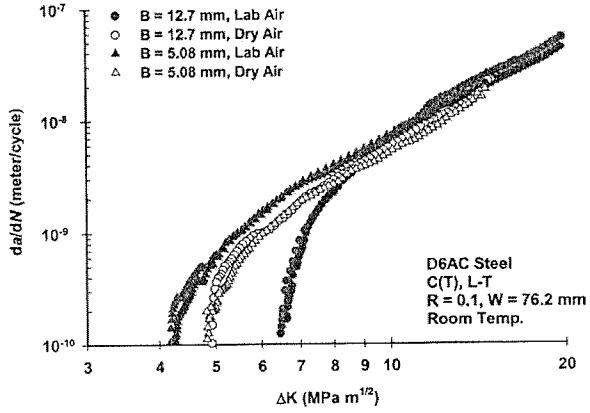


FIG. 5—*Crack growth rate vs. stress intensity factor range data for different environments.*

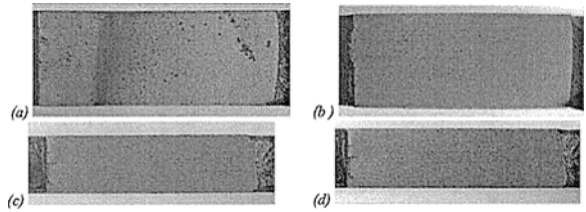


FIG. 6—*Photographs of representative fracture surfaces for C(T) specimens: (a) 76.2-mm wide, 12.7-mm thick in lab air; (b) 76.2-mm wide, 12.7-mm thick in dry air; (c) 76.2-mm wide, 5.08-mm thick in lab air; and (d) 76.2-*mm *wide, 5.08-mm thick in dry air.*

12.7-mm thick specimens tested in lab air produced a much higher fatigue crack growth threshold (Fig. 5) and had a different fracture surface appearance than any of the other conditions. The fracture surface of the 12.7-mm thick lab air tests appear to have noticeable oxidation [Fig. 6(*a*)] when compared to the 5.08-mm-thick lab air fracture surface [Fig. 6(*c*)]. Based on the appearance of oxide, fretting debris, it is plausible that environmental-induced crack closure caused the crack to arrest producing a high threshold. Initial verification of this theory is the 24 % lower threshold achieved by reducing the relative humidity of the testing environment using dry air and the reduction of observed oxide, fretting debris from the fracture surface [Fig. 6(*b*)]. In contrast to the 12.7-mm thick C(T) data, changing the environment had no apparent effect on the appearance of the fracture surface of the 5.08-mm thick C(T) specimens [Figs. 6(*c*) and 6(*d*)]; however, the crack growth rate was approximately 15 % slower over the entire range of ΔK. The trend of slower crack growth rates at lower humidity levels is not uncommon for most aerospace metallic materials that are chemically susceptible to hydrogen embrittlement [20].

Constant ΔK testing has traditionally been used to define steady-state conditions because the driving force is held constant, which in turn develops the steady-state plasticity condition [21]. Furthermore, if there is significant crack growth during a constant ΔK test, the steady-state roughness condition will also develop. Lastly, if the environment where the test is being conducted is also controlled, then steady-state environmental conditions will develop, and subsequently steady-state cracking will exist. Constant ΔK testing was performed to define the steady-state development in the 76.2-mm wide specimens [Fig. 6(*a*)]. A constant ΔK value of approximately 7.7 MPa $m^{1/2}$ was chosen because that is the point where the crack growth rate data presented in Fig. 5 diverge and the growth rate is fast enough to generate data during a reasonable amount of time. Figure 7 is a plot of crack growth, Δa, versus cycle count for constant ΔK $\sim$7.7 MPa $m^{1/2}$ tests performed in laboratory and dry air. The crack growth rate, the slope of the data presented in Fig. 7, is the same for lab and dry air for a little more than one million cycles, nearly 14 h. Then, the lab air test transitions to an eventual steady-state crack growth rate (9.32×10^{-10} m/cycle) that is one quarter that of the test in dry air (4.05×10^{-9} m/cycle).

The first subcomponent of the steady-state condition investigated was plasticity-induced crack closure because it is the simplest of the three closure conditions to identify. Plasticity-induced crack closure is a cyclic phenomenon, and steady-state plasticity develops rapidly at the crack tip during a constant ΔK test, within a million cycles [12]. For this study, it was presumed that plasticity-induced closure had developed a steady-state condition when the slope of the crack growth versus cycles plot became linear over one million cycles. This amount of cycles was chosen because it is significant with respect to the crack growth rate, i.e., enough damaging cycles accrue that a steady-state plasticity condition exists along both the crack tip and wake. Analyzing the data presented in Fig. 7, steady-state plasticity had developed over the first million cycles for both the lab and dry air conditions, leaving roughness- and environmental-induced crack closure as possible factors contributing to the different crack growth behavior of the lab air test.

Roughness-induced closure is a physical phenomenon, typically developing a steady-state condition with increasing crack length [16]. For this study, it was presumed that roughness-induced closure had developed a steady-state condition when the slope of the crack growth versus cycles plot became linear over crack growth of $\Delta a \sim 1$ mm. This amount of crack growth is significant with respect to the size of the microstructure of D6AC steel, approximately 2 to 30 μm in diameter, leading to a crack front and wake

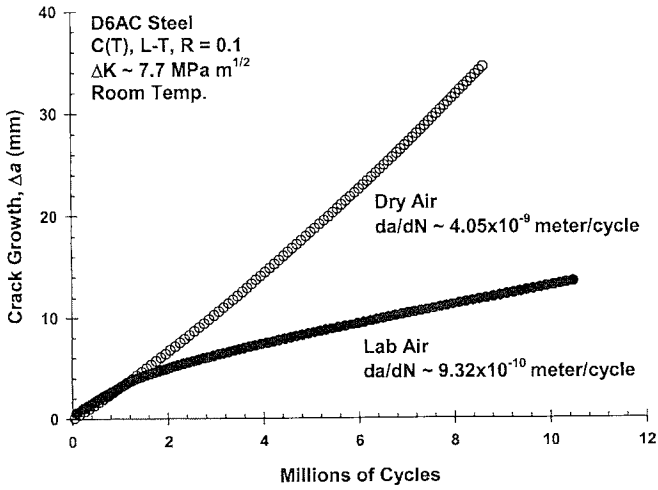


FIG. 7—*Constant ΔK crack growth vs. cycle count data for different environments.*

that will span several grains [13]. The results of the constant ΔK tests presented in Fig. 7 show that the steady-state roughness-induced crack closure condition developed concurrently with the plasticity-induced crack closure steady-state.

Consequently, environmental-induced closure remains as the primary reason for the retardation of crack growth rate in the constant ΔK tests (Fig. 7). Environmental-induced closure develops over time [20], as the crack tip is blunted and oxide/fretting debris builds on the crack face. For this study, steady-state environment-induced crack closure is defined as a linear relationship between crack growth rate and time. In this case, it took nearly 14 h for the environmental-induced closure to begin to noticeably affect the crack growth rate of the constant ΔK test in laboratory air. Furthermore, the steady-state condition in laboratory air took more than 80 h to develop. Photographs of the fracture surfaces of the constant ΔK tests, shown in Figs. 8(*a*) and 8(*b*) for lab and dry air, respectively, confirms that environment-induced crack closure, seen as oxide, fretting debris [Fig. 8(*a*)], is affecting the crack growth rate. The data presented in Fig. 5 show that the crack growth rate for the 12.7-mm thick C(T) at a ΔK of approximately 7.7 MPa $m^{1/2}$ is 1.93×10^{-9} and 2.56×10^{-9} m/cycle for lab and dry air, respectively. Neither of these values is within 20 % of the steady-state (constant ΔK) crack growth rate achieved using dry air. Nor are these values within a factor of two of the laboratory air steady-state (constant ΔK) crack growth rate. Therefore, assuming the constant ΔK data are representative of steady-state then the constant R test method is not generating a steady-state condition.

Based on the observed absence of environmental-induced debris on the fracture surface of the 5.08-mm thick, 76.2-mm wide C(T) specimen, [Fig. 6(*c*)] two other specimen widths (W=50.8 mm and 25.4 mm) were tested at this thickness to further evaluate similitude and the development of steady-state in the C(T) specimen. Constant R=0.1 testing was performed in both laboratory air (Fig. 9) and dry air (Fig. 10). Examining the data presented in Fig. 9, there appears to be little dependence in the crack growth rate on specimen width in laboratory air. However, once the tests were conducted in dry air, the

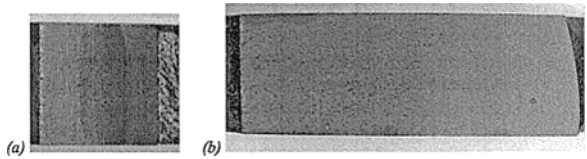


FIG. 8—*Photographs of fracture surfaces for constant ΔK tests: (a) lab air; (b) dry air.*

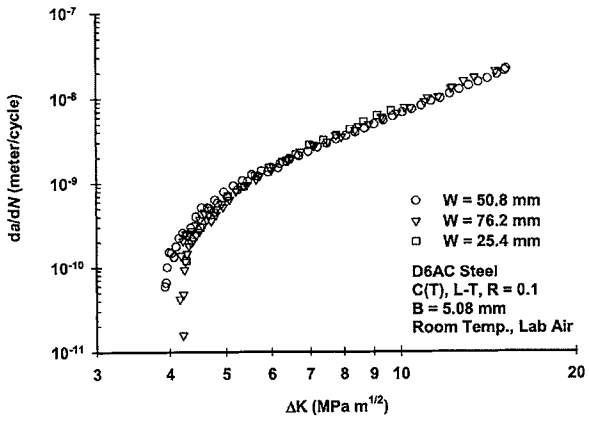


FIG. 9—*Crack growth rate vs. stress intensity factor range in lab air.*

76.4-mm wide specimen resulted in a 15 % lower crack growth rate than the 50.8- and 25.4-mm wide specimens. In an attempt to understand the variability seen between specimen configurations, Fig. 11 plots the 2 % offset measurement versus stress intensity factor range taken for one representative test of each specimen width for the lab and dry air environments. The 2 % offset measurement is useful for identifying trends in datasets where crack closure is expected to be prevalent, i.e., a rise in the offset value is typically an indication of crack closure [22]. The filled symbols represent the tests conducted in laboratory air, and while there are differences in offset measurements between the different specimen widths, the trend of an increasing amount of closure as ΔK is reduced is expected.

The crack growth rate data presented in Fig. 9 are relatively insensitive to specimen width because in each case crack closure is developing gradually until threshold is reached as shown in Fig. 11. The open symbols plotted in Fig. 11 represent the measurements taken during the dry air tests. The closure behavior of the 25.4- and 50.8-mm wide specimens in dry air is similar to the lab air experiments, explaining the comparable behavior in crack growth rate for these two specimen configurations in the lab and dry air environments, as shown in Figs. 9 and 10. However, the closure behavior of the 76.4-mm wide specimen in dry air is unusual. There is very little closure measured throughout the entire test and then the measurements peak near threshold. Initially, if there is little closure being measured in the 76.4-mm wide C(T), it would be expected that the growth rates would be faster at any given ΔK than either the 25.4- or

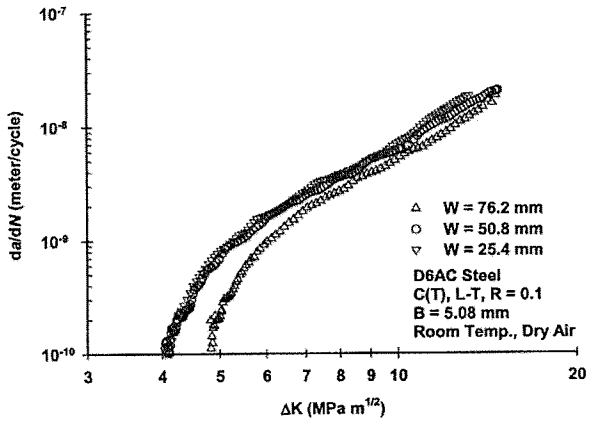


FIG. 10—*Crack growth rate vs. stress intensity factor range in dry air.*

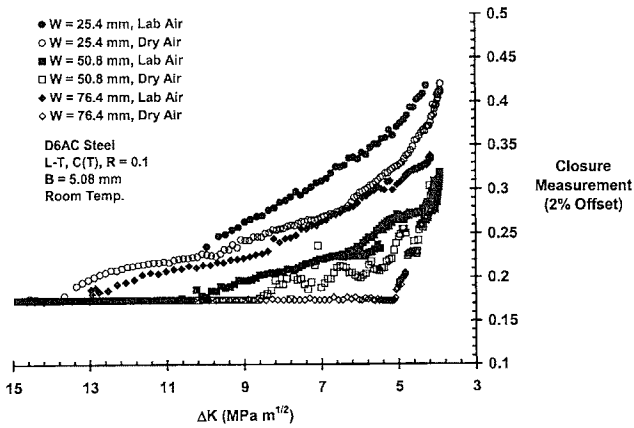


FIG. 11—*Closure measurements vs. stress intensity factor range.*

50.8-mm wide specimens because each of those specimen configurations develop measurable closure at a much higher ΔK. However, this is clearly not the case, as the growth rate of the 76.4-mm wide C(T) is consistently 15 % lower at any given value of ΔK than either of the other two specimens widths. Additionally, comparing the closure behavior of the 76.4-mm wide specimens tested in laboratory and dry air shows that the lab air test has more closure being measured, yet has higher growth rates at any value of ΔK and even a lower threshold. A previous note was made about hydrogen embrittlement being the possible cause for the behavior of the 76.4-mm wide specimen seen in Fig. 5. However, if hydrogen embrittlement were prevalent in this material system, the 50.8- and 25.4-mm wide specimens would also be affected, and the data presented in Figs. 9 and 10 show that they are not.

Constant K_{max}=22 MPa $m^{1/2}$ tests were performed using 76.4-mm wide, 12.7-mm thick, and 76.4-mm, 50.8-mm, and 25.4-mm wide, 5.08-mm thick C(T) specimens in both lab and dry air, shown respectively in Figs. 12 and 13, to develop crack growth rate data that have minimal influence from the previously described extrinsic effects. The crack growth rate data plotted in Figs. 12 and 13 show that for any value of ΔK, there is little difference between any of the tests, regardless of specimen width, thickness, or environment. The lack of sensitivity of the K_{max} test data to specimen configuration implies that the extrinsic effects such as crack closure have different effects on different specimens. Supporting this

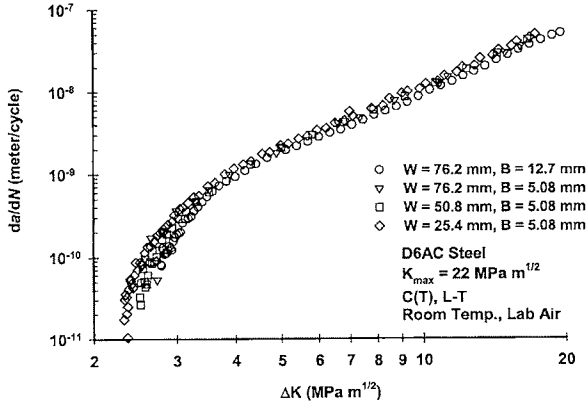


FIG. 12—*Crack growth rate vs. stress intensity factor range data for* K_{max}=22 MPa $m^{1/2}$ *in lab air.*

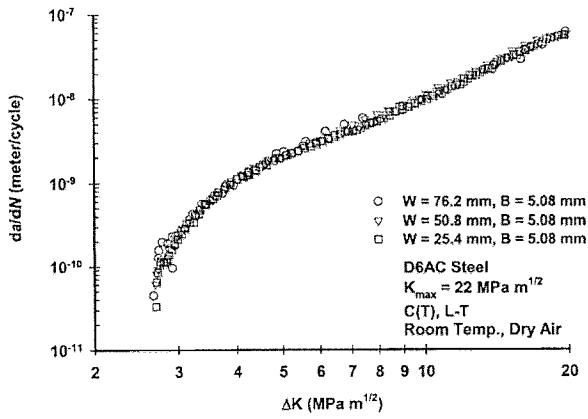


FIG. 13—*Crack growth rate vs. stress intensity factor range data for K_{max}=22 MPa $m^{1/2}$ in dry air.*

theory is the lack of dependence of the K_{max} tests on environment, which further infers that D6AC steel is insensitive to hydrogen embrittlement and that the previous discussions are correct in presuming the anomalous behavior observed being specimen dependent closure phenomena.

None of the tests conducted in laboratory air on 5.08-mm thick C(T) specimens, under normal conditions, exhibited signs of fretting/oxide debris on the fracture surface. However, there was a malfunction in the laboratory air conditioning system causing a spike in the relative humidity of the laboratory to approximately 60 %. Figure 14 is a plot of crack growth rate versus stress intensity factor range showing the effect of the spike during concurrent testing of 50.8- and 25.4-mm wide specimens. Figures 15(*a*) and 15(*b*) are photographs of the fracture surfaces of the 50.8- and 25.4-mm wide tests, respectively, with specific points where the air conditioning system malfunctioned is highlighted. Based on the photographs in Figs. 6 and 15, it is apparent that the 12.7-mm and 5.08-mm thick specimens are both susceptible to environmental-induced debris. However, the 12.7-mm thick specimens are sensitive to humidity levels within the normal operating range of the laboratory. The combination of the environment-dependent data presented in Figs. 5 and 14 with the K_{max} data presented in Figs. 12 and 13 suggest that different steady-state conditions develop for each C(T) specimen configuration because of differences in the way the specimens are reacting to environment-induced crack closure.

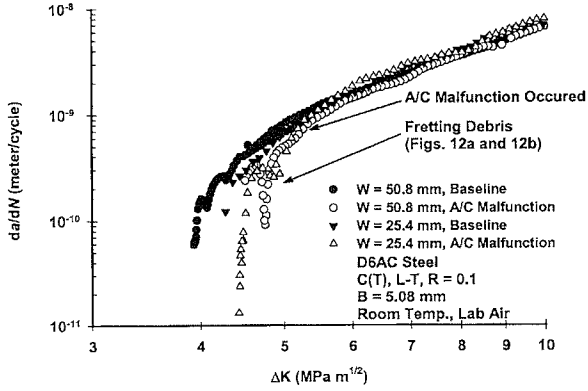


FIG. 14—*Crack growth rate vs. stress intensity factor range data for different specimen widths during a high humidity event.*

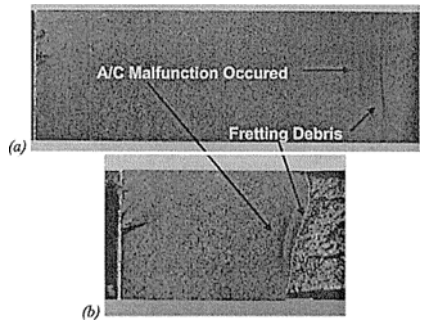


FIG. 15—*Photographs of the fracture surfaces for the 50.8-mm wide (a) and 25.4-mm wide (b) specimens tested during the A/C malfunction.*

Summary

It would be simple to dismiss the anomalous behavior of the D6AC steel as material dependent, and not an issue with the ASTM standard test specimens. However, Garr [6] has shown in testing of Inconel-718 that different sized C(T) specimens produce different crack growth rate responses. Forman [5] has shown that in several different steel alloys that the M(T) and C(T) response is different. Based on data presented within this paper and available in the literature, it appears that the crack growth behavior of the C(T) specimen is not well understood. The strong dependence of crack growth rate on specimen width, thickness and environment makes the C(T) specimen a poor choice for developing standard material response data.

The terminology of a steady-state crack growth condition is well defined in ASTM E 1823. However, the test approach to develop, and subsequent evaluation of, steady-state data is not well defined. The constant ΔK test method is an excellent tool for developing steady-state data. However, in the case of the D6AC steel, the steady-state crack growth rate developed in laboratory air did not correspond to any of the data generated using the standard test procedures. Therefore, it is arguable if any of the constant R laboratory air data generated using C(T) specimens is representative of steady-state. If fatigue crack growth rate data generated using the ASTM standard C(T) specimen are neither representative of similitude or steady-state, then the compact tension specimen is no longer viable as a tool for generating material data.

References

[1] Hudak, S J., Jr. , Saxena, S. J., Bucci, A., and Malcolm, R. C., "Development of Standard Methods of Testing and Analyzing Fatigue Crack Growth Rate Data—Final Report," AFML TR 78-40, Air Force Materials Laboratory, Wright Patterson Air Force Base, OH, 1978.

[2] Lincoln, J. W., "Damage-Tolerance—USAF Experience," *Proc. 13th Symposium of the Int. Comm. On Aeronautical Fatigue*, Pisa, Italy, 1985.

[3] Bucci, R. J., "Development of a Proposed ASTM Standard Test Method for Near-Threshold Fatigue Crack Growth Rate Measurement," *Fatigue Crack Growth Measurement and Data Analysis, ASTM STP 738*, ASTM International, West Conshohocken, PA, 1981, pp. 5–28.

[4] Forth, S. C., Newman, J. C., Jr., and Forman, R. G., "Evaluation of Fatigue Crack Thresholds Using Various Experimental Methods," *J. ASTM Int.*, Vol. 2, No. 6, 2005, pp. 1–16.

[5] Forman, R. G., "Development of Improved Fatigue Crack Growth Test Methods and Analytic Models Applicable to Aircraft Propellers," *Proc. of FAA NRTC Review*, 2005.

[6] Garr, K. R. and Hresko, G. C., "A Size Effect on the Fatigue Crack Growth Rate Threshold of Alloy 718," *Fatigue Crack Growth Thresholds, Endurance Limits, and Design*, ASTM International, West Conshohocken, PA, 2000, pp. 155–174.

[7] Forth, S. C., James, M. A., and Johnston, W. M., "Fatigue Crack Growth Thresholds in D6AC Steel,"

Proc. of the 15th European Conf. on Fracture, ECF15, 2004.

[8] "Damage Tolerance and Fatigue Evaluation of Structure," *Federal Aviation Regulations*, Title 14 Code of Federal Regulations, Part 25, Section 571.

[9] Kanninen, M. F. and Popelar, C. H., *Advanced Fracture Mechanics*, Oxford Engineering Science Series, 1985.

[10] NASGRO Material Database. ver. 4.2, www.nasgro.swri.org, 2005.

[11] Forth, S. C., Newman, J. C., Jr., and Forman, R. G., "On Generating Fatigue Crack Growth Thresholds," *Int. Journal of Fatigue*, Vol. 25, 2003, pp. 9–15.

[12] Elber, W., "The Significance of Fatigue Crack Closure," *Damage Tolerance in Aircraft Structures, ASTM STP 486*, ASTM International, West Conshohocken, PA, 1971, pp. 230–242.

[13] Liaw, P. K., Peck, M. G., and Rudd, G. E., "Fatigue Crack Growth Behavior of D6AC Pace Shuttle Steel," *Engineering Fracture Mechanics*, Vol. 43, 1992, pp. 370–400.

[14] Fracture Technology Associates, www.fracturetech.com.

[15] Dougherty, J. D., Srivatsan, T. S., and Padovan, J., "Fatigue Crack Propagation and Closure Behavior of Modified 1070 Steel: Experimental Results," *Engineering Fracture Mechanics*, Vol. 56, 1997, pp. 167–187.

[16] Ritchie, R. O. and Suresh, S., *Metall. Trans. A*, Vol. 13A, 1982, pp. 937–940.

[17] McEvily, A. J., *Mechanics of Fatigue Crack Closure, ASTM STP 982*, ASTM International, West Conshohocken, PA, 1988, pp. 35–43.

[18] Davidson, D. and Lankford, J., "The Effects of Aluminum Alloy Microstructure on Fatigue Crack Growth," *Metallurgical Science and Engineering*, Vol. 74, 1984, pp. 189–199.

[19] da Fonte, M., Romeiro, F., de Freitas, M., Stanzl-Tschegg, S. E., Tschegg, E. K., and Vasudevan, A. K., "The Effect of Microstructure and Environment on Fatigue Crack Growth in 7049 Aluminum Alloy at Negative Stress Ratios," *International Journal of Fatigue*, Vol. 25, 2003, pp. 1209–1216.

[20] Sadananda, K. and Vasudevan, A. K., "Fatigue Crack Growth Mechanisms in Steels," *Int. Journal of Fatigue*, Vol. 25, 2003, pp. 899–914.

[21] Gangloff, R. P., *Environmentally-Induced Cracking of Metals*, NACE-10, 1988, pp. 55–110.

[22] Newman, J. C., Jr., "A Nonlinear Fracture Mechanics Approach to the Growth of Small Cracks," AGARD Specialists' *Meeting on Behavior of Short Cracks in Airframe Components*, AGARD CP-328, 1983, pp. 6.1–6.26.

Journal of ASTM International, Vol. 3, No. 6
Paper ID JAI13210
Available online at www.astm.org

Bruce A. Young,[1] *W. Alan Van Der Sluys,*[2] *and Peter J. King*[3]

Development of a Circumferentially Throughwall Cracked Tube Specimen for Fatigue Crack Growth Rate Tests

ABSTRACT: This paper describes the development of a nonstandard specimen geometry for fatigue crack growth rate studies. Most fatigue crack growth rate data, available in open literature, for Alloy 690 and Alloy 600 were developed using standard, thick section C(T) specimens. Recently a need arose to study a circumferentially throughwall cracked tube specimen. The goal of the development was to use this tube specimen to determine any effects of section thickness or grain size on corrosion enhancement of fatigue crack growth rates in a simulated pressurized water reactor (PWR) primary side environment. Along with the final specimen geometry, the stress intensity equation and crack length monitoring equation are discussed. The stress intensity equation was converted to a standard polynomial equation in order to use a conventional automated fatigue crack growth rate software package. Symmetry arguments were made to justify the use of direct current potential drop (DCPD) and the use of the standard Johnson's equations for measuring crack lengths. Also, some discussions of the validity requirements for this geometry are presented such as stress intensity limits to remain with linear elastic fracture mechanics (LEFM) bounds and crack length limits to avoid excess bending stresses. A baseline test program was conducted on Alloy 690 tube specimens in ambient air and these results were compared with literature data. Also, a sensitivity investigation was preformed to determine the error between the polynomial equations developed and the actual equations in literature. The results of this study confirmed that a circumferentially cracked tube specimen could produce valid fatigue crack growth rate data.

KEYWORDS: steam generator, tube, fatigue, crack propagation, crack growth rate, specimen geometry, potential drop, stress intensity

Nomenclature

CGR_{air}	=	Crack growth rate in air (length/time)
CGR_{env}	=	Crack growth rate in environment (length/time)
da/dN	=	Crack growth rate per unit cycle (length/cycle)
$(da/dN)_{th}$	=	Threshold crack growth/cycle (length/cycle)
da/dt	=	Crack growth rate per unit time (length/time)
t_r	=	Rise time of the test waveform (time)
R	=	R-ratio (K_{min}/K_{max})
ΔK	=	K_{max} (1-R) (stress $\sqrt{}$length)
ΔK_{th}	=	Threshold stress intensity in fatigue(stress $\sqrt{}$length)
D, b, p, n	=	Empirical parameters
A, m	=	Material and environmental tting parameters
T	=	Temperature
P	=	Applied force (force)
B	=	Specimen thickness for a standard specimen (length)
W	=	Specimen width for a standard specimen (length)
α	=	Crack-length to width ratio

Manuscript received January 24, 2005; accepted for publication March 28, 2006; published online May 2006. Presented at ASTM Symposium on Fatigue and Fracture Mechanics on 18-20 May 2005 in Reno, NV; R. E. Link and K. M. Nikbin, Guest Editors.
[1] Research Engineer, The Babcock & Wilcox Research Center, Alliance, OH 44601.
[2] Consultant, Alliance, OH 44601.
[3] Program Manager, Life Cycle Engineering, Nuclear Engineering, Babcock & Wilcox Canada, Cambridge, Ontario, Canada N1R 5V3.

Copyright © 2006 by ASTM International, 100 Barr Harbor Drive, PO Box C700, West Conshohocken, PA 19428-2959.

θ = Half angle of the total crack length for a tube
t = Specimen thickness for a tube (length)
R_a = Average specimen radius (length)
l = Total crack length of the tube (length)
C = Circumference (length)

Introduction

Although the scientific community has agreed Alloy 690 exhibited superior corrosion resistance over Alloy 600, no one has said that Alloy 690 will never exhibit SCC under all circumstances. Thermally treated Alloy 600 (Alloy 600 TT) showed greater corrosion resistance than Alloy 600 in the mill annealed condition (Alloy 600 MA), but with time, Alloy 600 TT did crack in service. The studies on Alloy 690 have generally been on initiation of cracks and not on crack propagation. In producing a report for the USNRC [1], Argonne National Laboratory (ANL) compiled all the crack growth results on Alloy 690 available in open literature. The report stated the number of results were inadequate to determine effects of stress ratio, cyclic frequency, and stress intensity range on crack growth rate.

Another issue was testing in open literature was completed largely on thick section material (i.e., plate) in both pressurized water reactor (PWR) and boiling water reactor (BWR) environments. Since Babcock & Wilcox Canada, was concerned mainly with PWR environments, the database available on crack growth on alloy 690 was very small. Also, since the open literature was completed on thick section materials, the difference in microstructure between thick plate and thin tubes may be a variable in data analysis.

A research project was initiated by Babcock & Wilcox Canada at the Babcock & Wilcox Company's Research and Development to develop a specimen where heats of material currently in service could be investigated for fatigue crack growth rate properties in the tube configuration. Along with the specimen geometry, the stress intensity equation and crack length monitoring equation were investigated. The stress intensity equation was converted to a standard polynomial equation in order to use a conventional automated fatigue crack growth rate software package. Symmetry arguments were made to justify the use of direct current potential drop (DCPD) and the use of the standard Johnson's equations for measuring crack lengths. Also, some discussions of the validity requirements for this geometry are presented such as stress intensity limits to remain with linear elastic fracture mechanics (LEFM) bounds.

A baseline test program was conducted on Alloy 690 tube specimens in ambient air and these results were compared with literature data. Also, a sensitivity investigation was performed to determine the error between the polynomial equations developed and the actual equations in literature. The results of this study confirmed that a circumferentially cracked tube specimen could produce valid fatigue crack growth rate data.

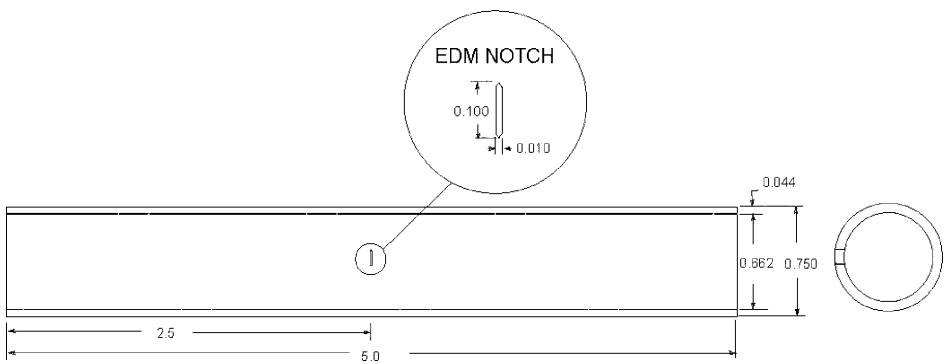


FIG. 1—*Alloy 690—base tube specimen sketch (dimensions in inches).*

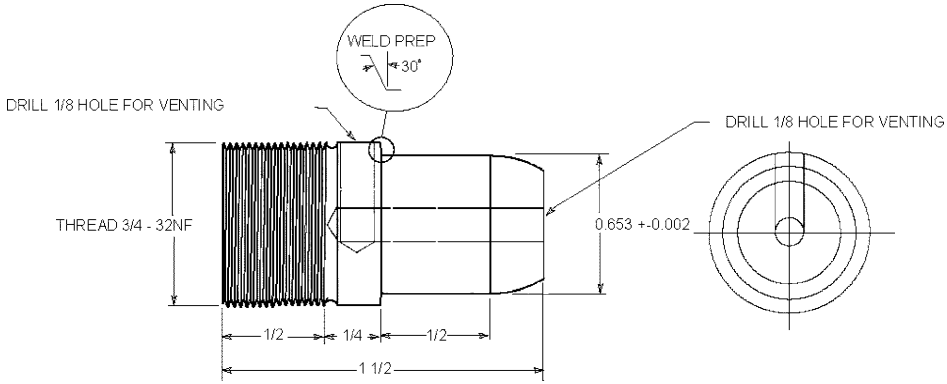


FIG. 2—*Alloy 690—tube plug sketch (dimensions in inches).*

Test Specimen

The first step, prior to obtaining any crack growth rate data, was to determine an appropriate specimen configuration for the project. After examining several loading and notch configurations, the decision was made to use a design similar to the one used by Westinghouse [2]. This design used a circumferentially oriented notch, machined via an electrical discharge machining (EDM) technique, along with electric potential drop (EPD) to measure the crack propagation. The variation was in the applied loading. Westinghouse used a complex loading technique, bending plus axial, to load their specimen while this project strived to load the specimen axially in tension.

To obtain the axial loading, several iterations of specimen threads and fixtures were needed. The first iteration was chosen because of previous experience with tube configurations for other tests, such as constant extension rate tests (CERT), as well as its simplicity in machining and low cost. The tube was threaded using a fine thread (3/4–32 NF) on each end. The grip was attached to the load frame using a threaded collar-and-bolt assembly. After testing the first specimen, the design proved to be flawed. The bolt assembly threads, at the test stress, fatigued to failure prior to the EDM notch initiating a crack.

The second iteration was to eliminate the threaded collar-and-bolt assembly. Again, this method failed due to fatigue in the threads of the tube. The thinning of the tube due to threading and the stress concentration due to the root of the thread lead to failure in the threads prior to the EDM notch initiating a crack.

The next iteration, shown in Figs. 1–3, proved to be the final iteration. This configuration used welded in plugs. This method proved to be useful not only in the air tests, but also in the environmental tests. The

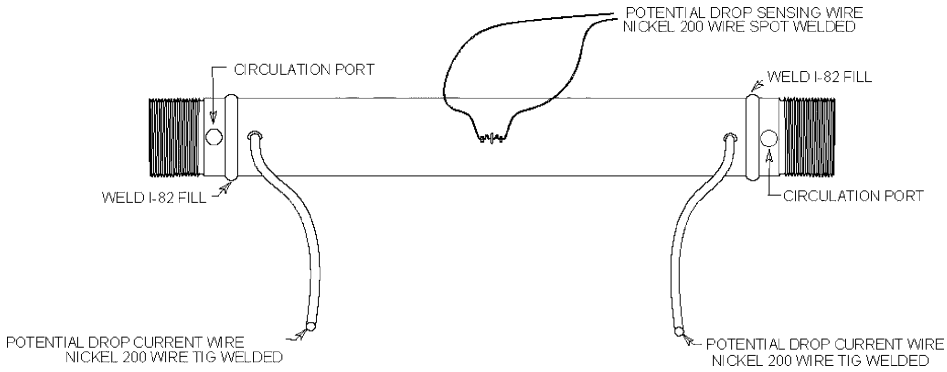


FIG. 3—*Alloy 690—composite sketch with potential leads.*

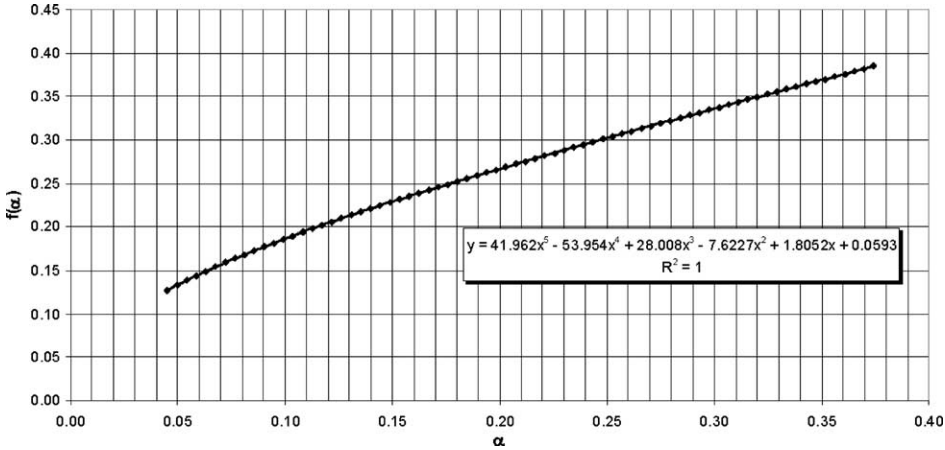


FIG. 4—*Series expansion for crack tip stress intensity equation.*

plugs were drilled with vent holes. These vent holes allowed the aqueous environment to flow through the inside of the tube without trapping gas. The threads on the plugs were also sized so the specimen would screw directly into the load frame.

Stress Intensity and Crack Length Monitoring Development

While gripping iterations were being developed, calculations for crack tip stress intensity (K) were being developed and verified. The issue was with the test control software. The necessary equations were obtained [3], but the form of the equations could not be used with the test software.

The form of the equation required by the software was the following:

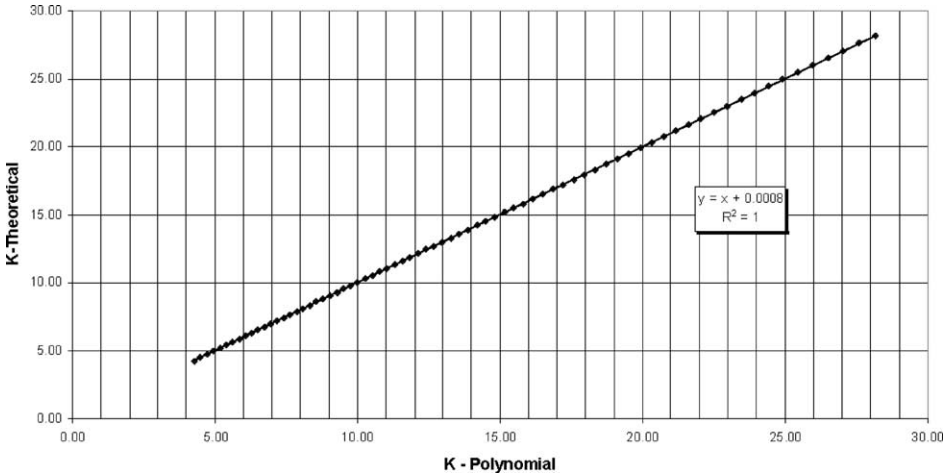


FIG. 5—*K comparison for constant load, varying alpha—P=1000(lb).*

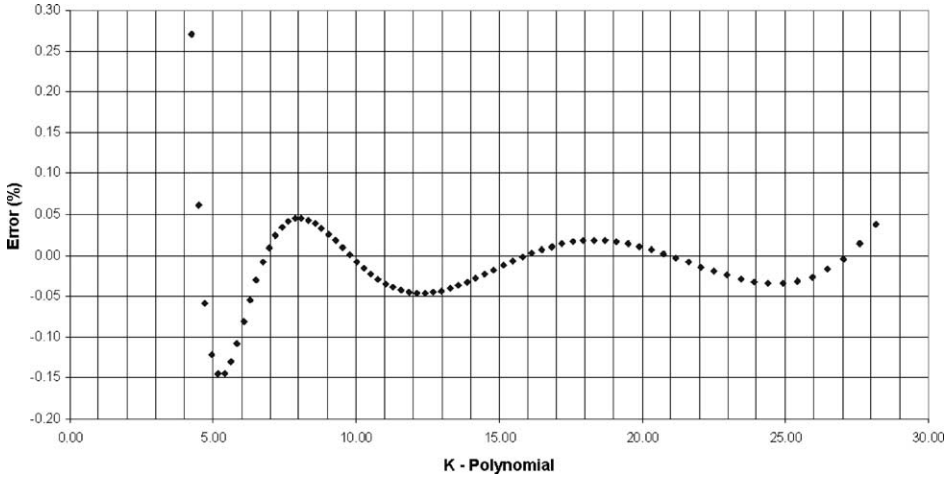


FIG. 6—*Constant load, varying alpha—polynomial K—error analysis.*

$$K_I = \left(\frac{P}{B\sqrt{W}}\right)\left[\frac{(2+\alpha)}{(1-\alpha)^{1.5}}\right] f(\alpha) \tag{1}$$

or

$$\Delta K_I = \left(\frac{\Delta P}{B\sqrt{W}}\right)\left[\frac{(2+\alpha)}{(1-\alpha)^{1.5}}\right] f(\alpha) \tag{2}$$

where $f(\alpha)$ is a fifth-order fitting polynomial

The form of the equation for the tubular geometry is given by the following:

$$K_I = \frac{P(\pi R_a \theta)^{0.5} F_t}{2\pi R t} \tag{3}$$

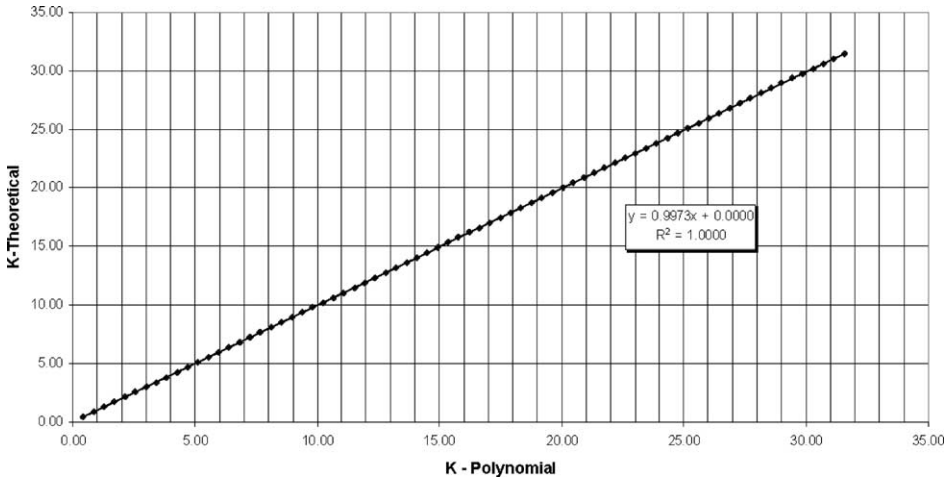


FIG. 7—*K comparison for constant alpha, varying load—alpha=0.10.*

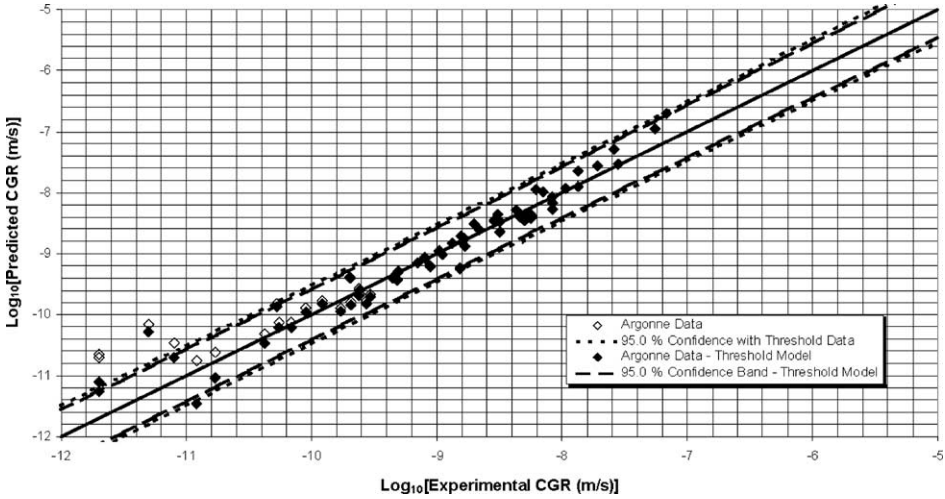


FIG. 8—*Threshold and nonthreshold model comparisons.*

TABLE 1—*Argonne model parameters.*

Parameter	Model[14]
b	0.82
p	−2.20
n	4.10

$$F_t = 1 + A\left[5.33\left(\frac{\theta}{\pi}\right)^{1.5} + 18.77\left(\frac{\theta}{\pi}\right)^{4.24}\right] \tag{4}$$

$$A = \left[0.125\left(\frac{R_a}{t}\right) - 0.25\right]^{0.25} \tag{5}$$

$$\frac{2\theta}{2\pi} = \frac{l}{2\pi R_i} = \frac{l}{C} \tag{6}$$

Rearranging variables, the formula was converted into the following form:

$$\alpha = \frac{l}{c} \tag{7}$$

TABLE 2—*Material pedigree for baseline fatigue tests.*

Specimens (B & W Mark)	4 and 5 (BWI-MK030895-2)
Description	Production Thermally Treated (TT) 690
Melter	Inco Alloys, Inc.
Manufacturer	Valinox
Heat Number	N/A
Melt Process	Vacuum Induction Melt plus Electro-Slag Remelt
Tube Process	Pilger
Mill Anneal	1099°C
Thermal Treatment	718°C for 10 h

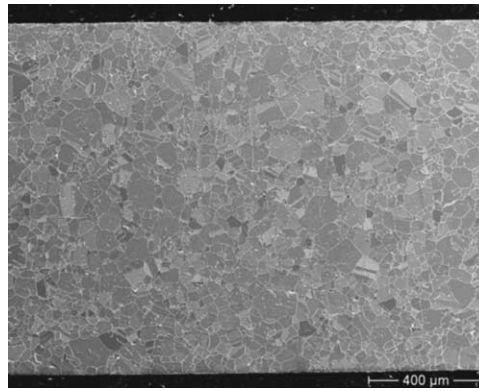


FIG. 9—*SEM photograph—60× BWI-MK030895-2.*

$$\Delta K_I = \frac{\Delta P}{t\sqrt{C}}\left(\frac{\pi\alpha}{2}\right)^{0.5} F_t \tag{8}$$

Assuming the following substitution via symmetry: t is equal to B and C is equal to W.

Setting the two Eqs 2 and 8 equal and reducing, a formula for f(α) was obtained. Recall, the tubes were tested with all the same diameter and thickness (R = 0.353 in., t = 0.044 in.). The equation was simplified to the following:

$$f(\alpha) = F_t\left(\frac{\pi\alpha}{2}\right)^{0.5}\left(\frac{(1-\alpha)^{1.5}}{(2+\alpha)}\right) \tag{9}$$

Since all of the specimens have the same nominal thickness and nominal radius, "A" in the F_t formula was a constant. The fifth-order polynomial for $f(\alpha)$ was determined by fitting a curve, Fig. 4, through a set of data pairs $(\alpha, f(\alpha))$. Additional validation analysis was shown in Figs. 5–7.

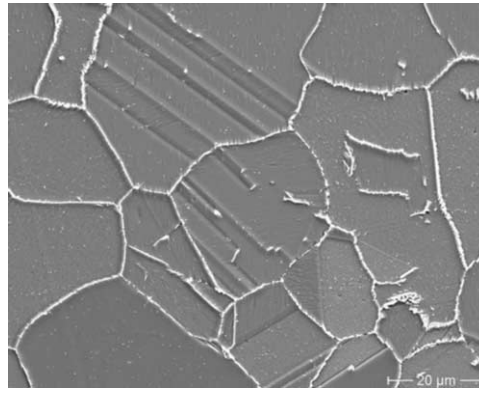


FIG. 10—*SEM photograph—1000× mid-wall BWI-MK030895-2.*

TABLE 3—*Ambient test results for Alloy 690 tubing at 24°C.*

Specimen	Rise Time (s)	ΔK (MPa √m)	R	Results da/dN (m/cycle)	Results da/dt (m/s)	Theoretical da/dt (m/s)
4	0.05	10.2	0.1	2.16E-9	4.32E-8	1.30E-8
4	0.05	17.5	0.1	8.47E-9	1.69E-7	1.68E-7
4	0.05	26.3	0.1	3.30E-8	6.60E-7	9.21E-7
4	0.05	33.9	0.1	1.61E-7	3.22E-6	2.62E-6
5	0.05	6.8	0.5	1.04E-9	2.08E-8	3.51E-9
5	0.05	9.8	0.5	2.95E-9	5.90E-8	3.68E-8
5	0.05	13.4	0.5	9.11E-9	1.82E-7	1.48E-7
5	0.05	15.5	0.5	1.21E-8	2.42E-7	2.74E-7
5	0.05	18.3	0.5	1.90E-8	3.80E-7	5.48E-7

$$f(\alpha) = c_0 + c_1\alpha + c_2\alpha^2 + c_3\alpha^3 + c_4\alpha^4 + c_5\alpha^5$$

$$c_0 = 0.0593 \quad c_1 = 1.8052$$

$$c_2 = -7.6227 \quad c_3 = 28.008$$

$$c_4 = -53.954 \quad c_5 = 41.962 \tag{10}$$

Once K solutions were obtained for the specimen, a method of obtaining crack lengths was employed. The method chosen was the common Johnson's equation which used the EPD technique. With the use of symmetry, as in the case of the K calculations, the Johnson equation [4,5] provided adequate results, but post test correction methods were employed in accordance with the American Society of Testing and Materials Test Specification (ASTM) E 647 (Standard Test Method for Measurement of Fatigue Crack Growth).

Literature Data and Model for Alloy 690

The existing fatigue crack growth rate data on Alloy 690 was very limited. There were approximately 100 tests in the database which cover three heats of material as well as high and low deoxygenated (DO) water

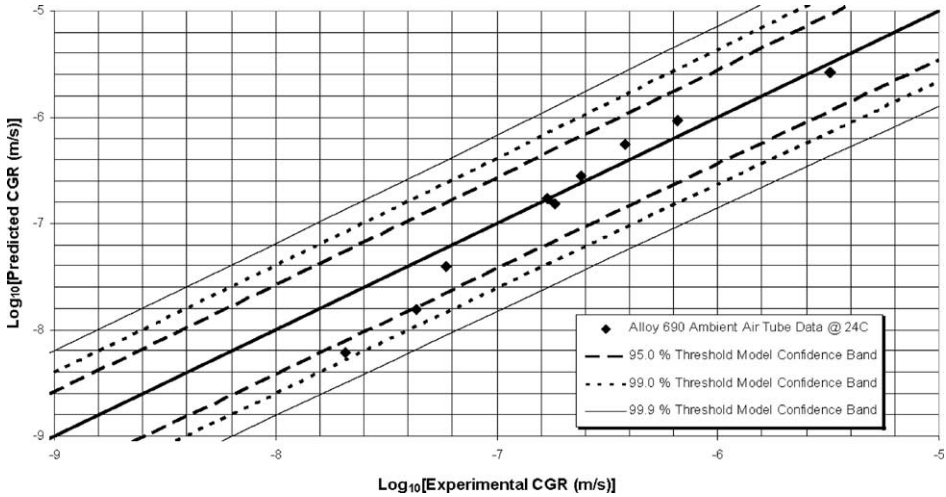


FIG. 11—*Ambient air, 24°C, data for Alloy 690 tubing plotted against the statistical boundaries for the Argonne model.*

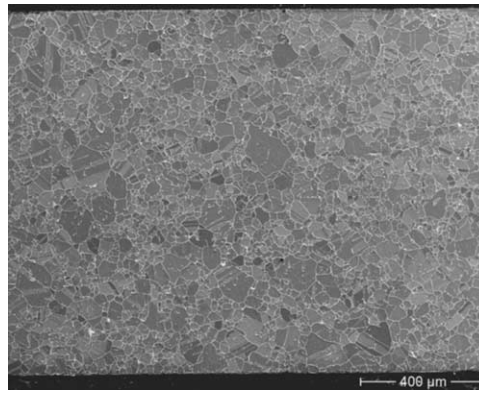


FIG. 12—*SEM photograph—65× ID surface BWI-MO620Y.*

TABLE 4—*Material pedigree for 600°F (316°C) fatigue tests.*

Specimens (B & W Mark)	I690-1 through I690-10
Description	Sumitomo ASME SB-183 Alloy 690 TT Tubing
Melter	Sumitomo
Manufacturer	Sumitomo
Heat Number	Heat SO20399 / Lot B636 / Tube MO620Y
Melt Process	Vacuum Oxygen Decarburization
Tube Process	Drawn
Mill Anneal	1095 °C
Thermal Treatment	716 °C for 10 h

with various r-ratios, K ranges, and rise times [6]. All of the data were compiled by Argonne National Labs (ANL). ANL also had compiled the available data on the Alloy 52 (Alloy 690 Weld Metal). All the available data on fatigue crack growth rate were completed on thick section plate material using a compact tension, C(T), geometry. The following equations were derived by Argonne for the data available [6,7]. Argonne also published a parameter list, shown in Table 1, for Alloy 690 in air at various temperatures [8].

$$D = C_0 + C_1T - C_2T^2 + C_3T^3 \text{ (T is in Degrees Celsius)}$$

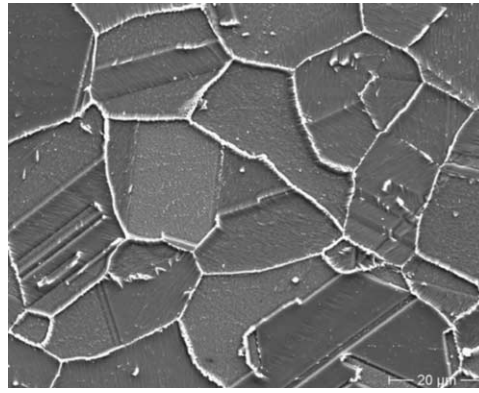


FIG. 13—*SEM photograph—1000× mid-wall BWI-MO620Y.*

TABLE 5—*Ambient test results for alloy 690 tubing at 315°C.*

Specimen	Rise Time (s)	ΔK (MPa √m)	R	Results da/dN (m/cycle)	Results da/dt (m/s)	Theoretical da/dt (m/s)
I690-1	0.05	9.8	0.1	4.11E-9	8.22E-8	2.56E-8
I690-1	0.05	14.5	0.1	6.32E-9	1.26E-7	1.52E-7
I690-1	0.05	18.6	0.1	8.62E-9	1.72E-7	4.31E-7
I690-1	0.05	25.5	0.1	3.00E-8	6.00E-7	1.59E-6
I690-2	0.05	12.0	0.1	6.80E-9	1.36E-7	6.65E-8
I690-2	0.05	21.0	0.1	2.19E-8	4.38E-7	7.14E-7
I690-2	0.05	31.0	0.1	1.84E-7	3.68E-6	3.55E-6

$$C_0 = 5.423 \times 10^{-14}$$

$$C_1 = 1.830 \times 10^{-16}$$

$$C_2 = 1.725 \times 10^{-18}$$

$$C_3 = 5.490 \times 10^{-21} \tag{11}$$

$$CGR_{air} = \left(\frac{1}{t_r}\right)\frac{da}{dN} = \left(\frac{1}{t_r}\right)D(1 - bR)^p \Delta K^n \tag{12}$$

As evident from the equations for the model, the model did not take into account the possibility for a material threshold. An effort was undertaken to expand the model to allow for threshold values. [9] According to ASTM specification E 647, the threshold stress intensity for a material is defined when the material reaches a crack length per cycle (da/dN) value of 1×10^{-10} m/cycle. Klensil and Lucas, to account for threshold values in fatigue crack growth, developed a modified equation to the Paris Law in 1972 [10].

The equation was as follows:

$$\frac{da}{dN} = C(\Delta K^n - \Delta K_{th}^n)$$

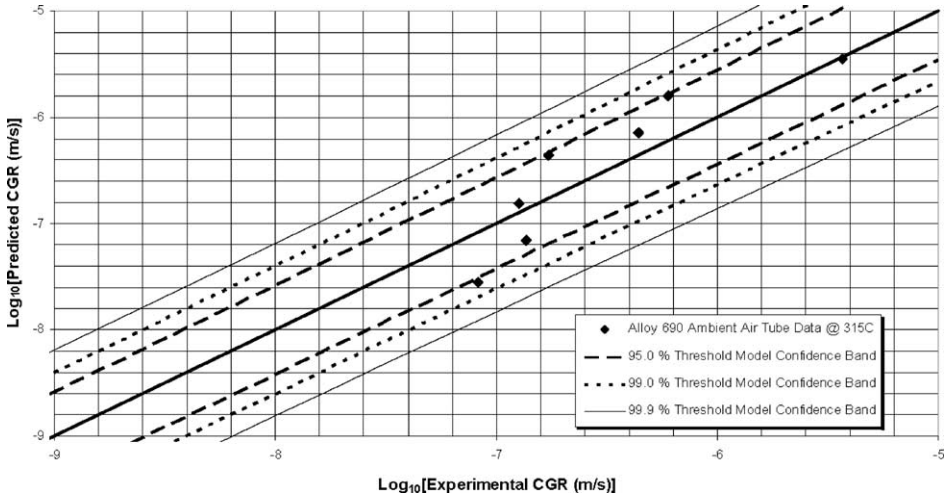


FIG. 14—*Ambient air, 315°C, data for Alloy 690 tubing plotted against the statistical boundaries for the Argonne model.*

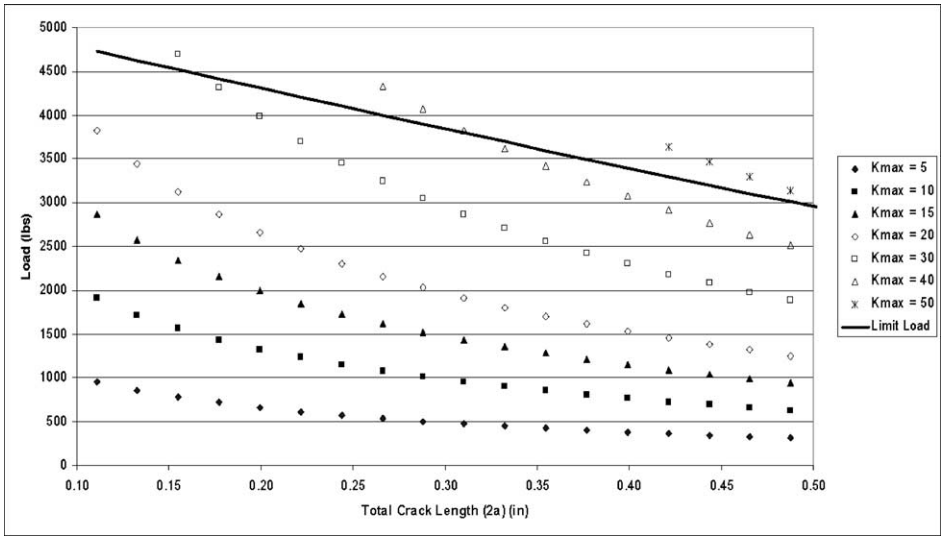


FIG. 15—*Limit load calculations for Alloy 690 tubing with 0.750 OD and 0.044 wall.*

$$\frac{da}{dN} = C(\Delta K^n) - C\Delta K_{th}^n$$

$$\left[\frac{da}{dN}\right]_{th} = C\Delta K_{th}^n$$

$$\frac{da}{dN} = C(\Delta K^n) - \left[\frac{da}{dN}\right]_{th} \tag{13}$$

Using the above concept, a crack growth rate formula was developed which took the material threshold into account.

$$CGR_{air} = \left(\frac{1}{t_r}\right) D(1 - bR)^p \Delta K^n - \left(\frac{1}{t_r}\right)\left[\frac{da}{dN}\right]_{th} \tag{14}$$

Although ASTM specification E 647 indicated a value of 1×10^{-10} m/cycle an optimum value for the dataset was found to be a value of 1.74×10^{-10} m/cycle. The statistical comparison between a "no-threshold" model and a "threshold" model were plotted in Fig. 8. As shown, the statistical analysis does not vary greatly, but the lower experimental crack growth rate had better agreement with the theoretical values.

Test Results

Initial testing was completed in an ambient air environment. These baseline tests were used to ensure the reliability of the equations. Since fatigue testing in air at ambient temperatures on Alloy 690 was well established, a comparison between the tube data and the Babcock & Wilcox Threshold Model (Modified Argonne Model) was completed. The material pedigree was outlined in Table 2. Along with the material pedigree, metallographic photographs, using a scanning electron microscope (SEM), were taken to show the carbide decoration on the grain boundaries and the nonuniformity of the grain size and presented in Figs. 9 and 10.

The baseline tests were conducted on two specimens. The test parameters and results were summarized in Table 3. The theoretical crack growth rate was determined from the threshold model.

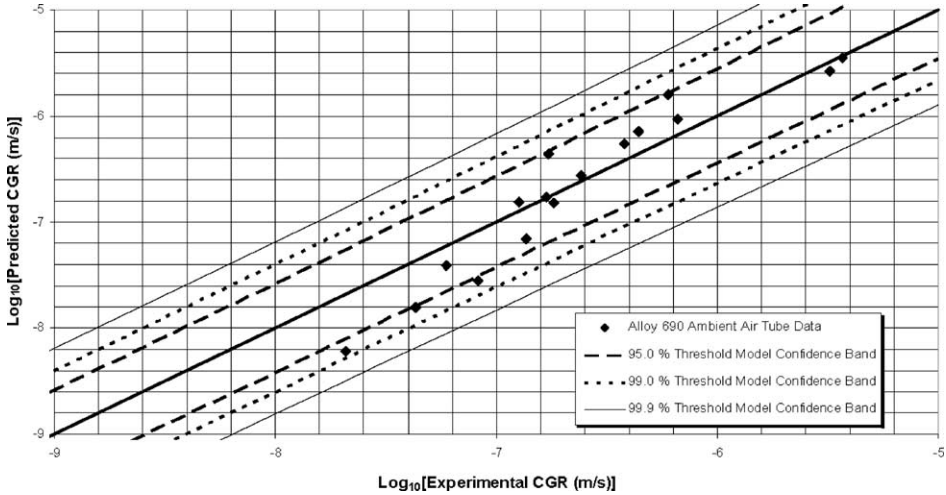


FIG. 16—*All ambient air data for Alloy 690 tubing plotted against the statistical boundaries for the Argonne model.*

As seen in Fig. 11, the baseline tests fell within the statistical variation of the Argonne data. Once the baseline tests were completed, the next step was to test a known heat and lot combination in 600°F (316°C) air conditions. A different material pedigree, obtained from Sumitomo, was outlined in Table 3.7. Along with the material pedigree, metallographic photographs, using a scanning electron microscope (SEM), were obtained to show the carbide decoration on the grain boundaries and the nonuniformity of the grain size for the new material and presented in Figs. 12 and 13 (Table 4).

Once the new Alloy 690 material was obtained, testing progressed to elevated temperature, ambient air tests. Results and test conditions for these tests were tabulated in Table 5. The data were plotted in Fig. 14 and compared to the statistical confidence band for the Argonne data. The theoretical crack growth rate was determined from the threshold model. As seen in Fig. 11, the laboratory air, elevated temperature tests also fell within the statistical variation of the Argonne data.

Summary

Along with the final specimen geometry, the stress intensity equation and crack length monitoring equation were discussed. The stress intensity equation was converted to a standard polynomial equation in order to use a conventional automated fatigue crack growth rate software package. Symmetry arguments were made to justify the use of direct current potential drop (DCPD) and the use of the standard Johnson's equations for measuring crack lengths. The validity requirements for this geometry, to stay within the limit load, are shown in Fig. 15. Also to avoid excess bending stress, a total crack length to circumference limit was set to 25 %.

A baseline test program was presented on Alloy 690 tube specimens in air both at ambient and elevated temperatures. These results were compared with literature data and determined to be favorable. Along with the baseline test data, a sensitivity investigation was presented which compared the error between the polynomial equations developed and the actual equations in literature.

The results of this study confirmed that a circumferentially cracked tube specimen could produce valid fatigue crack growth rate data. As shown in Fig. 16, most of the data falls with the 95 % confidence band of the original Argonne data while all of the data fall within the 99 % band. Based upon the results obtained during the air tests, the tube specimen geometry appears to be a viable geometry for studying the fatigue crack growth rate of materials.

References

[1] United States Nuclear Regulatory Commission, "Effects of Alloy Chemistry, Cold Work, and Water Chemistry on Corrosion Fatigue and Stress Corrosion Cracking of Nickel Alloys and Welds," NUREG/CR-6721, ANL-01/07, Argonne National Laboratory, April 2001, Office of Nuclear Regulatory Research, Washington, DC, pp. 9,17–18.

[2] Lott, R. G., Jacko, R. J., and Gold, R. E., "Primary Water Stress Corrosion Crack Growth Rates in Alloy 600 Steam Generator Tubing," *Environmental Degradation of Materials in Nuclear Power Systems—Water Reactors: Proceedings of the 5th International Symposium*, Monterey, CA, August 25–29, 1991, American Nuclear Society, Inc., La Grange Park, IL, p. 526.

[3] Anderson, T., *Fracture Mechanics: Fundamentals and Applications*, 2nd ed., CRC Press, Boca Raton, 1995, 634pp.

[4] Schwalbe, K.-H. and Hellmann, D. "Application of the *Electric Potential Method to Crack Length Measurements Using Johnson's Formula*," ASTM International, West Conshohoeken, PA, 1981, p. 218.

[5] McKeighan, P. C. and Smith, D. J., "Determining the Potential Drop Calibration of a Fatigue Crack Growth Specimen Subjected to Limited Experimental Observations," *J. Test. Eval.*, Vol. 22, No. 4, July 1994, pp. 291–301.

[6] United States Nuclear Regulatory Commission, NUREG/CR-6721, ANL-01/07, pp. 17–21.

[7] United States Nuclear Regulatory Commission, "Environmentally Assisted Cracking in Light-Water Reactors," NUREG/CR-4667, Vol. 27, ANL-99/11, Semiannual Report July 1998–December 1998, Argonne National Laboratory, October 1999, Office of Nuclear Regulatory Research, Washington, DC, pp. 46–47.

[8] United States Nuclear Regulatory Commission, "Environmentally Assisted Cracking in Light-Water Reactors," NUREG/CR-4667, Vol. 31, ANL-01/09, Semiannual Report July 2000–December 2000, Argonne National Laboratory, April 2002, Office of Nuclear Regulatory Research, Washington, DC, p. 40.

[9] Young, B. A., "The Incorporation of a Fatigue Threshold Concept into a Known Superposition Crack Growth Model for Alloy 690 in High Temperature, Low Oxygenated Water," American Society of Mechanical Engineers, ASME International, PVP 2004, PVP Vol. 480, July 2004, San Diego, CA.

[10] Anderson, "Metals—Mechanical Testing; Elevated and Low-Temperature Tests; Metallography," *Fracture Mechanics*, Vol. 3.01, 2004, p. 518.

Environmental Fracture

Journal of ASTM International, Vol. 3, No. 7
Paper ID JAI100485
Available online at www.astm.org

Kimberli Jones[1] *and David W. Hoeppner*[1]

Effect of Microstructure on Pit-to-Crack Transition of 7075-T6 Aluminum Alloy

ABSTRACT: The focus of this research was to gain an increased understanding of how microstructure influences pit growth, pit-to-crack transition, and critical crack propagation to fracture. Two thicknesses of 7075-T6 aluminum alloy were etched and subjected to corrosion fatigue in a 3.5 % sodium chloride environment. 7075-T6 aluminum alloy is of particular interest to the aging aircraft community, as this alloy has been used extensively on wing and fuselage structures for both military and commercial aircraft in the past. Testing was interrupted at various intervals to obtain information on pit generation, growth, and potential cracking. Results indicated that microstructure has a significant influence on pit-to-crack transition and fatigue crack propagation. Short cracks ($<$100 μm) in a corrosion fatigue environment were strongly influenced by grain boundaries and crystallographic grain orientation. Constituent particles competed with corrosion pits as critical crack nucleation sites. Post-fracture analysis confirmed the presence of noncritical cracks within the corroded region, related to pitting and constituent particles.

KEYWORDS: aluminum, corrosion fatigue, pitting corrosion, SEM

Introduction

Corrosion is a common occurrence in daily life. However, this same corrosion that seems harmless can in reality have potentially disastrous consequences. Aircraft are one of the areas in which corrosion's effects are frequently felt. A brief search for accidents and incidents related to corrosion in the aviation section of the National Transportation Safety Board's (NTSB) website yields pages and pages of corrosion related occurrences [1]. Upon closer investigation, many of these also are fatigue related. The importance of understanding the interaction between corrosion and fatigue becomes clear based on the lives that have already been lost, not to mention the serious potential for countless others.

A significant amount of work has been undertaken historically regarding corrosion fatigue, and more specifically, pitting corrosion fatigue. As early as 1837, failures from metal fatigue began to be noticed and early ideas for prevention were devised. The first documented mention of corrosion fatigue occurred in 1917 by Haigh, with corrosion fatigue testing performed by McAdam in 1929 [2]. Throughout the past 70 years, significant research has been conducted on the subject of pitting corrosion fatigue. Work in this area has been performed by many investigators, including Harmsworth [3], Chen et al. [4], Lindley et al. [5], Kondo [6], Kawai and Kasai [7], Hoeppner [8], and Goswami and Hoeppner [9]. Pitting is extremely common in aluminum alloys, with varying effects based on the extent of the pitting, operational environment, and other conditions.

Among the materials community, it is well known that corrosion, particularly pitting, dramatically reduces fatigue life. Exactly how and why this occurs have been the topic of many theories, as well as the subject of research and debate. The subject of corrosion as a safety issue is of particular interest. In a survey of corrosion and fretting related incidents and accidents for U.S. aircraft during 1975–1994 [10], Hoeppner et al. state that many aircraft and lives have been lost related to these serious issues. Many people do not believe corrosion to be an exceptional source of fatigue cracking. In some circumstances this may be true. Fatigue cracks will originate if the stress concentration is large enough to nucleate a crack, and, depending on the stresses at that location, microstructure may affect the rate and path of crack propagation.

Manuscript received April 7, 2005; accepted for publication April 4, 2006; published online May 2006. Presented at ASTM Symposium on Fatigue and Fracture Mechanics: 35th Volume on 18–20 May 2005 in Reno, NV; R. E. Link and K. M. Nikbin, Guest Editors.

[1] Research Assistant Engineer and Professor, respectively, University of Utah, Salt Lake City, UT 84112

Copyright © 2006 by ASTM International, 100 Barr Harbor Drive, PO Box C700, West Conshohocken, PA 19428-2959.

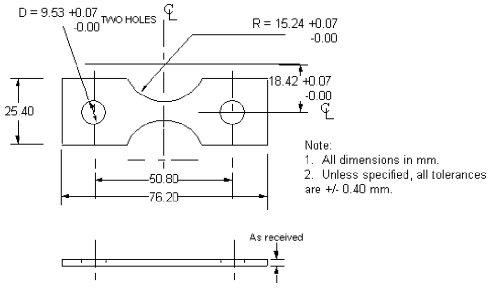


FIG. 1—*Dogbone specimen drawing.*

The focus of this research was to gain an increased understanding of the role of microstructure on pit growth, pit-to-crack transition, and critical crack propagation to fracture. Specimens in several forms of 7075-T6 sheet were etched and then subjected to corrosion fatigue. Testing was interrupted at various intervals to gain information on pit generation, growth, and potential cracking. In situ inspections were performed regularly throughout each interval. Critical pits and cracks were linked to microstructural features when possible. Characterization of each specimen's evolving discontinuity state was performed using metallurgical and scanning electron microscopy.

Corrosion fatigue is a complex phenomenon that has a substantial research component requirement for full understanding. Research has proven that corrosion can, and does, have a serious effect upon the fatigue life of a structure. Teardown inspections of the aging aircraft fleet have revealed multiple forms of corrosion, along with other types of damage. The full repercussions associated with these material degrading evolving discontinuity states have yet to be felt, as aircraft will continue to age, and no exact solution to the corrosion fatigue problem has been developed. With continuation of corrosion fatigue research, better solutions to the complexity of evolving and modified discontinuity states can be discovered.

Methodology

The purpose of the corrosion fatigue experimental program was to determine the role played by grain orientation, as well as relating this to corrosion pitting and the dissolution of grains. The rate of pitting growth (mainly depth) and the size and shape of pits at various times under corrosion fatigue conditions were investigated. Interrupted testing intervals were used to accomplish this goal. 7075-T6 aluminum alloy was selected for experimentation based on its applicability to the aging aircraft community, as this alloy has been used on wing and fuselage structures on both military and commercial aircraft. Center-pin-loaded dogbone specimens were machined from two sheets of varying thickness (B1=1.600 mm (0.063 in.), B2=4.064 mm (0.160 in.)) and an extruded plate of approximately the same thickness as B2. The specimen drawing is shown in Fig. 1.

A room temperature (~23°C) distilled water and 3.5 % sodium chloride (NaCl) solution was used as the corrosive medium. The pit-to-crack transition portion of the experiments investigated the time and cycles to detection of the first or first few cracks that nucleated from the corroded region of the specimen. Grain maps were generated prior to corrosion fatigue experimentation, and were used to identify, as much as possible, the microstructure within the corroded region and how microstructure related to the critical discontinuity. All specimens were cyclically loaded, in intervals, to fracture, for evolving discontinuity state (EDS) determination.

After machining, the surface of each specimen was polished using silicon carbide abrasive 200, 320, 400, and 600 grit papers with water as a lubricant. A 1.0 μm alpha alumina slurry was followed by 0.3 μm alpha alumina slurry to obtain a mirror finish. The final polishing step utilized a 0.05 μm gamma alumina slurry, necessitated by the etching procedure. The back surface of each specimen also was polished using silicon carbide abrasive up to the 600 grit finish. When polishing was completed, the specimens then were cleaned using acetone in an ultrasonic cleaner for a minimum of 15 min.

The next step in specimen preparation involved etching a small, centered area (~25 mm^2) in order to view the microstructure. A smaller portion of this same area would later be corroded. Etching was com-

TABLE 1—*Corrosion fatigue interval information.*

Exposure Interval	Time of Exposure Interval (h)	Interval Fatigue Cycles	Accumulated Exposure Time (h)	Accumulated Fatigue Cycles
A	2.142	72 000	2.142	72 000
B	4.285	144 000	6.427	216 000
C	8.570	288 000	14.997	504 000
D	8.570	288 000	23.567	792 000
Intervals continue at the 288 000 cycle level until fracture occurs.				

pleted as soon after polishing as possible. Clear, nonmetallic lacquer was used to protect the unexposed area from the etching solution. Etching was performed in accordance with ASTM Standard Practice for Microetching Metals and Alloys (E 407-99) for 7xxx series aluminum alloys [11].

Once the etching process was finished, grain mapping was performed, using the metallurgical microscope and a digital camera outfitted with a microscope adapter. The specimen was then prepared for the first corrosion fatigue interval by using a clear, nonmetallic lacquer to protect the surface, minus a 1.5 mm^2 rectangular area within the etched region, as near to the center of the specimen as possible.

Experimentation was started after the lacquer coating had dried, usually about 30 min. The 3.5 % NaCl solution was aerated for 1 h prior to the start of each interval. Once the experimental interval was started, solution flow was checked for regularity. The flow rate was approximately 1 mL/min.

Each type of specimen was exposed to the same exposure interval design, with fatigue cycling applied at a maximum tensile stress of 120.66 MPa (17.5 ksi), a frequency of 10 Hz, and a stress ratio of +0.1. Interval times and number of cycles are presented in Table 1. If a specimen had not fractured after interval K, the interval was continued without interruption until fracture did occur. An interval could be stopped before reaching the defined number of cycles if a fatigue crack was positively identified. Generally, this did not occur based on the resolution of the inspection system, as well as the slow growth rates of "short" cracks that may or may not actually propagate.

When an interval was completed, the specimen was removed from the load frame and the environmental chamber. The specimen was ready for inspection after completion of an ultrasonic cleaning process.

The metallurgical microscope was the first step in the analysis process. Each pit was documented via digital photography and measured for depth. The locations of cracks, if any, were noted. If cracks were present, the specimen then was investigated in the scanning electron microscope, mainly using backscattered electron (BSE) beams. Cracking was verified during this step, as the BSE 3-D mode assisted greatly in detecting fatigue cracks. If no surface cracks had been discovered, intervals were continued until cracks were present.

Once a specimen had fractured, fractographic analysis was performed to correctly identify the critical discontinuity that ultimately caused fracture. Interactions with other cracks, pits, and constituent particles were noted. In addition, noncritical crack locations were confirmed, and where possible, related to microstructure. Microstructural effects were noted whenever practical.

Results

Visual inspections using multiple microscopic techniques were performed after each interval completion. After each interval and its associated cleaning process were completed, corrosion products sometimes protruded above the surface and covered pits. Depths could not be obtained for these pits when this occurred, or might not have yielded entirely accurate depths if the deepest portion was obscured from view. Pit counts often changed slightly based on close proximity pits combining to form one larger pit. Pit depth sometimes decreased due to a thickness reduction over the entire corroded area, as pit depths were measured based on the surface height surrounding the pit.

Tables 2 and 3 summarize statistical results per material type for critical pits and fatigue lives, respectively. Figures 2–4 illustrate the relationship between critical pit depth and cycles to fracture for each specimen type. Figure 5 contrasts the time of critical pit formation and the number of cycles to fracture. Pit-to-crack transition and cycles to fracture are related in Fig. 6, with critical pit-to-crack transition and cycles to fracture considered in Fig. 7. Figure 8 shows a crack origin for KJ-8, an extruded

TABLE 2—*Critical pit depth statistics.*

	7075-T6 B1 (μm)	7075-T6 B2 (μm)	7075-T6 EXT (μm)
Mean	21.333	14.500	15.500
Standard Deviation	7.572	12.662	3.317
Maximum	30	33	20
Minimum	16	5	12

specimen, which exhibited subsurface pit growth. The interval H SEM inspection for KJ-11, a B2 specimen, is shown in Fig. 9. After this interval, eight surface cracks were visible within the specimen's corroded region. Figure 10 illustrates the occurrence of constituent particle related cracking, in this instance, for KJ-5, a B2 specimen that fractured due to the linkage of two particle originated cracks. Three

TABLE 3—*Cycles to fracture statistics.*

	7075-T6 B1 cycles	7075-T6 B2 cycles	7075-T6 EXT cycles
Mean	3 083 637	1 374 535	1 468 525
Standard Deviation	1 265 177	583 242	727 726
Maximum	4 543 071	2 015 150	2 256 028
Minimum	2 297 246	787 436	820 874

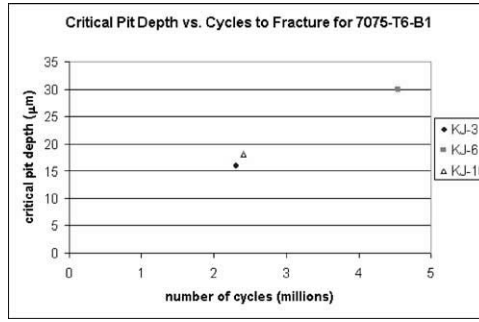


FIG. 2—*Critical pit depth versus cycles to fracture for 7075-T6-B1.*

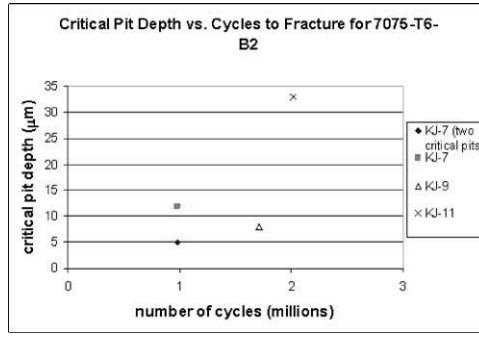


FIG. 3—*Critical pit depth versus cycles to fracture for 7075-T6-B2.*

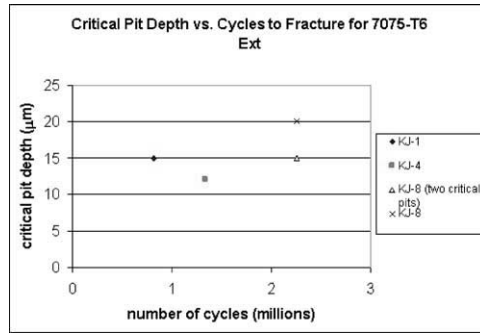


FIG. 4—*Critical pit depth versus cycles to fracture for 7075-T6 Ext.*

specimens of each type were subjected to corrosion fatigue testing. In addition to the corrosion fatigue specimens, a pristine, etched sample was tested for each of the three specimen types, with no fracture or visible surface cracking detected after 7.5 million cycles.

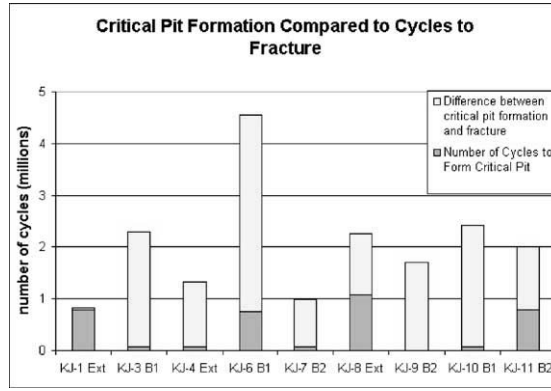


FIG. 5—*Critical pit formation compared to cycles to fracture.*

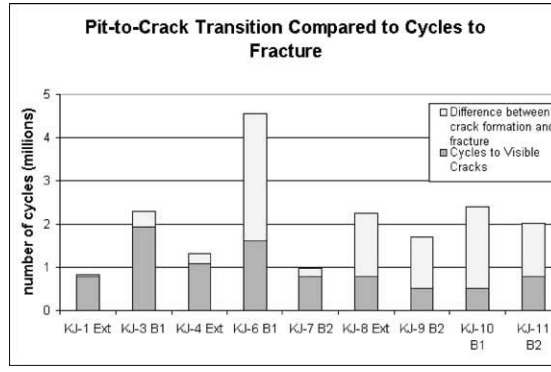


FIG. 6—*Pit-to-crack transition compared to cycles to fracture.*

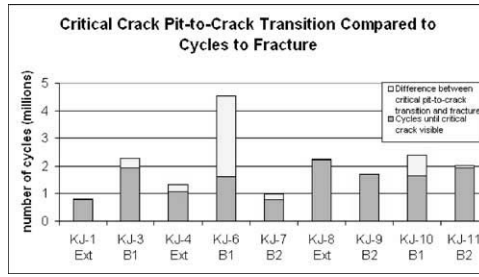


FIG. 7—*Critical crack pit-to-crack transition compared to cycles to fracture.*

Discussion

Results from the subject corrosion fatigue research, specifically Figs. 2–4, at first glance appear almost paradoxical: seemingly, more, and deeper, pitting corrosion damage increases fatigue life. Such a simple explanation for the phenomena experienced in this study, while appearing to contradict most research and logic, leads to the conclusion that further reasons must be acquired with the understanding that factors influencing fatigue life include more than the number of pits and pit depth.

Based on the fatigue life for each type of specimen, 7075-T6-B2 had the shortest average life, shown in Table 3. 7075-T6 Ext had approximately the same average fatigue life as 7075-T6-B2. 7075-T6-B1 had

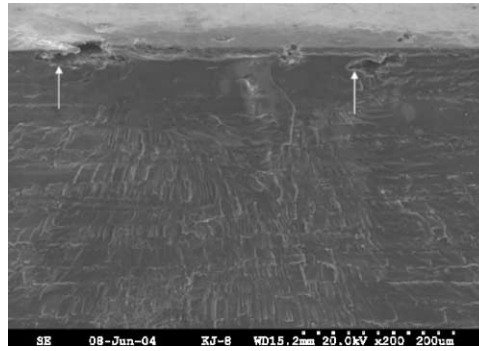


FIG. 8—*KJ-8 crack origin overview; note subsurface pit growth in the two outside pits (right side, 75°).*

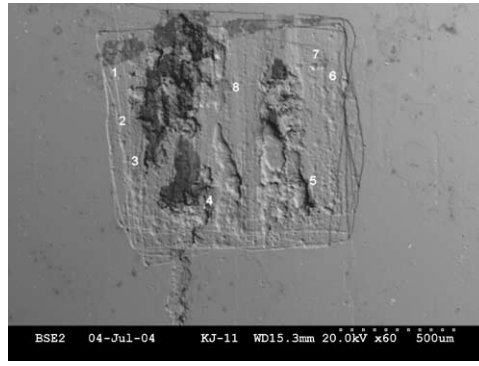


FIG. 9—*KJ-11 interval H BSE 3-D overview; numbers indicate location of cracks.*

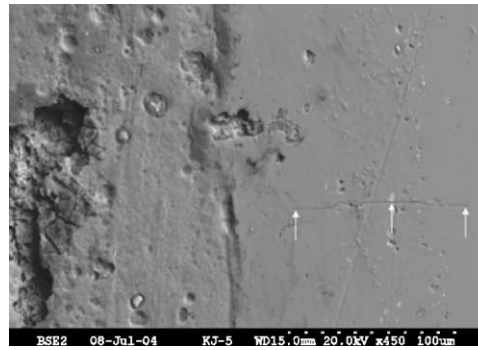


FIG. 10—*KJ-5 noncritical particle originated crack; this specimen fractured due to linkage of two constituent particle related cracks; however, pitting related cracks were present within the corroded area.*

a substantially longer fatigue life than either of the other types of specimens, with even the shortest number of cycles to fracture being greater than the maximum for the other specimen types. Critical pit depths were also deeper for 7075-T6-B1, but that is mainly explained by the extended fatigue life and time of corrosion.

The differences in microstructure, including overall grain size, between 7075-T6-B1, B2, and extruded materials help to explain the variation in fatigue life. The extruded and B2 specimens had comparable fatigue lives and more similar grain structures than the B1 material. Simply put, smaller grains in the B1 material meant that more grains were present within a given area to interfere with fatigue crack transition and growth, thereby extending the life by slowing pit-to-crack transition and the subsequent crack growth. Corrosion fatigue significantly reduced the fatigue life compared to pristine, etched specimens.

The maximum pit depth recorded for any specimen was 76 μm after interval I for KJ-10, a B1 specimen. Pits tended to elongate in the longitudinal direction of rolling and the specimen axis, especially for the 7075-T6-B2 and extruded specimens. For the rolled sheet material, both B1 and B2, pitting started out as preferentially corroded grains, often at grain boundaries. The extruded material tended to have more individual pits, and continued to have new pits form throughout the experiment, which occurred concurrently with pit coalescence. The 7075-T6-B1 and B2 specimens demonstrated similar pit growth, while the extruded material showed more overall corrosion resistance with initially smaller pit depths. The 7075-T6-B1 and B2 specimens were inclined towards more granular pit growth during the first few intervals, after which the pitting damage became widespread and few microstructural influences could be distinguished.

The extruded material seemed more susceptible to pitting along grain boundaries than the rolled sheet 7075-T6 aluminum alloys. 7075-T6-B1 specimens seemed to begin to corrode almost immediately upon exposure to the corrosive solution, while the 7075-T6-B2 required more time to begin corrosion processes, and the extruded specimens displayed more corrosion resistance. The extruded material was the most corrosion resistant of the three types tested, but still exhibited pitting after the first interval. Possible explanations for the difference in corrosion mechanisms include variations in constituent particles, particle distribution, grain orientation effects, and the level of homogeneity within grains. Since grain size and shape varied between material types, intergranular attack along grain boundaries would appear differently in various materials.

Figure 6 charts the comprehensive pit-to-crack transition for a given specimen. Cracking was present on most specimens for the majority of the fatigue life. In contrast to overall pit-to-crack transition, the critical crack tended to propagate to fracture quickly, especially considering the numerous other cracks present in the specimen that did not propagate. Figure 7 examines the difference between the number of cycles needed to produce a visible critical crack and the number of cycles to fracture. The 7075-T6-B1 specimens lasted longer than any other type of specimens with the critical crack, particularly so in the case of KJ-6. Most other specimens experienced critical crack nucleation and a continuous propagation in a relatively short number of cycles compared to their overall life.

Fatigue cracks in a corrosion fatigue environment propagated only when the crack growth rate was greater than the pit growth rate. This was proven time and time again as cracks transitioned from pits, then were never seen again, or were slowly removed over time as the pit continued to grow. Typically many other noncritical cracks were identified before a critical crack caused fracture. An example of this is shown in Fig. 9. Eight different cracks were present within the corroded region, with only one of these cracks eventually contributing to fracture.

Short cracks (<100 μm) in a corrosion fatigue environment were strongly influenced by grain boundaries and crystallographic grain orientation. Many cracks transitioned from pits and were not removed or reduced in size by corrosion, yet still did not propagate or grew slowly. If the crack tip was outside the corroded region, etching allowed for the tip to be located with respect to grains.

Many of the specimens either had a crack originate from a constituent particle, or had a particle influence a corrosion pit generated crack that became critical. The initial discontinuity state (IDS) of a material is very important, as any constituent particle of proper size and shape is capable of nucleating a fatigue crack, especially since crack-like discontinuities are most likely already present in the material. Corrosion can aggravate the situation, as a particle that may have been coherent with the matrix may have a corrosion pit form around the particle, causing a greater stress concentration than either the pit or the particle alone.

Three out of four 7075-T6-B2 specimens had fractures related to constituent particles, with KJ-5 being the only specimen to fracture solely due to particle related cracking. Other specimens had particles located in the same region from which the critical crack nucleated, but these particles could not be directly correlated with crack formation. Constituent particles often nucleated fatigue cracks in the specimens, with some affecting the critical crack by either nucleation or linkage. KJ-5 fractured due to the linkage and growth of two cracks that originated at two separate constituent particles outside of the corroded region, even with pit-originated cracks present on the specimen. The importance of IDS is beginning to be more widely recognized as a serious threat to extending structural fatigue lives. Some researchers understood the significance of intrinsic discontinuities related to fatigue crack growth decades ago [12], but these concepts were not immediately put into effect. Recent research is reiterating the importance of improving the IDS properties of materials [13].

After considering the various correlations with pit depths, it becomes obvious that something else plays a large role in pit-to-crack transition, especially at lower stress levels. Pit depth was not the most important factor in critical crack nucleation. Many other factors play important roles in pit-to-crack transition, especially at lower stresses where microstructure is more likely to affect crack transition and growth. These factors include:

- Microstructure and IDS,
- Pitting depth,
- Proximity to other pits,
- Pit size and shape (geometry), and
- Pit surface area.

Many fatigue life prediction models heavily rely on pitting depth. Unfortunately, this simplistic view does not account for many of the material properties and characteristics of corrosion fatigue that have been found to be significant. On a more positive note, models are continuing to increase in complexity and overall accuracy with improved research capability.

The differences in microstructure between 7075-T6-B1, B2, and extruded aluminum alloys seem to hold the key to understanding the pit-to-crack transition properties and crack propagation resistance. Theoretically, constituent particles should not be competing with pits as crack origins in high strength aluminum alloys used in aircraft applications, particularly during corrosion fatigue experiments as the pits typically create relatively large stress concentrations. The evidence of cracks stopping, or propagating very slowly while in the short crack regime, leads to the conclusion that microstructure, mainly crystallographic grain orientation, must be affecting the crack growth rate and crack path. Fractographic results, with the grain boundaries clearly visible on the fracture surface, also support this conclusion. The crack tips ending at or near grain boundaries, or cracks propagating slowly through a grain, also lend credence to this theory. As far as short crack propagation is concerned, it is well known that microstructure can alter the crack path, and even stop cracks from propagating altogether. However, short crack research within the corrosion fatigue domain is extremely limited due to its inherent complexity. Continuing to develop better and more

repeatable research techniques will extend knowledge into areas that are currently not well understood.

Conclusions and Recommendations

Microstructure has a significant influence on pit-to-crack transition and fatigue crack propagation for 7075-T6 aluminum alloy under corrosion fatigue conditions.

Fatigue cracks in a corrosion fatigue environment propagated only when the crack growth rate was greater than the pit growth rate.

Short cracks (<100 μm) in a corrosion fatigue environment were strongly influenced by grain boundaries and crystallographic grain orientation. Many cracks transitioned from pits and were not removed or reduced in size by corrosion, yet still did not propagate or grew only slowly.

Constituent particles within 7075-T6 aluminum alloys competed with corrosion pits formed during corrosion fatigue as critical crack nucleation sites.

For future experimentation regarding microstructural effects on pit-to-crack transition during corrosion fatigue, it is recommended to develop a technique for using orientation imaging microscopy (OIM) to determine the exact crystallographic grain orientation and relate this to the formation of corrosion pits and subsequent crack nucleation and propagation. Using this type of analysis tool will aid in a more quantitative microstructural approach.

Acknowledgments

The authors wish to acknowledge FASIDE International, Inc., for their financial support and the University of Utah for the use of their facilities. Sincere thanks are offered to Dr. Sachin Shinde, Dr. Paul Clark, Mr. Larry Smiltneek, Mr. Takao Okada, and Dr. Charles "Torch" Elliott for their assistance.

References

[1] http://www.ntsb.gov/aviation/aviation.htm.
[2] Schutz, W., "A History of Fatigue," *Eng. Fract. Mech.*, Vol. 54, No. 2, 1996, pp. 263–300.
[3] Harmsworth, C. L., "Effect of Corrosion on the Fatigue Behavior of 2024-T4 Aluminum Alloy," ASD Technical Report 61-121, 1961, pp. 1–7.
[4] Chen, G. S., Liao, C. M., Wan, K. C., Gao, M., and Wei, R. P., "Pitting Corrosion and Fatigue Crack Nucleation," *Effects of the Environment on the Initiation of Crack Growth, ASTM STP 1298*, W. A. Van Der Sluys, R. S. Piascik, and R. Zawierucha, Eds., ASTM International, West Conshohocken, PA, 1997, pp. 18–31.
[5] Lindley, T. C., McIntyre, P., and Trant, P. J., "Fatigue-Crack Initiation at Corrosion Pits," *Met. Technol. (London)*, Vol. 9, 1982, pp. 135–142.
[6] Kondo, Y., "Prediction of Fatigue Crack Initiation Life Based on Pit Growth," *Corrosion (Houston)*, Vol. 45, No. 1, 1989 pp. 7–11.
[7] Kawai, S. and Kasai, K., "Considerations of Allowable Stress of Corrosion Fatigue (Focused on the Influence of Pitting)," *Fatigue Fract. Eng. Mater. Struct.*, Vol. 8, No. 2, 1985, pp. 115–127.
[8] Hoeppner, D. W., "Model for Prediction of Fatigue Lives Based Upon a Pitting Corrosion Fatigue Process," *Fatigue Mechanisms, ASTM STP 675*, J. T. Fong Ed., ASTM International, West Conshohocken, PA, 1979, pp. 841–870.
[9] Goswami, T. and Hoeppner, D. W., "Transition Criteria—From a Pit to a Crack," *J. Mech. Behav. Mater.*, Vol. 10, No. 5–6, 1999, pp. 261–278.
[10] Hoeppner, D. W., Grimes, L., Hoeppner, A., Ledesma, J., Mills, T., and Shah, A., "Corrosion and Fretting as Critical Aviation Safety Issues," *ICAF 95 Estimation, Enhancement, and Control of Aircraft Fatigue Performance*, J. M. Grandage and G. S. Jost, Eds., Engineering Materials Advisory Services, London, Vol. I, 1995, pp. 87–107.
[11] ASTM Standard E 407, "Standard Practice for Microetching Metals and Alloys," *Annual Book of ASTM Standards*, (ASTM International, West Conshohocken, PA, 2001).
[12] Hoeppner, D. W., "Estimation of Component Life by Application of Fatigue Crack Growth Threshold

Knowledge," *Fatigue, Creep and Pressure Vessels for Elevated Temperature Service*, MPC-17, C. W. Lawton and R. R. Seeley, Eds., American Society of Mechanical Engineers, New York City, 1981, pp. 1–83.

[13] Merati, A., Tsang, J., and Kyle, K., "Exploratory Test Results for the Determination of Fatigue-Related Features of the Initial Discontinuity State (IDS) of Two Aluminum Alloys," LTR-SMPL-2001-0150, National Research Council Canada, Institute for Aerospace Research, Ottawa, 2001.

Journal of ASTM International, April 2006, Vol. 3, No. 4
Paper ID JAI13231
Available online at www.astm.org

Ajit K. Roy,[1] *Unnikrishnan Valliyil,*[2] *and Elumalai Govindaraj*[2]

The Role of Applied Potential on Environment-Assisted Cracking of Zirconium Alloys

ABSTRACT: Zircaloy-2 and Zircaloy-4 have been tested by the slow-strain-rate technique at ambient and elevated temperatures in an acidic environment relevant to the proposed geologic repository at the Yucca Mountain site. Tests were performed with and without cathodic and anodic applied potentials. The results of stress corrosion cracking testing without applied potentials indicate that the ductility of both alloys was enhanced in terms of percent elongation, percent reduction in area, failure strain, and the time-to-failure with increasing temperature indicating improved ductility. However, the magnitude of true failure stress was gradually reduced at higher testing temperatures. The application of anodic and cathodic controlled potentials during slow-strain-rate testing enhanced the cracking susceptibility of both alloys showing more pronounced effect at anodic applied potentials. The corrosion potential for both alloys, became more active at the elevated temperature. The morphology of failure at cathodic potentials was ductile, showing dimpled microstructure. However, transgranular brittle failure was observed with both alloys at anodic controlled potentials.

KEYWORDS: zirconium alloys, cracking, applied potential

Introduction

The Yucca Mountain site near Las Vegas, Nevada has been proposed to be the nationís geologic repository to contain spent-nuclear-fuels (SNF) generated from the operating nuclear power plants, and defense high level waste (HLW). Even though this repository has a natural barrier to prevent the seepage of water in it, substantial efforts have been made to prevent the breaching of the waste package through extensive design initiatives. The most recent waste package design is based on an all-metallic, multibarrier concept consisting of an outer corrosion-resistant metallic (Alloy 22) container over a thicker inner barrier made of Type 316NG stainless steel. The outer barrier is intended to provide the desired corrosion protection from the potential repository environments, while the inner container is added to provide the necessary structural support. Further, the use of a titanium (Ti) drip shield over the waste package is being considered to prevent direct contact of water, if any, with the waste package.

Cladding is the primary structural barrier that covers the SNF, which is in the form of pellets. It prevents the release of radionuclides contained in the SNF. Thus, the structural integrity of the cladding material plays an important role in either preventing or minimizing the release of radionuclides. Cladding used in most commercial light-water-reactors (LWR) and boiling-water reactors (BWR) in the United States is made of zirconium (Zr) alloys such as Zircaloy-2 (Zr-2) and Zircaloy-4 (Zr-4). Zr alloys are generally used due to their low neutron capture cross section, excellent corrosion resistance, and desired mechanical properties at elevated temperatures. However, there are indications in literature [1] that Zr alloys may become susceptible to stress corrosion cracking (SCC), hydrogen-embrittlement (HE), and localized (pitting and crevice) corrosion, should the waste package containers be breached by the aqueous environment inside the proposed repository. Even though the Ti drip shield may limit the contact of the waste package container to the dripping water, disruptive events such as seismicity can lift the water table located beneath the repository to higher levels. Thus, the waste package may come in contact with the ground water, leading to the breaching of this multibarrier package due to the occurrence of different types

Manuscript received April 7, 2005; accepted for publication December 8, 2005; published online January 2006. Presented at ASTM Symposium on Fatigue and Fracture Mechanics on 18ñ20 May 2005 in Reno, NV ; R. E. Link and K. M. Nikbin, Guest Editors.

[1] Associate Professor and Corresponding Author, Department of Mechanical Engineering, University of Nevada Las Vegas, Las Vegas, NV 89154-4027.

[2] Graduate Student, Department of Mechanical Engineering, University of Nevada Las Vegas, Las Vegas, NV 89154-4027.

Copyright © 2006 by ASTM International, 100 Barr Harbor Drive, PO Box C700, West Conshohocken, PA 19428-2959.

TABLE 1—*Chemical compositions of zirconium alloys tested (wt %).*

	Elemental analysis							
Material/Heat no.	Cr	Fe	Ni	Fe+Cr	Fe+Cr+Ni	O	Sn	Zr
Zr-2/242831	0.10	0.182	0.070	…	0.352	0.127	1.298	Balance
Zr-4/243195	0.12	0.225	…	0.342	…	0.132	1.283	Balance

of environment-induced degradations including SCC, HE, and localized attack.

Studies performed by several investigators [2–4] indicate that once the waste package is breached, the SNF cladding materials (Zr-2 and Zr-4) can come in contact with acidic species including hydrogen peroxide (H_2O_2) and nitric acid resulting from the radiolysis due to the gamma radiation. The formation of these radiolytic products and the presence of micro-organisms inside the repository can significantly influence the cathodic and anodic kinetics of the cladding materials while in contact with the surrounding aqueous environment that can result from the condensation, and tectonic events, as mentioned above. H_2O_2 having a very low pH (<3) has been detected in biofilms at millimolar levels [5] that has been cited to cause significant ennoblement of potential at which SCC can be initiated.

Previous studies [6,7] performed at the authors' laboratory have shown that neither Zr-2 nor Zr-4 may undergo SCC in an acidic solution at temperatures ranging from ambient to 90°C. One of the major failure mechanisms in Zr alloys is the hydrogen-induced subcritical crack growth resulting from the formation of hydrides [8,9]. Additionally, there are indications [10,11] in the open literature that these alloys may become susceptible to cracking in aqueous environments while loaded in tension under an anodic applied potential. In view of these rationales, SCC testing of Zr-2 and Zr-4 has been performed in an acidic environment under the influence of both anodic and cathodic applied potentials.

This paper presents the results of SCC testing of Zr-2 and Zr-4 under anodic and cathodic potentiostatic polarization using the state of the art experimental techniques. The results of localized corrosion studies and fractographic evaluations of the tested specimens are also presented in this paper.

Experimental

Smooth cylindrical specimens having 4-in. overall length (101.6 mm), 1-in. gage length (25.4 mm), and 0.25-in. gage diameter (6.35 mm) of Zr-2 and Zr-4 were machined by a qualified vendor using annealed bar stocks. These specimens were manufactured in such a way that the gage section was parallel to the longitudinal rolling direction. The room-temperature tensile properties of Zr-2 and Zr-4 were determined by using a commercially available tensile testing machine. The chemical composition, and the room-temperature tensile properties (based on duplicate testing) of both alloys are given in Tables 1 and 2, respectively. SCC testing without applied potential was performed using these cylindrical specimens. For SCC testing under controlled potentials (E_{cont}), the cylindrical specimens were modified by welding a conductive Type 304 stainless steel wire at the top shoulder of the specimens to apply the desired potential from a calibrated potentiostat. The welded wire was subsequently coated with a stop-off lacquer to prevent its contact with test solution while the desired potential was applied to the loaded specimen.

The operating temperature regime inside the proposed repository is yet to be established based on the emplacement distances amongst waste packages, and the age of the nuclear waste. Further, the precise environment surrounding the waste package inside the geologic repository is still unknown. Therefore, the susceptibility of Zr-2 and Zr-4 to SCC was evaluated in a simulated acidic aqueous solution containing concentrated chemical species [12,13] by using the slow-strain-rate (SSR) testing technique at ambient temperature, 60°C and 90°C. The composition of the test solution is given in Table 3. The specimens were continuously strained at a rate of 3.3×10^{-6} sec^{-1} until fracture. The application of this slow dynamic

TABLE 2—*Ambient temperature mechanical properties of Zr-2 and Zr-4.*

Material/ Heat no.	Yield strength ksi (MPa)	Ultimate tensile strength ksi (MPa)	%El	%RA
Zr-2/242831	53.0 (365.4)	76.2 (525.4)	31.0	47.9
Zr-4/243195	55.5 (382.7)	77.0 (530.9)	32.7	50.7

TABLE 3—*Chemical composition of the test solution (gram/liter).*

Environment (pH)	$CaCl_2$	K_2SO_4	$MgSO_4$	NaCl	$NaNO_3$	Na_2SO_4	HCl
Acidic solution (pH ~ 2 − 2.2)	2.77	7.58	4.95	39.97	31.53	56.74	To achieve the desired pH value

strain to the specimen caused failure that probably might not occur at a constant load or might have taken a prohibitively longer duration to cause failures in the tested specimens. This strain rate was selected to provide the most effective contributions of both the mechanical and environmental variables to promote SCC. The experimental setup used in the SSR testing is shown in Fig. 1.

During SSR testing, the specimens were subjected to a continuously changing stress. Therefore, the cracking susceptibility by this technique was characterized by the time-to-failure (TTF), failure strain (e_f) and a number of ductility parameters such as percent elongation (%El) and percent reduction in area (%RA). Further, the true failure stress (σ_f) based on the failure load, obtained from the engineering stress-strain diagram, and the final cross-sectional area of the specimen was used.

In order to study the effect of applied potential on the cracking susceptibility of Zr-2 and Zr-4 in an identical environment, the spot-welded specimens were strained at a similar rate of 3.3×10^{-6} sec^{-1} under either an anodic or a cathodic applied potential using potentiostatic polarization technique. During these tests, the specimen was used as a working electrode, silver/silver chloride (Ag/AgCl) acted as the reference electrode, and a graphite rod was used as a counter electrode. The magnitude of E_{cont} used during straining under cathodic polarization was based on the corrosion potential (E_{corr}) of each alloy, measured in an identical environment by a previous investigator [6]. However, during the SSR testing under an applied anodic potential, the magnitude of E_{cont} was based on the critical pitting potential (E_{pit}) determined [6] in an identical test solution. The experimental setup used in the SSR testing under E_{cont} is illustrated in Fig. 2.

The susceptibility of Zr-2 and Zr-4 to localized corrosion was determined by cyclic potentiodynamic polarization (CPP) technique in an identically simulated acidic solution at 30°C and 90°C. Once again, a three-electrode polarization method involving a working electrode (test specimen), a reference electrode (Ag/AgCl), and two counter electrodes (graphite) was employed. The potentiostat used in the CPP tests was calibrated according to the ASTM Designation: G 5-04 [14] prior to the localized corrosion testing. Duplicate tests were performed to evaluate the susceptibility of Zr-2 and Zr-4 to localized corrosion, and SCC with and without E_{cont}. The average value of each parameter was recorded for data analyses.

Metallographic and fractographic evaluations of all broken specimens were performed by optical

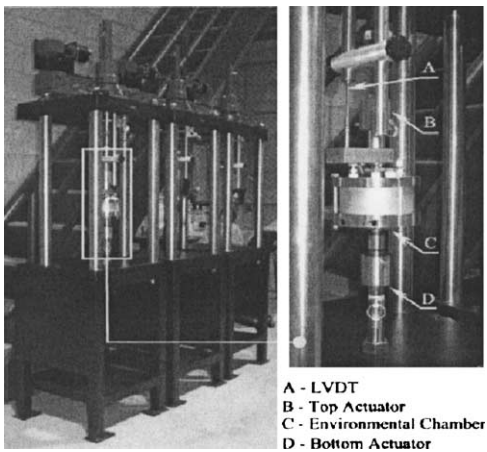


FIG. 1—*Slow-strain-rate setup.*

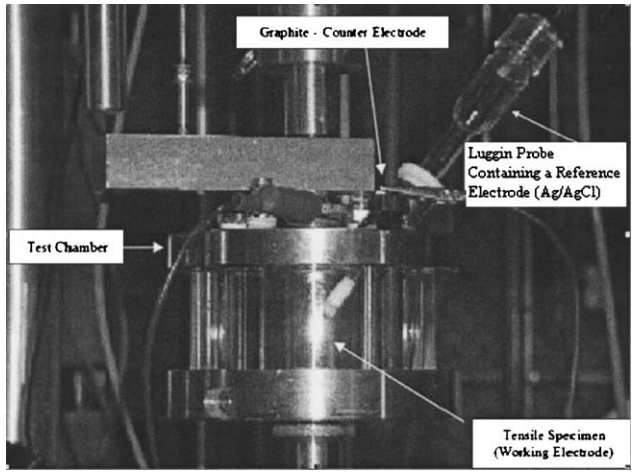


FIG. 2—*SSR Test setup under* E_{cont}.

microscopy and scanning electron microscopy (SEM), respectively. The characteristics of secondary cracks, if any, along the gage section of the tested specimens were evaluated by optical microscopy. The extent and morphology of cracking at the primary fracture surface of the tested specimens were determined by SEM.

Results and Discussions

The results of SCC testing involving Zr-2 and Zr-4 in the acidic solution at ambient temperature, 60°C and 90°C are shown in Figs. 3 and 4, respectively. The engineering stress-strain (s-e) diagram, obtained on either alloy in air at similar strain rate is also superimposed in these figures for comparison purpose. An examination of these figures indicate that the magnitude of the failure stress was generally reduced with increasing temperature, as expected. However, the extent of failure strain (e_f), was, in general, increased with an increase in the testing temperature, indicating enhanced ductility at higher temperatures. The effect of temperature on e_f was more pronounced with Zr-4. The magnitude of average σ_f, e_f, TTF, %El, and

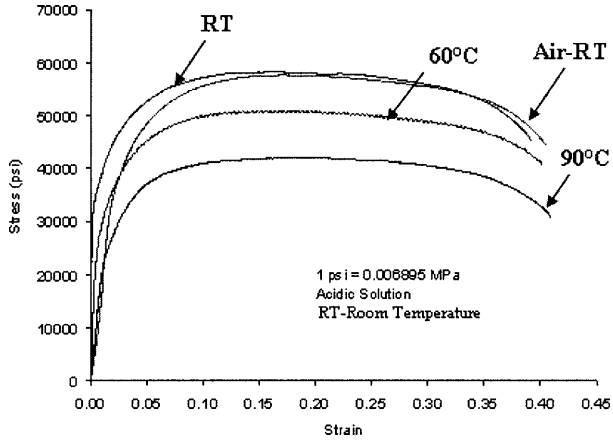


FIG. 3—*Stress-strain diagrams versus temperature for Zr-2.*

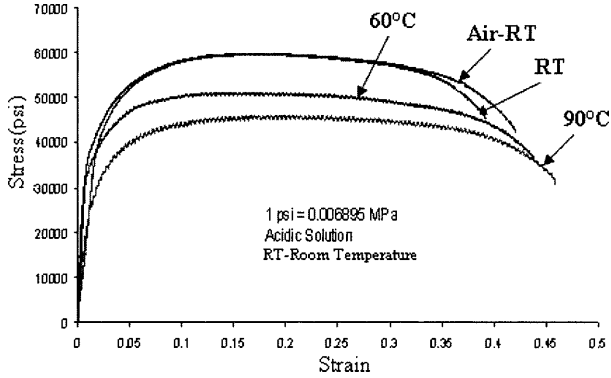


FIG. 4—*Stress-strain diagrams versus temperature for Zr-4.*

%RA, determined from these s-e diagrams, and the dimensions of the specimens (before and after testing), are given in Table 4. An evaluation of these data indicates that the TTF, e_f, and ductility parameters (%El and %RA) were gradually enhanced at higher testing temperatures, possibly due to increased plastic flow with increasing temperature. These results may suggest that both Zr alloys were immune to cracking even in the presence of an acidic solution at ambient and elevated temperatures. This phenomenon is consistent with the observation made by previous investigators [6,7] at the authors' laboratory. Nevertheless, the magnitude of the average σ_f was gradually reduced with increasing temperature for both alloys, as expected.

The comparisons of the s-e diagrams of Zr-2 and Zr-4 in the acidic solution at ambient temperature, with and without the application of cathodic E_{cont}, are shown in Figs. 5 and 6, respectively. An examination of these figures indicate that for both alloys, the engineering failure stress was reduced to some extent due to the application of cathodic E_{cont}. while the magnitude of the failure strain (e_f) for Zr-2 was not significantly influenced by E_{cont}, there was a gradual drop in e_f at more active (negative) E_{cont} values with Zr-4. The magnitudes of %El, %RA, σ_f, and TTF, determined from these s-e diagrams and the dimensions of the cylindrical specimens (before and after testing) are shown in Table 5. An evaluation of all four parameters indicates that they were gradually reduced with more active E_{cont}. Such a phenomenon may be attributed to the generation of hydrogen ion (H^+) and its enhanced concentration at more negative E_{cont} values, thus, causing reduced ductility due to the combined effect of hydrogen/hydrides and the applied stress during SSR testing. The failure of Zr alloys under the synergestic effect of hydrogen/hydrides and applied tensile stress is commonly referred to as hydrogen-induced-cracking (HIC) or delayed-hydride-cracking (DHC). The effect of cathodic applied potential in reducing the ductility, e_f and σ_f in susceptible materials have been reported by other investigators [15–21].

The results of SCC testing under anodic E_{cont} involving Zr-2 and Zr-4 in an identical environment using SSR technique at ambient temperature are illustrated in Fig. 7 and 8, respectively. Anodic potentials of +500 and +550 mV (versus Ag/AgCl), respectively were applied to Zr-2 and Zr-4, while they were strained at the same rate of 3.3×10^{-6} sec^{-1}. The magnitudes of ductility parameters (%El and %RA), TTF,

TABLE 4—*Results of SSR testing.*

Material/Heat no.	Environment	Temperature (°C)	Avg. %El	Avg. %RA	Avg. e_f	Avg. σ_f, ksi (MPa)	Avg. TTF (h)
Zr-2/242831	Air	Ambient	39.15	28.92	0.405	62.83 (433.21)	35.30
	Acidic solution	Ambient	36.36	26.36	0.381	62.12 (428.20)	34.00
		60	40.53	32.42	0.408	56.53 (389.77)	35.16
		90	41.54	33.17	0.413	48.95 (337.51)	35.92
Zr-4/243195	Air	Ambient	44.37	21.53	0.423	83.49 (575.66)	38.34
	Acidic Solution	Ambient	42.94	18.66	0.392	81.73 (563.52)	35.46
		60	44.10	19.65	0.422	69.77 (481.06)	36.97
		90	44.23	20.26	0.446	58.72 (404.87)	38.07

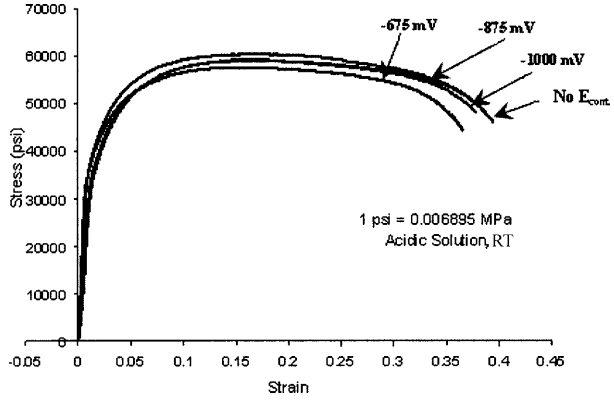


FIG. 5—*Stress-strain diagrams for Zr-2 under cathodic E_{cont}.*

and σ_f obtained from these s-e diagrams and the specimen dimensions are also shown in Table 5. A cursory examination of these data clearly reveals that the magnitude of %El, %RA, and TTF were drastically reduced due to the application of these anodic E_{cont} values. The magnitudes of e_f obtained from these plots are also shown in Table 5, indicating a significant drop due to the application of anodic E_{cont}. The detrimental effect of anodic applied potential on the cracking susceptibillity of both Zr alloys, as noted in this investigation, is consistent with the observations made by other investigators [11]. It is, however,

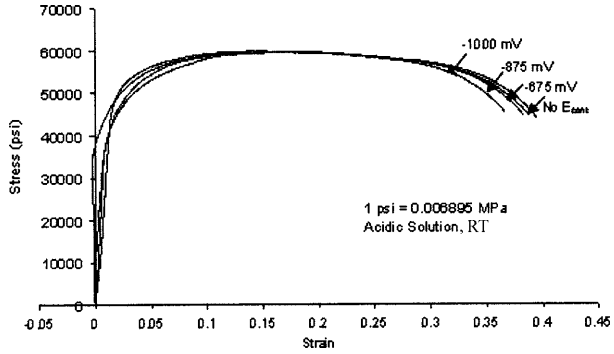


FIG. 6—*Stress-strain diagrams for Zr-4 under cathodic E_{cont}.*

TABLE 5—*Results of SSR testing under* E_{cont}.

Material/ Heat no.	Environment/ Temperature	E_{cont}, mV(Ag/AgCl)	Avg. %El	Avg. %RA	Avg. e_f	Avg. σ_f, ksi (MPa)	Avg. TTF (h)
Zr-2/242831	Acidic solution/ Room temperature	None	36.36	26.36	0.381	62.12 (428.32)	33.94
		−675	35.35	26.82	0.379	66.12 (455.90)	34.28
		−875	34.81	26.27	0.378	61.94 (427.04)	31.10
		−1000	33.80	24.69	0.378	59.65 (411.29)	33.87
		+500	21.84	16.60	0.172	60.61 (417.91)	15.90
Zr-4/243195	Acidic solution/ Room temperature	None	42.94	18.66	0.392	82.0 (565)	35.46
		−675	42.11	17.93	0.385	82.0 (565)	34.65
		−875	39.80	17.01	0.382	80.0 (551)	33.10
		−1000	37.73	16.56	0.376	76.0 (524)	32.43
		+550	35.65	16.22	0.308	76.2 (522.17)	28.96

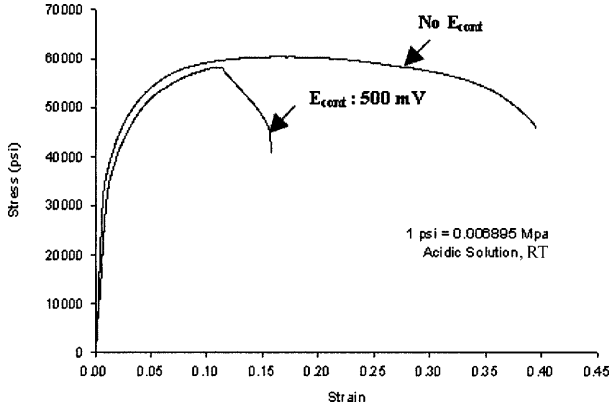


FIG. 7—*Stress-strain diagrams for Zr-2 under anodic E_{cont}.*

interesting to note that the magnitude of σ_f was not significantly varied by anodic applied potentials irrespective of the test materials.

The localized corrosion susceptibility of Zr-2 and Zr-4 evaluated by the CPP method in an identical aqueous environment at 30°C is shown in Figs. 9 and 10, respectively. An evaluation of these CPP diagrams indicates that both alloys exhibited an active-passive behavior showing a positive hysterisis loop. A similar trend was noted for both alloys at 90°C, as determined by the CPP technique. The magnitudes of E_{corr} and E_{pit}, determined from the CPP diagrams obtained at 30°C and 90°C, are shown in Table 6. An evaluation of these parameters indicates that the E_{corr} value became more active (negative) at the higher testing temperature. With respect to the E_{pit} value, it also became more active at 90°C for Zr-2. The temperature dependence of E_{corr} and E_{pit}, observed in this investigation, is consistent with the findings of other investigators [22–24]. This phenomenon may indicate the possibility of temperature-induced change in the protective properties of the passive film on the Zr alloy surface, resulting in a reduction of its resistance to breakdown as the temperature is increased. However, an anomaly in the E_{pit} value for Zr-4 was noted at 90°C, showing a more noble (positive) value at this temperature. While the data shown in Table 6 represent average values based on duplicate testing under each experimental condition, a viable

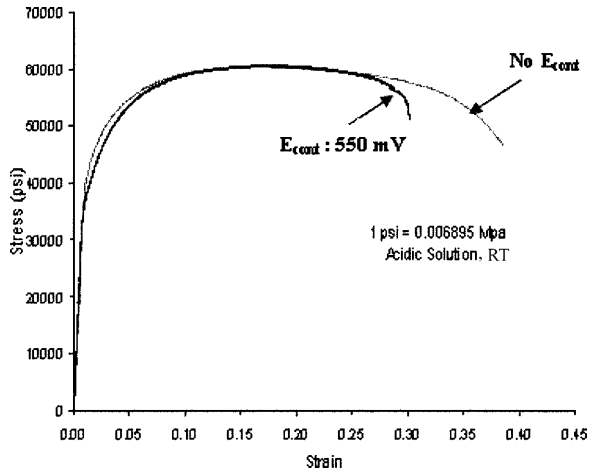


FIG. 8—*Stress-strain diagrams for Zr-4 under anodic E_{cont}.*

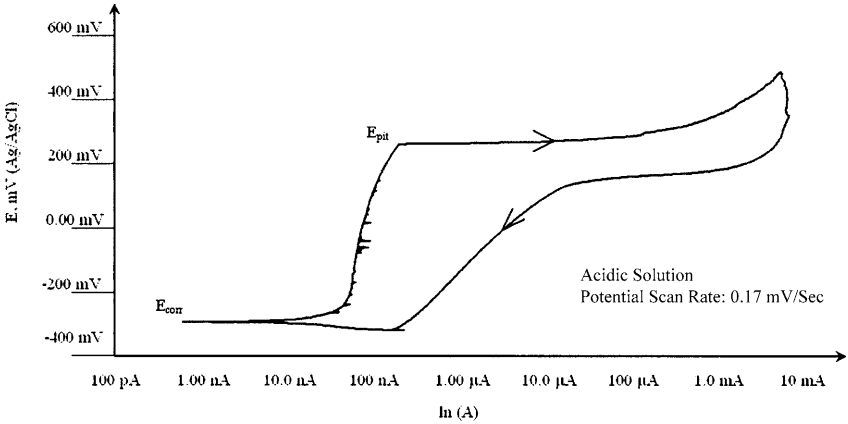


FIG. 9—*CPP diagram of Zr-2 at 30°C.*

explanation for such ennoblement of E_{pit} value for Zr-4 at 90°C is yet to be developed. It should also be noted that neither alloy exhibited pitting or crevice in the CPP testing.

The fractographic evaluations of the primary fracture surface of specimens tested under cathodic potentiostatic control revealed dimpled microstructures, indicating ductile failures. However, the specimens tested at anodic potentials showed transgranular brittle failures. The SEM micrographs of Zr-2 and Zr-4 are illustrated in Figs. 11–13 at different applied potentials (cathodic or anodic). Secondary cracks were observed along the gage section of the Zr-2 specimen tested under an anodic applied potential of +500 mV(Ag/AgCl), as shown in Fig. 14. However, no secondary cracks were observed with Zr-4 under an anodic control, even though transgranular brittle failures were observed in this alloy at the applied anodic potential.

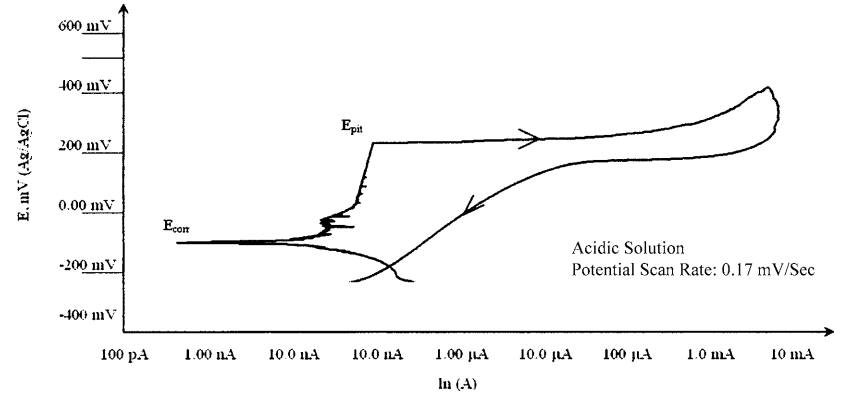


FIG. 10—*CPP diagram of Zr-4 at 30°C.*

TABLE 6—*Results of CPP testing.*

Material/Heat no.	Temperature (°C)	E_{corr}, mV (Ag/AgCl)	E_{pit}, mV (Ag/AgCl)
Zr−2/242831	30	−294	243
	90	−417	147
Zr−4/243195	30	−252	235
	90	−394	410

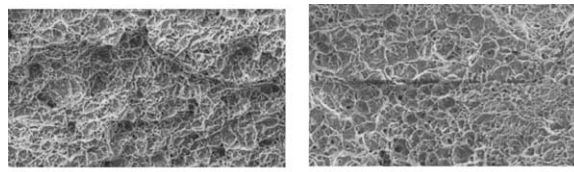


FIG. 11—*SEM micrigraphs of Zr-2.*

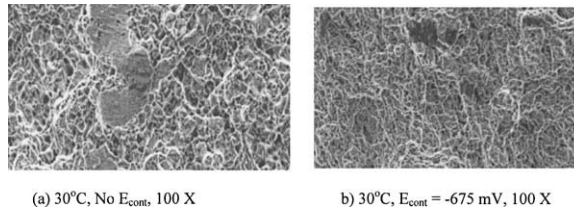


FIG. 12—*SEM micrographs of Zr-4.*

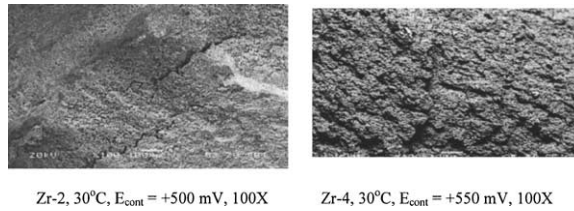


FIG. 13—*SEM micrographs of Zr-2 and Zr-4 under anodic* E_{cont}.

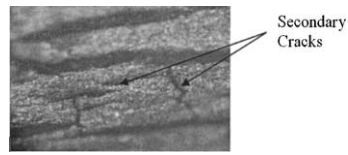


FIG. 14—*Optical micrograph of Zr-2 showing secondary cracks.*

Summary and Conclusions

The cracking susceptibility of Zr-2 and Zr-4 was evaluated in an acidic solution at ambient and elevated temperatures using the SSR technique under cathodic and anodic controlled potentials, respectively. The localized corrosion behavior was studied by the CPP technique in an identical environment. Metallographic and fractographic evaluations were performed by optical microscopy and SEM, respectively. The significant conclusions are summarized below.

- Both Zr alloys exhibited enhanced ductility at elevated temperatures in SCC tests without controlled potentials.

- The cracking susceptibility of both alloys in terms of the ductility (%El and %RA) parameters and the true failure stress (σ_f) was slightly enhanced at cathodic E_{cont} values. However, the magnitude of the failure strain (e_f) was not influenced at these potentials.
- The application of an anodic E_{cont} to both alloys resulted in enhanced cracking susceptibility in terms of %El, %RA, e_f, and TTF. However, the magnitude of σ_f was not significantly influenced due to the application of anodic E_{cont}.
- The application of E_{cont} (anodic/cathodic) during SCC testing under a SSR condition may simulate the variation of electrochemical potential resulting from radiolysis and presence of microorganisms inside the proposed repository. No localized attack was observed in specimens subjected to potentiostatic polarization.
- A consistent pattern on the effect of temperature on E_{corr} was noted for both Zr alloys. However an anomaly in the temperature dependence of E_{pit} was observed for Zr-4 at 90°C.
- Fractographic evaluations of the primary fracture surface by SEM revealed dimpled microstructures in both alloys under cathodic potential, indicating ductile failures. On the contrary, transgranular brittle failures were observed under an anodic applied potential.
- Secondary cracks were observed along the gage section of the Zr-2 specimens stressed under an anodic applied potential.

Acknowledgments

This work was funded by the United States Department of Energy under Grant No. DE-FG04-2001 Al67358. Assistance of Anand Venkatesh and Vikram Marthandam in editing this paper is thankfully acknowledged.

References

[1] Pestcatore, C., et al., "Zircaloy Fuel Performance under Spent Fuel Disposal Conditions, BNL-52235, DOE/OSTI-4500-R75, WMEM-ZRC Rev. 4/90," Progress Report for May 1-October 31, 1989, Brookhaven National Laboratory, 1990.

[2] Kim, Y. J., and Oriani, R. A., "Brine Radiolysis and its Effects on the Corrosion of Grade 12 Titanium," *Corrosion (Houston)* 43, 92–97 (1987).

[3] Kim, Y. J., and Oriani, R. A., "Corrosion Properties of the Oxide Film Formed on Grade 12 Titanium in Brine Under Gamma Radiation," *Corrosion (Houston)* 43, 85–91 (1987).

[4] Glass, R. S., Overtruf, G. E., Van Konynenburg, R. A, and McCright, R. D, "Gamma Radiation Effects of Corrosion - I. Electrochemical Mechanisms for the Aqueous Corrosion Processes of Austenitic Stainless Steels Relevant to Nuclear Waste Disposal in Tuff," *Corros. Sci.*, 26, 577–590 (1986).

[5] Shoesmith, D. W., and Ikeda, B. M., "The Resistance of titanium to Pitting, Microbially Induced Corrosion, and Corrosion Under Unsaturated Conditions," Atomic Energy of Canada Limited Report, AECL-11709, COG-96-557-I, April 1997.

[6] Pothana, S., "Evaluation of Cracking and Localized Corrosion Behavior of Cladding Materials," M.S. thesis, Dept. of Mechanical Engineering, University of Nevada, Las Vegas, 2003.

[7] Aquino, H., "Cracking of Zirconium Alloys at Constant Load with and without Applied Potentials," M.S. thesis, Dept. of Mechanical Engineering, University of Nevada, Las Vegas, 2003.

[8] Simpson, L. A., and Puls, M. P., "Effect of Stress, Temperature, and Hydrogen Content on Hydride-Induced Crack Growth in Zr-2.5% Nb," *Metall. Trans. A*, 10A, 1093–1105, (1979).

[9] Chung, H. M., "Corrosion and Hydride-Induced Degradation on Spent Fuel Cladding Under Repository Conditions," Research Report, Energy Technology Division, Argonne National Laboratory, 1999.

[10] Yucca Mountain Science and Engineering Report Rev 1, and DOE/RW-0539-1.

[11] Sharkawy, S. W., Hammad, F. H., Abou-Zahara, A. A., and Videm, K., "Influence of Some Factors on the Susceptibility of Zircaloy-2 Tubes to Iodine Stress Corrosion Cracking," *J. Nucl. Mater.*, 165, 184–192 (1989).

[12] BSC (Bechtel SAIC Company, "General Corrosion and Localized Corrosion of the Drip Shield," ANL-EBS-MD-000004 Rev.01, June 2003.

[13] Estill, J. C., "Long-Term Corrosion Studies," 2.2 of Engineered Materials Characterization Report, ed. R. D. McCright, UCRL-ID-119564, Vol. 3 Rev. 1.1, 1998.

[14] "Standard Reference Test Methods for Making Potentiostatic and Potentiodynamic Anodic Polarization Measurements," Designation: G 5-2004, American Society for Testing and Materials (ASTM), Vol. 03.

[15] Roy, A. K., and Spragge, M. K., "Effect of Controlled Potential on SCC of Nuclear Waste Package Container Materials," *Proceedings of NACE Corrosion/2000 Conference*, Paper No. 00188, Orlando, Florida, 2000.

[16] Roy, A. K., Spragge, M. K., Fleming, D. L., and Lum, B. Y., "Cracking of Titanium Alloys under Cathodic Applied Electrochemical Potential," *Micron* 32(2), 211–218 (2001).

[17] Azkarate, Pelayo, A., and Victori. L., "Hydrogen Assisted Stress Corrosion Cracking of Titanium Alloys in Aqueous Chloride Environments," *Progress in the Understanding and Prevention of Corrosion*, Vol. 2, Spain, 1993, 1573–1580.

[18] Raja, K. S., and Rao, K. P., "Effect of Applied Potentials on Room Temperature Stress Corrosion Cracking oF Austenitic Stainless Steel Weldments," *Corrosion (Houston)* 48(8), 634–640 (1992).

[19] Tsai, M. C., Tsai, W. T. and Lee, J. T., "The Effect of Heat Treatment and Applied Potential on the Stress Corrosion Cracking of Alloy 600 in Thiosulfate Solution," *Corros. Sci.*, 34(5), 741–757 (1993)

[20] Harima, T., Toyota, R., and Shibata, T., "The Effect of Potential on Initiation and Propagation of Stress Corrosion Cracks for Type 304L Stainless Steel in a Chloride Solution Containing Thiosulfate," *Corros. Sci.*, 39(10–11), 1873–1882 (1997).

[21] Congleton, J., and Yang, W., "The Effect of Applied Potential on the Stress Corrosion Cracking of Sensitized Type 316 Stainless Steel in High Temperature Water," *Corros. Sci.*, 37(3), 429–444 (1995).

[22] Wang, J. H., Su, C. C., and Szklarska-Smialowska, Z., "Effects of Cl^- Concentration and Temperature on Pitting of AISI 304 Stainless Steel," *Corrosion (Houston)* 44(10), 732–737 (1998).

[23] Roy, A. K., Fleming D. L., and Lum, B. Y., "Localized Corrosion Behavior of Candidate Nuclear Waste Package Container Materials," *Materials Performance*, 37(3), NACE International,.54–58 (1998).

[24] Postlethwaite, J., Scoular, R. J., and Dobbin, M. H., "Localized Corrosion of Molybdenum-Bearing Nickel Alloys in Chloride Solution," *Corrosion (Houston)* 44(4), 199–203 (1998).

Fracture Mechanics Analysis

Journal of ASTM International, Vol. 3, No. 6
Paper ID JAI100347
Available online at www.astm.org

Jie Qu[1] *and Xin Wang*[1]

Elastic *T*-Stress Solutions of Embedded Elliptical Cracks Subjected to Uniaxial and Biaxial Loadings

ABSTRACT: The elastic *T*-stress has been found to be an important parameter in characterizing the near crack tip elastic-plastic stress states of 2-D and 3-D crack problems. In addition to the *J*-integral, the *T*-stress provides an effective two-parameter characterization of 2-D and 3-D elastic-plastic crack tip fields in a variety of crack configurations under small scale yielding conditions. Embedded elliptical crack in an infinite solid subjected to uniaxial or biaxial tension conditions represents an excellent model for many engineering components with embedded cracks. Although extensive analyses are available for stress intensity factors (SIFs) for embedded elliptical cracks, to date no analytical *T*-stress solutions are available. This paper presents the exact close form solutions for elastic *T*-stress of an embedded elliptical crack in an infinite body under remote uniaxial or biaxial tension. The foundation of the derivation is based on the potential method for three-dimensional elasticity. Solutions of stress components parallel to and perpendicular to the cracked plane are derived first. *T*-stress is then obtained from the asymptotic stress field near the crack front. Complete solutions of *T*-stress along the crack front are established. Further, three-dimensional finite element analyses are conducted to verify the derived solutions; excellent agreements are achieved. When combined with the corresponding *K* or *J* solutions, these *T*-stress solutions are suitable for the analysis of constraint effects for embedded elliptical shaped cracks in engineering components.

KEYWORDS: elastic *T*-stress, constraint effects, embedded elliptical crack, biaxial loading, three-dimensional finite element analysis

Introduction

In an isotropic linear elastic body containing a three-dimensional crack subject to symmetric (mode I) loading, the leading terms in a series expansion of the stress eld vary near the crack front are [1]:

$$\sigma_{11} = \frac{K_I}{\sqrt{2\pi r}} \cos\frac{\theta}{2}\left(1 \bullet \sin\frac{\theta}{2}\sin\frac{3\theta}{2}\right) + T$$

$$\sigma_{22} = \frac{K_I}{\sqrt{2\pi r}} \cos\frac{\theta}{2}\left(1 + \sin\frac{\theta}{2}\sin\frac{3\theta}{2}\right)$$

$$\sigma_{33} = \frac{K_I}{\sqrt{2\pi r}} 2\nu\cos\frac{\theta}{2} + E\varepsilon_{33} + \nu T$$

$$\sigma_{12} = \frac{K_I}{\sqrt{2\pi r}} \sin\frac{\theta}{2}\cos\frac{\theta}{2}\cos\frac{3\theta}{2}$$

$$\sigma_{13} = \sigma_{23} = 0 \qquad (1)$$

where the subscripts 1, 2 and 3 suggests a local Cartesian coordinate system formed by the plane normal to the crack front and the plane tangential to the crack front point *s*; *r* and θ are the local polar coordinates; K_I is the mode I local stress intensity factor; *E* is the Young s modulus, and ν is the Poisson s ratio. The *T* in Eq 1 is the elastic *T*-stress, representing a tensile/compressive stress acting parallel to the crack plane.

Manuscript received April 18, 2005; accepted for publication March 7, 2006; published online April 2006. Presented at ASTM Symposium on Fatigue and Fracture Mechanics: 35th Volume on 18 20 May 2005 in Reno, NV; R. E. Link and K. M. Nikbin, Guest Editors.

[1] Research Assistant and Associate Professor, respectively, Department of Mechanical and Aerospace Engineering, Carleton University, Ottawa, Ontario, Canada, K1S 5B6.

Copyright © 2006 by ASTM International, 100 Barr Harbor Drive, PO Box C700, West Conshohocken, PA 19428-2959.

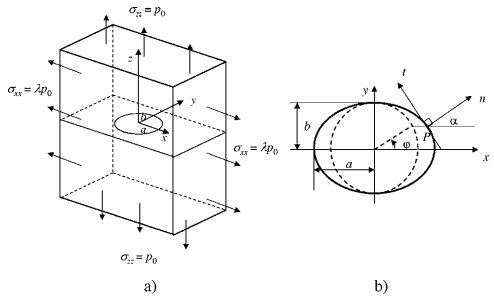


FIG. 1—*An embedded elliptical crack in an infinite body, with applied remote biaxial tension loadings, as shown in (a), crack is located in the x-y plane, as shown in (b).*

The elastic *T*-stress has been found to be an important parameter in characterizing the near crack tip elastic-plastic stress states of 2-D and 3-D crack problems. Larsson and Carlsson [2] and Rice [3] showed that the sign and magnitude of the *T*-stress substantially change the size and shape of the plane strain crack-tip plastic zone at finite load levels. Bilby et al. [4] showed that the *T*-stress can strongly affect the magnitude of hydrostatic triaxiality in the near crack tip elastic-plastic fields. The important features emerging from these works are that the sign and magnitude of *T*-stress can substantially alter the level of crack tip stress triaxiality, hence influence crack tip constraint. Positive *T*-stress strengthens the level of crack tip stress triaxiality and leads to high crack tip constraint; while negative *T*-stress reduces the level of crack tip stress triaxiality and leads to the loss of the crack tip constraint. The works by Betegon and Hancock [5], Du and Hancock [6], O'Dowd and Shih [7], and Wang [8] indicated that the *T*-stress, in addition to the *J*-integral, provides an effective two-parameter characterization of 2-D and 3-D elastic-plastic crack tip fields in a variety of crack configurations under small scale yielding conditions. Recently, the application of two-parameter fracture mechanics to include the constraint effect in the failure assessment procedure in engineering applications is becoming more and more established [9,10].

In addition to the elastic-plastic cracks, the effects of *T*-stress on other complex crack problems have also been studied most recently. For example, Ganti and Parks [11] and Zhang et al. [12] investigated the effect of *T*-stress on the constraint of elastic-plastic interface cracks; Ayatollahi et al. [13] studied the effect of *T*-stress on the constraint of cracks under mode II loadings; and Jayadevan et al. [14] studied the role of *T*-stress on fracture process under dynamic loading.

In order to apply these two-parameter fracture mechanics methodologies, it is important to provide *T*-stress solutions for the crack configurations under consideration. Similar to the stress intensity factors (SIFs), the values of *T*-stress strongly depend on the type of loading as well as on the relative crack length and the overall geometry. Note that the *T*-stress for the 2-D problem is independent of material property, but in the context of three-dimensional problems *T*-stresses (as well as SIFs) are also influenced by the Poisson's ratio of the material. Several numerical/analytical methods have been developed to calculate the elastic *T*-stresses. Many researchers have provided *T*-stress solutions for a wide range of 2-D cracked bodies under various loading conditions [15–21]. However, *T*-stress solutions for 3-D cracked specimens are very limited [22–24]. Elliptical crack embedded in an infinite solid subjected to uniaxial or biaxial tension loading represents an excellent model for many engineering components with embedded cracks. Although extensive analyses are available for stress intensity factors (SIFs) for embedded elliptical cracks [25,26], to the best of the authors' knowledge, no analytical *T*-stress solutions are available for embedded elliptical cracks. Recently, Wang [27] derived the exact *T*-stress solutions for the special case of embedded circular (penny shaped) cracks.

In the present paper, the exact *T*-stress solution for an embedded elliptical crack ($a > b$) in an infinite elastic body subjected to uniaxial or biaxial tension is developed. Figure 1 demonstrates the problem analyzed, with the biaxial loading ratio λ defined as the ratio of the stresses parallel to the crack plane (σ_{xx}) and perpendicular to the crack plane (σ_{zz}). The foundation of this derivation is based on the potential method for three-dimensional elasticity. Solutions of stress components parallel to and perpendicular to the cracked plane are derived first. Elastic *T*-stress is then obtained from the asymptotic stress field near the

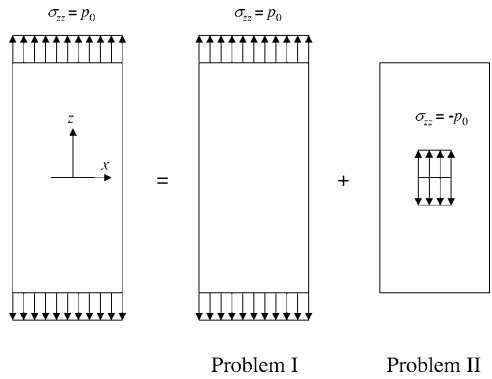


FIG. 2—*Superposition representation of problem.*

crack front. Further, three-dimensional finite element analyses are conducted to verify the derived solutions; excellent agreements are achieved.

Analysis of Elliptical Crack

Green and Sneddon [28] and Segedin [29] proposed potential functions to solve embedded elliptical cracks, which were extensively used to solve the elliptical crack problems for different loading conditions [25,26]. However, all the previous analyses have been focused on the determination of stress intensity factors. In this section, the terminology and analyses by Shah and Kobayashi [26] is summarized; it provides the background for the derivation of *T*-stress in the next section.

Embedded Elliptical Crack

Consider a flat elliptical crack in an infinite elastic body as demonstrated in Fig. 1. The boundary of the elliptical crack is described by:

$$\frac{x^2}{a^2} + \frac{y^2}{b^2} = 1 \quad \text{and} \quad z = 0 \tag{2}$$

The loading is applied at the remote ends, which is described by the following:

$$\sigma_{zz} = p_0 \tag{3}$$

In this section, the uniaxial tension case is considered here ($\lambda = 0$), the effect of λ will be discussed in a later section.

Using the superposition method, the problem is the summation of two problems: I and II (see Fig. 2). The first problem I is an uncracked body under remote tension, $\sigma^I_{zz} = p_0$, and the second problem II is the embedded elliptical cracks opened up by crack face pressure, $\sigma^{II}_{zz} = -p_0$, to the upper and lower surfaces of the crack.

The solution of stress components of the first problem I is simply

$$\sigma^I_{zz} = p_0 \tag{4}$$

with other stress components being zero.

Now concentrate on the second problem. For simplicity, from now on let's omit the superscript II. It is equivalent to the problem of a semi-infinite solid of $z > 0$ subject to the following boundary conditions:

$$\sigma_{xz} = \sigma_{yz} = 0; \quad \text{on } z = 0 \tag{5a}$$

$$\sigma_{zz} = -p_0; \quad \frac{x^2}{a^2} + \frac{y^2}{b^2} < 1, \; z = 0 \tag{5b}$$

$$u_z = 0; \quad \frac{x^2}{a^2} + \frac{y^2}{b^2} > 1, \; z = 0 \tag{5c}$$

The solution of the elliptical crack problem should then satisfy the above boundary conditions. In the context of three-dimensional elasticity, it becomes a mixed boundary value problem. This problem can be solved using the potential method by a single harmonic potential function ϕ. Appendix A summarized the resulting displacements and stress components for this harmonic function.

Using Eqs A2 and A3, (see Appendix A), condition 5a is satisfied and 5b and 5c take the following form:

$$\frac{\partial^2 \phi}{\partial z^2} = \frac{p_0}{2G}; \quad \frac{x^2}{a^2} + \frac{y^2}{b^2} < 1, \; z = 0 \tag{6a}$$

$$\frac{\partial \phi}{\partial z} = 0; \quad \frac{x^2}{a^2} + \frac{y^2}{b^2} > 1, \; z = 0 \tag{6b}$$

Now, the problem is reduced to find the harmonic function ϕ satisfying Eqs 6a and 6b.

Solution of Harmonic Function ϕ

To solve the boundary value problem represented by 6a and 6b for the elliptical crack, an ellipsoidal coordinate system (ξ, η, ζ) is introduced where ξ, η, and ζ are the roots of the equation in s,

$$\frac{x^2}{a^2 + s} + \frac{y^2}{b^2 + s} + \frac{z^2}{s} - 1 = 0 \tag{7}$$

The Cartesian coordinate (x, y, z) of any point can be expressed in terms of (ξ, η, ζ) by the relation:

$$a^2(a^2 - b^2)x^2 = (a^2 + \xi)(a^2 + \eta)(a^2 + \zeta) \tag{8a}$$

$$b^2(b^2 - a^2)y^2 = (b^2 + \xi)(b^2 + \eta)(b^2 + \zeta) \tag{8b}$$

$$a^2 b^2 z^2 = \xi \eta \zeta \tag{8c}$$

where

$$-a^2 \leqslant \zeta \leqslant -b^2 \leqslant \eta \leqslant 0 \leqslant \xi < \infty \tag{8d}$$

In the plane $z=0$, $\xi=0$ corresponds to the point (x, y) inside the ellipse, and $\eta=0$ corresponds to the point (x, y) outside the ellipse. Those points on the periphery of ellipse are identified by both $\xi=0$ and $\eta=0$. At a general point along the crack front, P, a local orthogonal system (n, t, z) can be established, where n and t are along the normal and tangential direction of the periphery of the ellipse as shown in Fig. 1(*b*).

Segedin [29] noted that the potential function, $V^{(n)}$ given by the following Eq 9a is harmonic.

$$V^{(n)} = \int_{\xi}^{\infty} \frac{\omega^n(s)ds}{\sqrt{Q(s)}} \tag{9a}$$

where

$$\omega(s) = 1 - \frac{x^2}{a^2 + s} - \frac{y^2}{b^2 + s} - \frac{z^2}{s} \tag{9b}$$

$$Q(s) = s(a^2 + s)(b^2 + s) \tag{9c}$$

and n is a positive integer. It has been found by Shah and Kobayashi [26] that for the loading condition represented by Eq 6, the corresponding potential function is in the form of $V^{(1)}$:

$$\phi = c_{00} V^{(1)} = c_{00} \int_{\xi}^{\infty} \frac{\omega(s)ds}{\sqrt{Q(s)}} \tag{10}$$

It can be shown that the above ϕ satisfies both Eqs 6a and 6b, if the following c_{00} is used:

$$c_{00} = \frac{p_0 a b^2}{8GE(k)} \tag{11}$$

where $E(k)$ is the complete elliptical integral of second kind, and k is the modulus of ellipse (see Appendix B). Once the ϕ is obtained, the stress components can be sought using Eq A.3. Using the derived ϕ, stress intensity factors for embedded elliptical cracks under remote tension were calculated in Refs [25] and [26].

Determination of Elastic *T*-Stress

In this section, the *T*-stress will be obtained from the difference between stress components σ_{nn} (stress parallel to the crack plane) and σ_{zz} (stress perpendicular to the crack plane) near the crack tip; therefore, solutions for these two stress components are derived first. Then, *T*-stress solutions are derived.

Solution of Stress Components

Having obtained the harmonic function ϕ, the stress components can be evaluated using Eq A.3. If at a point P along the crack front, the Cartesian system (x,y,z) is rotated α degree around z axis to a local coordinate system (n,t,z), see Fig. 1(*b*), the σ_{nn} is then related to the stress components in (x,y,z) coordinates in the following relationship:

$$\sigma_{nn} = \sigma_{xx}\cos^2\alpha + 2\sigma_{xy}\sin\alpha\cos\alpha + \sigma_{yy}\sin^2\alpha \tag{12}$$

From the geometry relationship as shown in Fig. 1(*b*), the angle α is related to angle φ as:

$$\cos^2\alpha = \frac{k'^2\cos^2\varphi}{\sin^2\varphi + k'^2\cos^2\varphi} \tag{13}$$

$$\sin^2\alpha = \frac{\sin^2\varphi}{\sin^2\varphi + k'^2\cos^2\varphi} \tag{14}$$

$$\sin\alpha\cos\alpha = \frac{k'\sin\varphi\cos\varphi}{\sin^2\varphi + k'^2\cos^2\varphi} \tag{15}$$

where $k' = b/a$, is the complementary modulus of the ellipse.

After substituting the expressions of σ_{xx}, σ_{xy}, and σ_{yy} in terms of harmonic function ϕ, Eq A.3, together with Eqs 13–15 into 12, the expression for σ_{nn} at $z=0$ plane can be written as:

$$\sigma_{nn} = A_1\frac{\partial^2\phi}{\partial x^2} + A_2\frac{\partial^2\phi}{\partial y^2} + A_3\frac{\partial^2\phi}{\partial x\,\partial y} \tag{16}$$

where

$$A_1 = 2G\frac{(k'^2\cos^2\varphi + 2\nu\sin^2\varphi)}{\sin^2\varphi + k'^2\cos\varphi} \tag{17a}$$

$$A_2 = 2G\frac{(\sin^2\varphi + 2\nu k'^2\cos^2\varphi)}{\sin^2\varphi + k'^2\cos\varphi} \tag{17b}$$

$$A_3 = 4G\frac{(1-2\nu)\sin\varphi\cos\varphi}{\sin^2\varphi + k'^2\cos\varphi} \tag{17c}$$

Note that at the $z=0$ plane, following Eq A.3, the σ_{zz} becomes:

$$\sigma_{zz} = -2G\frac{\partial^2\phi}{\partial z^2} \tag{18}$$

The potential function ϕ is given in Eqs 10 and 11, the partial derivatives of ϕ are then found as follows (using the results from Ref [25]):

$$\frac{\partial^2 \phi}{\partial x^2} = c_{00}\frac{\partial^2 V^{(1)}}{\partial x^2} = c_{00}\left(-2\int_{\xi}^{\infty}\frac{ds}{(a^2+s)\sqrt{Q(s)}} + \frac{4x^2\sqrt{Q(\xi)}}{(a^2+\xi)^2(\xi-\eta)(\xi-\zeta)}\right) \tag{19}$$

$$\frac{\partial^2 \phi}{\partial y^2} = c_{00}\frac{\partial^2 V^{(1)}}{\partial y^2} = c_{00}\left(-2\int_{\xi}^{\infty}\frac{ds}{(b^2+s)\sqrt{Q(s)}} + \frac{4y^2\sqrt{Q(\xi)}}{(b^2+\xi)^2(\xi-\eta)(\xi-\zeta)}\right) \tag{20}$$

$$\frac{\partial^2 \phi}{\partial x\,\partial y} = c_{00}\frac{\partial^2 V^{(1)}}{\partial x\,\partial y} = c_{00}\left(\frac{4xy\sqrt{Q(\xi)}}{(a^2+\xi)(b^2+\xi)(\xi-\eta)(\xi-\zeta)}\right) \tag{21}$$

and

$$\frac{\partial^2 \phi}{\partial z^2} = c_{00}\frac{\partial^2 V^{(1)}}{\partial z^2} = c_{00}\left(2\int_{\xi}^{\infty}\frac{ds}{(a^2+s)\sqrt{Q(s)}} + 2\int_{\xi}^{\infty}\frac{ds}{(b^2+s)\sqrt{Q(s)}} - \frac{4x^2\sqrt{Q(\xi)}}{(a^2+\xi)^2(\xi-\eta)(\xi-\zeta)} - \frac{4y^2\sqrt{Q(\xi)}}{(b^2+\xi)^2(\xi-\eta)(\xi-\zeta)}\right) \tag{22}$$

The integrals in Eqs 19, 20, and 22 can be further evaluated with the help of the following results (obtained from Ref [26]):

$$\int_{\xi}^{\infty}\frac{ds}{(a^2+s)\sqrt{Q(s)}} = \frac{2}{a^3k^2}[u_1 - E(u_1)] \tag{23a}$$

$$\int_{\xi}^{\infty}\frac{ds}{(b^2+s)\sqrt{Q(s)}} = \frac{2}{a^3k^2k'^2}[E(u_1) - k'^2u_1 - k^2 snu_1 cdu_1] \tag{23b}$$

where u_1, $E(u_1)$, snu_1, cdu_1 are Jacobian elliptical functions, outlined in Appendix B. Now, substituting the above Eqs 19–22 into Eqs 16 and 18, the stress results can be simplified into:

$$\sigma_{nn} = \frac{p_0ab^2}{E(k)(a^2\sin^2\varphi + b^2\cos^2\varphi)}\left\{\frac{b^2\cos^2\varphi + 2\upsilon a^2\sin^2\varphi}{a^3k^2}[E(u_1) - u_1]\right\} - \frac{p_0ab^2}{E(k)(a^2\sin^2\varphi + b^2\cos^2\varphi)}\left\{\frac{a^2\sin^2\varphi + 2\upsilon b^2\cos^2\varphi}{a^3k^2k'^2}[E(u_1) - k'^2u_1 - k^2 snu_1 cdu_1]\right\} + \frac{p_0ab^2}{E(k)\sqrt{Q(\xi)}} \tag{24}$$

and

$$\sigma_{zz} = \frac{p_0}{E(k)}[-E(u_1) + snu_1 cdu_1] + \frac{p_0ab^2}{E(k)\sqrt{Q(\xi)}} \tag{25}$$

Note that these solutions are for sub-problem II, after superposing the stress solutions for sub-problem I under tension, we have the stress solutions for remote tension:

$$\sigma_{zz} = \frac{p_0}{E(k)}[-E(u_1) + snu_1 cdu_1] + \frac{p_0ab^2}{E(k)\sqrt{Q(\xi)}} + p_0 \tag{26}$$

and σ_{nn} will remain as Eq 24.

Determination of Elastic T-Stress

William's [30] series expansion gives the asymptotic stress field very near the crack front, as demonstrated in Eq 1. For σ_{nn} and σ_{zz} we have

$$\sigma_{nn} = \frac{K_I}{\sqrt{2\pi r}}\cos\frac{\theta}{2}\left(1 - \sin\frac{\theta}{2}\sin\frac{3\theta}{2}\right) + T \tag{27}$$

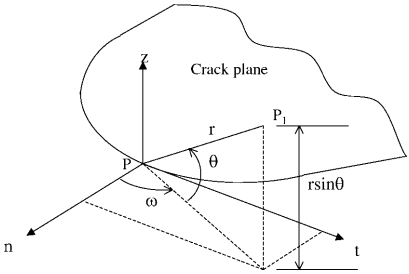


FIG. 3—*Local coordinates along the crack front.*

$$\sigma_{zz} = \frac{K_I}{\sqrt{2\pi r}} \cos\frac{\theta}{2}\left(1 + \sin\frac{\theta}{2}\sin\frac{3\theta}{2}\right) \tag{28}$$

Note here r and θ are the local polar coordinates around the crack tip. Using 27 and 28, and consider the location of $\theta=0$, the T-stress can be obtained from

$$T = \lim_{r\to 0+}(\sigma_{nn}|_{\theta=0} - \sigma_{zz}|_{\theta=0}) \tag{29}$$

From the relationship between the local coordinates (see Fig. 3) and the ellipsoidal coordinates, with ω being zero, the relationship between r and ξ is [31]:

$$\xi = abr(1+\cos\theta)(b^2\cos^2\varphi + a^2\sin^2\varphi)^{-\frac{1}{2}} \tag{30}$$

Therefore, Eq 29 becomes

$$T = \lim_{\xi\to 0}(\sigma_{nn}|_{z=0} - \sigma_{zz}|_{z=0}) \tag{31}$$

This equation is used here to determine the T-stress.

Substituting the stress components under tension loads Eqs 24 and 26 into Eq 31, and take the limit of $\xi\to 0$, the exact T-stress solution under tension can be obtained. Note that in the limit $\xi\to 0$, u_1 becomes the complete elliptic integral of first kind $K(k)$, $E(u_1)$ becomes the complete elliptic integral of second kind $E(k)$, and snu_1cdu_1 vanishes (see Appendix B). We have:

$$T(\varphi) = \frac{p_0 k'^2}{E(k)(\sin^2\varphi + k'^2\cos^2\varphi)}\{f_1 - f_2\} \tag{32}$$

or

$$t(\varphi) = \frac{T(\varphi)}{p_0} = \frac{k'^2}{E(k)\left(\sin^2\varphi + k'^2\cos^2\varphi\right)}\{f_1 - f_2\} \tag{33}$$

where $t(\varphi)$ is the normalized T-stress at specific angle φ, and p_0 is the applied nominal tensile stress, and

$$f_1 = \frac{k'^2\cos^2\varphi + 2\nu\sin^2\varphi}{k^2}[E(k) - K(k)] \tag{34}$$

$$f_2 = \frac{\sin^2\varphi + 2\nu k'^2\cos^2\varphi}{k^2 k'^2}[E(k) - k'^2 K(k)] \tag{35}$$

As shown in Eqs 32–35, T-stress depends on the Poisson's ratio, aspect ratio (b/a) and parametric angle φ. Figure 4 shows the results of T-stress along the crack front for various a/c ratios for Poisson's ratios of 0.3. It can be seen that the elastic T-stress is compressive along the crack front and strongly depends on the parametric angle. At the location of smaller radius (around 0 and 180 degrees), the T-stress

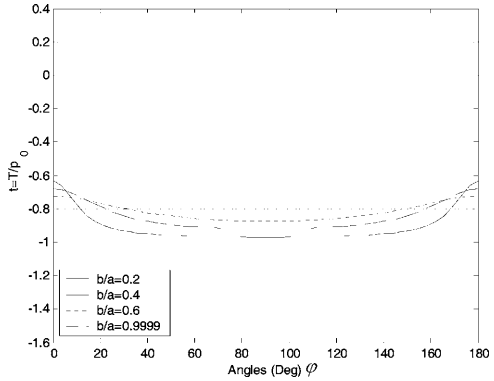


FIG. 4—*T-stress results for uniaxial loading,* $\lambda=0$, $\nu=0.3$.

increases for low aspect ratio cracks (b/a). The current T-stress solutions of elliptical cracks are used to calculate the T-stress for circular crack by setting $b/a=0.9999$, the results are the same numerically as the accurate solution of Wang [24]: $t(\varphi)=-(1+2\nu)/2=-0.8$.

Effect of Biaxial Loading

The T-stress solutions for embedded elliptical cracks under biaxial tension loading can be obtained using the superposition method, as demonstrated next. Consider the embedded crack under biaxial loading as demonstrated in Fig. 5(a). The stress field of this problem can be divided into two parts: the regular field which appears under the same loading conditions in the uncracked body (problem Fig. 5(b)), and a corrective field due to the presence of the crack (Fig. 5(c)). Note that the corrective field (Fig. 5(c)) is generated by the crack face pressure, $\sigma_{zz}(x)$, induced by the load system in the uncracked body. Therefore, the elastic T-stress for the problem (Eq 5(a)) at a general point P can be calculated from the summation of the T-stresses for these two problems:

$$T(P) = T_{uncrack}(P) + T_{crack\ pressure}(P) \tag{36}$$

where $T_{uncrack}(P)$ is the T-stress generated in the regular field, and $T_{crack\ pressure}(P)$ is the T-stress generated by crack pressure. Since the regular stress field (problem Fig. 5(b)) has no singularity at the crack tip, the corresponding stress intensity factor, K, is therefore zero. However, the same cannot be said for the elastic T-stress. Applying the crack tip stress field, Eq 1, and the relationship between local and global coordinates, we can find the corresponding T-stress for the regular field:

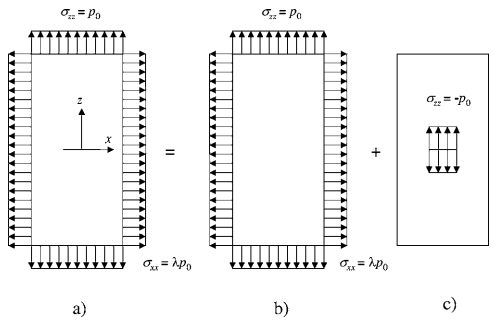


FIG. 5—*Superposition of T-stress calculation for biaxial loadings.*

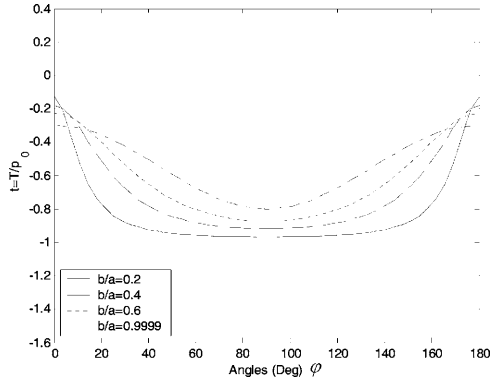


FIG. 6—*T-stress results for biaxial tension,* $\lambda=0.5$, $\nu=0.3$.

$$T_{uncrack}(P)=\left\{\lim_{r\to o+}\left(\sigma_{11}|_{\theta=0}-\sigma_{22}|_{\theta=0}\right)\right\}|_P=(\sigma_{nn}-\sigma_{zz})|_P \tag{37}$$

Here σ_{nn} and σ_{zz} are the stress components from the uncracked body under the applied load system, and the location is at the crack front point $P: x=a\sin\varphi$, $y=b\cos\varphi$, and $z=0$. Now, substitute Eq 37 into 36, the T-stress for the problem we are considering, Fig. 5(a), is then

$$T(P)=(\sigma_{nn}-\sigma_{zz})|_P+T_{crack\ pressure}(P) \tag{38}$$

For the uncracked body under uniaxial tension loading, $\lambda=0$, since both $\sigma_{xx}(P)$ and $\sigma_{yy}(P)$ are zeros, $\sigma_{nn}(P)$ is zero. The uncracked T-stress is then:

$$T^{\lambda=0}_{uncrack}(P)=(\sigma_{nn}-\sigma_{zz})|_P=-p_0 \tag{39}$$

For the cases of biaxial loading, $\sigma_{nn}(P)$ is no longer zero. From the geometry relation as shown in Fig. 1(b), as per Eq 12, we have, $\sigma_{nn}(P)=\sigma_{xx}\cos^2\alpha$, after substituting Eq 13 and applying Eq 37, the uncracked T-stress for biaxial loading can be written as

$$\left|T^{\lambda}_{uncrack}(P)=(\sigma_{nn}-\sigma_{zz})\right|_P=p_0\left(\frac{\lambda k'^2\cos^2\varphi}{\sin^2\varphi+k'^2\cos^2\varphi}-1\right)\Bigg|_P \tag{40}$$

Note that another portion of T-stress, $T_{crack\ pressure}(P)$, is the same for both the uniaxial loading and biaxial loading. Combing Eqs 39, 40, and 38, the following relation between T-stress solutions for uniaxial and biaxial tensions are established:

$$T^{\lambda}(P)=T^{\lambda=0}(P)+p_0\left|\frac{\lambda k'^2\cos^2\varphi}{\sin^2\varphi+k'^2\cos^2\varphi}\right|_P \tag{41}$$

Substituting the T-stress solution for uniaxial tension, obtained earlier, Eq 32, the T-stress solution for any biaxial tension ratio, λ, is found to be:

$$T(\varphi)=\frac{p_0k'^2}{E(k)(\sin^2\varphi+k'^2\cos^2\varphi)}\{f_1-f_2\}+\frac{\lambda p_0k'^2\cos^2\varphi}{\sin^2\varphi+k'^2\cos^2\varphi} \tag{42}$$

or

$$t(\varphi)=\frac{T(\varphi)}{p_0}=\frac{k'^2}{E(k)(\sin^2\varphi+k'^2\cos^2\varphi)}\{f_1-f_2\}+\frac{\lambda k'^2\cos^2\varphi}{\sin^2\varphi+k'^2\cos^2\varphi} \tag{43}$$

where f_1 and f_2 are given in Eqs 34 and 35. The T-stress results for $\lambda=0.5$ and 1.0 and aspect ratio $b/a=0.2$, 0.4, 0.6, and 0.9999 are plotted in Figs. 6 and 7. It can be seen that the T-stress levels are unchanged around $\varphi=90$ degrees, but increases significantly around $\varphi=0$ and 180 degrees, indicating the increase in constraint levels. It is because the σ_{nn} is not affected by the external load from the x-direction

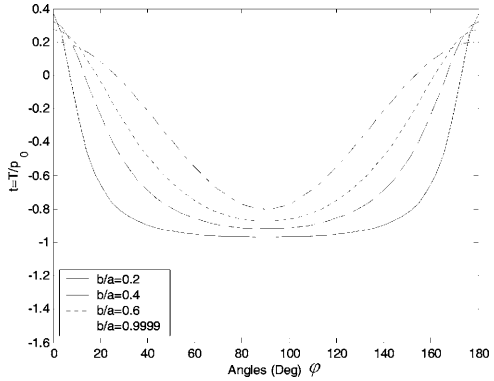


FIG. 7—*T-stress results for biaxial tension,* $\lambda = 1.0$, $\nu = 0.3$.

around $\varphi = 90$ degrees, but it increased significantly by the x-direction load around φ of 0 and 180 degrees.

Finite Element Verifications

To verify the above analytical solutions, three-dimensional finite element analyses are conducted to calculate the elastic T-stress for embedded elliptical cracks in an infinite body under remote tension. As illustrated by Nakamura and Parks [1] and Wang [24], effective finite element techniques using an interaction integral are available to calculate the elastic T-stress for three-dimensional crack problems. In this section, these techniques are employed to analyze the elliptical crack problem.

Finite Element Analyses

Three-dimensional finite elements are used to model the symmetric 1/8 of a embedded elliptical shaped crack in a thick plate. The thickness of the plate is more than six times of the crack radius, and this ensures that two bounding free surface of plate will have practically no effect on the stress distribution in the vicinity of the embedded crack [26]. The finite element analysis are made using ABAQUS [32], version 6.2, with 20-noded isoparametric three-dimensional solid elements. In order to model the square root singularity at the crack tip, three-dimensional prism elements with four mid-side nodes at the quarter points (a degenerate cube with one face collapsed) are used and the separate crack tip nodes are constrained to have the same displacements [33].

The loads are applied to the far ends of the plate. Remote tension loadings are considered. Note that both the geometry and loading conditions are symmetric for tension loads. These properties are utilized in the finite element calculations so that only 1/8 of the geometry is modeled. Appropriate displacement boundary conditions are applied on the symmetric planes. The finite element mesh used in the analysis is plotted in Fig. 8.

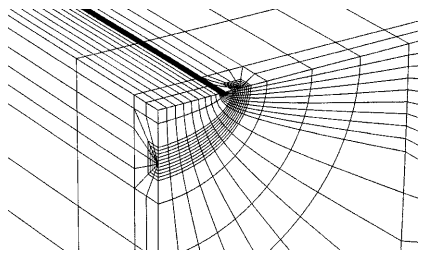


FIG. 8—*Finite element mesh (part,* $b/a = 0.6$*).*

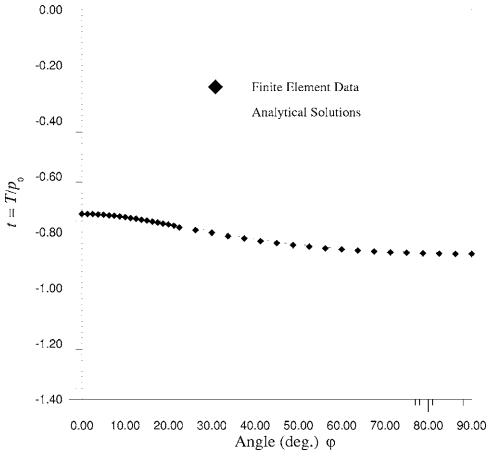


FIG. 9—*Comparison between analytical T-stress solution and FEM data, b/a=0.6, λ=0, ν=0.3.*

The interaction integral introduced by Nakamura and Parks [1] is used in the current analysis to extract the elastic *T*-stress. The calculation of *T*-stress along the crack front using domain integral formula of the interaction integral is conducted within the ABAQUS program. Five contours are used in the current analyses. Good independence of the *T* value on the choice of contour was obtained. In the current calculations, the average value of *T* results from the outer two contours is used to calculate crack *T*-stress distributions. Detail descriptions of the finite element analyses for obtaining *T*-stress for 3-D crack problems can be found in Ref [24].

Results

The *T*-stress distributions along the crack front for embedded elliptical crack of aspect ratio, a/b=0.6, in a thick plate under far-end tension has been determined. The Poisson's ratio used in the analysis is 0.3.

The normalized *T*-stress results, $t(\varphi)=T(\varphi)/p_0$, from the finite element analysis, together with the analytical solutions, are plotted in Fig. 9. Excellent agreements with the derived analytical solutions are achieved. The maximum differences are within 1.23 % for all the points along the crack front. Through these comparisons, it can be concluded that the analytical solutions for *T*-stress have been verified.

These derived *T*-stress solution, then, can be applied to the problem of a thick specimen containing an embedded elliptical crack under uniaxial and biaxial loadings, if the thickness is sufficiently large in comparison to the crack diameter (thickness $\geqslant 3\times$ crack diameter). This ensures that the two bounding free surfaces of the plate will have practically no effect on the stress distribution in the vicinity of the embedded crack [26].

Conclusions

Close form exact solutions for elastic *T*-stress of an elliptical shaped crack in an infinite body under remote uniaxial and biaxial tension are derived. *T*-stress solutions for uniaxial tension were derived first using the potential method. Solutions of stress components parallel to and perpendicular to the cracked plane were derived, based on which *T*-stress is then obtained from the asymptotic stress field near the crack front. *T*-stress solutions for biaxial tension were derived using the superposition method. Three-dimensional finite element analysis was conducted to verify the derived analytical solutions. It was found that *T*-stress depends on the material's Poisson's ratio, the parametric angle, crack aspect ratio b/a, and biaxial ratio λ. These results can be applied to thick plate containing an embedded elliptical shaped crack if the plate thickness is at least three times greater than the crack diameter. When combined with the corresponding *K* or *J* values, these *T*-stress results are suitable for the analysis of constraint effects for engineering components with embedded elliptical cracks.

Acknowledgments

The authors gratefully acknowledge the financial supports from the Natural Sciences and Engineering Research Council (NSERC) of Canada and Materials and Manufacturing Ontario (MMO). Thanks also go to Hibbit, Karlsson, and Sorensen, Inc., for making ABAQUS available under an academic license to Carleton University.

Appendix A

For embedded elliptical crack under general loads, the general equations of three-dimensional elasticity are described here following Shah and Kobayashi [26]. In the absence of body forces and shear stresses σ_{xz} and σ_{yz} on $z=0$ plane, Navier's equations of elastic equilibrium are satisfied by a harmonic function ϕ defined as follows:

$$\nabla^2\phi = 0 \tag{A.1}$$

where ϕ is a suitable harmonic function and ∇^2 is Laplacian operator in three dimensions. Cartesian components u_x, u_y, and u_z of the displacement vector are given by

$$u_x = z\frac{\partial^2\phi}{\partial x\,\partial z} + (1-2\nu)\frac{\partial\phi}{\partial x} \tag{A.2a}$$

$$u_y = \frac{\partial^2\phi}{\partial y\,\partial z} + (1-2\nu)\frac{\partial\phi}{\partial y} \tag{A.2b}$$

$$u_z = z\frac{\partial^2\phi}{\partial z^2} - 2(1-\nu)\frac{\partial\phi}{\partial z} \tag{A.2c}$$

where ν is the Poisson's ratio. The stress components are given by

$$\sigma_{xx} = 2G\left\{z\frac{\partial^3\phi}{\partial x^2\,\partial z} + \frac{\partial^2\phi}{\partial x^2} + 2\nu\frac{\partial^2\phi}{\partial y^2}\right\} \tag{A.3a}$$

$$\sigma_{yy} = 2G\left\{z\frac{\partial^3\phi}{\partial y^2\,\partial z} + \frac{\partial^2\phi}{\partial y^2} + 2\nu\frac{\partial^2\phi}{\partial x^2}\right\} \tag{A.3b}$$

$$\sigma_{zz} = 2G\left(z\frac{\partial^3\phi}{\partial z^3} - \frac{\partial^2\phi}{\partial z^2}\right) \tag{A.3c}$$

$$\sigma_{xy} = 2G\left\{z\frac{\partial^3\phi}{\partial x\,\partial y\,\partial z} + (1-2\nu)\frac{\partial^2\phi}{\partial x\,\partial y}\right\} \tag{A.3d}$$

$$\sigma_{yz} = 2G\left(z\frac{\partial\phi^3}{\partial y\,\partial z^2}\right) \tag{A.3e}$$

$$\sigma_{xz} = 2G\left(z\frac{\partial\phi^3}{\partial x\,\partial z^2}\right) \tag{A.3f}$$

where G is the shear modulus. Note that same set of equations is presented in Ref [34].

Appendix B

Various elliptic integrals are encountered in the text, and they are evaluated in terms of incomplete elliptic integrals of first kind u_1, incomplete elliptic integrals of second kind $E(u_1)$, and Jacobian elliptic functions snu_1 and cdu_1. The Jacobian elliptic function snu_1 is related to ξ by

$$sn^2u_1 = \frac{a^2}{a^2 + \xi} \tag{B.1}$$

and

$$cn^2u_1 = 1 - sn^2u_1 \tag{B.2}$$

$$dn^2u_1 = 1 - k^2sn^2u_1 \tag{B.3}$$

$$cdu_1 = \frac{cnu_1}{dnu_1} \tag{B.4}$$

where the modulus k and complementary modulus k' of ellipse are defined as:

$$k^2 = \frac{a^2 - b^2}{a^2}, \quad k'^2 = 1 - k^2 \ (a > b > 0) \tag{B.5}$$

when take the limit $\xi \to 0$, u_1 becomes the complete elliptic integral of fist kind $K(k)$, $E(u_1)$ becomes the complete elliptic integral of second kind $E(k)$, which are

$$K(k) = \int_0^{\frac{\pi}{2}} \frac{1}{\sqrt{1 - k^2 \sin^2 \theta}} d\theta = \int_0^1 \frac{1}{\sqrt{(1 - u^2)(1 - k^2u^2)}} du \tag{B.6}$$

$$E(k) = \int_0^{\frac{\pi}{2}} \sqrt{(1 - k^2 \sin^2 \theta)} d\theta = \int_0^1 \frac{\sqrt{(1 - k^2u^2)}}{\sqrt{(1 - u^2)}} du \tag{B.7}$$

References

[1] Nakamura, T. and Parks, D. M., "Determination of Elastic *T*-stress Along Three-dimensional Crack Fronts Using an Interaction Integral," *Int. J. Solids Struct.*, Vol. 29, 1992, pp. 1597–1611.

[2] Larsson, S. G. and Carlsson, A. J., "Influence of Nonsingular Stress Terms and Specimen Geometry on Small-scale Yielding at Cracktips in Elastic-Plastic Materials," *J. Mech. Phys. Solids*, Vol. 21, 1973, pp. 447–473.

[3] Rice, J. R., "Limitations to the Small Scale Yielding Approximation for Crack Tip Pasticity," *J. Mech. Phys. Solids*, Vol. 22, 1974, pp. 17–26.

[4] Bilby, B. A., Cardew, G. E., Goldthorpe, M. R., and Howard, I. C., "A Finite Element Investigation of the Effect of Specimen Geometry on the Fields of Stress and Strain at the Tips of Stationary Cracks," in *Size Effects in Fracture*, Mechanical Engineering Publications Limited, London, 1986, pp. 37–46.

[5] Betegon, C. and Hancock, J. W., "Two-parameter Characterization of Elastic-Plastic Crack Tip Fields," *ASME J. Appl. Mech.*, Vol. 58, 1991, pp. 104–110.

[6] Du, Z. Z. and Hancock, J. W., "The Effect of Nonsingular Stresses on Crack Tip Constraint," *J. Mech. Phys. Solids*, Vol. 39, 1991, pp. 555–567.

[7] O'Dowd, N. P. and Shih, C. F., "Family of Crack Tip Fields Characterized by a Triaxiality Prameter—I. Structure of Fields," , Vol. 39, 1991, pp. 989–1015.

[8] Wang, Y. Y., "On the Two-Parameter Characterization of Elastic-Plastic Crack Front Fields in Surface Cracked Plates," *Constraint Effects in Fracture, ASTM STP 1171* E. M. Hackett, K. H. Schwalbe, and R. H. Dodds, Eds., ASTM International, West Conshohocken, PA, 1993, pp. 120–138.

[9] Ainsworth, R. A. and O'Dowd, N. P., "Constraint in the Failure Assessment Diagram Approach for Fracture Assessment," *ASME J. Pressure Vessel Technol.*, Vol. 117, 1995, pp. 260–267.

[10] Ainsworth, R. A., Sattari-Far, I., Ferry, A. H., Hooton, D. G., and Hadley, I., "Methods for Including Constraint Effects Within SINTAP Procedures," *Eng. Fract. Mech.*, Vol. 67, 2000, pp. 563–571.

[11] Ganti, S. and Parks, D. M., "Elastic-Plastic Fracture Mechanics of Strength-Mismatch Interface Cracks," *Recent Advances in Fracture*, R. K. Mahudhara, et al., Eds., The Minerals, Metals and Material Society, 1997, pp. 13–25.

[12] Zhang, Z. L., Hauge, M., and Taulow, C., "The Effect of *T*-Stress on the Near Tip Stress Field of an Elastic-Plastic Interface Crack," *Proceedings of the Ninth International Conference on Fracture*, Karihaloo, B. L., et al., Eds., Vol. 4, Pergamon, Amsterdam, 1997, pp. 2643–2650.

[13] Ayatollahi, M. R., Smith, D. J., and Pavier, M. J., "Crack Tip Constraint in Mode II Deformation," *Int. J. Fract.*, Vol. 113, 2002, pp. 153–173.

[14] Jayadevan, K. R., Narasimhan, R., Ramamurthy, T. S., and Dattaguru, B., "A Numerical Study of *T*-Stress in Dynamically Loaded Fracture Specimens," *Int. J. Solids Struct.*, Vol. 38, 2001, pp. 4987–5005.

[15] Leevers, P. S. and Radon, J. C., "Inherent Stress Biaxiality in Various Fracture Secimen Geometries," *Int. J. Fract.*, Vol. 9, 1982, pp. 311–325.

[16] Cardew, G. E., Goldthorpe, M. R., Howard, I. C., and Kfouri, A. P., "On the Elastic *T*-Term," *Fundamentals of Deformation and Fracture*, B. A. Bilby, K. J. Miller, and J. R. Willis, Eds., Cambridge University Press, Cambridge, 1984, pp. 465–476.

[17] Kfouri, A. P., "Some Evaluation of the Elastic *T*-Term Using Eshelby's Method," *Int. J. Fract.*, Vol. 30, 1986, pp. 301–315.

[18] Chen, Y. Z., "Closed Form Solutions of *T*-Stress in Plane Elasticity Crack Problems," *Int. J. Solids Struct.*, Vol. 37, 2000, pp. 1629–1637.

[19] Sham, T. L., "The Determination of Elastic *T*-Term Using Higher Order Weight Functions," *Int. J. Fract.*, Vol. 48, 1991, pp. 81–102.

[20] Fett, T., "A Green's Function for *T*-Stress in an Edge Cracked Rectangular Plate," *Eng. Fract. Mech.*, Vol. 57, 1997, pp. 365–373.

[21] Wang, X., "Elastic *T*-Stress for Cracks in Test Specimens Subjected to Nonuniform Stress Distributions," *Eng. Fract. Mech.*, Vol. 69, 2002, pp. 1339–1352.

[22] Wang, Y. Y. and Parks, D. M., "Evaluation of the Elastic *T*-Stress in Surface Cracked Plates Using the Line-Spring Method," *Int. J. Fract.*, Vol. 56, 1992, pp. 25–40.

[23] Zhao, L. G., Tong, J., and Byrne, J., "Stress Intensity Factor and Elastic *T*-Stress for Corner Cracks," *Int. J. Fract.*, Vol. 109, 2001, pp. 209–225.

[24] Wang, X., "Elastic *T*-Stress Solutions for Semi-Elliptical Surface Cracks in Finite Thickness Plates," *Eng. Fract. Mech.*, Vol. 70, 2003, pp. 731–756.

[25] Kassir, M. K. and Sih, G. C., *Fracture Mechanics, Three-Dimensional Crack Problems*, Noordhoff International Publishing, Leyden, The Netherlands, 1975.

[26] Shah, R. C. and Kobayashi, A. S., "Stress Intensity Factor for an Elliptical Crack Under Arbitrary Normal Loading," *Eng. Fract. Mech.*, Vol. 3, 1971, pp. 71–96.

[27] Wang, X., "Elastic *T*-Stress Solutions for Penny-Shaped Cracks Under Tension and Bending," *Eng. Fract. Mech.*, Vol. 71, 2004, pp. 2283–2298.

[28] Green, A. E. and Sneddon, I. N., "The Distribution of Stress in the Neighborhood of a Flat Elliptical Crack in an Elastic Solid," *Proceedings of the Cambridge Philosophical Society*, Vol. 46, 1950, pp. 159–164.

[29] Segedin, C. M., "Some Three-Dimensional Mixed Boundary Value Problems in Elasticity," University of Washington, Dept. of Aeronautics and Astronautics, Report No. 67-5, 1967.

[30] Williams, M. L., "On the Stress Distribution at the Base of a Stationary Crack," *ASME J. Appl. Mech.*, Vol. 24, 1957, pp. 109–114.

[31] Zhu, X. K., Liu, G. T., and Chao, Y. J., "Three-Dimensional Stress and Displacement Fields Near an Elliptical Crack Front," *Int. J. Fract.*, Vol. 109, 2001, pp. 383–401.

[32] *ABAQUS Manual*, Version 6.2, Hibbitt, Karlsson & Sorensen, Inc., 2001.

[33] Barsoum, R. S., "Triangular Quarter-Point Elements as Elastic and Perfectly-Plastic Crack Tip Elements," *Int. J. Numer. Methods Eng.*, Vol. 11, 1977, pp. 85–98.

[34] Barber, J. R., *Elasticity*, Kluwer Academic Publishers, Dordrecht, The Netherlands, 1992.

Journal of ASTM International, Vol. 3, No. 7
Paper ID JAI13237
Available online at www.astm.org

Nitesh Jain,[1] *Ravinder Chona,*[2] *and Arun Shukla*[3]

Asymptotic Stress Fields for Thermomechanically Loaded Cracks in FGMs

ABSTRACT: The problem of a stationary crack in functionally graded materials (FGM), subjected to a combination of thermal and mechanical loading is considered. An asymptotic analysis coupled with Westergaard's stress function approach is used to characterize the stress field around the crack tip. Thermal and mechanical properties (e.g., elastic modulus, coefficient of thermal expansion, and thermal conductivity) are assumed to vary exponentially. The crack is assumed to be inclined to the direction of the property gradation. The thermal loading is taken to be a uniform heat flow in a direction inclined to the crack. The principal of superposition from linear elasticity is used to solve the problem, whereby the problem is divided into a number of subproblems. The first four terms in the expansion of the stress field are derived to explicitly bring out the influence of nonhomogeneity on the structure of the stress field. It is observed that the presence of heat flow produced no additional singularity and hence the classical inverse square root singularity still prevails around the crack tip. Using these stress field contours of constant maximum shear stress are generated and the effect of thermal loading on the crack-tip stress field is discussed.

KEYWORDS: FGMs, thermomechanical loading, crack-tip, isochromatics

Nomenclature

E = Young's modulus
ΔT = Temperature gradient
K = Thermal conductivity
α = Coefficient of thermal expansion
δ, γ, λ = Nonhomogeneity parameter
η_1, η_2 = Mapped coordinate system
φ = Property gradation direction
G_n, J_n, H_n, K_n: = Series solution of Mode I and II stress functions (mechanical loading)
L_n, M_n, N_n, T_n: = Series solution of Mode I and Mode II stress functions (thermal loading)
σ = Stress
σ = Stress
ε = Strain
u, v = In-plane displacements
F = Airy stress function
ϕ, ψ = Series stress function
$2a$ = Crack length
β = Direction of heat flow

Manuscript received July 13, 2005; accepted for publication March 31, 2006; published online May 2006. Presented at ASTM Symposium on Fatigue and Fracture Mechanics: 35th Volume on 18–20 May 2005 in Reno, NV; R. E. Link and K. M. Nikbin, Guest Editors.

[1] Senior Research Engineer, Corporate Research, Goodyear Tire and Rubber Company, Akron, OH 44305.
[2] Senior Scientist, Vehicles Directorate, AFRL, AFMC, Wright-Patterson AFB, OH.
[3] Simon Ostrach Professor and Chair, Dept. of Mech. Eng., University of Rhode Island, Kingston, RI 02881.

Copyright © 2006 by ASTM International, 100 Barr Harbor Drive, PO Box C700, West Conshohocken, PA 19428-2959.

Introduction

Ultra-super-hypersonic airplanes for supersonic transport, nuclear fusion reactors, and similar structures are often subjected to severe thermal and mechanical loading that gives rise to intense stresses in various components belonging to these systems. These components are subjected to severe structural loading as well as ultrahigh temperature, temperature gradient, and cyclic changes of ultrahigh temperature. At such operating temperatures the only practical group of materials appears to be structural ceramics. The application of homogeneous ceramic bonded to metal, however, involves some technical issues that may adversely affect performance and durability. First, because of the mismatch in the material properties of ceramics and metal, the temperature changes during processing and operation would give rather high residual and thermal stresses. Second, the strength of bonding between a ceramic layer and a metal layer is generally very poor. Finally, ceramics are brittle (even at relatively high temperatures). Consequently, the ceramic layer would be highly susceptible to cracking and spallation.

Recently, a new class of materials called functionally graded materials (FGMs), have gained considerable attention as a potential structural material in extremely high temperature environments. FGMs are microscopically inhomogeneous, composite materials in which the mechanical properties vary continuously from one surface to the other. This is achieved by gradually varying the volume fraction of the constituent materials. The characteristic feature of the FGMs are that the material combination and the composition gradation can be tailored to optimize their performance to meet single or multiple functions like thermal resistance, structural integrity, etc. In order for these FGMs to be used without significant reliability shortcomings, it is important to develop a fundamental understanding of their mechanical behavior, specifically the failure by fracture. Very often the failure process begins with the formation of microcracks at locations of corrosion pits, surface flaws, or severe stress concentrations. Generally a number of microcracks coalesce and form a local dominant crack, which would then propagate subcritically under cyclic or sustained loading.

Since the idea of FGMs was proposed, the majority of investigations into the failure of graded materials have been limited to situations where only one type of loading was assumed to exist, either mechanical or thermal. Several researchers [1–6] have investigated the behavior of embedded and edge cracks in graded materials subjected to quasistatic mechanical or thermal loading.

Fundamental investigation into the thermomechanical response of the graded materials is paramount before they can be incorporated into the design of structural components. To date, there has been little research on thermomechanical characterization of graded materials. Recently, Walter et al. developed the stress-intensity factor expression for surface cracks in functionally graded materials under Mode I thermomechanical loading [7]. Despite this initial study, the behavior of a cracked FGM under combined thermomechanical loading is still not completely understood. In this paper an asymptotic analysis coupled with Westergaard's stress function approach is used to develop the stress field around the stationary crack tip in FGMs under thermomechanical loading. These stress fields are subsequently used in generating synthetic contours of constant maximum shear stress (isochromatic), and the effect of thermomechanical loading on the crack-tip stress field is discussed.

Theoretical Formulation

Consider the plane elasticity problem of an FGM containing a finite crack on $y=0$ plane as shown in Fig. 1. The crack is subjected to a combination of thermal and mechanical loading. Thermal loading is taken to be a temperature gradient (ΔT) in a direction making an angle β with the positive x-axis.

The Young's modulus is assumed to vary exponentially in the x_1 direction as given in Eq 1 and the Poisson's ratio, ν, is assumed to be constant. The property gradient direction is at an angle φ to the $y=0$ plane.

$$E(x_1) = E_o e^{\delta x_1} \tag{1}$$

where E_o is the Young's modulus at the crack tip ($x=x_1=0$) and δ is the nonhomogeneity parameter having dimension (Length)$^{-1}$. Equation 1 can be written in terms of (x, y) coordinates by using simple coordinate transformation as

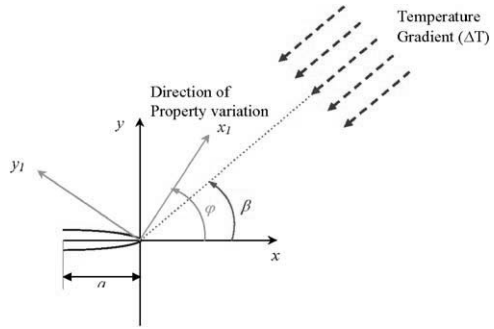


FIG. 1—*Reference coordinate system ($\varphi = 0$ for straight crack).*

$$E(x,y) = E_o e^{\alpha_1 x + \beta_1 y} \tag{2}$$

$$\alpha_1 = \frac{\delta}{\sqrt{1+\tan^2\varphi}}, \quad \beta_1 = \frac{\delta \tan\varphi}{\sqrt{1+\tan^2\varphi}} \tag{3}$$

The coefficient of thermal expansion (α) and thermal conductivity (k) are also assumed to be varying exponentially as

$$\alpha(x,y) = \alpha_o e^{\gamma x_1} \tag{4}$$

$$k(x,y) = k_o e^{\lambda x_1} \tag{5}$$

A similar coordinate transformation can also be applied for α and k in terms of parameters (α_2, β_2) and (α_3, β_3), respectively.

For any plane elasticity problem the equilibrium equation can be written as

$$\begin{aligned} \frac{\partial \sigma_{xx}}{\partial x} + \frac{\partial \sigma_{xy}}{\partial y} = 0, \\ \frac{\partial \sigma_{xy}}{\partial x} + \frac{\partial \sigma_{yy}}{\partial y} = 0 \end{aligned} \tag{6}$$

Strain-displacement relations can be given as

$$\varepsilon_{xx} = \frac{\partial u}{\partial x}, \quad \varepsilon_{yy} = \frac{\partial v}{\partial y}, \quad \varepsilon_{xy} = \frac{1}{2}\left(\frac{\partial u}{\partial y} + \frac{\partial v}{\partial x}\right) \tag{7}$$

The compatibility equation for plane problems as:

$$\frac{\partial^2 \varepsilon_{xx}}{\partial y^2} + \frac{\partial^2 \varepsilon_{yy}}{\partial x^2} = 2\frac{\partial^2 \varepsilon_{xy}}{\partial x\, \partial y} \tag{8}$$

The inplane stress components (σ_{ij}, i, j ε $\{x,y\}$) can be defined in terms of the Airy's stress function $F(x,y)$, as given in Eq 9.

$$\sigma_{xx} = \frac{\partial^2 F}{\partial y^2}; \quad \sigma_{yy} = \frac{\partial^2 F}{\partial x^2} \quad \text{and} \quad \sigma_{xy} = -\frac{\partial^2 F}{\partial x\, \partial y} \tag{9}$$

For a thermomechanical loading problem the Hooke's law can be written as

$$\varepsilon_{xx} = \frac{1}{E}(\sigma_{xx} - \upsilon\sigma_{yy}) + \alpha T,$$

$$\varepsilon_{yy} = \frac{1}{E}(\sigma_{yy} - \upsilon\sigma_{xx}) + \alpha T, \tag{10}$$

$$\varepsilon_{xy} = \frac{2(1+\upsilon)}{E}\sigma_{xy}$$

where T represents the change in temperature with respect to the stress free state.

The problem of thermomechanical loading on a cracked FGM is solved using the principal of superposition, a well known principal in linear elasticity. The problem is divided into two subproblems: (a) mechanical loading, and (b) thermal loading. The solution of the two problems is superimposed in the end in order to obtain the complete solution of the thermomechanical problem.

Mechanical Loading Subproblem

For solving this problem stresses due to thermal loading are neglected (T=0). Expressing the strain components in terms of the stress function through Hooke's law, the compatibility equation can be written as below [6].

$$\nabla^2(\nabla^2 F) - 2\alpha_1\frac{\partial}{\partial x}(\nabla^2 F) - 2\beta_1\frac{\partial}{\partial y}(\nabla^2 F) + (\alpha_1^2 + \beta_1^2)(\nabla^2 F) - \alpha_1^2(1+\nu)\frac{\partial^2 F}{\partial y^2}$$
$$- \beta_1^2(1+\nu)\frac{\partial^2 F}{\partial x^2} + 2(1+\nu)\alpha_1\beta_1\frac{\partial^2 F}{\partial x\,\partial y} = 0 \tag{11}$$

where $\nabla^2 = \partial^2/\partial x^2 + \partial^2/\partial y^2$

It may be observed from Eq 11 that the first term is the biharmonic term and the additional lower order differentials are due to the nonhomogeneity. The solution for Eq 11 is obtained through an asymptotic analysis coupled with Westergaard's stress function approach as explained in the following sections [6].

Asymptotic Analysis

In the asymptotic analysis, first a new set of coordinates are introduced through the transformation given in Eq 12

$$\eta_1 = \frac{x}{\varepsilon}, \quad \text{and} \quad \eta_2 = \frac{y}{\varepsilon}, \quad 0 < \varepsilon \leqslant 1 \tag{12}$$

For small values of ε, points very close to the crack tip are mapped into the range of observation in the (η_1, η_2) plane. Equation 11 now can be expressed in terms of scaled coordinates (η_1, η_2) as

$$\nabla^2(\nabla^2 F) - 2\alpha_1\varepsilon\frac{\partial}{\partial\eta_1}(\nabla^2 F) - 2\beta_1\varepsilon\frac{\partial}{\partial\eta_2}(\nabla^2 F) + (\alpha_1^2 + \beta_1^2)\varepsilon^2(\nabla^2 F)$$
$$- \alpha_1^2\varepsilon^2(1+\nu)\frac{\partial^2 F}{\partial\eta_2^2} - \beta_1^2\varepsilon^2(1+\nu)\frac{\partial^2 F}{\partial\eta_1^2} + 2(1+\nu)\alpha_1\beta_1\varepsilon^2\frac{\partial^2 F}{\partial\eta_1\,\partial\eta_2} = 0 \tag{13}$$

where $\nabla^2 = \partial^2/\partial\eta_1^2 + \partial^2/\partial\eta_2^2$

It is assumed at this stage that the stress function $F(\varepsilon\eta_1, \varepsilon\eta_2)$ can be expanded in powers of the parameter ε as follows

$$F_{mech}(\varepsilon\eta_1, \varepsilon\eta_2) = \sum_{m=0}^{\infty} \varepsilon^{\left(m+\frac{3}{2}\right)}(\phi_m)_{mech}(\eta_1, \eta_2) + \sum_{n=0}^{\infty} \varepsilon^{(n+2)}(\psi_n)_{mech}(\eta_1, \eta_2) \tag{14}$$

The first part of the above series $(\phi_m)_{mech}$ represents the singular series and the second part containing $(\psi_n)_{mech}$ is to account for the finiteness of the domain. The above series on substitution into Eq 13 leads to an infinite series involving differential equations associated with each power of ε as written below.

$$\sum_{m=0}^{\infty}\left\{\epsilon^{\left(m+\frac{3}{2}\right)}\nabla^2(\nabla^2(\phi_m)_{mech})-\epsilon^{\left(m+\frac{5}{2}\right)}\left[2\alpha_1\frac{\partial}{\partial\eta_1}(\nabla^2(\phi_m)_{mech})+2\beta_1\frac{\partial}{\partial\eta_1}(\nabla^2(\phi_m)_{mech})\right]\right]$$
$$+\epsilon^{\left(m+\frac{7}{2}\right)}\left[(\alpha_1^2+\beta_1^2)\nabla^2(\phi_m)_{mech}-\alpha_1^2(1+\nu)\frac{\partial^2(\phi_m)_{mech}}{\partial\eta_2^2}\right]$$
$$-\left\{\left[\beta_1^2(1+\nu)\frac{\partial^2(\phi_m)_{mech}}{\partial\eta_2^2}+2(1+\nu)\alpha_1\beta_1\frac{\partial^2(\phi_m)_{mech}}{\partial\eta_1\,\partial\eta_2}\right]\right\} \tag{15}$$

$$+\sum_{n=0}^{\infty}\left\{\epsilon^{(n+2)}\nabla^2(\nabla^2(\psi_n)_{mech})-\epsilon^{(n+3)}\left[2\alpha_1\frac{\partial}{\partial\eta_1}(\nabla^2(\psi_n)_{mech})+2\beta_1\frac{\partial}{\partial\eta_1}(\nabla^2(\psi_n)_{mech})\right]\right]$$
$$+\epsilon^{(n+4)}\left[(\alpha_1^2+\beta_1^2)\nabla^2(\psi_n)_{mech}-\alpha_1^2(1+\nu)\frac{\partial^2(\psi_n)_{mech}}{\partial\eta_2^2}\right]$$
$$-\left\{\left[\beta_1^2(1+\nu)\frac{\partial^2(\psi_n)_{mech}}{\partial\eta_2^2}+2(1+\nu)\alpha_1\beta_1\frac{\partial^2(\psi_n)_{mech}}{\partial\eta_1\,\partial\eta_2}\right]\right\}=0$$

For Eq 15 to be valid, the differential equations corresponding to each power of ε ($\varepsilon^{3/2}$, ε^2, $\varepsilon^{5/2}\ldots$) should vanish independently. This leads to the following set of differential equations.

$$m=n=0,\quad \nabla^2(\nabla^2(\phi_m)_{mech})=0,\quad \nabla^2(\nabla^2(\psi_m)_{mech})=0 \tag{16}$$

$$m=n=1,\quad \begin{aligned}&\nabla^2(\nabla^2(\phi_m)_{mech})-2\alpha_1\frac{\partial}{\partial\eta_1}(\nabla^2(\phi_{m-1})_{mech})-2\beta_1\frac{\partial}{\partial\eta_2}(\nabla^2(\phi_{m-1})_{mech})=0,\\&\nabla^2(\nabla^2(\psi_m)_{mech})-2\alpha_1\frac{\partial}{\partial\eta_1}(\nabla^2(\psi_{m-1})_{mech})-2\beta_1\frac{\partial}{\partial\eta_2}(\nabla^2(\psi_{m-1})_{mech})=0\end{aligned} \tag{17}$$

It can be observed that Eq 16 is the same as that for homogeneous materials for which the solution is available. However, the differential Eq 17, associated with higher powers of ε is no more the classical biharmonic equation and contains lower order differentials whose coefficients are the nonhomogeneity factors α_1 and β_1. The solution for Eq 17 consists of two parts: the classical solution, and additional terms due to nonhomogeneity, which can be obtained recursively.

Since the crack is inclined to the direction of property gradation, the stress field near the crack tip is mixed mode. However, due to the continuous variation of the elastic properties, the opening and shear mode components of the stress field can be superposed in the same way as that for a mixed mode crack in a homogenous material. Hence for $m=0$, the first term in the expansion can be written as

$$(\phi_0)_{mech}=\mathrm{Re}\{\overline{\overline{G_0}}\}+\eta_2\,\mathrm{Im}\{\overline{G_0}\}-\eta_2\,\mathrm{Re}\{\overline{J_0}\} \tag{18}$$

$\overline{\overline{G_0}}$ and $\overline{\overline{J_0}}$, which are the same as the first term in the series solution of Mode I and Mode II stress functions, respectively, for homogeneous materials, are defined as follows [8]

$$\overline{\overline{G_0}}=\frac{4}{3}A_0\varsigma^{\frac{3}{2}},\quad \overline{\overline{J_0}}=\frac{4}{3}C_0\varsigma^{\frac{3}{2}},\quad \varsigma=\eta_1+i\eta_2,\quad i=\sqrt{-1},\quad \overline{G_0}=\frac{\partial\overline{\overline{G_0}}}{\partial\varsigma},\quad \overline{J_0}=\frac{\partial\overline{\overline{J_0}}}{\partial\varsigma}$$

A_0 and C_0 are real constants proportional to the Mode I and Mode II stress intensity factors, respectively.

As indicated earlier, the solution of Eq 17 consists of two parts: complimentary solution and the particular solution. The complimentary solution is obtained from the series expansion of the stress function for homogeneous material and the particular solution is derived from already known $(\phi_0)_{mech}$. The complete solution for $m=1$ is given below.

$$(\phi_1)_{mech} = \mathrm{Re}\{\overline{\overline{G_1}}\} + \eta_2 \,\mathrm{Im}\{\overline{G_1}\} - \frac{\alpha}{2}\eta_2^2 \,\mathrm{Re}\{\overline{G_0}\} + \frac{\beta}{2}\eta_2^2 \,\mathrm{Im}\{\overline{G_0}\} - \eta_2 \,\mathrm{Re}\{\overline{J_1}\} - \frac{\alpha}{2}\eta_2^2 \,\mathrm{Im}\{\overline{J_0}\} - \frac{\beta}{2}\eta_2^2 \,\mathrm{Re}\{\overline{J_0}\} \tag{19}$$

where $\overline{\overline{G_1}} = \frac{4}{15}A_1\varsigma^{\frac{5}{2}}$, $\overline{\overline{J_1}} = \frac{4}{15}C_1\varsigma^{\frac{5}{2}}$, $\overline{G_1} = \frac{\partial\overline{\overline{G_1}}}{\partial\varsigma}$, $\overline{J_1} = \frac{\partial\overline{\overline{J_1}}}{\partial\varsigma}$

A_1 and C_1 are real constants. It should be noticed that $\overline{\overline{G_1}}$ and $\overline{\overline{J_1}}$ are the same as the second term in the series solution of the Mode I and Mode II stress functions, respectively, for homogeneous materials.

Similarly for $n=0$ and 1, the solutions can be written as below in terms of the functions $\overline{H_0}$, $\overline{K_0}$, $\overline{\overline{K_0}}$, $\overline{H_1}$, $\overline{K_1}$ and $\overline{\overline{K_1}}$, which are the same as the first two terms of the series solution for a mixed mode crack in homogeneous materials [9].

$$(\psi_0)_{mech} = \eta_2 \,\mathrm{Im}\{\overline{H_0}\} + \mathrm{Im}\{\overline{\overline{K_0}}\} - \eta_2 \,\mathrm{Re}\{\overline{K_0}\} \tag{20}$$

$$(\psi_1)_{mech} = \eta_2 \,\mathrm{Im}\{\overline{H_1}\} + \mathrm{Im}\{\overline{\overline{K_1}}\} - \eta_2 \,\mathrm{Re}\{\overline{K_1}\} \tag{21}$$

where $\overline{H_0} = B_0\varsigma$, $\overline{H_1} = \frac{1}{2}B_1\varsigma^2$, $\overline{\overline{K_0}} = \frac{1}{2}D_0\varsigma^2$, $\overline{\overline{K_1}} = \frac{1}{6}D_1\varsigma^3$, $\overline{K_0} = \frac{\partial\overline{\overline{K_0}}}{\partial\varsigma}$, $\overline{K_1} = \frac{\partial\overline{\overline{K_1}}}{\partial\varsigma}$, and B_0, B_1,D_0, and D_1 are real constants. The solutions for higher values of m and n can be obtained recursively [6].

By substituting the Eqs 18 to 21 in Eq 14 and converting them into (x,y) coordinates, we can obtain a four-term expansion for stresses using Eq 9.

$$\begin{aligned}(\sigma_{xx})_{mech} = &\sum_{n=0}^{1} [\mathrm{Re}\{P_n\} - y \,\mathrm{Im}\{P_n'\} + 2 \,\mathrm{Im}\{R_n\} + y \,\mathrm{Re}\{R_n'\} + 2 \,\mathrm{Re}\{Q_n\} + \mathrm{Im}\{S_n\} + y \,\mathrm{Re}\{S_n'\}] \\ &+ \alpha_1\left[- \mathrm{Re}\{\overline{P_0}\} + 2y \,\mathrm{Im}\{P_0\} + \frac{y^2}{2}\mathrm{Re}\{P_0'\} - \mathrm{Im}\{\overline{R_0}\} - 2y \,\mathrm{Re}\{R_0\} + \frac{y^2}{2}\mathrm{Im}\{R_0'\}\right] \\ &+ \beta_1\left[\mathrm{Im}\{\overline{P_0}\} + 2y \,\mathrm{Re}\{P_0\} - \frac{y^2}{2}\mathrm{Im}\{P_0'\} - \mathrm{Re}\{\overline{R_0}\} + 2y \,\mathrm{Im}\{R_0\} + \frac{y^2}{2}\mathrm{Re}\{R_0'\}\right]\end{aligned} \tag{22}$$

$$\begin{aligned}(\sigma_{yy})_{mech} = &\sum_{n=0}^{1} [\mathrm{Re}\{P_n\} + y \,\mathrm{Im}\{P_n'\} - y \,\mathrm{Re}\{R_n'\} + \mathrm{Im}\{S_n\} - y \,\mathrm{Re}\{S_n'\}] \\ &+ \alpha_1\left[\frac{-y^2}{2}\mathrm{Re}\{P_0'\} - \frac{y^2}{2}\mathrm{Im}\{R_0'\}\right] + \beta_1\left[\frac{y^2}{2}\mathrm{Im}\{P_0'\} - \frac{y^2}{2}\mathrm{Re}\{R_0'\}\right]\end{aligned} \tag{23}$$

$$\begin{aligned}(\sigma_{xy})_{mech} = &\sum_{n=0}^{1} -[y \,\mathrm{Re}\{P_n'\} + y \,\mathrm{Im}\{R_n'\} + \mathrm{Im}\{Q_n\} + y \,\mathrm{Re}\{Q_n'\} - \mathrm{Re}\{R_n\}] \\ &+ \alpha_1\left[y \,\mathrm{Re}\{P_0\} - \frac{y^2}{2}\mathrm{Im}\{P_0'\} + y \,\mathrm{Im}\{R_0\} + \frac{y^2}{2}\mathrm{Re}\{R_0'\}\right] \\ &+ \beta_1\left[- y\mathrm{Im}\{P_0\} - \frac{y^2}{2}\mathrm{Re}\{P_0'\} + y \,\mathrm{Re}\{R_0\} - \frac{y^2}{2}\mathrm{Im}\{R_0'\}\right]\end{aligned} \tag{24}$$

where $P_n = A_n z^{n-1/2}$, $Q_n = B_n z^n$, $R_n = C_n z^{n-1/2}$ and $S_n = D_n z^n$ in the (x,y) coordinates, are counterparts of the functions G_n, H_n, J_n and K_n, respectively. It can be noticed that by setting α_1 and β_1 to zero, the stresses collapse to their homogeneous counterparts.

Thermal Loading Subproblem

In this section analysis is performed to obtain the solution for the thermal loading problem. Similar to the mechanical loading problem, a complex variable technique is employed to obtain the solution.

Defining a complex temperature potential

$$\Omega(z) = T(x,y) + iT_I(x,y) \tag{25}$$

$$\Omega'(z) = \frac{\partial T(x,y)}{\partial x} - i\frac{\partial T(x,y)}{\partial y} = -\frac{1}{k(x)}(q_x - iq_y) \tag{26}$$

where the real part of this complex temperature potential $(T(x,y))$ represent the actual temperature change from stress free reference state and the imaginary part $(T_I(x,y))$ represents the solution of the conjugate problem; q_x and q_y are the heat flux in the x and y directions.

On the same lines defining a complex strain as

$$\varepsilon(z) = \alpha T + i\alpha T_I, \quad z = x + iy \tag{27}$$

Using Westergaard notation the integration of $\varepsilon(z)$ can be defined as

$$U(z) = \bar{\epsilon} = \int \epsilon(z)\mathrm{d}z = U_R + iU_I \tag{28}$$

The Cauchy-Riemann equations are

$$\frac{\partial U_R}{\partial x} = \frac{\partial U_I}{\partial y}, \quad \frac{\partial U_R}{\partial y} = -\frac{\partial U_I}{\partial x} \tag{29}$$

Using Eqs 27–29 the strains due to the thermal effects (αT) can be expressed as

$$\alpha T = \frac{\partial U_R}{\partial x} = \frac{\partial U_I}{\partial y} \tag{30}$$

At this point, the displacement (u,v) is defined as the sum of two parts such that the first part leads to an isothermal state and the second part can be imposed as an extra displacement boundary condition. By decomposing the original 2-D in-plane displacement in two factors as

$$\begin{aligned} u &= u' + \rho U_R \\ v &= v' + \rho U_I \end{aligned} \tag{31}$$

where ρ is a constant to be determined.

By substituting these decomposed displacements into Hooke's law for plane problems:

$$\begin{aligned} \sigma_{xx} &= \frac{E'}{1-v^2}\left(\frac{\partial u'}{\partial x} + v\frac{\partial v'}{\partial y}\right) + \frac{E'}{1-v}\rho\alpha T - \frac{E'}{1-v}\alpha T, \\ \sigma_{yy} &= \frac{E'}{1-v^2}\left(\frac{\partial v'}{\partial y} + v\frac{\partial u'}{\partial x}\right) + \frac{E'}{1-v}\rho\alpha T - \frac{E'}{1-v}\alpha T, \\ \sigma_{xy} &= \frac{E'}{2(1+v)}\left(\frac{\partial u'}{\partial y} + \frac{\partial v'}{\partial x}\right) \end{aligned} \tag{32}$$

By choosing

$$\begin{Bmatrix} \rho = 1,\ E' = E & \textit{plane stress} \\ \rho = (1+v) \text{ and } E' = E/(1-v^2) & \textit{plane strain} \end{Bmatrix} \tag{33}$$

in Eq 32 the temperature terms can be eliminated from the Hooke's law and the problem reduces to the isothermal case in terms of the displacements u' and v'.

The stress and displacements for this general thermal loading subproblem can be formulated by complex variable theory as [10]

$$\sigma_x + \sigma_y = 2(\gamma'(z) + \overline{\gamma'(z)})$$

$$\sigma_y - \sigma_x + 2i\tau_{xy} = 2(\bar{z}\gamma''(z) + \psi'(z)) \tag{34}$$

$$2\mu(u + iv) = \kappa\gamma(z) - z\overline{\gamma'(z)} - \overline{\psi(z)} + 2\mu\rho\chi^*(z)$$

where μ is shear modulus.

These equations show that the expressions for in-plane stresses are exactly the same to that of an isothermal problem and are given in terms of Kolsov-Muskhelishvili potential [11]. However, in the expression for in-plane displacements an extra term $(2\mu\rho\chi^*(z))$ appears. This suggests that this term can be used as an extra displacement boundary condition along with the original boundary conditions of the problem.

Thus, the original thermal loading problem can be solved by superposition of an isothemal state with original boundary conditions and a displacement field given by $u+iv=\chi^*(z)$. The solution methodology of this reduced isothermal problem is exactly similar to that of the mechanical loading problem as shown in the previous section. The compatibility equation (biharmonic equation) for an isothermal problem is same as given by Eq 13; however, due to the extra displacement boundary condition the stress function will be different. To solve the biharmonic equation an asymptotic analysis is performed.

$$F_{thermal}(\varepsilon\eta_1, \varepsilon\eta_2) = \sum_{m=0}^{\infty} \varepsilon^{\left(m+\frac{3}{2}\right)}(\phi_m)_{thermal} + \sum_{n=0}^{\infty} \varepsilon^{(n+2)}(\psi_n)_{thermal} \tag{35}$$

where the first part of the above series $(\phi_m)_{thermal}$ represents the singular series and the second part containing $(\psi_m)_{\text{thermal}}$ is to account for the finiteness of the domain. The above series on substitution into biharmonic leads to an infinite series involving differential equations associated with each power of ε similar to Eq 15.

Now the differential equation corresponding to different powers of (ε) (or corresponding to different values of m and n) can be given as follows:

$$m = n = 0, \quad \nabla^2(\nabla^2(\phi_m)_{thermal}) = 0, \quad \nabla^2(\nabla^2(\psi_m)_{thermal}) = 0 \tag{36}$$

$$m = n = 1, \quad \begin{aligned} &\nabla^2(\nabla^2(\phi_m)_{thermal}) - 2\alpha_1\frac{\partial}{\partial\eta_1}(\nabla^2(\phi_{m-1})_{thermal}) - 2\beta_1\frac{\partial}{\partial\eta_2}(\nabla^2(\phi_{m-1})_{thermal}) = 0, \\ &\nabla^2(\nabla^2(\psi_m)_{thermal}) - 2\alpha_1\frac{\partial}{\partial\eta_1}(\nabla^2(\psi_{m-1})_{thermal}) - 2\beta_1\frac{\partial}{\partial\eta_2}(\nabla^2(\psi_{m-1})_{thermal}) = 0 \end{aligned} \tag{37}$$

The solution to the governing equation corresponding to $m=n=0$ is the same as the solutions to the homogeneous problem. These solutions are already known and can be given as

$$(\phi_0)_{thermal} = \text{Re}\{\overline{\overline{L_0}}\} + \eta_2\,\text{Im}\{\overline{L_0}\} - \eta_2\,\text{Re}\{\overline{M_0}\} \tag{38}$$

$$(\psi_0)_{thermal} = \eta_2\,\text{Im}\{\overline{N_0}\} + \text{Im}\{\overline{\overline{T_0}}\} - \eta_2\,\text{Re}\{\overline{T_0}\} \tag{39}$$

$\overline{\overline{L_0}}$ and $\overline{\overline{M_0}}$, are the same as the first term in the series solution of thermal stress problem for homogeneous materials, and are defined as follows

$$\overline{\overline{L_0}} = \frac{8\,\text{Re}\{A\}}{3(2a)^{1/2}}\varsigma^{\frac{3}{2}}, \quad \overline{\overline{M_0}} = \frac{8\,\text{Im}\{A\}}{3(2a)^{1/2}}\varsigma^{\frac{3}{2}}, \quad \varsigma = \eta_1 + i\eta_2, \quad i = \sqrt{-1}, \quad A = -\frac{iE\alpha(\Delta T)a^2\sin\beta}{8k(1+\kappa)} \tag{40}$$

This solution satisfies the crack face boundary conditions as well as the extra boundary condition $\{u+iv=\chi^*(z)\}$ due to thermal loading. Now the solution for the higher values of m and n can be obtained recursively

The solution for $m=1$ is given as

$$(\phi_1)_{thermal} = \mathrm{Re}\{\overline{\overline{L_1}}\} + \eta_2 \,\mathrm{Im}\{\overline{L_1}\} - \frac{\alpha_1}{2}\eta_2^2 \,\mathrm{Re}\{\overline{M_0}\} + \frac{\beta_1}{2}\eta_2^2 \,\mathrm{Im}\{\overline{L_0}\} - \eta_2 \,\mathrm{Re}\{\overline{M_1}\} - \frac{\alpha_1}{2}\eta_2^2 \,\mathrm{Im}\{\overline{M_0}\} - \frac{\beta_1}{2}\eta_2^2 \,\mathrm{Re}\{\overline{M_0}\} \tag{41}$$

$\overline{\overline{L_1}}$ and $\overline{\overline{M_1}}$ are the same as the second term in the series solution for homogeneous materials.

Similarly for $n=1$, the solutions can be written as below.

$$(\psi_1)_{thermal} = \eta_2 \,\mathrm{Im}\{\overline{N_1}\} + \mathrm{Im}\{\overline{\overline{T_1}}\} - \eta_2 \,\mathrm{Re}\{\overline{T_1}\} \tag{42}$$

By substituting the Eqs 38 to 42 in Eq 35 and converting them into (x,y) coordinates, we can obtain a four-term expansion for stresses using Eq 9.

$$\begin{aligned}(\sigma_{xx})_{thermal} = \sum_{n=0}^{1} &[\mathrm{Re}\{Pt_n\} - y \,\mathrm{Im}\{Pt_t'\} + 2 \,\mathrm{Im}\{Rt_n\} + y \,\mathrm{Re}\{Rt_t'\} + 2 \,\mathrm{Re}\{Qt_n\} + \mathrm{Im}\{St_n\} + y \,\mathrm{Re}\{St_n'\}] \\ &+ \alpha_1\left[-\mathrm{Re}\{\overline{Pt_0}\} + 2y \,\mathrm{Im}\{Pt_0\} + \frac{y^2}{2}\mathrm{Re}\{Pt_0'\} - \mathrm{Im}\{\overline{Rt_0}\} - 2y \,\mathrm{Re}\{Rt_0\} + \frac{y^2}{2}\mathrm{Im}\{Rt_0'\}\right] \\ &+ \beta_1\left[\mathrm{Im}\{\overline{Pt_0}\} + 2y \,\mathrm{Re}\{Pt_0\} - \frac{y^2}{2}\mathrm{Im}\{Pt_0'\} - \mathrm{Re}\{\overline{Rt_0}\} + 2y \,\mathrm{Im}\{Rt_0\} + \frac{y^2}{2}\mathrm{Re}\{Rt_0'\}\right]\end{aligned} \tag{43}$$

$$\begin{aligned}(\sigma_{yy})_{thermal} = \sum_{n=0}^{1} &\left[\mathrm{Re}\{Pt_n\} + y \,\mathrm{Im}\{Pt_n'\} - y \,\mathrm{Re}\{Rt_{nn}'\} + \mathrm{Im}\{St_n\} - y \,\mathrm{Re}\{St_n'\}\right] + \alpha_1\left[\frac{-y^2}{2}\mathrm{Re}\{Pt_0'\} - \frac{y^2}{2}\mathrm{Im}\{Rt_0'\}\right] \\ &+ \beta_1\left[\frac{y^2}{2}\mathrm{Im}\{Pt_0'\} - \frac{y^2}{2}\mathrm{Re}\{Rt_0'\}\right]\end{aligned} \tag{44}$$

$$\begin{aligned}(\sigma_{xy})_{thermal} = \sum_{n=0}^{1} &-\left[y \,\mathrm{Re}\{Pt_n'\} + y \,\mathrm{Im}\{Rt_n'\} + \mathrm{Im}\{Qt_n\} + y \,\mathrm{Re}\{Qt_n'\} - \mathrm{Re}\{Rt_n\}\right] + \alpha_1\left[y \,\mathrm{Re}\{Pt_0\} - \frac{y^2}{2}\mathrm{Im}\{Rt_0'\}\right. \\ &\left. + y \,\mathrm{Im}\{Rt_0\} + \frac{y^2}{2}\mathrm{Re}\{Rt_0'\}\right] + \beta_1\left[-y \,\mathrm{Im}\{Pt_0\} - \frac{y^2}{2}\mathrm{Re}\{Pt_0'\} + y \,\mathrm{Re}\{Rt_0\} - \frac{y^2}{2}\mathrm{Im}\{Rt_0'\}\right]\end{aligned} \tag{45}$$

The complex functions used above (Pt_n, Qt_n, Rt_n, and St_n) in the (x,y) coordinates are counterparts of the functions L_n, M_n, N_n and T_n, respectively.

Discussions on Solutions

The asymptotic representation of crack-tip stress field is many times used to extract fracture parameters from experimental data. The fracture parameters such as stress intensity factor and nonsingular stress components are related to the coefficients of the asymptotic expansion of the crack-tip stress, strain, and displacement fields. These coefficients can be obtained by using experimentally obtained full field data such as the isochromatics, isopachics, Moiré fringes or CGS contours. To get an insight into the effects of nonhomogeneity and relative value of thermal and mechanical loading, contours of constant maximum shear stress (isochromatics) are generated for different values of the nonhomogeneity parameter using crack-tip stress fields developed in the previous sections. The contours are generated for an assumed value of the dynamic stress intensity factor (coefficient A_0), whereas the higher order coefficients A_1, A_2, B_1, and B_2 are assumed to be zero. However, the nonhomogeneity specific part of the higher order terms, which have A_0 and B_0 as the coefficients is retained. The higher order terms can be given specific values; however, this will not add to the discussion, which is to show the influence of the nonhomogeneity parameter on stress fields near the crack tip for fixed values of stress field coefficients. Following are some typical materials attributes used in plotting these contours: Thickness=0.5 in. (12.7 mm), Elastic modulus=200 GPa, Coefficient of thermal expansion=10.5e−6/°C, $\beta = 90^\circ$.

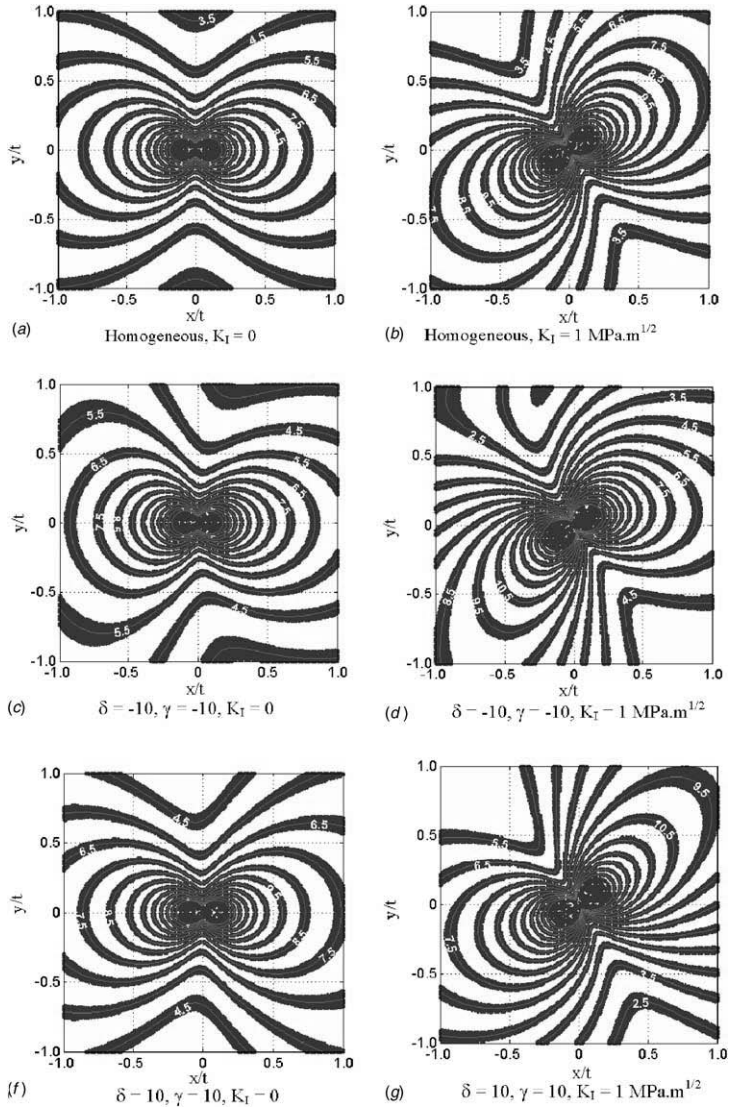


FIG. 2—*Contours of the constant maximum shear stress around the crack tip for a thermomechanically loaded FGM.*

Contours of Constant Maximum Shear Stress

Maximum shear stress, τ_{max}, at each point around the crack tip can be determined by substituting the stress field equation, obtained in the previous sections, in the relation:

$$\tau_{max} = \sqrt{\left(\frac{\sigma_{yy} - \sigma_{xx}}{2}\right)^2 + \sigma_{xy}^2} \tag{46}$$

In an experimental investigation, the constants A_0, A_1, B_0, B_1, C_0, C_1, D_0, and D_1 of the various terms

in the expansion of the stresses are determined by fitting Eq 46 to the experimental data. The Mode I and Mode II stress intensity factors, K_I and K_{II}, and the nonsingular stress, σ_{0x}, are related to the constants A_0, C_0, and B_0 as shown below:

$$A_0 = \frac{K_I}{\sqrt{2\pi}}, \quad C_0 = \frac{K_{II}}{\sqrt{2\pi}}, \quad \sigma_{0x} = -2B_0 \tag{47}$$

Figures 2(*a*)–2(*f*) shows the effect of nonhmogeneity and thermomechanical loading on the contours of constant maximum shear stress (MPa) (isochromatics). These contours are generated for $\Delta T = 1500\ ^\circ\mathrm{K/m}$ and two different cases of mechanical loading namely: $K_I = 0$ and 1.0 MPa-$\mathrm{m}^{1/2}$. The property gradation direction is assumed to be along the crack ($\varphi = 0$). The crack is assumed to be on the negative *x*-axis and the crack tip is located at (0,0). The figure shows that the nonhomogeneity does not alter the structure of the contours very close to the crack tip ($|x/t| < 0.25$) as compared to homogeneous material. However, slightly removed from the crack tip, the size and tilt of contours changes with the introduction of nonhomogeneity in material properties. Figure 2(*a*) shows the contours for homogeneous materials corresponding to only thermal loading ($K_I = 0$), these contours look similar to those obtained by pure shear mode mechanical loading. It can be observed from Fig. 2 that the size and number of the contours increases towards the stiffer side of the materials (positive *x* axis for $\delta > 0$ and negative *x* axis for $\delta < 0$). Figure 2(*b*) shows the contours for homogeneous materials corresponding to combined thermomechanical loading ($T = 1500\ ^\circ\mathrm{K}$ and $K_I = 1.0$ MPa-$\mathrm{m}^{1/2}$), these contours clearly represent the presence of mixed mode loading at the crack tip even though applied mechanical loading is pure tensile in nature. It can also be seen that number of fringes around the crack tip decreases for $\delta < 0$ and increases for $\delta > 0$.

Summary

Crack-tip stress fields for a thermomechanically loaded stationary crack inclined to the direction of property gradation were obtained through an asymptotic analysis coupled with Westergaard's stress function approach. The first four terms in the expansion of the stress field are derived to explicitly bring out the influence of nonhomogeneity on the structure of the stress field. It is observed that the presence of heat flow produced no additional singularity and hence the classical inverse square root singularity still prevails around the crack tip. These stress fields are useful in extracting fracture parameters during the analysis of full field data around crack tips in experimental techniques such as photoelasticity and CGS. Using these stress fields, synthetic contours of constant maximum shear stress were developed. It was found that the contours very close to the crack tip were found to be identical to the homogeneous materials. However, as one moves away from crack tip, contours start deviating from the homogeneous materials showing the affect of nonhomogeneity.

Acknowledgments

The support of Air Force Office of Scientific Research under grant # FA9550-06-1-0162 and National Science Foundation under grant # CMS 0244330 are gratefully acknowledged.

References

[1] Jin, Z. H. and Noda, N., "Crack-tip Singular Fields in Inhomogeneous Materials," *J. Appl. Mech.*, vol. 61, 1994, pp. 738–739.

[2] Erdogan, F., "Fracture Mechanics of Functionally Graded Materials," *Composites Eng.*, vol. 5, No. 7, 1995, pp. 753–770.

[3] Jin, Z. H. and Batra, R. C., "Some Fracture Mechanics Concepts in Functionally Graded Materials," *J. Mech. Phys. Solids*, vol. 44, No. 8, 1996, pp. 1221–235.

[4] Gu, P. and Asaro, R. J., "Cracks in Functionally Graded Materials," *Int. J. Solids Struct.*, vol. 34, No. 1, 1997, pp. 1–17.

[5] Parameswaran, V. and Shukla, A., "Asymptotic Stress Fields for Stationary Cracks Along the Gradient in Functionally Graded Materials," *Transactions of ASME*, vol. 69, 2002, pp. 240–243.

[6] Jain, N., Rousseau, C. E., and Shukla, A., "Crack-Tip Stress Fields in Materials with Linearly Varying Properties," *Theor. Appl. Fract. Mech.*, vol. 42, No. 2, 2004, pp. 155–170.
[7] Walters, M. C., Paulino, G. H., and Dodds, R. H., "Stress-Intensity Factors for Surface Cracks in Functionally Graded Materials Under Mode-I Thermomechanical Loading," *Int. J. Solids Struct.*, vol. 41, 2004, pp. 1081–1118.
[8] Westergaard, H. M., "Bearing Pressures and Cracks," *J. Appl. Mech.*, vol. 6, 1939, pp. A49–A53.
[9] Sanford, R. J., "A Critical Re-examination of the Westergaard Method for Solving Opening Mode Problem," *Mech. Res. Comm.*, vol. 6, No. 5, 1979, pp. 289–294.
[10] Bogdanoff, J. L., "Note on Thermal Stress," *J. Appl. Mech.*, vol. 77, 1954, p. 88.
[11] Muskhelishvili, N. I., *Some Basic Problems of the Mathematical Theory of Elasticity*, Kluwer Academic Publishers, 1977.

Journal of ASTM International, April 2006, Vol. 3, No. 4
Paper ID JAI13221
Available online at www.astm.org

C. M. Davies,[1] M. Kourmpetis,[1] N. P. O'Dowd,[1] and K. M. Nikbin[1]

Experimental Evaluation of the *J* or *C** Parameter for a Range of Cracked Geometries

ABSTRACT: In the current ASTM Standard Test Method for Measurement of Creep Crack Growth Rates in Metals (E 1457) the experimental C^* parameter is related to the load and creep load line displacement rate through the geometry related η factor. In this work η factors for a range of geometries are presented. The geometries examined are the compact tension specimen, C(T), single edge notch specimen in tension, SEN(T), and bending, SEN(B), double edge notch specimen in tension, DEN(T), middle crack specimen in tension, M(T) and the C-shaped specimen in tension CS(T). Calculations have been performed for a linear elastic-power law hardening material but the resulting η factors are applicable to either power law plastic or power law creeping materials. Values for η^{LLD} and η^{CMOD}, based on the load line displacement and crack mouth opening displacement, respectively, have been determined. A wide range of crack depths, $0.1 \leqslant a/W \leqslant 0.7$, where a is crack length and W is specimen width, and hardening exponents, $3 \leqslant N \leqslant 10$, under plane stress and plane strain conditions have been examined using the finite element method. The influence of specimen length, crack length, material properties and out of plane stress state on the η factor has also been considered. It has been found that for shallow cracks the value of η depends quite strongly on the exponent, N in the material power law, regardless of whether η is defined based on the load line displacement or crack mouth opening displacement. The η^{LLD} factor has also been found to be strongly sensitive to plane stress/strain conditions imposed, a/W and specimen length, whereas η^{CMOD} depends more weakly on a/W and is almost independent of specimen length for the cases examined. There is, however, no clear trend in these variations over the range of specimen geometries and a/W examined. These results are found to be consistent with those in the literature. Recommendations are made regarding the most appropriate values for η, depending on the specimen type and geometry while taking into account the variability due to the material properties, out of plane stress state and variations between the numerical analyses.

KEYWORDS: eta factor, creep crack growth, finite element, specimen geometry, C^*, J, load line displacement, crack mouth opening displacement

Nomenclature

a = Crack length or crack half length
b = Uncracked ligament size ($=W-a$)
n = Power-law creep stress exponent
x = Ratio of crack length to specimen width, a/W
A = Appropriate area on a load displacement record
A_c = Area of the cracked surface
B, B_n = Specimen thickness and (net) thickness between side grooves
C = Coefficient in the power-law creep strain rate relation
C_e = Elastic compliance function
C^* = Steady-state creep fracture mechanics parameter
E = Elastic (Young's) modulus
E' = Effective elastic modulus, $E/(1-\nu^2)$ for plane strain and E for plane stress
H^{CMOD} = Geometric function to calculate C^* from crack mouth opening displacement rate
H^{LLD} = Geometric function to calculate C^* from load line displacement rate
J = Elastic-plastic fracture mechanics parameter

Manuscript received April 28, 2005; accepted for publication January 30, 2006; published online March 2006. Presented at ASTM Symposium on Fatigue and Fracture Mechanics: 35th, on 18–20 May 2005 in Reno, NV; R. E. Link and K. M. Nikbin, Guest Editors.
[1] Department of Mechanical Engineering, Imperial College London, South Kensington Campus, London, SW7 2AZ, UK.
Copyright © 2006 by ASTM International, 100 Barr Harbor Drive, PO Box C700, West Conshohocken, PA 19428-2959.

J_e, J_p = Elastic and plastic components of J
K = Linear elastic stress intensity factor
L = Gage length over which load line displacement, Δ^{LLD}, is measured
N = Power-law plasticity hardening exponent
P = Applied load
R_i = Inner radius of CS(T) specimen
R_o = Outer radius of CS(T) specimen
W = Specimen width or half width
X = Load hole offset in CS(T) specimen
$Y(a/W)$ = Linear elastic shape factor
α = Constant in Ramberg-Osgood law
ε = Strain
ε_0 = Normalizing strain in the Ramberg-Osgood law
$\dot{\varepsilon}^c$ = Creep strain rate
η^{CMOD} = Geometric factor to calculate C^* from crack mouth opening displacement rate
η^{LLD} = Geometric factor to calculate C^* from load line displacement rate
ν = Poisson's ratio
σ_0 = Normalizing stress in the Ramberg-Osgood law
σ = Stress
Δ_e, Δ_p = Elastic and plastic components of displacement
$\dot{\Delta}_c$ = Creep displacement rate
$\Delta^{LLD}, \dot{\Delta}^{LLD}$ = Load line displacement, load line displacement rate
$\Delta^{CMOD}, \dot{\Delta}^{CMOD}$ = Crack mouth opening displacement, crack mouth opening displacement rate

Introduction

Creep crack growth (CCG) is often characterized by the C^* parameter [1], which is analogous to J for rate independent nonlinear materials [2]. In a CCG test the value of C^* is estimated experimentally from load-load line displacement rate (LLD) records. C^* can also be estimated from experimental load-crack mouth opening displacement rate (CMOD) records, which, under certain conditions, has been found to provide a more robust measurement than LLD [3]. The ASTM Standard Test Method for measurement of Creep Crack Growth Rates in Metals (E 1457) [4] proposes the Compact Tension, C(T), specimen geometry. While the use of the C(T) specimen for testing and analysis is expected to provide a safe, upper bound to the CCG rate of the material, a wider range of test geometries is needed in order to apply the results from experimental laboratory test specimens to the range of conditions experienced by engineering components under service conditions. This trend towards CCG testing using nonstandard specimens has drawn attention to the need for accurate determination of C^* in order to analyze the data [1].

In order to determine the value of C^* from the displacement rate, a dimensionless parameter, η, which depends on specimen geometry but is independent of load magnitude (see, e.g., [5]), is required. In this study the geometric η factors, used to derive experimental C^* values, have been evaluated for a number of geometries: the compact tension, C(T), C-shaped tension, CS(T), double edge notched tension, DEN(T), single edge notch bend, SEN(B), single edge notched tension, SEN(T), and middle cracked tension, M(T) (sometimes referred to as center crack tension, CC(T)). These geometries are shown schematically in Fig. 1. For the SEN(B) specimen, loading is under three point bending. Values of the η factor have been obtained from the literature and additional values have been generated using finite element analysis.

A brief review of the analysis methods for the derivation of η factors is first presented. The application to a nonlinear power law plastic material is provided and the generalization to a power law creeping material is then considered. The effect of material properties, specimen geometry and out-of-plane stress state (plane stress or plane strain) on the value of η is examined. On the basis of the analyses presented, recommendations for mean and upper/lower bound values of η factors are made for each geometry examined. This will allow a user to determine values of C^* for a wide range of cracked geometries.

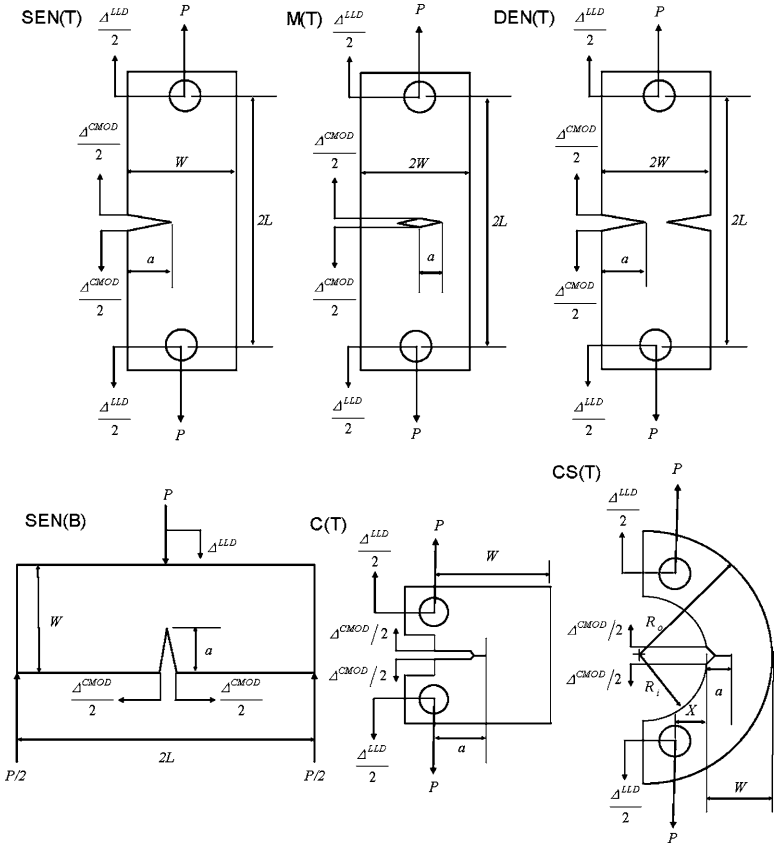


FIG. 1—*Specimen geometry definition.*

Material Behavior

In this work, the elastic-plastic behavior is assumed to be represented by a Ramberg-Osgood type material law. The uniaxial stress-strain response is represented as

$$\varepsilon = \frac{\sigma}{E} + \alpha \frac{\sigma_0}{E}\left(\frac{\sigma}{\sigma_0}\right)^N \tag{1}$$

where E is the Young's modulus, σ_0 denotes a normalizing stress, often taken to be the yield strength, N is the hardening exponent and α is the yield offset.

For a power law creeping material, the creep strain rate, $\dot{\varepsilon}^c$, may be described by

$$\dot{\varepsilon}^c = C\sigma^n \tag{2}$$

where the creep stress exponent, n, and the constant C, are temperature dependent material properties.

Estimation of *J* and *C** from Load-Displacement History

The nonlinear elastic crack tip parameter, J, may be evaluated from a line integral along a contour surrounding a crack tip [2]. Alternatively the value of J may be obtained from the potential energy release rate of a cracked body,

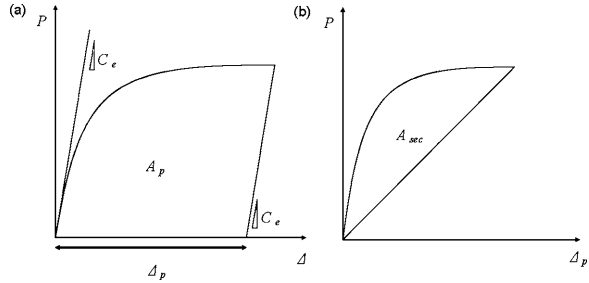


FIG. 2—*Definition of the (a) plastic displacement Δ_p and plastic area A_p, under the load-displacement curve, and (b) plastic secant area A_{sec}, under the load-plastic displacement curve.*

$$J = -\frac{\partial U}{\partial A_c} \tag{3}$$

where U is the potential energy stored in the system, and A_c is the crack area. For geometries with a single crack tip, e.g., SEN(T), C(T), CS(T), the crack area, $A_c = B \times a$, whereas for geometries with two crack tips, e.g., M(T), DEN(T), $A_c = B \times 2a$, where B is the crack front length (specimen thickness for a through-thickness crack) and a is the crack length or half crack length (see Fig. 1). The potential energy, U, may be related to the load, P, and the displacement along the load line, Δ^{LLD}.

For a nonlinear material, in order to obtain the value of J directly from a load-displacement history, it is convenient to split J into elastic and plastic parts [6],

$$J = J_e + J_p \tag{4}$$

The elastic component of J, J_e, is related to the linear elastic stress intensity factor, K, and the effective elastic modulus of the material, E', (E in plane stress and $E/(1-\nu^2)$ in plane strain) by the well known relation,

$$J_e = \frac{K^2}{E'} \tag{5}$$

The plastic component of J, J_p may be estimated using the equation,

$$J_p = \frac{A}{B(W-a)}\eta \tag{6}$$

where the η factor relates J_p to an appropriate area, A, on the load displacement record generated during a fracture toughness test. The dimensionless factor, η, for a given geometry, is generally considered to be a function of crack dimension, a/W only, where W is the specimen width or half width. However, η may also depend on material hardening exponent, N, normalized length, L/W, and specimen thickness B.

The displacement, Δ, used to determine the area, A, in Eq. 6 may be separated into linear elastic, Δ_e, and plastic, Δ_p, components,

$$\Delta = \Delta_e + \Delta_p \tag{7}$$

The linear elastic component of the displacement of a cracked geometry is directly related to the applied load, P, through the linear elastic compliance function, C_e, which is a function of crack length, a,

$$\Delta_e = C_e(a)P \tag{8}$$

The plastic component of dispacement, Δ_p, may then be determined as shown graphically in Fig. 2(*a*).

In order to obtain values of η that are consistent with those used historically, i.e., $\eta = 1$ for a tension specimen and $\eta = 2$ for a bend specimen [5], η in Eq. 6 is related to an appropriately chosen area of the load-displacement curve for each specimen. Two areas are used, the plastic area, A_p, and plastic secant area, A_{sec}, shown in Figs. 2(*a*) and 2(*b*), respectively. These areas may be expressed as

TABLE 1—*Definitions of H, H′ and A for each specimen.*

Specimen Type	H^{LLD}	H^{CMOD}	Associated Area, A	H'^{LLD}	H'^{CMOD}
C(T)	$N/(N+1)$	$N/(N+1)$	A_p	1	1
SEN(T)	$N/(N+1)$	$N/(N+1)$	A_p	1	1
DEN(T)	$1/2(N-1)(N+1)$	$1/2(N-1)/(N+1)$	A_{sec}	1	1
M(T)	$1/2(N-1)/(N+1)$	$1/2(N-1)/(N+1)$	A_{sec}	1	1
SEN(B)	$N/(N+1)$	$(2L/W)N/(N+1)$	A_p	1	$2L/W$
CS(T)	$N/(N+1)$	$N/(N+1)$	A_p	1	1

$$A_p = \int_0^{\Delta_p} P d\Delta_p \tag{9}$$

$$A_{\text{sec}} = \int_0^{\Delta_p} P d\Delta_p - \frac{1}{2} P\Delta_p \tag{10}$$

and may be obtained from the load-displacement record produced during a test. For a power-law hardening material these areas can be calculated from

$$A_p = \frac{N}{N+1} P\Delta_p \tag{11}$$

$$A_{sec} = \frac{1}{2}\frac{N-1}{N+1} P\Delta_p \tag{12}$$

Equations 11 and 12 are only appropriate for materials where the plastic component of displacement, Δ_p, can be represented by a power law as in the Ramberg-Osgood material law, Eq. 1. Replacing the area A in Eq 6 with Eq 11 or 12, the solution for J_p, Eq 6, can be rewritten as

$$J_p = \frac{P\Delta_p}{B(W-a)} H\eta \tag{13}$$

The parameter, H, is included in Eq 13, to simplify the definition of η for a range of geometries, and in general, H will depend on N and specimen geometry. During testing, the displacement of the specimen is often measured along the load line, Δ^{LLD}, which is generally taken at the point of load application. Alternatively the specimens crack mouth opening displacement, Δ^{CMOD}, may be measured. These quantities are defined for the geometries of interest in Fig. 1. As will be discussed later, the value of H and η will depend on whether J is calculated using load line or crack mouth opening displacement. While Δ^{CMOD} is defined unambiguously, if J is to be evaluated using Δ^{LLD}, the value of H and η may depend on the point at which Δ^{LLD} is measured. Note that the length $2L$ in Fig. 1 for the M(T), DEN(T), and SEN(T) specimen is strictly speaking not the specimen length but the gage length over which Δ^{LLD} is measured. For SEN(B) under three point loading, $2L$ is the spacing between the support points.

The function H is defined through Eqs. 6 and 11–13. For the SEN(B) specimen an additional normalizing factor is included in H to account for the dependency of Δ^{CMOD} on L/W. The values of H^{LLD} and H^{CMOD} for each specimen examined are provided in Table 1 along with the appropriate area to use in Eq 6. The superscripts LLD and CMOD are used with H to indicate that they are associated with the load line and crack mouth opening displacement, respectively. The values of H in Table 1 are appropriate for a power law hardening material. More generally the plastic component of J, J_p, in Eq 13 may be determined from

$$J_p = \frac{A}{B(W-a)} H'\eta \tag{14}$$

where A represents the associated area used in the calculation of η and H' is an additional normalizing parameter. The value of H' for each geometry examined is also included in Table 1.

The steady-state creep crack tip characterizing parameter, C^*, defined under widespread (steady-state) creep conditions, is analogous to J_p for a nonlinear elastic material. Hence for a power law creeping material (Eq 2) C^* may be determined from the load displacement rate record during a creep crack growth test using the relations,

$$C^* = \frac{P\dot{\Delta}_c}{B(W-a)}H\eta \tag{15}$$

In Eq 15 the value of H and η for a power law creeping material, with creep exponent n, is the same as that for a power law plastic material with exponent, $N=n$.

Review of η Factors in the Literature

A review has been performed of η factors available in the literature. Summaries are provided in Tables 2–4 for studies based on numerical and analytical methods, respectively. Some variations in the values of η from each source have been found, which may be due to differences in the numerical code used (all analyses reviewed have used the finite element method), the mesh design (e.g., mesh size and/or element type), the application of boundary conditions (e.g., point loads/distributed load, the method of modeling the loading pin, displacement or load controlled analysis, etc.) and in the precise method used to calculate η. Also, the displacement measuring positions and the material properties used vary among the analyses.

Numerical Analysis

In this work numerical methods have been employed to estimate η factors for different crack geometries, using the commercial finite element (FE) package, ABAQUS [7]. The specimen geometries analyzed are a standard compact tension, C(T), middle tension, M(T), C-shaped tension, CS(T), double edge notched tension, DEN(T) and the single edge notch bend specimen under three point bend loading, SEN(B). The Ramgerg-Osgood material model (Eq 1) has been employed throughout. The J-integral value is obtained using a domain integral within the FE software [7] and the total displacements at the relevant positions on the specimen, Δ, are extracted. In an elastic-plastic analyses, the elastic components, J_e and Δ_e, are then subtracted from the total values to obtain J_p and Δ_p, respectively, for use in Eq 13. Linear-elastic analyses were performed for each case in order to obtain the elastic compliance value $C_e(a)$ and the linear elastic stress intensity factor, K, for each crack length considered, enabling J_e and Δ_e to be determined in the elastic-plastic analyses. The values obtained are found to be in good agreement with those available in the literature [4,8,9]. The value of η has then been calculated according to the relation

$$\eta = \frac{B(W-a)J_p}{HP\Delta_p} \tag{16}$$

Two-dimensional, plane stress, and plane strain analyses have been performed. Each specimen has been modeled with a focused mesh and multiple nodes at the crack tip to capture the crack tip singularity. Small geometry change conditions are used. Symmetry conditions are fully employed. For all specimens except the CS(T), four noded plane strain and plane stress continuum elements (type CPE4H and CPS4) are used. For the CS(T) specimen eight-noded elements have been used. A typical mesh consists of over 2000 elements and nodes and the J integral and K values have been averaged over 41 contours.

Three values of $N=3$, 5, and 10 are examined in order to determine the sensitivity of η to N (or n). The value of η obtained from Eq 16 initially shows some dependence on load but reaches a constant value once the plastic strains are sufficiently high that power law material behavior prevails throughout the specimen. This constant value is taken as the η value for the specimen. It is assumed that N is the only material property that effects η as it is evaluated where plasticity dominates and $J_p \gg J_e$.

Results

The results of the FE analysis are presented in this section. The η factor values determined in this work are compared with the values found in the literature under various conditions. For the SEN(T), M(T), DEN(T),

TABLE 2—*Summary of numerical studies in literature.*

Author	Specimen Type	N	Material Properties	LLD / CMOD	a/W	Dimensions	$P\sigma/P\varepsilon$[a] or 3-D
Kim et al. [3]	DEN(T)				0.25		
		5					$P\sigma$
			E/σ_0=667,	LLD	0.5	B/W=0.5,	
		10					$P\varepsilon$
			1000, 500	CMOD	0.75	1, 5, 10	
		∞					3-D
					0.9		
Kim et al. [10]	M(T)	5			0.1		$P\sigma$
	SEN(B)-3PB		E/σ_0=500	LLD		B/W=0.5,	
	SEN(T)	10			0.3		$P\varepsilon$
	C(T)		α=1	CMOD		0.25, 0.125	
					0.5		3-D
Panontin et al. [16]	C(T)				0.4		
		5	E/ε_0=800		0.45		
		10	E/ε_0=500	CMOD	0.5	…	$P\varepsilon$
		20	E/ε_0=250		0.6		
					0.7		
Nevalainen and Dodds [19].	SEN(B)-3PB	5	E/ε_0=500	SEN(B):LLD	SEN(B):	L/W=2	
	C(T)	10	ν=0.3	CMOD	0.1,0.5	B/W=1,	3-D
		20	α=1	C(T):LLD	C(T):0.6	0.5, 0.25	$P\varepsilon$
O'Dowd et al. [20]	SEN(T)	4	Bimaterial	LLD	0.25	L/W=2.5	$P\varepsilon$
O'Dowd et al. [21]	CC(T)	4	E/σ_0=500		0.1		
							$P\sigma$
		10	α=1	LLD	0.25	L/W=2	
		20					P_ε
			ν=0.3		0.5		
Kirk and Dodds [22,23]	SEN(B)-3PB	4		LLD	0.05	L/W=2	$P\varepsilon$
		5	yield offset	CMOD	0.15		
		10	$\varepsilon_0=\sigma_0/E$		0.25		
		50	α=1		0.5		
					0.7		
Joyce et al. [24]	SEN(T)		High strength				
	DEN(T)		structural				
	SEN(B)-3PB		steel		SEN(T):		
			σ_y=747		0.12–0.8		$P\varepsilon$
		…		LLD		…	
			UTS=877		DEN(T)		
			MPa		0.72,0.84,0.9		
			E/σ_0=388				
			ν=0.3				
Lei et al. [25]	SEN(B)-3PB		E/ε_0=500				
		3					
			α=1	LLD			
		10			0.1–0.7	L/W=2,3	$P\varepsilon$
			ν=0.3	CMOD			
		20					
Kim et al. [26]	CS(T)		Steel 304L			R_o=18.29	3-D
		…		LLD	0.54		
			21-6-9			R_i=9.14	$P\varepsilon$
Wang and Gordon [27,28]	SEN(B)-3PB	…	…	…	0.1–0.5	…	…
Griffiths [29]	SEN(T)					L/W=2.5,	
		4	Bimaterial	LLD	0.25		$P\varepsilon$
						5, 7.5	

[a] $P\sigma \equiv$ Plane stress, $P\varepsilon \equiv$ Plane strain.

and SEN(B) a summary highlighting the effects of normalized length, L/W on the η factor are also presented.

TABLE 3—*Summary of* η *and J estimation studies in literature.*

Author	Specimen Type	LLD / CMOD	a/W	Dimensions	$P\sigma/P\varepsilon$[a] or 3-D	Comments
Merkle and Corten [14]	C(T)	LLD	…	…	…	Limit Load Analysis.
Clarke and Landes [13]	C(T)	LLD	0.45–0.62	…	…	Provides a linear fit to the analysis in Ref. [14].
Junnan [18]	CS(T)	LLD	…	X/W=0.5	…	Load-Separation Analysis.
Kim and Schwalbe [28]	M(T) C(T) SEN(B)-3PB	LLD CMOD	M(T), SE(B): 0.1–0.7 C(T):0.45–0.7	…	M(T): $P\sigma P\varepsilon$ C(T) & SE(B): $P\varepsilon$	Reviews accuracyof J estimation from various η solutions.
Kim and Budden [30]	SEN(T)	LLD CMOD	0.1–0.8	…	$P\sigma$ $P\varepsilon$	Limit load solutions, comparisons with FE analysis of Ref. [20].
Sumpter [31]	SEN(B)-3PB	CMOD	0.1 – 0.5	…	…	Fit made to limited range of data.
Wu et al. [32]	3PB CC(T) SEN(T) DEN(T)	LLD	0.125 – 0.875	L/W=2	…	Slip Line Field & EPRI Solutions.

[a]$P\sigma\equiv$ Plane stress, $P\varepsilon\equiv$ Plane strain.

Single Edge Notched Tension Specimen, SEN(T)

The effect of normalized length, L/W, on η^{LLD} and η^{CMOD} for the SEN(T) specimen are shown in Fig. 3 for the two extremes of crack length examined (a/W=0.1 and 0.7). Note that this specimen is modeled with uniform remote stress and thus bending is allowed in the specimen, which can be significant for deep cracks. Figure 3(*a*) provides the results for a shallow crack, a/W=0.1 and Fig. 3(*b*) the results for a deeply cracked specimen, a/W=0.7. The results shown are for hardening exponent N=10 under plane stress and plane strain conditions. The trends given for N=3 are similar and thus not shown here. It may be seen that η^{LLD} is strongly sensitive to L/W for the shallow crack, a/W=0.1, but for the deep crack, a/W=0.7, is insensitive to L/W. This sensitivity for a shallow crack is related to the significant amount of remote plasticity which increases with increasing specimen length. It may be seen in Fig. 3 that the value of η^{CMOD} is insensitive to specimen length for both shallow and deep cracks. Similar trends are seen under plane stress and plane strain conditions (the plane strain and plane strain results for η^{CMOD} are almost coincident in Fig. 3(*b*) and η is insensitive to the plane stress/strain assumption.

Figure 4 illustrates the influence of the hardening exponent, N, on η^{LLD} and η^{CMOD} for the SEN(T) specimen over a range of crack lengths. For deep cracks, $a/W \geqslant 0.6$, N has a weak effect on η^{LLD} (Fig. 4(*a*)) and η^{CMOD} is almost independent of N over the range of a/W (Fig. 4(*b*)). The same trend is seen under plane stress conditions, since, as shown in Fig. 3, there is little variation in the values of η^{LLD} and η^{CMOD} from a plane stress or plane strain analysis.

Figure 5 shows the full set of results for η^{LLD} and η^{CMOD} from the current analysis (indicated by circles) and data taken from Ref. [10] for the SEN(T) specimen. The values shown cover the range of conditions examined (i.e., plane stress/plane strain, $0.1 \leqslant a/W \leqslant 0.7$; $3 \leqslant N \leqslant 10$; $2 \leqslant L/W \leqslant 10$). It may be seen in Fig. 5(*a*) that there is some irregularity in the values of η^{LLD}at a/W=0.6. This is consistent with the trend shown by existing solutions (see, e.g., [11]).

In Fig. 5(*a*) and 5(*b*) piecewise linear fits are made to the combined data sets. The line labeled "mean fit" is an approximate fit to the mean value of the dataset at each value of a/W, and the upper bound and lower bound line have been estimated to cover between one and two standard deviations of the dataset within the region of the linear fit. These simple fits and associated bounds quantify the variation in η under

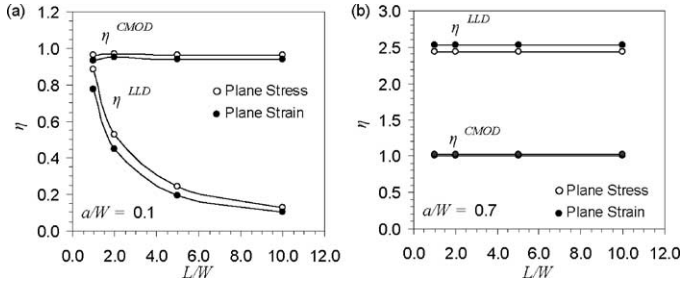


FIG. 3—*Specimen length effects on* η^{LLD} *and* η^{CMOD} *under plane stress and plane strain conditions for (a) shallow and (b) deeply cracked SEN(T) specimens,* $N=10$.

various conditions; no attempt has been made to describe the individual dependence on material or geometric parameters (apart from a/W). The equations for the mean fit and the measure of uncertainty are given in Appendix A.

As seen in Fig. 5(a) the value of η^{LLD} is strongly sensitive to crack length for shallow cracks ($a/W<0.5$) and approaches 2.5 for $a/W>0.6$. This high value of η^{LLD} for deep cracks is an indication of the level of bending in the specimen (for a tension specimen η^{LLD} is generally taken to be 1). The variability in η^{LLD} (indicated by the upper/lower bound lines in Fig. 5(a)) can be over 80 % of the mean value for shallow cracks ($a/W=0.1$). This variability is mostly indicative of the strong sensitivity to specimen length, L/W, as indicated in Fig. 3(a).

It is seen in Fig. 5(b) that η^{CMOD} is almost independent of crack length over the range considered. The variability is approximately 5 % of the mean value for the cases examined. The recommended solutions for η^{LLD} and η^{CMOD} are provided in Appendix A. The bilinear fit provided for η^{LLD} in Appendix A has been restricted to the range $1\leqslant L/W\leqslant 3$, since the majority of the data presented are for $L/W=2$. As the value of η^{CMOD} has a weak dependence on problem parameters for the SEN(T) specimen, it is recommended that, where practicable, J or C^* be estimated using Δ^{CMOD} rather than Δ^{LLD}.

Middle Cracked Tension Specimen, M(T)

Following the findings for the SEN(T) specimens the effect of normalized length, L/W, has only been examined under plane strain conditions and $N=10$ for the M(T) specimen. Figure 6 shows that the dependence on L/W is similar to that seen for the SEN(T) specimen, with η^{LLD} for the shallow crack, $a/W=0.1$, being strongly sensitive to specimen length, while η^{CMOD} is unaffected by the specimen length. Note that for $a/W=0.7$ (Fig. 6(b)) η^{LLD} and η^{CMOD} are independent of specimen length and their values almost coincide. This indicates that for deep cracks the majority of the deformation is occurring in the vicinity of the crack and Δ^{LLD} and Δ^{CMOD} are almost the same.

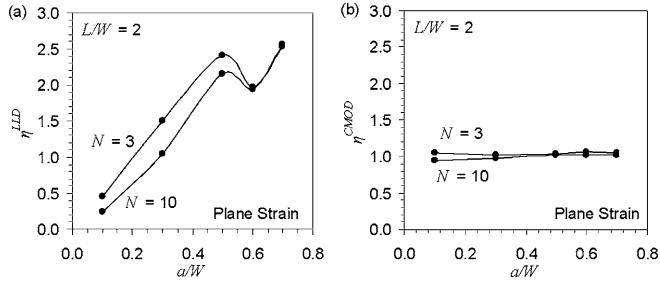


FIG. 4—*Example of the influence of N on (a)* η^{LLD} *and (b)* η^{CMOD}*, under plane strain conditions, over a range of crack lengths for a SEN(T) specimen.*

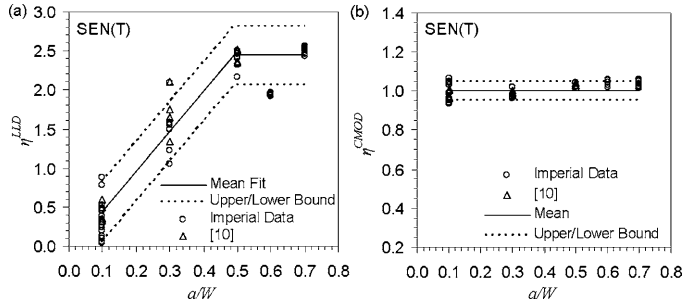


FIG. 5—*Variation in (a)* η^{LLD} *and (b)* η^{CMOD} *with crack length for SEN(T) specimen data from various sources.*

In Fig. 7 the sensitivity to N and to plane stress or plane strain conditions is examined. It is seen, that as for the SEN(T) specimen the influence of out of plane constraint is insignificant compared to the influence of N. For deep cracks, $a/W \geq 0.5$, η^{LLD} and η^{CMOD} are relatively insensitive to N.

The full set of results, including those taken from the literature, is shown in Fig. 8. Good agreement is found between the values of η^{LLD} and η^{CMOD} obtained here with those in the literature. As for the SEN(T) specimen η^{LLD} shows a strong dependence on crack length, a/W, and for shallow cracks has a high variability, indicated by the upper and lower bounds in Fig. 8(*a*) (this variability is mainly due to dependence on length, L/W, and N). It may be noted that for deep cracks, $a/W > 0.4$, η^{LLD} is close to unity.

A bilinear fit is made for η^{LLD}, while a single linear fit adequately describes the dependence of η^{CMOD} on a/W. The same specimen length restrictions are imposed as for the SEN(T) specimen. In Fig. 8(*b*) it is seen that some of the data for $a/W = 0.1$ and 0.3 lie above the upper bound line. These data correspond to results for $N = 3$ (see also Fig. 7(*b*)) and thus the additional restriction, that $N > 3$, is imposed on this specimen calibration. It may be seen in Fig. 7 that variability in η^{CMOD} is somewhat less than that for η^{LLD} particularly for shallow cracks. It is therefore recommended that, where practicable, J or C^* be estimated using Δ^{CMOD} rather than Δ^{LLD}.

Double Edge Notched Tension Specimen, DEN(T)

Figures 9 and 10 illustrate the sensitivity to specimen length, out of plane constraint and strain hardening for the DEN(T) specimen. The trends are similar to those for the M(T) specimen, though the dependence on strain hardening, N, is somewhat greater for deep cracks and out-of-plane constraint effects on the value of η are also greater.

A bilinear fit is made to both η^{LLD} and η^{CMOD} in Fig. 11. The uncertainty bands are considered constant over the range of crack lengths considered. The variability in η^{CMOD} is on the order of 20 % of

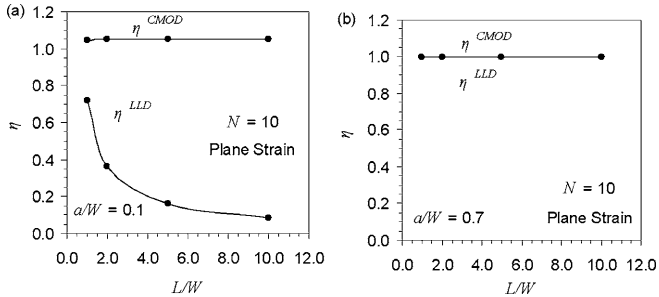


FIG. 6—*Specimen length effects on* η^{LLD} *and* η^{CMOD} *under plane strain conditions for (a) shallow and (b) deeply cracked M(T) specimens.*

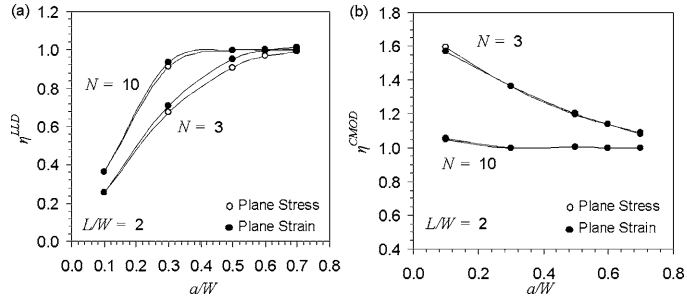


FIG. 7—*Example of the influence of N on (a) η^{LLD} and (b) η^{CMOD}, under plane stress and plane strain conditions, over a range of crack lengths for a M(T) specimen.*

the mean fit over the range of crack lengths. For η^{LLD} the variability is between approximately 75 % for shallow cracks to approximately 25 % for deep cracks. Since, both η^{LLD} and η^{CMOD} have a relatively large variability and strong dependence on a/W, care should be used when determining J or C^* from this geometry. For shallow cracks it is recommended that J or C^* be evaluated using Δ^{CMOD}.

Single Edge Notched Bend Specimen, SEN(B)

The specimen has been analyzed under three point bending. Results under plane strain conditions are shown in Fig. 12 for three specimen lengths, L/W. There is some influence of L/W on η^{LLD}, though this effect is weaker than that seen for the tension specimens (DEN(T), SEN(T), and M(T)). Through the use of the additional normalizing factor included in H^{CMOD}, length effects on η^{CMOD} have been eliminated for the cases examined, indicated by the constant value of η^{CMOD} in Fig. 12(*b*).

The out of plane stress state and N effects on η^{LLD} and η^{CMOD} are presented for $L/W=4$, in Fig. 13. The main source of variation in η^{LLD} is due to the hardening exponent, N, particularly for shallow cracks, $a/W<0.5$, for η^{LLD} and $a/W<0.3$ for η^{CMOD}. For deeper cracks ($a/W>0.5$), η^{LLD} is essentially independent of out-of-plane stress state and strain hardening and is close to 2, as expected for a deeply cracked bend geometry. For $a/W<0.3$, η^{CMOD} for the SEN(B) specimen is independent of out of plane stress state and strain hardening and has a near linear variation with a/W.

In Fig. 14(*a*) the available data for η^{LLD} are shown. The data fall into two regions: for $a/W<0.4$ there is significant variability, due primarily to dependence on strain hardening, and η^{LLD} depends strongly on a/W; for $a/W>0.3$ the variability is lower and η^{LLD} is more weakly dependent on a/W. On average, the values of η^{LLD} deviate from the mean by about 35 % for $0.1\leqslant a/W\leqslant 0.3$, but variability is less than 4 % for $a/W>0.3$. The value of η^{CMOD} decreases linearly with crack length over the whole range of a/W considered. The relatively small variations at a given a/W are mainly due to the dependence on N. Over

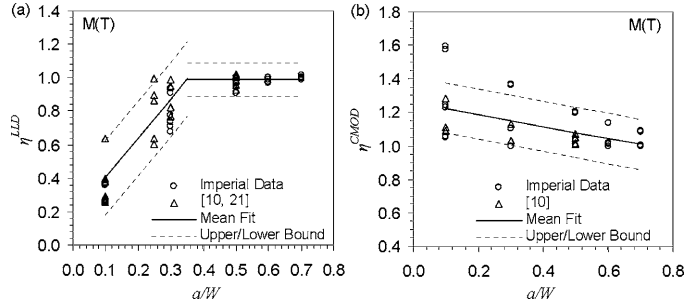


FIG. 8—*Variation in (a) η^{LLD} and (b) η^{CMOD} with crack length for M(T) specimen data from various sources.*

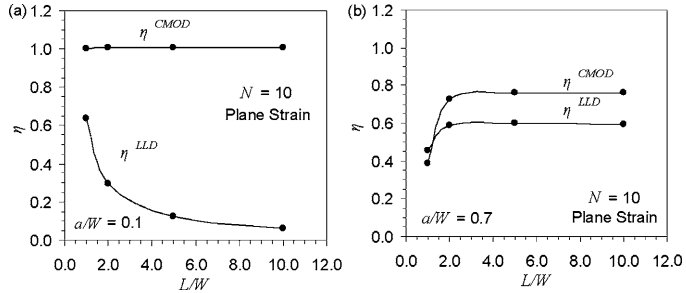


FIG. 9—*Specimen length effects on* η^{LLD} *and* η^{CMOD} *under plane strain conditions for (a) shallow and (b) deeply cracked DEN(T) specimens.*

the range $0.1 \leqslant a/W \leqslant 0.7$ the value of η^{CMOD} deviates from the mean value by about 10 % for the cases examined. The value of η^{CMOD} for $N=3$ and $a/W=0.1$ falls outside the upper bound line (see Fig. 14(*b*)). Therefore, the equation fitting the data is restricted to $N>3$.

The results indicate that when $a/W<0.3$ the value of J or C^* may be more accurate if Δ^{CMOD} is used, while for $a/W>0.3$, it is expected that a more accurate value will be obtained using Δ^{LLD}.

Compact Tension Specimen, C(T)

The C(T) specimen is the only specimen examined where the crack mouth opening displacement is measured along the load line, as opposed to the front face as, for example, in the SEN(T) specimen (see Fig. 1). Thus, the displacement measured at the crack mouth is often considered to be equivalent to that measured at the point of load application. This assumption has been confirmed by the analyses carried out here: displacement measurements from the crack mouth (along the load line) and those at the loading point have been compared, and these are almost identical. Note that due to differences between the specimen and finite element model geometry for the cases examined here, the position of the node used to determine Δ^{CMOD} is not precisely coincident with the point indicated in Fig. 1. Note further that for the majority of the results presented here the pin hole indicated in Fig. 1 was not modeled explicitly.

The ASTM Standard Test Method for Plane-Strain Fracture Toughness of Metallic Materials (E 399) [9] and ASTM E 1457 [4] is η solution for the C(T) specimen is widely used and is given by

$$\eta = 2 + 0.522\frac{W-a}{W} \tag{17}$$

Equation 17 was first proposed in Ref. [12] and was taken from a linear fit in Ref. [13], over the region $0.45 \leqslant a/W \leqslant 0.62$, to the fully plastic limit load analysis of Ref. [14]. This formula is derived based on the

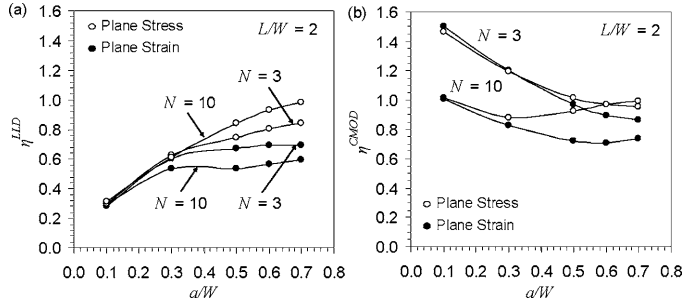


FIG. 10—*Example of the influence of N on (a)* η^{LLD} *and (b)* η^{CMOD}*, under plane stress and plane strain conditions, over a range of crack lengths for a DEN(T) specimen.*

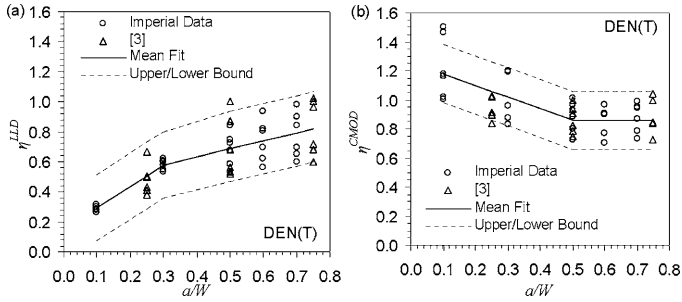


FIG. 11—*Variation in (a)* η^{LLD} *and (b)* η^{CMOD} *with crack length for DEN(T) specimen data from various sources.*

assumption that the displacement is measured at the loading point, though in Refs. [12,15] J values found experimentally using Δ^{CMOD} were in excellent agreement with values for J obtained from multi specimen techniques. Equation 17 has since been widely used to determine η using displacements measured at both the load point and at the crack mouth.

Figure 15 shows the influence of out-of-plane stress state and N on η over a range of crack lengths. It is seen that there is no general trend but the largest differences are due to the variation in N (though these are small). Figure 16 presents the η data from the current analysis and from the literature. No distinction is made between η^{CMOD} and η^{LLD}, though the data presented form the current analysis were obtained using Δ^{LLD}while those from Refs. [10,16] used Δ^{CMOD}. The results for η obtained from the current analysis are in good agreement with those of Ref. [16], except at $a/W=0.4$. The reason for this discrepancy has not been identified but the trend indicated by the current data (open circles) seems more reasonable. Equation 17, which was originally fitted within the range $0.45 \leqslant a/W \leqslant 0.62$ and is indicated in Fig. 16 by the dash line, provides an upper bound to the data at $a/W=0.45$ and a lower bound at $a/W=0.7$. Thus an adequate fit is provided by the ASTM formula, which may be used to evaluate η using either Δ^{LLD} or Δ^{CMOD} for $0.45 \leqslant a/W \leqslant 0.7$. However, following the approach for the other geometries examined here a mean line fit has been made to the dataset, in the range of $0.45 \leqslant a/W \leqslant 0.7$, which is independent of crack length ($\eta=2.2$). The upper and lower bounds are less than 5 % of the mean fit value in the range of crack lengths considered.

C-shaped Specimen, CS(T)

The final specimen examined is the CS(T) specimen, which has a somewhat similar geometry to the C(T) specimen. The results presented here are only considered valid for a CS(T) specimen of outer radius $R_o=50$ mm, with $R_i/R_o=0.5$ and $X/W=0.5$.

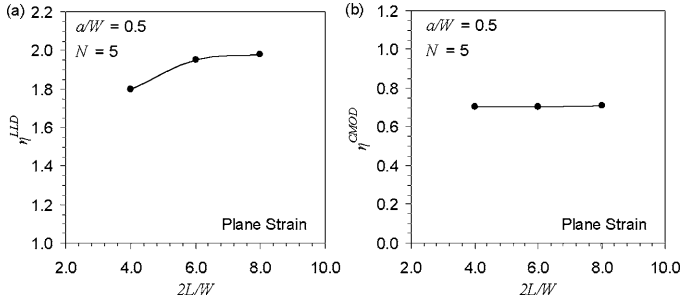


FIG. 12—*Specimen length effects on (a)* η^{LLD} *and (b)* η^{CMOD} *under plane strain conditions for SEN(B) specimens of* $a/W=0.5$, $N=5$.

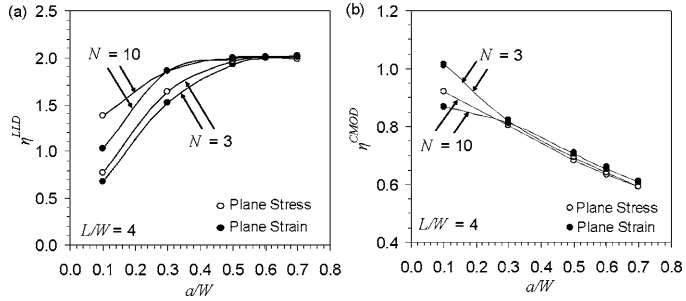


FIG. 13—*Example of the influence of N on (a) η^{LLD} and (b) η^{CMOD}, under plane stress and plane strain conditions, over a range of crack lengths for a SEN(B) specimen.*

The variation in η^{LLD} from the plane stress and plane strain analyses is relatively small compared with the variation due to N, as seen in Fig. 17(*a*). In Fig. 17(*b*) it is demonstrated that for $a/W=0.1$, N has the greatest influence on η^{CMOD}; however, for $a/W \geq 0.4$ the influence of out-of-plane stress state dominates. This result is similar to that observed for the DEN(T) specimen.

A very limited amount of data are available in the literature for the CS(T) specimen. No appropriate numerical data for comparison have been found hence only the values determined from the current analysis are shown in Fig. 18. As before, mean, upper, and lower bound lines are provided, though the data are relatively sparse. In Ref. [17] a 2-D plane strain and a 3-D analysis were performed for a specimen of somewhat different dimensions (see Table 2) to that considered in this work, for a single crack length of $a/W=0.54$. Values of η^{LLD} of approximately 2.24 and 2.44 were obtained from 2-D and 3-D analyses, respectively. These results are consistent with the values shown in Fig. 18(*a*). An analytical estimate for η^{LLD}, based on the load separation technique, is provided in Ref. [18], values from which are consistent with the upper bound for $a/W=0.4$ and the mean fit at $a/W=0.55$. However, the solution is only relevant for deep cracks and there is a large discrepancy between this solution and the data for shallower cracks.

No solutions were found in the literature for η^{CMOD}. Our analyses indicate that for the CS(T) specimen, unlike the C(T) specimen, there is a significant difference between η^{CMOD} and η^{LLD} for the cases examined as seen in Fig. 18. Figure 18(*b*) shows that η^{CMOD} decreases with a/W, and has a variability of approximately 5 % of the mean value. This variability is mainly due to the dependence on N for shallow cracks, and dependence on out of plane stress state for deeper cracks (see Fig. 17(*b*)).

The limited number of crack depths examined here makes it difficult to provide definitive recommendations for the CS(T) specimen. It may be seen that there is a large variability in η^{LLD} for $0.2 \leq a/W < 0.4$ (the variability ranges from to 79 to 30 % of the mean value). A more definite trend is shown for η^{CMOD} and the variability is significantly less than that for η^{LLD} in the region $0.2 \leq a/W < 0.4$. The variability in η^{CMOD} and η^{LLD} are comparable for $a/W > 0.4$.

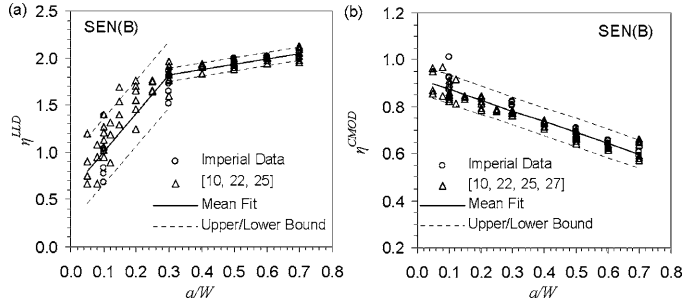


FIG. 14—*Variation in (a) η^{LLD} and (b) η^{CMOD} with crack length for SEN(B) specimen data from various sources.*

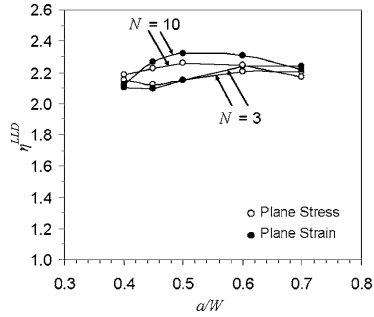


FIG. 15—*Example of the influence of N on* η^{LLD} *under plane stress and plane strain conditions, over a range of crack lengths for a C(T) specimen.*

Due to the limited data available for this specimen and the relatively large variability for shallow cracks, it is recommended that *J* or *C** values for the CS(T) specimen are evaluated using the crack mouth opening displacement, Δ^{CMOD}.

Discussion

Analyses have been reported which allow the fracture mechanics parameters *J* and *C** to be evaluated from load-displacement and load-displacement rate histories, respectively. The geometry parameters η and *H* used to evaluate *J* or *C** have been tabulated and η values plotted for a range of crack geometries using either the load line displacement or crack mouth opening displacement. The influence of material response (power law exponent), out-of-plane stress state (plane stress/plane strain), and specimen length on the parameters η^{LLD} and η^{CMOD} have been examined and results compared with existing solutions in the literature, where available. For most specimens η^{LLD} is sensitive to crack length especially for shallow cracks. A lower sensitivity to crack length is generally seen for η^{CMOD}, though this is not always the case.

Most of the results presented here are from a 2-D analysis. There may also be an influence from specimen thickness, *B*/*W*, and specimen side-grooving which has not been fully explored. It is expected that the plane stress and plane strain solutions for η will bound the values for different thickness specimens. Some 3-D calculations and discussion on thickness and side-grooving effects can be found in Refs. [3,10,17,19].

In an analysis, the appropriate bound of η should be used to provide a conservative prediction. When material properties are being determined the lower bound will provide a conservative measure of the material toughness. If a structural assessment is being carried out using the η factor then a conservative assessment is obtained using the upper bound value. Alternatively, the mean value of η can be used and the uncertainty, evaluated as a percentage of the mean, should be quantified in each case. Since *C** is linearly

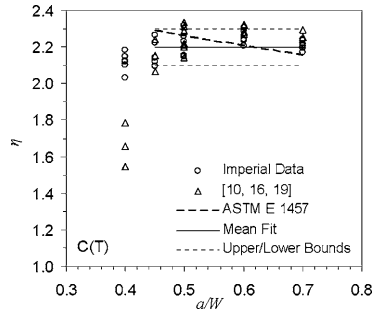


FIG. 16—*Variation in* η *with crack length for C(T) specimen data from various sources.*

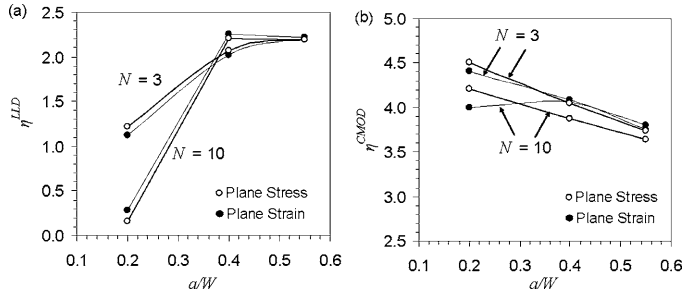


FIG. 17—*Example of the influence of N on (a)* η^{LLD} *and (b)* η^{CMOD}*, under plane stress and plane strain conditions, over a range of crack lengths for a CS(T) specimen.*

related to η (see Eq. 15) then, for example, a 20 % uncertainty in η would lead to a 20 % uncertainty in C^*, in addition to other experimental uncertainties. In some experiments both Δ^{LLD} and Δ^{CMOD} may be available. The values of J or C^* obtained from the two measurements should agree within the quoted variability for the specimen. Note that, agreement between C^* values from Δ^{CMOD} and Δ^{LLD} does not imply that the "exact" value of J or C^* has been obtained, since the degree of uncertainty in both η^{LLD} and η^{CMOD} are sometimes comparable. If an exact value is required then the η value for the particular geometry (accounting for the effects of a/W, B/W, and L/W) and particular material should be obtained from FE analysis or otherwise. The analysis carried out here indicates that for most specimens the variability in the η factors is sufficiently low that a separate specimen calibration is not required. Note, finally, that within the FE analysis certain assumptions have been made, e.g., in most cases the rigid pin has not been modeled and for the SEN(T), M(T), and DEN(T) specimens a remote uniform stress has been applied to the specimen at the specimen boundaries. In an experiment a minimum gage length is required for a pin loaded structure to ensure a relatively uniform stress distribution to be achieved in the region of the crack plane.

For most of the specimens it has been found that typically the variability of η^{CMOD} is much less than that for η^{LLD}. Thus it is recommend that, where practicable, C^* or J values should be obtained using the crack mouth opening displacements and the geometric functions presented here.

Conclusions

Values for η^{LLD} and η^{CMOD}, based on the load line displacement and crack mouth opening displacement, respectively, have been presented for a range of geometries. The geometries examined are the compact tension specimen, C(T), single edge notch specimen in tension, SEN(T), and bending, SEN(B), double edge notch specimen in tension, DEN(T), middle crack specimen in tension, M(T) and the C-shaped

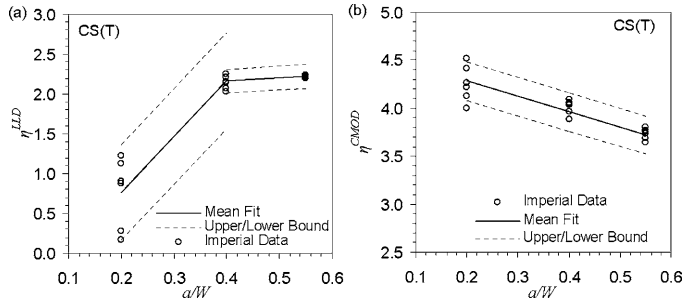


FIG. 18—*Variation in (a)* η^{LLD} *and (b)* η^{CMOD}*, with crack length for CS(T) specimen data of* X/W=0.5*,* R_i/R_o=0.5.

TABLE 4—*Details of the numerical models for each specimen.*

Specimen Type	Material Properties	a/W	L/W	Comments
SEN(T)	$E/\sigma_0 = 318$ $\alpha = 1$ $\nu = 0.3$ $N = 3, 5, 10$	0.1 0.3 0.5 0.6 0.7	1 2 5 10	Uniform stress applied to top surface elements. Load line displacement is the average displacement of the top surface nodes.
M(T)	$E/\sigma_0 = 318$ $\alpha = 1$ $\nu = 0.3$ $N = 3, 5, 10$	0.1 0.3 0.5 0.6 0.7	1 2 5 10	Uniform stress applied to top surface elements. Load line displacement is the average displacement of the top surface nodes.
DEN(T)	$E/\sigma_0 = 318$ $\alpha = 1$ $\nu = 0.3$ $N = 3, 5, 10$	0.1 0.3 0.5 0.6 0.7	1 2 5 10	Uniform stress applied to top surface elements. Load line displacement is the average displacement of the top surface nodes.
SEN(B)	$E/\sigma_0 = 318$ $\alpha = 1$ $\nu = 0.3$ $N = 3, 5, 10$	0.1 0.3 0.5 0.6 0.7	4 6 8	Three point bend loading.
C(T)	$E/\sigma_0 = 318$ $\alpha = 1$ $\nu = 0.3$ $N = 3, 5, 10$	0.4 0.45 0.5 0.6 0.7	...	Elements directly surrounding concentrated point load given elastic material properties.
CS(T)	$E/\sigma_0 = 318$ $\alpha = 1$ $\nu = 0.3$ $N = 3, 5, 10$	0.2 0.4 0.55	...	Eight noded reduced integration elements. $X/W = 0.5$ $R_o/R_i = 0.5$ $W = 25$ mm

specimen tension CS(T). Calculations have been performed for a Ramberg-Osgood (power law hardening) material and the resulting η factors are applicable to either power law plastic or power law creeping materials. A wide range of crack depths, $0.1 \leqslant a/W \leqslant 0.7$, and hardening exponents, $3 \leqslant N \leqslant 10$, under plane stress and plane strain conditions have been examined using the finite element method. Specimen length has been found to have a strong influence on η^{LLD} for shallow cracked SEN(T), M(T), and DEN(T), but little or no influence on η^{CMOD}. The influence of stress state on the η factor varies with specimen type and crack length. These results are generally consistent with those in the literature. Mean linear fits, that are dependent on crack length, are provided and the variations in η due to N, length, out-of-plane stress state, and other effects, are accommodated by providing an upper and lower bound to the data. Generally, more confidence is expected in J or C^* values derived from crack mouth opening displacement measurements.

Acknowledgments

The mesh for the CS(T) specimen was kindly provided by VTT Industrial Systems, Finland. Helpful discussions with Prof. C. E. Turner are gratefully acknowledged.

APPENDIX A—Equations for the Mean Fit to η Including a Measure of Uncertainty

Equations of the mean fits to the data, describing the dependency of η^{LLD} and η^{CMOD} on the normalized crack length, $x = a/W$, are given below, together with an approximate absolute measure of the uncertainty in the data, thus providing an upper and lower bound estimate. The restrictions on specimen geometry and hardening exponent, N, are also specified.

SEN(T)

$$0.1 \leqslant x \leqslant 0.5 \quad \eta^{LLD} = (5.0x - 0.06) \pm 0.38 \quad \begin{matrix} 1 \leqslant L/W \leqslant 3 \\ 3 \leqslant N \leqslant \infty \end{matrix} \tag{A-1}$$

$$0.5 < x \leqslant 0.7 \quad \eta^{LLD} = 2.44 \pm 0.38 \quad \begin{matrix} 1 \leqslant L/W \leqslant 3 \\ 3 \leqslant N \leqslant \infty \end{matrix} \tag{A-2}$$

$$0.1 \leqslant x \leqslant 0.7 \quad \eta^{CMOD} = 1.0 \pm 0.05 \quad \begin{matrix} 1 \leqslant L/W \leqslant 4 \\ 3 \leqslant N \leqslant \infty \end{matrix} \tag{A-3}$$

M(T)

$$0.1 \leqslant x \leqslant 0.35 \quad \eta^{LLD} = (2.32x + 0.18) \pm 0.22 \quad \begin{matrix} 2 \leqslant L/W \leqslant 4 \\ 3 \leqslant N \leqslant \infty \end{matrix} \tag{A-4}$$

$$0.35 < x \leqslant 0.7 \quad \eta^{LLD} = 0.99 \pm 0.10 \quad \begin{matrix} 2 \leqslant L/W \leqslant 4 \\ 3 \leqslant N \leqslant \infty \end{matrix} \tag{A-5}$$

$$0.1 \leqslant x \leqslant 0.7 \quad \eta^{CMOD} = (1.26 - 0.36x) \pm 0.15 \quad \begin{matrix} 2 \leqslant L/W \leqslant 4 \\ 3 < N \leqslant \infty \end{matrix} \tag{A-6}$$

DEN(T)

$$0.1 \leqslant x \leqslant 0.3 \quad \eta^{LLD} = (1.43 + 0.15) \pm 0.22 \quad \begin{matrix} 2 \leqslant L/W \leqslant 4 \\ 3 \leqslant N \leqslant \infty \end{matrix} \tag{A-7}$$

$$0.3 < x \leqslant 0.7 \quad \eta^{LLD} = (0.53x + 0.42) \pm 0.22 \quad \begin{matrix} 2 \leqslant L/W \leqslant 4 \\ 3 \leqslant N \leqslant \infty \end{matrix} \tag{A-8}$$

$$0.1 \leqslant x < 0.5 \quad \eta^{CMOD} = (1.26 - 0.80x) \pm 0.20 \quad \begin{matrix} 2 \leqslant L/W \leqslant 4 \\ 3 < N \leqslant \infty \end{matrix} \tag{A-9}$$

$$0.5 \leqslant x \leqslant 0.7 \quad \eta^{CMOD} = 0.86 \pm 0.20 \quad \begin{matrix} 2 \leqslant L/W \leqslant 4 \\ 3 \leqslant N \leqslant \infty \end{matrix} \tag{A-10}$$

SEN(B)–3PB

$$0.1 \leqslant x \leqslant 0.3 \quad \eta^{LLD} = (4.06x + 0.60) \pm 0.35 \quad 3 \leqslant N \leqslant \infty \tag{A-11}$$

$$0.3 < x \leqslant 0.7 \quad \eta^{LLD} = (0.56x + 1.65) \pm 0.07 \quad 3 \leqslant N \leqslant \infty \tag{A-12}$$

$$0.1 \leqslant x \leqslant 0.7 \quad \eta^{CMOD} = (0.92 - 0.46x) \pm 0.06 \quad 3 < N \leqslant \infty \tag{A-13}$$

C(T)

$$0.45 \leqslant x \leqslant 0.7 \quad \eta^{LLD} = \eta^{CMOD} = 2.2 \pm 0.1 \quad 3 \leqslant N \leqslant \infty \tag{A-14}$$

CS(T)

$$0.2 \leqslant x < 0.4 \quad \eta^{LLD} = (7x - 0.64) \pm 0.06 \quad \begin{matrix} R_i/R_o = 0.5 \\ X/W = 0.5 \\ 3 \leqslant N \leqslant 10 \end{matrix} \tag{A-15}$$

$$0.4 \leqslant x \leqslant 0.55 \quad \eta^{LLD} = (0.4x + 2) \pm 0.15 \quad \begin{matrix} R_i/R_o = 0.5 \\ X/W = 0.5 \\ 3 \leqslant N \leqslant 10 \end{matrix} \tag{A-16}$$

$$0.2 \leqslant x \leqslant 0.55 \quad \eta^{CMOD} = (4.6 - 1.6x) \pm 0.2 \quad \begin{matrix} R_i/R_o = 0.5 \\ X/W = 0.5 \\ 3 \leqslant N \leqslant 10 \end{matrix} \tag{A-17}$$

References

[1] Webster, G. A. and Ainsworth, R. A., *High Temperature Component Life Assessment*, 1st ed., Chapman and Hall, London, 1994.

[2] Rice, J. R., "A Path Independent Integral and the Approximate Analysis of Strain Concentration by Notches and Cracks," *ASME Trans. J. Appl. Mech.*, Vol. 35, 1968, pp. 379–386.

[3] Kim, Y.-J., Son, B.-G., and Kim, Y.-J., "Elastic-Plastic Finite Element Analysis for Double-Edge Cracked Tension (DE(T)) Plates," *Eng. Fract. Mech.* Vol. 71, 2004, pp. 945–966.

[4] ASTM Standard E 1457, "Standard Test Method for Measurement of Creep Crack Growth Rates in Metals," , *Annual Book of ASTM Standards*, Vol. 3, No. 1, 2001, pp. 936–950.

[5] Turner, C. E., The Ubiquitous η Factor, in *Fracture Mechanics: Twelfth Conference, ASTM STP 700*, ASTM International, West Conshohocken, PA, 1980, pp. 314–337.

[6] Ainsworth, R. A., "The Assessment of Defects in Structures of Strain Hardening Material", *Eng. Fract. Mech.*, Vol. 19, 1984, pp. 633–642.

[7] ABAQUS, *Users Manual*, in *Version 6.2*. 2001.

[8] Tada, H., Paris, P. C., and Irwin, G. R., *The Stress Analysis of Cracks Handbook*, Paris Productions & (Del Research Corp.), Saint Louis, 1985.

[9] ASTM Standard E 399-90, "Standard Test Method for Plane-Strain Fracture Toughness of Metallic Materials", *Annual Book of ASTM Standards*, Vol. 3, No. 1, 2001, pp. 434–464.

[10] Kim, Y.-J., Kim, J.-S., Cho, S.-M., and Kim, Y.-J., "3-D Constraint Effects on J Testing and Crack Tip Constraint in M(T), SE(B), SE(T) and C(T) Specimens: Numerical Study," Vol. 71, No. 9, 2004, pp. 1203–1219.

[11] Kanninen, M. F. and Popelar, C. H., *Advanced Fracture Mechanics*, The Oxford Engineering Science Series, Clarendon Press, Oxford, 1985.

[12] Ernst, H. A., Paris, P. C., and Landes, J. D., Estimations on J-Integral and Tearing Modulus T from a Single Specimen Test Record, in *Fracture Mechanics: Thirteenth Conference, ASTM STP 743*, R. Roberts, Ed., ASTM International, West Conshohocken, PA, 1981, pp. 476–502.

[13] Clarke, G. A. and Landes, J. D., "Evaluation of the J Integral for the Compact Specimen, *J. Test. Eval.*, Vol. 7, No. 5, 1979, pp. 264–269.

[14] Merkle, J. G. and Corten, H. T., "A J Integral Analysis for the Compact Specimen, Considering Axial Force as Well as Bending Effects," *ASME J. Pressure Vessel Technol.*, Vol. 96, 1974, pp. 286–292.

[15] Landes, J. D., Walker, H., and Clarke, G. A., "Evaluation of Estimation Procedures Used in J-Integral Testing, in *Elastic-Plastic Fracture, ASTM STP 668*," J. D. Landes, J. A. Begley, and G. A. Clarke, Eds., ASTM International, West Conshohocken, PA, 1979, pp. 286–287.

[16] Panontin, T. L., "Crack Tip Opening Displacement Estimation Formulae for C(T) Specimens," *Eng. Fract. Mech.*, Vol. 67, No. 3, 2000, p. 293.

[17] Kim, Y., Chao, Y. J., Pechersky, M. J., and Morgan, M. J., "C-Specimen Fracture Toughness Testing: Effect of Side Grooves and η Factor," *J. Pressure Vessel Technol.*, Vol. 126, No. 3, 2004, pp.

293–299.

[18] Junnan, C., "The Elastic-plastic Parameters of the C-shaped Specimen," *Eng. Fract. Mech.*, Vol. 37, No. 1, 1990, pp. 119–125.

[19] Nevalainen, M. and Dodds, R. H., Jr., "Numerical Investigation of 3-D Constraint Effects on Brittle Fracture in SE(B) and C(T) Specimens, *International Journal of Fracture*, Vol. 74, No. 2, 1995, pp. 131–161.

[20] O'Dowd, N. P., Budden, P. J., and Griffiths, E. R. J., "Finite Element Analysis of a Bi-Material SENT Specimen under Elastic-Plastic Loading, in *Proceedings IUTAM Symposium Nonlinear Analysis of Fracture*, Kluwer Academic Publisher, Dordrecht, The Netherlands, 1997, pp. 33–42.

[21] O'Dowd, N. P., Kolednik, O., and Naumenko, V. P., "Elastic-Plastic Analysis of Biaxially Loaded Center-Cracked Plates," *Int. J. Solids Struct.*, Vol. 36, 1999, pp. 5639–5661.

[22] Kirk, T. M. and Dodds, R. H. J., "J and CTOD Estimation Equations for Shallow Cracks in Single Edge Notch Bend Specimens", Department of Civil Engineering, University of Illinois at Urbana, Champaign Urbana, Illinois, No. 570, January 1992.

[23] Kirk, T. M. and Dodds, R. H. J., "*Effect of Weld Strength Mismatch on Elastic-Plastic Fracture Parameters*", Department of Civil Engineering, University of Illinois at Urbana, Champaign Urbana, Illinois, No. 570, August 1992.

[24] Joyce, J. A., Hackett, E. M., and Roe, C., "Effects of Crack Depth and Mode of Loadings on the J-R Curve Behavior of High Strength Steel," in *Constraint Effects in Fracture, ASTM STP 1171*, E. M. Hackett, K.-H. Schwalbe, and R. H. Dodds, Eds., ASTM International, West Conshohocken, PA, 1993, pp. 239–263.

[25] Lei, Y., Webster, G. A., and O'Dowd, N. P., *Investigation of Residual Stresses in Welded Joints Part II: Finite Element Modelling*, Department of Mechanical Engineering, Imperial College London, GR/L42926, December 1998.

[26] Kim, Y., "C-Specimen Fracture Toughness Testing: Effect of Side Grooves and η Factor, *J. Pressure Vessel Technol.*, Vol. 126, No. 3, 2004, pp. 293–299.

[27] Wang, Y.-Y. and Gordon, J. R., "The Limits of Applicability of J and CTOD Estimation Procedures for Shallow-Cracked SENB Specimens," in International Conference on Shallow Crack Fracture Mechanics, Toughness Test and Applications, M. G. Dawes, Ed., 1992, Cambridge, UK.

[28] Kim, Y.-J. and Schwalbe, K.-H., "On the Sensitivity of J Estimation to Materials' Stress-Strain Curves in Fracture Toughness Testing Using the Finite Element Method," *J. Test. Eval.*, Vol. 29, No. 1, 2001, pp. 18–31.

[29] Griffiths, E. R. J., "Finite Element Modelling of Cracks in Homogeneous and BiMaterial SENT Specimens," 3M Project Report, Department of Mechanical Engineering, Imperial College London, 1994.

[30] Kim, Y.-J. and Budden, P. J., "Plastic Eta Factor Solutions of Homogeneous and Bi-Material SE(T) Specimens for Toughness and Creep Crack Growth Testing," *Fatigue and Fracture of Engineering Materials and Structures*, Vol. 24, No. 11, 2001, pp. 751–751.

[31] Sumpter, J. D. G., "J_c Determination for Shallow Notch Welded Bend Specimens," *Fatigue and Fracture of Engineering Materials and Structures*, Vol. 10, No. 6, 1987, pp. 479–193.

[32] Wu, S.-X., Mai, Y.-W., and Cottrell, B., "Plastic η-Factor (η_p) of Fracture Specimens with Deep and Shallow Cracks," *International Journal of Fracture*, Vol. 45, 1990, pp. 1–18.

Fracture Toughness and Constraint

Journal of ASTM International, Vol. 3, No. 6
Paper ID JAI13183
Available online at www.astm.org

Timo Björk,[1] *Gary Marquis,*[1] *Veli Pellikka,*[2] *and Reijo Ilvonen*[3]

An Experimental and Numerical Study of the Fracture Strength of Welded Structural Hollow Section X-Joints

ABSTRACT: The effect of the geometry and material properties on the fracture strength of welded X-joints fabricated from structural hollow section (SHS) profiles has been studied experimentally and by using nonlinear finite element analysis (FEA). The current paper focuses on four joints tested at −40°C. This was one part of an extensive series of laboratory experiments performed at temperatures +20°C…−60°C. At sub-zero temperatures the primary fracture mode was mainly ductile followed by final brittle failure. The radius and material properties in the corner area of a SHS are dependent on the fabrication method of the SHS. In cold-formed sections the corner radius is typically large and the yield strength is greater than the nominal yield strength of the base material. This bigger corner radius can provide different stiffness and load carrying capacity as compared to joints fabricated from hot-formed sections. Numerical simulation and experimental tests focused on the importance of this corner effect and the separate role geometry, yield strength, and fracture toughness on the total fracture strength of the joint.

KEYWORDS: structural hollow section, X-joint, ductile fracture, brittle fracture

Nomenclature

A_5 = percentage elongation at fracture of the gage length
b_0 = width of chord member, mm
b_w = distance from weld to toe weld toe of brace member, mm
b_1 = width of brace member, mm
F_u = ultimate load carrying capacity, N
$F_{u,test}$ = ultimate load carrying capacity de ned by test, N
F_y = capacity related to yield strength, N
$F_{y,0.2}$ = calculated capacity related to measured yield strength, N
$F_{y,355}$ = calculated capacity related to nominal yield strength=355 N/mm^2, N
$F_{3\ \%}$ = load corresponding to 3 % relative deformation, N
f_u = ultimate tensile strength, N/mm
f_y = yield strength (of chord member), N/mm^2
$f_{y,1}$ = yield strength of brace member, N/mm^2
$f_{y,0.2}$ = yield strength relating 0.2 % plastic deformation, N/mm^2
h_0 = height of chord member, mm
h_1 = height of brace member, mm
h_w = distance from weld to toe weld toe of brace member, mm
r_0 = outer radius of corner in chord member, mm
r_1 = outer radius of corner in brace member, mm
s = distance along perimeter, mm
$T_{50\ \%}$ = temperature, which obtain 50 % ductile area of fractured surface, C
t_0 = wall thickness of chord member, mm

Manuscript received April 7, 2005; accepted for publication March 6, 2006; published online April 2006. Presented at ASTM Symposium on Fatigue and Fracture Mechanics: 35th Volume on 18 20 May 2005 in Reno, NV; R. E. Link and K. M. Nikbin, Guest Editors.

[1] Project Manager and Professor, respectively, Lappeenranta University of Technology, FIN-53851 Lappeenranta, Finland.
[2] Structural Analyst, Stress eld Oy, FIN-53851, Lappeenranta, Finland.
[3] Technical Support Manager, Ruukki Metals, Rautaruukki Oyj, FIN-13300 Hameenlinna, Finland.

Copyright © 2006 by ASTM International, 100 Barr Harbor Drive, PO Box C700, West Conshohocken, PA 19428-2959.

t_1 = wall thickness of brace member, mm
β = width ratio=b_1/b_0
δ_p = plastic deformation, mm
ε = strain
η = h_1/b_0
θ = joint angle between brace and chord member, degree
σ = stress, N/mm^2

Introduction

Structural hollow sections (SHS) are widely used structural components mostly due to their good structural properties and esthetic appearances. Many experimental tests and numerical analyses on the capacity and fracture mechanics of structural hollow section joints have been performed. However, most of those investigations involved joints fabricated using hot-formed structural hollow section (HFSHS) members and testing has been at room or elevated temperatures. Only limited test data are available for cold-formed structural hollow section (CFSHS) joints at lower temperatures [1].

Tubular joints fall generally into two categories: X- and K-joints. Both categories include multiple variations, but a common feature for X-joints is that the load will be transmitted from the flange to the web of the chord member causing high stresses in the corner area. Material and geometric features of the corner area are, therefore, very important for X-joints. The importance of the SHS corner, therefore, highlights the two main differences between HFSHS and CFSHS. The corner radius is the main geometrical difference between hot- and cold-formed sections of the same nominal size. Theoretically, the larger corner radius of a chord member makes the transverse face of the brace member more effective, when the width ratio, β, between the brace and chord members is near unity. This is due to the increased stiffness of a curved shell as opposed to a flat shell. If β is small, e.g., $\beta \leqslant 0.85$, the failure mechanism changes, but again the larger radius of the chord member increases the stiffness and strength of the chord flange. Consequently, independent β, the larger corner radius of the chord member for CFSHS should increase the ultimate load-carrying capacity of the X-joint if other dimensions remain unchanged. From a fabrication point of view, however, the large corner radius makes joint preparation more time consuming when β is close to 1.

Yield and ultimate strength and ductility are the most important material properties. In X-joints the corner areas of the chord are loaded mainly by transverse stresses independent of β. Hence, the transverse material properties in the chord corner are critical. However, in design guidance documents the load and deformation capacities of X-joints are usually calculated based on material properties defined in longitudinal direction of the chord member. In hot-formed sections this is probably sufficient but for cold-formed sections the corner area is highly strain hardened in the transverse direction. Strain hardening increases the material strength but decreases the plastic deformation capacity. In addition, the heat input due to welding can alter the material properties. These effects may increase the probability of brittle fracture as the failure mode for an X-joint fabricated with CFRHS and, hence, restrictions for welding on corner areas are given [2].

For $\beta \leqslant 0.85$, the elastic-plastic capacity of the X-joint depends more on the local bending load-carrying capacity than on the membrane load-carrying capacity of the chord flange. The residual stresses through the wall thickness of the cold-formed flange are large and dramatically alter the effective strength in tension and bending. For this reason bending strength, rather than tensile strength, was judged to better describe the material properties for analysis purposes.

Considering all the previously described phenomena, the maximum load-carrying capacity and deformation behavior of an X-joint is so complex that numerical simulation must be calibrated based on experiments. An extensive test program of X-joints of different geometries and at different temperatures was carried out. In total 20 joints were tested at temperatures ranging from +20°C…−60°C. In these tests the load and deformation capacities for X-joints fabricated from HFSHS and CFSHS were measured. The current paper focuses on four of the joints tested at −40°C. Two of the joints were fabricated from HFSHS and two nominally identical joints were fabricated from CFSHS. Finite element (FE) analyses were used to define the theoretical ultimate load-carrying capacity and expected failure mechanism. Experimental results have also been compared with analytical joint strength capacities calculated using current design

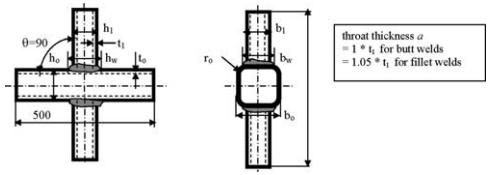


FIG. 1—*Test specimen geometry.*

guidance documents (EC3) [3]. Failure analyses of the observed fractures have been performed.

Experimental Study

Geometry of Test Specimens

The effect of corner radius on the ultimate capacity and fracture behavior of X-joints has been studied using test specimens illustrated in Fig. 1. Nominal dimensions of the test specimens are given in Table 1. Whenever possible the chord and brace members of the X-joints are joined with fillet welds. However, when the width of the brace and chord members were equal, butt welds were used for the welds parallel to the longitudinal axis of the chord member. In all cases a manual MAG welding process was used. The joints were prepared according to the instructions obtained in the design code [4].

Material Properties

Chemical Composition—The chemical composition of the SHS base material was measured and is shown in Table 2.

Tensile and Charpy V-tests—The material properties ($f_{0.2}$, f_u, and A_5) seen in Table 3 were measured using tensile tests on coupons cut from the tube flange. The transition temperature value $T_{50\ \%}$ is based on the surface analyses of the tested Charpy V-notch specimens ($T_{50\ \%}$= temperature where about 50 % of the fractured surface is ductile). In some cases the fracture toughness for two orientations was examined. The locations in the SHS from which the tensile coupon and Charpy V-notch test specimens were cut are illustrated in Fig. 2.

Test Setup

X-joint Tests—The test specimens were mounted in the loading rig and pretension was applied to the chord member. The magnitude of the pretension load was selected as approximately 60 % of the nominal

TABLE 1—*The nominal dimensions of the test X-joints.*

		Chord			Brace			Joint	
ID.	SHS Type	$b_0 \times h_0 \times t_0$ (mm)	b_0/t_0	r_0 (mm)	$b_1 \times h_1 \times t_1$ (mm)	b_1/t_1	r_1 (mm)	$\beta=b_1/b_0$	θ (°)
X18	CF	100×100×10	10.0	25	100×100×10	10.0	25	1.0	90
X20	CF	100×100×10	10.0	25	50×50×5	10.0	10	0.5	90
X22	HF	100×100×10	10.0	<25	100×100×10	10.0	<25	1.0	90
X23	HF	100×100×10	10.0	<25	50×50×5	10.0	<10	0.5	90

TABLE 2—*Chemical compositions of the SHSs.*

Tube	SHS	C	Si	Mn	P	S	Al	Nb	V	Cu	Cr	Ni	Mo	Ti	B	Ca	N
100×100×10	CF	0.145	0.202	0.60	0.009	0.006	0.037	0.001	0.004	0.016	0.023	0.037	0.000	0.019	0.0002	0.002	0.0042
50×50×5	CF	0.097	0.206	1.39	0.012	0.005	0.039	0.003	0.008	0.023	0.028	0.039	0.003	0.016	0.0003	0.003	0.0052
100×100×10	HF	0.138	0.200	1.39	0.020	0.004	0.044	0.041	0.004	0.012	0.030	0.022	0.001	0.002	0.0003	0.002	0.0035
50×50×5	HF	0.151	0.149	1.32	0.030	0.014	0.065	0.049	0.001	0.022	0.041	0.033	0.006	0.001	0.0002	0.000	0.0059

TABLE 3—*Measured material properties.*

SHS	Cold- or Hot-formed	$f_{0.2}$ (MPa)	f_u (MPa)	A_5 (%)	$T_{50\ \%}$ T-L (C)	$T_{50\ \%}$ L-T (C)
100×100×10	CF	468	551	30.0	−10	−15
100×100×10	HF	424	561	35.1	−40	−70
50×50×5	CF	480	541	30.0	···	−65
50×50×5	HF	561	641	28.3	···	−100

yield strength of the chord, i.e., 690 kN for joints reported here. Test temperature was −40°C. Temperature of the test specimens was measured by thermocouple elements installed on the chord member near the critical joint area. Joint temperature was controlled by adjusting the flow rate of an ethanol-based coolant that was cooled using dry ice. The coolant was circulated inside the hollow test specimen via small holes. The brace members were then loaded until failure. Brace loading was quasi-static displacement controlled at the rate of 1–2 mm/min. Total test time for a single joint was in the range of 30 min. A photograph and schematic of the test setup are shown in Fig. 3.

Bending and SHS Distortion Tests—One bending test was performed on a strip cut from the flange of the CFSHS. This was performed in order to define the bending load-carrying capacity of the chord flange. The test also served as a simple comparison study for the finite element analyses (FEA) and was used to assess the potential effect of through thickness residual stresses on the bending capacity. The test setup is illustrated in Fig. 4(*a*).

Because the material properties in the transverse direction of the cross section play an important role in defining the ultimate capacity of the X-joint, one SHS distortion test was carried out in order. In this test the transverse elastic-plastic behavior of the material in the corner region was derived. The distortion test setup is illustrated in Fig. 4(*b*). In both these tests, strain values were measured by strain gages. The tests were executed at room temperature and the material was cut from the same tube, from which the test specimen X18 was fabricated.

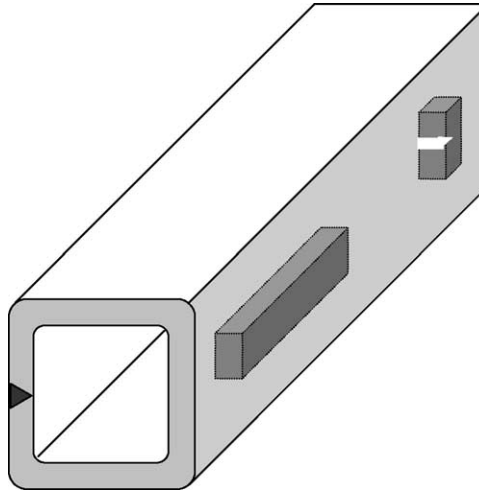


FIG. 2—*Locations of the coupon and Charpy V-notch test specimens.*

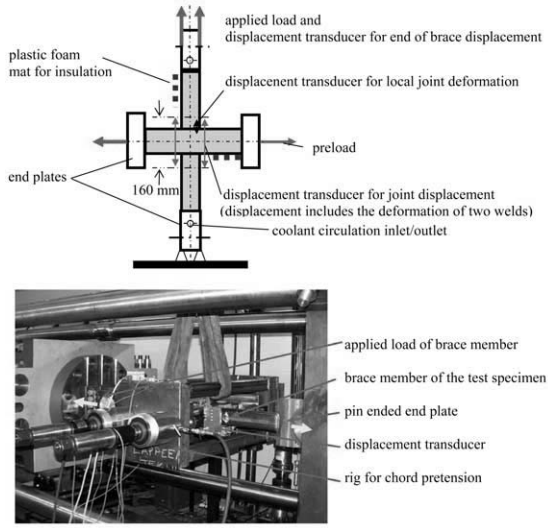


FIG. 3—*Test setup in schematic and in practice.*

Test Results

Force and Displacement Capacities

The experimental results for the X-joint tests are presented as force-displacement curves. A typical force-displacement curve is illustrated in Fig. 5. The ultimate load carrying capacity F_u and plastic deformations δ_p for each test specimen is determined and the results are shown in Table 4. Due to the symmetry of the test specimen, two welds were tested simultaneously, thus the measured displacement of the X-joint is $2\delta_p$. Note that the distance between displacement measuring points was 160 mm as shown in Fig. 3. The local displacement reported in Fig. 5 was based on a single small displacement transducer connected to either side of the weld. This local value is shown in Fig. 5 but is not further discussed in this paper.

Failure Modes

Based on the analytical equations given in the design guidance documents, the joints were sized so as to avoid failure in the brace members. However, due to the conservative assumption used in these equations it was not always possible to know in advance the failure mode. During the extensive X-joint test series, the following failure modes were identified:

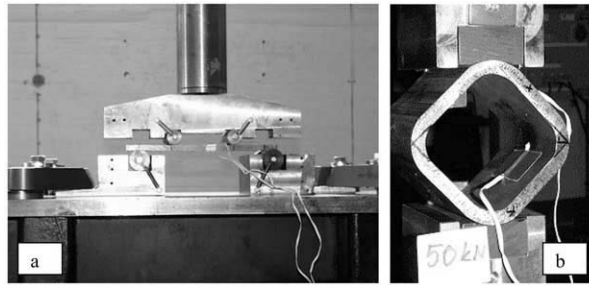


FIG. 4—*Bending and SHS distortion tests.*

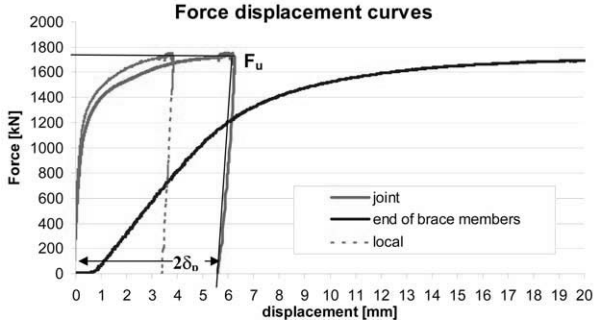


FIG. 5—*Typical force-displacement curve for an X-joint. Measured displacement quantities depend on the measurement points.*

W = failure in the web of the chord
F = failure in the flange of the chord
Bw = failure in the brace in or next to the weld
B = failure in the brace remote from the welded joint

The desired failure modes were W and F. However, B and Bw failure were also observed for some joints. In some cases the fracture was of a mixed type including at least two different failure modes. The failure is categorized only according to the primary failure. Failure type F was not observed for any of the joints reported here. Failures of the four specimens reported here are shown in Fig. 6.

Numerical Investigations

Design Code-Based Capacity of an X-joint

Formulas found in the design guidance documents [2,3], can be used to estimate the load-carrying capacity of an X-joint. Because the chord is in tension, the tensile brace loading capacity can be found by the lowest capacity estimated using Eqs 1–4. In the case $\beta \leq 0.85$, the chord flange capacity, failure mode F, is computed using

$$F_y = \frac{f_y \cdot t_0^2}{(1-\beta)\sin\theta}\left[\frac{2\eta}{\sin\theta} + 4\sqrt{1-\beta}\right] \tag{1}$$

In the case $\beta = 1.0$, the chord web capacity, failure mode W, is computed using

$$F_y = \frac{f_y \cdot t_0}{\sin\theta}\left[\frac{2h_1}{\sin\theta} + 10t_0\right] \tag{2}$$

In the case $\beta > 0.85$, the brace capacity in the region of the web, failure mode Bw, is computed using

TABLE 4—*Results from test and theoretical capacities.*

	Test				Calculated F, Eqs 1–4				Comparison			
ID.	Max. $\frac{\delta_p}{b_0}$ (%)	F_u (kN)	Load at $\frac{\delta_p}{b_0}$=0.03 (kN)	Experiment Failure Mode W=web B=brace F=flange	$F_{y,355}$ (kN)	$F_{y,02}$ (kN)	F_u (kN)	Predicted Failure Mode W=web B=brace F=flange	$\frac{F_{u,test}}{F_{y,355}}$	$\frac{F_{u,test}}{F_{y,0.2}}$	$\frac{F_{u,test}}{F_u}$	$\frac{F_{u,test3}\ \%}{F_u}$ or $\frac{F_{u,test}}{F_u}$
×18	2.5[a]	1750		B/d	1068	1408	1657	W	1.64	1.24	1.06	1.06
×20	1.5[a]	455		B/d	273	360	423	F	1.67	1.26	1.08	1.08
×22	6.5	1720	1507	W/$d \rightarrow b$	994	1187	1570	W	1.73	1.45	1.10	0.96
×23	3.5	400	392	Bw/$d \rightarrow b$	245	293	387	W	1.63	1.37	1.03	1.01

[a]Failure took place outside the measured joint displacement.

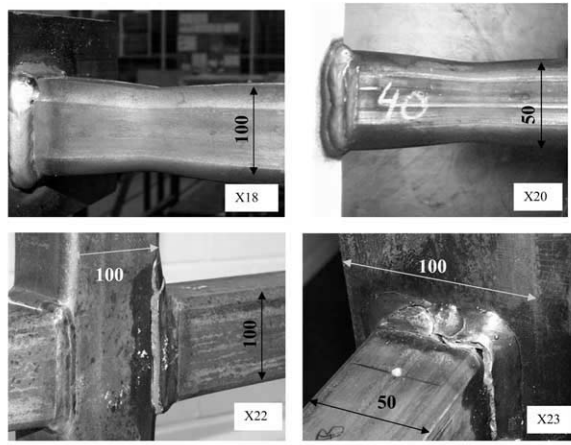


FIG. 6—*Failure modes (a) joint* X18 *failure mode B, (b) joint* X20 *failure mode B, (c) joint* X22 *failure mode W, and (d) joint* X23 *failure mode Bw.*

$$F_y = f_y \cdot t_0[2h_1 - 4t_1 + 2b_{\text{eff}}]$$

where

$$b_{\text{eff}} = \frac{10b_1 \cdot t_0^2 \cdot f_y}{b_0 \cdot t_1 \cdot f_{y,1}} \leqslant b_1 \tag{3}$$

The brace capacity, failure mode B, is computed using

$$F_y = f_{y,1} \cdot t_1[2h_1 - 4t_1 + 2b_1] \tag{4}$$

Table 4 gives both test results and the analytical strength values computed using Eqs 1–4. Analytical joint strength values are computed based on both nominal strength of the RHS material, $F_{y,355}$, and the measured yield strength, $F_{y,0.2}$. The ultimate capacity based on ultimate tensile strength is also presented, F_u. In these calculations the measured geometry values of a joint were used as opposed to the nominal values. Table 4 also indicates the expected failure mode based on Eqs 1–4 and the failure modes observed during the experiments. If the failure from the experiments was judged to be ductile, the letter *d* is shown in the failure mode column. In some tests the primary failure from the experiment was observed to be ductile fracture followed by secondary brittle fracture, *b*. This is represented by the symbol $d \rightarrow b$ in Table 4. The deformation capacity is presented in relation to the chord width, δ_p/b_0.

Finite Element Analyses

Element Models—Finite element analyses were performed in order to assess the assumptions regarding the effects of fabrication process on the strength capacity of the X-joints [5]. The four joints from the experimental tests reported here were analyzed using nonlinear FEA. Geometrically the major difference between the CFSHS and the HFSHS X-joints was the SHS corner geometries. The dimensions for each model are seen in Table 5.

Due to symmetry it was necessary to model only 1/8 of the X-joint. Eight node solid elements were used for most of the model, but some tetra elements were placed in the transition zone. For the CFSHS models two material models were included in the analyses in order to take into account the difference in materials properties in the corner areas and the flat sections of the SHS. The FEA meshes are shown in Fig. 7. For the X18 and X20 meshes, the regions of different material properties are indicated with different shading. The effect of the corner radius alone was assessed by using the precise geometries from HFSHS and CFSHS joints but with an identical material model for both, i.e., properties from the cold-formed

TABLE 5—*The analyzed X-joints.*

ID.	Chord	r_0 (mm)	t_0 (mm)	Brace	r_1 (mm)	t_1 (mm)	β	Weld	Throat Thickness (mm)
X18	CF 100×100×10	26.2	9.93	CF 100×100×10	26.2	9.93	1.0	single bevel	10
X20	CF 100×100×10	26.2	9.97	CF 50×50×5	9.5	4.90	0.5	fillet	5.5
X22	HF 100×100×10	10.5	9.93	HF 100×100×10	10.5	9.93	1.0	single bevel	10
X23	HF 100×100×10	10.5	9.97	HF 50×50×5	5.7	4.90	0.5	fillet	5.5

section.

The boundary conditions used reflected the experimental X-joints test fixtures. The preload of the chord member is modeled as a load rather than as a displacement. This was felt to better reflect the true load conditions. Large displacements were allowed in the FE analyses. A von Mises yield criterion was used and a Newton-Raphson iteration method was applied. The MCS-Marc FEA package was used for analyzing [6].

Material Models, Strip Bending, and SHS Distortion Tests—Material σ-ε models for FEA were defined based on tensile tests with test coupons taken from the flat faces of the sections as shown in Fig. 2 and, in the case of CFSHS, also from longitudinal coupons taken from the corner areas of the section. For HFSHS the materials were assumed to be homogeneous. An example of a stress-strain curve obtained from coupon tests is seen in Fig. 8. For FEA the true stress-strain curve is used in place of the engineering stress-strain curve measured during tensile testing. The true stress-strain curve is inputted into the FEA program as a piecewise linear curve. The open symbols in Fig. 8 indicate the stress-strain combinations

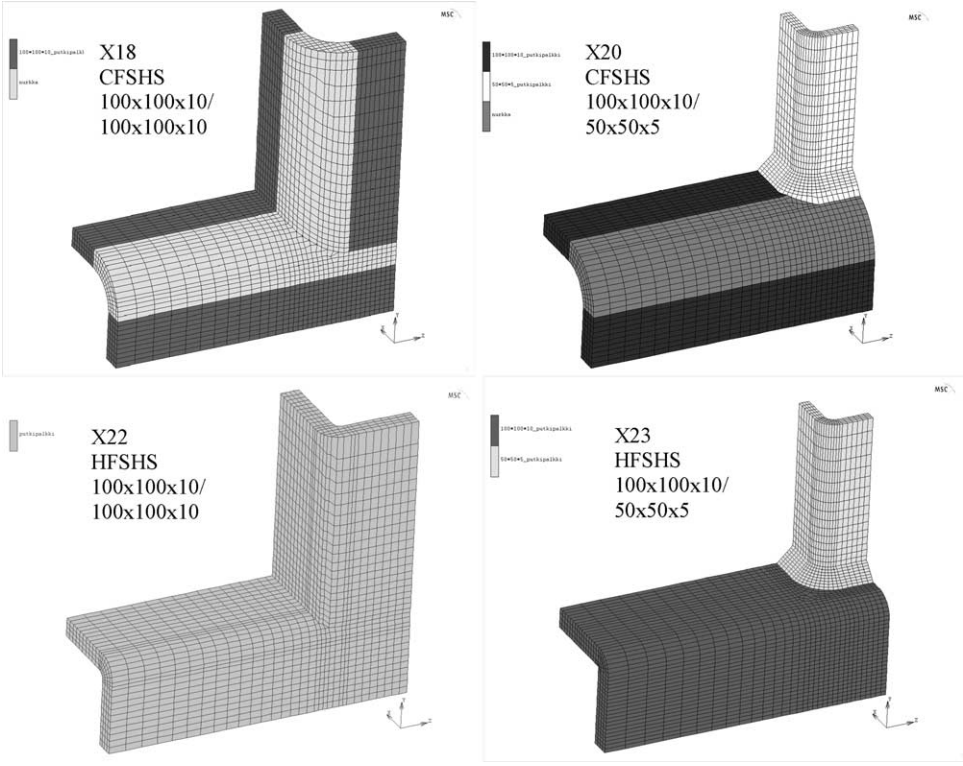


FIG. 7—*The X-joint models with material section.*

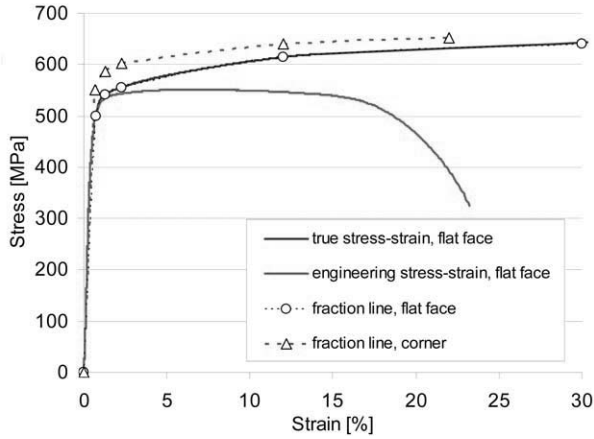


FIG. 8—*Measured σ-ε curve for the SHS flat face and true stress-strain curves for flat and corner sections of specimen* X18*. The point to point linear curves used in FEA are also indicated.*

used to define the piecewise linear curves.

Due to the extensive cold working of the CFSHS corners, the material is expected to be anisotropic. However, FEA of the SHS distortion tests showed that anisotropy had little influence on the force deformation curves. Therefore, all further FEA was performed using an isotropic material model, but with different σ-ε behavior for material on the flat edges and in the corner region of a section. In order to compare different material models, the strip bending test and the section distortion test were modeled and analyzed by nonlinear FE. In the bending test $\frac{1}{4}$ of the strip was modeled using solid elements and the material σ-ε model obtained from the tensile coupon test from material taken from the chord flange. FE models for the strip bending and SHS distortion tests are shown in Fig. 9.

Results from the bending and SHS distortion evaluations are illustrated in Fig. 10. The experimental tests curves in those figures are based on measured forces and strains. From the bending test curve, Fig. 10(*a*), it can be seen that in the region near first yielding the FE results using the measured σ-ε model slightly underestimates the load when compared to the experimental test. In the region of high plastic strain the FEA results were not fully stable due to convergence problems, but the lower bound solutions were in good agreement with the experimental results. Similar correlation would be found if the force-

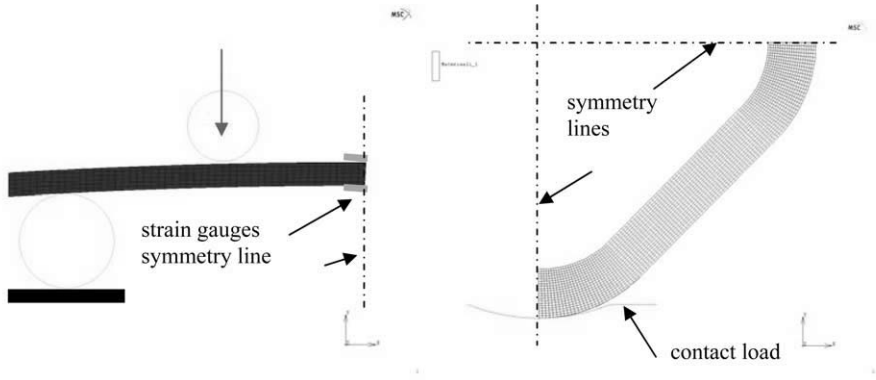


FIG. 9—*Bending and SHS distortion tests for assessing the material σ-ε models.*

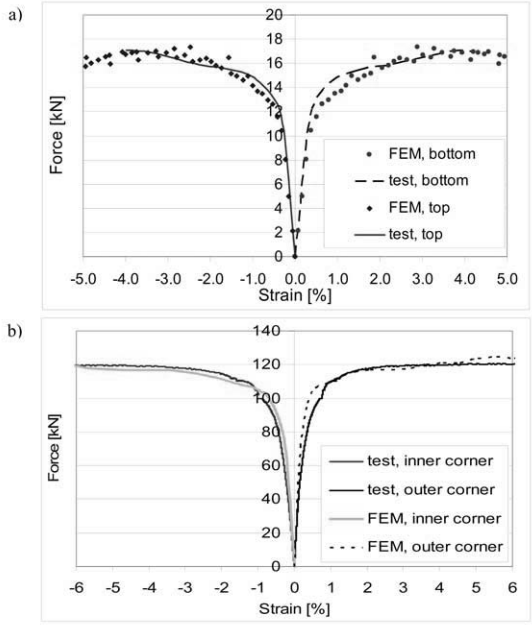


FIG. 10—*Experimental and FE results for the (a) bending, and (b) SHS distortion tests.*

deformation curve would be plotted.

Based on a comparison of the bending and SHS distortion test results and the simulation of these tests using FEA, it was judged that σ-ε model defined by tensile testing of a coupon taken from the longitudinal SHS flange was sufficient. The material, therefore, was assumed to be isotropic except for the properties in the corner and along the flat face. The analyzed X-joint with material sections are seen in Fig. 11.

The FE based force-displacement results for the four X-joint tests are seen in Fig. 11. For comparison, the experimental test results are plotted in the same figures. The X-axes in these figures represent the joint displacement as illustrated in Fig. 5. For the CFSHS material model 1 means the corner section has different material properties and in material model 2 the whole section is homogenous.

These effects of corner radius were studied numerically and the results are seen in Fig. 12. In these analyses the same material σ-ε curve is used for all models. Only the SHS geometries have been modified. All the dimensions are held constant except that the measured corner radii from the respective CFSHS and HFSHS were used. Figure 12(*a*) shows the result for X-joint with $\beta = 1.0$. This shows that the strength of the HFSHS is slightly greater for all displacements. Further evaluation revealed that the sharper corner of the brace member meant that the flat faces of the section are larger and thus there is a better load transfer between chord and brace flanges. In Fig. 12(*b*) the same type of analysis is done for joints with $\beta = 0.5$. Here it can be noticed that the CFSHS has slightly greater strength. This is due to the increased stiffness of the chord flanges caused by the greater radius.

Discussion

The current experimental investigations did not reveal any significant differences in the ultimate strength capacity of joints fabricated from HFSHS and those fabricated from CFSHS and all joints fulfill the requirements obtained in EC3. The ultimate deformation capacities are more difficult to compare, because the failure of the CFSHS joints was remote from the welded region. In all joints evaluated here, even for

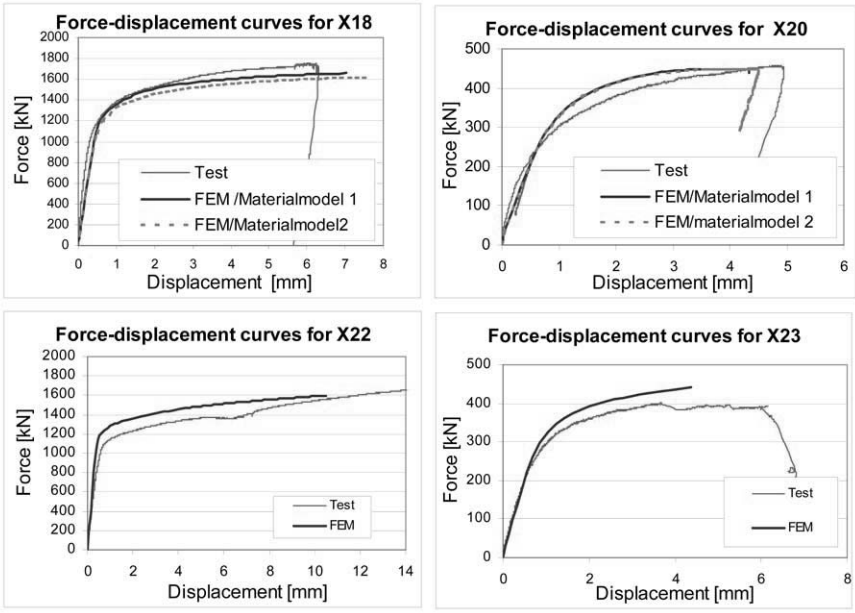


FIG. 11—*Force-joint displacement curves for X-joints in comparison.*

those exhibiting brittle fracture, the plastic deformation capacity was always larger than the 1 % value that is normally considered as good design limits for $\beta = 1$ and $\beta < 1$ joints. Some significant differences in the failure mechanisms, however, were observed. The ultimate failure mode for CFSHS was in the brace member due to large plastic deformation. In HFSHS the failure was located in the region of the welded joint.

Closer investigation of the fractured surfaces of the HFSHS joints revealed that the failure was initiated in a ductile mode but also includes evidence of brittle fracture. The fracture surface of HFSHS joint X22 is shown in Fig. 13. The fracture surface shows that the weld filler metal was ductile, but once the failure crack penetrated to the base material the joint failed in a brittle manner. The brittle fracture of the base material near the weld is probably due to the effects of welding and the very low test temperature. The base metal itself (unwelded) was fully ductile at this temperature. The initiation point of the crack is easy to understand based on the computed strain distribution around the weld as illustrated in Fig. 14. The

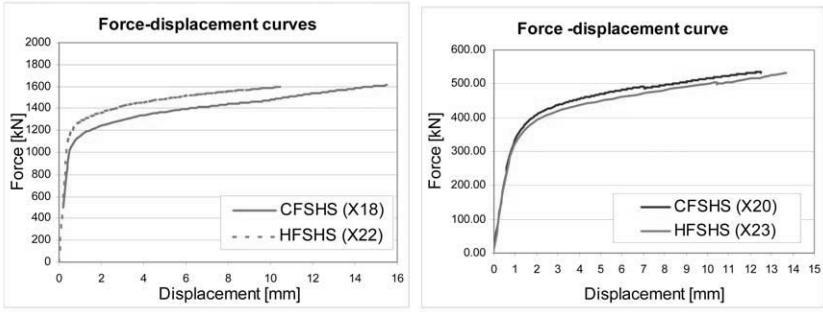


FIG. 12—*Effects of corner radius.*

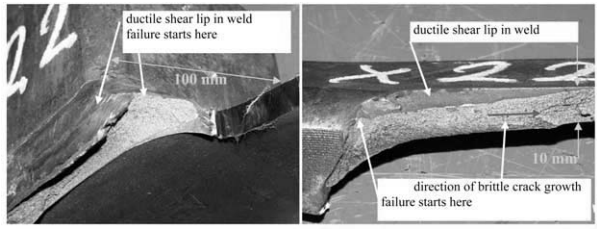


FIG. 13—*Brittle ultimate failure mode and ductile shear lip cross the weld in* X22.

sharper corners of the HFSHS resulted in significantly larger strain concentration in the corner of the X-joint. For the CFSHS the estimated maximum strain at 1580 kN was less than 14 % while for the HFSHS at the same load the strain was more than 25 %.

In X23 the fracture initiated at a lack of penetration in the middle of the flange of chord. This is a common feature for MAG welding. The crack is grown partly brittle and partly ductile manner as seen in Fig. 15.

The large degree of cold forming in the transverse direction of CFSHS due to the fabrication process seems to have relatively little effect on the load-carrying capacity of the X-joints. The isotropic material model was judged to be adequate for estimating the ultimate capacity of the joint.

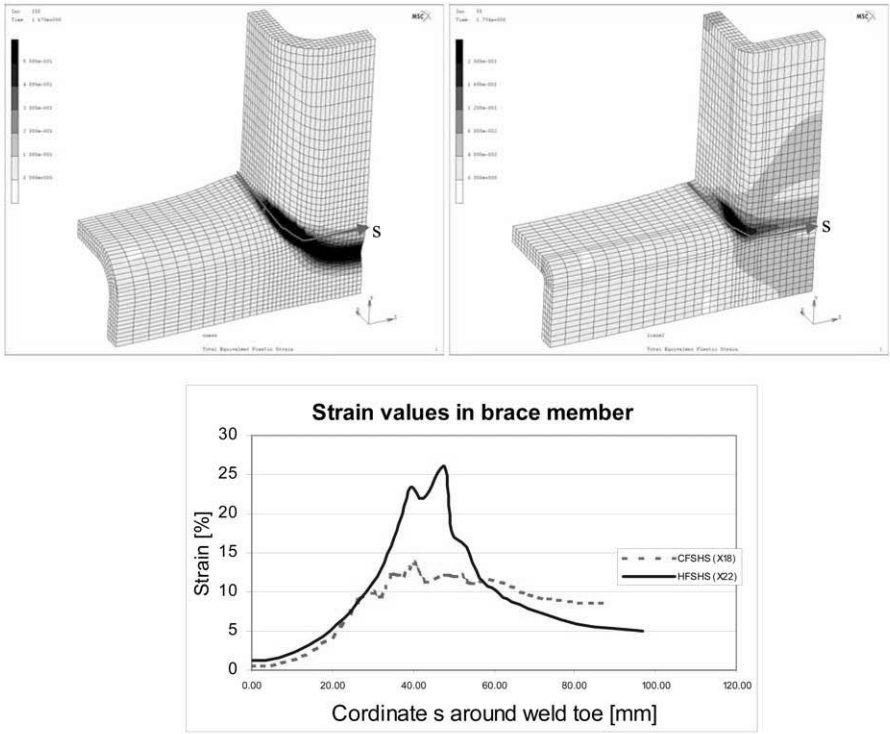


FIG. 14—*Vertical strain values in the brace member having large (CFSHS) and small (HFSHS) corner radius, the curves represent force level of ultimate load (1580 kN).*

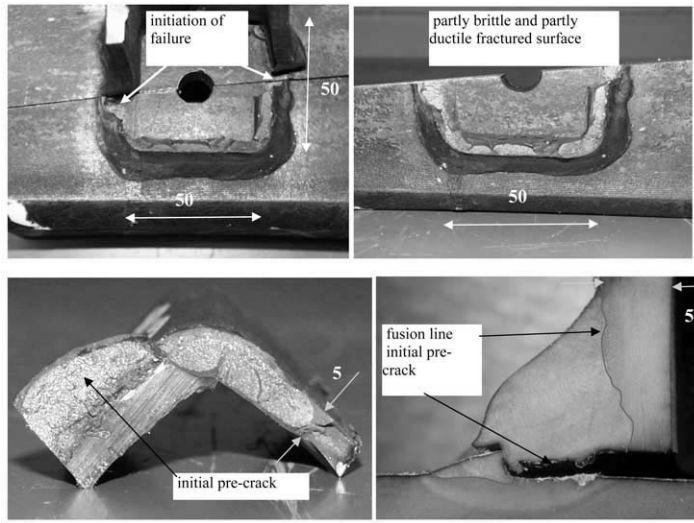


FIG. 15—*Fractured surfaces and lack of penetration* X23.

It was expected that the larger corner radius of the chord member would make the transverse face of the brace member more effective for $\beta = 1$. Experimentally it was found that the large corner radius actually resulted in a slightly smaller load-carrying capacity for CFSHS than for HFSHS with sharper corners. However, FEA revealed that this is not due to the corner radius of the chord member but due to the corner radius of the brace. The length of the flat face of the brace parallel to chord web is an important dimension. Consequently, a larger load-carrying capacity would be obtained if the brace member would be of a HFSHS and the chord a CFSHS having large corner radius.

As β decreases, a chord member with large radius has greater flange stiffness and strength. When $\beta = 0.5$, the corner radius of the brace member is less critical than for $\beta = 1.0$ and the capacity of the joint follows the stated assumptions and the larger corner radius of the chord member slightly increases the ultimate capacity of the joint. The larger corner radius of the chord member for CFSHS increases the ultimate load-carrying capacity of an X-joint if other dimensions remain unchanged.

Conclusions

The effect of the geometry and material properties on the ultimate strength of welded X-joints fabricated from CFSHS and HFSHS profiles have been studied experimentally and by using nonlinear finite element analysis. Laboratory experiments were performed at temperature $-40\,^{\circ}C$. The main differences between CFSHS and HFSHS profiles are the corner geometry and the increased material strength and lower ductility properties in the corners of the CFSHS due to coldforming. Numerical simulation and experimental tests focused on the importance of this corner effect and the separate role geometry, yield strength, and fracture toughness on the total fracture strength of the joint. The following conclusions can be made:

(1) Equations found in design guidance document, EC3, could be used to estimate the capacity of CHSHS at temperatures as low as $-40\,^{\circ}C$.
(2) Equations found in EC3 did not correctly predict the ultimate failure mode for the low width to thickness ratio CFSHS X-joints evaluated in this study.
(3) For HFSHS joints, the primary failure model was ductile fracture in the region of the welds followed by brittle fracture.
(4) For CFSHS joints, the primary failure mechanism was ductile yielding of the brace members remote from the weld region.

(5) The force-displacement behavior of the X-joint could be adequately modeled using the assumption of isotropic material behavior.
(6) The method of SHS fabrication had only a small influence on the ultimate capacity of the X-joints but it significantly altered the final failure mode.
(7) The corner radius of the SHS has a small but clear effect on the behavior of the X-joint.

References

[1] Soininen, R., "Fracture Behavior and Assessment of Design Requirement Against Fracture in Welded Steel Structures Made of Cold-formed Rectangular Hollow Sections," Ph.D. Thesis, Lappeenranta University of Technology, 1996.
[2] prEN1993-1-8. "*Design of Steel Structures, Part 1–8: Design of Joints*," European Committee for Standardization, 2003.
[3] SFS-ENV 1993-1-1:1992, Eurocode 3, *Design of Steel Structures, Part 1–1, General Rules and Rules for Buildings*, European Prestandard, CEN, European Committee for Standardization.
[4] N37B, *Execution of Steel Structures and Aluminum Structures*, prEN1090, Chapter 7, Welding, European Committee for Standardization, 2002.
[5] Pellikka, V., "On the Definition of Material Model, Stiffness and Ultimate Strength for Cold-formed Structural Hollow Section X-joint," Master's Thesis, Lappeenranta University of Technology, 2004 (in Finnish).
[6] MSC.Marc 1997, Volume A, *Theory and User Information*, Version 1997, Santa Ana, MSC.Software Corporation.

Journal of ASTM International, Vol. 3, No. 6
Paper ID JAI13209
Available online at www.astm.org

Xian-Kui Zhu[1] *and Brian N. Leis*[1]

Constraint Corrected *J-R*- Curve and Its Application to Fracture Assessment for X80 Pipelines

ABSTRACT: Single specimen *J-R* curve testing for X80 pipeline steel was conducted using single edge notched bend (SENB) and single edge notched tension (SENT) specimens with various crack lengths. Test data indicate that the *J-R* curves for this steel are strongly constraint dependent. To facilitate transferability of experimental *J-R* curves to those for actual cracked components, this paper develops a constraint corrected *J-R* curve for X80 steel. A modified *J-Q* theory that can consider the global bending stress influence is proposed so as to correctly quantify constraint effect on the crack-tip fields and the *J-R* curves. Results show that the modified *J-Q* solution can well match numerical crack-tip fields for bending specimens, with *Q* being a load-independent constraint parameter under large scale yielding. Based on the experimental data and numerical analysis, a constraint corrected *J-R* curve is formulated as a function of the parameter *Q* and crack extension Δa for X80 steel. A general procedure to predict *J-R* curves for actual cracked components is then outlined.Comparison indicates that the predicted *J-R* curves developed in this paper agree well with the experimental data for both SENB and SENT specimens. To demonstrate its application in failure assessment, the constraint corrected *J-R* curve for X80 steel is used to determine failure loads for a surface cracked pipeline. Reasonable agreement to available analytic solution is achieved.

KEYWORDS: constraint effect, *J-Q* theory, *J-R* curve, fracture toughness, failure assessment, X80 steel, pipeline

Introduction

Fracture toughness experiments [1–3] have shown that fracture resistance curves against ductile crack growth, i.e., *J-R* curves, depend on geometry or constraint at the crack tip for ductile materials. The constraint dependence has been an issue for transferability of experimental *J-R* curves determined using standard laboratory specimens to actual cracked components. Standard specimens for fracture toughness testing include SENB and compact tension (CT) specimens with deep cracks and strict size requirements to ensure high constraint levels at the crack tip, as specified in ASTM E 1820-01 [4], while other specimens or actual surface cracked components usually involve low constraints. In general, application of *J-R* curves from high-constraint specimens to low-constraint geometry introduces a degree of conservatism into design analysis. Conversely, for some special cases, fracture toughness data are obtained from relatively low-constraint specimens and used in high-constraint applications, which could result in a nonconservative design [2]. A more detailed review with respect to the investigations of constraint effect on *J-R* curves can be found in Zhu and Jang [5].

Structural integrity assessment of pipelines is a critical concern for both designers and operators for the design and operation of onshore and offshore oil and gas facilities. Conventional failure assessment methods applicable to pipelines containing service-induced defects generally use simplified failure criteria, such as ASME B31G criterion [6] and RSTRENG criterion [7], which were empirically derived from experimental analysis. Ductile material failure including leakage and sudden rupture in a flawed pipeline may occur after large amounts of slow stable crack growth until a critical crack size is reached. For sustained ductile tearing of a crack, a large increase in the loading-carrying capacity, as characterized by *J-R* curves, is possible beyond the limits by the conventional analysis. Therefore, a realistic elastic-plastic fracture analysis is useful in integrity assessment of pipelines. However, it relies on reasonable application

Manuscript received April 8, 2005; accepted for publication March 6, 2006; published online May 2006. Presented at ASTM Symposium on Fatigue and Fracture Mechanics: 35th Volume on 18–20 May 2005 in Reno, NV; R. E. Link and K. M. Nikbin, Guest Editors.

[1] Senior Research Scientist and Senior Research Leader, respectively, Battelle Memorial Institute, 505 King Avenue, Columbus, OH 43201.

Copyright © 2006 by ASTM International, 100 Barr Harbor Drive, PO Box C700, West Conshohocken, PA 19428-2959.

of measured *J-R* curves, and correct understanding of the constraint dependence of *J-R* curves. As a result, a viable method needs to be developed to transfer the fracture resistance data measured with small laboratory specimens to those for actual components and structures.

In recent years, more and more researchers have been attracted to investigate the constraint dependence of fracture resistance for pipeline steels. Pisarski and Wignall [8] presented experimental data of constraint-dependent CTOD fracture resistance curves for X52 pipeline steel. Dong et al. [9] experimentally investigated the coupled effects of out-of-plane constraint and delamination on fracture toughness for X60 pipeline steel. Hippert et al. [10] reported the constraint dependence of experimental *J-R* curves for X70 (or X65) pipeline steel. Pavankumar et al. [11] performed fracture testing of *J-R* curves for SA333 Gr 6 steel using full-scale cracked pipes under four point bending and their experimental results were geometry dependent. Most recently, Shen et al. [12] reported the detailed experimental results of *J-R* curves using SENB and SENT specimens for various cracks, and again their results indicated significant constraint effect on the *J-R* curves for X80 and X100 pipeline steels.

To quantify the crack-tip constraint levels, different fracture constraint theories have been proposed, and many numerical analyses have been performed under both two- and three-dimensional conditions [13–20]. To improve the single-parameter solution, several two-parameter fracture approaches have been developed [20], including the *J-Q* theory proposed by O'Dowd and Shih [13–15] and the *J-*A_2 three-term solution proposed by Yang et al. [18,19], where Q and A_2 are constraint parameters. Zhu and Jang [5] extended the *J-Q* theory to quasi-static cracks, and developed a new methodology for constructing a family of *J-R* curves corrected by a load-independent constraint parameter for ductile crack growth, with incorporation of experimental and numerical analyses. Similarly, Refs. [21–23] studied the constraint corrected *J-R* curves based on the *J-*A_2 solution. This paper will modify the *J-Q* theory to consider the global bending influence, and then extend the methodology proposed in Ref. [5] to determine a constraint corrected *J-R* curve for X80 pipeline steel.

Experimental *J-R* curves for X80 pipeline steel were obtained using SENB and SENT specimens, and used to determine the fracture initiation toughness at crack extension of 0.2 mm and the *J*-integral values at the crack extension of 1.0 mm. To consider the global bending stress influence on the crack-tip field for bending specimens, a modified *J-Q* theory was proposed with Q as a load-independent constraint parameter under large scale yielding (LSY). Using the power-law relationship suggested in ASTM E 1820, a mathematical expression representing a family of constraint dependent *J-R* curves for X80 steel was formulated as a function of the constraint parameter Q and crack extension Δa. With this expression, the *J-R* curve for a specific cracked geometry can be predicted, provided that the Q is known for that geometry. Correspondence between the predicted *J-R* curves and the experimental data was evaluated for both SENB and SENT specimens. Application of the constraint corrected *J-R* curve was demonstrated by determining failure load for a surface cracked pipeline.

Experimental Measurements

Material and Specimen Descriptions

The material used was a high strength pipeline steel: API 5L X80 or N550, as detailed in Ref. [8]. The chemical compositions of X80 steel (wt %) are C: 0.05, Mn: 1.80, P: 0.006, S: 0.002, Si: 0.27, Cu: 0.28, Ni: 0.11, Cr: 0.04, Mo: 0.13, Nb: 0.035, and Ti: 0.01. Figure 1 presents the engineering stress-strain data and the true stress-strain curve for X80 steel, where the 0.2 % offset yield stress of 570 MPa, ultimate tensile stress of 675 MPa, Young's modulus $E=207$ GPa and Poisson's ratio $\nu=0.3$. As shown in Fig. 1, the true stress-strain curve is best fitted by the Ramberg-Osgood power-law relation:

$$\frac{\varepsilon}{\varepsilon_0}=\frac{\sigma}{\sigma_0}+\alpha\left(\frac{\sigma}{\sigma_0}\right)^n \tag{1}$$

where $\sigma_0=570$ MPa, $\varepsilon_0=\sigma_0/E=0.00275$, $\alpha=1.07$, and $n=13$.

SENB and SENT specimens were used to measure *J-R* curves for X80 pipeline steel. Dimensions for SENB specimens recommended by ASTM E 1820 were used, except for the initial crack length which was varied to develop different constraint levels at the crack tip. The specimen width, W, is 23 mm, and the initial crack length a varies producing ratios of a/W between 0.24 and 0.64. The ligament length $b=W$

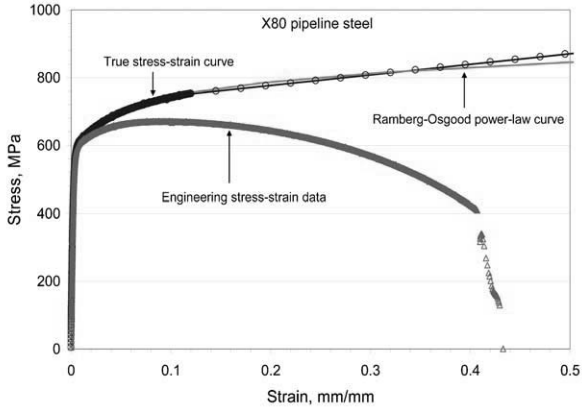


FIG. 1—*Stress-strain responses of X80 pipeline steel.*

$-a$, specimen thickness is 11.5 mm, and beam span is 92 mm. For SENT specimens, $W=B=11.5$ mm, specimen length is 92 mm, and $a/W=0.22\sim0.61$. While SENB specimens were loaded in three-point bending, SENT specimens were loaded by fixed-grip tension. All specimens were fatigue precracked according to the procedure in ASTM E 1820, and then side grooved using a Charpy cutter to a total thickness reduction of 20 %, in an attempt to develop plane strain conditions along the crack front. All specimens were oriented in the L-C direction, and tested at room temperature (about 20°C).

Experimental Data of J-R Curves

Single-specimen *J-R* curves for X80 pipeline steel was measured by Shen et al. [12] using both SENB and SENT specimens under quasi-static loading at room temperature. For the SENB specimens, determination of *J-R* curves followed the standard procedures of ASTM E 1820 except that η and γ factors provided in Ref. [2] for shallow cracks of $a/W<0.282$ were used. Note that *J-R* curve testing for shallow cracked SENB is outside the standard and can lead to inaccurate results. After test, the specimens were heat tinted and then broken in liquid nitrogen. The initial and final crack lengths were measured on the fracture surface by the 9-point technique as described in E 1820. Severe splitting was observed during tests with difference as high as 40 % for final crack length. However, splitting was not observed for small crack extension $\Delta a\leqslant0.2$ mm. Similar splitting (or delamination) during crack growth was found for X70 pipeline steel [24]. Figure 2 shows the experimental *J-R* curves obtained by Shen et al. [12] for the X80 SENB specimens. Considerable difference of *J-R* curves between the shallow and deep cracks is observed from this figure.

The initiation toughness (J_i) used to characterize fracture resistance at the onset of stable ductile crack growth can be defined on the *J-R* curve at the critical stretch zone width (Δa_i), which can be measured on the fracture surface using a scanning electron microscope [11,25]. It was reported that $\Delta a_i\approx0.2$ mm for XCrNi1811 structural steel [26] and for SA333 Gr6 pressure vessel steel [11]. Since splitting was not observed as $\Delta a\leqslant0.2$ mm for X80 steel, the crack extension of 0.2 mm is used to define approximate fracture initiation in this work. From Fig. 2, initiation toughness of X80 steel at $\Delta a=0.2$ mm are obtained as 420, 407, 290, 370, 250, and 287 kJ/m^2 for $a/W=0.24$, 0.25, 0.42, 0.43, 0.63, and 0.64, respectively. In contrast, ASTM E 1820 defines the fracture initiation toughness as J_Q at the intersection of the measured *J-R* curve and the 0.2 mm offset line: $J=M\sigma_Y(\Delta a-0.2)$, where $M\geqslant2$ and σ_Y is the effective yield strength. For X80 steel, $M\approx3$, $\sigma_Y=622.5$ MPa, the 0.2 mm offset line is $J=1868(\Delta a-0.2)$, as included in Fig. 2. It is seen that the 0.2 mm offset toughness J_Q varies from 400 to 1010 kJ/m^2, which represents a much larger range than the initiation toughness defined at 0.2 mm crack extension.

For the SENT specimens, a standardized procedure to determine the *J-R* curves is not available yet. Based on an estimation method, Shen et al. [12] obtained the experimental *J-R* curves for SENT speci-

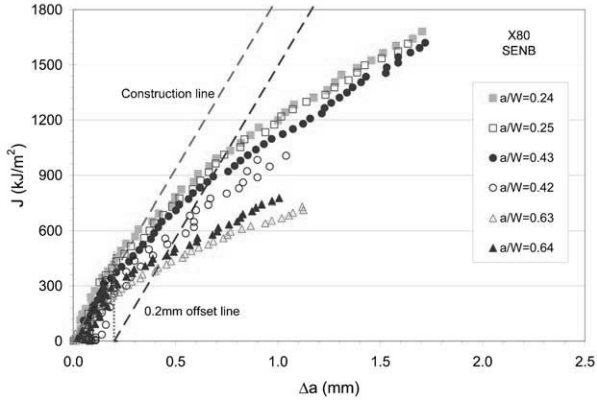


FIG. 2—*Experimental J-R curves for SENB specimens.*

mens, as shown in Fig. 3. It is evident again that significant difference of *J-R* curves exists between the shallow and deep cracks for X80 pipeline steel. The experimental results of *J-R* curves for the SENT specimens will be used to validate the predicted *J-R* curves, which are formulated using the test data for the SENB specimens.

Numerical Calculations and Constraint Analyses

Finite Element Modeling

Plane strain elastic-plastic finite element analysis (FEA) was performed using the general purposed FEA software, ABAQUS Standard [27], to calculate the full-field stress and strain fields and to determine fracture constraint parameters for the test specimens. Due to symmetry, only one-half of each specimen was modeled using the typical FEA mesh illustrated in Fig. 4. A fine mesh was used with the smallest element size of 0.002 mm focused on the crack tip, and an increasingly coarse mesh was generated elsewhere. The FEA mesh consists of 1925 nodes and 604 eight-node plane strain isoparametric elements with reduced integration. The local mesh encircling the crack tip contains 23 rings of elements with each

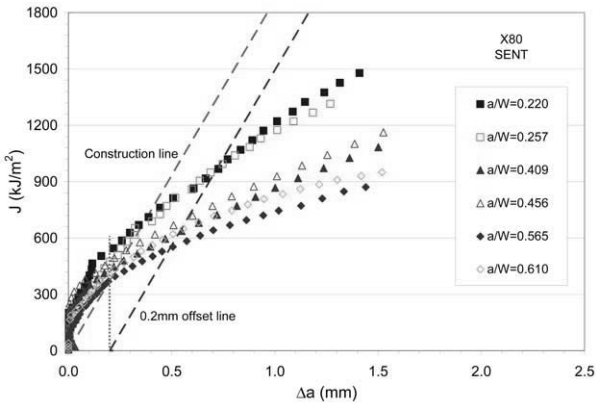


FIG. 3—*Experimental J-R curves for SENT specimens.*

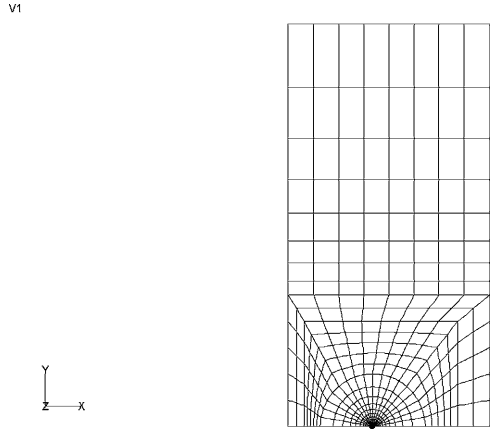


FIG. 4—*Typical finite element mesh used for test specimens.*

ring having 18 elements. The same number of elements and nodes were used for all test specimens. For the SENB specimens, a concentrated load was applied on the top of ligament. For the SENT specimens, a uniform distributed load was applied on the ends.

In the FEA simulation, the incremental theory of plasticity with the von Mises yield criterion was employed. The incremental form of nonlinear stress-strain relation can be generally expressed as:

$$\frac{d\varepsilon_{ij}}{\varepsilon_0} = (1+\nu)\frac{d\sigma_{ij}}{\sigma_0} - \nu\frac{d\sigma_{kk}}{\sigma_0}\delta_{ij} + \frac{3}{2}n\alpha\left(\frac{\sigma_e}{\sigma_0}\right)^{n-2}\frac{d\sigma_e}{\sigma_0}\frac{s_{ij}}{\sigma_0} \tag{2}$$

where δ_{ij} is the Kronecker delta, $s_{ij}=\sigma_{ij}-\sigma_{kk}\delta_{ij}/3$ is the deviatoric stress, and $\sigma_e=(3s_{ij}s_{ij}/2)^{1/2}$ is the Mises equivalent stress. It is noted that for simple loading, the deformation theory of plasticity can obtain FEA results identical to the incremental theory of plasticity for large-scale yielding (LSY) or fully plasticity, but saves a lot of computation time.

Figures 5 and 6 show distributions of the crack opening stress, $\sigma_{\theta\theta}$, obtained from the FEA (as denoted by symbols) at different deformation levels as a function of distance from the crack tip for the SENB specimens with a shallow crack of $a/W=0.24$ and a deep crack of $a/W=0.64$, respectively. The numerical results in these figures show that the opening stress near the crack tip decreases as loading increases for normalized distance r. Under LSY (or $b\sigma_0/J<70$), for both shallow and deep cracks, the distribution of $\sigma_{\theta\theta}$ with the normalized distance is nearly linear when $r/(J/\sigma_0)\geq 1$, which indicates the significant influence of global bending stress on the crack-tip stress fields. The following sections will discuss how to use the *J-Q* theory to correctly describe the crack-tip fields, and quantify the constraint levels at the crack tip.

The J-Q Theory

From detailed FEA analysis, O'Dowd and Shih [13,14] found that the difference between the full-field solution, σ_{ij}, and the HRR field, σ_{ij}^{HRR}, is approximately a uniform hydrostatic stress ahead of the crack tip. Thus, they developed the following crack-tip stress field:

$$\sigma_{ij} = \sigma_{ij}^{HRR} + Q_{HRR}\sigma_0\delta_{ij} \quad \text{for } r > J/\sigma_0 \quad \text{and} \quad |\theta| \leq \pi/2 \tag{3}$$

where Q_{HRR} (i.e., Q, originally denoted in [13]) is a triaxial stress parameter reflecting the hydrostatic stress level at the crack tip, and σ_{ij}^{HRR} is the well known HRR singularity stress field [28,29], and is expressed by

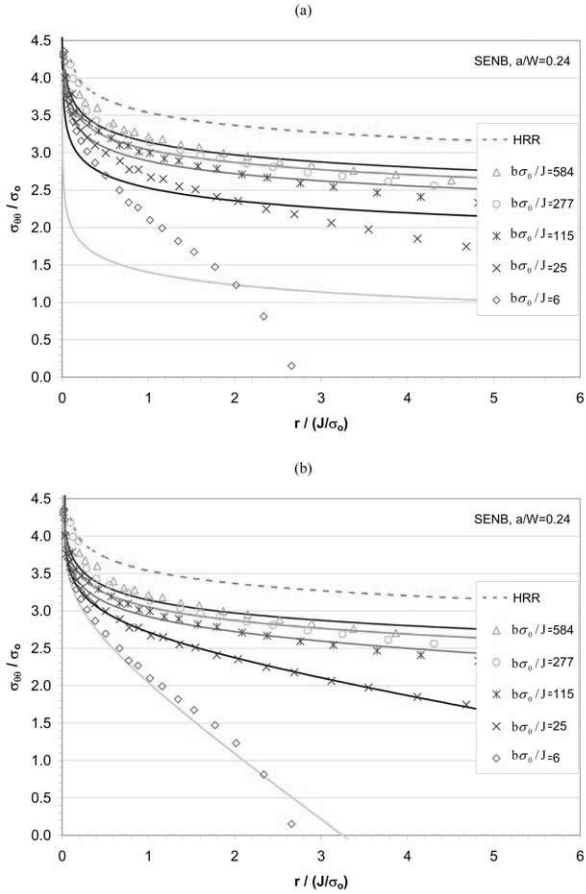


FIG. 5—*Distribution of crack opening stress along the uncracked ligament from the crack tip for a/W = 0.24 (symbols represents FEA results, and lines represents J-Q solutions), based on: (a) the J-Q theory, (b) the modified J-Q theory.*

$$\frac{\sigma_{ij}^{HRR}}{\sigma_0} = \left[\frac{J}{\alpha\varepsilon_0\sigma_0 I_n r}\right]^{\frac{1}{n+1}} \tilde{\sigma}_{ij}(\theta, n) \tag{4}$$

where J is the J-integral, (r, θ) are the polar coordinates centered at the crack tip, I_n is an integration constant and $\tilde{\sigma}_{ij}(\theta, n)$ are dimensionless stress functions. The values of I_n and $\tilde{\sigma}_{ij}(\theta, n)$ were tabulated in Ref. [30].

A Modification of J-Q Theory

Due to simplicity, the *J-Q* theory is widely used in engineering fracture constraint analysis [1,2,16]. However, the Q in Eq 3 is a load-dependent parameter, and thus it varies during the crack extension [17]. For a specific *J-R* curve, one may expect a constant constraint parameter during ductile crack growth. For this purpose, Zhu et al. [31] introduced a modified parameter Q by

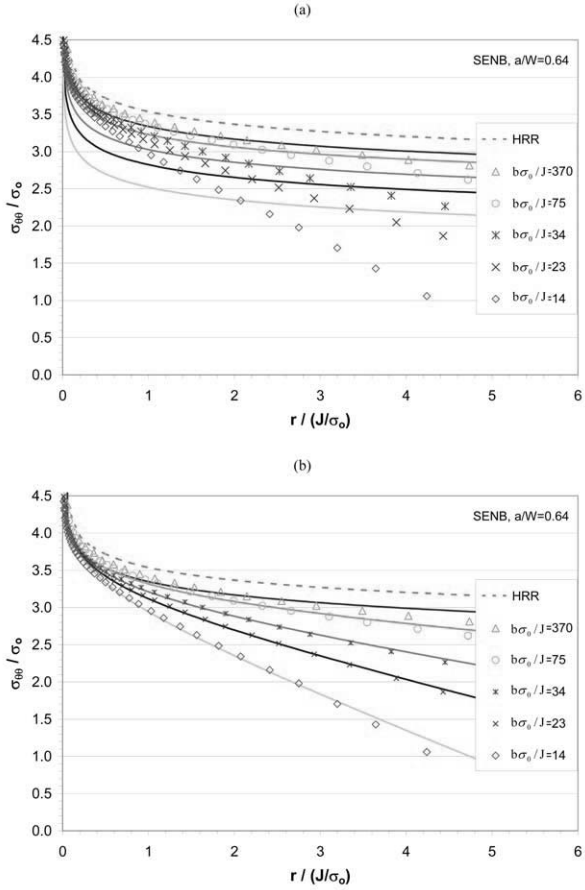


FIG. 6—*Distribution of crack opening stress along the uncracked ligament from the crack tip for a/W=0.64 (symbols represents FEA results, and lines represents J-Q solutions), based on: (a) the J-Q theory, (b) the modified J-Q theory.*

$$Q = \left[\frac{J}{\alpha\varepsilon_0\sigma_0 I_n L}\right]^{-\frac{1}{n+1}} Q_{HRR} \tag{5}$$

By substituting Eqs 4 and 5 into Eq 3, the *J-Q* field becomes

$$\frac{\sigma_{ij}}{\sigma_0} = \left[\frac{J}{\alpha\varepsilon_0\sigma_0 I_n L}\right]^{\frac{1}{n+1}} \left[\left(\frac{1}{r/L}\right)^{\frac{1}{n+1}} \tilde{\sigma}_{ij}(\theta,n) + Q\delta_{ij}\right] \quad \text{for } r > J/\sigma_0 \quad \text{and} \quad |\theta| \leq \pi/2 \tag{6}$$

where L is a characteristic length and chosen as 1 mm. Numerical analysis has showed that the Q defined in Eq 6 was a load-independent constraint parameter for most deformation levels in the region of interest. Moreover, Refs. [5,31] pointed out that the modified parameter Q is theoretically independent of applied J under fully plastic deformation.

Reference [14] indicated that the original parameter Q is somewhat distance-dependent under large applied loads, although Eq 3 was valid for most deformation levels in the region of interest, $1 < r/(J/\sigma_0) < 5$. The small-scale yielding (SSY) solution, $(\sigma_{ij})_{SSY}$, was then suggested to replace the HRR

field so that Q can be approximately distance-independent in the region of interest [15]. However, recent work [16] indicated that the SSY solution-based parameter Q was still distance-dependent in the interest region for different bending specimens (e.g., SENB, CT, and SENT) under LSY. Apparently, the distance dependence of Q for these specimens is caused by the global bending stress. Under such circumstance, the J-Q theory fails to correctly describe the crack-tip field. Therefore, an attempt is made here to modify the J-Q theory for reflecting the global bending stress influence on the crack-tip fields. As an approximation, it is assumed that actual crack-opening stress at $\theta=0^\circ$ ahead of the crack tip in bending specimens is a simple superposition of the J-Q stress solution and a linearized global bending stress:

$$\frac{\sigma_{\theta\theta}(r,0)}{\sigma_0}=\left[\frac{J}{\alpha\varepsilon_0\sigma_0 I_n L}\right]^{\frac{1}{n+1}}\left[\left(\frac{1}{r/L}\right)^{\frac{1}{n+1}}\tilde{\sigma}_{\theta\theta}(0,n)+Q\right]-\frac{\alpha M r}{\sigma_0 b^3} \tag{7}$$

where the plane strain condition is adopted, M is the global bending moment, α is a linearization factor for the nonlinear bending stress, which can be determined using a two-point matching approach. A similar bending stress modification was proposed for the J-A_2 solution [32].

For a given applied load J under LSY, the constraint parameter Q is expected being distance-independent. If the opening stresses determined by FEA at two points $r=r_1$ and $r=r_2$ within $1<r/(J/\sigma_0)<5$ are denoted as $\sigma_{\theta\theta}^{FEA}(r_1,0)$ and $\sigma_{\theta\theta}^{FEA}(r_2,0)$, from Eq 7, the factor α for the geometry can be determined by

$$\alpha=\frac{\sigma_0 b^3}{M(r_2-r_1)}\left\{\left[\frac{J}{\alpha\varepsilon_0\sigma_0 I_n}\right]^{\frac{1}{n+1}}\left(\left(\frac{1}{r_2}\right)^{\frac{1}{n+1}}-\left(\frac{1}{r_1}\right)^{\frac{1}{n+1}}\right)\tilde{\sigma}_{\theta\theta}(0,n)+\left(\frac{\sigma_{\theta\theta}^{FEA}(r_2,0)}{\sigma_0}-\frac{\sigma_{\theta\theta}^{FEA}(r_1,0)}{\sigma_0}\right)\right\}. \tag{8}$$

With the values of α, the constraint parameter Q can be determined by matching the opening stress from the modified J-Q solution, i.e., Eq 7, with the FEA result at $r/(J/\sigma_0)\approx 2$:

$$Q=\left[\frac{J}{\alpha\varepsilon_0\sigma_0 I_n L}\right]^{-\frac{1}{n+1}}\left(\frac{\sigma_{\theta\theta}^{FEA}(r,0)-\sigma_{\theta\theta}^{HRR}(r,0)}{\sigma_0}+\frac{\alpha M r}{\sigma_0 b^3}\right) \tag{9}$$

Determination of Constraint Parameter Q

The constraint parameter Q is determined using the FEA results and Eq 9. Figure 7 plots the variations of Q with the applied loading J for the three SENB specimens with $a/W=0.24$, 0.42, and 0.64. The Q in Fig. 7(*a*) is determined by the J-Q solution or Eq 6, while the Q in Fig. 7(*b*) is determined by the modified J-Q solution or Eq 7, with the parameter α determined by Eq 8 as $\alpha\approx 6$ for the shallow crack of $a/W=0.24$ and $\alpha\approx 12$ for the deep cracks of $a/W=0.42$ and 0.64. Figure 7(*a*) shows that the parameter Q determined by Eq 6 strongly depends on loads under LSY ($b\sigma_0/J<70$ or $Log(J/b\sigma_0)>-1.85$) for all three specimens. This implies that the global bending stress has significantly impinged the crack-tip fields for bending specimens under LSY. In contrast, Fig. 7(*b*) shows that after considering the global bending influence, the parameter Q determined by Eq 7 is nearly a load-independent constant for all specimens. The constant values of Q are -0.475, -0.236, and -0.120, respectively, for $a/W=0.24$, 0.42, and 0.64. This load-independent parameter Q is thus a reasonable candidate used to quantify the constraint level of J-R curve for a specific geometry.

With the values of Q, the crack-tip stress fields can be determined from the (modified) J-Q solution for a given load of J (and M). Figures 5(*a*) and 6(*a*) show distributions of the opening stress determined from the J-Q solution or Eq 6 at five deformation levels from SSY to LSY for the SENB specimens with a shallow crack of $a/W=0.24$ and a deep crack of $a/W=0.42$, respectively. In comparison, Figs. 5(*b*) and 6(*b*) show distributions of the opening stress determined from the modified J-Q solution or Eq 7 at the same deformation levels for the two specimens. All these figures include the HRR solution. It clearly indicates that the modified J-Q solution matches the FEA results well at all deformation levels. From these results and our other experience, a basic guidance for choosing the asymptotic solutions is drawn as: (1) the single parameter HRR field can be used for deep cracked bending specimens under small loading or SSY; (2) the two-parameter J-Q solution can be used for bending specimens at intermediate loading or contained yielding and for any tensile geometry; (3) the proposed modified J-Q solution should be used for bending specimens under large loading or LSY (e.g., $b\sigma_0/J<70$). The following sections will use the

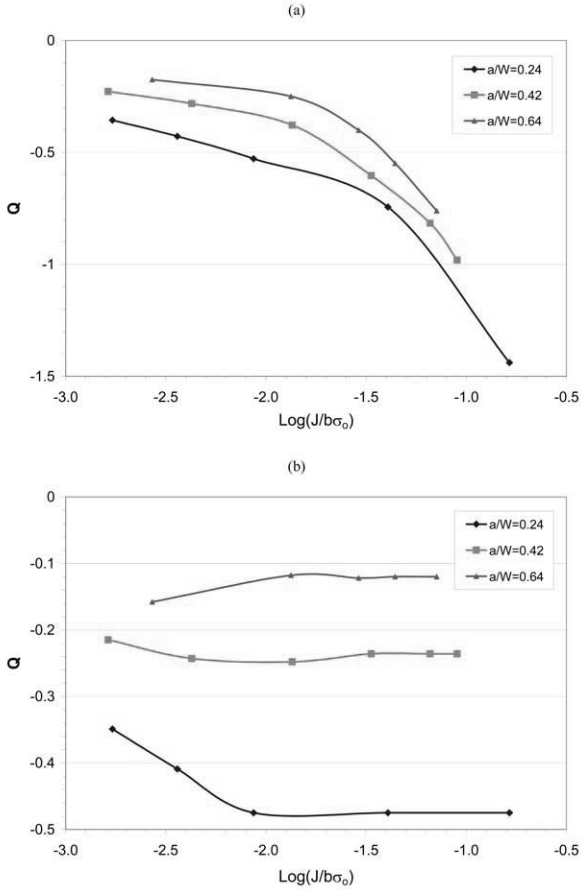


FIG. 7—*Variation of Q with J for SENB specimens based on (a) the J-Q theory, (b) the modified J-Q theory.*

modified *J-Q* solution to characterize the crack-tip field and quantify the crack-tip constraint level for X80 pipeline steel.

Constraint Correction of *J-R* Curves for X80 Pipeline Steel

General Methodology

Following the concept of *J*-controlled crack growth, Zhu and Jang [5] proposed a concept of *J-Q* controlled crack growth by extending the *J-Q* two-parameter description for stationary cracks to quasi-static growing cracks for small crack extension. They applied the *J-Q* theory to analyze ductile crack growth, and developed an engineering method to quantify the constraint effect on the *J-R* curves for ductile materials.

As demonstrated above for X80 steel, the constraint parameter *Q* in the modified *J-Q* field or Eq 7 is nearly load-independent for bending specimens under LSY, and thus the *Q* determined at the crack initiation load can remain constant for subsequent stable crack growth within the *J-Q* dominant region.

Under which conditions, the curve of J-resistance versus crack extension, Δa, can be expressed by a power-law relationship, as suggested in ASTM E 1820:

$$J(\Delta a, Q) = C_1(Q)\left(\frac{\Delta a}{k}\right)^{C_2(Q)} \tag{10}$$

where $k=1$ mm, the coefficients $C_1(Q)$ and $C_2(Q)$ are undetermined functions of Q, which are different from the constants used in the original E 1820 formulation. Equation 10 extends the current ASTM constraint-independent formulation of J-R curves, $J(\Delta a)$, to a constraint-dependent formulation of J-R curves, $J(\Delta a, Q)$. Once the functional forms of $C_1(Q)$ and $C_2(Q)$ are obtained, a family of constraint dependent J-R curves is completely determined.

Zhu and Jang [5] proposed a procedure to determine the functions C_1 and C_2 in reference to the initiation toughness and the ductile tearing modulus defined in E 1820. More generally, one can establish two equations at any two points of crack extension based on experimental J-R curves. The crack extensions at the two points are denoted as Δa_1 and Δa_2, and the J-integrals at the two points are denoted by

$$J_1 = J_{\Delta a_1}(Q)$$

$$J_2 = J_{\Delta a_2}(Q) \tag{11}$$

where $J_{\Delta a_1}(Q)$ and $J_{\Delta a_2}(Q)$ are two known functions of Q determined by best-fitting test data from at least three experimental J-R curves. In principle, if crack extension $\Delta a_i (i=1-2)$ is chosen between 0.2 mm and 2 mm, it automatically satisfies the E 1820 criterion for acceptable data. However, if a specimen exhibits much longer crack extension ($\Delta a > 2$ mm), choosing Δa_2 outside of that range may yield a better overall fit for the J-R curves [23].

Substituting Eqs 11 into 10, one obtains the following simultaneous equations:

$$C_1(Q)\left(\frac{\Delta a_1}{k}\right)^{C_2(Q)} = J_{\Delta a_1}(Q)$$

$$C_1(Q)\left(\frac{\Delta a_2}{k}\right)^{C_2(Q)} = J_{\Delta a_2}(Q) \tag{12}$$

Equation 12 can be used to determine the functions C_1 and C_2 of Q. Based on past studies, a valid range of Q is between -1 and 0, as the crack-tip constraint varies from low to high. For a series of Q values within this range ($-1 < Q < 0$), functions C_1 and C_2 can be solved with dependencies of Q. And then, the least-square regression analysis provides the desired functional forms of C_1 and C_2 with respect to the constraint parameter Q.

For a given material, once the mathematical expression for constraint dependent J-R curves, or Eq 10, is obtained, the J-R curve can be simply predicted for any specific cracked geometry (e.g., nonstandard specimens or actual flawed components), provided that the constraint parameter Q is determined for that geometry.

Determination of Constraint Corrected J-R Curve

Following the general procedures described above and using the experimental data of J-R curves for SENB specimens shown in Fig. 2, a family of constraint-dependent J-R curve in reference to the load-independent constraint parameter Q can be constructed for X80 pipeline steel. Two points: $\Delta a_1 = 0.2$ mm and $\Delta a_2 = 1.0$ mm with $J_1 = J_{0.2\ \mathrm{mm}}$ and $J_2 = J_{1.0\ \mathrm{mm}}$ are chosen to set up two equations for solving for C_1 and C_2. At the loading level of $J_{0.2\ \mathrm{mm}}$, the Q is determined for each SENB specimen using the modified J-Q solution, and it remains constant at the loading of $J_{1.0\ \mathrm{mm}}$. Figure 8 illustrates the $J_{0.2\ \mathrm{mm}}$ versus Q and $J_{1.0\ \mathrm{mm}}$ versus Q relations, which can be approximated by the following linear curves:

$$J_{0.2\ \mathrm{mm}} = -406.32Q + 225.46$$

$$J_{1.0\ \mathrm{mm}} = -1275Q + 634.6 \tag{13}$$

where the J-integral has unit in kJ/m^2. Substitution of Eq 13 into Eq 12 leads to:

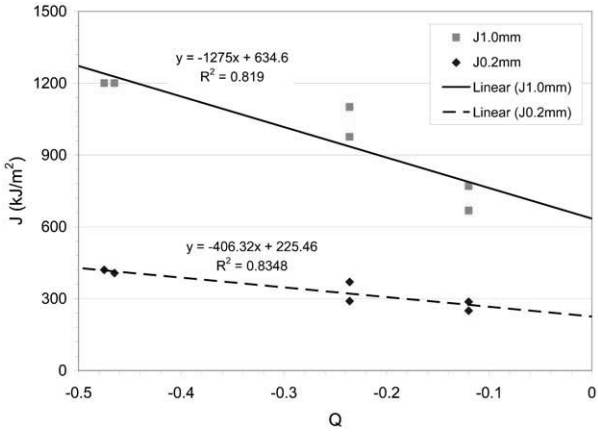


FIG. 8—*Variation of $J_{0.2\ mm}$ and $J_{1.0\ mm}$ with the constraint parameter Q for SENB specimens.*

$$C_1 0.2^{C_2} = -406.32Q + 225.46$$

$$C_1 1.0^{C_2} = -1275Q + 634.6 \tag{14}$$

Solving Eq 14 results in the approximated functions of C_1 and C_2 as

$$C_1(Q) = -1275Q + 634.6$$

$$C_2(Q) = -0.04Q + 0.65 \tag{15}$$

Finally, substituting Eq 15 to Eq 10, one obtains the constraint-corrected *J-R* curve for X80 pipeline steel as follows:

$$J(\Delta a, Q) = (-1275Q + 634.6)\left(\frac{\Delta a}{1\ \text{mm}}\right)^{(-0.04Q+0.65)} \tag{16}$$

where the *J*-integral has unit of kJ/m^2. Equation 16 indicates that the constraint-corrected *J-R* curve is a function of Q and Δa, which represents a family of constraint-dependent *J-R* curves for X80 pipeline steel. If Q is known for a specific geometry, the *J-R* curve can be easily predicted from Eq 16.

Validation of Predicted J-R Curves

For the SENB specimens with $a/W = 0.24$, 0.42, and 0.64, Q is determined as −0.475, −0.236, and −0.12, respectively, at $J_{0.2\ mm}$. The *J-R* curves are then predicted from Eq 16, and compared with the experimental ones for the three SENB specimens in Fig. 9. Similarly, Fig. 10 compares the predicted *J-R* curves with the experimental *J-R* curves for three SENT specimens with $a/W = 0.26$, 0.41, and 0.57, respectively. Comparisons show that the predicted *J-R* curves from Eq 16 can match the experimental data with reasonable degrees for both SENB and SENT specimens. The *J-R* curve match in Fig. 9 is not surprising as C_1 and C_2 were calibrated on the SENB. The match for SENT validates the proposed method as this geometry did not use for the calibration. Therefore, the constraint-corrected *J-R* curve or Eq 16 can be effectively used to predict the *J-R* curve for fracture specimens and actual cracked components for X80 steel, provided that the constraint parameter Q is known a priori.

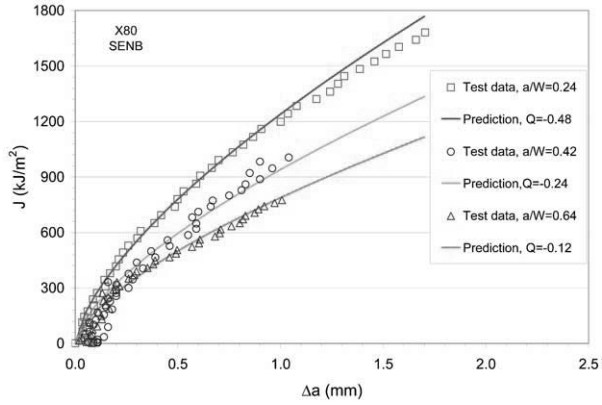


FIG. 9—*Comparison of predicted and experimental J-R curves for SENB specimens.*

Application to Failure Predictions of Cracked Pipelines

Numerical Analysis and Constraint Quantification for Cracked Pipeline

A pipeline with an outside diameter 762 mm and a thickness 23 mm under internal pressure is considered. For purposes of analysis, it is assumed that the pipeline contains a very long axial surface crack on its exterior with the crack depth being 50 % of the wall thickness, and thus the plane strain deformation can reasonably approximate this cracked pipeline. Due to symmetry, only one-half of the circular cross section was modeled using the FEA mesh shown in Fig. 11. In this FEA model, a very fine mesh was generated near the crack tip with the smallest element size of 0.003 mm, and coarse mesh was used elsewhere. The mesh involves 3107 nodes and 944 eight-node plane strain isoparametric elements with reduced integration. The boundary conditions include the symmetry conditions, and the applied load is internal pressure.

Figure 12(*a*) shows distributions of the opening stress determined from FEA and the *J-Q* solution (Eq 6) along the normalized distance from the crack tip for the X80 pipeline with a surface crack of $a/t = 0.5$, and the constraint parameter Q being −0.344, −0.393, −0.486, −0.626 and −0.767, respectively, at five deformation levels from SSY to LSY. Likewise, Fig. 12(*b*) compares the opening stress determined from FEA and from the modified *J-Q* solution (Eq 7) with the linearization factor $\alpha = 5$ and the constraint parameter $Q = -0.335$ for the smallest loading, and −0.373 for the other four loadings. For comparison, the

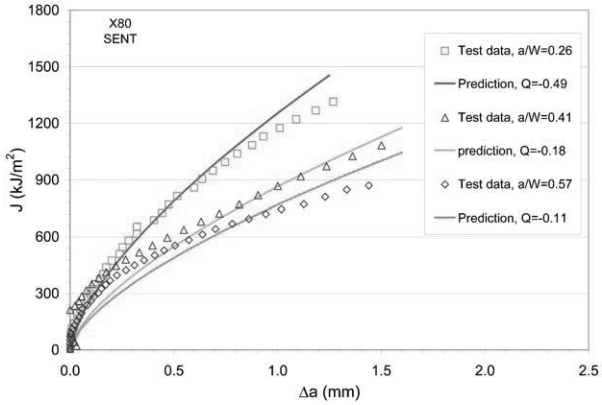


FIG. 10—*Comparison of predicted and experimental J-R curves for SENT specimens.*

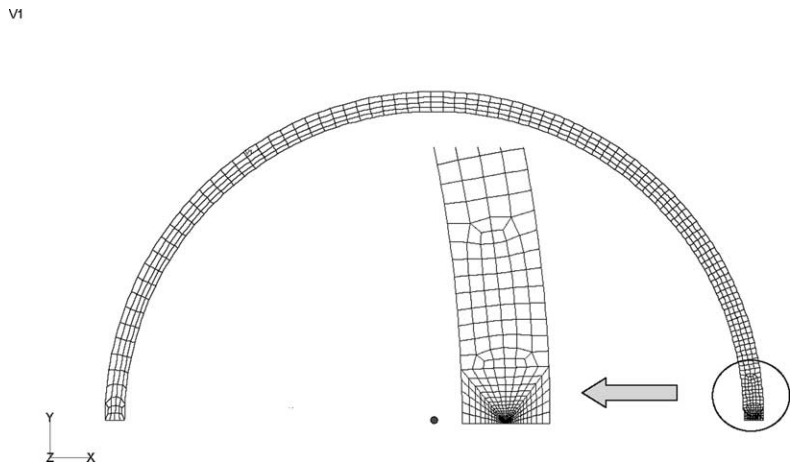


FIG. 11—*Finite element mesh for 762 mm × 23 mm pipe with an axial surface crack of a/t = 0.5.*

HRR solution is included in Fig. 12. It is observed that the global bending stress has significant influence on the crack-tip field for this cracked pipeline, the modified *J-Q* solution can well match the FEA results for all deformations with *Q* being constant under LSY, whereas the *J-Q* solution is good only for SSY and containing yielding. Since the crack is dominated by tension, the HRR field does not fit the FEA results even at SSY. Accordingly, the modified *J-Q* solution is appropriate to be used for characterizing the crack-tip field and quantifying the constraint level for this cracked pipeline.

Predicted J-R Curve of Cracked Pipeline

Replacing the value of −0.373 for *Q* in Eq 16 of the constraint-corrected *J-R* curve yields the predicted *J-R* curve for the X80 pipe with a long axial surface crack of $a/t = 0.5$ as

$$J(\Delta a) = 1110\left(\frac{\Delta a}{1\ \text{mm}}\right)^{0.665} \tag{17}$$

where the *J*-integral is in kJ/m^2. As shown in Fig. 13, the *J-R* curve for the cracked pipeline is much higher than that for the standard SENB specimen with $a/W = 0.64$, and may coincide with that for the SENB specimen with $a/W = 0.35$. Therefore, the *J-R* curve obtained from the ASTM standard specimen could overly underestimate the fracture resistance for the X80 pipeline.

Prediction of Failure Pressure

Plastic Collapse Pressure—For a pipe containing a longitudinal surface defect under internal pressure, the burst pressure P_d at the plastic collapse can be predicted by the PCORRC criterion [33] using the following equation:

$$P_d = \sigma_{uts}\frac{2t}{D}\left(1 - \frac{d}{t}\left(1 - \exp\left(-0.157\frac{L}{\sqrt{R(t-d)}}\right)\right)\right) \tag{18}$$

where σ_{uts} is the ultimate tensile stress (UTS), $D = 2R$ is the average diameter of the pipe, t is the wall thickness, d is the defect depth, and L is the defect length. PCORRC is a UTS based plastic collapse criterion for blunt defects derived independent of fracture mechanics analysis. Thus what is determined by Eq 18 is a plastic collapse failure pressure.

If a defect is very long, Eq 18 is simplified as $P_d = \sigma_{uts} 2t/D(1 - d/t)$. For the cracked X80 pipeline, $\sigma_{uts} = 675$ MPa, $D = 739$ mm, $t = 23$ mm with $d/t = 0.5$. Therefore, the burst pressure is predicted as $P_d = 21$ MPa. Because ductile crack tips blunt initially under LSY, this prediction should provide a reasonable

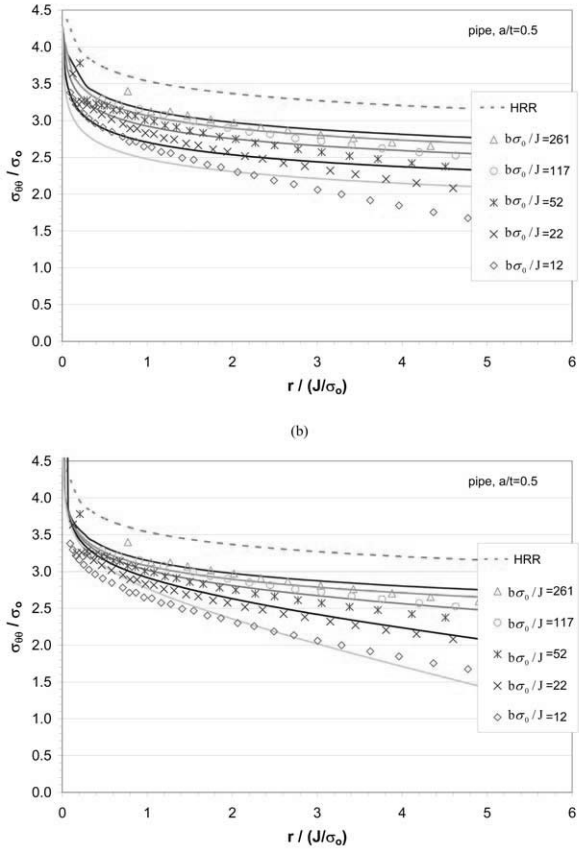


FIG. 12—*Distribution of crack opening stress determined by FEA and theories along the uncracked ligament from the crack tip for cracked pipe of a/t=0.5: (a) the J-Q theory, (b) the modified J-Q theory.*

estimate of plastic collapse pressure for the X80 pipeline. The next paragraphs assess the consistency between this plastic collapse model and the behavior characterized by fracture mechanics.

Crack Initiation Pressure—It is possible to predict the crack initiation pressure by comparing the initiation toughness determined from Eq 17 with a calculated crack driving force. Figure 13 shows that the initiation toughness at crack extension 0.2 mm, and at the 0.2 mm offset line are $J_{0.2\ mm}$=380 kJ/m^2, and J_Q=833 kJ/m^2, respectively, for the cracked pipeline. Figure 14 shows the calculated crack driving force curve, i.e., the *J*-integral versus the internal pressure for the X80 cracked pipe. From this figure, the crack initiation pressures corresponding to the initiation toughness of $J_{0.2\ mm}$ and J_Q are approximately determined as 19.6 and 22.8 MPa. These values are almost identical to the plastic collapse pressure of 21 MPa for this cracked pipe. This indicates that ductile crack initiation is very close to plastic collapse for such a thin wall pipe. Therefore, at least for this case, crack initiation is followed by nearly simultaneous plastic collapse, and the failure pressure for the deeply cracked pipeline could be bounded by pressures corresponding to the 0.2 mm toughness and 0.2 mm offset toughness, respectively. As a result, the X80 cracked pipeline will be safe if the applied pressure is less than the smaller failure pressure.

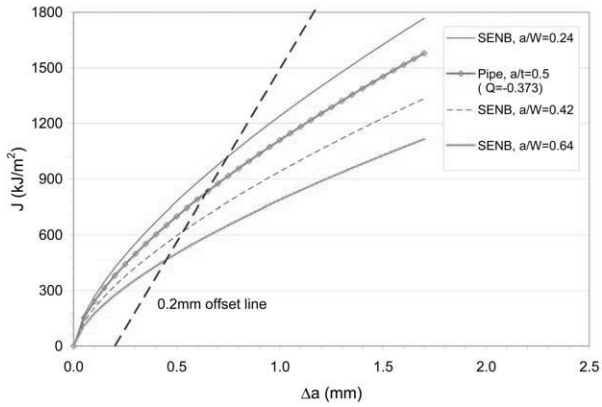


FIG. 13—*Predicted J-R curve for X80 surface cracked pipeline and compared with those for the three SENB specimens.*

Conclusions

The constraint effect on the *J-R* curves for X80 pipeline steel was examined in this paper. Based on the experimental data, the numerical calculations, and the modified *J-Q* fracture theory, a general method for determining a constraint corrected *J-R* curve has been developed, and the application to an actual cracked pipeline was demonstrated. The primary results are summarized as follows:

(1) Experimental *J-R* curves determined for the X80 steel using SENB and SENT specimens with various crack lengths showed strong geometry or constraint dependence.

(2) A modified *J-Q* theory and a load-independent constraint parameter*Q* were proposed for bending specimens under LSY, resulting in a great improvement to match the FEA results. As a basic guidance, the single parameter HRR field is only good to be used for deep cracked bending specimens under SSY; the two parameter *J-Q* theory can be used for bending specimens at containing yielding and for tensile specimens at any deformation level; and the proposed modified *J-Q* solution should be used for bending specimens at LSY so as to eliminate the global bending stress influence on the crack-tip field.

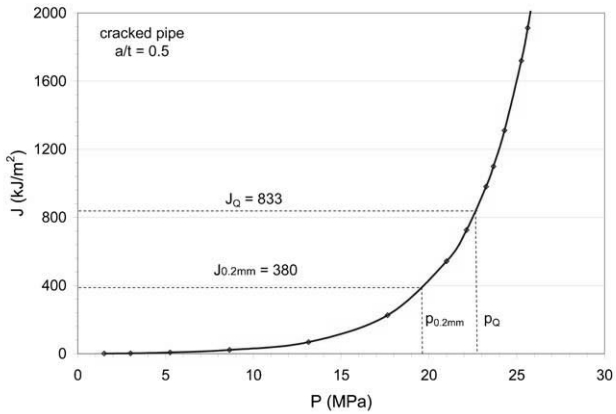


FIG. 14—*Crack driving force: J-integral versus applied pressure for the surface cracked pipeline with a/t = 0.5.*

(3) A general method to construct a constraint-corrected *J-R* curve was developed, and a mathematical expression representing a family of the constraint-dependent *J-R* curves was formulated as a function of the load-independent constraint parameter Q and crack extension Δa. Specifically, a constraint-corrected *J-R* curve was constructed for X80 pipeline steel based on the experimental data for SENB specimens. The predicted *J-R* curves were validated by the experimental *J-R* curves for SENT specimens.

(4) A pipeline containing a long axial surface crack of 50 % of the wall thickness was analyzed for demonstrating the application of the proposed constraint corrected *J-R* curves to failure assessment of structures. The predicted results showed that ASTM standard specimens may underestimate the fracture resistance for this deeply cracked X80 pipe.

(5) The results also showed that crack initiation was followed by nearly simultaneous plastic collapse, and the crack initiation pressure determined using the *J-R* curve method was almost identical to the plastic collapse pressure for the surface cracked X80 pipeline. This indicated the consistency of fracture analysis and plastic collapse analysis for a surface cracked thin-wall pipe, and proved the proposed constraint-corrected *J-R* curves viable in fracture analysis and integrity assessments of flawed pipelines.

Acknowledgments

The authors gratefully acknowledge Drs. Bill Tyson and Guowu Shen at the Material Technology Laboratory, Natural Resource Canada for their support in providing the original experimental data used in this work. The authors also thank the support by Battelle internal research and development program, and the useful suggestions from anonymous reviewers.

References

[1] Joyce, J. A. and Link, R. E., "Effects of Constraint on Upper Shelf Fracture Toughness," *Fatigue and Fracture Mechanics: 26th Volume, ASTM STP 1256*, ASTM International, West Conshohocken, PA, 1995, pp. 142–177.

[2] Joyce, J. A. and Link, R. E., "Application of Two Parameter Elastic-Plastic Fracture Mechanics to Analysis of Structures," *Eng. Fract. Mech.*, Vol. 57, 1997, pp. 431–446.

[3] Neimitz, A., Dzioba, I., Galkiewicz, J., and Molasy, R., "A Study of Stable Crack Growth Using Experimental Methods, Finite Elements and Fractography," *Eng. Fract. Mech.*, Vol. 71, 2004, pp. 1325–1355.

[4] ASTM Standard E 1820-01, "Standard Test Method for Measurement of Fracture Toughness," *Annual Book of ASTM Standards*, ASTM International, West Conshohocken, PA, 2004.

[5] Zhu, X. K. and Jang, S. K., "J-R Curves Corrected by Load-Independent Constraint Parameter in Ductile Crack Growth," *Eng. Fract. Mech.*, Vol. 68, 2001, pp. 285–301.

[6] American Society of Mechanical Engineers, *Manual for Determining the Remaining Strength of Corroded Pipelines*, ASME B31G, New York, 1991.

[7] Kiefner, J. F. and Vieth, P. H., "A Modified Criterion for Evaluating the Remaining Strength of Corroded Pipe," Final report on project PR 3-805 to the Pipeline Research Committee of the American Gas Association, 1989.

[8] Pisarksi, H. G. and Wifnall, C. M., "Fracture Toughness Estimation for Pipeline Girth Welds," *Proceedings of the 4th International Pipeline Conference, September 29–October 3*, 2002, Calgary, Alberta, Canada.

[9] Dong, H. R., Guo, W. L., Yang, Z., Lu, M. X., Zhao, X. W., and Luo, J. H., "Study on Fracture of Non-Through Crack Bodies of X60 Pipeline Steel," *Acta Metallurgica Sinica*, Vol. 37, 2001, pp. 579–584.

[10] Hippert, E., Dotta, F., and Ruggieri, C., "Structural Integrity Assessment of Pipelines Using Crack Growth Resistance Curves," *Proceedings of the 4th International Pipeline Conference, September 29–October 3*, 2002, Calgary, Alberta, Canada.

[11] Pavankumar, T. V., Chattopadhyay, J., Dutta, B. K., and Kushwaha, H. S., "Transferability of Specimen J-R Curve to Straight Pipes with Throughwall Circumferential Flaws," *Int. J. Pressure Vessels Piping*, Vol. 79, 2002, pp. 127–134.

[12] Shen, G., Tyson, W. R., Glover, A., and Horsley, D., "Constraint Effects On Linepipe Toughness,"

Proceedings of the 4th International Conference on Pipeline Technology, Volume 2, May 9–13, 2004, Ostend, Belgium, pp. 703–720.

[13] O'Dowd, N. P. and Shih, C. F., "Family of Crack-Tip Fields Characterized by a Triaxiality Parameter—I. Structure of Fields," *J. Mech. Phys. Solids*, Vol. 39, 1991, pp. 989–1015.

[14] O'Dowd, N. P. and Shih, C. F., "Family of Crack-Tip Fields Characterized by a Triaxiality Parameter—II. Fracture Applications," *J. Mech. Phys. Solids*, Vol. 40, 1992, pp. 939–963.

[15] O'Dowd, N. P. and Shih, C. F., "Two-Parameter Fracture Mechanics: Theory and Applications," *Fracture Mechanics: 24th Volume*, ASTM STP 1207, ASTM International, West Conshohocken, PA, 1994, pp. 21–47.

[16] Cravero, S. and Ruggieri, C., "Correlation of Fracture Behavior in High Pressure Pipelines with Axial Flaws Using Constraint Designed Test Specimens—Part I: Plane-Strain Analyses," *Eng. Fract. Mech.*, Vol. 72, 2005, pp. 1344–1360.

[17] Faleshog, J., "Effects of Local Constraint Along Three-dimensional Crack Fronts—A Numerical and Experimental Investigation," *J. Mech. Phys. Solids*, Vol. 43, 1995, pp. 447–493.

[18] Yang, S., Chao, Y. J., and Sutton, M. A., "Higher-Order Asymptotic Fields in a Power-Law Hardening Material," *Eng. Fract. Mech.*, Vol. 45, 1993, pp. 1–20.

[19] Chao, Y. J., Yang, S., and Sutton, M. A., "On the Fracture of Solids Characterized by One or Two Parameters: Theory and Practice," *J. Mech. Phys. Solids*, Vol. 42, 1994, pp. 629–647.

[20] Chao, Y. J. and Zhu, X. K., "*J*-A_2 Characterization of Crack-Tip Fields: Extent of *J*-A_2 Dominance and Size Requirements," *Int. J. Fract.*, Vol. 89, 1998, pp. 285–307.

[21] Chao, Y. J. and Zhu, X. K., "Constraint-Modified *J-R* Curves and Its Applications to Ductile Crack Growth," *Int. J. Fract.*, Vol. 106, 2000, pp. 135–160.

[22] Chao, Y. J., Zhu, X. K., Lam, P. S., Louthen, M. R., and Iyer, N. C., "Application of the Two-Parameter *J*-A_2 Description to Ductile Crack Growth," *Fatigue and Fracture Mechanics: 31th Volume, ASTM STP 1389*, G. R. Halford and J. P. Gallagher, Eds., ASTM International, West Conshohocken, PA, 2000, pp. 165–182.

[23] Lam, P. S., Chao, Y. J., Zhu, X. K., Kim, Y., and Sindelar, R. L., "Determination of Constraint-Modified J-R Curves for Carbon Steel Storage Tanks," *J. Pressure Vessel Technol.*," Vol. 125, 2003, pp. 136–142.

[24] Guo, W., Dong, H., Lu, M., and Zhao, X., "The Couple Effects of Thickness and Delamination on Cracking Resistance of X70 Pipeline Steel," *Int. J. Pressure Vessels Piping*, Vol. 79, 2002, pp. 403–412.

[25] Schealbe, K. H., Newman, J. C., and Shannon, J. L., "Fracture Mechanics Testing on Specimens with Low Constraint—Standardization Activities with ISO and ASTM," *Eng. Fract. Mech.*, Vol. 72, 2005, pp. 557–576.

[26] Schwalbe, K. H., Cornec, A., and Baustian, K., "Application of Fracture Mechanics Principles to Austenitic Steels," *Int. J. Pressure Vessels Piping*, Vol. 65, 1996, pp. 193–207.

[27] *ABAQUS Standard User's Manual* (version 6.4), Hibbitt, Karlsson and Sorensen, Inc., Pawtucket, RI, 2004.

[28] Hutchinson, J. W., "Singular Behavior at the End of a Tensile Crack in a Hardening Material," *J. Mech. Phys. Solids*, Vol. 16, 1968, pp. 13–31.

[29] Rice, J. R. and Rosengren, G. F., "Plane Strain Deformation Near a Crack Tip in a Power Law Hardening Material," *J. Mech. Phys. Solids*, Vol. 16, 1968, pp. 1–12.

[30] Shih, C. F., "Tables of HRR Singular Field Quantities," Report MRL E-147, Materials Research Laboratory, Brown University, Providence, RI, 1983.

[31] Zhu, X. K., Jang, S. K., and Chen, Y. F., "A Modification of *J-Q* Theory and Its Applications," *Int. J. Fract.*, Vol. 111, 2001, pp. L47–L52.

[32] Chao, Y. J., Zhu, X. K., Kim, Y., Lam, P. S., Pechersky, M. J., and Morgan, M. J., "Characterization of Crack-Tip Fields and Constraints for Bending Specimens under Large-Scale Yielding," *Int. J. Fract.*, Vol. 127, 2004, pp. 283–302.

[33] Stephens, D. R. and Leis, B. N., "Development of an Alternative Criterion for Residual Strength of Corrosion Defects in Moderate- to High-Toughness Pipe," *Proceedings of the 3rd International Pipeline Conference*, October 1–5, 2002, Calgary, Alberta, Canada.

Journal of ASTM International, Jan. 2006, Vol. 3, No. 1
Paper ID: JAI13235
Available online at: www.astm.org

Enrico Lucon,[1] *Marc Scibetta,*[2] *Rachid Chaouadi,*[1] *and Eric van Walle*[3]

Use of Miniaturized Compact Tension Specimens for Fracture Toughness Measurements in the Upper Shelf Regime

ABSTRACT: In the nuclear field, the importance of direct fracture toughness measurements on reactor pressure vessel (RPV) materials has been nowadays widely recognized, as opposed to Charpy-based estimations. However, sample dimensions have to be kept small in order to optimize the use of available material (often in the form of previously broken Charpy specimens) or, in the case of new irradiations, make effective use of the limited space available inside irradiation facilities. One of the most appealing geometries for fracture toughness measurements is the miniature Compact Tension specimen, MC(T), which has the following dimensions: B = 4.15 mm, W = 8.3 mm, cross section 10 × 10 mm². Four MC(T) specimens can be machined out of a broken half Charpy, and in the case of irradiation ten MC(T) samples occupy approximately the same volume as a full-size Charpy specimen. A comprehensive investigation is presented in this paper, aimed at assessing the applicability of MC(T) specimens to measure fracture toughness in fully ductile (upper shelf) conditions. In this study, 18 1TC(T) and 20 MC(T) specimens have been tested at different temperatures from three RPV steels and one low-alloy C-Mn steel. The results obtained clearly show that MC(T) samples exhibit lower fracture toughness properties, both in terms of initiation of ductile tearing (according to various test standards) and resistance to ductile crack propagation (J-R curve). The reduction of tearing resistance might be attributed to work hardening prevailing over loss of constraint in the uncracked ligament for a side-grooved specimen, or to the inadequacy of J-integral to represent ductile crack extension in very small specimens. Both arguments need to be verified with further investigations.

KEYWORDS: ductile fracture toughness measurement, miniature compact tension specimen, ductile tearing initiation, J-R curve, work hardening, loss of constraint

Introduction

The knowledge of mechanical properties for structural materials of plant components is among the key points for producing reliable integrity assessments and accurate residual life predictions. Particularly when embrittlement and degradation of structural materials are present due to service exposure under neutron irradiation, elevated temperatures or aggressive environment, the actual mechanical behavior of the components must be confidently assessed, possibly without being overconservative.

The evaluation of mechanical properties, with the sole exception of hardness measurements, is by definition a destructive technique, since it requires direct sampling from the component (whenever this is feasible). When direct sampling is possible and if the component has to be

Manuscript received April 14, 2005; accepted for publication Aug. 11, 2005; published Jan. 2006.
[1] Senior researchers, SCK•CEN, Dep. RMO, Boeretang 200, B-2400 Mol (Belgium).
[2] Head of Mechanical Testing Section, Dep. RMO, Boeretang 200, B-2400 Mol (Belgium).
[3] Head of RMO Department, SCK•CEN, Boeretang 200, B-2400 Mol (Belgium).

maintained in service, the sample size has to be small enough so that easy repair or even no repair at all is needed to allow further operation of the component. Furthermore, in the nuclear field, the space available inside irradiation facilities is normally quite limited and the exploitation of material has to be optimized. All these circumstances make the use of very small specimens, usually not complying with the requirements of tests standard, very appealing.

In the specific domain of fracture toughness, the importance of direct toughness measurements is nowadays widely recognized, rather than relying on indirect correlations with other mechanical properties, such as for instance Charpy impact test results. This has justified the intensive effort spent during recent years in the development and validation of various subsized or miniaturized specimen geometries to be used for fracture toughness measurements.

Namely, the miniature Compact Tension specimen, MC(T) has a cross section of approximately 10 × 10 mm², equivalent to that of a full-size Charpy specimen, and a thickness of B = 4.15 mm (roughly corresponding to 1/6 in.). In the framework of past investigations carried out at SCK•CEN, its use has been validated in the ductile-to-brittle transition region, where the Master Curve approach has been successfully applied on both unirradiated and irradiated materials [1,2]. An assessment of their applicability in fully ductile conditions, by comparison with standard-type 1TC(T) samples, is illustrated in this study.

Background: Size Effects in Fracture Toughness

The influence of specimen dimensions (and configuration) on the results of fracture toughness tests has always been an intensely debated issue, since the early developments of fracture mechanics.

If the material's behavior is typical of lower shelf conditions, it is generally accepted that the critical value of toughness, expressed in terms of the linear elastic parameter K_{Ic}, is practically size-insensitive, provided that the validity requirements expressed for example in the ASTM E 399-90 standard are met.

In the ductile-to-brittle transition region, the influence of sample size has a very significant effect on fracture, which can be synthetically summarized as follows: in a larger specimen the crack front samples more material and has therefore a higher probability of intercepting a cleavage initiation point which can trigger fracture; therefore, larger samples tend to exhibit lower toughness. Moreover, thinner samples are prone to loss of constraint, and the loss of triaxiality in the stress/strain state along the crack front produces an apparent increase of toughness. Nowadays, the Master Curve methodology offers a powerful tool to represent the inherent statistical nature of cleavage in the transition region, and even allows to quantify size effects by a relatively simple normalization procedure.

As far as specimen size effects in case of fully ductile behavior are concerned, indications are often contradictory when one examines the available literature. A few selected examples are given below:

- In 1979, Ingham and Morland [3] tested 25 mm and 12.5 mm thick SE(B) specimens of A533B Cl.1 steel, using the multi-specimen technique; they did not find any significant influence of specimen size on either initiation values or crack resistance curves.
- In 1987, Ingham et al. [4] published fracture toughness data obtained on A533B Cl.1 at RT and 288°C using plane-sided and side-grooved C(T) specimens with thicknesses ranging from 10 to 100 mm. Once again, the multi-specimen method was employed.

Their results showed that size-independent J-R curves were only obtained for specimens thicker than 40 mm; in the case of samples with B = 10 and 20 mm, the slope of the J-R curve tended to increase with decreasing specimen size, although the effect was small and appeared to be minimized by side-grooving.

- In 1991, Link et al. [5] remarked that "J-R curve size effects are not generally observed in any consistent trend." They reported that J-R curves measured from C(T) specimens of five different steels (A508, A533B, A736, 5NiCrMoV, and AISI 304) with thicknesses ranging from ½ to 10 in. (12.5 to 254 mm) were independent of specimen size. However, when using other sample geometries (CCT, DEN, SEN) in conjunction with C(T) specimen, they found "classical effects of changing constraint by varying specimen thickness," meaning that reducing thickness reduced through-thickness constraint and led to an elevation of toughness; nevertheless, a "non-classical effect" was observed for two highly ductile materials (A736 and 304 SS), for which toughness was seen to decrease with decreasing specimen size.
- In 1993, Heerens et al. [6] reported an evident thickness effect on J-R curves obtained from C(T) specimens with B = 25 and 50 mm of 20MnMoNi55 and an Al alloy (Al2024 FC); in all cases, the resistance curves of the thicker specimen fell below those of the thinner. The authors also contended that both the crack tip opening displacement δ_5 and Ernst's modified J-integral J_m [7] can provide size-insensitivity up to larger amounts of crack extension than the conventional parameter J.
- In 2002, Wardle [8] published a comparison of initiation toughness values and J-R curve data for a series of geometrically scaled C(T) and SE(B) specimens of A533B Cl.1, with thicknesses ranging from 5 to 100 mm. He concluded that there is little effect of specimen size and geometry on initiation toughness when the specimen is side-grooved; moreover, even the thinnest specimens (B = 5 mm) could provide J-R curve data equivalent to larger specimens up to J levels of about 600 kJ/m² and crack extensions up to 40 % of their initial remaining ligament.
- In 2003, Neimitz et al. [9] observed no influence of specimen thickness on J-R curves or fracture initiation values using SE(B) specimens of typical RPV steels with thicknesses from 10 to 20 mm, provided that side-grooves are present. For plane-sided samples, a clear thickness effect can be seen, with two materials providing, however, completely opposite indications: increasing toughness with decreasing thickness for 40HNMA (equivalent to 4340H) and flatter resistance curves from thinner samples for 40H (equivalent to 5140 or 41Cr4).
- In 2004, Ono et al. [10] reported upper shelf fracture toughness results on a Japanese reduced-activation ferritic-martensitic steel, JLF-1, using C(T) with thicknesses = ¼ in., ½ in., and 1 in. They observed a decrease of initiation toughness (J_Q) and slope of the resistance curve with decreasing specimen thickness, which they explained in terms of increase of plane stress state region and plastic zone size at the crack tip of the specimen.

What is reported above is in no way meant to represent a comprehensive literature review on the subject. Rather, it is just intended to give the reader a "feel" of the contradictory indications that can be found in the literature.

Materials and Experimental

Three well-known RPV steels (22NiMoCr37, 18MND5, A533B) and a typical low-alloy C-Mn steel (A106) have been used for this study. The chemical compositions are given in Table 1.

TABLE 1—*Chemical compositions (weight %, Fe balance) of the steels selected for this study.*

Steel	C	Si	P	S	Cr	Mn	Ni	Cu	Mo	Al
22NiMoCr37	0.22	0.23	0.006	0.004	0.39	0.88	0.84	0.08	0.51	...
18MND5	0.18	0.25	0.007	0.002	0.17	1.6	0.64	0.13	0.5	0.02
A533B Cl.1	0.183	0.231	0.0073	0.0031	0.17	1.49	0.642	0.062	0.479	0.022
A106	0.24	0.23	0.011	0.011	0.09	1.08	0.11	0.09	0.04	...

For each material, Compact Tension specimens with thicknesses B = 25 mm, 1TC(T), and B = 4.15 mm, MC(T), have been tested at RT and in some cases also at higher temperatures (150 and 290°C). Additionally, two multi-specimen J-R curves have been obtained on 1TC(T) and MC(T) specimens of 18MND5 at 150°C. All specimens were side-grooved up to 80 % of their original thickness after fatigue precracking.

The geometry of the MC(T) specimens is shown in Fig. 1. The grooves on the outer side of the pin holes are used to accomodate the clip-gage, which is mounted externally, whereas in the case of bigger samples the arms of transducer are placed inside the machined notch. The clip-gage, in addition to measuring load-line displacement, is also used for measuring the voltage drop across the crack plane when the PD technique is applied. All tests have been performed using a constant crosshead displacement rate of 0.2 mm/min for MC(T) and 1 mm/min for 1TC(T).

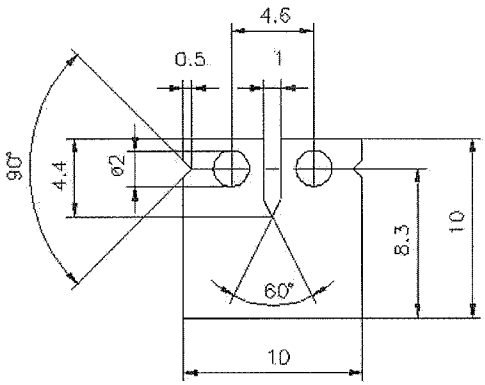


FIG. 1—*Drawing of the MC(T) specimen.*

A post-test quantitative evaluation has been carried out of the effect of clip-gage position for MC(T) specimens (outside the loading pin holes), with respect to the "conventional" configuration (inside the pin holes), by accounting for

- plastic deformation of the pin holes;
- geometrical effects on the rotation between the two specimen halves.

By considering specimen dimensions, measured plastic deformations of the pin holes and measured load-line displacement values, these latter have been found to underestimate the actual crack mouth opening by less than 4 % at ductile crack initiation (J_Q) and less than 7.5 % at test termination; these differences play a role only on the plastic part of the J-integral. On account of the intrinsic uncertainties associated with the test, a specific correction to the measured load-line displacement values for MC(T) specimens was therefore deemed unnecessary.

For the analysis of all tests, the procedure prescribed by ASTM Standard Test Method for Measurement of Fracture Toughness (E 1820) has been followed; in addition, for a few selected tests, alternative procedures have been used (ISO 12135, use of alternative crack growth corrections, etc). Such investigations will be addressed in separate sections.

Comparison of J-R Test Results Between 1TC(T) and MC(T) Specimens

Critical (Initiation) Toughness Values

For most test standards, the engineering approximation of ductile crack growth initiation is defined at the intersection of the J-R curve (fitted through all data points contained within a so-called "validity box") with a straight line, parallel to the blunting (construction) line and having an offset of 0.2 mm. In other words, initiation is assumed for practical purposes at 0.2 mm of ductile crack extension beyond blunting (apparent crack extension due to plastic stretching of the crack tip). This parameter is denominated J_Q (or J_{Ic} if qualified according to a list of validity criteria) in ASTM E1820 and $J_{0.2BL}$ in ISO 12135.

For MC(T) specimens, the maximum J-integral capacity according to ASTM E 1820-01 is exceeded very early during all tests, way before ductile crack growth is initiated.

Overall results are summarized in Table 2, where values for the two tests performed under the same conditions (material + temperature + specimen type) using the single-specimen technique (Unloading Compliance) are reported, as well as J_{max}. The results obtained using the multi-specimen technique on 18MND5 at 150°C are also included.

The values presented in Table 2 are also plotted in Fig. 2.

Crack Resistance (J-R) Curves

When comparing test results in terms of J-R curves, it is observed that crack resistance curves measured on MC(T) specimens are consistently flatter than those obtained from 1TC(T) samples. An example is shown in Fig. 3, for 22NiMoCr37 tested at room temperature.

For each material and test temperature, J-R curves start significantly deviating above approximately 200 kJ/m² in terms of J-integral and 0.2–0.3 mm in terms of ductile crack extension. In most cases, the curves obtained from the tests performed under the same nominal conditions (material, specimen type, and temperature) are in satisfactory agreement with each other.

TABLE 2—*Maximum J-integral capacity and J_Q/J_{Ic} results (kJ/m²) obtained from 1TC(T) and MC(T) specimens. Values in bold are valid J_{Ic} according to ASTM E 1820-01.*

Material	T (°C)	Single-specimen				Multi-specimen			
		MC(T)		1TC(T)		MC(T)		1TC(T)	
		J_{max}	J_Q/J_{Ic}	J_{max}	J_Q/J_{Ic}	J_{max}	J_Q/J_{Ic}	J_{max}	J_Q/J_{Ic}
22NiMoCr37	RT	130.2	439.5	734.1	INVALID				
		124.5	372.7	735.1	666.7				
	150	114.2	132.3	697.8	579.4				
		109.3	340.8	705.6	628.6				
	290	112.4	305.4	679.1	**271.3**				
		114.1	310.3	686.9	479.8				
18MND5	RT	136.6	407.0	823.4	853.3				
		135.1	451.9	820.6	569.4				
	150	130.6	334.2	775.4	523.4	134.8	308.7	812.3	**467.0**
		131.9	348.1	792.7	561.1				
	290	130.7	243.3	780.3	**371.4**				
		135.6	239.7	770.6	**284.0**				
A106	RT	89.7	256.2	540.1	252.9				
		86.7	232.7	522.6	329.5				
A533B	RT	145.6	348.5	889.9	**505.4**				
		150.2	297.9	889.6	**392.5**				
	290	126.5	262.3	753.3	**304.8**				
		128.0	240.6	749.4	**294.9**				

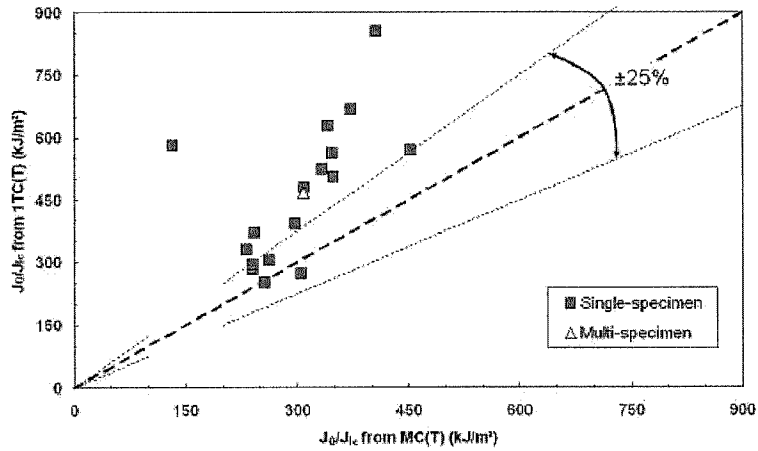


FIG. 2—*Relationship between J_Q/J_{Ic} values measured from 1TC(T) and MC(T) specimens.*

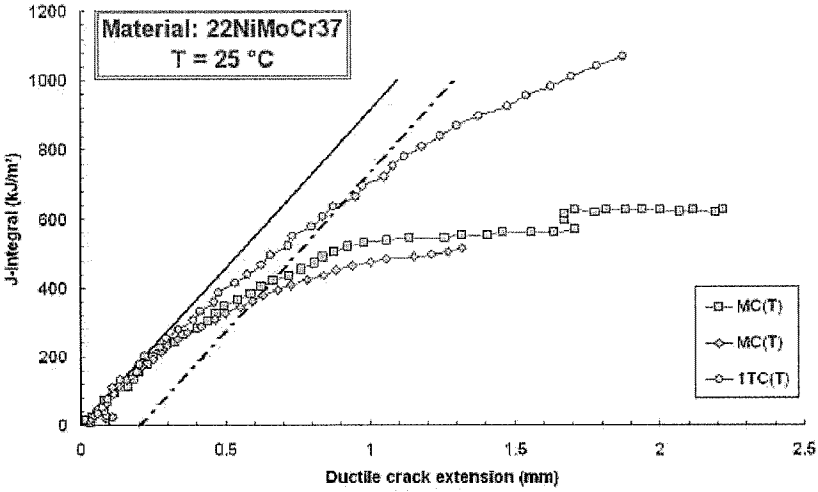


FIG. 3—*J-R curves obtained from 1TC(T) and MC(T) specimens on 22NiMoCr37 at RT.*

Multi-Specimen Curves (18MND5, T = 150°C)

As previously mentioned, two multi-specimen J-R curves have been obtained on 18MND5 at 150°C, one for 1TC(T) and one for MC(T) specimens. These are shown in Fig. 4, directly compared with single-specimen data.

The trend shown in Fig. 4 for multi-specimen J-R curves substantially reflects the situation observed for single-specimen data. Therefore, no relevance can be attributed to the choice of the experimental technique (multi- or single-specimen).

It is also worth pointing out that the multi-specimen curve of 1TC(T) specimens is in much better agreement with the single-specimen ones than in the case of MC(T) samples. This circumstance can be explained in terms of crack growth correction (a subject which will be more extensively treated below).

The present version of ASTM E 1820-01 does not include a crack growth correction for the so-called "*basic test method*" (which corresponds to the multi-specimen approach),[4] whereas for single-specimen methods the plastic part of the J-integral is corrected for crack extension. Such correction is proportional to Δa and inversely proportional to the current ligament length. As a consequence, for MC(T) specimens the correction is much more significant than for 1TC(T) samples, and the relevant multi-specimen J-R curve clearly departs from the single-specimen curves starting from crack extension values greater than ~ 0.6 mm.

[4] We should also emphasize, however, that the "*basic test method*" is specifically restricted to the evaluation of initiation toughness, and is not intended for the derivation of resistance curves.

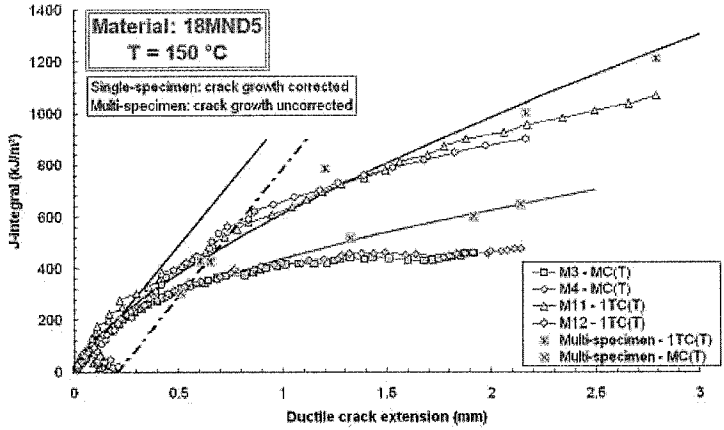


FIG. 4—*Single-specimen and multi-specimen data obtained from 1TC(T) and MC(T) specimens on 18MND5 at 150°C.*

Use of a Different Test Standard (ISO 12135:2002) and Influence of the Crack Growth Correction

The ISO standard 12135:2002, Metallic Materials—Unified Method of Test for the Determination of Quasistatic Fracture Toughness, stems from the ESIS P2-92 procedure, which was developed during the 1980s and 1990s by the European Working Group TC1/4 lead by K.-H. Schwalbe (GKSS, Germany).

While the actual experimental procedure and the basic J-integral calculations are virtually identical to ASTM E 1820-01, the following aspects in the determination of upper shelf fracture toughness (critical values and resistance curves) are significantly different:

- Form of the crack growth correction, which is not applied incrementally as in E 1820:

$$J_{corr} = J_{el,o} + J_{pl,o} \cdot \left[1 - \frac{\Delta a}{2(W - a_o)}\right] \tag{1}$$

  where J_{corr} is the crack growth corrected J-integral and $J_{el,o}$ and $J_{pl,o}$ the uncorrected elastic and plastic components, respectively.
- Analytical expression of the blunting (or construction) line, which is much steeper than in the ASTM standard:

$$J = 3.75 \cdot \sigma_m \Delta a \tag{2}$$

  where σ_m is the tensile strength at the test temperature.
- Form of the data regression curve, which has three parameters (offset power law) rather than two (simple power law):

$$J = \alpha + \beta \Delta a^{\gamma} \tag{3}$$

with $\alpha,\beta = 0$ and $0 = \gamma = 1$.

- Qualification requirements for $J_{0,2BL}$ (which corresponds to J_Q), which are more stringent than in E 1820:

$$J_{\max} = \min\left(a_o, B, b_o\right) \cdot \frac{\sigma_Y}{20} \tag{4}$$

$$\Delta a_{\max} = 0.10 \cdot (W - a_o) \tag{5}$$

The consequences of such differences in the comparison between MC(T) and 1TC(T) specimens have been investigated by re-analyzing the twelve tests (six per specimen type) performed on 22NiMoCr37 in accordance with the ISO 12135:2005 standard.

Additionally, we have examined the influence of the crack growth correction on the results by comparing data calculated according to ASTM and ISO with and without crack growth correction. A third expression of crack growth correction, recently proposed by Wallin and Laukkanen [11], has also been considered:

$$J = \frac{J_O}{1 + \left(\frac{1-m}{1+m}\right) \cdot \frac{\Delta a}{W - a_o}} \tag{6}$$

where J_O is the uncorrected value and m is the power of the J-R curve (to be evaluated by successive iterations).

As previously mentioned, for any form of crack growth correction, the smaller the specimens the larger is the effect on J-integral values for crack extensions larger than ~0.5 mm. For instance, using the expression given in the ISO standard (Eq 1), and assuming that $a_o/W = 0.5$ and $\Delta a = 2$ mm, the correction amounts to 33.5 % for an MC(T) specimen and only 5.6 % for a 1TC(T).

Single-specimen critical values J_Q/J_{Ic}/$J_{0,2BL}$ for 22NiMoCr37 (average values from two tests performed at the same temperature on the same sample type) calculated according to ISO and ASTM, with and without correction, are shown in Fig. 5. The values at initiation obtained using the ISO standard are significantly lower than ASTM critical parameters, due to the steepness of the construction line, and therefore show less discrepancy between MC(T) and 1TC(T) specimens, falling in proximity of the –25 % line.

Moreover, removing the crack growth correction slightly moves the data points upwards and to the right, without significantly affecting the comparison between MC(T) and 1TC(T) specimens; the effect appears similar for both ASTM and ISO standards. The influence of Wallin and Laukkanen's correction is very similiar to the incremental one already implemented in E 1820-01.

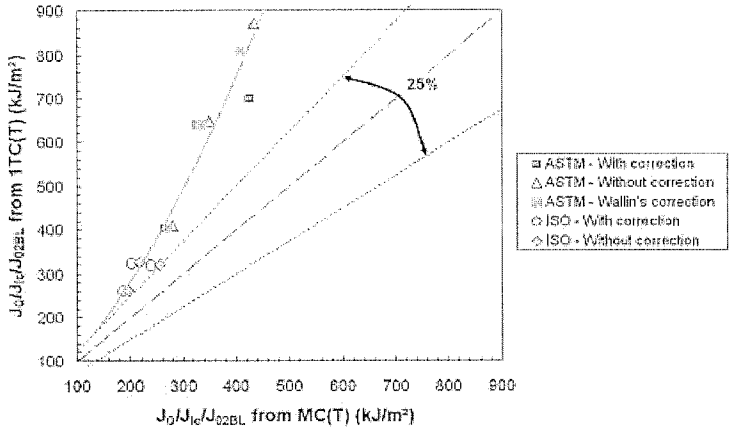


FIG. 5—*Critical toughness values calculated at 0.2 mm crack extension beyond blunting for 22NiMoCr37.*

As far as crack resistance curves are concerned, crack growth correction starts to play a role only after at least 0.5 mm of ductile crack extension; as an example, Fig. 6 shows data for 22NiMoCr37 at 290°C, obtained in accordance with ASTM E 1820-01. For both ASTM and ISO standards, removing the correction has a much larger effect for MC(T) specimens, as expected, and therefore brings the J-R curves closer. Although the ranking between MC(T) and 1TC(T) does not significantly change, it might be contended that crack growth corrections should be less dependent on specimen size.

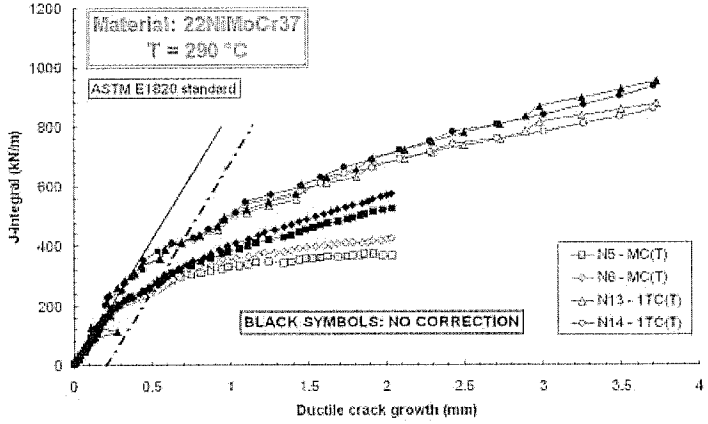


FIG. 6—*Crack resistance data obtained on 22NiMoCr37 at 290°C using ASTM E1820-01, with and without crack growth correction.*

Use of a J-R Curve Scaling Approach Based on Plastic Constraint Factors

With the aim of finding a more physical interpretation of the differences observed between MC(T) and 1TC(T) specimens, a model recently proposed by Brocks et al. [12] has been considered, based on the concept of energy dissipation rate. A concise summary of this approach is given below.

The energy dissipation rate, R, has been proposed as the "true driving force" for elastic-plastic fracture mechanics by Turner [13], in alternative to J-integral, on the basis of its consistency with incremental plasticity. It characterizes the increment of non-recoverable mechanical work per unit of crack extension, and includes two contributions: the specific work of remote plastic deformation and the specific local work of separation. It has been claimed that solving the problem of the geometry dependency of J-R curves can only be achieved using the concept of dissipation rate [14].

If the J-R curve is known, R can be evaluated for a C(T) or SE(B) specimen as a function of the plastic component of J (J_{pl}) and crack size from [15]:

$$R = \left(\frac{W-a}{\eta}\right)\frac{dJ_{pl}}{da} + J_{pl}\frac{\gamma}{\eta} \tag{7}$$

where η and γ are plastic factors given in ASTM E 1820-01. If Eq 7 is scaled to a different specimen size and then integrated, the plastic J-R curve for this new specimen size can be obtained. According to Brocks's model, therefore, all that is needed is to scale R, which in turn allows scaling of the conventional crack resistance curve (or at least its plastic component).

The typical curve shape of R as a function of crack growth can be effectively represented by a decreasing exponential function [15]:

$$R = R_{\infty}\left[1 + \alpha \exp\left(-\lambda\frac{\Delta a}{W}\right)\right] \tag{8}$$

where R_{∞} is the final stationary value, also known as "crack propagation energy" [16], α is a parameter that determines the initial value at $\Delta a = 0$, and λ is another parameter that describes the rate of decay from the initial to the stationary value.

Brocks's approach consists in scaling R-Δa curves by the following geometrical factor, in order to eliminate the geometry dependence:

$$f_G = (W - a_o)\cdot f_Y\left(\frac{a_o}{W}\right) \tag{9}$$

with f_Y being the ratio of the plastic limit load of the cracked structure to the net section yield load. If Eq 8 is used to represent R, then the only parameter that needs to be scaled is R_{∞}.

Given this theoretical framework, the following has been done in this study using single-specimen test results obtained on 22NiMoCr37:

- J_{pl} versus Δa data from MC(T) specimens have been converted into $R_{MC(T)}$ versus Δa data using Eq 7.

- The latter have been fitted using Eq 8 in order to obtain R_∞, α, and λ.
- The predicted energy dissipation rate curve for 1TC(T), $R_{1TC(T)}$ versus Δa, has been reconstructed using again Eq 8, where α and λ remain the same as for MC(T) specimens and R_∞ is scaled by the ratio of the respective geometrical factors calculated according to Eq 9.
- $R_{1TC(T)}$ versus Δa data are integrated by inverting Eq 7 in order to obtain a predicted J_{pl}-Δa curve.
- This latter is compared directly with the experimental (measured) plastic J-R curves for 1TC(T) specimens.

The results obtained at 290°C are shown, in terms of comparison between predictions and measurements, in Fig. 7.

Based on the results obtained at three temperatures (only data for 290°C are shown in Fig. 7), the agreement between predictions and measurements is unsatisfactory at RT, acceptable at 150°C, and good at 290°C. Actually, Brocks himself admits that "*the scaling failed in some cases, which has to be further analyzed*" and "*the present procedure does not claim for generality.*"

Nevertheless, all predictions show that 1TC(T) are expected to deliver steeper J-R curves than MC(T), which are associated with a lower energy dissipation rate, and therefore confirm the experimental results obtained.

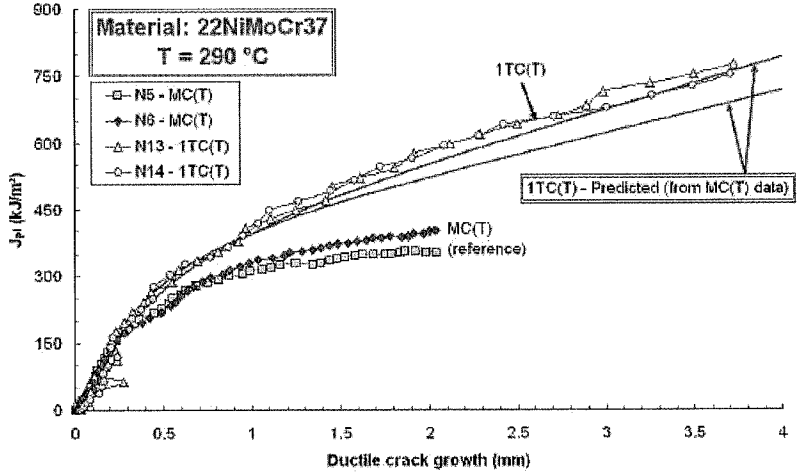


FIG. 7—*Comparison between predicted and measured plastic J-R curves for 1TC(T) specimens of 22NiMoCr37 tested at 290°C. The green prediction line was obtained from the analysis of MC(T) specimen N5, the red one from specimen N6.*

"Real" Initiation of Ductile Crack Extension: Stretch Zone Width (SZW) Measurements

The results shown so far have demonstrated that, above approximately 200 kJ/m², where "engineering" approximations of crack initiation (J_Q or $J_{0.2BL}$) are measured, MC(T) and 1TC(T) specimens deliver significantly different results.

But what happens at the instant of "real" ductile crack initiation, i.e., when crack tip blunting is exhausted and coalescence of voids starts to generate new fracture surfaces?

To answer this question, we have applied the procedure outlined in Annex A of ISO 12135:2002 for the determination of the "real" initiation parameters J_i and δ_i, based on the measurement of the local stretch zone width (SZW) on the fracture surface of the broken specimen using calibrated photographs taken in a SEM (Scanning Electron Microscope). One MC(T) specimen and one 1TC(T) specimen tested at RT from 18MND5 have been used for the measurements.

The initiation parameters are calculated from best-fit curves fitted through all data points having $\Delta a > \Delta a_{SZW}$, at an abscissa value corresponding to the measured Δa_{SZW}.

The results obtained for the specimens of 18MND5 tested at RT are summarized in Table 3; the assumption has been made that the Δa_{SZW} value measured on one specimen of a given size can also be attributed to the other specimen of the same size.

Since in several instances (especially for MC(T) specimens) we observed that the best-fit curve did not suitably follow the experimental data, we also estimated J_i by averaging the J values of the two points closer to the $\Delta a = \Delta a_{SZW}$ vertical line (i.e., the last one with $\Delta a < \Delta a_{SZW}$ and the first one with $\Delta a > \Delta a_{SZW}$); an example is shown in Fig. 8. These estimates are given in the right section of Table 3; the values in the central section are calculated strictly in accordance with ISO 12135:2002.

Table 3 clearly shows that crack tip blunting is much larger for 1TC(T) than MC(T) specimens. As a consequence, initiation values from MC(T) samples are clearly lower than those calculated for 1TC(T), the difference being higher than for the conventional critical parameters (J_Q, J_{Ic}, $J_{0,2BL}$) discussed in previous chapters.

In summary, it appears that, with respect to a standard-sized specimen, in a MC(T) sample the crack initiates sooner and propagates more easily.

TABLE 3—*"Real" initiation values measured in accordance with Annex A of ISO 12135:2002 on the specimens of 18MND5 tested at RT.*

Specimen type	Specimen code	Δa_{SZW} (mm)	J_i (kJ/m²) From fit	J_i (kJ/m²) From data
MC(T)	M1	0.119	168.4	127.6
	M2		186.4	146.6
	Average values		***177.4***	***137.1***
1TC(T)	M9	0.318	371.7	360.8
	M10		301.0	292.5
	Average values		***336.3***	***326.7***

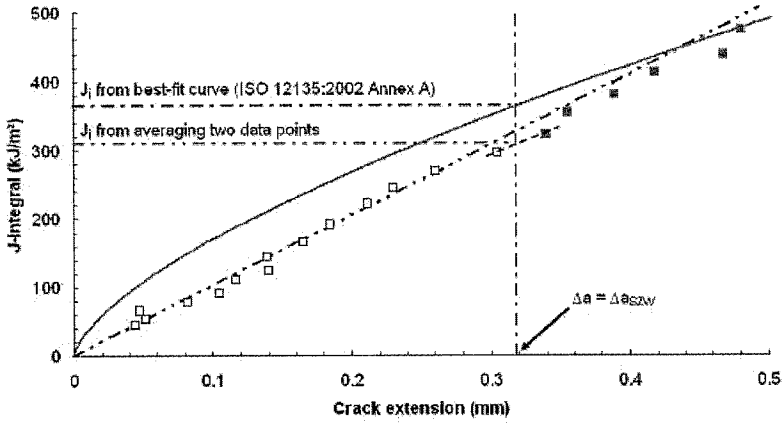


FIG. 8—*Evaluation of J_i using two different approaches: example for specimen M10.*

Conclusions

A comprehensive study has been conducted on the applicability of miniature Compact Tension specimens (with thickness B = 4.15 mm) for fracture toughness measurements in the upper shelf regime.

Results obtained from MC(T) specimens have been compared at different temperatures with data measured from standard-size 1TC(T) samples of four well-characterized materials (three RPV steels and one C-Mn steel).

As a general conclusion, we observed that MC(T) specimens consistently and systematically underestimate the elastic-plastic fracture toughness as measured from 1TC(T) samples, both in terms of ductile crack initiation ("real" initiation and its engineering estimates) and crack resistance curve.

One of the possible explanations is related to work hardening in the region ahead of the crack tip, which would occur on a much larger scale in a very small specimen and induce a significant decrease of tearing resistance. In the absence of side-grooves, however, it is loss of constraint that prevails over work hardening and causes generalized plastic yielding of the whole specimen even before actual crack initiation. This was observed on a plain-sided MC(T) sample tested within a previous investigation.[5]

Another hypothesis is that J-integral is not an adequate parameter for representing ductile crack extension for MC(T) specimens (as shown by the very early violation of the J limit criterion), and use of alternative parameters, such as CTOD (crack tip opening displacement) or CTOA (crack tip opening angle), would improve the agreement with larger specimens.

All these issues require further investigations, which are foreseen in the near future.

[5] This information is contained in the restricted SCK•CEN report R-3845 (April 2004).

Acknowledgments

The collaboration of the scientific and technical staff of the RMO department is gratefully acknowledged. This work is partially sponsored by Electrabel/Tractebel Engineering, whose support is kindly appreciated.

References

[1] Scibetta, M., Lucon, E., and van Walle, E., "Optimum Use of Broken Charpy Specimens from Surveillance Programs for the Application of the Master Curve Approach," *International Journal of Fracture,* Vol. 116, 2002, pp. 231–244.

[2] Scibetta, M., Lucon, E., and van Walle, E., "Use of Broken Charpy V-notch Specimens from a Surveillance Program for Fracture Toughness Determination," *22nd ASTM Symposium on Effect of Radiations on Materials*, 8–10 June 2004, Boston.

[3] Ingham, T. and Morland, E., "Measurement of Ductile Crack Initiation: A Comparison of Data from Multiple and Single Specimen Methods and Some Considerations of Size Effects," UKAEA Report ND-R-408(R), November 1979.

[4] Ingham, T., Wardle, G., and Bland, J. T., "The Influence of Test Piece Size and Geometry on the Upper Shelf Fracture Toughness of an A533B Pressure Vessel Steel," UKAEA Report ND-R-1333(R), August 1987.

[5] Link, R. E., Landes, J. D., Herrera, R., and Zhou, Z., "Something New on Size and Constraint Effects for J-R Curves," *Defect Assessment in Components – Fundamentals and Applications*, ESIS/EGF9, MEP London, 1991. pp.707–721.

[6] Heerens, J., Schwalbe, K. -H., and Nix, C., "Influence of Specimen Size on *J*-, J_m- and δ_5-R-Curves for Side-Grooved Compact-Tension Specimens," *Constraint Effects in Fracture, ASTM STP 1171,* 1993, pp. 429–472.

[7] Ernst, H. A., "Material Resistance and Instability Beyond *J*-Controlled Crack Growth," *Elastic-Plastic Fracture: Second Symposium, Volume I – Inelastic Crack Analysis, ASTM STP 803,* 1983, pp. 191–213.

[8] Wardle, G., "A Study of Specimen Size Effects on the Initiation Toughness and Tearing Resistance of an A533B-1 Steel," *Small Specimen Test Techniques, ASTM STP 1418,* 2002, pp. 48–66.

[9] Neimitz, A., Dzioba, I., Galkiewicz, J., and Molasy, R., "A Study of Stable Crack Growth Using Experimental Methods, Finite Elements and Fractography," *Engineering Fracture Mechanics,* Vol. 71, 2004, pp. 1325–1355.

[10] Ono, H., Kasada, R., and Kimura, A., "Specimen Size Effects on Fracture Toughness of JLF-1 Reduced-Activation Ferritic Steel," *Journal of Nuclear Materials,* 329-333, 2004, pp. 1117–1121.

[11] Wallin, K. and Laukkanen, A., "Improved Crack Growth Corrections for *J-R*-curve Testing," *Engineering Fracture Mechanics*, Vol. 71, 2004, pp. 1601–1614.

[12] Brocks, W., Anuschewski, P., and Hellmann, D., "A Concept for Scaling J_R-curves by Plastic Constraint Factors," *International Journal of Fracture,* Vol. 130, 2004, pp. 455–469.

[13] Turner, C. E., "A Re-assessment of Ductile Tearing Resistance," *Fracture Behavior and Design of Materials and Structures, Proceeedings of ECF 8, Vol. II,* 1990, pp. 933–949 and 951–968.

[14] Sumpter, J. D. G., "The Energy Dissipation Rate Approach to Tearing Instability," *Engineering Fracture Mechanics,* Vol. 64, 2004, pp. 17–37.

[15] Memhard, D., Brocks, W., and Fricke, S., "Characterization of Ductile Tearing Resistance by Energy Dissipation Rate," *Fatigue and Fracture of Engineering Materials and Structures,* Vol. 16, 1993, pp. 1109–1124.

[16] Klemm, W., "Material Resistance Against Fast Ductile Fracture in Pipeline Steels," *Dynamic Fracture Mechanics for the 1990s, Proceedings of 1989 ASME Pressure Vessels and Piping Conference*, 1989, pp. 99–104.

Journal of ASTM International, Vol. 3, No. 8
Paper ID JAI13193
Available online at www.astm.org

J. A. Joyce[1] *and P. J. Joyce*[1]

An Investigation of Specimen Geometry Effects on the Fracture Behavior of a Polytetrafluoroethylene Polymer

ABSTRACT: Recent interest by the U.S. Navy in metal filled polymers for weapons applications has resulted in a desire to characterize interactions between polymer properties associated with strain rate sensitivity, pressure sensitivity, failure mechanisms, damage mechanisms, spall strength, crystalline response to shock loading, and dynamic fracture mechanics as well as the effects of loading the polymer with various metal fillers [1]. Polytetrafluoroethylene (PTFE) is an important structural polymer that in the "7C" derivative is used for gaskets, bearing pads, piston rings, and diaphragms and when 5μm aluminum spheres are added, has important ballistic properties. Prior work [2–4] evaluated the fracture toughness of PTFE and aluminum filled PTFE over a range of temperatures and loading rates using compact tension (C(T)) specimens and the normalization method [5–7] described in Annex A15 of ASTM E 1820. Moreover, prior work [3] has shown that filling the PTFE with 10 to 25 % aluminum 5μm spheres can increase stiffness and strength while the effect on toughness can be either positive or negative depending on the loading rate and test temperature. The overall effect on fracture toughness properties derived from adding the aluminum spheres to the PTFE is small and for that reason the unfilled PTFE material was used here to study the effects of geometry on fracture toughness in this material. The normalization method was initially chosen for this project because of the scarcity and cost of specimen material, especially the filled, reactive material, the many different test conditions to be investigated, and the inadequacy of alternative methods. It was quite fortunate that the normalization method was used initially to characterize this polymer since the fracture toughness resistance curves of this material often contains ductile instabilities or "pop-ins" which would not have been well characterized by multispecimen methods. The objective of this work is to compare the fracture toughness measurements obtained from C(T) and precracked Charpy (SE(B)) specimens tested under similar test conditions. A comparison is also made between *J-R* curves obtained using the single specimen normalization method and the "Basic" or multispecimen procedure. A limited study of the effects of side grooving on the crack extension and on the resulting *J-R* curves is included here.

KEYWORDS: *J*-integral, elastic-plastic fracture, polytetrafluorethylene (PTFE), pop-in behavior, geometry effects, side grooves, crack growth corrections

Introduction

Prior work [2–4] evaluated the fracture toughness of PTFE and aluminum filled PTFE over a range of temperatures and loading rates using compact tension (C(T)) specimens and the normalization method [5–7] described in Annex A15 of ASTM E 1820 (Standard Test Method for Measurement of Fracture Toughness). Prior work [3] has shown that filling the PTFE with 10 to 25 % aluminum 5μm spheres can increase stiffness and strength while the effect on toughness can be either positive or negative depending on the loading rate and test temperature. The overall effect on fracture toughness properties derived from adding the aluminum spheres to the PTFE is small and for that reason the unfilled PTFE material was used here to study the effects of geometry on fracture toughness in this material.

The normalization method was chosen before the work was started on this project because of the scarcity and cost of specimen material, especially the filled, reactive material, the many different test conditions to be investigated, and the inadequacy of alternative methods. The standard elastic compliance method was not acceptable since most of the testing was to be done at elevated loading rates, while the multispecimen or "basic" method requires at least six times as much material and poses its own difficulties when matching loading rates over different stroke ranges using servohydraulic test equipment. It was quite fortunate that the normalization method was used initially to characterize this polymer since the fracture

Manuscript received May 9, 2005; accepted for publication March 29, 2006; published online August 2006. Presented at ASTM Symposium on Fatigue and Fracture Mechanics: 35th Volume on 18–20 May 2005 in Reno, NV; R. E. Link and K. M. Nikbin, Guest Editors.

[1] Professor and Associate Professor of Mechanical Engineering, respectively, U.S. Naval Academy, Annapolis, MD 21402.

Copyright © 2006 by ASTM International, 100 Barr Harbor Drive, PO Box C700, West Conshohocken, PA 19428-2959.

toughness resistance curves of this material often contains ductile instabilities or "pop-ins" which would not have been well characterized by multispecimen methods.

While the research work conducted previously on this material was done using C(T) specimens, it is expected that smaller and simpler precracked Charpy type specimens, loaded as a single-edge-notched bend specimen (SE(B)) in a standard pendulum machine, will ultimately be used for quality assurance. This requires that similar fracture toughness resistance curves and J_{Ic} values be measured from these two geometries. A straightforward comparison of the results of two different geometries also would provide a demonstration of the transferability of the fracture toughness properties measured on this polymeric material to other test geometries and ultimately to the structural application. If comparable fracture properties cannot be obtained from C(T) and precracked Charpy (SE(B)) geometries, the transferability of these properties to structural applications would certainly not be expected. While this seems obvious, there does not seem to be an example which makes this type of comparison for other polymeric materials available in the literature.

The objective of this work is to compare the fracture toughness measurements obtained from C(T) and precracked Charpy (SE(B)) specimens tested under similar test conditions. A comparison is also made between the *J-R* curves obtained using the single specimen normalization method and the "Basic" or multispecimen procedure. A limited study on the effects of side grooving on the crack extension and on the resulting *J-R* curves is included here. Many of the temperature and rate test conditions studied in the previous work resulted only in crack tip blunting. This study avoids such conditions and explores phenomena known to produce crack extension due to crack tearing. This generally means that tests conducted here will be done at the lower temperatures and higher loading rates studied in the earlier work.

Material Description

Polytetrafluoroethylene (PTFE 7C) is a semicrystalline polymer. The percentage of crystallinity depends upon the thermal processing used to manufacture the component. The PTFE phase diagram shows that at atmospheric pressure the crystalline component can change structure from hexagonal to triclinic just below room temperature. The PTFE material of interest here is obtained by preforming PTFE 7C powder under pressure into a cylindrical puck with a diameter of 89 mm and a thickness of approximately 39 mm. Then the puck is sintered using a precise heating and cooling cycle to consolidate the material. The result of this process is a cylindrical "puck" with a diameter of approximately 80 mm and a height of approximately 40 mm. Since the percentage of crystallinity of PTFE is temperature and pressure dependent it is expected that the mechanical properties will also be temperature and pressure dependent. PTFE 7C was studied previously [2–4] and tensile data were obtained for commercial sheet using round tensile specimens. The tensile test results for the PTFE 7C polymer were strongly temperature and rate dependent.

Tensile Properties

Only limited mechanical property data are available on polytetrafluoroethylene since it is commonly used only as a coating material with its dominant properties being a low friction coefficient and high application temperature. Tensile properties were measured [2] using round tensile specimens with a 25-mm (1-in.) gage length and 7.1-mm (0.28-in.) diameter obtained from commercially available PTFE 7C sheet material of 13.7-mm thickness. Tensile specimens were tested at three test temperatures between −73 and 21 °C and at three loading rates between 2.5×10^{-5} to 2.5×10^{-2} m/s as shown in Figs. 1 and 2. Higher test rates and lower test temperatures result in stiffer and dramatically more brittle tensile results with typical elongations to failure being reduced from in excess of 300 % to approximately 20 %, while lower test temperatures increased yield and failure loads, but only by 10 to 20 %.

Fracture Toughness

J-integral based fracture toughness properties have been measured for polymeric materials throughout the development of the *J*-integral method. Early tests [8–12] utilized the multiple specimen method of ASTM E 813-81, (ASTM, 1987), and this gave good results in most cases but requires the availability of many specimens to obtain each J_{Ic} measurement. Chung and Williams [13] used the elastic compliance method to obtain single specimen J_{Ic} measurements, but they found that the hysteresis loop resulting from the

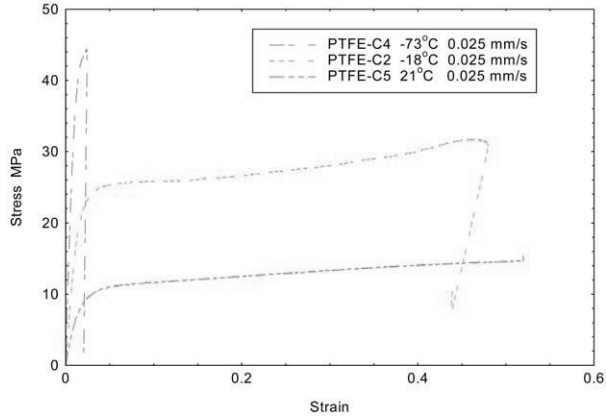


FIG. 1—*Effect of test temperature on tensile stress-strain curves of the PTFE polymer.*

viscoelastic nature of the polymer obtained during the elastic unloading and reloading sequence caused considerable uncertainty in the crack extension estimates. The normalization method was applied in Refs. [5–7] to rubber toughened polymers and ultrahigh molecular weight polyethylene, which yielded excellent results at slow loading rates. The recent work of Bernal and associates [14–16] has demonstrated that a load separation criterion is valid for polymeric materials using the methods developed by Sharobeam and Landes [17]. Load separability is required for application of the normalization method. This work shows the equivalence in polymers of the J resistance curves obtained from multispecimen methods and the normalization method.

This equivalence also was shown to exist for a glassy PVC polymer over a range of relatively slow crosshead loading rates by Che et al. [18]. The normalization method has recently been added to the ASTM Elastic-Plastic Fracture Toughness Standard E 1820, and is well accepted for fracture toughness of metals when elastic compliance techniques are not applicable. In this work the normalization method is assumed to be suitable for defining the *J-R* curve and fracture initiation values for the PTFE polymer.

The present authors [2,4] previously applied the normalization technique to the PTFE 7C polymer with tests conducted over a range of loading rates from 2.5×10^{-5} to 0.39 m/s and a range of test temperatures from −73 to 21°C. Using the normalization method, a fracture initiation property more equivalent to the J_{Ic} or $J_{Ic}(t)$ of ASTM E 1820 could be measured as well as the *J-R* curve for each test condition. The offset

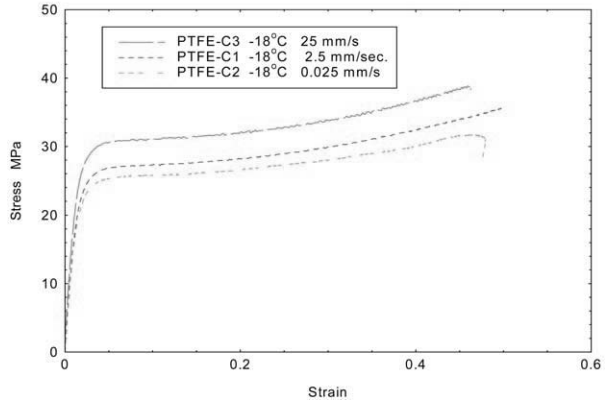


FIG. 2—*Effect of loading rate on tensile stress-strain curves of the PTFE polymer.*

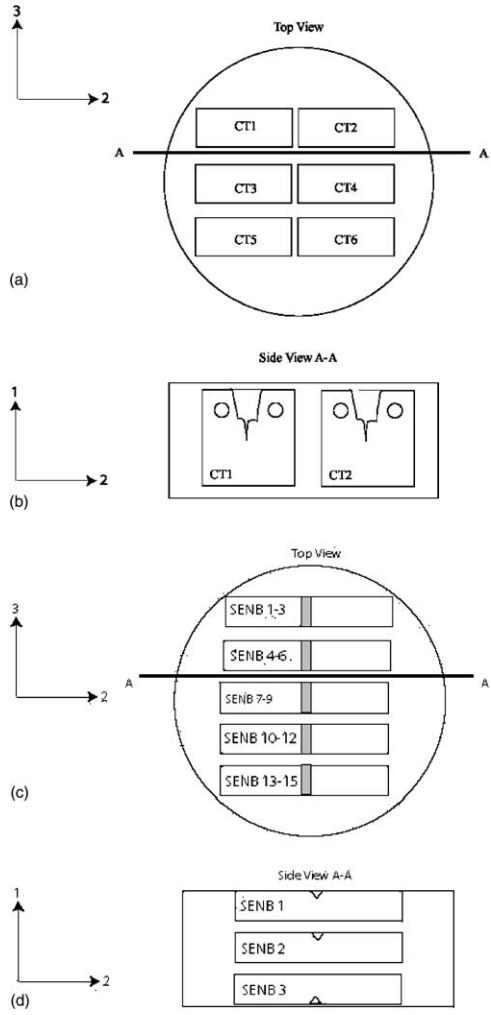


FIG. 3—*Schematic drawings showing specimen orientations and cutting diagrams for obtaining the test specimens from the fabricated "puck."*

blunting line approach of ASTM E 1820 was used to define J_{Ic} or $J_{Ic}(t)$ with the blunting line slope taken from $J=2\sigma_Y\Delta a$ with the yield stress defined in terms of the static tensile properties. Specimens were machined using standard $\frac{1}{2}$T C(T) (W=2B=25.4 mm) and sharp-notched Charpy (W=B=10 mm, S =4W) specimen geometries, with specimens oriented in the PTFE "pucks" in the (2-1) orientation as shown in Fig. 3. Specimen notches were sharpened by pressing a razor blade into the notch, as is typically done in fracture testing of polymeric materials. Most specimens were tested without side grooves, but a comparison between side grooved and nonside grooved specimen results is included in this paper for both the C(T) and sharp-notched Charpy specimen geometries. A standard load line mounted COD gage was used on integral knife edges to measure the COD/Load line displacement on the C(T) specimens. A small "ring gage" mounted at the surface of the specimen was used to measure the COD on the Charpy specimens while the load line displacement was obtained directly from the stroke transducer. Because of the small size of the Charpy specimens a direct measurement of load line displacement was not accom-

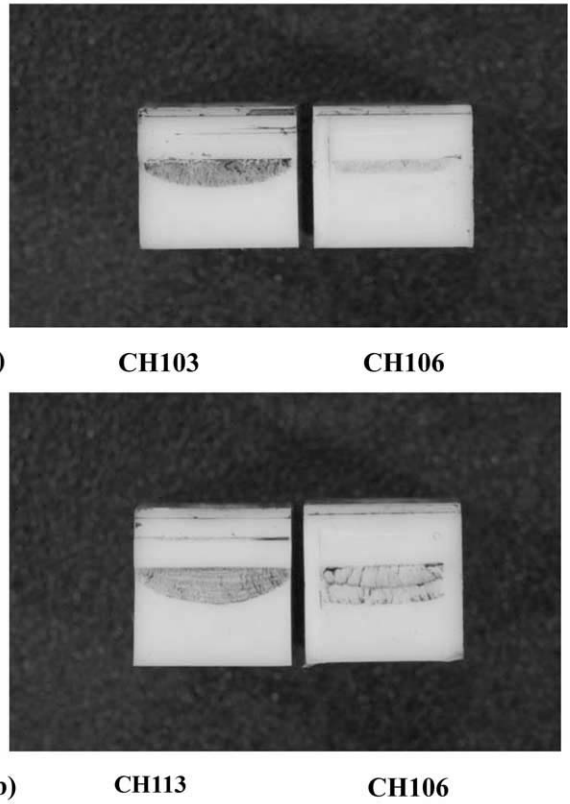


FIG. 4—*Crack extensions on sharp notched Charpy specimens marked using lay-up dye.*

plished. However, the very soft and flexible test specimens and the rigid test machine means that little error in load line displacement was likely to be introduced by this type of measurement. Nonetheless, the *J* integral was obtained by using the COD measurement as described below.

After loading, the crack extension was marked by introducing a blue "lay-up" dye into the notches, letting the dye dry, then breaking the specimens open after immersion in liquid nitrogen. Typical fracture surfaces are shown in Figs. 4 and 5 for sharp-notched Charpy specimens and C(T) specimens, respectively.

Typical *J-R* curves obtained for the C(T) specimen geometry in the previous study [4] are presented in Figs. 6 and 7 with Fig. 6 showing the strong effect of temperature and Fig. 7 showing the smaller effect of applied loading rate on the *J* resistance curves of this material with about each order of magnitude in loading rate corresponding to a temperature shift of approximately 10°C. These results show clearly that specimens loaded at or above room temperature tend to demonstrate only crack tip blunting and that as the loading rate is increased, fracture instabilities are observed that tend to become smaller and more numerous as the loading rate is further increased. The *J-R* curves become smoother at the highest test rates utilized, but observations from the fracture surfaces show that the process remains discontinuous, just disguised by the smaller scale of the run-arrest (pop-in) events.

Analysis

The basic input data consist of a load versus displacement record for the test, a measured initial crack length, a_i, and a measured final crack length, a_f. The load is normalized according to:

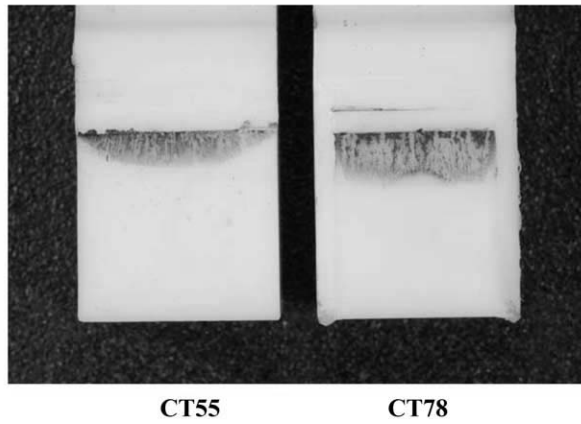


FIG. 5—*Typical specimen fracture surfaces of C(T) specimens with the crack extension marked using lay-up dye.*

$$P_{Ni} = \frac{P_i}{WB\left[\frac{W - a_{bi}}{W}\right]^{\eta_{pl}}} \tag{1}$$

where a_{bi} is the blunting corrected crack length at the ith data point and $\eta_{pl}=2+0.522(W-a_{bi})/W$, with W denoting the width of the fracture specimen. The plastic (inelastic) component of the crack opening displacement (COD) is normalized as:

$$COD'_{pl} = COD_{pl}/W \tag{2}$$

A normalized load displacement record for a PTFE $\frac{1}{2}$T C(T) specimen is shown in Fig. 8. The initial tangent stiffness measured from the load displacement record and the measured specimen crack length were used in the compliance relationship of ASTM E 1820 to define an effective elastic modulus for each specific loading rate; these values are tabulated in Table 1. This effective modulus was used to separate the elastic and "plastic" or inelastic components of the total *COD* to obtain COD_{pl}.

Figure 8 shows the full dataset for a typical specimen (specimen CT58) normalized using the above relationships based on the initial crack length with the exception of the final data point, shown as a

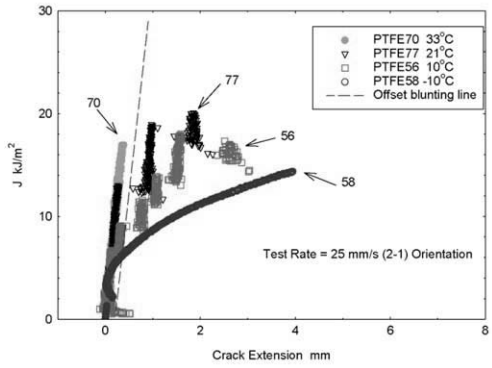


FIG. 6—*Effect of test temperature on the J-R curve fracture toughness.*

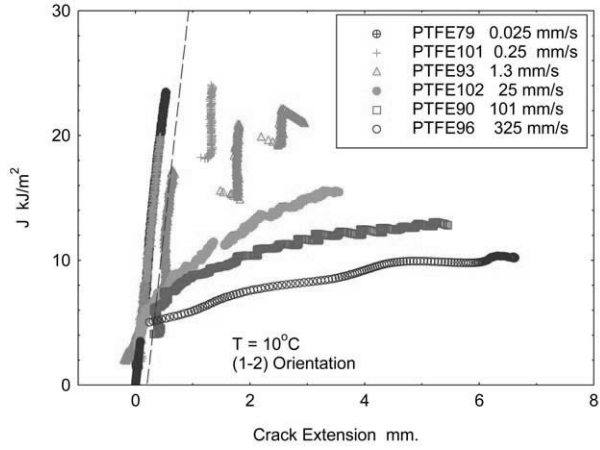


FIG. 7—*Effect of specimen loading rate on the J-R curve fracture toughness.*

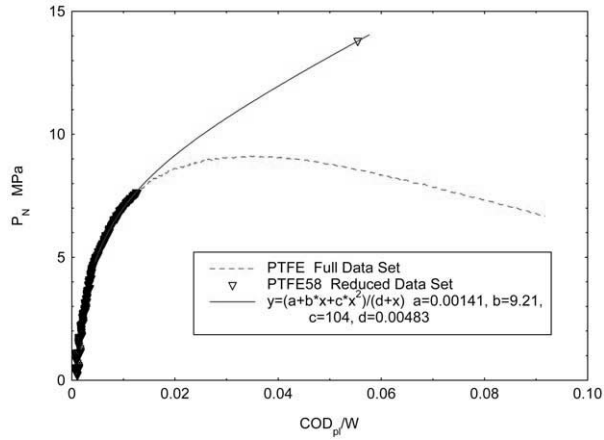


FIG. 8—*Example application of normalization method.*

TABLE 1—*C(T) specimen data.*

Specimen ID	Temp. °C	Loading Rate mm/s	E_{eff} MPa	a_o mm	a_f mm	Side Groove %	dJ/dt kJ/m² s
CT58	−10	25	1780	13.26	17.22	0	160
CT56	10	25	1440	13.46	15.75	0	193
CT77	21	25	960	13.26	15.11	0	117
CT55	−10	0.25	1230	13.28	15.04	0	2.18
CT57	10	0.25	1370	13.31	13.66	0	1.69
CT76	21	0.25	820	12.50	12.67	0	0.89
CT78	−10	0.25	1390	13.67	16.67	20	3.37

triangle, which was normalized using the optically measured nine-point average final crack length. A reduced dataset is then obtained including data short of maximum load, and if possible, short of the onset of ductile crack initiation. These data are corrected slightly by using an estimated blunting corrected crack length.

A normalization function of the form:

$$P_N = \frac{a + b * COD'_{pl} + c * (COD'_{pl})^2}{d + COD'_{pl}} \tag{3}$$

is then fit to the reduced dataset as shown in Fig. 8. Next the full dataset is analyzed to determine the crack length required to place each load displacement pair on the normalization function of Eq 3. Associating each *COD*-load pair with the proper crack length between the initial and final optically measured crack lengths will place the data point on the normalization function. In this way the crack length corresponding to each *COD*-load pair can be estimated. The result is that each *COD*-load pair can be associated with a crack extension, and the data necessary to obtain a *J-R* curve according to ASTM E 1820 are determined. The resulting *J-R* curve for specimen CT58 is shown in Fig. 6. After completion of the analysis, load, *COD*, *J*, crack extension and elapsed time data are available, with generally between 500 and 2000 datasets being measured or computed for each test.

Because of the small size of the Charpy size specimen it is difficult to measure the load-line displacement directly for *J* estimation as required by ASTM E 1820. For this reason recent proposed revisions to E 1820 allow evaluating *J* from the crack mouth opening displacement using the relationship [19]:

$$J_{pl} = \frac{\eta_{pl(i)} A_{pl(i)}}{B_N b_i} \tag{4}$$

where:

A_{pl} = area under load versus crack mouth opening displacement record,
$\eta_{pl(i)} = 3.785 - 3.101(a_i/W) + 2.018(a_i/W)^2$
$b_i = W - a_i$.

This relationship does not include a crack growth correction to the *J* integral and the new E 1820 revision Annex A16 obtains an estimate of the crack growth correction by first correcting *J* values using the following relationship:

$$J = J_{elo} + \frac{J_{plo}}{1 + \left(\frac{\alpha - 0.5}{\alpha + 0.5}\right)\frac{\Delta a}{b_o}} \tag{5}$$

with $\alpha = 1$ for SE(B) specimens and $\alpha = 0.9$ for C(T) specimens and then fitting a power law expression $J = J_{1mm}\Delta a^m$ to the corrected $J(\Delta a)$ data for crack growths exceeding $\Delta a/b_o \geq 0.05$, and finally calculating the final crack growth corrected $J(\Delta a)$ data using:

$$J = J_{elo} + \frac{J_{plo}}{1 + \left(\frac{\alpha - m}{\alpha + m}\right)\frac{\Delta a}{b_o}} \tag{6}$$

Discussion of Results

Specimen Geometry Effects

Load displacement records for typical C(T) and Charpy size SE(B) specimens are presented in Figs. 9 and 10. The Charpy specimens generally demonstrate lower maximum loads and less load-line displacement at maximum load and at the end of the test. The *COD* gage used for the precracked Charpy specimens was a typical "ring gage" that was fit into the crack mouth at the specimen surface and had a range of approximately 2 mm. A standard E399 style *COD* gage was used for the C(T) specimens mounted on

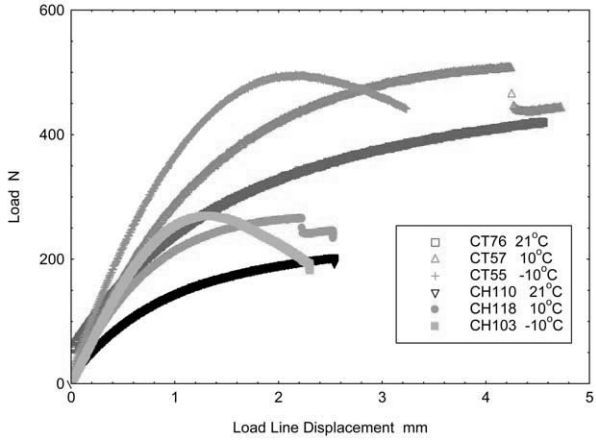


FIG. 9—*Load versus load-line displacement records for PTFE specimens obtained at 0.25 mm/s.*

integral load-line knife edges. Looking more closely at the records in Figs. 9 and 10 shows that at 21°C the specimens demonstrate only a rising load, consistent with crack blunting behavior in a fracture toughness specimen. All four specimens tested at 10°C show "pop-in" behavior, and show only a rising load before and after the pop-ins. The coldest tests, at −10°C, demonstrate a much more typical ductile fracture behavior with the distinct rise to a maximum load followed by a smooth load drop until the test was completed. Tables 1 and 2 include crack length measurement data for the C(T) and Charpy specimens tested in this study. The loading rate presented in column 2 of these tables is obtained from the load line displacement for both specimen geometries. The J integral and dJ/dt in column 8 of these tables was obtained from COD measurements for both specimens.

Figures 11–13 show the comparisons of *J-R* curves obtained from C(T) and Charpy specimen geometries at 21, 10, and −10°C, respectively. At 21°C (Fig. 11) all four specimens demonstrate predominant crack tip blunting behavior, with only the highest loading rate C(T) specimen demonstrating any crack extension, and this crack extension is two "pop-in" instability events characterized by an unstable crack jump and a subsequent crack blunting behavior. Figure 12 shows pop-ins occurring in both specimen geometries with smaller and more numerous pop-ins corresponding to higher loading rates. Figure 14

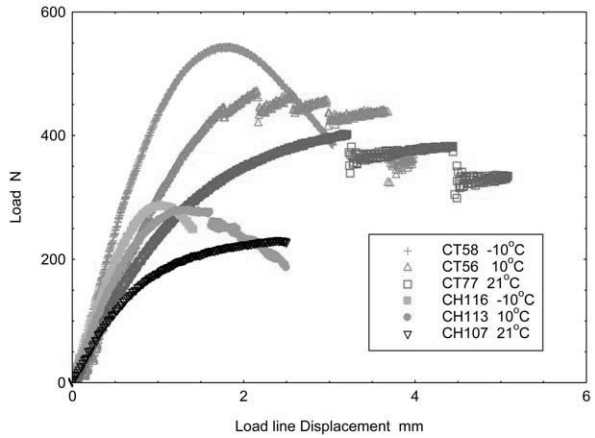


FIG. 10—*Load versus load-line displacement records for PTFE specimens obtained at 25 mm/s.*

TABLE 2—*Precracked Charpy specimen data.*

Specimen ID	Temp. °C	Loading Rate mm/s	E_{eff} MPa	a_o mm	a_f mm	Side Groove %	d*J*/dt kJ/m^2 s
CH116	−10	25	1730	3.73	5.38	0	202
CH113	10	25	1340	3.75	5.58	0	217
CH107	21	25	1290	3.91	4.16	0	178
CH114	−10	25	1460	3.85	4.01	0	156
CH97	−10	25	1590	3.71	5.65	0	91.9
CH111	−10	25	1660	3.75	4.61	0	90.0
CH105	−10	25	1500	3.65	3.65	0	130
CH106	10	25	1150	3.97	6.41	20	215
CH117	10	2.5	1190	3.74	4.83	0	21.0
CH118	10	0.25	1110	3.78	4.22	0	1.92
CH110	21	0.25	665	3.57	3.73	0	1.37
CH103	−10	0.25	1250	3.65	5.16	0	2.54
CH112	−10	0.25	1210	3.76	4.61	20	2.15
CH99	−10	0.0025	1160	3.82	4.23	0	0.0204
CH115	10	0.0025	760	3.76	4.83	0	0.0150

presents fracture surface photographs of specimens CT77 and CH113 showing the presence of clear markings corresponding to two large pop-ins in specimen CT77 and many smaller pop-ins in specimen CH113. Figure 13 shows that at −10°C the pop-ins have been eliminated, not being observable on the *J-R* curve and also not visible on the fracture surfaces. The comparison between the C(T) and Charpy *J-R* curves is good in most cases with the biggest differences occurring in the smooth −10°C results of Fig. 13.

Figures 15–18 present plots of *J* versus time obtained showing the evaluation of d*J*/dt for four C(T) and four Charpy test samples. Values of d*J*/dt are presented for all specimens in Tables 1 and 2. Comparing the *J-R* curves of Figs. 11–13 with the estimated d*J*/dt rates of Tables 1 and 2 show that the differences observed between *J-R* are consistent with the measured differences in the loading rates, with lower *J-R* curves corresponding to higher d*J*/dt loading rates in all cases. For example, as shown in Fig. 17, Specimen CT58 is loaded 20 % slower than specimen CH116 resulting in a *J-R* curve on Fig. 13 that is approximately 15 % higher throughout its extent.

Crack Growth Correction of the J Integral

Because of the small size of the Charpy specimen it is difficult to measure the load-line displacement directly as recommended by E 1820 and many investigators obtain *J* using the *COD* gage measurement

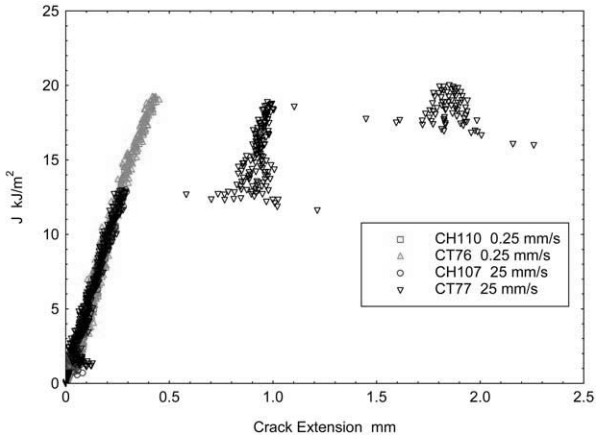


FIG. 11—*J-R curves obtained at 21°C.*

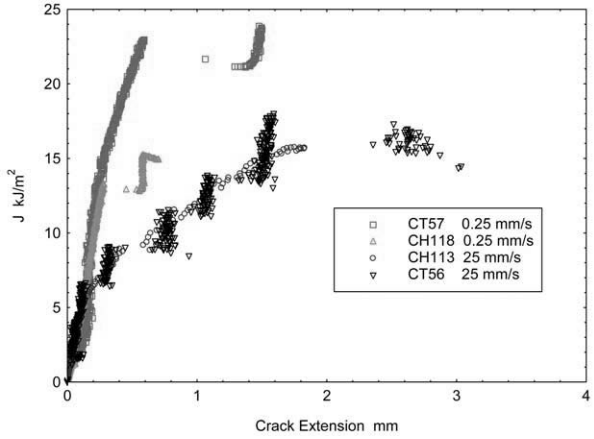


FIG. 12—*J-R curves obtained at 10°C.*

and Eq 4 presented previously. Use of this equation for *J* causes an error since it does not account for the crack growth correction that is included in the E 1820 incremental method for evaluating *J*. In E 1921 the *COD* method of evaluating *J* is used to obtain the Master Curve reference temperature T_o, and in that case it is an effective method since ductile crack growth is required to be small and the crack growth correction is inconsequential. When the *COD* measurement is used to evaluate *J* for a *J-R* curve application as done here, accurate results require the incorporation of a crack growth correction. The newest version of E 1820, which is presently being balloted by ASTM Committee E08, includes the procedure presented above to include an estimate of the crack growth correction in the *J* integral, and this correction has been used for the above *J-R* curves, for those specimens which exhibited substantial crack extension.

Figure 19 shows the magnitude of this correction for specimen CH113 which exhibited about 2 mm of crack extension. The crack growth correction causes a reduction in the *J* value of about 15 %, which is typical of metals. A *J-R* curve obtained for the same specimen using the E 1820 incremental *J* evaluation method is presented for comparison, and the correspondence is excellent. The latter curve was obtained here using the load-line displacement measured using a remote actuator LVDT, which can introduce

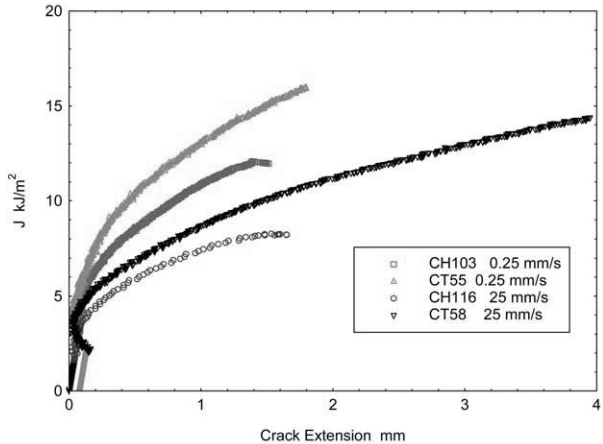


FIG. 13—*J-R curves obtained at −10°C.*

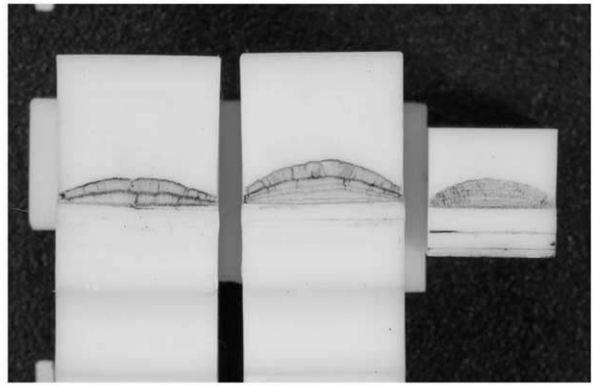


FIG. 14—*Fracture surfaces showing two pop-ins on specimen CT77, five pop-ins on specimen CT56 and multiple smaller pop-ins in the Charpy specimen CH113.*

inaccuracies of its own, but in this case, since the specimens are so flexible and the loads are so low, it is felt to give reasonably accurate results. Crack growth corrected, *COD* based, *J* integral calculations have been used throughout this paper.

Effect of Side Grooves

All of the testing conducted previously on this material by the present authors [2–4] was done on nonside grooved specimens. Most of the specimens tested in this study were also nonside grooved, but in order to investigate the effect of side grooves, two side grooved Charpy size specimens and one side grooved C(T) specimen were tested here. Figures 20 and 21 show the effect of side grooves on the Charpy specimens tested at two different loading rates in comparison with nonside grooved specimens. Clearly in the higher loading rate case which results in smooth *J-R* curves the effect of the side groove on the *J-R* curve is very slight, even though the crack straightness is affected, as shown in Fig. 4(*a*) for these two samples. When "pop-ins" intervene, however, the *J-R* curves are quite different, and it is not surprising that it was the side groove specimen that demonstrated the pop-in behavior. The fracture surfaces for the two specimens

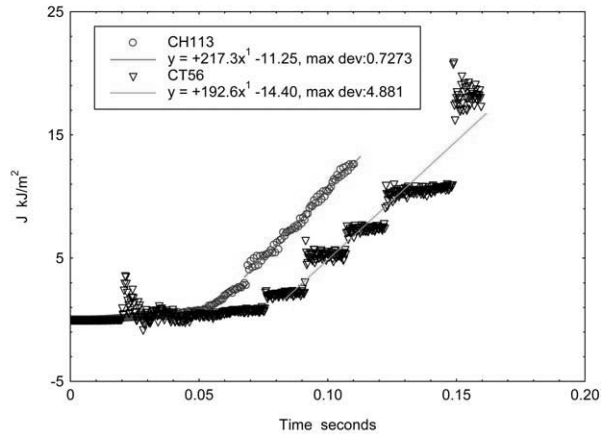


FIG. 15—*Comparison of dJ/dt for C(T) and Charpy specimens tested at 25 mm/s at 10°C.*

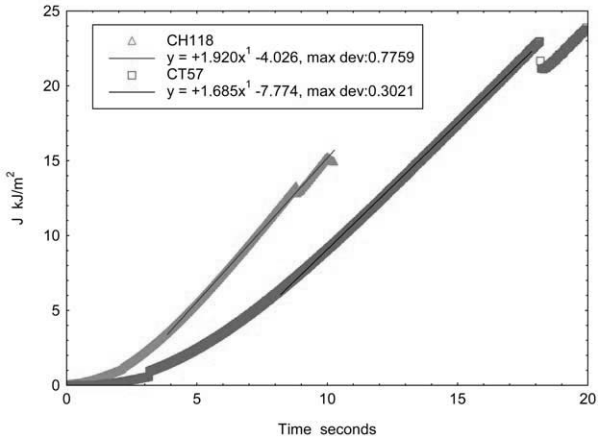


FIG. 16—*Comparison of dJ/dt for C(T) and Charpy specimens tested at 25 mm/s at 10°C.*

plotted in Fig. 21 are presented in Fig. 4(*b*), and show that the nonside grooved specimen, CH113, also demonstrated pop-ins, though they were smaller and more numerous. It is not clear from the single pair of specimens available whether this would be demonstrated in general.

Figure 22 shows a comparison between side grooved and nonside grooved C(T) specimens. These results show the side grooved specimen *J-R* curve falling below the nonside grooved curve, at least once the crack extension has proceeded far enough that the thumbnail curvature of the nonside grooved specimen crack front has fully developed. The fracture surfaces of these two C(T) specimens were presented previously in Fig. 5. The two Charpy specimens were included in Fig. 22 to again demonstrate the excellent agreement between *J-R* curves obtained using the two different specimen geometries.

Multispecimen J-R Curve Comparison

The fracture toughness of polymers has generally been investigated using a multispecimen technique [8–12]. The multispecimen procedure is difficult to apply for loading rates and temperatures where pop-in

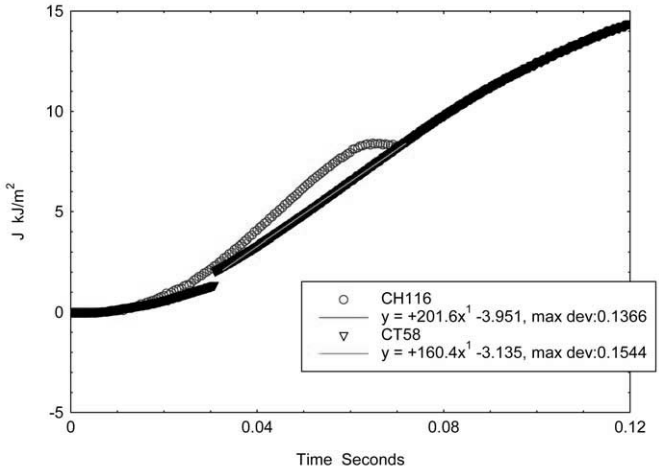


FIG. 17—*Comparison of dJ/dt for C(T) and Charpy specimens tested at 25 mm/s at −10°C.*

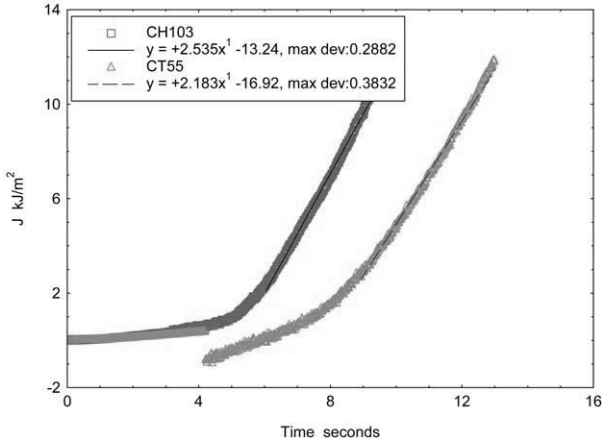


FIG. 18—*Comparison of dJ/dt for C(T) and Charpy specimens tested at 25 mm/s at −10°C.*

instabilities are present, and hence it seems to be a somewhat undesirable procedure in general, especially since so many specimens are required to obtain a complete *J-R* curve. Four specimens were tested here at −10°C and 25 mm/s, specifically because under these conditions smooth *J-R* curves were expected. These results were analyzed using the normalization method, but without using crack growth corrections. One specimen did not demonstrate any crack extension; the other three are plotted in Fig. 23. Not surprisingly the three resistance curves fall directly on top of each other. The final point in each case is filled in, since in the case one had run only a multispecimen test; only this point would be available to plot. The three points would certainly give a decent representation of the material *J-R* curve under these loading conditions, but the normalization method obtains full *J-R* curves for each specimen, giving much additional information about the material toughness. One can emphasize again that results from the normalization method were used here to choose conditions under which the multispecimen method would give reasonable results. Many other choices of test conditions and loading rates would not have yielded any meaningful results if only the multispecimen method had been available.

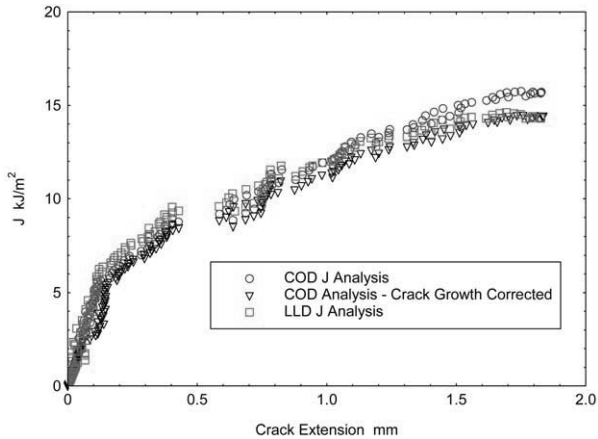


FIG. 19—*Comparison of J-R curves for Charpy specimen CH113 with the J integral calculated using COD and load-line displacement relationships according to E 1820.*

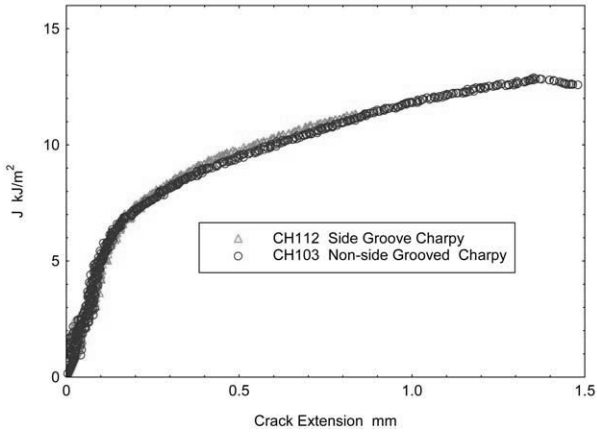


FIG. 20—*Comparison of side grooved and nonside grooved notched Charpy J-R curves at 25 mm/s.*

Conclusions

The normalization method was found to be an excellent method of evaluating the *J-R* curves of this material across a range of toughness properties from notch blunting to ductile crack extension. Comparison of the *J-R* curves obtained using the multispecimen and normalization methods showed excellent agreement, but it also showed that the normalization method is applicable to test conditions which produced pop-in behavior, conditions which could not be handled effectively using the multispecimen method. The normalization method also showed details in the *J-R* curves that would not have been observed using the multispecimen method, especially the small ductile instabilities or "pop-ins" that occurred regularly with this material under some test conditions.

Excellent agreement was found to exist between *J-R* curves obtained from the $\frac{1}{2}$T C(T) and the Charpy size SE(B) specimens of the polytetrafluoroethylene (PTFE) used in this study. In cases where differences between the *J-R* curves were observed they corresponded to differences in the applied loading rate dJ/dt with lower *J-R* curves consistently observed when the loading rate defined in terms of dJ/dt was higher.

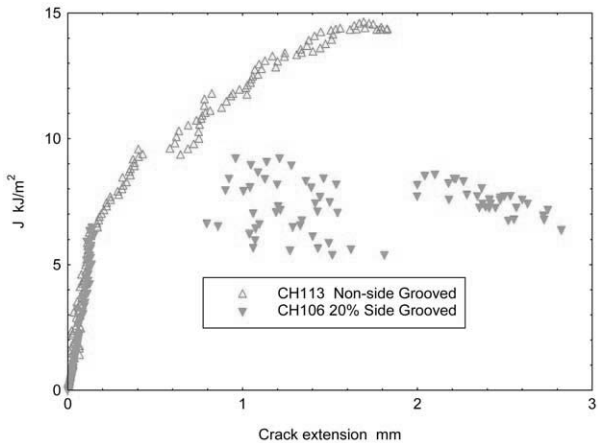


FIG. 21—*Comparison of side grooved and nonside grooved notched Charpy J-R curves at 25 mm/s.*

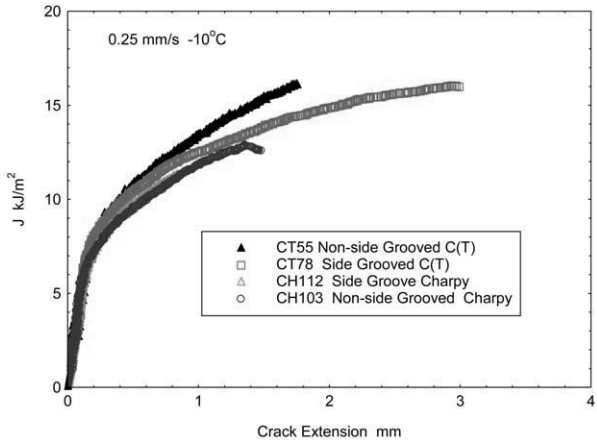


FIG. 22—*Comparison of J-R curves for side grooved and nonside grooved C(T) and Charpy specimens all tested at 25 mm/s.*

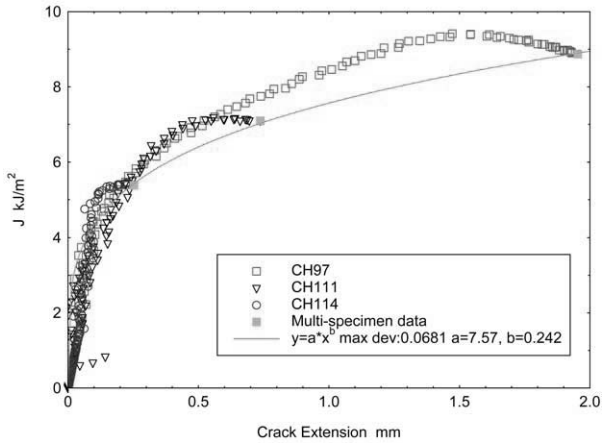


FIG. 23—*Comparison of multispecimen and normalization method J-R curves.*

Application of the new E 1820 Annex A16 procedure to obtained crack growth corrected *J-R* curves worked well for the Charpy size SE(B) specimens of this material.

Side grooves removed the "thumb-nail" crack extension in both the C(T) and Charpy specimen geometries but had little effect on the measured *J-R* curve. When effects of side grooves were present on the *J-R* curves, the side grooved specimen did exhibit somewhat lower *J-R* curves, as has been typically observed in metals. Side grooved specimens also demonstrated more pop-ins than the equivalent nonside grooved specimens.

References

[1] Kirby, G., Garrett, R., and Dyka, C., "Review of Progress in Modeling Constitutive, Damage and Fracture Behavior of PTFE Subject to Dynamic Loading," *9th International Conference of Plasticity*, A. S. Khan, Ed., Quebec, July 7–10, 2003.

[2] Joyce, J. A., "Fracture Toughness Evaluation of Polytetrafluorethylene," *Polym. Eng. Sci.*, Vol. 43, 2003, pp. 1702–1714.

[3] Joyce, J. A. and Joyce, P. J., "Toughness Characterization of a Metal Filled Polytetrafluoroethylene Using the *J*-Integral," *Eng. Fract. Mech.*, Vol. 71, 2004, pp. 2513–2531.

[4] Joyce, P. J. and Joyce, J. A., "Evaluation of the Fracture Toughness Properties of Polytetrafluoroethylene," *International Journal of Fracture*, Vol. 127, 2004, pp. 361–385.

[5] Landes, J. D. and Zhou, Z., "Application of Load Separation and Normalization Methods for Polycarbonate Materials," *International Journal of Fracture*, Vol. 63, 1993, pp. 383–393.

[6] Zhou, Z., Landes, J. D., and Huang, D., "*J-R* Curve with the Normalization Method for Toughened Polymers," *Polym. Eng. Sci.*, Vol. 34, 1994, pp. 128–134.

[7] Landes, J. D., Bhambri, S. K., and Lee, K., "Fracture Toughness Testing of Polymers Using Small Compact Specimens and Normalization," *J. Test. Eval.*, Vol. 31, No. 3, 2003, pp. 126–132.

[8] Chan, M. G. V. and Williams, J. G.,"*J*-Integral Studies of Crack Initiation of a Tough High Density Polyethylene," *International Journal of Fracture*, Vol. 23, 1983, pp. 145–159.

[9] Hashemi, S. and Williams, J. G., "Fracture Characterization of Tough Polymers Using the *J* Method," *Polym. Eng. Sci.*, Vol. 26, 1986, pp. 760–767.

[10] Huang, D. D. and Williams, J. G., "*J* Testing of Toughened Nylons," *J. Mater. Sci.*, Vol. 22, 1987, pp. 2503–2508.

[11] Huang, D. D., "A Comparison of Multispecimen J-Integral Methods as Applied to Toughened Polymers," *Advances in Fracture Research*, Vol. 4, 7th International Conference on Fracture, University of Houston, 1989, pp. 2725–2732.

[12] Takemori, M. T. and Narisawa, I., "*J*-Integral Characterization of Impact-Modified Polymers," *Advances in Fracture Research*, Vol. 4, 7th International Conference on Fracture, University of Houston, 1989, pp. 2733–2737.

[13] Chung, W. N. and Williams, J. G., "Determination of J_{Ic} for Polymers Using the Single Specimen Method," *Elastic-Plastic Fracture Test Methods: The User's Experience (2nd Volume)*, ASTM STP 1114, ASTM International, West Conshohocken, PA, 1991, pp. 320–339.

[14] Bernal, C. R. Cassanelli, A., Anibal, N., and Frontini, P. M., "A Simple Method for *J-R* Curve Determination in ABS Polymers," *Polym. Test.*, Vol. 14, 1985, pp. 85–96.

[15] Bernal, C. R., Cassanelli, A., and Frontini, P., "On the Applicability of the Load Separation Criterion to Acrylonitrile/Butadiene/Styrene Terpolymer Resins," *Polymer*, Vol. 37, 1996, pp. 4033–4039.

[16] Bernal, C. R., Montemartini, P. E., and Frontini, P. M., "The Use of Load Separation Criterion and Normalization Method in Ductile Fracture Characterization of Thermoplastic Polymers," *J. Polym. Sci.*, Vol. 34, 1996, pp. 1869–1880.

[17] Sharobeam, H. M. and Landes, J. D., "The Load Separation Criterion and Methodology in Ductile Fracture Mechanics," *International Journal of Fracture*, Vol. 47, 1991, pp. 81–104.

[18] Che, M., Grellman, W., Seidler, S., and Landes, J. D., "Application of a Normalization Method for Determining *J-R* Curves in Glassy Polymer PVC at Different Crosshead Speeds," *Fatigue and Fracture of Engineering Materials*, Vol. 20, 1997, pp. 119–127.

[19] Kirk, M. T. and Dodds, R. H., Jr., "*J* and *CTOD* Estimation Equations for Shallow Cracks in Single Edge Notch Bend Specimens," *J. Test. Eval.*, Vol. 21, No. 4, 1993, pp. 228–238.

Journal of ASTM International, January 2006, Vol. 3, No. 1
Paper ID JAI13188
Available online at www.astm.org

Timothy O. Lawrence,[1] *M.Sc. and David M. Boyajian,*[2] *Ph.D.*

Surface Roughness, Quasi-Static Fracture, and Cyclic Fatigue Effects on GFRP- and CFRP-Concrete Bonded Interfaces

ABSTRACT: The recently developed experimental fracture approach known as the Single Contoured-Cantilever Beam (SCCB) was used to characterize the interface bonds between concrete substrates and two varieties of FRP: glass and carbon (abbreviated GFRP and CFRP, respectively). Limited research has been performed concerning the FRP-concrete interface bond relative to three surface-roughness grades: *low*- (<10 μm), *moderate*- (≈ 10–50 μm), and *high*- (>50 μm), to establish the optimal formation for bonding. By use of the SCCB approach, Mode I critical strain energy release rate results are measured and quantified. Finally, considering that a majority of externally strengthened FRP concrete structures involves bridges and girders that are subjected to repeated (as opposed to static) loads, a preliminary study is conducted on cyclically fatigued FRP-concrete interfaces under varying load-ratio and frequency effects.

KEYWORDS: Surface Roughness, CFRP-Concrete, GFRP-Concrete, SCCB, Fracture, Fatigue

Introduction

In today's growing awareness of sustainability within the infrastructure, more and more engineered structures are utilizing composite systems to enhance and maintain structural efficiency. Use of these technologies has been shown to positively extend the service life of structures slated to be built and even eliminate the need to replace or remove existing ones due to age or other measures that may deem the system deficient, and, consequently, reduce the overall resources allocated for such construction.

Composite systems with particular applications of internal/external reinforcement of concrete have seen increased usage in recent years, though one area of research—arguably the most critical of all under this context—namely, that of the interface bond, has not received its due attention among the published literature. The interface bond must necessarily be a focal point within this framework as it is the location wherein stresses are transferred between the composite and concrete constituents through the resin matrix. Poor bond or inadequately prepared constituent surfaces can result in a reduction in load carrying capacities, and, as such, may negate the inherently beneficial properties to have otherwise been gained by the use of FRP materials in the first place.

In an attempt to address such vitally important issues as these, answers are furnished by use of the novel experimental fracture mechanics specimen known as the Single Contoured-Cantilever Beam (SCCB). By use of such a methodology, the effects of surface roughness from

Manuscript received 27 April 2005; accepted for publication 13 July 2005; published January 2006. Presented at ASTM Symposium on Fatigue and Fracture Mechanics: 35th Volume on 18-20 May 2005 in Reno, NV.
[1] Ph.D. Research Assistant, Department of Civil Engineering, The University of North Carolina at Charlotte, 9201 University City Blvd, Charlotte, NC 28223.
[2] Corresponding Author, Assistant Professor, Department of Civil Engineering, The University of North Carolina at Charlotte, 9201 University City Blvd, Charlotte, NC 28223.

Copyright © 2005 by ASTM International, 100 Barr Harbor Drive, PO Box C700, West Conshohocken, PA 19428-2959.

the underlying concrete substrate on the interface bond are evaluated through the measuring and evaluation of the Mode I critical strain energy release rates, G_{Ic}, of a variety of specimens. Finally, the results of a preliminary study on the interface bond as subjected to cyclic-fatigue testing under varied load ratio and frequency effects are also reported and presented herein in hopes of motivating a move toward the standardization of future experimental investigations relative to such an important phenomenon.

Materials

The materials chosen for use within this research study, though not strictly identical, were based on comparability to those of previous investigations as conducted by Boyajian [1] and Kodkani [2], for purposes of streamlining the corroboration of data among past research efforts.

Substrate Design

The cross-section of the concrete member was intentionally designed to be trapezoidal in shape (see Figs. 1 and 2) so as to not only prevent the SCCB specimen from becoming dislodged vertically during the opening mode of loading, but also to impart an adequate degree of lateral clamping pressures to the member and thereby confine the underlying (brittle) substrate from any undue cracking that might have otherwise occurred in this bulk-region as unrelated to the interface itself. From a manageability standpoint, the overall length of the SCCB specimen was also reduced slightly in this study to 457.2 mm (18 in.) as compared with that of Kodkani's [2] 482.6 mm (19 in.) and Boyajian's [1] 685.5 mm (27 in.) beam sizes. The concrete substrate, though cast monolithically, can be separated into two parts: 1) the portion that is being referred to as the concrete step (having a height of 5.74 mm (0.25 in.) and a width to match the LVL contour of 43.94 mm (1.73 in.)) that constitutes the interface-region once the FRP laminate is adhered to it, and 2) the bulk concrete substrate which was intentionally designed to be trapezoidal in cross-section (as just described above). Incidentally, the concrete step does not extend over the entire length of the substrate so as to allow a 50.80 mm (2 in.) void which can accommodate the load strap used. As for the concrete mixture proportions of the substrate, the following recipe was adhered to: 1C:1.16FA:1.13CA:0.40W, with the addition of 6 % air entrainment in anticipation of future freeze/thaw research. The average 28-day compressive strength of the 100 × 200 mm (4 in. × 8 in.) cylinders was found to be 60 MPa (8 700 psi) ± 1.6 MPa (240 psi).

FRP Types

Two varieties of unidirectional fiber reinforced polymers (FRPs) were investigated using the SCCB fracture specimen. The first, involving a carbon FRP (abbreviated, CFRP), consisted of the SikaWrap® Hex 103C, and the second, a glass FRP (GFRP), was the SikaWrap® Hex 100G; the saturant/primer used was the Sikadur® Hex 306. Again, the individual material properties (see Table 1) were chosen to be adequately similar to the systems as used by Boyajian [1] and Kodkani [2] for the purposes of corroborating test results.

Testing and Loading

The SCCB loading apparatus (Fig. 3) was made of 31.75 mm (1.25 in.) thick 6061 T-651 aluminum and was similar in design to that introduced by Kodkani [2]. The loading apparatus was designed to allow for quick and easy removal and placement of the specimens for testing and to be compatible with the various load frame machines, i.e., two servo-hydraulic MTS and

one Instron 5582, which were utilized in this research to acquire the quasi-static and cyclic-fatigue data. The displacement-controlled, quasi-static testing was accomplished at a constant load-rate of 0.6096 mm/min (0.02400 in./min).

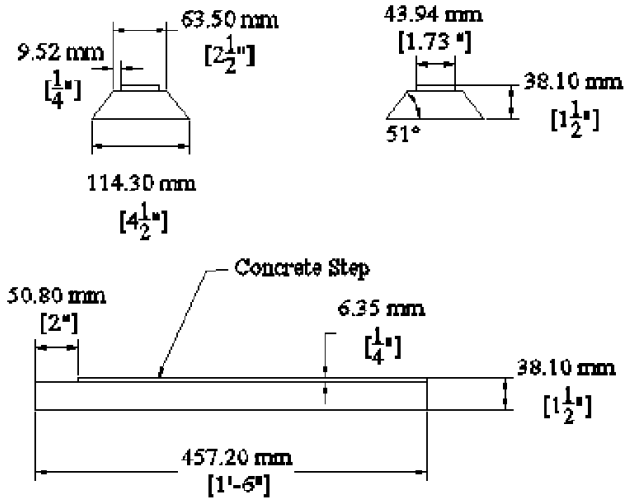


FIG. 1—*Concrete substrate dimensions.*



FIG. 2—*Finished concrete substrate samples.*

TABLE 1—*FRP material properties.*[3]

	SikaWrap® Hex 103C	SikaWrap® Hex 100G	Sikadur® Hex 306
Tensile Strength	3.793 GPa (550 ksi)	2.275 GPa (330 ksi)	72.5 MPa (10.5 ksi)
Tensile Modulus	234.5 GPa (34 000 ksi)	72.413 GPa (10 500 ksi)	3.174 GPa (4 600 ksi)
Elongation	1.5 %	4 %	4.8 % @ break

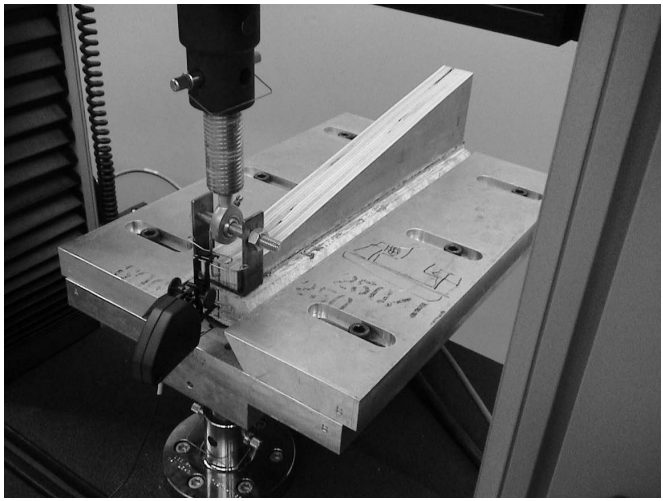


FIG. 3—*SCCB loading apparatus in Instron 5582.*

Laminated Veneer Lumber

The material used to create the desired contoured-shape of the cantilevered-member utilized the orthotropically engineered wood product of laminated veneer lumber (LVL) possessing, in this case, a longitudinal modulus of elasticity of 131 GPa (1.91 Msi)[4] and a uniform thickness, b, of 43.94 mm (1.73 in.). The shape of the contour was arrived at through finite element modeling and experimental compliance calibration verifications (see following section) to obtain a shape that provided a constant compliance with linear results over various specified crack lengths. Creating a contoured shape that maintains a constant value of the compliance gradient (dC/da) during fracture enables determination of the critical strain energy release rates (see Eq 2 later) without the need of measuring the instantaneous location of the crack, a—a rather formidable undertaking experimentally speaking.

[3] Material Properties obtained from the Sika® manufacturer.
[4] Material properties obtained from manufacture, Trus Joist, for 1.9E Microllam LVL.

Compliance Calibration

The compliance, C, is related to the inverse of the stiffness of the member (or the ratio of the displacement (u) and the load (P)—see Eq 1), and its gradient, dC/da, is a measure of the rate-change of this quantity with respect to the instantaneous location of the crack length, a. Formerly, research involving the fracture and fatigue of interfaces has relied on the well-known Double Cantilever Beam (DCB) technique or a variant thereof, such as the Contoured Double Cantilever Beam (CDCB) specimen (e.g., the works of Trimble [4], Davalos et al. [6], and Jia and Davalos [16]). The SCCB specimen was conceived and fashioned after such techniques to overcome the arm-breakoff phenomenon (for more details of this, the reader is referred to Boyajian et al. [5] and Boyajian [1]) that was found to hinder extending methods like that of the CDCB to study FRP-concrete interfaces.

$$C = u / P \tag{1}$$

Finite Element Analysis

Using ANSYS 8.1, together with SOLID 92—an element type having a three-dimensional ten-node tetrahedral structure—the contours and compliance gradient results of Boyajian [1] and Kodkani [2] were first successfully duplicated and then extended to arrive at a similar shape for the (shortened) contoured-cantilever of this present study.

The optimum shape that was used in Boyajian's [1] research cited a compliance gradient, dC/da, of 1.61×10^{-5} N^{-1} (7.2×10^{-5} lb^{-1}) with a corresponding r^2 value of 0.9988, relative to the finite element (FE) results. From the current FE analysis, a comparable value of dC/da was found as being 1.63×10^{-5} N^{-1} (7.3×10^{-5} lb^{-1}) with an r^2 value of 0.9981—results that are within 1.2 %. Similarly, Kodkani's [2] contour that was designed as a CDCB—i.e., having two contours instead of the one for the SCCB—reported a dC/da value of 2.59×10^{-5} N^{-1} (11.5×10^{-5} lb^{-1}), which, when halved to account for the single-contour, corresponds closely with the FE compliance gradient value of 1.26×10^{-5} N^{-1} (5.6×10^{-5} lb^{-1}; with $r^2 = 0.9982$).

Contour Design

The basis for selecting the optimal contour shape for the cantilevered-portion of the SCCB specimen was achieved by minimizing the deviation of the r^2 value from 1 (i.e., read as "r-squared" and technically known as the coefficient of determination ($0 \le r^2 \le 1$)—a measure of how closely estimated values of a trend-line correspond to actual data) from among the various FE shapes considered. From the FE studies, it was determined that the optimal contour for this study possessing an initial height, h_i, of 20.6 mm (0.81 in.), required a final height, h_f, of 95.25 mm (3.75 in.); corresponding to such a geometry, the LVL contour (Fig. 4) was found to have a compliance gradient, dC/da, of 1.397×10^{-5} N^{-1} (6.2×10^{-5} lb^{-1}) at an $r^2 = 0.9999$.

Compliance-Gradients and -Calibrations

After determining the proper contour shapes resulting from the two separate varieties of FRPs being considered for this study, the individual compliance gradient (dC/da) values for the carbon and glass materials were found to be, respectively: 1.13×10^{-5} N^{-1} (5.0×10^{-5} lb^{-1}) and 1.27×10^{-5} N^{-1} (5.6×10^{-5} lb^{-1}).

Following the FE studies, actual compliance calibration tests were performed in the laboratory with specimens having crack lengths of 101.6 mm (4 in.), 152.4 mm (6 in.), and 203.2 mm (8 in.). A pair of calibration tests was conducted on the CFRP specimens, yielding the

following compliance gradient values: 1.153×10^{-5} N^{-1} (5.1×10^{-5} lb^{-1}) with an $r^2 = 0.9999$ and 1.130×10^{-5} N^{-1} (5.0×10^{-5} lb^{-1}) at an $r^2 = 0.9997$. A comparison of these results is shown in Fig. 5, illustrating the good match between the FE and experimental compliance calibration results. Similarly, close agreements were found to result with the GFRP specimens as well.

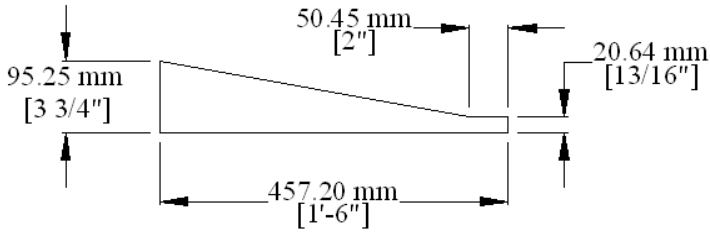


FIG. 4—*Contour dimensions.*

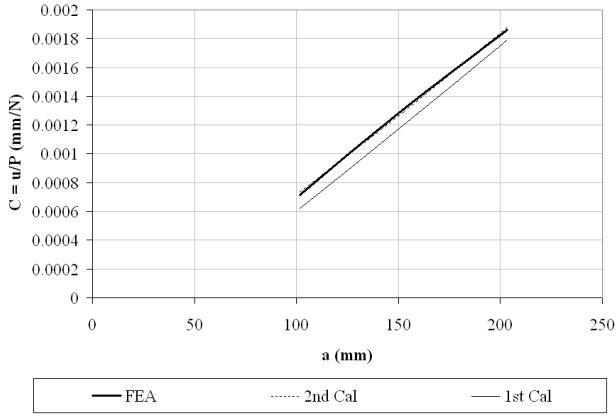


FIG. 5—*FEA compliance of the selected 95.25 mm (3.75 in.) contour with CFRP.*

Surface Preparations

The surface preparation of the substrate is an important step in the application of composite materials, as it is the primary means of enhancing the interface bond. According to the American Concrete Institute (ACI) [7], in addition to requiring surfaces to be strong, dense, and sound, such vital areas should also be cleansed thoroughly of all foreign substances that may otherwise hinder the proper formation of bond with the epoxy compounds.

To date, there has been limited research on the topic of enhancing the FRP-concrete interface bond by consideration of various surface roughness gradations. Prior tests have concluded that the bond behavior cannot be predicted easily and have suggested that more reliable tests methods

be developed [8]. It is noted that having too smooth a surface will result in a poor bond, while, on the other hand, a very rough surface will require use of a putty filler for which the optimal surface roughness has not yet been characterized [9].

Roughness

In this context, the so-called "surface preparation" involved the roughening and abrading of the vital concrete bonding zones as achieved through mechanical means and was found to have a significant effect on the overall interface strength. Three gradations of surface roughness-ranges were evaluated during the course of this research characterized herein as being low (<10 μm), moderate (10–50 μm), and high (>50 μm), as achieved through, respectively: the resulting surface of the de-molded specimens (from the formwork) directly, as well as by subsequent belt-sanding and sandblasting measures. The molds used in casting the concrete beams were constructed of an ultra-high molecular weight polyethylene material allowing for both durability and precision machining to achieve the trapezoidal shapes and concrete-step surfaces (see Fig. 1). The belt-sanded surface was accomplished by use of a 50-grit aluminum oxide belt-sander; lastly, the sandblasted surface was prepared using fine (No. 20 mesh) sand.

To measure and quantify the various toughness grades considered in this study, a Federal Products Surfanalyzer 5000 was used (accurate to 125 nm (0.005 mil)) to record the profile of the surface being investigated through a moving stylus (Fig. 6 shows some typical trace-plots). The average roughness (R_a) is defined as the area between the roughness profile and its mean line divided by the evaluation length. The mold surface was found to have a R_a = 8.0 μm, and the belt-sanded and sandblasted surfaces yielded values of R_a = 32.8 μm and R_a = 57.7 μm, respectively.

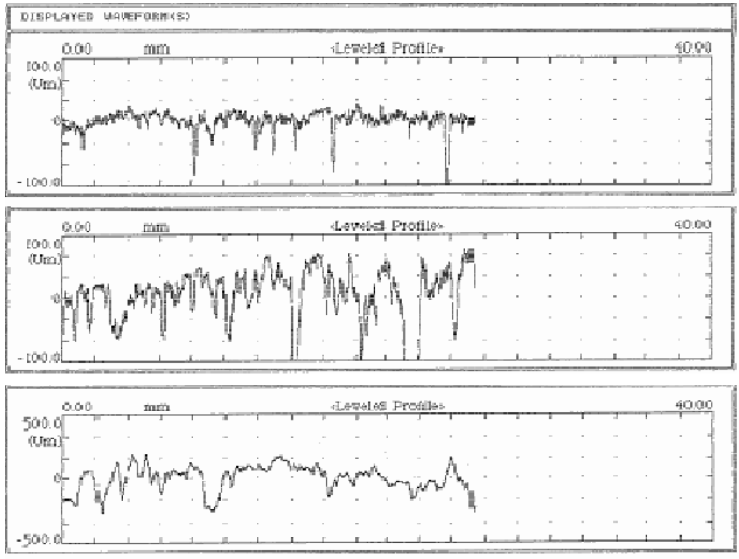


FIG. 6—*Trace profiles from Surfanalyzer (from top to bottom: mold-surface, belt-sanded, and sandblasted).*

Other surface-roughening procedures, such as water jetting or acid etching, were not performed in this study. The former, as explained by Galecki et al. [10], has been found to have complications associated with such factors as water pressure, rotational speed, nozzle size, and standoff distance. In the latter approach (e.g., see Xiong et al. [11]), the concrete surface is chemically etched by a solution of hydrochloric acid, and as per ACI Committee 515 recommendations, should only be used as a last alternative due to the potential for corrosion [12].

Adhesion Tests

Adhesion pull-off tests were conducted to determine the performance of the epoxy-resin being used and to ensure that proper interface bonding was being achieved. Simply, the pull-off tests determine the greatest tensile force required to induce failure as occurring along the weakest plane of the system, i.e., either within the concrete substrate, the composite matrix, or the glue-line of the dolly. In this study, pull-off strengths were measured using the Elcometer Model 106 Adhesion Tester with a scale range of 2 (i.e., 0–7 MPa (0–1000 psi)) and an accuracy of ±15 % of the given reading. Sika® states that the minimum tensile strength of the concrete substrate failure should be at least 1.4 MPa (200 psi); this was achieved or exceeded in all test cases.

Static Fracture Toughness

Dry (i.e., unweathered) quasi-static tests were performed by use of the SCCB specimen to obtain the Mode I critical strain energy release rate (G_{Ic}) values of the FRP-concrete interface bond. The G_{Ic} values measure the amount of strain energy required to initiate a crack of unit area (related to the fracture toughness, K_{Ic}) and are computed using Eq 2, where b = width of the interface, P_c = critical (fracture) load, and dC/da = compliance gradient (refer back to the subsection titled *Compliance-Gradients and -Calibrations*). It should be noted that although the effects of Mode II were ignored in this paper, efforts are currently underway to consider and quantify such effects as well.

$$G_{Ic} = \frac{P_c^2}{2b}\frac{dC}{da} \tag{2}$$

Quasi-Static Tests Results

It is noticed from the comparison chart for the CFRP specimens (Fig. 7) that the mold and sandblasted surfaces failed in a similar manner, though the peak load of the latter was 50 % greater in magnitude. In contrast, the belt-sanded surface was found to have a more gradual decrease in load over a much wider range of crack opening displacement (*COD*) before failing—affirming the greater expense of energy required to cause interface failure due to the moderately-roughened surface—in spite of the fact that its peak loads were comparable to those of the mold surface failure values.

Inspection of the undersides of the post-fracture mold surface samples (Fig. 8) indicated an even separation with no substantial damage to the concrete substrate, characteristic of an adhesive failure. The belt-sanded and sandblasted specimens, on the other hand, yielded much more cohesive forms of failure, which again corroborates the heightened achievement of bond due to the roughened-surfaces.

As was done with the CFRP specimens, a comparison chart for the GFRP specimens was also generated (see Fig. 9). In contrast, the GFRP specimens yielded different failure characteristics. As an example, though the belt-sanded specimen in this case did not exhibit the

elongated COD ranges of its CFRP counterpart, the peak-failure loads were, however, discovered to be much more comparable with that of the sandblasted specimen and substantially higher than those of the mold surfaces. Qualitatively, the fracture surfaces of the GFRP specimens appeared to be slightly more substrate-dominant than those of the CFRP.

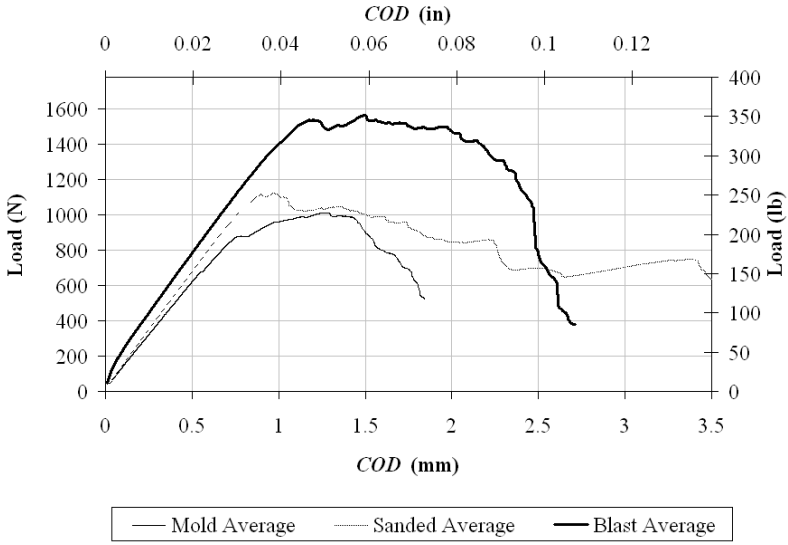


FIG. 7—*CFRP average sample comparison of surface preparations.*

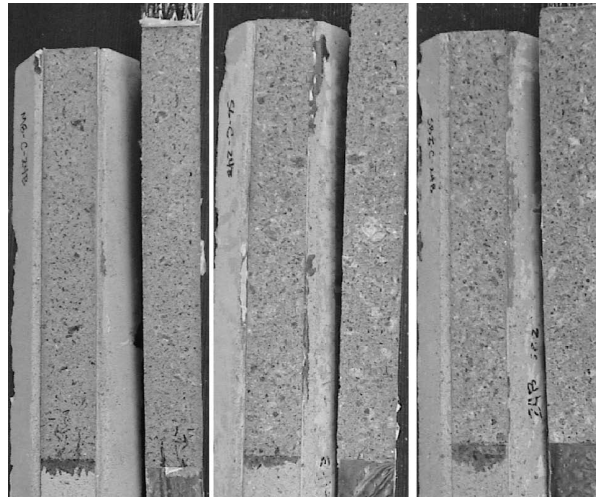


FIG. 8—*Post fracture surfaces of CFRP specimens (from left to right: mold-surface, belt-sanded, and sandblasted).*

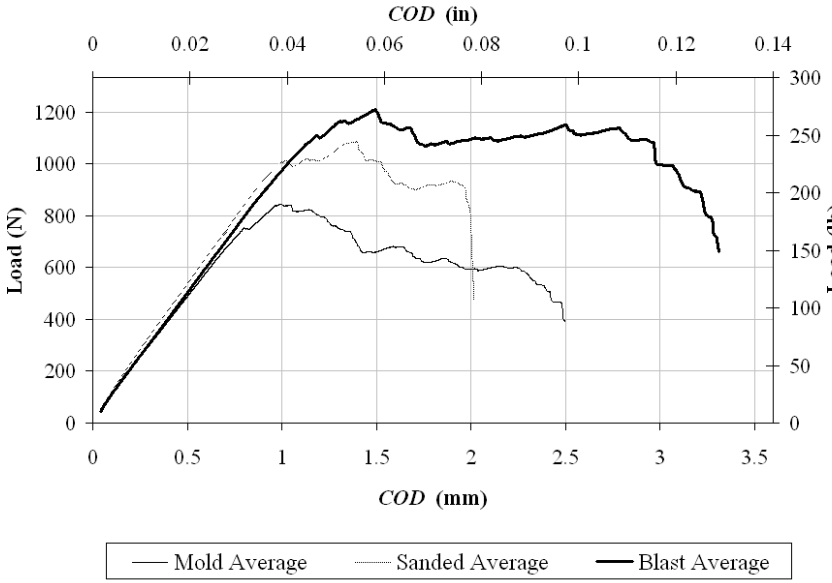


FIG. 9—*GFRP average sample comparison of surface preparations.*

The critical load has a significant effect on the value of the fracture toughness, as it is the square of this value that is used to determine the G_{Ic} magnitudes—i.e., any error in identifying the appropriate P_c digresses the value of G_{Ic} by the square of this deviation, assuming, of course, that this absolute difference is greater than unity. (For greater discussion of this subject, the reader is referred to the work of Boyajian et al. [13].) The determined critical loads and calculated fracture toughness values are provided in Tables 2 and 3 for both of the FRP types. The surface preparation that yielded the highest G_{Ic} values resulted from the sandblasted specimens with values of G_{Ic} = 307.2 J/m^2 (1.75 lb/in.) for the CFRP and, likewise, G_{Ic} = 190.3 J/m^2 (1.08 lb/in.) for the GFRP dry fracture specimens.

TABLE 2—*CFRP fracture toughness comparison of surface preparations.*[5]

Specimen	Critical Load, P_c	G_{Ic} (Initiation)
CFRP - Mold	948.7 N (213.3 lb)	115.7 J/m^2 (0.66 lb/in.)
CFRP – Belt Sanded	1 085.4 N (244.0 lb)	151.5 J/m^2 (0.86 lb/in.)
CFRP – Sandblasted	1 545.8 N (347.5 lb)	307.2 J/m^2 (1.75 lb/in.)

[5] G_{Ic} is typically given in SI units of J/m^2. This is equivalent to N/m and converts to US customary units as lb/in.

TABLE 3—*CFRP fracture toughness comparison of surface preparations.*[5]

Specimen	Critical Load, P_c	G_{Ic} (Initiation)
GFRP - Mold	838.0 N (188.4 lb)	101.5 J/m^2 (0.57 lb/in.)
GFRP – Belt Sanded	1 045.3 N (235.0 lb)	157.9 J/m^2 (0.89 lb/in.)
GFRP – Sandblasted	1 147.6 N (258.0 lb)	190.3 J/m^2 (1.08 lb/in.)

Data Comparisons

From the bar graphs of Fig. 10, it can be seen that while the mold and belt-sanded surface preparations of the CFRP and GFRP samples provided relatively comparable fracture toughness values, the sandblasted G_{Ic} magnitudes were considerably higher. This suggests, therefore, that among the three varieties of surfaces considered for this study, the optimal roughness grade was realized through the method of sandblasting.

From previous research, Kodkani [2] presented a high-performance concrete (HPC) with a compressive strength slightly higher than what was used for this research, wherein she achieved a load of 1055 N (237 lb) with her GFRP specimens exhibiting a fracture-profile that is quite similar in form when superimposed on the test-data resulting this research (see Fig. 11). This is further corroborated by the surface preparation used in that study in which a coarse belt sander was used.

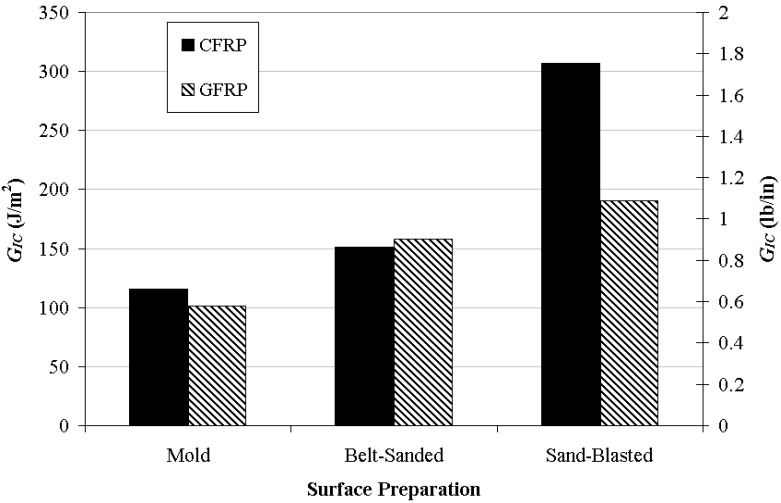


FIG. 10—*Comparison of fracture toughness values for CFRP to GFRP due to surface preparations.*

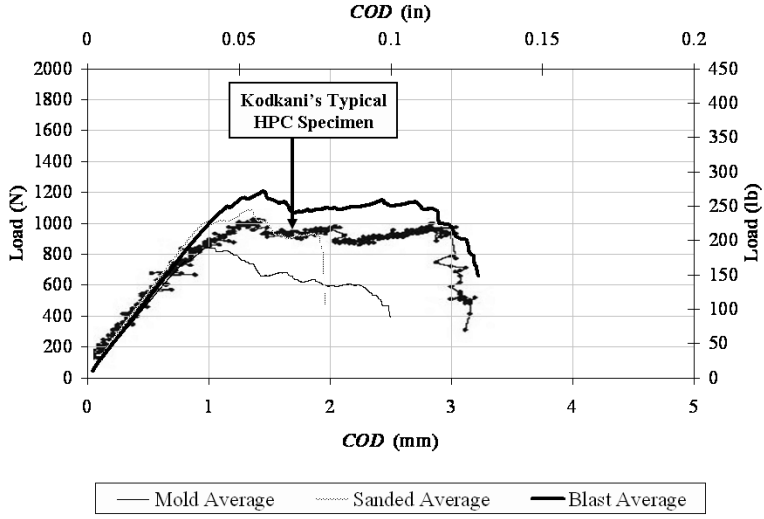


FIG. 11—*GFRP comparison with Kodkani's research [2].*

Another factor that may hinder the direct comparison to works of other researchers is the strength of the concrete substrate that was used. Lower compressive strengths could mean that the concrete being used was more porous, which, in turn, might account for better adhesion and the realization of higher failure loads. There is also the difference in the composite lay up procedures used. The system of this study called for the primer to become tacky (achieved in a matter of minutes) before application of the saturant to bond the carbon or glass fibers to the concrete, while the systems that were used by Boyajian [1] and Kodkani [2] required the primer to cure completely (usually achieved in a day or two), after which the fibers were applied. Another possible reason is the shape of the contours themselves. Each contour, as discussed earlier provided different dC/da values. This was accomplished by varying the shape, specifically the final height of the contour for the different lengths used. As previously mentioned, Boyajian's contour provides a slope of 0.11, and Kodkani's contour has a slope of 0.15, while the designed contour within this research is 0.184. All of these parametric differences may therefore contribute to some variations in fracture behavior and outcomes, although they are not expected to be responsible for significant differences.

Cyclic Fatigue Effects

The investigation of fatigue is an important aspect of the FRP-concrete bond. Structures such as bridges, overpasses, and parking decks can experience upwards of 58×10^8 loading cycles [14]—cyclic loading being considered as the main cause of degradation in these joints [15]. In a recent study by Ferrier et al. [14], it was stated that the durability and performance is directly dependent on the fatigue behavior of the FRP itself.

In the initial stages of this research, a preliminary look into the durability under fatigue loading was conducted on the CFRP specimens. The specimens investigated were tested with a varying load ratio and frequency using a sinusoidal wave. In research conducted on the fatigue

crack growth of aluminum DCB specimens, Pirondi et al. [16] concluded that the load ratio had a more pronounced effect than did the frequency on the critical strain energy release rate values, attributing this to the crack closure effect.

The compliance method was utilized to determine the crack propagation rate (da/dN), primarily because of its ease in collecting *COD* readings over the more formidably measured crack length (a) locations. The equation for utilizing the crack opening displacement propagation rate (d*COD*/dN) to obtain the da/dN value is given in Eq 3. The d*COD*/dN term is obtained from the equation of the trendline of the plot of *COD* versus the number of cycles (N) and is a material constant that is representative of the frequency and load ratio effects. The k term is a constant that is equal to the dC/da value obtained under the compliance calibration tests.

$$\frac{da}{dN} = \frac{da}{dC}\frac{dC}{dN} = \frac{1}{kP}\frac{dCOD}{dN} \tag{3}$$

Load Ratio

The load ratio (R) describes the ratio of the minimum to maximum load under cyclic conditions. Based on research conducted by Jia [17], the load ratio is a very significant parameter in the fatigue crack growth rate. The tested load ratios were based on the achieved quasi-static tests, with the maximum loads being nearly 70 % of that obtained at crack initiation for the mold surface preparation.

In comparing da/dN values due to varying load ratios, Eq 3 was used with the k value equal to the dC/da of 1.13×10^{-5} N^{-1} (5.0×10^{-5} lb^{-1}) for the CFRP specimens. Looking at a specimen with an R = 0.25 and a frequency of 5 Hz, P_{max} was set at 711.7 N (160 lb). This specimen yielded a d*COD*/dN of 7.0×10^{-6} mm/cycle (2.58×10^{-7} in/cycle) for a da/dN of 8.2×10^{-4} mm/cycle (3.2×10^{-5} in./cycle). For a specimen that is being cycled with a frequency at 10 Hz, an R = 0.5, and a P_{max} = 667.2 N (150 lb), the d*COD*/dN was 8.2×10^{-7} mm/cycle (3.23×10^{-8} in./cycle) for a da/dN = 1.1×10^{-4} mm/cycle (4.0×10^{-6} in./cycle).

One noticeable effect to the results obtained in investigating the load ratio is that the surface preparation is a big factor in the da/dN obtained. In testing the CFRP specimens with sandblasted surfaces at load ratios of 0.25 and 0.5 under the same 5 Hz frequency, over 20 million cycles were achieved with no *COD* recorded. This would indicate that the surface preparation is a very important preliminary step to perform in safeguarding FRP-concrete joints against fatigue effects. Another point of consideration that is somewhat related to this finding is the assertion that stems from the research of Abou-Hamda et al. [14], wherein it was found that an increase in the bondline thickness effected a heightened resistance to fatigue as well.

Frequency

The frequency represents the number of cycles per second that the specimen is subjected to. In this initial research stage, a change of frequency from 3 Hz to 5 Hz was examined. The specimens were maintained at the same load ratio 0.25 and were tested with a mold surface preparation. The 3 Hz specimen yielded a larger d*COD*/dN value of 2.9×10^{-5} mm/cycle (1.61×10^{-6} in./cycle) while the 5 Hz specimen had a d*COD*/dN value of 0.0307×10^{-5} mm/cycle (0.0121×10^{-6} in./cycle). Utilizing these values, the obtained dC/da value for k and a P of 622.7 N (140 lb), and Eq 3, the respective da/dN values are 5.84×10^{-3} mm/cycle (2.3×10^{-4} in./cycle) and 4.4×10^{-5} mm/cycle (2.0×10^{-6} in./cycle). This indicates that at higher frequencies, the rate of crack propagation is reduced dramatically. Jia [16], who reported that the crack growth rate decreased as frequency increased, also observed such findings.

In another look at the effects of frequency, a GFRP specimen was compared to the CFRP specimen under a frequency of 3 Hz. The GFRP yielded a d*COD*/d*N* value of 7.9×10^{-5} mm/cycle (3.1×10^{-6} in./cycle), which in turn gives a d*a*/d*N* value of 1.0×10^{-2} mm/cycle (3.95×10^{-4} in./cycle). This indicates that the GFRP specimen will have a faster crack propagation than the CFRP due to its much lower stiffness.

Conclusions

In this preliminary study, the carbon- and glass-fiber varieties of the FRP-concrete interface bond were studied through implementation of the novel SCCB experimental fracture mechanics specimen under both quasi-static and cyclic-fatigue conditions; moreover, parametric studies of the effects of roughening the underlying concrete substrate as a surface preparation measure were also considered and found to have a significant impact on the overall performance of this most crucial adhesive region.

To initiate the study, FE models of the contoured-cantilever portion of the SCCB specimen were formulated and shown to provide nearly identical results to the experimentally-derived compliance-calibrations. Through such an approach, it was established that the CFRP had a slightly lower d*C*/d*a* value than the GFRP, thus requiring the use of distinct compliance gradient values in the calculation of the G_{Ic} values with regard to these two materials.

Proper preparation of the underlying concrete surface with an appropriate degree of roughness was found to be a most significant preliminary-step to enhancing the G_{IC} values of the FRP-concrete interface bond, as well. The sandblasted surface preparation with a measured roughness of 57.7 μm was found to provide the highest G_{Ic} values, when compared to the mold and belt-sanded surfaces; it was thus determined to be the optimum surface roughness for the cases considered herein.

Under quasi-static testing, the CFRP specimens were found to achieve higher failure loads under each surface preparation as compared to their GFRP counterparts; however, the d*C*/d*a* values (being different) rendered nearly equivalent critical strain energy release rates to the mold and belt-sanded surfaces. In comparison to previous research, it was seen that under the quasi-static tests, similar results were obtained when factors such as the surface preparation, FRP type, and concrete strength were comparable.

From the preliminary fatigue tests that were conducted, the crack propagation rates, d*a*/d*N*, were determined by collecting *COD* versus *N* data. The cyclic fatigue tests show that as the frequency is increased, the crack opening reduces, supporting other research results. It was also noticed under this preliminary fatigue investigation that the surface roughness once again played a significant role in the delaying of cracking initiation. This was seen through a comparison of mold and sandblasted surfaces while maintaining identical frequency and load ratio values, wherein the mold-surface sample failed at 151 000 cycles, the sandblasted surface sample cycled over 20 million with no increase in the *COD*.

Future Research

This paper represents only a portion of the information from the research currently being conducted at the University of North Carolina at Charlotte. Ongoing research on the topics presented within includes the following:

- Mode II effect on quasi-static loading.
- Freeze/Thaw durability testing.
- Environmental conditioning durability tests.

- Cyclic Tests under varying waveforms.
- Determine Modified Paris Law equations for crack propagation rates.

Acknowledgments

The authors gratefully acknowledge the generous donations of materials that were extended by Sika® and Trus Joist MacMillan used for this research study.

References

[1] Boyajian, D.M., "Mode I Fracture and Durability of the CFRP-Concrete Interface Bond," Doctoral Dissertation, West Virginia University, 2002.

[2] Kodkani, S., "Interface Durability of Externally Bonded GFRP to Normal and High-Performance Concrete," Masters Thesis, West Virginia University, 2004.

[3] Davalos, J.F, Kodkani, S., Boyajian, D.M., and Ray, I., "Freeze-Thaw Durability of Interface for Externally Bonded GFRP to Normal and High-Performance Concrete," *18th Annual Technical Conference*, CRC Press, American Society of Composites, 2003, 9 pp.

[4] Trimble B.S., "Durability and Mode-I Fracture of Fiber-Reinforced Plastic (FRP)/Wood Interface Bond," Masters Thesis, West Virginia University, 1999.

[5] Boyajian, D.M., Davalos, J.F., and Ray, I., "Appraisal of the Novel Single Contoured-Cantilever Beam," *Materials and Structures*, Vol. 38, No. 275, 2005, pp. 11-16.

[6] Davalos, J.F., Madabhusi-Raman, P., and Qiao, P., "Characterization of Mode-I Fracture of Hybrid Material Interface Bonds by Contoured DCB Specimens," *Engineering Fracture Mechanics*, Vol. 58, No. 3, 1997, pp. 173-192.

[7] ACI 503R-93, "Use of Epoxy Compounds with Concrete; American Concrete Institute," 1998.

[8] Shen X., Myers J.J., Maerz N., and Galecki G., "Effect of Surface Roughness on the Bond Performance between FRP Laminates and Concrete," *Proceedings of the Second International Conference (CDCC 02), Durability of Fiber Reinforced Polymer (FRP) Composites for Construction*, Montreal, Quebec, Canada, May 29th-31st, 2002.

[9] Maerz, N., Nanni A., Myers J., and Galecki G., "Laser Profilometry for Concrete Substrate Characterization Prior to FRP Laminate Application," *Concrete Repair Bulletin*," May/June 2001, pp. 4-8.

[10] Galecki, G., Maerz, Nanni, A., and Myers, J., "Limitations to the Use of Waterjets in Concrete Substrate Preparation," *2001 WJTA American Waterjet Conference*, August 18-21, 2001.

[11] Xiong, G., Cui, Y., Chen, L., and Jiang, H., "Influence of Hydrochloric Acid Etching on Bond Strength Between Concrete Substrate and Repair Materials," *Cement & Concrete Composites 26,* 2004.

[12] Mailvaganam N.P., Pye G.B., and Arnott M.R., *Surface Preparation of the Concrete Substrate, Construction Technology Update No. 24*, Institute for Research in Construction, Canada, 1998.

[13] Boyajian, D.M., Davalos, J.F., Ray, I. and Kodkani, S., "The CFRP-Concrete Interface Subjected to Sodium -Sulfate and -Hydroxide Attack," *17th Annual Technical Conference*, CRC Press, American Society of Composites, 2002, 9 pp.

[14] Ferrier, E., Bigaud, D., Hamelin, P., Bizindavyi, L., and Neale, K.W., "Fatigue of CFRPs Externally Bonded to Concrete," *Materials and Science*, Vol. 38, January-February, 2005, pp. 39-46.

[15] Abou-Hamda, M.M., Megahed, M.M., and Hammouda, M.M.I., "Fatigue Crack Growth in Double Cantilever Beam Specimen with an Adhesive Layer," *Engineering Fracture Mechanics*, Vol. 60, No. 5-6, 1998, pp. 605-614.

[16] Pirondi, A. and Nicoletto, G., "Fatigue Crack Growth in Bonded DCB Specimens," *Engineering Fracture Mechanics*, Vol. 71, 2004, pp. 859-871.

[17] Jia, J., and Davalos, J.F., "Loading Variable Effects on Mode I Fatigue of Wood-FRP Composite Bonded Interface," *Composite Science and Technology*, Vol. 64, 2004, pp. 99-107.

Ductile-Brittle Transition

Journal of ASTM International, January 2006, Vol. 3, No. 1
Paper ID JAI13230
Available online at www.astm.org

T. R. Leax[1]

Temperature Dependence and Variability of Fracture Toughness in the Transition Regime for A508 Grade 4N Pressure Vessel Steel

ABSTRACT: A508 Grade 4N is a high nickel (3.4 %) pressure vessel steel with a relatively high yield strength (585 MPa minimum for Class 1) and a relatively low transition temperature (47 J transition temperature of -29°C or below). Published fracture toughness data on this steel are nonexistent, and so they have not been included in prior assessments of the applicability of the Master Curve approach to pressure vessel steels. The purpose of this study is to compare the temperature dependence and data scatter for this steel with the behavior predicted by the Master Curve. The available database consists of approximately 800 fracture toughness tests on 51 material heats, some of which were given a temper embrittling heat treatment. As an additional basis of comparison, test data on A508 Grades 2 and 3, 1 % nickel weld metal, and several high nickel (1.3–3.8 %) steels (NiCrMo and NiCrMoV) were included in the assessment. Maximum likelihood techniques were used to fit the toughness data, and Monte Carlo methods were used to assess the observed distribution of Weibull slopes (related to the extent of variability). The results of this assessment show that the Master Curve provides a good description of the shape (temperature dependence) of the toughness curve for moderate and high transition temperatures. However, for heats with low transition temperatures below the range observed in other pressure vessel steels, the shape of the toughness curve deviates from the Master Curve. The lower the transition temperature, the larger the deviation from the Master Curve. Based on the test data, a model describing the behavior of A508 Grade 4N has been developed. This model also accurately describes the toughness behavior of the other pressure vessel steels included in this study. With respect to variability, the Weibull slope of A508 Grade 4N is consistent with the value of four prescribed by the Master Curve. However, the Weibull slope for the other pressure vessel steels included in this assessment is close to 3.4. This lower value of the Weibull slope, which indicates larger variability, is likely the result of material inhomogeneity.

KEYWORDS: fracture toughness, data scatter, pressure vessel steels, Master Curve

Nomenclature

P_f is the probability of failure.
B is the crack front length (mm).
B_0 is a reference thickness (usually taken as 25.4 mm).
K_{Jc} is the measured fracture toughness (MPa√m).
$K_{Jc(med)}$ is the median toughness corresponding to 50 % failure probability (MPa√m).
$K_{Jc(1T)}$ is the size corrected measured toughness (MPa√m).
K_{min} is the minimum possible toughness (= 20 MPa√m).
K_0 is the characteristic toughness (MPa√m) corresponding to a probability of failure of 0.632.
T is the temperature (°C).

Manuscript received 12 April 2005; accepted for publication 13 July 2005; published January 2006. Presented at ASTM Symposium on Fatigue and Fracture Mechanics: 35th Volume on 18-20 May 2005 in Reno, NV.
[1] Principal Engineer, Bechtel Bettis, Inc., West Mifflin, PA 15122.

Copyright © 2005 by ASTM International, 100 Barr Harbor Drive, PO Box C700, West Conshohocken, PA 19428-2959.

T_0 is a reference transition temperature (°C) at which the median toughness is 100 MPa√m for a 1T size specimen.
A and C are empirical constants.
β is the Weibull slope.
$\sigma(\beta)$ is the standard deviation of the Weibull slope.
r is the number of uncensored toughness measurements in a given data set.

Introduction

A508 Grade 4N is a high nickel pressure vessel steel that has an attractive combination of strength and low temperature fracture toughness. The purpose of the study described in this paper is to compare the temperature dependence and variability of fracture toughness for this steel with the behavior predicted by the Master Curve. For the purposes of this evaluation, it has been assumed that the minimum toughness, K_{min}, and the statistical (weakest-link) scaling of toughness with crack size can be described by the Master Curve methodology. In evaluating the temperature dependence, maximum likelihood techniques were used to fit the fracture toughness data to an equation of the same form as the Master Curve. To evaluate variability, the experimentally determined data scatter was compared to the expected data scatter using Monte Carlo techniques. In addition to comparing the A508 Grade 4N data to the Master Curve, fracture toughness data on A508 Grades 2 and 3, 1 % nickel weld metal, and several high nickel steels (NiCrMo and NiCrMoV) were included in the evaluation to provide an independent benchmark (these steels will be referred to hereafter as the comparison database). The total database used in this evaluation contains over 2600 fracture toughness measurements. Such a large database is necessary to overcome the large inherent variability (factor of three or more) in transition regime fracture toughness measurements that makes it difficult to unambiguously identify trends in the data.

Database

The database includes previously unpublished fracture toughness measurements on A508 Grade 4N, A508 Grade 2, and 1 % nickel weld metal. Also included are test data on A508 Grades 2 and 3 and on high nickel steels (NiCrMo and NiCrMoV) taken from the EPRI Master Curve database [1–15]. The complete database used in this evaluation consists of the following test results:

- A508 Grade 4N: 51 heats, 74 data sets, 805 toughness measurements
- A508 Grades 2 & 3: 23 heats, 42 data sets, 1470 toughness measurements
- 1 % nickel weld metal: 11 heats, 24 data sets, 210 toughness measurements
- NiCrMo & NiCrMoV: 3 heats, 3 data sets, 176 toughness measurements

The number of data sets exceeds the number of heats since some heats were given one or more temper embrittling heat treatments, resulting in an increase in T_0.

Summary of the Master Curve Approach

The Master Curve methodology assumes that the cumulative fracture toughness probability distribution in the transition regime can be described by a three parameter Weibull distribution:

$$P_f = 1 - \exp\left\{ -\frac{B}{B_0}\left[\frac{K_{Jc} - K_{\min}}{K_0 - K_{\min}} \right]^{\beta} \right\} \quad (1)$$

The temperature dependence (shape) of the Master Curve is given by:

$$K_{Jc(med)} = A + (100 - A)e^{C(T - T_0)} \quad (2)$$

K_0 in Eq 1 is related to the median toughness, $K_{Jc(med)}$, in Eq 2 by:

$$K_0 = K_{\min} + \frac{K_{Jc(med)} - K_{\min}}{LN(2)^{1/\beta}} \quad (3)$$

Due to the large variability in toughness that occurs in the transition regime, it is not feasible to independently determine all five adjustable parameters (A, C, β, K_{min}, and T_0) in Eqs 1 and 2 for every pressure vessel steel forging and material condition. Fortunately, fracture toughness assessments performed during the last 25 years have shown that it is unnecessary to determine each of the parameters for every forging in order to adequately characterize the fracture toughness. These assessments (e.g., [16]) have shown that all ferritic steels follow the same fracture toughness curve when the test temperature is normalized by T_0. This means that the constants A and C are the same for all pressure vessel steels. The variation in fracture toughness (data scatter) for all ferritic steels at any given temperature also appears to follow the same Weibull distribution. For physical reasons, one would also expect the statistical crack size effect for all pressure vessel steels to be the same. These two factors allow the constants K_{min} and β to be specified. Consequently, the only parameter that needs to be determined for a given forging and material condition is the reference temperature, T_0. Fortunately, this parameter, unlike the other four adjustable parameters, can be accurately determined by testing a relatively small number of specimens (six to eight) in the transition regime. ASTM E 1921-02 [17] specifies all the parameters to be used in Eqs 1 and 2 except for T_0. In addition, ASTM E 1921 specifies the procedure for determining the reference temperature, T_0. When these specified parameters are used, Eq 2 is referred to as the Master Curve. The parameters prescribed by ASTM E 1921-02 are as follows:

$$\begin{aligned} &K_{min} = 20\ \text{MPa}\sqrt{\text{m}} \\ &A = 30\ \text{MPa}\sqrt{\text{m}} \\ &C = 0.019\ (1/°\text{C}) \\ &\beta = 4 \end{aligned} \quad (4)$$

Evaluation of the Fracture Toughness Temperature Dependence

The simplest way to assess whether the temperature dependence of A508 Grade 4N can be described reasonably by the Master Curve is to plot the toughness data against the Master Curve. Such a plot is given in Fig. 1 and shows that the A508 Grade 4N data are consistent with the Master Curve.

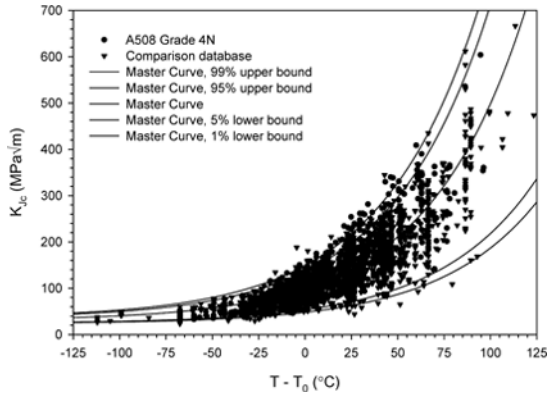


FIG. 1—*Comparison of the fracture toughness data to the Master Curve.*

Another way to assess the temperature dependence is to compare a plot of K_0 as a function of excess temperature ($T - T_0$) with the Master Curve. For this assessment, K_0 was determined according to ASTM E 1921 for those heats where four or more tests were performed at a single temperature and where test results were available at more than a single test temperature (in order to get a multi-temperature estimate of T_0). A comparison of the K_0 values to the Master Curve is shown in Fig. 2. The Master Curve provides a reasonable description of the temperature dependence for all the steels in the database. However, for A508 Grade 4N, the Master Curve does appear to slightly over-predict the toughness at moderate and low excess temperature ($T < T_0$) and slightly under-predict the toughness at high excess temperature ($T > T_0 + 50°C$). It should be noted that the higher than expected toughness of A508 Grade 4N at high excess temperatures may be due, at least in part, to constraint loss or to the effects of ductile crack growth on cleavage toughness. Constraint loss results in a reduction in the stress near the crack tip and is a function of the geometry (size of the crack tip plastic zone compared to the remaining ligament). The measured toughness increases with decreasing constraint.

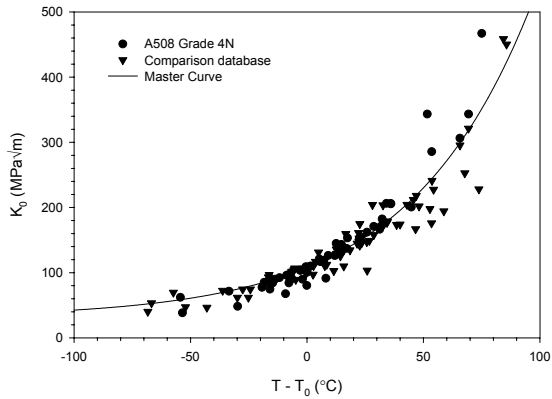


FIG. 2—*K_0 determined from single temperature tests compared to the Master Curve.*

One purported benefit of the Master Curve is that the estimate of T_0 one obtains from a set of test data does not depend on the temperature at which the tests were performed (as long as the test temperature is within 50°C of T_0). To evaluate whether T_0 estimates for A508 Grade 4N are similarly unbiased, K_0 values were determined from tests at a single temperature, and T_0 values were determined from both single and multiple temperature tests. The difference between the single temperature determination of T_0 and the multi-temperature T_0 is shown in Fig. 3 and is plotted as a function of excess temperature. It should be noted that the requirement for a minimum of six tests in determining T_0 was relaxed for this analysis, and some T_0 values were estimated from as few as four tests, increasing the uncertainty in the T_0 estimate. As shown in Fig. 3, there can be a considerable bias in the T_0 estimate for tests at very low excess temperature. This bias at low excess temperatures will result in conservative estimates of T_0 (i.e., an overestimate of the transition temperature). It should be noted that the large bias occurs at test temperatures outside the range allowed by E 1921 (i.e., not within 50°C of T_0).

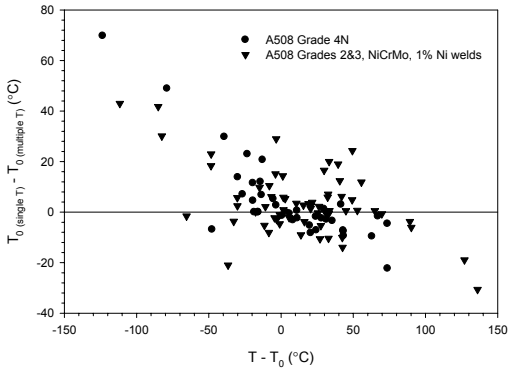


FIG. 3—*Bias in T_0 determinations.*

It is clear from examining Eq 2 that the temperature dependence of the toughness depends primarily on the value of the parameter, C. If C is equal to zero, then the toughness is a constant (100 MPa√m), irrespective of test temperature. The larger the value of C, the more rapidly the toughness increases with test temperature. This observation provides a means to determine whether a single curve applies to all pressure vessel steels. One can independently fit the model represented by Eq 2 to each data set in the database where test results are available at more than one test temperature. If the fitted values for C are the same within data scatter for all the steels in the database, then one can reasonably conclude that a single curve shape (temperature dependence) applies to all pressure vessel steels. Consequently, the constants C and T_0 in Eq 2 were determined independently, by maximum likelihood, for each data set where toughness tests were performed at more than one temperature. The toughness values were size-corrected prior to performing the analysis. The two constants, K_{min} and A, were assumed equal to the values prescribed in E 1921 since the specified values, 20 MPa√m and 30 MPa√m, respectively, reasonably describe the lower bound and median toughness on the lower shelf. The only remaining constant specified by E 1921 is the Weibull slope, β, used to describe size scaling and data scatter. This constant was also fitted for each data set (after size correcting). Please note that for convenience in performing this analysis, the requirement in E 1921 that the test temperatures

be within 50°C of T_0 was not followed. Ignoring this requirement has only a modest effect on the analysis results and no effect on the conclusions. Also, modest constraints were placed on the allowable values for C ($0.009 \leq C \leq 0.045$). This resulted in two data sets where the value of C was constrained to be a minimum value and three data sets where the value of C was constrained to a maximum value.

A plot of the fitted values of C versus T_0 is shown in Fig. 4. There are several noteworthy features of this plot:

- It is clear that there is a large amount of data scatter. This is the result of the relatively small number of data points in many of the data sets (19 out of 119 data sets had only four or five valid test results) combined with the large toughness variation that occurs in the transition regime.
- For A508 Grade 4N, the mean value for C is 0.0291, and the median value is 0.0228. For the comparison database, the mean value is 0.0210, and the median value is 0.019.
- There is a trend of decreasing C with increasing T_0. A simple regression line through the data highlights this trend. As shown in the plot, the value of C for the Master Curve is fixed at a value of 0.019 per °C independent of T_0.
- The value of C appears to be the same, or nearly the same (it is statistically indistinguishable), for all the pressure vessel steels included in this evaluation.
- With the exception of several 1 % nickel weld metal heats, all the data at low T_0 are from A508 Grade 4N.
- The value of C is consistent with the Master Curve specified value over the range of T_0 from approximately -100°C to +50°C. Interestingly, this is the range of transition temperatures from which the Master Curve was developed.

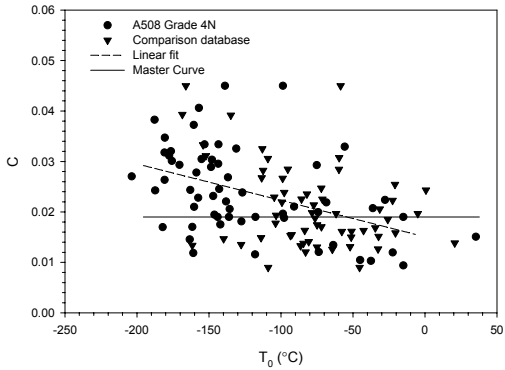


FIG. 4—*Variation of the fitting parameter, C, with T_0.*

One commonly used method for determining whether a model adequately accounts for the effects of the independent (controlling) variables (e.g., temperature) is to examine the residuals. The residuals are simply the differences between the measured values and the values predicted by the model. A plot of the standardized residuals versus T_0 for the Master Curve is shown in Fig. 5. The standardized residuals are given by:

$$\text{Standardized Residuals} = \beta\left[Ln(K_{Jc(1T)} - K_{\min}) - Ln(K_0 - K_{\min})\right] \quad (5)$$

In this expression, the Weibull slope was assumed equal to four, and K_0 (MPa√m) is the predicted characteristic toughness determined from Eqs 2 and 3 with the constant A fixed at 30 MPa√m and the constant C fixed at 0.019 per °C.

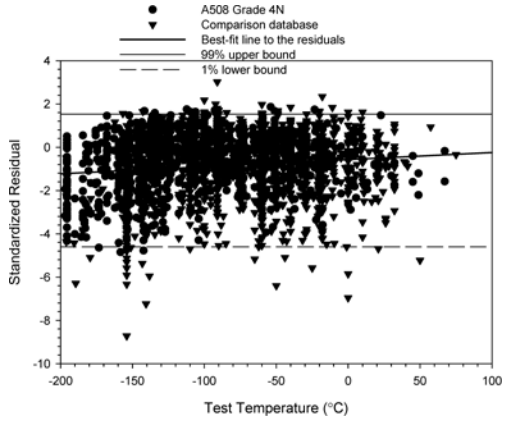


FIG. 5—*Residuals versus test temperature for the Master Curve. A best-fit indicates there is a bias in the residuals with respect to test temperature.*

For a Weibull distribution, the standardized residuals are expected to follow the (smallest) extreme value distribution. Figure 5 provides the 99 % and 1 % probability bounds based on the extreme value distribution for a Weibull slope of four. The toughness data are reasonably consistent with these bounds. Also shown in the plot is the best-fit line through the residuals as a function of test temperature. It is clear that the Master Curve does not completely account for the effect of test temperature.

Based on these analysis results, the Master Curve was modified, by trial and error, to allow for a temperature dependent value of C. Regression analysis using maximum likelihood techniques resulted in the following "temperature modified" Master Curve:

$$K_{Jc(med)} = 30 + 70\exp\left[\frac{0.303}{\sqrt{T+273}}(T - T_0)\right] \quad (6)$$

Please note that, for this analysis, the values of A, K_{min}, and β were constrained to those specified in ASTM E 1921-02. A plot of the standardized residuals versus T_0 for the temperature modified Master Curve is shown in Fig. 6. While the bias with temperature is less than for the Master Curve, the Eq 6 model appears to slightly over correct for the effect of test temperature.

Since C is a measure of how rapidly toughness changes with temperature, its value may be related to how rapidly the yield strength changes with temperature (Fig. 7). While Fig. 7 strictly applies only to A508 Grade 4N, a similar relationship is expected for other ferritic steels.

A plot of the temperature modified Master Curve is shown in Fig. 8 for a range of T_0 values. The Master Curve is shown on the plot for comparison. As shown in Fig. 8, there is a relatively small difference between the Master Curve and the temperature modified curves for T_0 values in the range of -100°C to +50°C. This is consistent with the nearly constant value of C for this temperature range, as discussed above.

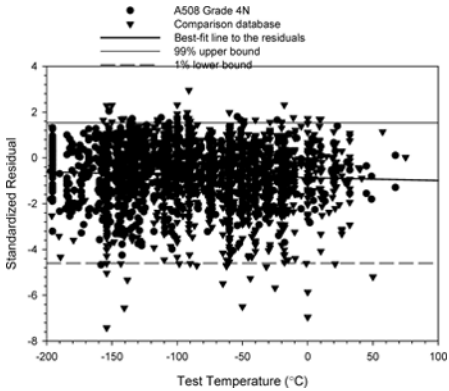


FIG. 6—*Residuals versus test temperature for the temperature modified Master Curve. A best-fit indicates there is still a small bias in the residuals with respect to test temperature.*

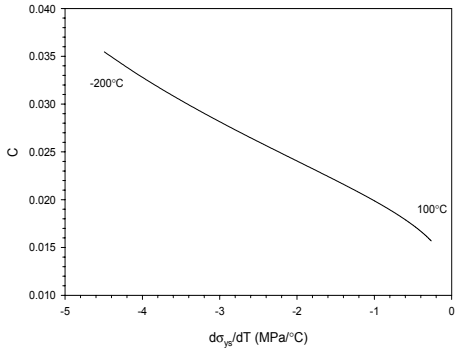


FIG. 7—*Relationship between the value of "C" and the change in yield strength with temperature for A508 Grade 4N.*

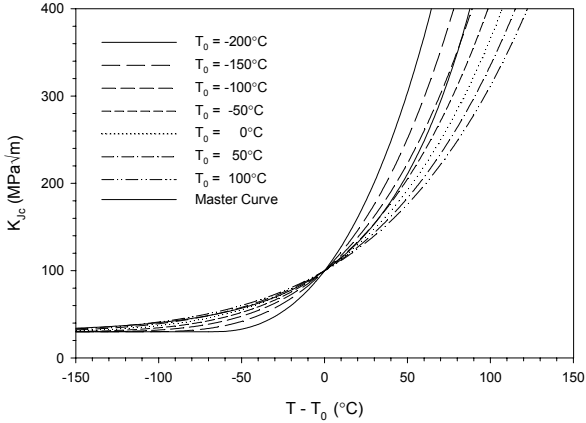
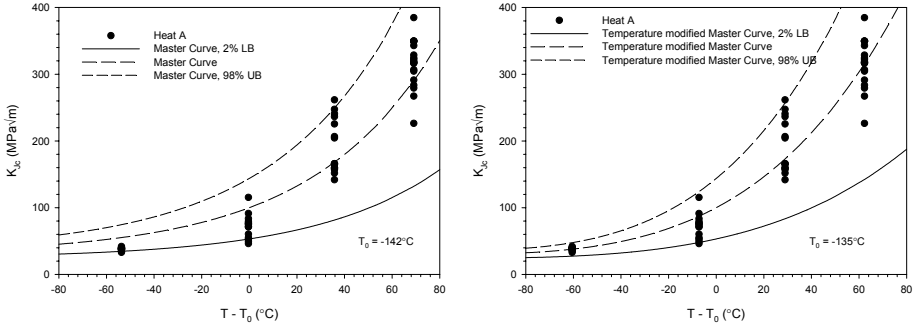


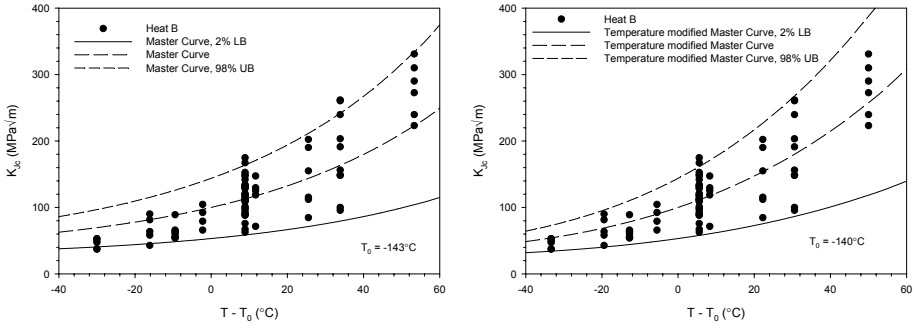
FIG. 8—*Comparison of the Master Curve to the temperature modified Master Curve.*

Plots comparing A508 Grade 4N test data to the Master Curve and to the temperature modified Master Curve are shown in Figs. 9–12. Plots are shown for the two heats with the largest amount of test data and for one heat with a very low T_0 and one temper embrittled heat with a very high T_0. As shown in the plots, the differences between the Master Curve and the temperature modified Master Curve are relatively small.



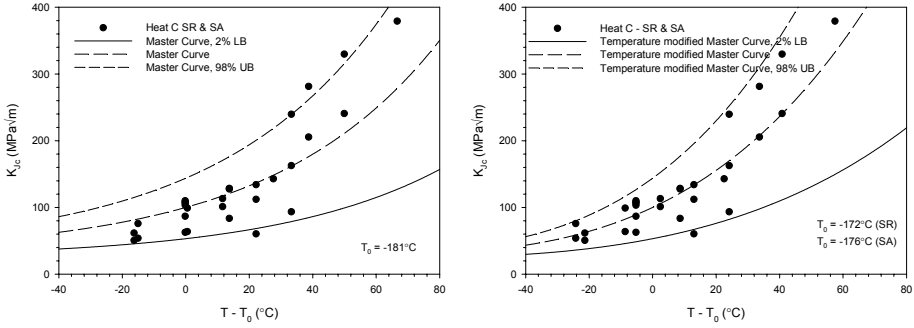
a) b)

FIG. 9—*Comparison of the toughness data from Heat A to* a*) the Master Curve and* b*) the temperature modified Master Curve.*



a) b)

FIG. 10—*Comparison of the toughness data from Heat B to* a*) the Master Curve and* b*) the temperature modified Master Curve.*



a) b)

FIG. 11—*Comparison of the toughness data from Heat C to* a*) the Master Curve and* b*) the temperature modified Master Curve (SR = stress relieved, SA = strain aged).*

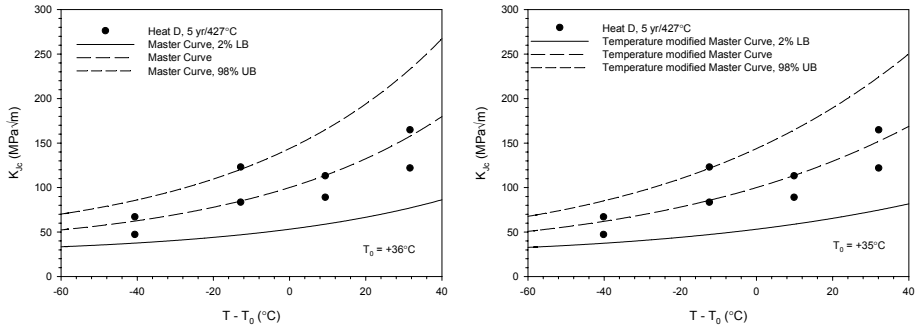


FIG. 12—*Comparison of the toughness data from Heat D to* a*) the Master Curve and* b*) the temperature modified Master Curve.*

Regression analyses using maximum likelihood were performed to determine whether the parameters in the Master Curve and in the temperature modified Master Curve could be optimized to give significantly better fits. In these analyses, the value of K_{min} was fixed at a value of 20 MPa√m, and the data were size corrected using E 1921 prior to the regression analysis. In the regressions, one or more of the remaining parameters (the T_0 values were always fit) were determined by maximum likelihood. When A and C were fit, they were assumed the same for all the pressure vessel steels in the database. When the Weibull slope, β, was fit, separate values were assumed for A508 Grade 4N and for the remaining combined heats in the database (comparison database). This was done in order to determine whether the degree of data scatter for A508 Grade 4N is the same as for other pressure vessel steels. The results of these fits are given in Tables 1 and 2 for the Master Curve and the temperature modified Master Curve, respectively. Based on the results of this analysis, the following conclusions can be made:

- When all the parameters (other than T_0) are fixed, the temperature modified Master Curve provides a significantly better fit to the data than the Master Curve (when assessing the significance of including an additional parameter in a model, a change in the log likelihood of 2.56 or larger is statistically significant at the 0.025 level). Even when all the parameters are fitted, the temperature modified Master Curve provides a significantly better fit to the pressure vessel steel toughness data.
- There is a significant improvement in the fit of the data to the Master Curve when the parameters A and β are optimized. The values for the optimized parameters are: A = 21.3 MPa√m, and β = 3.7 (A508 Grade 4N) and 3.4 (comparison database).
- For the temperature modified Master Curve, there is no significant improvement in the fit when the value for A is optimized. However, there is a significant improvement when the Weibull slope is optimized. The optimized values for β are 4.0 (A508 Grade 4N) and 3.4 (comparison database). The slightly lower Weibull slope for the comparison database indicates that the data scatter is somewhat larger for the comparison database than for A508 Grade 4N (an increase in the standard deviation of approximately 15 % from what would be expected based on a Weibull slope of four).

- The optimized values of A and C do not change significantly when the Weibull slopes are optimized. That is, the shape of the toughness versus temperature curve is independent of whether or not the Weibull slope is optimized.

TABLE 1*a—Regression analysis results for a Master Curve based toughness model-log likelihood values.*

MODEL	LOG LIKELIHOOD		
	A508 Grade 4N	Comparison database	Total
Fix A, C, β	-3687	-7927	-11614
Fix A, β	-3671	-7923	-11594
Fix C, β	-3652	-7906	-11558
Fix β	-3651	-7907	-11557
Fix A, C	-3679	-7895	-11574
Fix A	-3644	-7882	-11526
Fix C	-3644	-7869	-11513
All Fitted	-3639	-7873	-11512

TABLE 1*b—Regression analysis results for a Master Curve based toughness model-parameter estimates.*

MODEL	PARAMETER			
	A	C	β (A508 Grade 4N)	Comparison database
Fix A, C, β	30	0.019	4	4
Fix A, β	30	0.0200	4	4
Fix C, β	22.3	0.019	4	4
Fix β	22.9	0.0192	4	4
Fix A, C	30	0.019	3.6	3.5
Fix A	30	0.0214	3.7	3.4
Fix C	21.3	0.019	3.7	3.4
All Fitted	23.8	0.0200	3.7	3.4

TABLE 2*a—Regression analysis results for a temperature modified Master Curve based toughness model-log likelihood values.*

MODEL	LOG LIKELIHOOD		
	A508 Grade 4N	Comparison database	Total
Fix A, β	-3582	-7896	-11478
Fix C, β	-3583	-7894	-11477
Fix β	-3582	-7893	-11476
Fix A, C	-3581	-7860	11441
Fix A	3581	-7860	11441
Fix C	-3581	-7860	-11441
All Fitted	-3581	-7859	11440

TABLE 2*b*—*Regression analysis results for a temperature modified Master Curve based toughness model-parameter estimates.*

MODEL	PARAMETER			
	A	C	β (A508 Grade 4N)	Comparison database
Fix A, β	30	0.303	4	4
Fix C, β	30.5	0.303	4	4
Fix β	31.3	0.309	4	4
Fix A, C	30	0.303	4.0	3.4
Fix A	30	0.306	4.0	3.4
Fix C	29.8	0.303	4.0	3.4
All Fitted	30.7	0.309	4.0	3.4

The temperature modified Master Curve can be used to assess whether the shape (temperature dependence) of the toughness curve is the same for A508 Grade 4N as for the comparison database. Separate fits of the A508 Grade 4N database and the comparison database were made to the temperature modified Master Curve. The values for A, K_{min}, and β were fixed at the Master Curve prescribed values (30, 20, and 4 MPa√m, respectively) and the remaining two empirical parameters (C and T_0) were optimized by maximum likelihood. For A508 Grade 4N, the best-fit value for C was 0.311, and the log likelihood value changed by 1.0, which is not statistically significant. For the comparison database, the best-fit value for C was 0.300, and the log likelihood value for the comparison database changed by 0.3, which is not statistically significant. This analysis provides convincing evidence that the toughness temperature dependence for A508 Grade 4N is the same as for other pressure vessel steels.

Assessment of Fracture Toughness Variability

If the toughness variability is strongly material dependent, it may not be possible to use a Weibull distribution with a single fixed value of the Weibull slope, β, for all pressure vessel steels (β equal to four is specified by the Master Curve). Quantification of the variability is necessary for developing a statistically based lower bound design curve (as noted above, the shape of the curve is not sensitive to the value of β). To address this issue, the fracture toughness variability was evaluated, and the results are described below.

There are two methods that are in common use for assessing variability in any material property. One way is to determine the standard deviation of the material property, which provides a direct measure of variability. For a Weibull distribution, the Weibull slope, β, is analogous to the standard deviation in a normal distribution (a decrease in β corresponds to an increase in variability). Another method, described briefly above, is to examine the residuals from fitting a model to the data. In assessing the variability in the pressure vessel steel toughness database, residuals and Weibull slopes were determined from the temperature modified Master Curve. The reason for using the temperature modified Master Curve, rather than the Master Curve, is that the former model provides a somewhat better fit to the data, particularly for low transition temperature A508 Grade 4N heats and so will provide a better estimate of the true inherent toughness variability.

As noted above, the residuals are expected to follow the extreme value distribution. A probability plot of the standardized A508 Grade 4N residuals is provided in Fig. 13*a*. As shown

in the figure, the A508 Grade 4N data follow the extreme value distribution except in the lower tail. This plot suggests that a design curve for A508 Grade 4N based on the lower tail of the assumed Weibull distribution will underestimate the minimum toughness and so be conservative. This conservatism in the lower tail has been noted previously [18].

A similar probability plot for the comparison database is shown in Fig. 13*b*. In this case, the assumed probability distribution appears to fit the lower tail, but it is not the optimum description for the majority of the data. Consequently, the toughness data were refit to the temperature modified Master Curve, allowing for separate values of the Weibull slope for A508 Grade 4N and for the comparison database. As noted previously, the value of the Weibull slope for this latter case (comparison database) is 3.4. A revised probability plot for the comparison database using a Weibull slope of 3.4 is shown in Fig. 14. As was the case for A508 Grade 4N, the comparison database follows the extreme probability distribution fairly well except in the lower tail (and perhaps in the upper tail), indicating that a probability distribution for the comparison database using a Weibull slope of 3.4 will underestimate the toughness in the lower tail.

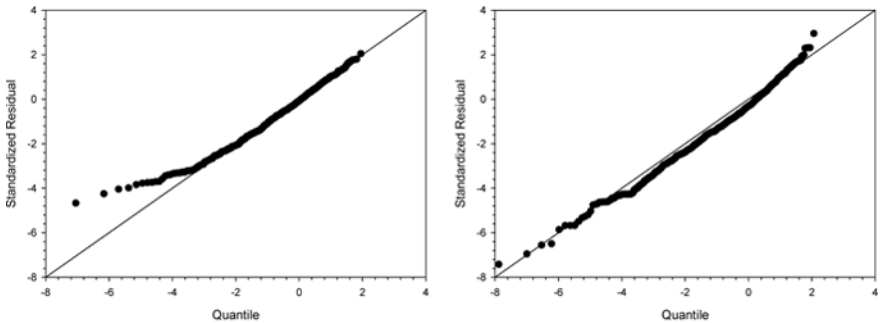


FIG. 13—*Extreme value probability plot of* a*) the A508 Grade 4N standardized residuals (β = 4) and* b*) the comparison database standardized residuals (β = 4).*

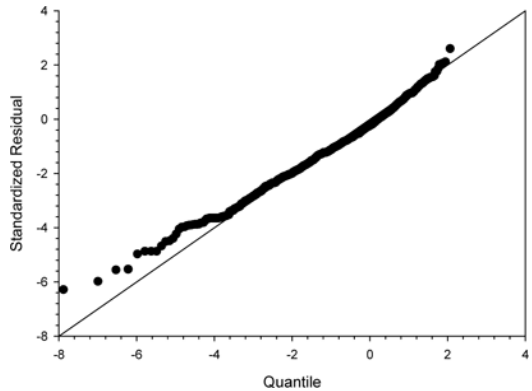
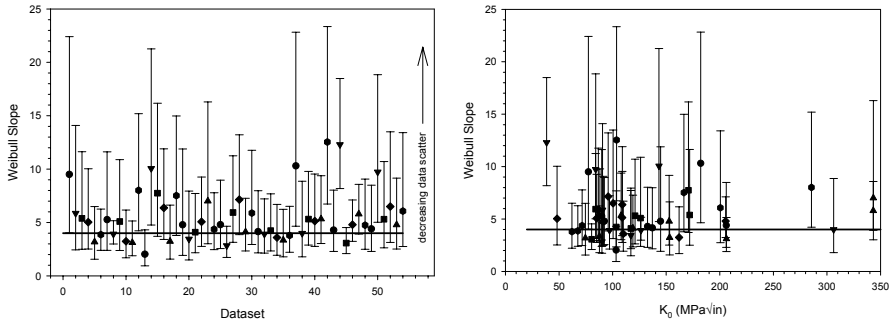


FIG. 14—*Extreme value probability plot of the comparison database standardized residuals (β = 3.4).*

Another way to assess variability is by directly determining the Weibull slope, β, which, as noted above, is analogous to the standard deviation in a normal distribution. It is, however, difficult to accurately assess the variability of a single material heat by determining the Weibull slope, since a large number of tests is required to accurately determine β [16]. As noted in [16], even when as many as one hundred specimens from a single heat are tested, variations of plus or minus one in the value of β can be expected, and much larger variations can be expected when far fewer specimens are tested. To overcome this limitation, one can compare the distribution of Weibull slopes obtained from a large number of data sets with the expected distribution. This was done in the current evaluation, and the results are described below.

Where sufficient test data were available (four or more test results) at a single temperature for a given material heat and condition, the (size corrected) toughness data were fit to a Weibull distribution by maximum likelihood using the commercial software code, NCSS. NCSS also provides upper and lower bounds on the estimated Weibull slope. A threshold value (K_{min}) of 20 MPa√m was assumed when fitting the data. Fifty-four separate estimates of the Weibull slope are shown in random order in Fig. 15*a* and plotted against K_0, determined from each dataset using E 1921, in Fig. 15*b*. The data at both very high and very low K_0 (outside the allowable temperature range for a valid T_0 determination per ASTM E 1921) appear to show less variability than for intermediate K_0s. The Weibull slopes of the remaining data sets are consistent with the Master Curve value of four. The median value for the Weibull slope for all the data is 4.9, which is slightly higher than the expected value of four. This indicates that the variability in the A508 Grade 4N fracture toughness for the heats represented by this plot is roughly the same, or perhaps slightly less, than assumed in the Master Curve approach. Thus, use of a Weibull slope of four to characterize the variability in fracture toughness is a reasonable assumption for A508 Grade 4N.



a) b)

FIG. 15—*Estimated Weibull slopes for A508 Grade 4N from single temperature tests* a*) in random order and* b*) plotted versus K_0. The red horizontal line is at a Weibull slope of four and is plotted as a reference.*

Weibull slopes can also be determined for toughness data obtained over a range of temperatures using maximum likelihood techniques. In determining the Weibull slopes, all the fracture toughness data were first size corrected assuming β equal to four. The toughness data were then fit to the temperature modified Master Curve, fixing all the adjustable parameters except T_0 and β (A = 30 MPa√m, K_{min} = 20 MPa√m, C = $0.303/(T+273)^{1/2}$ 1/°C). The

distribution of the experimentally determined Weibull slopes was then compared to the expected distribution. The expected distribution was obtained by Monte Carlo techniques with β taken equal to four, and the test temperature taken equal to T_0. For the Monte Carlo analysis, four thousand data sets with either six or twelve toughness values per data set were used to characterize the Weibull distribution. A comparison of the two Monte Carlo distributions is provided in Fig. 16. As expected, the distribution of Weibull slopes is fairly broad, particularly when there are only six toughness values per data set. For the A508 Grade 4N database, the number of uncensored toughness measurements per data set varied from 4 to 128, with a median value of 8. For the comparison database, the number of uncensored toughness measurements varied from 4 to 483, with a median of 9. Combined, the two Monte Carlo data sets have a median number of toughness measurements of nine, the same (or nearly so) as the median number of toughness measurements for the two pressure vessel steel data sets. A comparison of the observed and simulated distributions is shown in Fig. 17. As shown in the plot, the A508 Grade 4N distribution is very similar to the Monte Carlo distribution. For the comparison database, the shape (slope) of the distribution is the same as the Monte Carlo distribution, but the median value of β is less than four. The median value of the Weibull slope for the A508 Grade 4N distribution is 4.2, while the median value of the comparison database is 3.6. This compares to estimated Weibull slopes of 4.0 and 3.4 determined from fits to the temperature modified Master Curve. Finally, the distribution of standardized Weibull slopes was determined and compared to the distribution from the Monte Carlo calculations (Fig. 18). The standardized Weibull slope is given by:

$$\beta_{\text{standardized}} = \frac{\beta - \overline{\beta}}{\sigma(\beta)} \tag{7}$$

In this expression, the Weibull slope was assumed equal to four for A508 Grade 4N and for the Monte Carlo distribution, and was assumed equal to 3.4 for the comparison database. The standard deviation for β was estimated from the following expression (derived from Monte Carlo simulations) taken from [19]:

$$\sigma(\beta) = \frac{2.91 + 6.32(r-1)^{-0.693}}{\sqrt{r}} \tag{8}$$

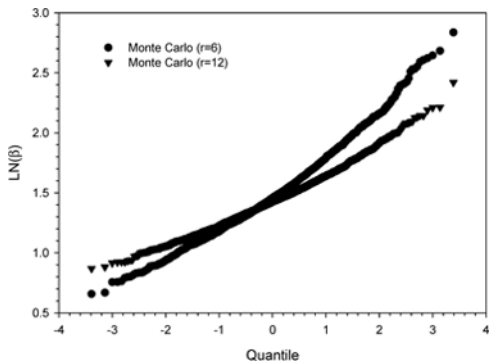


FIG. 16—*Lognormal probability plot showing the dependence of the expected distribution of Weibull slopes on the number of toughness measurements in the data set.*

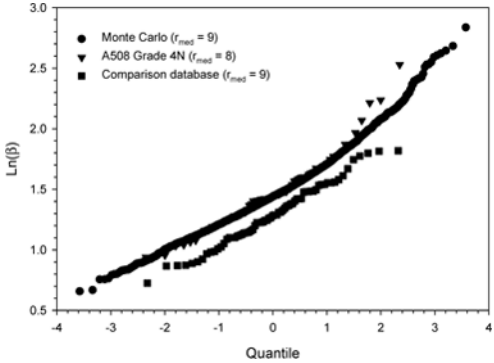


FIG. 17—*Probability plot comparing the expected distribution of Weibull slopes from Monte Carlo analysis with the measured distributions.* r_{med} *is the median number of data points per data set.*

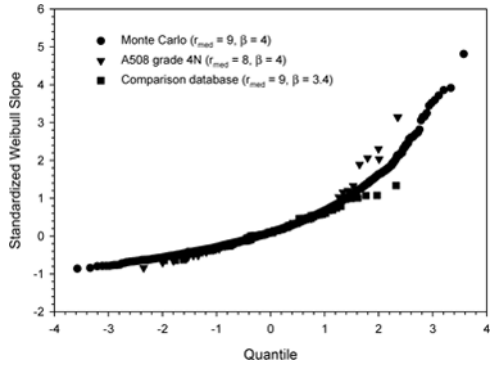


FIG. 18—*Probability plot comparing the expected distribution of standardized Weibull slopes from Monte Carlo analysis with the measured distributions.*

Figure 18 shows that the experimentally determined Weibull slope distribution closely matches the distribution determined from Monte Carlo calculations.

In summary, the distribution in measured Weibull slopes for A508 Grade 4N has the same shape and median value as the Master Curve distribution. For the comparison database, the distribution in measured Weibull slopes is close to the Master Curve distribution, but the median value of the Weibull slope is lower (3.4), indicating the variability is, on average, larger than would be expected from the Master Curve Weibull distribution. Larger variability in Charpy impact energy for A508 Grade 2 compared to A508 Grade 4N has been reported in [20]. In [20], the authors noted that for A508 Grade 2: "*This [Charpy] scatter in the transition regime is greater than would be obtained with a homogeneous tempered martensite structure, and is characteristic of the heterogeneous bainitic structure in this grade.*" This heterogeneous microstructure can be attributed to inadequate hardenability in thick sections.

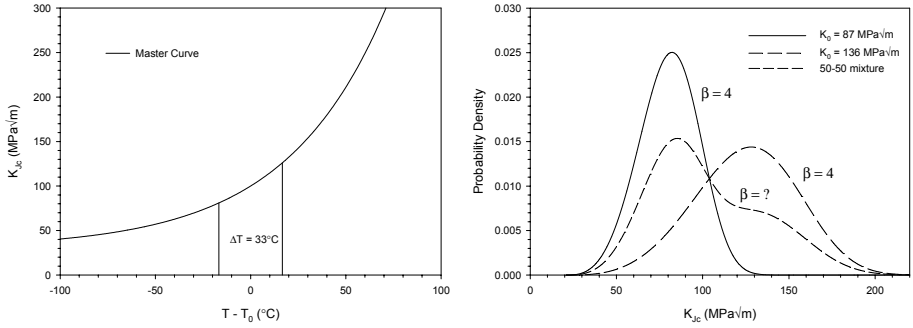
Effect of Material Inhomogeneity on Fracture Toughness Variability

A brief discussion of how local (short range) variability due to mesoscale material inhomogeneity can contribute to the observed variability in fracture toughness in the transition regime is provided below.

For pressure vessel steels, the final microstructure is determined by the composition (which affects the hardenability), the cooling rate from the austenitizing temperature, and the tempering temperature. The toughness (at a given test temperature) is strongly dependent on the microstructure. For slow cooling rates and low hardenability, primary ferrite and pearlite (depending on carbon content) will form, and the transition temperature will be so high as to render the forging unusable for a pressure vessel. For fast cooling rates and high hardenability, the microstructure will consist of martensite or lower bainite with a fine, uniform distribution of carbides, and the transition temperature will be low. The variability in toughness in both these cases is expected to be described by a Weibull distribution with a Weibull slope near four. For intermediate hardenability and cooling rates, a mixed microstructure will develop (e.g., upper and lower bainite), leading to a moderate transition temperature, but increased variability with a Weibull slope less than four. The extent of the deviation from a Weibull slope of four depends on the details of the microstructure. The greater the difference in inherent toughness between two (or more) microstructural constituents, the greater the expected variability.

As noted above, the median Weibull slope is 3.4 for the comparison database. Since it is expected that the test specimens for most data sets were taken from roughly the same locations and forging depths, this lower than expected Weibull slope suggests that mesoscale material inhomogeneity is contributing to the variability. An estimate of what this means in terms of the uncertainty in the transition temperature was made using the following approach. First, it was assumed that the larger variability was due to a mixed microstructure (e.g., a mixture of upper and lower bainite) that gives rise to two separate toughness distributions. Secondly, it was assumed that the T_0 value from the combined distribution ($T_{0(comb)}$) is an average of two T_0 values located a distance $T_{0(comb)} \pm \Delta T/2$ apart along the median toughness curve as illustrated in Fig. 19*a*. The combined toughness distribution is assumed to be the sum of two toughness distributions, each of which contributes equally to the combined distribution, as illustrated in Fig. 19*b*. Monte Carlo techniques were used to determine the relationship between the experimentally determined Weibull slope and the temperature difference (ΔT) along the median toughness curve between the two toughness distributions.

The results of the Monte Carlo simulations are shown in Fig. 20 and indicate that a measured Weibull slope of 3.4 would result from the combination of two toughness distributions located at approximately $T_0 \pm 10°C$. This assumes six test specimens per data set. For larger data sets, the temperature difference would be slightly smaller. While this analysis is only an approximation due to the simplifying assumptions used, it does provide a rough estimate of how far apart on the median fracture toughness curve, in terms of temperature, the toughness distributions would need to be to result in a median Weibull slope of 3.4.



a) b)

FIG. 19—*Schematic illustrating* a*) the two temperatures at which the toughness distributions were obtained and* b*) the original and combined toughness distributions.*

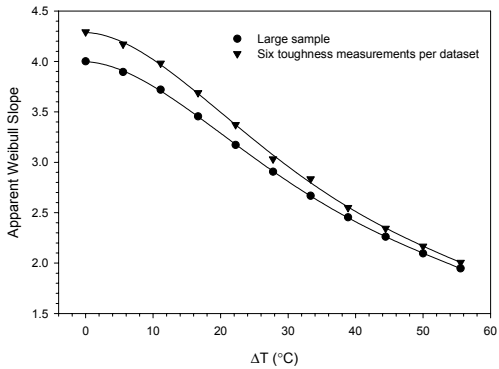


FIG. 20—*Relationship between the apparent Weibull slope and the excess temperature difference from which the toughness distributions were obtained.*

Conclusions

Based on the assessment described above, the following conclusions are offered:

- All the pressure vessel steels evaluated fall on a single fracture toughness curve.
- The Master Curve, while not an exact description of the toughness behavior, provides a simple and accurate means to estimate toughness as the temperature of interest.
- While the temperature modified Master Curve provides a slightly better description of the toughness behavior than the Master Curve, its use requires a family of curves, rather than a single curve. As a consequence, a design procedure using this approach would be more complex than one based on the Master Curve. Further, the difference in the two curves is small relative to the inherent variability. For likely operating temperatures, the differences are particularly small.

- A508 Grade 4N shows less fracture toughness variability, on average, than the other pressure vessel steels evaluated. The increased variability displayed by the heats in the comparison database can be attributed to material inhomogeneity.
- A design curve for A508 Grade 4N based on the lower tail of the assumed Weibull distribution will underestimate the minimum toughness and so be conservative. For the comparison database, the assumed Weibull distribution provides a reasonable description of the lower tail of the distribution.

References

[1] Marston, T. U., "Flaw Evaluation Procedures, Background and Application of ASME Sec. XI App. A", *EPRI Report NP-719-SR*, EPRI, 1978.

[2] VanDerSluys, W.A. and Miglin, M.T., "Results of MPC/JSPS Cooperative Testing Program in the Ductile-to-Brittle Transition Region", *Fracture Mechanics, 24th Volume, ASTM STP 1207*, Landes, J.D., McCabe, D.E., and Boulet, J.A.M., ed., ASTM, pp. 308-324, 1994.

[3] Alexander, D.J. and Cheverton, R.D., "Fracture Properties of Specially Heat Treated ASTM A508 Cl. 2 Pressure Vessel Steel", *Fracture Mechanics, 23rd Symposium, ASTM STP 1189*, Chona, R., ed., ASTM, pp. 365-380, 1993.

[4] Iwadate, T., Tanaka, Y., Ono, S. and Watanabe, J., "An Analysis of Elastic Plastic Fracture Toughness Behavior for J_{Ic} Measurement in the Transition Region", *Elastic Plastic Fracture, Second Symposium, Vol. 2, ASTM STP 803*, Shih, C.F., Gudas, J.P., ed., ASTM, pp. 531-561, 1983.

[5] Lidbury, D. and Moskovic, R., "Assessment of the Ductile-to-Brittle Transition Toughness Behavior of an A508 Cl. 3 PWR Pressure Vessel Steel By a Statistical Approach", *ASME PVP Conference Proceedings, Vol. 250, Pressure Vessel Integrity*, ASME, pp. 283-294, 1993.

[6] Hawthorne, J.R., Menke, B.H., Loss, F.J., Watson, H.E., Hiser, A.L., and Gray, R.A., "Evaluation and Prediction of Neutron Embrittlement in Reactor Pressure Vessel Materials", *EPRI NP-2782*, EPRI, 1992.

[7] Miranda, Carlos, Landes, John, Andrade, Arnaldo, McCabe, Don and Swain, Ronald, "Accuracy in the T_0 Determination: Numerical vs. Experimental Results", *Proceedings of the 1999 Pressure Vessel and Piping Conference*, ASME, 1999.

[8] Valo, Matti, Wallin, Kim, Torronen, Kari and Ahlstrand, Ralf, "Irradiation Response of the IAEA CRP-3 Material FFA Measured by Fracture Toughness Specimens", *Radiation Embrittlement of Nuclear RPV Steels, ASTM STP 1170*, L.E. Steele, ed., ASTM, pp. 238-248, 1993.

[9] Havel, R., Vacek, M. and Brumovsky, M., "Fracture Properties of Irradiated A533B Cl.1, A508 Cl. 3, and 15Ch2NMFAA Reactor Pressure Vessel Steel", *Radiation Embrittlement of Nuclear RPV Steels, STP 1170*, Steele, L.E., ed., ASTM, pp. 163-171, 1993.

[10] Kodaira, T., Miyazono, S., Ishimoto, K. and Itami, H., "Evaluation of Neutron Irradiation Embrittlement of Heavy Section Nuclear RPV Steels in Terms of Elastic-Plastic Fracture Toughness", *Nuclear Engineering and Design*, Vol. 85, pp. 1-13, 1985.

[11] Wallin, K., "Master Curve Analysis of Ductile to Brittle Transition Region Fracture Toughness Round Robin Data, The 'EURO' Fracture Toughness Curve", *VTT-367*,

VTT, 1998.
[12] Pluvinage, G. and Marandet, B., "Application of Local Fracture Criteria to Dynamic Fracture Toughness", *Advances in Fracture Research: Fracture 84, Proc. of the 6th ICF*, New Delhi, India, Dec 84, pp. 3151-3158, 1984.
[13] Marandet, B., Phelippeau, G. and Sanz, G., "Influence of Loading Rate on the Fracture Toughness of Some Structural Steels in the Transition Regime", *Fracture Mechanics, 15th Symposium, ASTM STP 833*, Sanford, R.J. , ed., ASTM, pp. 622-647, 1984.
[14] Holzmann, M., Man, J., Valka, L. and Vlach, B.,"R-Curves and Fracture Toughness Transition Behavior at Static, Rapid, and Impact Loading of CrNiMoV Reactor Pressure Vessel Steel", *International Journal of Pressure Vessels and Piping*, Vol. 62, pp. 39-47, 1995.
[15] Soulat, P. and Petrequin, P., "The Effect of Irradiation on the Toughness of Pressurized Water Reactor Vessel Steels Under Different Service Conditions", *Nuclear Engineering and Design*, Vol. 81, pp. 61-68, 1984.
[16] J. G. Merkle, K. Wallin and D. E. McCabe, "Technical Basis for an ASTM Standard on Determining the Reference Temperature, T_0, for Ferritic Steels in the Transition Temperature Range", *NUREG/CR-5504, ORNL/TM-13631*, Oak Ridge National Laboratory, 1998.
[17] ASTM E 1921-02, "Standard Test Method for Determination of Reference Temperature, T_0, for Ferritic Steels in the Transition Range", *Annual Book of ASTM Standards*, Vol 03.01, ASTM, 2003.
[18] U. Zerbst, J. Heerens, M. Pfuff, B. U. Wittkowsky and K. H. Schwalbe, "Engineering Estimation of the Lower Bound Toughness in the Transition Regime of Ferritic Steels", *Fatigue & Fracture of Engineering Materials & Structures*, Vol. 21, pp. 1273-1278, 1998.
[19] E. Lucon, M. Scibetta and E. Van Walle, "Assessment of the Master Curve Approach on Three Reactor Pressure Vessel Steels", *International Journal of Fracture*, Vol. 119, pp. 161-178, 2003.
[20] T. D. Nelson, R. L. Bodnar and J. E. Fielding, "A Critical Assessment of ASTM A508 Class 2 Steel for Pressure Vessel Applications", *32nd Mechanical Working and Steel Processing Proceedings*, Vol. XXVIII, Cincinnati, Ohio, 21-24 Oct. 1990, pp. 323-341, 1991.

Journal of ASTM International, Vol. 3, No. 5
Paper ID JAI13191
Available online at www.astm.org

Stephen M. Graham,[1] *Gerard P. Mercier,*[2] *and Brian P. L'Heureux*[2]

Application of the Reference Temperature to the Evaluation of Cleavage Fracture in HSLA-100 Steel

ABSTRACT: The purpose of this study was to evaluate the fracture behavior of HSLA-100 steel at a temperature of −40°C (−40°F). Tests were conducted on three different compositions and two orientations of HSLA-100. HY-100 was also tested to provide a baseline for comparison. Various fracture-related tests were conducted, including traditional test methods, such as the Charpy V-notch and the Dynamic Tear, and more recent methods, such as ductile crack growth initiation (J_{ic}) and the reference temperature. Transition temperatures from the Charpy tests were all very similar, falling around −129°C (−200°F), although the upper shelf Charpy energy for the HY-100 was lower than the HSLA-100 steels. Dynamic tear energies at −40°C for the four steels ranged from 800 to 1800 J. The average reference temperature of all four steels, measured according to ASTM E 1921, was around −151°C (−240°F), with one composition of HSLA-100 coming in as low as −179°C (−290°F) and another as high as −123°C (−190°F). Fracture toughness tests were conducted according to E 1820 at temperatures of −40, −29, and −18°C. These temperatures were more than 83°C above the highest of the reference temperatures, so cleavage fracture was not expected to occur. The HY-100 specimens exhibited an average initiation toughness of 227 kJ/m^2 (1296 lb/in.) and crack growth remained ductile throughout the tests. Even though the HSLA-100 exhibited initiation toughnesses more than twice as high as the HY-100, many of the tests terminated in cleavage fracture after amounts of ductile crack growth varying from 0 to 1.85 mm (0.073 in.). This was an unexpected result based on good Charpy and dynamic tear energies at −40°C, and low reference temperatures. The higher initiation toughness and tearing resistance of HSLA-100 allowed very high stresses to develop in the fracture process zone. As ductile crack growth occurred, the fracture process zone swept through an increasing volume of metal, which increased the probability of cleavage fracture. It is shown that the load required to reach these levels of crack driving force may be above gross section yielding of a typical structure. In this case failure by gross section yielding would occur before fracture. This is demonstrated with the aid of a failure assessment diagram.

KEYWORDS: fracture mechanics, reference temperature, cleavage, HSLA-100

Introduction

In the 1960s high yield (HY) steels were developed that had high yield strength, low transition temperatures, and high upper shelf tearing resistance. This combination of properties made these HY steels good candidates for critical structural applications. However, construction of large structures from HY steels is expensive because of the precautions that must be taken to prevent cracking in the welds [1]. Over the past 40 years, considerable research has been conducted in an effort to develop more easily weldable steels with high strength and toughness. One of the fruits of that research is HSLA (high strength low alloy) steel. Changes in chemistry, such as lowered carbon content, allow this steel to be made with strengths similar to the HY steels, and with better weldability.

Ferritic steels show a transition in fracture behavior from rapid, brittle fracture to stable tearing as the temperature is increased. Figure 1 shows this transition behavior graphically as an increase in Charpy V-notch (CVN) energy absorbed with increasing temperature. At low temperatures, the material is brittle and absorbs low amounts of energy during fracture. At high temperatures, the material is ductile and absorbs larger amounts of energy. In the transition between lower shelf and upper shelf, there is large variability in fracture toughness and ductile fracture can transition to brittle at any time. Consequently, material behavior in this transition region is dif cult to predict. Therefore, it is desirable to have the lowest

Manuscript received March 30, 2005; accepted for publication January 30, 2006; published online April 2006. Presented at ASTM Symposium on Fatigue and Fracture Mechanics: 35th Volume on 18 20 May 2005 in Reno, NV; R. E. Link and K. M. Nikbin, Guest Editors.

[1] Ph.D., U.S. Naval Academy, Annapolis, MD21402.

[2] Naval Surface Warfare Center, Carderock Division, Bethesda, MD 20817

Copyright © 2006 by ASTM International, 100 Barr Harbor Drive, PO Box C700, West Conshohocken, PA 19428-2959.

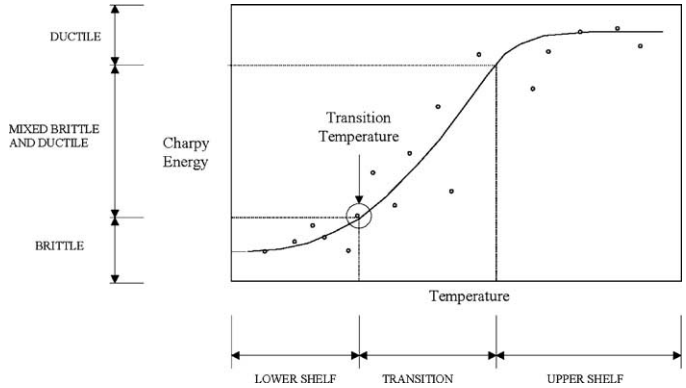


FIG. 1—*Typical transition behavior of low alloy steels.*

service temperature for a particular application fall in the upper shelf region, and to have a high upper shelf tearing resistance. HSLA-100 steel shows higher upper-shelf toughness than HY-100 steel [2], which is attributed to very small prior austenite grain size and classic copper precipitation [3]. The availability, improved weldability, and mechanical properties of HSLA steels make them an attractive choice for large structures. The objective of this study was to investigate the fracture properties and transition behavior of HSLA-100 and to compare it with HY-100.

Materials

Tests were conducted on four HSLA-100 plates, ranging in thickness from 19.1 mm (Comp. 1) to 50.8 mm (Comp. 3), and one 31.8-mm thick HY-100 plate. The multiple compositions of HSLA-100 are designed to improve toughness properties as plate thickness increases. This is accomplished by increasing nickel, copper, and molybdenum content with plate thickness [4]. Table 1 shows the designations, steel type, and dimensions of the plates tested in this study.

Transition Behavior

Tests were conducted in accordance with ASTM Standard Test Methods for Notched Bar Impact Testing of Metallic Materials (E 23), ASTM Standard Test Method for Dynamic Tear Testing of Metallic Materials (E 604), and ASTM Standard Test Method for Determination of Reference Temperature, T_o, for Ferritic Steels in the Transition Regime (E 1921) to qualitatively and quantitatively define the transition behaviors of HSLA-100 and HY-100. Full Charpy V-notch transition curves were developed for four of the plates in the T-L orientation, which typically has the lowest fracture resistance for rolled plate. These transition curves are given in Fig. 2 and the average Charpy toughnesses of all five plates at −40°C (−40°F) are summarized in Table 2. Note that based on the Charpy data, there does not appear to be much difference in the transition temperatures of these steels. Note also that the HSLA-100 steels had greater upper-shelf impact toughness than HY-100.

TABLE 1—*Plate IDs and thicknesses.*

Plate Designation	Steel	Thickness mm (in.)
HIC	HY-100	31.8 (1.25)
HDB	HSLA-100, Comp. 1	19.1 (0.75)
HDU	HSLA-100, Comp. 2	31.8 (1.25)
HIZ	HSLA-100, Comp. 2	41.3 (1.625)
GPP	HSLA-100, Comp. 3	50.8 (2.00)

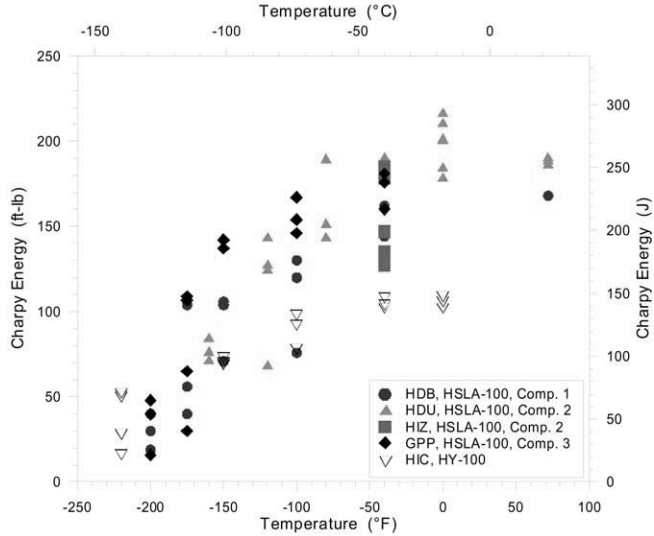


FIG. 2—*Charpy V-notch impact data for the T-L orientation.*

Dynamic tear tests were conducted at −40°C on two specimens from each of the five plates. Once again, the plates were tested in the T-L orientation. Tests from the composition two plates are averaged together for ease of comparison. The results are shown in Fig. 3 and are consistent with the expected behavior

TABLE 2—*Charpy V-notch results at −40°C in the T-L orientation.*

	HDB HSLA-100 Comp.1	HDU HSLA-100 Comp.2	HIZ HSLA-100 Comp.2	GPP HSLA-100 Comp.3	HIC HY-100
CVN Energy @ −40°C, J (ft-lb)	204.3	250.4	183.7	233.6	142.0
	(150.7)	(184.7)	(135.5)	(172.3)	(104.7)

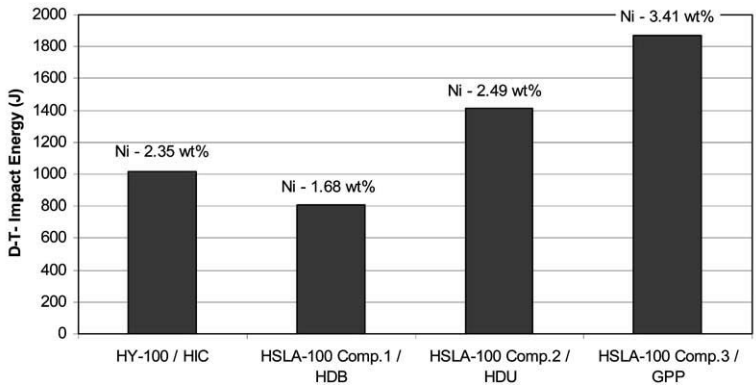


FIG. 3—*Dynamic tear results in the T-L orientation at −40°C.*

TABLE 3—*T_o reference temperature test results.*

Steel ID	Composition	Thickness mm (in)	Orientation	T_o Temperature °C (°F)
HIC	HY-100	31.8 (1.25)	L-T	−152 (−242)
			T-L	−155 (−247)
HDB	HSLA-100 Comp.1	19.1 (0.75)	T-L	−153 (−244)
HDU	HSLA-100 Comp.2	31.8 (1.25)	L-T	−138 (−216)
			T-L	−123 (−190)
GPP	HSLA-100 Comp.3	50.8 (2.0)	T-L	−179 (−290)

based on the amount of nickel present in each composition. Nickel, in general, improves low temperature toughness. The DT energy for the HSLA-100 Comp. 1 is about 20 % lower than HY-100, while Comp. 2 and Comp. 3 are approximately 40 and 85 % higher, respectively.

ASTM E 1921 provides a quantitative way to compare toughness of steels that exhibit transition behavior. This is accomplished by means of a reference temperature, T_o, defined as the temperature at which the median fracture toughness is 100 MPa$\sqrt{}$m (91 ksi$\sqrt{}$in). This fracture toughness level is just above lower shelf for ferritic steels, and provides a more accurate means of identifying transition than either Charpy or Dynamic tear tests. Research has shown that fracture toughness for ferritic steels in transition tends to conform to a common toughness versus temperature curve [5], similar to the American Society for Mechanical Engineers K_{IC} and K_{IR} lower bound design curves found in their Pressure Vessel Design Code [6]. This toughness transition curve, referred to as the "Master Curve," is defined by the following equation.

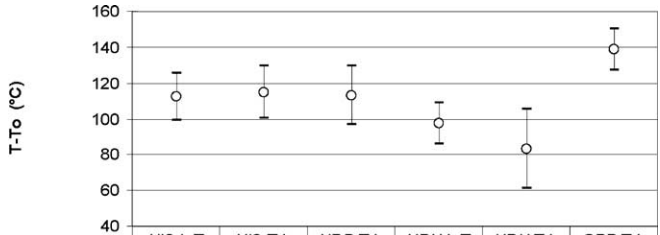
$$K_{Jc} = 30 + 70 \exp\left[0.019(T - T_o)\right] \tag{1}$$

where K_{Jc} is in MPa$\sqrt{}$m and T is the test temperature in °C. Once T_o is determined, the transition behavior of the steel can be inferred by Eq 1 and fracture toughness values can be calculated at other temperatures of interest throughout the transition region.

Four of the five plates were tested to determine the reference temperature, T_o. HSLA-100, Comp. 1 and Comp. 3 were tested in the T-L orientation, while Comp. 2 and the HY-100 were evaluated in both T-L and L-T orientations. Only one of the two Comp. 2 plates (HDU) was tested. Test specimens were single edge bend [SE(B)] with a thickness of 12.7 mm (0.5 in.), a width of 25.4 mm (1.0 in.), and were not side-grooved. Tests were conducted at temperatures near lower shelf that ranged from −84°C (−120°F) to −151°C (−240°F). A summary of the measured reference temperatures is given in Table 3.

The behavior of a steel in a particular application will depend on where the lowest service temperature is relative to the reference temperature. Therefore, it is informative to look at the excess temperature, which is the difference between the two $(T-T_o)$. This is shown in Fig. 4 for a service temperature of −40°C. The large excess temperature for these steels at −40°C indicates that the behavior should be on upper shelf, or at least close to it. The vertical bars in Fig. 4 represent 95 % confidence bounds at the 10 and 90 percentile levels, which were calculated using the equations provided in ASTM E 1921, and are based on the number of valid tests available to determine T_o. This statistical treatment shows that HSLA-100, Comp. 3 clearly has a higher excess temperature than HY-100 and the other HSLA-100 compositions, which is consistent with DT results. HSLA-100, Comp. 2 in the T-L orientation has the lowest excess temperature at 83°C, although the upper confidence bound overlaps the lower confidence bounds of all but the Comp. 3, indicating that there is some probability that the difference is not statistically significant at the 95 % confidence level. This is contrary to the DT test results, where Comp. 1 had the lowest DT energy. It does not appear that orientation has a strong effect on reference temperature.

Tensile tests were conducted in accordance with ASTM Standard Test Methods for Tension Testing of Metallic Materials (E 08) on all five plates in the longitudinal orientation. The tensile tests on plate HIZ, which was not evaluated for T_o, were conducted at room temperature (22°C). The other four plates were tested at or near the respective T_o temperatures. The measured tensile properties are shown in Fig. 5. The brittle fracture morphology shown in the tensile fractures was unique. The fracture surface was very flat with no visible shear lips. However, the location of the fracture was at the beginning of the necked-down region instead of at the minimum diameter in the necked region. The minimum diameter was used to calculate reduction of area.



	HIC L-T HY-100	HIC T-L HY-100	HDB T-L Comp.1	HDU L-T Comp.2	HDU T-L Comp.2	GPP T-L Comp.3
– 90% UCB	126	130	130	109	105	150
– 10% LCB	99	100	97	86	61	128
○ T-To	112	115	113	98	83	139

UCB – Upper Confidence Bound on 90-percentile

LCB – Lower Confidence Bound on 10-percentile

FIG. 4—*Excess temperature at minimum service temperature −40°C.*

Fracture Toughness

Elastic-plastic fracture toughness tests were conducted in accordance with ASTM Standard Test Method for Measurement of Fracture Toughness (E 1820) to compare initiation toughness and resistance to ductile crack extension between HY-100 and HSLA-100 steels. Thirty-one fracture toughness tests were conducted on the five plates at temperatures ranging from −40 to −18°C (−40 to 0°F). Compact tension specimens [C(T)] with $B=25.4$ mm (1.0 in.) and $W=50.8$ mm (2.0 in.) were used for all tests except HDB, which had $B=19.1$ mm (0.75 in.) and $W=38.1$ mm (1.5 in.). All specimens were side-grooved 20 %. ASTM E 1820 has many validity requirements that must be met for a valid J_{Ic} result. If these requirements are not achieved, the ductile initiation toughness value is designated J_Q. If a test ended in cleavage, a valid J_{Ic} could not be obtained. In those cases, if more than 0.2 mm of ductile crack growth

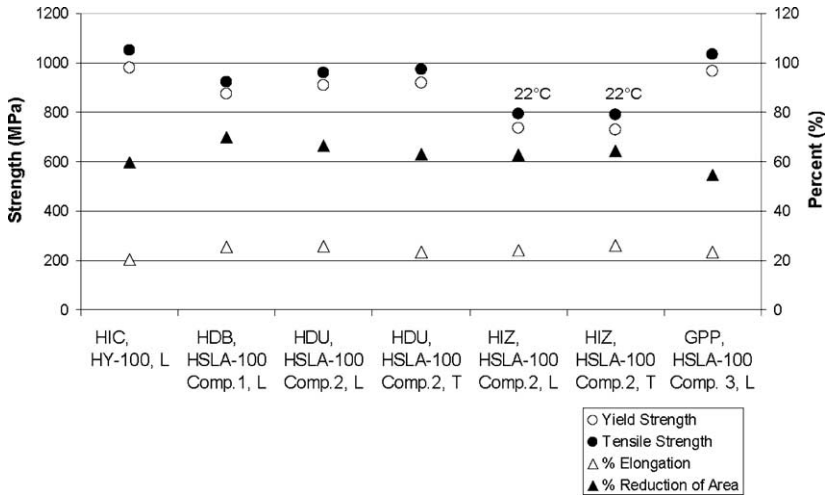


FIG. 5—*Tensile test results at various temperatures near the reference temperature for each alloy (except as noted for HIZ).*

TABLE 4—*E 1820 fracture toughness test results.*

Type	Orien-tation	Test Temp. (°C)	Excess Temp. (°C)	J at Ductile Initiation, J_Q (kJ/m^2)	Valid J_{Ic}?	J at Cleavage, J_c (kJ/m^2)	Ductile Crack Growth at Cleavage (mm)
HDB	T-L	−40	113			926.1	1.40
HSLA-		−40	113			726.8	1.50
100,		−40	113	449.0	Yes		
Comp. 1		−40	113	534.8	No		
		−40	113	397.9	Yes		
HIZ	L-T	−40		601.4	Yes		
HSLA-		−40		775.5	No		
100,		−40		617.3	Yes		
Comp. 2	T-L	−40		436.4		663.9	1.68
		−40		421.5		573.6	0.89
		−40				246.4	0.23
HDU	L-T	−40	98	727.0		899.5	1.02
HSLA-		−29	109	640.8		1063.6	1.68
100,		−29	109	736.1		1053.9	1.80
Comp. 2	T-L	−40	83			259.7	0.16
		−40	83	571.1		619.1	0.79
		−40	83	496.0		591.2	0.81
		−40	83	599.3		639.0	0.69
		−29	94	671.3		794.9	0.79
		−29	94	528.4	No		
		−18	106	542.2	No		
		−18	106	576.5	No		
GPP	L-T	−40	139			179.9	0.10
HSLA-		−29	150	567.2	Yes		
100,		−29	150	549.4	No		
Comp. 3	T-L	−40	139			428.5	0.33
		−40	139	548.5		615.9	0.66
		−40	139	477.6		643.4	0.86
HIC	T-L	−40	115	225.2	Yes		
HY-100		−40	115	211.9	Yes		
		−40	115	242.7	Yes		

preceded cleavage, both J_Q and J at cleavage (J_c) are reported, otherwise, only J_c is reported. Six of the 14 tests that did not end in cleavage were invalid, mostly due to problems with crack front straightness and crack extension prediction.

The T-L orientation typically has lower toughness than other orientations as the crack propagates along the plate rolling direction and can progress along the elongated grains. Therefore, early fracture toughness testing in this program focused on testing in this lower toughness orientation to provide a lower bound of expected plate toughness properties. Tests were also conducted in the L-T orientation for some of the plates to evaluate orientation effects. Table 4 shows the plate ID, orientation, test temperature, excess temperature, initiation toughness, J at cleavage, and amount of ductile crack growth (including blunting) that preceded cleavage. The values for J at cleavage have been corrected for crack growth. The fracture toughnesses for the five plates are compared in Fig. 6 where the solid symbols represent ductile crack growth initiation (J_Q) and the open symbols represent cleavage (J_c).

HY-100 — The HY-100 steel, HIC, was only tested in the T-L orientation at −40°C, which corresponds to an excess temperature of 115°C. These three specimens all exhibited ductile tearing to crack extensions of at least 2.5 mm, and yielded an average J_{Ic} of 227 kJ/m^2.

HSLA-100 Comp. 1 — Plate HDB was also tested in the T-L orientation at −40°C, which is an excess temperature of 113°C. Crack growth in three of the five specimens remained ductile to the end of the test, which was at least 4.22 mm of crack extension. These three specimens had an average J_Q of 461 kJ/m^2, which is about double the initiation toughness of HY-100. For the remaining two tests, cleavage occurred at elevated J values in excess of 727 kJ/m^2 after considerable stable ductile crack growth (>1.4 mm). The

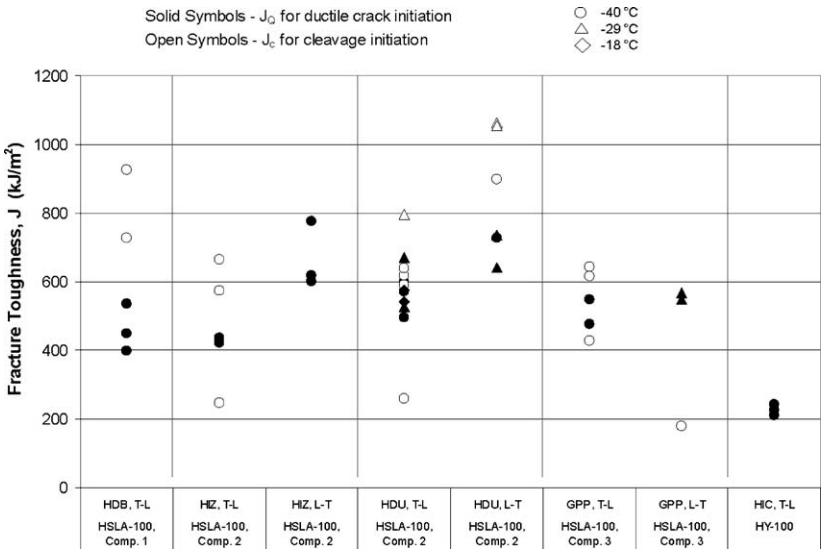


FIG. 6—*Summary of all ASTM E 1820 fracture toughness test results.*

specimens from this plate were thinner than the other plates (19.1 versus 25.4 mm), which may lead to an elevation in J at cleavage initiation.

HSLA-100, Comp. 2 — HIZ had three T-L and three L-T tests, all at −40°C. One T-L specimen cleaved at J of 246 kJ/m^2 with only 0.23 mm of ductile crack growth. The others failed by cleavage after stable ductile growth of 0.89 and 1.68 mm and resulted in an average J_Q of 429 kJ/m^2. This is about 7 % lower than the Comp. 1 plate. They did not cleave until J exceeded about 574 kJ/m^2. This is a good example of the large variability in toughness and the unpredictability that is characteristic of transition behavior. The tests in the L-T orientation all remained stable throughout the test and the average J_Q was 665 kJ/m^2, which is 55 % higher than the T-L orientation.

Four tests were run on plate HDU in the T-L orientation at −40°C (excess temperature of 83°C), all of which cleaved. One specimen cleaved with almost no ductile crack growth at a J of 260 kJ/m^2. The others had at least 0.7 mm of ductile growth and an average J_Q of 555 kJ/m^2. They cleaved at J values in excess of 619 kJ/m^2. Compared to the same orientation in the other Comp. 2 plate, the J_Q is about 29 % higher, but the minimum J at cleavage is about the same. The temperature was increased to −29°C for the next two T-L tests. One specimen exhibited a very high J_Q of 671 kJ/m^2 and then cleaved soon after, while the other had a lower J_Q of 528 kJ/m^2 and crack growth remained ductile. Two more T-L tests were run at -18°C (excess temperature of 106°C), both of which exhibited high initiation toughness and were ductile with 2.1 mm of ductile growth at test completion. One test in the L-T orientation was conducted at −40°C, and it cleaved with a J_Q of 727 kJ/m^2, which is 31 % higher than in the T-L orientation. Two more L-T tests were conducted at −29°C and yielded an average J_Q of 688 kJ/m^2, which is only about 15 % higher than the T-L orientation at this temperature. They both ended in cleavage at J values in excess of 1054 kJ/m^2.

HSLA-100 Comp. 3 — GPP had three T-L tests at −40°C (excess temperature of 139°C). Two failed via cleavage after some ductile growth and resulted in an average J_Q of 513 kJ/m^2, and one specimen cleaved at a J of 428 kJ/m^2 with no ductile tearing. This average J_Q is about 2.3 times the J_Q for HY-100, but falls between the average J_Q values for the two Comp. 2 plates. Even though the initiation toughness is high, the metal is still in transition at an excess temperature of 139°C while the HY-100 appears to be on upper shelf at an excess temperature of 112°C. This implies that HSLA-100 has a very wide transition region. Three tests were conducted on GPP in the L-T orientation, two at −29°C and one at −40°C. The test at −40°C resulted in cleavage failure at a surprisingly low J of 180 kJ/m^2. No cleavage occurred in the two tests at −29°C and the average J_Q value was 558 kJ/m^2, which is only 9 % higher than the T-L

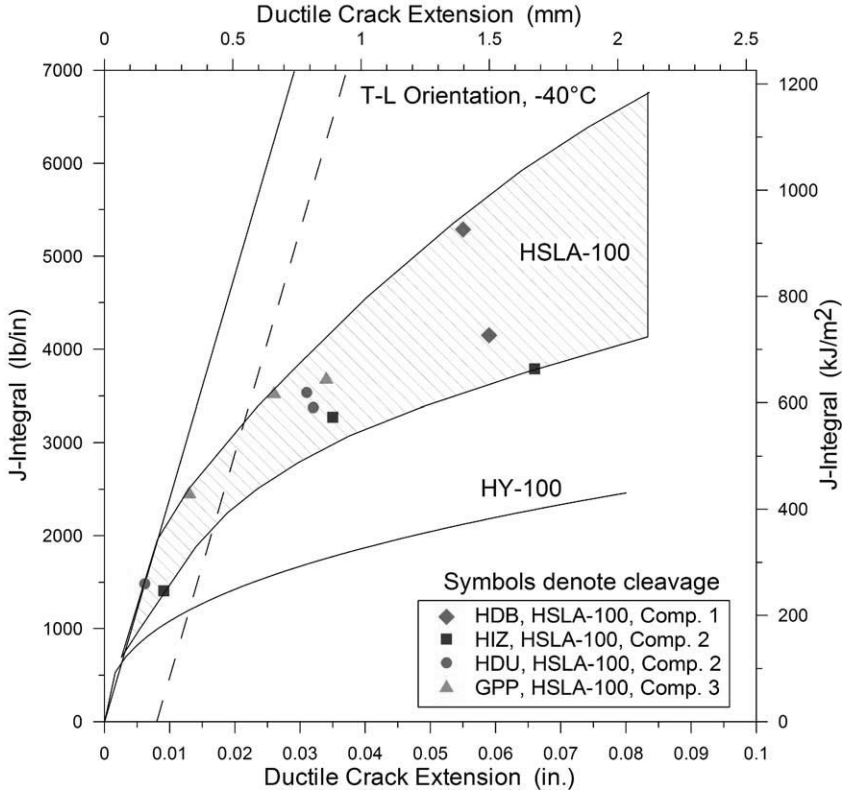


FIG. 7—*Crack growth resistance curves for HY-100 and HSLA-100 for T-L orientation at −40°C.*

orientation. Based on a limited number of tests, it does not appear that orientation has as much effect on fracture toughness for the 50.8 mm thick Comp. 3 plate as it does for the two Comp. 2 plates, which were 31.8 and 41.3 mm thick.

Discussion

The tearing resistance curves for HY-100 and HSLA-100 for the T-L orientation at −40°C are compared in Fig. 7. The cross-hatched band represents the range of J-R curves measured on HSLA-100 and the symbols represent cleavage initiation. This graph shows the high initiation toughness values and elevated J-R curves that were measured for all HSLA-100 compositions where cleavage did not occur. As shown in Fig. 8, these results are in line with historical testing of HSLA-100 [7], which shows that the tearing resistance and initiation toughness for HSLA-100 is substantially above HY-100. However, Fig. 7 also shows that cleavage can occur in HSLA-100 at J-values only slightly above the initiation toughness of HY-100. The two lowest cleavage initiation points on the curve are both Comp. 2, which also had the highest reference temperature (lowest excess temperature). The high Comp. 1 cleavage initiation toughness is partly due to lower constraint. This composition has lower nickel and shows lower CVN and DT toughness, yet because the in-plane thickness is 19.1 mm (as opposed to 25.4 mm for other compositions), four of six fracture tests exhibited ductile behavior in the T-L orientation at −40°C. In comparison, only one of ten tests in the same orientation of the other compositions exhibited ductile behavior at −40°C.

The cleavage initiation toughnesses for all specimens in the T-L orientation are compared with the Master Curve in Fig. 9. The graph includes data from both E 1921 tests, where cleavage occurred with

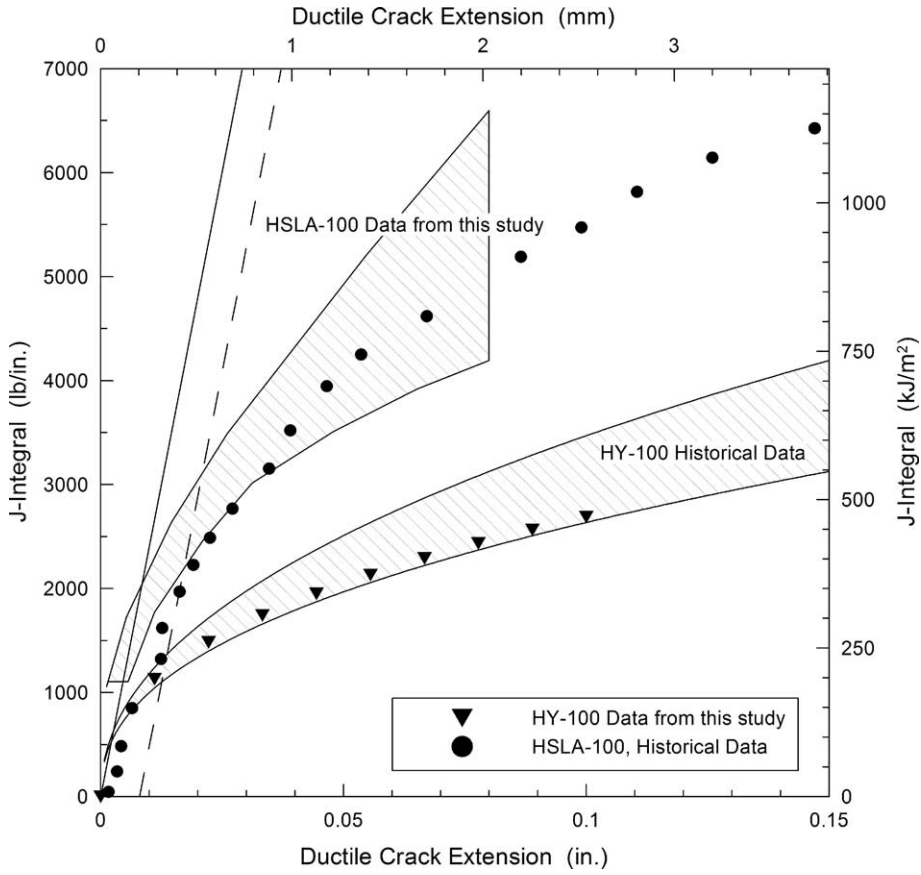


FIG. 8—*Comparison of HY-100 and HSLA-100 data from this study with historical room temperature data.*

little or no ductile crack growth (open symbols), and E 1820 tests that ended in cleavage after some ductile tearing (solid symbols). The E 1820 J values have been corrected for crack growth and converted to K_{Jc} values. An estimated reference temperature of −118°C (−180°F) was used for Comp. 2 plate HIZ and the Comp. 1 J values were not thickness corrected to 1T. The dashed lines in the graph represent the upper and lower 95 % confidence bounds on the 90 and 10 percentiles. It can be stated with 95 % confidence that there is only a 10 % chance that cleavage will occur below the lower dashed line and there is a 90 % chance that cleavage will occur before reaching the upper dashed line. The Comp. 1 and 2 E 1820 data fall within the bounds, even at excess temperatures of 113°C (203°F). The Comp. 3 E 1820 data fall below the lower 10 % curve with an excess temperature of 139°C (250°F). This graph shows that the combination of high crack driving force and ductile tearing lead to cleavage fracture at excess temperatures even as high at 139°C.

The majority of HSLA-100 tests at −40°C experienced cleavage failures after ductile crack growth. This phenomenon seems contrary to the expectation that increasing deformation (loading) in a finite specimen results in a large plastic zone and a corresponding loss in crack tip constraint. The loss of constraint should increase the energy required to extend the crack, and thereby enhance the tearing resistance [8]. However, others have also observed a transition from ductile to brittle behavior after significant ductile tearing and attributed it to the effect of crack extension on the stress field directly ahead

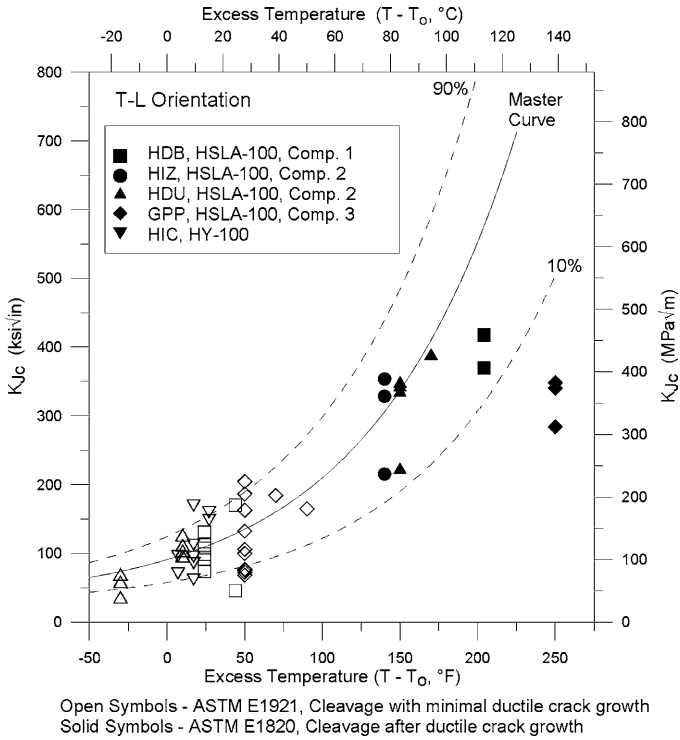


FIG. 9—*Comparison of E 1921 fracture test results with cleavage failures in E1820 tests and the Master Curve, T-L orientation.*

of the crack tip [9–12]. They show that the stress field ahead of a growing crack is elevated above that of a stationary crack, and that the cumulative volume of highly stressed material is increased as ductile tearing occurs and the stress field advances with the crack tip. Cleavage failure in ferritic steels is governed by microstructural features ahead of the crack tip [13]. These features such as inclusions, carbides, and dislocation pile-ups are randomly distributed and have a critical local stress level that will trigger cleavage failure. The distance these features are from the crack tip dictates cleavage toughness. If the features are distant or scarce, higher toughness values will result. In the case of a growing crack, the larger cumulative volume of highly stressed material increases the likelihood of tripping one of the cleavage-causing features.

At high crack driving force values like those shown in Fig. 7, J is roughly proportional to the amount of plastic deformation that is occurring in the material. While these high crack driving forces are relatively easy to generate in a deep cracked, high constraint test specimen, reaching these levels in a structure may not be possible before exceeding other design criteria that are based on yielding of the material. There are two competing failure modes for any structure, fracture, and plastic collapse by extensive yielding. These two failure modes can be illustrated in a failure assessment diagram (FAD), such as shown in Fig. 10. The vertical axis represents the relative crack driving force and the horizontal axis represents the relative magnitude of applied loading. The points on the failure curve represent combinations of crack size and loading that lead to crack growth. The vertical dashed line represents the load ratio at gross section yielding for a 254-mm wide by 25.4-mm thick plate made from HSLA-100, Comp. 2 with a yield strength of 896 MPa (130 ksi). Also shown in the figure is the assessment line for a 6.2-mm long edge crack in a plate with a fracture toughness of 236 MPa$\sqrt{\text{m}}$ (215 ksi$\sqrt{\text{in.}}$), which corresponds to the lowest measured value for the T-L orientation at −40°C. For this particular geometry and crack size, the applied load will

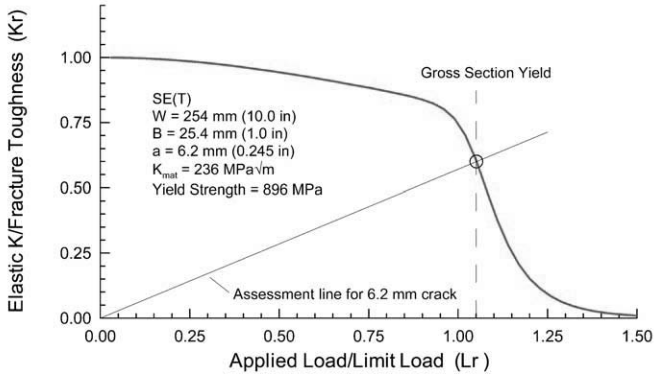


FIG. 10—*Failure assessment diagram for HSLA-100.*

reach gross section yielding just as the crack begins to grow. For smaller cracks, the slope of the assessment line would decrease and gross section yielding would precede crack growth. Conversely, for larger cracks, crack growth would occur first. Since the tests presented here show that HSLA-100 in the T-L orientation has a propensity to transition to cleavage fracture at low temperatures, the fitness for service of this plate is contingent on conducting inspections to ensure that no cracks larger than the critical size for the geometry and loading are present.

Conclusions

Charpy test results showed that HSLA-100 has higher upper shelf impact toughness than HY-100. Dynamic tear testing showed that the toughness at −40°C scaled with nickel content and that HSLA-100 Comp. 2 and 3 DT energy exceeded that of HY-100 at this temperature. Reference temperature testing showed that HY-100 and HSLA-100 exhibit similar transition behavior, and that HSLA-100 Comp. 3 had the lowest reference temperature. This was attributed to the high nickel content.

Fracture test results did not necessarily correlate with either Charpy or DT test results. While HSLA-100 Comp. 3 exhibited good Charpy transition behavior, the highest DT energy, and the lowest transition temperature, the ductile initiation toughness and propensity for cleavage at −40°C were no better than the other compositions.

Fracture toughness testing confirmed historical data showing that the ductile initiation toughness of HSLA-100 is double that of HY-100, and that the tearing resistance is higher. Unfortunately, the high tearing resistance leads to high crack driving force and increases the probability of cleavage fracture. Tests in the T-L orientation showed that the potential for unstable fracture exists in all compositions at −40°C. The L-T orientation generally exhibited higher fracture toughness, but cleavage failures still occurred. Both Comp. 2 and 3 plates had test results where cleavage fracture occurred at −40°C with little or no ductile crack growth. At temperatures below –29°C, numerous cleavage failures occurred after significant ductile crack growth in all compositions. It was shown that for the case of a large edge cracked structure at −40°C, gross section yielding could occur before crack growth in HSLA-100 as long as there are no cracks larger than the critical size in the structure.

The dramatic difference in fracture resistance of HY and HSLA-100 may be attributed to microstructural differences. The reduction in carbon in the HSLA-100 steels greatly improves toughness and weldability by changing the basic microstructure from a martensitic quench and tempered product to a more banitic steel. However, to maintain strength and hardenability, copper and nickel were added [14]. Nickel increases hardenability and low temperature toughness. Copper precipitates at dislocations and ferrite grain boundaries during aging [15], which improves strength but may act to cause dislocation pile-up that could initiate cleavage failures.

References

[1] Czyryca, E. J., Franke, G. L., Hackett, E. M., Holserg, P. W., Montemarano, T. W., Vassilaros, M. G., and Wong, R. J., DTRC-SME-90/12, "Advances in High Strength Steel Technology and Fabrication for Future Naval Hull Construction," November 1991.

[2] Czyryca, E. J., Link, R. E., and Wong, R. J., DTRC-SME-89/15, "Evaluation of HSLA-100 Steel for Surface Combatant Structural Certification," August 1989.

[3] Mattes, V. R., "Microstructures and Mechanical Properties of HSLA-100 Steel," Naval Post Graduate School December 1990.

[4] NAVSEA Technical Publication *T9074-BD-GIB-010/0300* "Base Materials for Critical Applications: Requirements for Low Alloy Steel Plate, Forgings, Castings, Shapes, Bars, and Heads of HY-80/100/130 and HSLA-80/100," August 9, 2002.

[5] Wallin, K., "Fracture Toughness Transition Curve Shape for Ferritic Structural Steels," *Fracture of Engineering Materials & Structures*, S. T. Teoh and K. H. Lee, Eds., Elsevier Applied Science, 1991, pp. 83–88.

[6] ASME Boiler and Pressure Vessel Code. An American National Standard, Sect. XI, *Rules for In-service Inspection for Nuclear Power Plant Components*, Article A-4000, American Society of Mechanical Engineers, New York, 1993.

[7] Czyryca, E. J. and Link, R. E., NSWCCD Report DTRC-SME-88/64 "Fracture Toughness of HSLA-100, HSLA-80 and ASTM A710 Steel Plate," January 1990.

[8] Joyce, J. A. and Link, R. E., "Effects of Constraint on Upper Shelf Fracture Toughness," in *Fracture Mechanics: Vol. 26, ASTM STP 1256*, W. Reuter, J. Underwood, and J. Newman, Eds., ASTM International, West Conshohocken, PA, 1995, pp. 142–177.

[9] O'Dowd, N. P., Shih, C. F., and Dodds, R. H., "The Role of Geometry and Crack Growth on Constraint and the Implications for Ductile/Brittle Fracture," in *Constraint Effect in Fracture Theory and Application: Vol. 2, ASTM STP 1244*, M. Kirk and A. Bakker, Eds., ASTM International, West Conshohocken, PA, 1995, pp. 134–159.

[10] Wu, S.-X., Mai, Y.-W., and Cottrell, B., "Ductile-Brittle Fracture Transition as a Result of Increasing In-Plane Constraint in a Medium Carbon Steel," in *Fracture Mechanics: Vol. 24, ASTM STP 1207*, J. Landes and D. McCabe, Eds., ASTM International, West Conshohocken, PA, 1994, pp. 376–386.

[11] Ruggieri, C. and Dodds, R. H., "A Transferability Model for Brittle Fracture Including Constraint and Ductile Tearing Effects: A Probabilistic Approach," *International Journal of Fracture*, Vol. 79, 1996, pp. 309–340.

[12] Yan, C., Mai, Y-W., and Wu, S-X., "Finite Element Analysis and Experimental Evaluation of Ductile-Brittle Transition in Compact Tension Specimen," *International Journal of Fracture*, Vol. 87, 1997, pp. 345–362.

[13] Anderson, T. L., Stienstra, D., and Dodds, R. H., "A Theoretical Framework for Addressing Fracture in the Ductile-Brittle Transition Region," in *Fracture Mechanics: 24th Volume, ASTM STP 1207*, J. D. Landes, D. E. McCabe, and J. A. M. Boulet, Eds., ASTM International, West Conshohocken, PA, 1994, pp. 186–214.

[14] Focht, E. M., "Control Rolling and Interrupted Cooling of a High Strength Nickel-Copper Naval Steel," *Proceedings from Material Solutions '97 on Accelerated Cooling/Direct Quenching Steels*, Indianapolis, IN, September 1997.

[15] Wilson, A. D., Hamburg, E. G., Colvin, D. J., Thompson, S. W., and Krauss, G., "Properties and Microstructures of Copper Precipitattion Aged Plate Steels," Microalloyed HSLA Steels, *Proceedings of Microalloying '88*, Chicago, IL, September 1998.

Journal of ASTM International, Vol. 3, No. 9
Paper ID JAI13208
Available online at www.astm.org

G. Wardle[1] *and W. Geary*[2]

Prediction of the Shape of the K_J Ductile-to-Brittle Transition Temperature Curve for Ferritic Pressure Vessel Steels Using the Material's Resistance to Crack Extension K_J versus Δa Curve

ABSTRACT: Fracture toughness ($K_{J\ (cleavage)}$) measurements made within the ductile-to-brittle transition region for ferritic pressure vessel steels are not always described by the shape of the Master Curve currently given in ASTM Standard E 1921. The objective of this paper is to show how the shape of the transition toughness curve may be related to the shape of the material's resistance to crack extension curve (K_{JR}) once the crack tip starts to blunt and ductile crack extension precedes cleavage failure. Using an empirical relationship between the mean ductile crack extension (Δa) prior to the onset of cleavage failure and temperature ($\Delta a = \lambda \exp(\phi T)$), then the relationship between K_J and T may simply be given by $K_J = K_A + \alpha[\lambda \exp(\phi T)]^{\beta}$, where K_A, α, and β are simply the coefficients to an offset power law to K_J versus Δa data given by $K_{JR} = K_A + \alpha(\Delta a)^{\beta}$. For specimens of different sizes, a reference temperature T_K may be defined for a given reference level of Δa or equivalent K_J. Unique curves may be defined for materials with differing crack extension resistance curves through plots of K_J versus $(T - T_{\Delta a(\mathrm{ref})})$ or $(T - T_{K(\mathrm{ref})})$. The generalized form of the transition curve may be given by $K_J = K_A + \alpha\{\Delta a_{(\mathrm{ref})} \exp[\phi(T - T_{\Delta a(\mathrm{ref})})]\}^{\beta}$ or $K_J = K_A + (K_{(\mathrm{ref})} - K_A)\{\exp[\phi(T - T_{K(\mathrm{ref})})]\}^{\beta}$. Experimentally, ϕ has been estimated as approximately 0.08 for nuclear pressure vessel materials such as A533B/A508. Using a specific situation wherein the value of $K_A = 30$ MPa$\sqrt{}$m, $K(\mathrm{ref}) = 100$ MPa$\sqrt{}$m, and $\beta = 0.25$ then, for a $B = 25$-mm specimen, within experimental scatter this provides an almost exact match to the Master Curve given by $K_J = 30 + 70 \exp[0.019(T - T_{K100})]$. The predictions of transition curve shape using the material's resistance to crack extension curve are believed to be complementary to the Master Curve method, and may describe the shape of the transition curve when there is ductile crack extension prior to cleavage failure. Further work is recommended to investigate the relationship between the predicted ductile-to-brittle transition curve and the Master Curve for probabilities of cleavage failure post-initiation.

KEYWORDS: fracture toughness, transition curve shape, resistance curve, Master Curve

Nomenclature

a_o = Initial crack length, mm
Δa = Ductile crack extension (including blunting), mm
b_o = Initial remaining ligament $(W - a_o)$, mm
B = Specimen thickness, mm
E = Young's modulus $(E' = E/(1 - \nu^2))$, GPa
J = Experimental equivalent of J-integral, kJ/m^2
K = Stress intensity factor, MPa$\sqrt{}$m
K_J = K derived from J, where $K = \sqrt{(E'J)}$, MPa$\sqrt{}$m
$K_J - R$ = Material's resistance to ductile crack extension Δa, MPa$\sqrt{}$m
K_A = Value of K_J at zero crack extension, defined from an offset power law $K_J = K_A + \alpha(\Delta a)^{\beta}$, MPa$\sqrt{}$m
$K_{J0.2}$ = K_J defined at 0.2 mm of crack extension (i.e., onset of ductile tearing), MPa$\sqrt{}$m

Manuscript received May 10, 2005; accepted for publication July 14, 2006; published online October 2006. Presented at ASTM Symposium on Fatigue and Fracture Mechanics: 35th Volume on 18–20 May 2005 in Reno, NV; R. E. Link and K. M. Nikbin, Guest Editors.

[1] Technical Director, Warhelle Consulting Ltd, Lowton, Cheshire WA3 2TR, UK.
[2] Section Head (Metallurgy & Materials) Health and Safety Laboratory, Buxton, SK17 9JN, UK.

Copyright © 2006 by ASTM International, 100 Barr Harbor Drive, PO Box C700, West Conshohocken, PA 19428-2959.

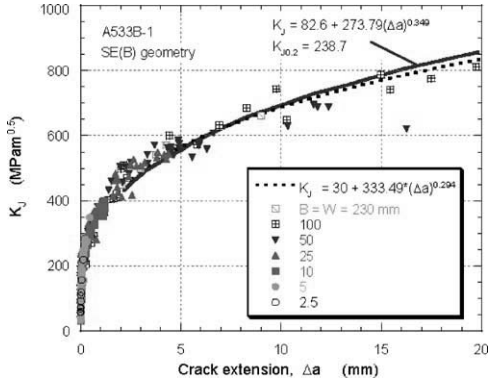


FIG. 1.

$K_{J(\text{lim})}$ = Maximum value of K_J used to censor cleavage fracture toughness data, MPa$\sqrt{\text{m}}$
K_{Ic} = LEFM fracture toughness, MPa$\sqrt{\text{m}}$
T = Test temperature, °C
T_0 = ASTM Standard E 1921 definition of Reference Temperature, i.e., The temperature at which the median K_J cleavage failure equals 100 MPa$\sqrt{\text{m}}$ for a 25-mm-thick specimen, °C
$T_{1.0}$ = Temperature at which the average ductile crack extension prior to cleavage (including blunting) is 1.0 mm, °C
UTS = Ultimate tensile strength, MPa
W = Specimen width, mm
α = K_J–R curve coefficient ($K_A+\alpha=K_J$ value at $\Delta a=1$ mm), MPa$\sqrt{\text{m}}$
β = K_J–R curve exponent
ϕ = Coefficient in exponential fit $\Delta a=\lambda \exp(\phi T)$
λ = Coefficient in exponential fit $\Delta a=\lambda \exp(\phi T)$, mm
σ_y = Yield (0.2 % proof) strength, MPa
ν = Poisson's ratio

Introduction

During Phase I of the UK Health and Safety Executives "Joint Industry Programme (JIP) on miniaturized testing," fracture toughness studies were undertaken, within the ductile-to-brittle transition regime, on several ferritic pressure vessel steels [1–3]. These included a thick section (257-mm-thick) A533B Class 1 plate, a thick section (280-mm-thick) DIN 22NiMoCr37 (A508 Class 2/3 equivalent) forging and a thin section (29-mm-thick) BS1501-213 Grade 32A high-pressure storage vessel (HPSV) steel [2]. Within Phase 2 [3] of this study, opportunity has arisen to examine the relationships between the mean ductile crack extension prior to cleavage failure, specimen size, and test temperature. The available fracture toughness data [1] including original data from earlier programs on the thick section nuclear reactor pressure vessel (NRPV) steels [4,5] have been analyzed along with data from a fourth thick section NRPV material, namely, an A508 Class 3 studied in the 1980s [6].

It is suggested that the shape of a the ductile-to-brittle transition curve may be estimated using the material's resistance to crack extension curve (K_J versus Δa), since it is commonly observed that the K_J resistance curve is, to a first approximation, constant throughout the transition region and independent of specimen size. An example is given in Fig. 1. The general expression is given by:

$$K_J = K_A + \alpha(\Delta a)^{\beta} \tag{1}$$

The hypothesis is that the mean crack extension prior to cleavage failure (including data where $\Delta a=0$), follows a simple exponential relationship with temperature:

$$\Delta a = \lambda \exp(\phi T) \tag{2}$$

where ϕ is the slope of the relationship and λ (i.e., Δa at $T=0$) a parameter that varies with specimen size. It is assumed that ϕ will be approximately constant for a given material and independent of specimen size. A plot of average ductile crack extension versus temperature is expected to produce a series of curves for different specimen sizes. If so, then, by estimating the temperature for a given reference average crack extension Δa(ref), all data from different specimen sizes may (for a given material) be represented by a general curve given by

$$\Delta a = \Delta a_{(\text{ref})} \exp[\phi(T - T_{\Delta a(\text{ref})})] \tag{3}$$

For example, $T_{\Delta a(\text{ref})}$ is the temperature at which there is a given amount of crack extension prior to cleavage. If $T_{\Delta a}$ is chosen at $\Delta a=1$ mm, then $\Delta a_{(\text{ref})}=1$, likewise if $T_{\Delta a}$ is chosen at $\Delta a=0.2$ mm, then $\Delta a_{(\text{ref})}=0.2$. Although ϕ may be constant for a given material, different sizes of specimens would be expected to provide different values of $T_{\Delta a(\text{ref})}$, since the temperature at which ductile crack extension starts to take place would be expected to vary with size; i.e., smaller specimens provide lower $T_{\Delta a}$ values due to a loss of constraint and a move away from plane strain towards plane stress conditions.

Thus, if ϕ is constant and $T_{\Delta a}$ can be determined, then links among Δa, T, and K_J may be made. Furthermore, it is then possible to simply make a plot of measured K_J versus a normalized temperature $(T-T_{\Delta a})$, and, unlike the Master Curve, to not have to introduce any size corrections to the K_J data or to apply any censoring limits. (The levels of censoring for test data and the assumption of a $B^{0.25}$ size correction have been issues that have often prompted discussion.) This empirical method uses all data as measured and provides an estimate of the shape of the transition curve. What this method does not do at present is to attempt to predict probabilities of failure, but merely describes the shape of the transition curve and the positioning of the data with respect to the curve. Thus, it is seen as a complementary tool to the Master Curve method for situations where there is ductile crack extension prior to cleavage failure.

If the general case of Eq 3 holds, then the relationship between K_J and temperature within the transition regime may be given by

$$K_J = K_A + \alpha\{\Delta a_{(\text{ref})} \exp[\phi(T - T_{\Delta a(\text{ref})})]\}^{\beta} \tag{4}$$

The use of the equation in the above format, rather than a mathematically more correct style, is to enable the parameters K_A, α, and β to be input directly from measured K_J resistance curve determinations, and to allow the equation to be deconstructed into its two component equations.

The implication is that the shape of the ductile-to-brittle transition curve is influenced by the shape of the material's crack extension resistance curve within the transition regime. This may possibly explain why the shape of the Master Curve [7] is not always observed to be constant [8,9] once there is evidence of ductile crack extension.

Plotting the as measured K_J data versus $T-T_{\Delta a(\text{ref})}$ would provide a general curve (given above) that simply describes the overall relationship between K_J and temperature such that the curve passes through the point ($K_{J\Delta a}$, $T_{\Delta a}$). For example, if the reference level of average crack extension is 0.2 mm (i.e., initiation of ductile tearing) then the curve passes through the point $K_{J0.2}$, $T_{0.2}$.

If the reference level $\Delta a_{(\text{ref})}$ value is fixed then this will in turn fix the $K_{(\text{ref})}$ level through the resistance curve relationship (Eq 1) i.e.,

$$\Delta a_{(\text{ref})} = \left(\frac{K_{(\text{ref})} - K_A}{\alpha}\right)^{1/\beta} \tag{5}$$

Substituting Eq 5 into Eq 4 provides

$$K_J = K_A + \alpha\left(\left(\frac{K_{(\text{ref})} - K_A}{\alpha}\right)^{1/\beta} \exp\{\phi[T - T_{(\text{ref})}]\}\right)^{\beta} \tag{6}$$

Rearranging Eq 6 provides

$$\left(\frac{K_J - K_A}{K_{(\text{ref})} - K_A}\right)^{1/\beta} = \exp[\phi(T - T_{K(\text{ref})})] \tag{7}$$

or

TABLE 1—*Chemical composition (wt. %) of plate materials studies [1].*

Material	C	Mn	Si	Mo	Ni	Cr	S	P	Cu	Al	
BS1501		0.90									Min
213-32A	0.24	1.60	0.60	0.13	0.35	0.30	0.055	0.055	0.35	0.09	Max
A533B-1	0.21	1.44	0.28	0.48	0.67	0.18	0.005	0.006	0.05	0.021	

$$K_J = K_A + (K_{(\text{ref})} - K_A)\{\exp[\phi(T - T_{K(\text{ref})})]\}^{\beta} \tag{8}$$

Equation 8 gives the identical result to Eq 4. The above equation will be contrasted to the Master Curve equation (for 50 % probability of failure) given below:

$$K_J = 30 + 70\exp[0.019(T - T_0)] \tag{9}$$

Material Properties and Test Results

The chemical composition and tensile properties of the materials studied are given in Refs. [1–6]. The A533B-1, DIN 22NiMOCr37, and A508-3 materials are of approximately similar specification, with the DIN 22NiMOCr37 and A508-3 materials being the forging equivalents of the A533B-1 plate material. The differences between the typical NRPV thick section (200 mm) A533B-1 material and a thinner section (30 mm) BS1501-213 general pressure vessel material are provided in Table 1 (chemistry) and Table 2 (tensile strength).

Analysis of Test Results

The test data analyzed here[3] are to be found compiled in Refs. [1,11]. The analyses of these data were simply as follows:

- For an individual specimen, ductile crack extension prior to cleavage was estimated using a nine-point averaging method across the crack front (as given in testing standards). Individual measurements of crack extension at the nine points on the crack front were, for the smaller specimens tested, made to 0.002 mm. In some instances, the only crack extension was that due to blunting. In other instances, there was no evidence of blunting prior to cleavage failure.
- The average (arithmetic mean) crack extension prior to cleavage (including specimens where $\Delta a = 0$) was, for each material studied, calculated for each individual size of specimen and at each given test temperature. In some instances, it was necessary to bound groups of data (e.g., $T \pm 5\,^{\circ}\text{C}$), in which case the mean test temperature for that group was also calculated:

$$\Delta a(\text{mean}) = \frac{\sum(\Delta a)}{n} \tag{10}$$

- For some of the higher transition test temperatures, a few specimens did not fail by cleavage and the tests were stopped. In these situations the average ductile crack extensions were calculated, but the resultant $\Delta a - T$ data were not included in the analyses. These data are, however, shown on the figures, noting that the Δa value should be greater than the value indicated.

TABLE 2—*Tensile yield strength (0.2 % proof strength) at* 20°C *(taken from Ref. [1]).*

	Yield (0.2 % Proof), MPa	*UTS*, MPa
BS1501-213-32A	373[a]	538[a]
A533B-1	458	627

[a]Estimated from lower temperature data [10].

[3]The A533B-1 and DIN 22NiMoCr37 materials provided the most comprehensive data sets on a variety of specimen sizes. However, one of the main problems in assessing the crack extension data is that in many instances where $\Delta a < 1.0$ mm (and particularly for $\Delta a < 0.05$ mm), there was a tendency for the operator to ascribe a value of zero to Δa, since the amount of crack extension was secondary to the determination of K_J measurements.

TABLE 3—*Average values of ϕ (slope) in $\Delta a = \lambda \exp(\phi T)$.*

Material	ϕ (slope) in $\Delta a = \lambda \exp(\phi T)$
A533B-1 (Ingham et al.)	0.080
A508-3	0.079
DIN 22NiMoCr37 (Europroject)	0.077
BS 1501-213	0.098

- For each specimen size, simple exponential fits were made to the average crack extension versus temperature and the slope ϕ was determined. For a given specimen size and temperature, a typical number of specimens used to define the average crack extension prior to cleavage would be 8. The grand average slope from all sizes of specimens (Table 3) was estimated and this average slope was used to define a series of parallel exponential curves ($\ln(\Delta a)$ versus T). From these curves the value of $T_{\Delta a}$ may be determined at an appropriate level of crack extension (e.g., $\Delta a = 1$ mm (or 0.2 mm) for each specimen size (e.g., $T_{\Delta a=1}$ is a temperature at which there is 1 mm of crack extension prior to cleavage), and a unique curve is plotted through the mean Δa versus $(T - T_{\Delta a=1})$ data. This was done for each material studied. Values of $T_{\Delta a}$ are simply given by

$$T_{\Delta a} = \frac{1}{\phi}\left[\ln \frac{\Delta a}{\lambda}\right] \tag{11}$$

  Figures 2 and 3 provide example plots of average crack extension prior to cleavage Δa(mean) versus temperature T for each specimen size tested (DIN 22NiMoCr37 and A533B materials), and Fig. 4 provides, for example, a reference curve for Δa(mean) versus $(T - T_{\Delta a=1})$ for each of the thick section RPV materials studied. An averaged value of slope for the A533B, DIN 22NiMoCr37, and A508-3 materials is shown as $\phi = 0.078$ (i.e., $\phi = 0.080$, 0.079, and 0.075, respectively (Table 3)).

Thus, if ϕ is known and the resistance curve is known then it follows that the ductile-to-brittle transition curve shape is known. For a given level of average crack extension Δa(ref) then $K_{J\Delta a}$ is known (e.g., for Δa(ref) = 0.2 mm; $K_{J0.2}$) and may be used as a reference $K_{J(\text{ref})}$ level. $T_{K(\text{ref})} = T_{KJ0.2} = T_{\Delta a=0.2\ \text{mm}}$. For the situation given,

$$K_J = K_A + (K_{J0.2} - K_A)\{\exp[\phi(T - T_{KJ0.2})]\}^{\beta} \tag{12}$$

Figure 5 provides a plot of "as measured" K_J values versus $T_{KJ0.2}$ for a series of single-edge bend specimens, of size range 2.5 to 230 mm in thickness B, for the A533B-1 material studied. Also shown is the shape of the predicted ductile-to-brittle transition curve based on the material's resistance to crack extension curve given by Eq 4 (Fig. 1) and which is equivalent to the Eq 12 expression above:

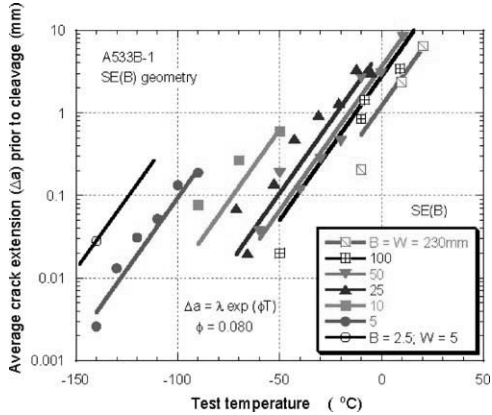


FIG. 2.

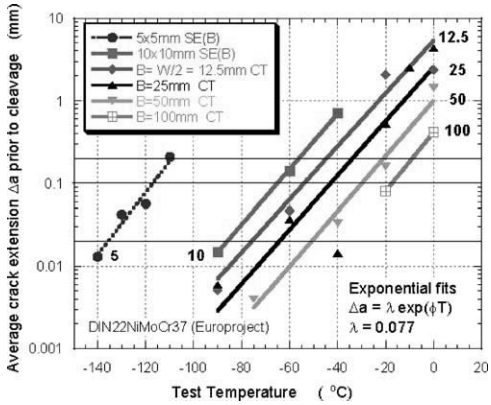


FIG. 3.

$$K_J = 30 + 333.49\{0.2 \exp[\phi(T - T_{KJ0.2})]\}^{0.294} \tag{13}$$

It is evident from Fig. 5 that the predicted ductile-to-brittle transition curve is a good representation to the data shown. It is also interesting to note that the positioning of the smallest specimens tested (B =2.5 mm) show good correspondence to the larger specimens (cf. B=50-mm specimens). In the above work none of the K_J data have been censored, and the K_J values are the "as measured" values for all sizes of specimen tested.

Size correction may be determined through the shift of the K_J-$T_{\Delta a(\text{ref})}$ transition curve. The variation in $T_{\Delta a(\text{ref})}$ may be determined empirically, or through consideration of the change from plane-strain to plane-stress conditions. The relationships among $T_{\Delta a(\text{ref})}$, specimen size, geometry, stress state, and temperature is an area of study that needs to be performed for a variety of materials of different material properties (e.g., $\sigma_{\text{yield}}/\sigma_{\text{UTS}}$ ratios). Current studies [11] suggest that the empirical variation in $T_{\Delta a}$ with specimen size (thickness B) appears to follow a $(\ln(B))^{0.25}$ relationship (Fig. 6) and which is thought to reflect loss of constraint as specimen size decreases (for geometrically scaled specimens). This work is ongoing.

$$T_{\Delta a(\text{ref})} = m(\ln(B))^{0.25} - C \tag{14}$$

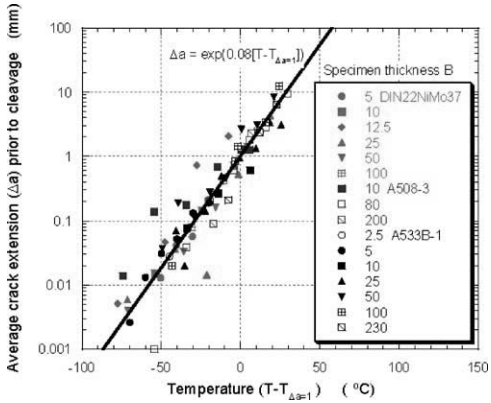


FIG. 4.

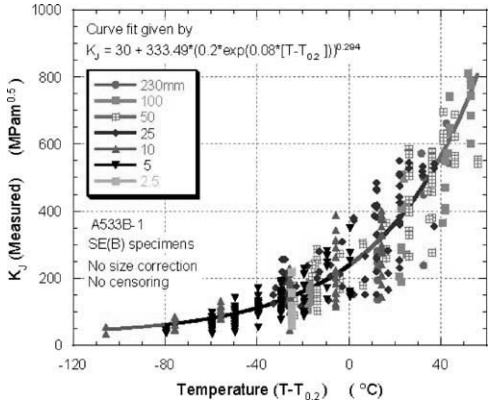


FIG. 5.

Comparison of the Predicted (Resistance Curve Method) Ductile-to-Brittle Transition Curve With the ASTM Standard E 1921 Master Curve

If we consider that the relationship between Δa(mean) as defined by a K_J level of 100 MPa$\sqrt{\text{m}}$ via the material's resistance to crack extension curve, and $[T-T_{\Delta a}]$, where $T_{\Delta a}$ is equivalent to the K_J level of K_J (ref) = 100 MPa$\sqrt{\text{m}}$, as used in the ASTM Standard E 1921 Master Curve (such that $[T-T_{\Delta a}]=[T-T_0] = \Delta T_x$), then the equation given below:

$$K_J = K_A + (K_{(\text{ref})} - K_A)\{\exp[\phi(T - T_{K(\text{ref})})]\}^{\beta} \tag{8'}$$

may be compared with the Master Curve (for 50 % probability of failure) curve given by:

$$K_J = 30 + 70\exp[0.019(T - T_0)] \tag{9'}$$

For the specific situation (25-mm-thick specimen) of setting $K_A = 30$ and $\beta = 0.25$ then the relationship between Eq 8 and 9 becomes

$$\frac{K_J - 30}{70} = \{\exp[\phi(\Delta T_x)]\}^{0.25} = \exp[0.019(\Delta T_x)] \tag{14'}$$

When $\phi = 0.076$ then both Eqs 8 and 9 yield identical results. Alternatively, if the value of $\phi = 0.08$ is used (as determined from this current work) for the Δa(mean) relationships then the slope to the Master Curve

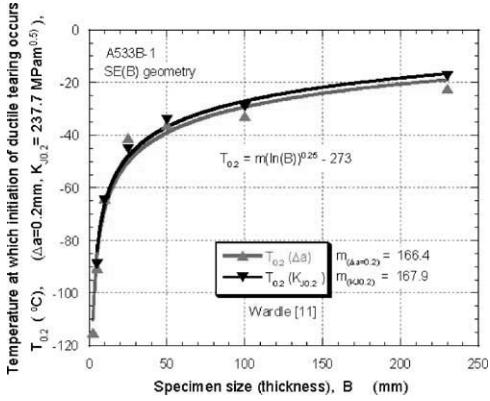


FIG. 6.

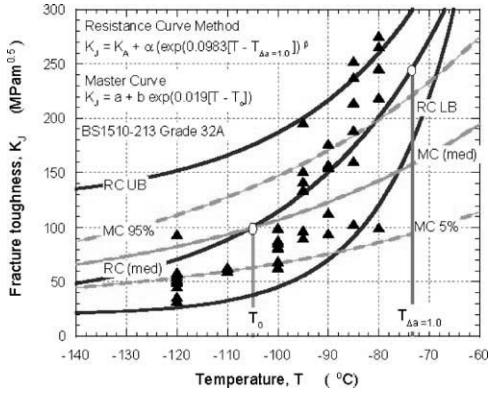


FIG. 7.

expression would need to be 0.02. Since both expressions were developed empirically from different standpoints then the closeness of the results is very good. Thus, the Master Curve would also seem to predict the ductile-to-brittle transition curve for a specific material's resistance curve when $\beta = 0.25$. For materials with other power law exponent (β) and slope (ϕ) then this implies that the Master Curve Eq 9 may produce a different ductile-to-brittle transition curve shape than that predicted on the basis of the crack resistance curve—particularly post-initiation of ductile tearing prior to cleavage.

An example of where the Master Curve did not fit the data very well was given [1] for BS1501 steel; here the Master Curve overestimated data points at low temperatures, and underestimated data points at higher temperature. A transition curve fit using the K_J resistance curve indicated a much better description of the transition (Figs. 7 and 8).

Discussion and Conclusions

From the data presented for the four materials considered, it would appear that if mean crack extensions prior to cleavage failure are calculated based on the fracture surface of tested specimens then there is a relationship between this crack extension and temperature that may be represented by a simple exponential relationship between Δa and T (Eq 2). If, as appears to be the case, the slope of this relationship ϕ is a constant for all sizes of specimens then all data may be normalized for a given material, by plotting Δa

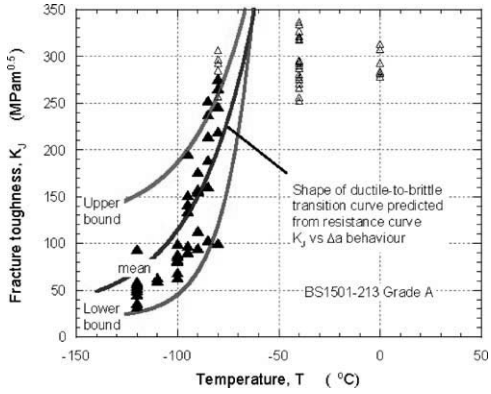


FIG. 8.

versus ($T-T_{\Delta a}$) and a unique expression defined (Eq 3). It may even be the case that for a given class of materials that (e.g., NRPVs) the slope ϕ is a constant for all these materials. Further data studies are required to confirm this assertion.

The implication of a known relationship between Δa and $T-T_{\Delta a}$ (or a theoretical one based on plane-stress or strain) is that an empirical relationship may be used to relate the shape of the materials K_J resistance curve to the shape of the ductile-to-brittle transition curve based on simple measured values. In these instances there would be no need to size correct K_J data, or indeed to apply censoring limits to those data.

From the ongoing work it is concluded that:

1. Analyses of the variation in mean ductile crack extension prior to cleavage initiation Δa(mean) versus test temperature T within the ductile-to-brittle regime, for a series of pressure vessel materials, shows that Δa(mean) may be related to T through a simple exponential function:

$$\Delta a = \lambda \exp(\phi T)$$

   where ϕ is the slope of the relationship and λ (i.e., Δa at $T=0$) (this parameter varies with specimen size (B or W)).
2. The slope of the relationship ϕ does not appear to be significantly influenced by test specimen size, and may be considered approximately constant for a given material. Thus, for a range of specimen sizes there is a unique relationship between Δa(mean) and a normalized temperature ($T-T_{\Delta a}$), where $T_{\Delta a}$, is the temperature at which Δa(mean) is equal to a reference level of Δa (e.g., 1.0 or 0.2 mm). $T_{\Delta a}$ is dependent on specimen size, and decreases as specimen size decreases.
3. For a given class of material (e.g., thick section NRPV A533B/A508) the slope of the exponential relationship ϕ appears to be constant. In the case of the three NRPV materials studied, the average value of ϕ approximates to 0.08. In the case of the general pressure vessel BS1501 material, ϕ was found to approximate to 0.098, but could also be reasonably approximated using a value of $\phi = 0.08$.
4. For situations where ϕ and $T_{\Delta a(\mathrm{ref})}$ (and thus $T_{K(\mathrm{ref})}$) can be determined and a unique relationship defined, it is a fairly simple step to relate the K_J ductile-to-brittle temperature relationship to the materials resistance to crack extension curve.

$$K_J = K_A + (K_{(\mathrm{ref})} - K_A)\{\exp[\phi(T - T_{K(\mathrm{ref})})]\}^{\beta}$$

   This has the advantage that as measured K_J values are used without the need for censoring or crack front length correction. The shift in the transition curve with size is made on the basis of the relationship between $T_{K(\mathrm{ref})}$ and size (B).

It is believed that the method used here may be complementary to that of the Master Curve, and may prove useful when fracture toughness measurements are being made on small/miniature specimens, and where the censoring would otherwise necessitate an unacceptable level of testing in order to obtain "valid" data. As part of future work programs it is hoped to establish the influence of specimen size and geometry (constraint) in the shifting of the raw K_J versus T data relative to each other, and the statistical size effect on the probability of failure as embodied within the Master Curve concept.

Recommendations

From the evidence relating to the data obtained from these pressure vessel materials it appears that more consideration needs to be given to the role of ductile crack extension prior to cleavage, and censoring limits, on the shape of the ductile-to-brittle transition curve. These factors need to be investigated for a range of ferritic steels. In addition, the relationship between a transition curve based on the material's resistance curve and that derived from a consideration of Master Curve assumptions needs to be reconciled.

One of the problems that the authors have found is that when going through fracture toughness databases there has been little emphasis on the accurate measurement of ductile crack extension prior to cleavage. In many instances crack extensions have been measured for $\Delta a > 0.2$ mm (occasionally 0.1 mm), but below this level a value of zero has generally been stated. For values of practical interest

($K_J < 200$ MPa$\sqrt{\text{m}}$; i.e., <0.2 mm) the need is for good (precise and accurate) crack extension measurements. The authors would strongly recommend that in all fracture toughness tests within the brittle-to-ductile regime individual nine-point measurements are made to 0.002 mm.

Accurate measurement of ductile crack extension prior to cleavage may well reconcile the differences between the Resistance Curve Measurement method and the Master Curve technique. It may well help to define a better censoring limit to Master Curve K_J data (e.g., no data where crack extension is greater than blunting), thus limiting the statistical effect (Monte Carlo) to a stationary crack. Once there is crack extension (i.e., blunting and ductile crack extension) then the Resistance Curve Measurement method may well come into play. The challenge is to link the two.

Acknowledgments

The authors wish to thank their colleagues on the HSE (Minaturized testing—Phase 2) Joint Industry Project (JIP) committee, and in particular H. Bainbridge (Health and Safety Executive), and J. Dutton (Health and Safety Laboratory) for their encouragement throughout this work. Financial support through HSE is greatly appreciated.

References

[1] Shuter D. M., Geary W., Dutton J. T., Birkett R. P., and Wardle G., "Summary Report on Fracture Toughness Testing and Analysis Methodologies for Miniaturised Specimens of Ferritic Steels; HSE Sponsored Joint Industry Programme 1999-2002," Health and Safety Laboratory Report, HSL MM/02/28, May 2003. Available (through HSL) on CD.

[2] Shuter D. M., Dutton J. T., Hobbs J. W., Geary W., Birkett R. P., and Wardle G., "Miniature Specimen Fracture Toughness Testing and Analysis," *Proceedings of the Sixth International Conference on Engineering Structural Integrity Assessment*, held at the Manchester Conference Centre UMIST, UK, 8-9 October 2002, pp. 243–251; *Engineering Structural Integrity Assessment: Needs and Provision*, P. E. J. Flewitt et al., Eds., EMAS publications, Sheffield, 2002.

[3] Wardle G., Geary W., Dutton J. T., and Shuter D., "Influence of Specimen Size on the Fracture Toughness of Pressure Vessel Steels Within the Ductile to Brittle Transition Regime," *Proceedings of the UK Forum for Engineering Structural Integrity: Seventh International Conference on Engineering Structural Integrity Assessment*, held at the Manchester Conference Centre UMIST, UK, 20-21 October 2004, pp. 259–268; *Integrity for Life: Structural Integrity Assessment for Life Cycle Management*, P. E. J. Flewitt et al., Eds., EMAS publications, Sheffield, 2004.

[4] Ingham T., Knee N., Milne I., and Morland E., "Fracture Toughness in the Transition Regime for A533B-1 Steel: Prediction of Large Specimen Results From Small Specimen Tests," United Kingdom Atomic Energy Authority Report, UKAEA—ND-R-1354(R), July 1987.

[5] Heerens J. and Hellmann D., "Development of the Euro Fracture Toughness Dataset," *Eng. Fract. Mech.*, Vol. 69, 2002, pp. 421–449.

[6] Lidbury D. and Moskovic R., "Assessment of Ductile-to-Brittle Transition Toughness Behaviour of an A508 Class 3 PWR Pressure Vessel Steel by a Statistical Approach," ASME Pressure and Piping Conference, PVP-Vol. 250, 1993, pp. 283–294.

[7] ASTM Standard E-1921: 97, "Standard Test Method for Determination of Reference Temperature, T_0 for Ferritic Steels in the Transition Range," *Annual Book of ASTM Standards*, Vol. 03.01, ASTM International, West Conshocken, PA, 2000.

[8] Ortner S. R., "Outstanding Issues in Master Curve Applications," in *Use and applications of the master curve for determining fracture toughness*, Master Curve Workshop, K. Wallin, Ed., Helsinki, 12-14, June, 2002.

[9] Ortner S. R. "Factors Affecting the Shape of the Ductile-to-Brittle Transition," *Int. J. Pressure Vessels Piping*, Vol. 79, 2002, pp. 693–700.

[10] Wright K. and Swankie T., "Statistical Assessment of Fracture Toughness Data From High Pressure Storage Vessel Material," Advantica Technology (Formerly British Gas Research) Report No. R4515, March 2002.

[11] Wardle G., Report in preparation.

Dynamic Fracture

Journal of ASTM International, Vol. 3, No. 9
Paper ID JAI13218
Available online at www.astm.org

Farid Reza Biglari,[1] *Alireza Rezaeinasab,*[1] *Kamran Nikbin,*[2] *and Iradj Sattarifar*[1]

Finite Element Simulation of Dynamic Crack Propagation for Complex Geometries Without Remeshing

ABSTRACT: Simulation of the crack growth for complex geometries is presented in this paper. Determination of the crack propagation direction under mixed mode conditions is one of the most important parameters in fracture mechanics. There are several criteria that have been developed to predict crack growth and its direction using linear elastic fracture mechanics (LEFM), many of which have recently been incorporated into finite element codes. These criteria are commonly adopted in the prediction of crack propagation in simple geometries and in straight crack paths. In more complex geometries, a more accurate determination of the crack propagation path, using remeshing methods can be employed. However, the remeshing technique usually suffers from the loss of strain energy density that can occur at the tip of the crack during the interpolation of field solutions. In this research work, the crack growth simulation is presented which allows for crack path deviation without the use of remeshing of the model. This method deals with a nonstraight crack growth path, is based on a node releasing technique and appropriate fracture criteria. The maximum principal stress and maximum strain energy release rate criteria is used in this paper exclusively. The results of simulation have been compared with experimental results as well as with numerical works of others that have been found in the recently published literature.

KEYWORDS: finite element method, crack propagation, node releasing, maximum energy release rate, strain energy density

Introduction

An important problem in linear elastic fracture mechanics (LEFM) is the prediction of crack growth and its direction in a component. Since the rst introduction of LEFM theories in 1920 s substantial research in developing new theories and applications have been carried out. For example, several fatigue crack propagation and crack growth criteria under impact loading have been developed. Essentially, there have been two strategies for solving these problems. These are to

Use an analytical approach for calculation of stress intensity factors (SIFs) as a function of crack length.

Use general numerical methods such as the nite element method (FEM) and boundary element method (BEM) which can be applied for different boundary conditions and more complex geometries.

Using the FEM method the crack is denoted as a discontinuity displacement eld that consists of two free surfaces during the separation. The change of mesh topology is one of the methods for discontinuity modeling. Many researchers have employed the mesh topology modi cation technique that uses the node release [1 4] element kill [5,6] and element split methods. Because of sudden variations due to stress gradient and complex stress distribution on the crack tip, the application of a ne mesh is necessary to be employed in order to achieve acceptable results. To prevent the excessive increase of computation time when using a ne mesh, the crack tip remeshing techniques have been introduced by Bittencourt et al. [3] and Bouchard et al. [4]. Moreover, the crack tip remeshing can help to modify distorted elements located right at the crack tip. However, for the cases with large deformation, the mesh distortion at the crack tip involves a loss of accuracy during the interpolation of eld variables.

Other techniques can model crack discontinuity without using remeshing. Belytschko et al. [7] have

Manuscript received May 23, 2005; accepted for publication April 17, 2006; published online September 2006. Presented at ASTM Symposium on Fatigue and Fracture Mechanics: 35th Volume on 18 20 May 2005 in Reno, NV; R. E. Link and K. M. Nikbin, Guest Editors.

[1] Mechanical Engineering Dept., Amirkabir University of Technology, Tehran, Iran.

[2] Mechanical Engineering Dept., Imperial College, London, SW7 2AZ.

Copyright © 2006 by ASTM International, 100 Barr Harbor Drive, PO Box C700, West Conshohocken, PA 19428-2959.

introduced a meshless method where the discretisation is achieved by a model which consists of only nodes. Rashid [8] has developed the arbitrary local mesh replacement method based on two distinct meshes. First, localized mesh moves with the crack tip and then fills the rest of the domain. Recently, the extended finite element method for modeling of discontinuity in mesh has been developed by other researches [9,10]. Sukumar and Prevost [10] have implemented a discontinuous function and the near-tip asymptotic functions which are added to the finite element approximation using the framework of partition of unity. This permits the crack to be represented without explicitly meshing the crack surfaces and crack propagation simulations can be conducted without the need for any remeshing.

Because of the recent development of general FEM codes, they are becoming more popular for modeling of crack growth for difficult geometries and complex mechanical conditions such as contact surfaces in addition to convenient output data manipulation during the advanced post processing. In this paper a program has been adapted to the general purpose finite element code (ABAQUS™)[3] by reviewing the different criteria for determination of kinking angle, crack propagation by node release technique without using remeshing. In the following sections some examples have been implemented and the results have been compared with experimental results and numerical results of other published works.

Criteria Used in Crack Initiation and Growth

In order to extend the crack through the mesh in the modeled component during the FEM process, criteria for crack extension need to be in place concurrent with the FEM calculation. Furthermore if the direction of the crack extension needs to be determined the criteria for crack extension needs to be further improved to deal with this, Therefore for modeling of crack growth, in each time step three procedural items must be checked:

(1) The critical loading condition for crack to initiate.
(2) The direction that the crack is to propagate.
(3) The extent to which the crack needs to grow.

For the evaluation of these criteria, the stress intensity factors (SIFs) and strain energy release rate needs to be calculated at every increment. For the prediction of crack initiation a critical value of SIFs is often used. Therefore it is possible to calculate values of SIFs for each time step and compare it to critical values of the material failure properties and if the values of SIFs are greater than critical values, the first condition is satisfied.

For an elastic-plastic material, crack tip opening displacement criterion is also used. This was originally introduced by Wells in 1961 [11]. In each time step, crack tip opening displacement value is calculated and compared with critical value. Also according to the Griffith and Irwin theory, crack initiation can be predicted by the calculation of the strain energy release rate G. Potential energy of the elastic body is defined as below

$$\Pi = U - F \tag{1}$$

where U is the strain energy stored in body and F is the work done by external forces. G is the rate of potential energy variations with respect to crack area that has been shown in Eq 2.

$$G = -\frac{\partial \Pi}{\partial A} \tag{2}$$

According to this definition, Griffith criterion for crack growth is written as below

$$\left.\begin{cases} G < G_f \Rightarrow \delta_a = 0 & \text{no propagation} \\ G = G_f \Rightarrow \delta_a \geqslant 0 & \text{propagation could start} \end{cases}\right\} \tag{3}$$

where G_f is critical strain energy release rate, and a is crack length and δ_a is crack length variation [12].

Fortino and Bilotta [13] has introduced an algorithm for evaluation of crack growth extension in two-dimensional (2D) LEFM problems. The mentioned method is based on the energetic formulation of the coupled displacement-crack propagation problems. In addition, the G-R curve can be used to calculate

[3]Hibbitt, Karlsson and Sorensen Ltd. ABAQUS, version 6.3.1, 2003.

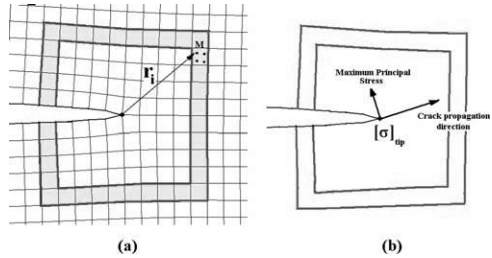


FIG. 1—*Kinking angle of crack propagation based on maximum principal stress criterion.*

crack length. For example, in virtual finite element (VFE) method introduced by Gerken and Smith [14,15], the calculation of virtual crack length variation between two elements in each step time uses the *G-R* curve as a criterion.

For the determination of crack kinking angle, researchers have introduced several criteria. Some of these criteria determine the crack growth direction based on stresses and strains field at the crack tip. These criteria generally give acceptable results for LEFM, such as maximum principal stress, maximum circumferential stress [16], and maximum strain [17]. However, for (NLFM) more complicated methods are needed such as criteria that determine the crack growth direction based on energy distribution on a cracked body. The most commonly used criterion is the maximum strain energy release rate [18]. Some other criteria are based on the nature of crack creation such as criteria that use microvoid continuum damage for determination of crack growth direction. In these theories, the crack growth is controlled by the creation and propagation of microvoids in the vicinity of the crack tip. Therefore, the crack propagates in the direction that most of the voids have been nucleated [19,20].

In the next section criteria relating to maximum principal stresses, maximum circumferential stress, minimum strain density energy, and maximum strain energy release rate for crack growth direction are described in further detail. However, the maximum principal stress and maximum strain energy release rate criteria is used in this paper exclusively.

Maximum Principal Stress Criterion

According to this criterion crack propagates in the direction that is perpendicular to the maximum principal stress. To derive more accurate results from this method, the size of the mesh must be fine compared to other regions. Also for LEFM, it is better to use singular elements. Bouchard et al. [21] have studied the effect of mesh size and element type used in the crack tip. The accuracy of this method depends on the mesh size and for achieving accurate results, therefore, the application of remeshing is necessary. The approach that the present paper takes is described below:

(1) A ring of elements around the crack tip is selected as shown in Fig. 1(*a*).
(2) Stress tensor of each Gaussian point of ring elements is calculated by FEM.
(3) Depending on the distance of crack tip from Gaussian point a weight function for stress tensor is considered (w_i).
(4) Stress tensor of crack tip is calculated according to Gaussian point's stress tensor and weight function of that point (Eq 4).
(5) The directions of principal stresses of crack tip stress tensor and direction perpendicular to maximum principal stresses is calculated.

$$[\sigma]_{\text{tip}} = \frac{\sum_{i=1}^{\text{Elements}} \sum_{j=1}^{\text{Int}-P} w_i [\sigma]_{ij}^{M}}{\sum_{i=1}^{\text{Int}-P} w_i} \tag{4}$$

The results of this method are independent of the crack tip mesh structure and it gives the same results for meshes of different sizes. However, the method used by Bouchard et al. [21] is strongly depended on

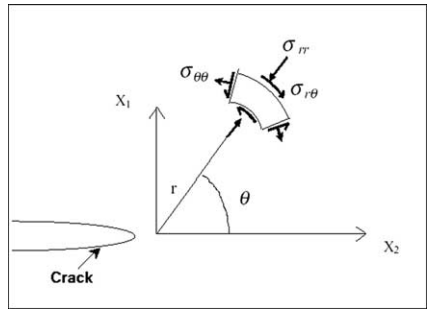


FIG. 2—*Crack tip stresses according to polar coordinate system.*

the mesh structure and to get acceptable results remeshing is needed in their case. Acceptable results under a linear elastic condition have been achieved by the present method which implements four-node elements with four Gaussian points without considering the effect of singularity.

Maximum Circumferential Stress Criterion

This criterion which was introduced by Erdogan and Sih [16] for elastic materials uses the maximum circumferential stress around the crack tip to allow propagation of the crack. Stresses on a circle with a radius centered at the crack tip in polar coordinates as shown in Fig. 2 are expressed as [22]

$$\sigma_r = \frac{1}{\sqrt{2\pi r}}\cos(\theta/2)\left\{K_{\mathrm{I}}[1+\sin^2(\theta/2)] + \frac{3}{2}K_{\mathrm{II}}\sin(\theta) - 2K_{\mathrm{II}}\tan(\theta/2)\right\}$$

$$\sigma_\theta = \frac{1}{\sqrt{2\pi r}}\cos(\theta/2)\left\{K_{\mathrm{I}}\cos^2(\theta/2) - \frac{3}{2}K_{\mathrm{II}}\sin(\theta)\right\}$$

$$\tau_{r\theta} = \frac{1}{\sqrt{2\pi r}}\cos(\theta/2)\{K_{\mathrm{I}}\sin(\theta) + K_{\mathrm{II}}[3\cos(\theta) - 1]\} \tag{5}$$

These equations are valid for both plane stress and plane strain cases. According to maximum circumferential stress criterion there is an angle (θ) that σ_θ is maximum. To find maximum σ_θ, the derivative equation of σ_θ is equated by zero.

$$\frac{\partial\sigma_\theta}{\partial\theta} = \frac{1}{\sqrt{2\pi r}}\{K_{\mathrm{I}}\sin(\theta) + K_{\mathrm{II}}[3\cos(\theta) - 1]\} \tag{6}$$

Solving Eq 6 gives the θ corresponding to the maximum σ_θ

$$\theta = 2\arctan\left[\frac{1}{4}\frac{K_{\mathrm{I}}}{K_{\mathrm{II}}} \pm \frac{1}{4}\sqrt{\left(\frac{K_{\mathrm{I}}}{K_{\mathrm{II}}}\right)^2 + 8}\right] \tag{7}$$

The result that gives the sign as opposite to sign of K_{II} is the correct one. Using Eq 6 in mode I loading (K_{II}=0), the crack propagation angle is zero. In mode II loading, by solving the equation $K_{\mathrm{II}}[3\cos(\theta) - 1]$=0, the crack propagation angle is ±70.5°. So the maximum range of the crack propagation angle under LEFM is limited to an angle range of [−70.5° to 70.5°]. Figure 3 illustrates the plots of σ_θ and $\tau_{r\theta}$ versus propagation angle for arbitrary K_{I} and K_{II}. It can be seen that when the circumferential stress is maximum, the shear stress tends to become zero.

Minimum Strain Energy Density Criterion

This method which was introduced by Sih and MacDonald [23] in 1974 suggests that the crack propagates in the direction in which strain energy density is minimum. Sih and MacDonald supposed that the factor

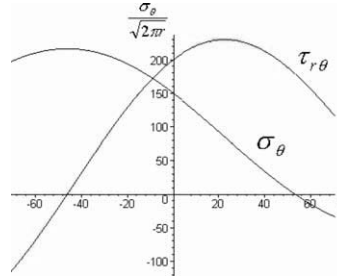


FIG. 3—*Typical circumferential and shear stresses around crack tip versus* θ *angle in mixed mode.*

preventing crack growth is strain energy (W_e). Therefore, crack extension is more probable to occur in the direction that the preventing factor is minimal. Strain energy density for those points ahead of the crack tip can be written as a function of angle θ (Fig. 2) is [1]

$$S(\theta) = a_{11}K_{\mathrm{I}}^2 + 2a_{12}K_{\mathrm{I}}K_{\mathrm{II}} + a_{22}K_{\mathrm{II}}^2 \tag{8}$$

where the above factors a_{11}, a_{12}, and a_{22} are defined as below

$$a_{11} = \frac{1}{16\pi\mu}[(1 + \mathrm{Cos}\,\theta)(k - \mathrm{Cos}\,\theta)]$$

$$a_{12} = \frac{1}{16\pi\mu}[2\,\mathrm{Cos}\,\theta - (k-1)]$$

$$a_{22} = \frac{1}{16\pi\mu}[(1 - \mathrm{Cos}\,\theta)(k+1) + (1 + \mathrm{Cos}\,\theta)(3\,\mathrm{Cos}\,\theta - 1)]. \tag{9}$$

To obtain the kinking angle of the crack, the minimum value of $S(\theta)$ for different values of θ have to be found.

Maximum Strain Energy Release Rate Criterion

Strain energy release rate G is the required energy to increase the length of the crack one unit ahead. The crack propagates in the direction that G is maximum. Therefore, crack propagation direction will be derived from the following equations:

$$\left\{ \begin{array}{l} \left(\dfrac{dG}{d\theta}\right)_{\theta=\theta_0} = 0 \\ \left(\dfrac{d^2G}{d^2\theta}\right)_{\theta=\theta_0} \leqslant 0 \end{array} \right\} \tag{10}$$

To use this criterion, first G is calculated by the use of J integral. This is a common method to calculate G in fracture mechanics. Under LEFM conditions, the J integral is equal to G. J integral is introduced by Rice [24] as

$$J = \int_\Gamma \left(U dy - t_i \frac{\partial u_i}{\partial x} d_S \right) \tag{11}$$

where U is strain energy density, t_i is the traction vector perpendicular to path Γ, u_i is displacement vector, and d_S is an element on the contour Γ.

If no forces are applied on the crack surfaces, J value for quasistatic and isothermal condition is independent of path. Another method of calculating G is using a surface integral that is more accurate. de Lorenzi [25], derived a method to calculate G using the formulation of continuum mechanics of virtual crack extension. According to this method for 2D condition, G value is

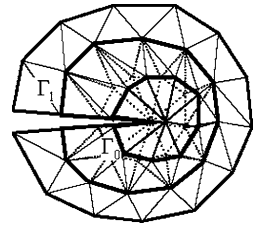


FIG. 4—*Calculation of J using surface integral method.*

$$G = \frac{1}{\delta a} \int \int_A \left(\sigma_{ij} \frac{\partial u_j}{\partial x_1} - w\delta_{i1} \right) \frac{\partial \Delta x_1}{\partial x_i} d_A \tag{12}$$

where A is the surface between paths Γ_0, Γ_1 as shown in Fig. 4. Δx_1 is the virtual crack propagation value. This method is more accurate compared to contour integral computation especially for elastic-plastic conditions.

The procedure to calculate J integral for a four-noded element with linear shape function according to the contour integral method is given in [26].

If $N_1, \ldots, N_4$ is considered as shape function for nodes of a four-noded element, then

$$\begin{Bmatrix} N_1 = 1/4(1-\xi)(1-\eta) \\ N_2 = 1/4(1+\xi)(1-\eta) \\ N_3 = 1/4(1+\xi)(1+\eta) \\ N_4 = 1/4(1-\xi)(1+\eta) \end{Bmatrix} \tag{13}$$

Jacobian matrix of this element is

$$[Jac^{(e)}] = \begin{bmatrix} \frac{\partial x}{\partial \xi} & \frac{\partial y}{\partial \eta} \\ \frac{\partial y}{\partial \xi} & \frac{\partial y}{\partial \eta} \end{bmatrix} = \begin{bmatrix} \sum_{i=1}^{r} \frac{\partial N_i^e}{\partial \xi} x_i^e & \sum_{i=1}^{r} \frac{\partial N_i^e}{\partial \xi} y_i^e \\ \sum_{i=1}^{r} \frac{\partial N_i^e}{\partial \eta} x_i^e & \sum_{i=1}^{r} \frac{\partial N_i^e}{\partial \eta} y_i^e \end{bmatrix} \tag{14}$$

$$[Jac^{(e)}]^{-1} = \begin{bmatrix} \frac{\partial \xi}{\partial x} & \frac{\partial \eta}{\partial x} \\ \frac{\partial \xi}{\partial y} & \frac{\partial \eta}{\partial y} \end{bmatrix} = \frac{1}{|J^{(e)}|} \begin{bmatrix} \frac{\partial y}{\partial \eta} & -\frac{\partial y}{\partial \eta} \\ -\frac{\partial x}{\partial \eta} & \frac{\partial x}{\partial \xi} \end{bmatrix} \tag{15}$$

Using these two equations, the Jacobian mapping of the isoparametric elements are defined for the area or line integration of the J integral.

If $J_i^{(e)}$ is considered as the J integral value for the part of the path that passes from element i (Fig. 5),

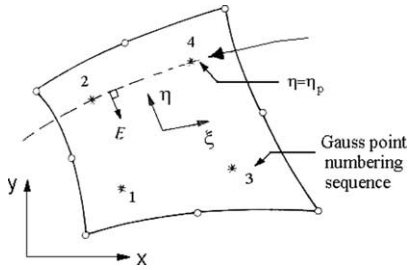


FIG. 5—*Contour path along direction of constant* η *value [26].*

then the total value of J integral for whole path is

$$J^{(\text{Contour})} = \sum_{i=1}^{n} J_i^{(e)} \tag{16}$$

where n is the number of elements that contour integral passes through.

To calculate $J_i^{(e)}$, the known values of stress, strain, and displacement of element Gaussian point, will be used. The $J_i^{(e)}$ value for both ξ=constant and η=constant values will be calculated and added together. The following equation shows the method of calculating $J_i^{(e)}$:

$$J_\xi^{(e)} = \sum_{q=1}^{\text{NGAUS}} I(\xi_p, \eta_q) W_q \tag{17}$$

where $J_\xi^{(e)}$ is for the part of path that ξ=constant and NGAUS is the number of the integration point on this path. W_q is the weight factor related to η_q.

$$J_\eta^{(e)} = \sum_{p=1}^{\text{NGAUS}} I(\xi_p, \eta_q) W_p \tag{18}$$

where $J_\eta^{(e)}$ is for the part of the path that η=constant and NGAUS is the number of the integration point on this path. W_p is the weight factor related to ξ_p.

$$J^{(e)} = J_\xi^{(e)} + J_\eta^{(e)} \tag{19}$$

The strain energy is

$$U = U_e + U_P \tag{20}$$

$$U_e = \frac{1}{2}\sigma_{ij}(\varepsilon_{ij})_e \quad U_P = \int_0^{\bar{\varepsilon}_p} \bar{\sigma} d\bar{\varepsilon}_P \tag{21}$$

where U_e is the elastic strain energy and U_P is the plastic strain energy.

The following equations give the traction vector perpendicular to path:

$$t_i = \begin{Bmatrix} \sigma_{xx} n_1 + \sigma_{xy} n_2 \\ \sigma_{xy} n_1 + \sigma_{yy} n_2 \end{Bmatrix} \tag{22}$$

$$n^T = [n_1, n_2] = \left[\frac{E_1}{\sqrt{E_1^2 + E_2^2}}, \frac{E_2}{\sqrt{E_1^2 + E_2^2}} \right] \tag{23}$$

$$E = \begin{Bmatrix} E_1 \\ E_2 \end{Bmatrix} = \begin{Bmatrix} \dfrac{\partial y}{\partial \xi}\left(\dfrac{\partial y}{\partial \eta}\dfrac{\partial x}{\partial \xi} - \dfrac{\partial x}{\partial \eta}\dfrac{\partial y}{\partial \xi} \right) \\ \dfrac{\partial x}{\partial \xi}\left(\dfrac{\partial x}{\partial \eta}\dfrac{\partial y}{\partial \xi} - \dfrac{\partial y}{\partial \eta}\dfrac{\partial x}{\partial \xi} \right) \end{Bmatrix} \text{ For } \eta = \eta_P \tag{24}$$

$$dx = \frac{\partial x}{\partial \xi} d\xi, \quad dy = \frac{\partial y}{\partial \xi} d\xi \quad \text{For } \eta = \eta_P \tag{25}$$

$$ds = \sqrt{\left(\frac{\partial x}{\partial \xi}\right)^2 + \left(\frac{\partial y}{\partial \xi}\right)^2}\, d_\xi \quad \text{For } \eta = \eta_P \tag{26}$$

$$\frac{\partial(u,v)}{\partial x} = \sum_{i=1}^{n} \frac{\partial N_i^{(e)}}{\partial x}(u_i, v_i), \quad \frac{\partial(u,v)}{\partial y} = \sum_{i=1}^{n} \frac{\partial N_i^{(e)}}{\partial y}(u_i, v_i) \tag{27}$$

$$J_i^{(e)} = \int_{\Gamma_e} \left(U dy - t_i \frac{\partial u_i}{\partial x} d_S \right) = \int_{-1}^{1} I d\xi \quad \text{For } \eta = \eta_P \tag{28}$$

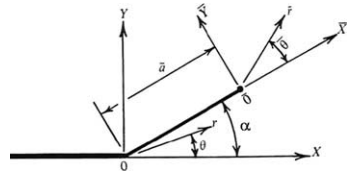


FIG. 6—*Geometry and coordinate systems for the branched crack [27].*

$$\int_{-1}^{1} Id\xi = \sum_{p=1}^{\text{NGAUS}} I(\xi_p,\eta_q)W_p = \sum_{P=1}^{\text{NGAUS}} \left\{ \frac{1}{2}[\sigma_{xx}(\varepsilon_{xx})_e + \sigma_{xy}(\varepsilon_{xy})_e + \sigma_{yy}(\varepsilon_{yy})_e]\frac{\partial y}{\partial \xi} + U_P\frac{\partial y}{\partial \xi} - \left[(\sigma_{xx}n_1 + \sigma_{xy}n_2)\frac{\partial u}{\partial x} + (\sigma_{xy}n_1 + \sigma_{yy}n_2)\frac{\partial v}{\partial x} \right] \sqrt{\left(\frac{\partial x}{\partial \xi}\right)^2 + \left(\frac{\partial y}{\partial \xi}\right)^2} \right\}_P W_P \tag{29}$$

For $\xi=\xi_P$ equations are the same as before except for $\partial x/\partial\xi$ and $\partial y/\partial\xi$ should be replaced with $\partial x/\partial\eta$ and $\partial y/\partial\eta$.

If crack propagates self-similarly under mixed mode loading, stress intensity factor and strain energy release rate are related as following equations:

$$G = \frac{\pi(k+1)}{8\mu}(K_{\text{I}}^2 + K_{\text{II}}^2) \tag{30}$$

$$\begin{Bmatrix} k = 3 - 4\nu & \text{For plane strain} \\ k = \dfrac{3-\nu}{1+\nu} & \text{For plane stress} \end{Bmatrix} \tag{31}$$

where ν is the Poisson ratio, μ is the shear modulus of material and K_{I}, K_{II} are the stress intensity factors.

When a part is under mixed mode loading, kinking angle is not zero, so Eq 30 does not stand. Nuismer [27], has developed the stress intensity factor in a branched crack tip with angle α as shown in Fig. 6

$$\bar{K}_{\text{I}} = \frac{1}{2}\cos\frac{\alpha}{2}[K_{\text{I}}(1+\cos\alpha) - 3K_{\text{II}}\sin\alpha] \tag{32}$$

$$\bar{K}_{\text{II}} = \frac{1}{2}\cos\frac{\alpha}{2}[K_{\text{I}}\sin\alpha + K_{\text{II}}(3\cos\alpha - 1)] \tag{33}$$

Therefore, the G value for the present crack tip is

$$\bar{G}_{(\alpha)} = \frac{\pi(k+1)}{8\mu}(\bar{K}_{\text{I}}^2 + \bar{K}_{\text{II}}^2) \tag{34}$$

Substituting $\bar{K}_{\text{I}}$ and $\bar{K}_{\text{II}}$ in Eq 34 gives

$$\bar{G}_{(\theta)} = \frac{\pi(k+1)}{32\mu}\cos^2\frac{\theta}{2}[K_{\text{I}}^2(1+\cos\theta)^2 + 9K_{\text{II}}^2\sin^2\theta - 6K_{\text{I}}K_{\text{II}}\sin\theta(1+\cos\theta)] \tag{35}$$

According to the maximum strain energy release rate criterion, crack propagates in the direction that $\bar{G}_{(\theta)}$ is maximum. To find the maximum $\bar{G}_{(\theta)}$, the derivative of $\bar{G}_{(\theta)}$ is equated to zero ($\partial\bar{G}_\theta/\partial\theta = 0$). This equation gives the crack propagation angle

$$\cos(\theta) = \frac{3K_{\text{II}}^2 + K_{\text{I}}\sqrt{K_{\text{I}}^2 + 8K_{\text{II}}^2}}{K_{\text{I}}^2 + 9K_{\text{II}}^2} \tag{36}$$

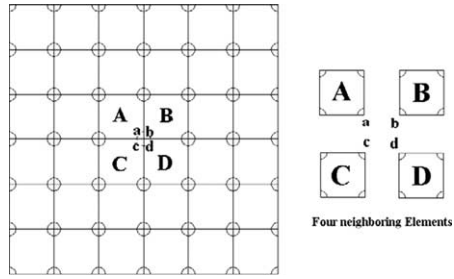


FIG. 7—*2D mesh with multinode construction.*

Equation 36 is equivalent to Eq 7. On the other hand, under LEFM conditions, maximum circumferential stress criterion and maximum strain energy release rate criterion are the same. When crack is not self-similar, the maximum strain energy release rate under mixed mode loading can be defined by substituting Eq 36 in Eq 35.

$$\bar{G}_{\theta\,\max} = \frac{\pi(k+1)}{16\mu} \frac{K_{\mathrm{I}}^4 + 24K_{\mathrm{II}}^4 + 12K_{\mathrm{I}}^2K_{\mathrm{II}}^2 + K_{\mathrm{I}}(K_{\mathrm{I}}^2 + 8K_{\mathrm{II}}^2)^{3/2}}{K_{\mathrm{I}}^2 + 9K_{\mathrm{II}}^2} \tag{37}$$

Implementation of Automatic Node Release in ABAQUS

User subroutines are used in the ABAQUS code to introduce new and nonconventional required numerical conditions. In crack propagation problems, because of dynamic boundary condition updates, it is necessary to change the boundary condition (crack surfaces) during each solving time step. Therefore, node release technique implemented into the multipoint constraint subroutine (MPC) has been used. In this method instead of conventional meshing that uses one node at each element corner, four nodes are located at an identical coordinates. Figure 7 shows this mesh. Nodes *a*, *b*, *c*, and *d* of four elements *A*, *B*, *C*, and *D* are coupled together. This means that their displacements are forced to be the same.

$$u_a = u_b = u_c = u_d \tag{38}$$

To create a crack surface, it is necessary for these nodes to be separated following the crack growth direction. Consequently equal displacement of remaining attached nodes is estimated. Figure 8 shows three different possible situations that the direction of a crack can take.

If for a point that contains nodes *a*, *b*, *c*, and *d* the constraint equation can be written as

$$k_1^1 u_a + k_2^1 u_b + k_3^1 u_c + k_4^1 u_d = 0$$

$$k_1^2 u_b + k_2^2 u_c + k_3^2 u_d = 0$$

$$k_1^3 u_c + k_2^3 u_d = 0 \tag{39}$$

The above-mathematical representation of multipoint constraint for nodes *a*, *b*, *c*, and *d* can be

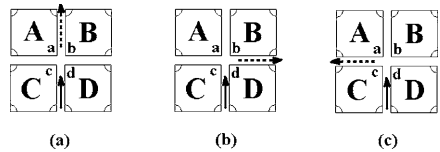


FIG. 8—*Representation of three possible node release situation for creation of crack surfaces: (a) Crack extension is straight* $u_a = u_c$ *and* $u_b = u_d$*; (b) crack extension is right direction* $u_a = u_b = u_c$*; (c) crack extension is left direction* $u_a = u_b = u_d$.

TABLE 1—*Factors of Eq 39 for three possible node release situation.*

Crack extension is left handed	Crack extension is right handed	Crack extension is straight
$k_1^1=k_1^2=1$	$k_1^1=k_1^2=1$	$k_1^1=k_1^2=1$
$k_2^1=k_3^2=-1$	$k_2^1=k_2^2=-1$	$k_3^1=k_3^2=-1$
$k_3^1=k_4^1=k_2^2=k_1^3=k_2^3=0$	$k_3^1=k_4^1=k_3^2=k_1^3=k_2^3=0$	$k_2^1=k_4^1=k_2^2=k_1^3=k_2^3=0$

reexpressed in the ABAQUS input file format as

```
*MPC
  a,a,b,c,d
  b,b,c,d
  c,c,d
```

According to crack propagation direction, the factors in Eq 39 will take the values of 0, 1, or −1. Table 1 shows the factors in Eq 39 for three different situations, shown in Fig. 8.

This strategy can only be used to model three possible situations of crack propagation, which differs approximately by 90° from each other. Any crack propagation angle less than 90° between each case is extrapolated to one of the above cases. This mean that some localized error in the evaluation of the crack growth direction can reduce the accuracy in short term. In Ref. [2], a method to solve this problem has been introduced. This is shown in Fig. 9. The nearest node ahead of the crack growth direction path can be moved in a way that one of the element faces is aligned in the new crack direction.

The method that has been used in this paper is as follows:

(1) Amount of crack propagation in each step is calculated by the program or defined by user (Δa). According to crack propagation angle and Δa value, the new candidate of crack tip point will be defined (t').
(2) The nearest nodes to the tt' line will be defined (see Fig. 10).
(3) The nodes around the tt' line will be released according to the given algorithm.

The element size used in this method should be at least five times smaller than Δa. So in each step of crack propagation modeling, more than one node can be released. Therefore, it is possible to model every crack propagation angle with a good degree of approximations by releasing the nodes around propagation line. Figure 11 shows the algorithm of crack propagation simulation.

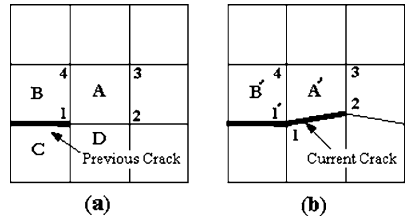


FIG. 9—*Automatic remeshing strategy for crack propagation: (a) previous mesh; (b) current; mesh [2].*

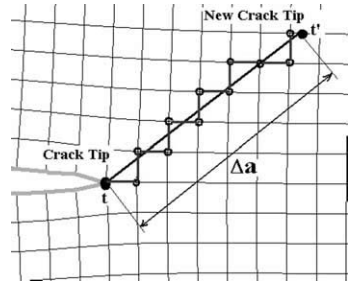


FIG. 10—*Method of approximation of crack trajectory with node release technique.*

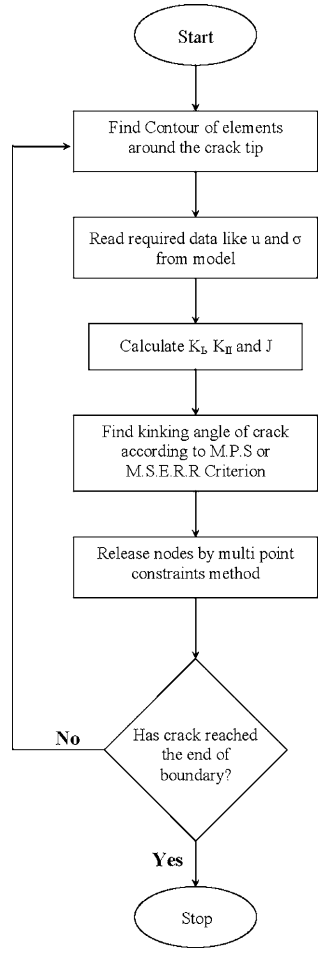


FIG. 11—*Flowchart used for crack propagation modeling.*

Numerical Examples

To model crack propagation using maximum principal stress criterion and maximum strain energy release rate criterion, different programs have been written in VISUAL-FORTRAN language and linked to the ABAQUS 6.3.1 code. This program has been implemented for four-noded linear elements with four Gaussian points successfully. The examples have been selected from Refs. [3,4] to compare the results with those that used remeshing techniques.

Example 1: A Rectangular Block with an Oblique Precrack

Figure 12 shows the geometrical properties of a plate with the rectangular shape that contains an oblique precrack. The dimensions are in millimeter. The material is purely elastic with a Young modulus of $E = 98000$ MPa and a Poisson ratio of $v = 0.3$.

In Fig. 13 the mesh for the rectangular plate has been shown and the plane strain condition was used with four-noded elements containing four integration points. The element type used in this analysis is CPE4. A total number of 20 975 elements and 83 900 nodes have been used in this example. The element

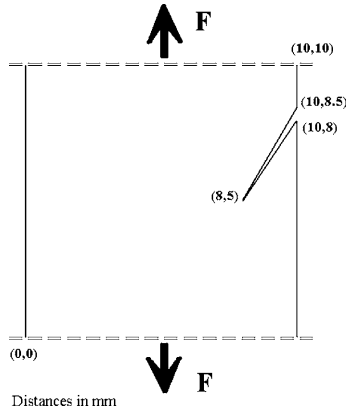


FIG. 12—*Rectangular block with an oblique precrack [4].*

size around crack tip is about 40 μm. The crack propagation length in each step has been numerically tested for a range of 4–15 elements and similar results were obtained. Therefore, a length of seven elements was selected arbitrarily. Figure 14 shows crack propagation trajectory according to the maximum principal stress criterion. To use the maximum strain energy release rate criterion, it is necessary to calculate *J* integral and stress intensity factors around the crack tip. Figure 15 shows *G* values for example 1 around the crack tip during crack propagation.

Figure 16 shows the results of the crack propagation path modeling using maximum strain energy release rate criterion for the rectangular part with an oblique crack.

Figure 17 illustrates the comparison of the result from the present work with the remeshing technique results published in [4].

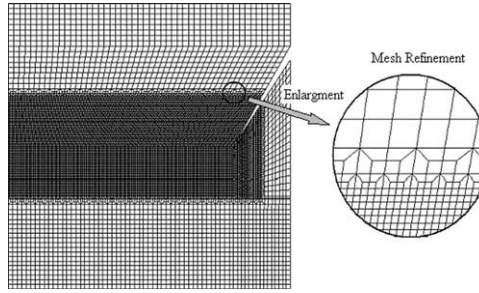


FIG. 13—*Mesh used for modeling of crack propagation of rectangular part with an oblique precrack.*

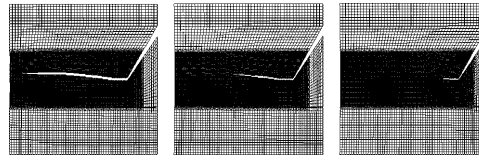


FIG. 14—*Crack trajectory based on maximum principal stress criterion.*

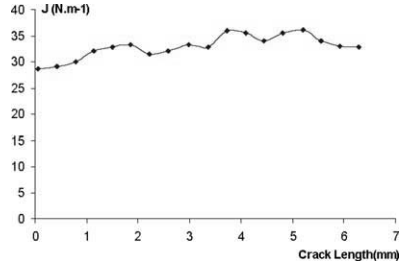


FIG. 15—*J integral histories for example 1.*

Example 2: Drilled Plate with Two Supporting Point

The geometrical properties and loading condition of example 2 are shown in Fig. 18. The material of this part is polymethyl methacrylate (PMMA). It has a preliminary notch with a defined length in a particular distance from centerline. The experimental results of this model have been studied at Cornel University and published in Ref. [3]. The experimental results have also been compared with a finite element modeling result using the remeshing technique. Elastic modulus of material used were $E=2.94$ GPa and the Poisson ratio is $\nu=0.3$ [28]. Because of the holes in the model acting as stress concentrators, the shape of the crack propagation path is seen to be as a curvature. Figure 19 shows the mesh of this model. The element type is the same as example 1 but because of the boundary condition, the plane stress element has been used (CPS4 from the ABAQUS library). A total number of 17 657 elements and 70 628 nodes have been used in this example and the element size around the crack tip is 0.1524 mm.

Figure 20 shows the crack propagation path using maximum principal stress criterion for this model. Figure 21 compares the result from this model using maximum principal stress and maximum strain energy release rate criteria with experimental results and also results from Ref. [3].

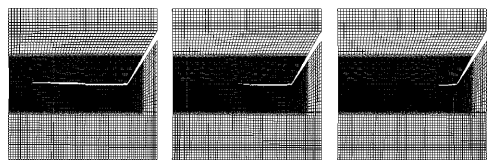


FIG. 16—*Crack trajectory based on maximum strain energy release rate criterion.*

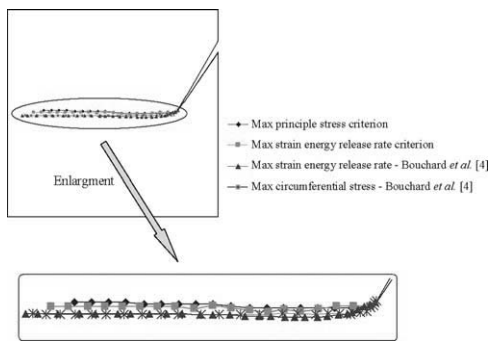


FIG. 17—*Comparison of crack trajectory based on maximum principal stress and maximum strain energy release rate criteria with results of remeshing.*

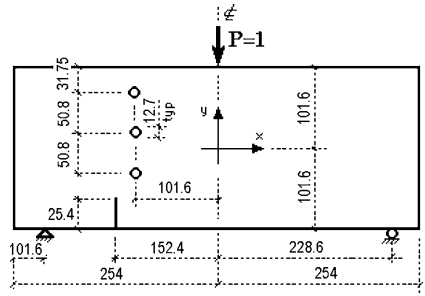


FIG. 18—*Initial geometry of specimen. All dimensions in millimeters [3].*

Conclusions

The simulation of the crack growth for complex geometries using LEFM methods is presented in this paper. A program which deals with assessing the stress/strain distribution local to the crack tip in 2D has

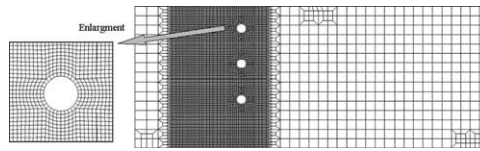


FIG. 19—*Mesh used for modeling of crack propagation of rectangular part.*

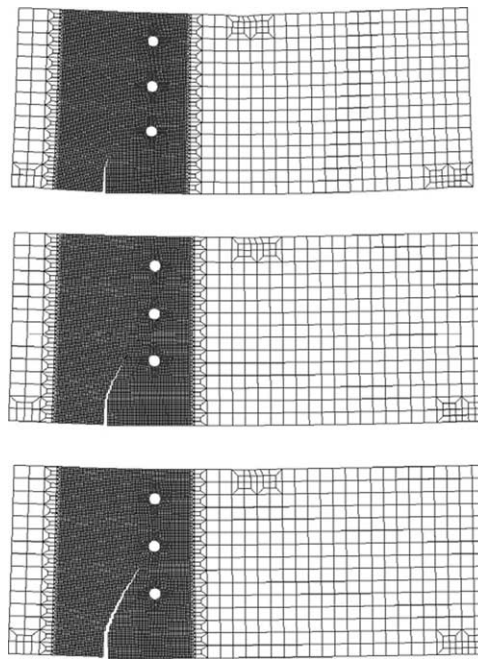


FIG. 20—*Crack trajectory based on maximum principal stress criterion.*

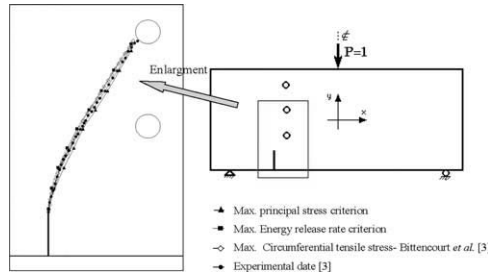


FIG. 21—*Comparison of crack trajectory based on maximum principal stress and maximum strain energy release rate criteria with results of remeshing.*

been developed to link with a general purpose finite element program. This development allows for the modeling of complex geometries in the engineering applications. The maximum principal stress and maximum strain energy release rate criteria have been used to find the extent of crack growth, its direction, and length. Since the remeshing technique usually suffers from the loss of strain energy density that can occur at the tip of the crack during the interpolation of field solutions, a regular quad mesh with no remeshing has been adopted in this research work. It has been shown that the presented method can conveniently deal with a nonstraight crack growth path, which is based on a node releasing technique. The results of the simulation have been favorably compared with published experimental and numerical results from the literature. The presented results showed a good agreement with the published experimental data and results from numerical simulations that employed remeshing techniques. Since the present technique is sufficiently robust and adaptable, it is also suggested that this method can be used to simulate crack growth for more ductile materials that undergo elastic-plastic and creep deformation.

References

[1] Bittencourt, T. N., "Computer Simulation of Linear and Nonlinear Crack Propagation in Cementitious Materials," Phd Thesis, Cornell University, 1993.

[2] Tabiei, A. and Jin Wu, "Development of the DYNA3D Simulation Code With Automated Fracture Procedure for Brick Elements," *Int. J. Numer. Methods Eng.*, Vol. 57, 2003, pp. 1–28.

[3] Bittencourt, T. N. and Wawrzynek, P. A., "Quasi-Automatic Simulation of Crack Propagation for 2D LEFM Problems," *Eng. Fract. Mech.*, Vol. 55, No. 2, 1996, pp. 321–334.

[4] Bouchard, P. O., Bay, F., and Chastel, Y., "Numerical Modeling of Crack Propagation: Automatic Remeshing and Comparison of Different Criteria," *Comput. Methods Appl. Mech. Eng.*, Vol. 192, 2003, pp. 3887–3908.

[5] Beissel, S., Johnson, G., and Popelar, C., "An Element Failure Algorithm for Dynamic Crack Propagation in General Directions," *Eng. Fract. Mech.*, Vol. 61, 1998, pp. 407–426.

[6] Biglari, F. R., Tavakoli, A., Parsa, M. H., Nikbin, K., and O'Dowd, N. P., "Comparison of Fine and Conventional Blanking Based on Ductile Fracture Criteria," *7th Biennial ASME Conference on Engineering Systems Design and Analysis*, July 19–22, Manchester, UK, 2004.

[7] Belytschko, T., Lu, Y. Y., and Gu, L., "Element Free Galerkin Methods," *Int. J. Numer. Methods Eng.*, Vol. 37, 1994, pp. 229–256.

[8] Rashid, M. M., "The Arbitrary Local Mesh Replacement Method: An Alternative to Remeshing for Crack Propagation Analysis," *Comput. Methods Appl. Mech. Eng.*, Vol. 154, 1998, pp. 133–150.

[9] Moës, N., Dolbow, J., and Belytschko, T., "A Finite Element Method for Crack Growth Without Remeshing," *Int. J. Numer. Methods Eng.*, Vol. 46, 1999, pp. 131–150.

[10] Sukumar, N., and Prevost, J. H., "Modeling Quasi-Static Crack Growth With the Extended Finite Element Method. Part I: Computer Implementation," *Int. J. Solids Struct.*, Vol. 40, 2003, pp. 7513–7537.

[11] Wells, A. A., "Unstable Crack Propagation in Metals: Cleavage and Fast Fracture," *Proceedings of*

the Crack Propagation Symposium, Vol. 1, Paper 84, Cranfield U.K., 1961.
[12] Anderson, T. L., *Fracture Mechanics Fundamentals and Applications*, 2nd Ed., Texas A&M University, College Station, Texas, 1995.
[13] Fortino, S. and Bilotta, A., "Evaluation of the Amount of Crack Growth in 2D LEFM Problems," *Eng. Fract. Mech.*, Vol. 71, 2004, pp. 1403–1419.
[14] Gerken, J. M., "An Implicit Finite Element Method for Discrete Dynamic Fracture," MS thesis, Colorado State University, 1998.
[15] Smith, F. W., "Software Tools for Dynamic Cracking Analysis," Final Report, 2000.
[16] Erdogan, F. and Sih, G. C., "On the Crack Extension in Plane Loading and Transverse Shear," *J. Basic Eng.*, Vol. 85, 1963, pp. 519–527.
[17] Maiti, S. K. and Smith, R. A., "Comparison of the Criteria for Mixed Mode Brittle Fracture Based on the Preinstability Stress-Strain Field. Part II: Pure Shear and Uniaxial Compressive Loading," *Int. J. Fract.*, Vol. 24, 1984, pp. 5–22.
[18] Hussain, M. A., Pu, S. L., and Underwood, J. H., "Strain Energy Release Rate for a Crack Under Combined Mode I and Mode II," *Fract. Analysis*, ASTM STP 560, ASTM, Philadelphia, PA, 1974, pp. 2–28.
[19] Gurson, A. L., "Continuum Theory of Ductile Rupture by Void Nucleation and Growth: Part I. Yield Criteria and Flow Rules for Porous Ductile Media," *J. Eng. Mater. Technol.*, Vol. 99, 1997, pp. 2–15.
[20] Biglari, F. R., Nikbin, K. M., and O'Dowd, N. P., "Numerical Simulation of Crack Growth Based on Void Volume Fraction," *Proceedings of ISME2002 Conference*, Tehran, Iran, May, 2002.
[21] Bouchard, P. O., Bay, F., Chastel, Y., and Tovena, I., "Crack Propagation Modeling Using an Advanced Remeshing Technique," *Comput. Methods Appl. Mech. Eng.*, Vol. 189, 2000, pp. 723–742.
[22] Miranda, A. C. O., Miggiolaro, M. A., Castro, J. T. P., Martha, L. F., and Bittencourt, T. N., "Fatigue Life and Crack Path Predictions in Generic 2D Structural Components," *Eng. Fract. Mech.*, Vol. 70, 2003, pp. 1259–1279.
[23] Sih, G. C. and Macdonald, B., "Fracture Mechanics Applied to Engineering Problems-Strain Energy Density Fracture Criterion," *Eng. Fract. Mech.*, Vol. 6, 1974, pp. 361–386.
[24] Rice, J. R., "A Path Independent Integral and the Approximate Analysis of Strain Concentrations by Notches and Cracks," *J. Appl. Phys.*, Vol. 35, 1968, pp. 379–386.
[25] de Lorenzi, H. G., "Energy Release Rate Calculations by the Finite Element Method," *Eng. Fract. Mech.*, Vol. 21, No. 1, 1985, pp. 129–143.
[26] Owen, D. R. J. and Fawkes, A. J., *Engineering Fracture Mechanics: Numerical Methods and Applications*, Pineridge Press Ltd, 1983.
[27] Nuismer, R. J., "An Energy Release Rate Criterion for Mixed Mode Fracture," *Int. J. Fract.*, Vol. 11, No. 2, 1975, pp. 245–250.
[28] Nishioka, T., Tokudome, H., and Kinoshita, M., "Dynamic Fracture-Path Prediction in Impact Fracture Phenomena Using Moving Finite Element Method Based on Delaunay Automatic Mesh Generation," *Int. J. Solids Struct.*, Vol. 38, 2001, pp. 5273–5301.

Journal of ASTM International, January 2006, Vol. 3, No. 1
Paper ID JAI13236
Available online at www.astm.org

Richard E. Link,[1] *Ph.D.*

Analysis of Dynamic Fracture and Crack Arrest of an HSLA Steel in an SE(T) Specimen

ABSTRACT: A single edge notch tension, SE(T), specimen was used to measure the dynamic fracture toughness and the crack arrest toughness of a tough HSLA steel in the ductile-brittle transition region. The SE(T) specimen was considerably smaller (W = 152 mm) than wide-plate specimens that have been typically used in other crack arrest tests. A thermal gradient was applied across the ligament of the specimen to facilitate a brittle crack initiation in the low temperature region of the specimen. The cleavage crack propagated into warmer and, consequently, tougher material which led to crack arrest. Transient, three-dimensional, finite element analyses of the tests were performed to determine the dynamic fracture and crack arrest toughness of the steel. The analyses employed both linear elastic and visco-plastic constitutive models. Dynamic strain measurements recorded during the run-arrest event were used to determine the crack tip position as a function of time during the event. This information was used as a boundary condition for the analysis. The measured strains were compared with strains predicted by the finite element analysis to validate the model. The dynamic response of the specimen, the effect of crack speed on the driving force, and the evolution of crack tip plasticity during the run-arrest event are discussed.

KEYWORDS: fracture mechanics, crack arrest, dynamic fracture, finite element analysis, toughness

Introduction

The ASTM Standard Test Method for Determining Plane-Strain Crack-Arrest Fracture Toughness, K_{Ia}, of Ferritic Steels (E 1221), was approved in 1988 and is the principal method for characterizing the crack arrest fracture toughness of steels. The crack is initiated by driving a wedge through a pair of split-pins inserted in the notch until a brittle crack initiates from the crack starter notch. The crack propagates into a decreasing K-field due to the fixed displacement loading condition and arrests when the driving force falls below the crack arrest fracture toughness of the material. The crack arrest fracture toughness, K_{Ia}, is inferred from measurement of the arrested crack length and the crack mouth opening displacement a short time, approximately 1 ms, after arrest using a static analysis of the specimen. A static analysis has been demonstrated to provide a satisfactory approximation to the true dynamic response of the compact crack arrest (CCA) specimen provided certain restrictions on crack jump, specimen size, and other restrictions are met [1] [2].

Several researchers have noted problems using the ASTM E 1221 procedure to measure the crack arrest fracture toughness of steel alloys and weldments [3] [4] [5]. The success rate during the round-robin in support of the standard development was less than 50 % [2]. It can be difficult to achieve valid results for some alloys depending upon the test temperature, strength, toughness, and plate thickness. The reasons for invalid test results included insufficient or excessive crack jump from the starter notch and a tendency for the crack path to deviate from the intended crack

Manuscript received April 8, 2005; accepted for publication July 13, 2005; published Jan. 2006. Presented at ASTM Symposium on Fatigue and Fracture Mechanics: 35th Volume on 18–20 May 2005 in Reno, NV.
[1] Associate Professor, United States Naval Academy, Annapolis, MD 21402.

Copyright © 2005 by ASTM International, 100 Barr Harbor Drive, PO Box C700, West Conshohocken, PA 19428-2959.

plane. Crosley and Ripling [6] have proposed a modified crack arrest testing procedure for full-thickness plates that lack sufficient thickness to meet ASTM E 1221 requirements, but their procedure suffers from some of the same problems as the ASTM E 1221 approach.

The standard crack arrest test is an isothermal test and it can be difficult or impossible to perform a valid test at all temperatures of interest, particularly for tough materials that have a large shift in the transition curves between the static initiation and crack arrest toughness. The initiation and crack arrest transition curves for two different materials are compared in Fig. 1. Material A has a small to moderate shift in the fracture toughness transition curves between initiation and arrest. In this case it may be possible to measure the crack arrest toughness successfully over a significant portion of the transition region. Material B has a large shift in the transition curve between initiation and arrest. It may be possible to generate a valid crack arrest toughness value at very low temperatures for Material B, but the initiation toughness at the temperature of interest may be too high to initiate a brittle crack before extensive plasticity and tearing develop in the specimen. Furthermore, if a brittle crack is initiated, the stored energy in the specimen is sufficient to drive the crack completely through the specimen or lead to crack branching. Brittle crack starter welds may assist in shifting the initiation toughness curve closer to the arrest curve, but this practice may not help in the upper transition.

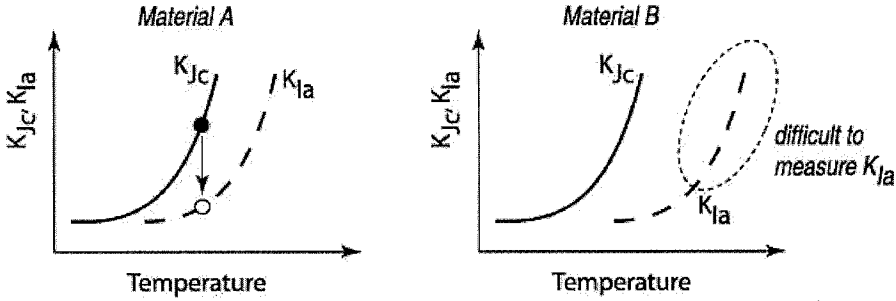


FIG. 1—*Comparison of fracture toughness transition curves for two hypothetical materials with different shifts between the crack initiation and arrest fracture toughness.*

A wide-plate, single-edge notch tension, SE(T), specimen was developed to measure the crack arrest fracture toughness of reactor pressure vessel steels in the upper transition region [7]. The wide plate specimens were very large, 1 m wide, 10 m long, and 0.1 m thick, and were very expensive to test. The large specimen size was selected primarily to minimize dynamic effects due to reflected stress waves interacting with the crack during the run-arrest events. Assuming fixed displacement conditions, the SE(T) specimen exhibits an increasing K field until the crack exceeds about 50 % of the width and then it decreases monotonically. A thermal gradient was employed to establish a gradient in the fracture toughness across the width of the plate. The initial crack tip was maintained at a low temperature and the temperature increased linearly across the specimen width. As the crack propagated under the increasing K field, it encountered progressively tougher material owing to the increase in temperature. The crack arrested when the crack arrest toughness exceeded the instantaneous driving force. The dynamic stress intensity and the crack arrest fracture toughness were determined by a combination of finite element

analysis and correlation of the dynamic strain response of the specimen with a three-parameter approximation of the theoretical strain field of a dynamically propagating crack [7] [8] [9].

This paper examines the feasibility of using a much smaller SE(T) specimen for measuring the crack arrest toughness of a high toughness steel alloy. The experiments are described and the results of finite element analysis of the experiments are presented.

Experimental Procedure

All of the experiments described in this paper were conducted during the period 1990–1991. No additional material from the original tests was available for making supplemental measurements of fracture initiation or arrest toughness.

Material Description

The material used in this investigation was a 25.4-mm (1-in.) thick, high strength, low alloy steel, HSLA 100, typically used for naval surface ships and structures [10]. This steel is a quenched and aged, low carbon, copper precipitation strengthened alloy that has a microstructure that has been described as low carbon martensite with granular bainite forming in plate gages greater than 50-mm (2-in.) thick [11]. The plate was austenitized at 900°C, quenched and aged at 675°C for 150 min, and air-cooled. The chemical composition of the plate and the room temperature mechanical properties of the plate are listed in Tables 1 and 2.

TABLE 1—*Chemical composition of the HSLA-100 steel plate used in this investigation.*

Element	C	Mn	P	S	Si	Cu	Ni	Cr	Mo	Al	Cb
Wt. %	0.04	0.86	0.004	0.002	0.27	1.58	3.55	0.57	0.60	0.032	0.030

TABLE 2—*Room temperature mechanical properties for the HSLA-100 steel plate.*

0.2 % Yield Strength (MPa)	Tensile Strength (MPa)	Elongation in 51 mm (%)	Reduction of Area (%)
807	848	25	74

Representative quasi-static stress-strain curves for HSLA-100 steel plate over a range of temperatures are plotted in Fig. 2. High strain rate stress-strain data at several temperatures were also available for this material.

The fracture toughness of the plate in the T-L orientation was determined over a range of temperatures and is plotted in Fig. 3. These tests were conducted in accordance with ASTM E 813 and ASTM E 1152. It was not possible to determine a valid reference temperature, T_o, from the available data because there was an insufficient number of results near T_o; however, an estimate of the reference temperature, T_{oq}, for the plate is – 160°C. This estimate was based on the available cleavage fracture toughness values measured high in the transition region, using the procedure of ASTM E 1921. The average fracture toughness for ductile tearing, determined from the data plotted in Fig. 3 was J_{Ic} = 385 kJ/m^2 (2200 in.-lb/in.^{2}) and K_{JIc} = 291 MPa-m$^{1/2}$ (265 ksi-in.$^{1/2}$).

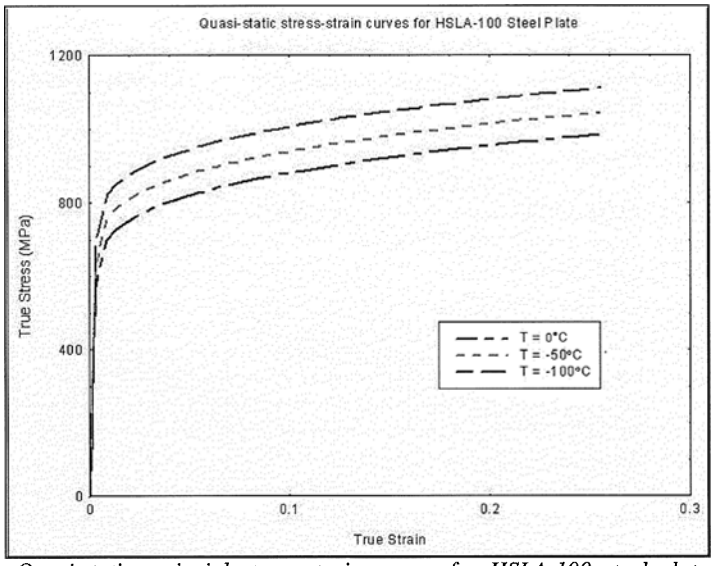


FIG. 2—*Quasi-static, uniaxial stress-strain curves for HSLA-100 steel plate at several temperatures.*

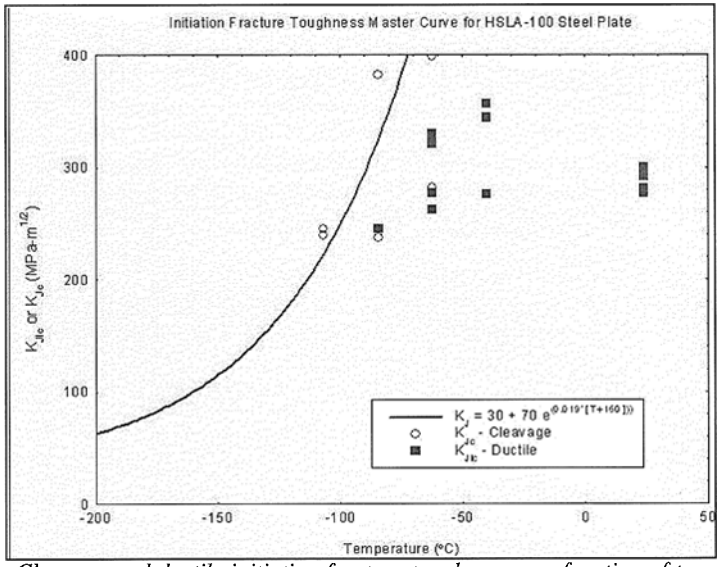


FIG. 3—*Cleavage and ductile initiation fracture toughness as a function of temperature for the HSLA-100 steel plate and the master curve for cleavage initiation.*

Specimen Details

The crack arrest specimens were pin-loaded SE(T) specimens with a width, W = 152 mm (6 in.) and an initial crack length, a_0 = 38 mm (1.50 in.), a_0/W = 0.25. The specimen length between the pinholes was 711 mm (28 in.) and the reduced section in the center of the specimen was 305 mm (12 in.). The specimens were 25.4-mm-thick (1.0-in.) and were side-grooved, 2.5 mm (0.10 in.), on each face. A fatigue precrack was extended from the machined notch to the desired initial crack length of 38 mm. Precracking was conducted by loading the specimen in three-point bending and K_{max} was less than 25 MPa–$m^{1/2}$. The specimen is shown in Fig. 4.

The specimens were instrumented with strain gages placed along lines parallel to the crack plane a distance of 15 mm above and below the crack plane. This offset distance was necessary to keep the gages away from the influence of three-dimensional effects due to the side grooves. The strain gages were positioned as shown in Fig. 5. A single element gage was oriented at an angle of 61.3° to the crack plane and the remaining gages were 90° rosettes configured to measure the difference between the two gages ($\varepsilon_{y'y'} - \varepsilon_{x'x'}$). The orientation of the first gage allowed for a three-parameter measure of the stress intensity factor at initiation [12]. The rosette orientation was selected to support an over deterministic method to determine the crack tip position and the dynamic stress intensity factor, K_{ID}, as the crack traversed the specimen [13]. The strain gages were connected to high-frequency bridge amplifiers (Vishay Model 2310, freq. response 0–25 kHz, –0.5 dB) for signal conditioning and the amplifiers were connected to digital storage oscilloscopes. The oscilloscopes were set to trigger off of the falling edge of the transient strain signal from the first gage as the crack ran past the gage.

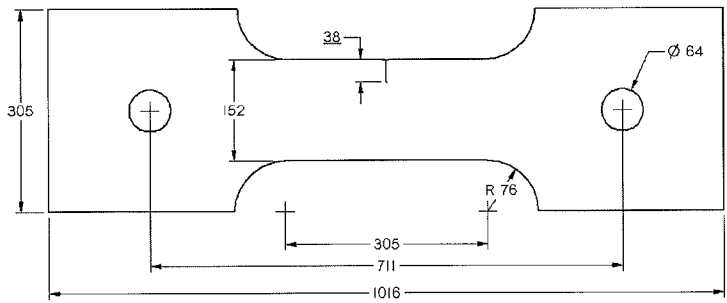


FIG. 4—*Schematic drawing of the SE(T) specimen used in this investigation. The specimen was 25-mm thick and had 10 % side grooves on each face. All dimensions are in mm.*

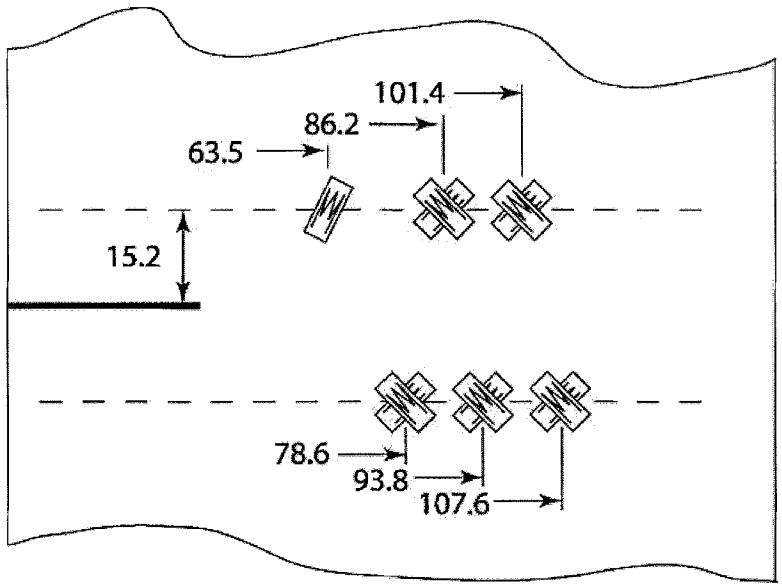


FIG. 5—*Locations of strain gages along crack path relative to the crack plane and the front face of the SE(T) specimen. All dimensions are in mm.*

Aluminum cooling fins were bolted to the notched edge of the specimen in the reduced section and a stainless steel chamber was fabricated from thin sheet to enclose the cooling fins and to hold liquid nitrogen for cooling the notched edge of the specimen. The chamber was secured to the specimen using screws and silicone sealant designed to minimize any closing forces across the crack plane. An aluminum block with three electrical resistance heaters was attached to the back face of the specimen. A variable transformer was used to control the power supplied to the heaters. A series of 11 thermocouples was uniformly spaced along the specimen width just above the side groove. The thermocouples were peened into small holes drilled into the surface of the specimen and were used to monitor the temperature gradient and determine when an equilibrium linear gradient was achieved. The typical temperature profile across the test section of Specimen GLC-502 at the commencement of testing is plotted in Fig. 6. The gradient is very linear with a maximum deviation of 5°C from the linear fit shown.

The applied force and the crack mouth opening displacement were recorded on an analog x-y plotter. A photograph of an instrumented specimen is shown in Fig. 7.

Experimental Results

Two crack arrest tests were conducted with varying degrees of success. Both of the tests had brittle initiations followed by rapid crack growth and arrest. For one of the tests, GLC-502, the load was accidentally applied rapidly, in less than one second. The analog recorder did not accurately capture the initiation load but the digital oscilloscopes did capture the strain gage signals. After the test, the specimen was heat tinted to mark the arrested crack front and subsequently broken open and the initial fatigue crack and arrested crack lengths were measured.

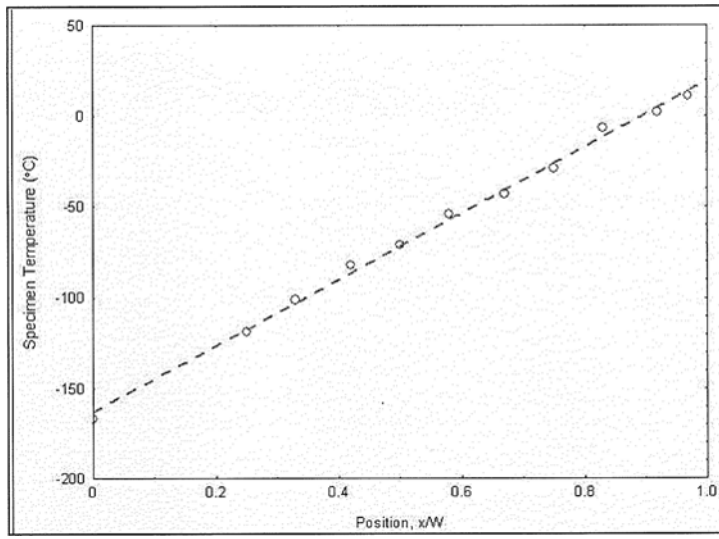


FIG. 6—*Temperature gradient across Specimen GLC-502 immediately prior to test.*

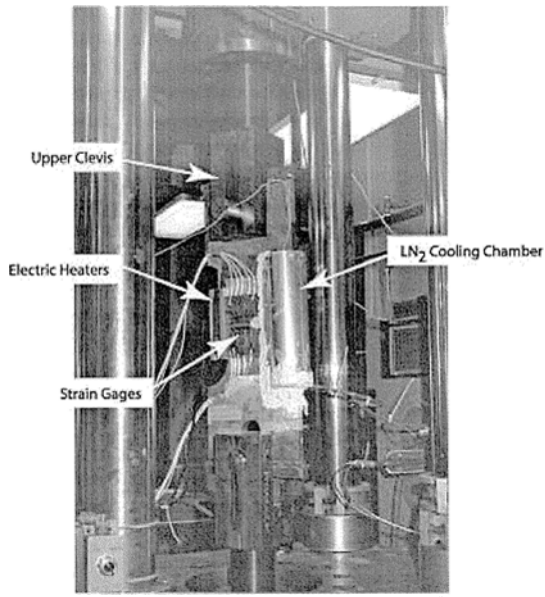


FIG. 7—*Photograph of an instrumented specimen in the testing machine.*

In the second test, GLC-501, the load was applied in a quasi-static manner and an accurate initiation load was recorded; however, in this case, the digital oscilloscopes failed to trigger and capture the strain signals. The specimen was nearly broken in two and the final crack front was marked by fatigue cycling. Once the specimen was fully broken, it was clear that a cleavage crack initiated from the fatigue precrack, arrested, and reinitiated as ductile tearing after arrest, leaving only a small ligament, approximately 15 mm ($b/W = 0.1$).

The initial and arrested crack lengths were measured using a nine-point average of the crack front measurements. The initiation and arrest temperatures were determined from the crack lengths and the measured thermal gradient. Photographs of the fracture surfaces are shown in Fig. 8. Specimen GLC-502 had a relatively straight crack front at arrest. The arrested crack front from Specimen GLC-501 had considerable tunneling in the center of the specimen and the cleavage crack extension at the side groove was much less than at the center of the specimen. A nine-point average crack length was used in all subsequent analyses.

The strain signals recorded from Specimen GLC-502 are plotted in Fig. 9. Only the traces from the first five gages are shown because the crack did not propagate past the fifth gage and the strain signals contain no information about the passage of the crack. The strain signals exhibited the expected characteristic peak and rapid decay due to the crack propagating past the strain gage location. For this specimen, the crack arrested before the crack reached Gage 3. The peak in the strain response occurs well before the crack actually reaches the strain gage. Gage 4 was close enough to the crack tip to record a peak and some decay, while Gage 5 was far enough ahead of the crack that the peak had not been achieved prior to crack arrest.

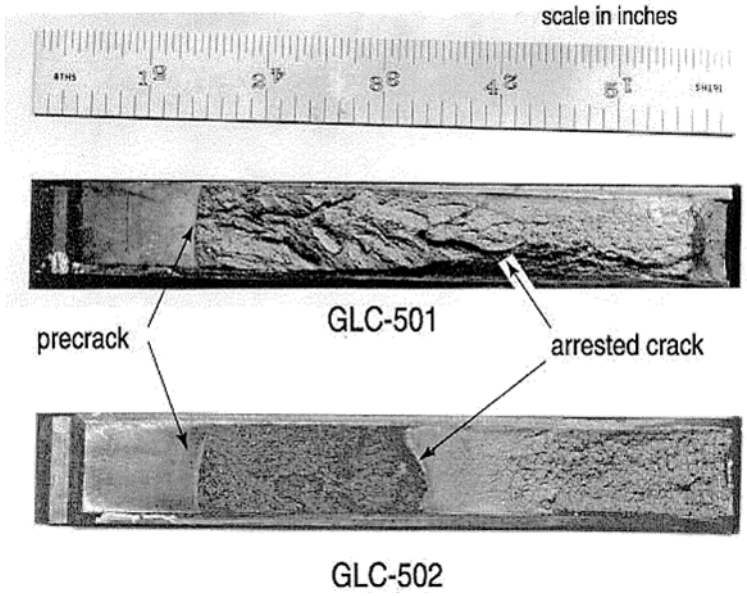


FIG. 8—*Photographs of the fracture surfaces of the crack arrest specimens.*

An attempt was made to correlate the strain gage signals to the dynamic crack tip strain fields and to extract the crack position and K as a function of time. The analyses failed to converge and were unsuccessful. The technique requires that the gages be positioned close to the crack tip relative to the crack size and specimen width, and this condition was not met very well in the small specimen. In addition, the gages had to be about half a plate thickness away from the crack line to minimize the influence of the side groove on the strain field [12] [13]. The relatively small size of the SE(T) specimen prevented these two requirements from being met simultaneously and was a likely reason that the approach was unsuccessful. The crack speed could be estimated from key characteristics of the strain response, such as the relative time between strain peaks or zero crossings of the strain signals. By assuming that the peak strain occurs at a fixed location relative to the moving crack tip, a rough estimate of the crack speed can be made. Based on the time of the peaks of the strain signals and the spacing of the strain gages, the average crack speed was approximately 500 m/s. This crack speed is consistent with the typical range of crack speeds reported in other dynamic fracture investigations of steels [9].

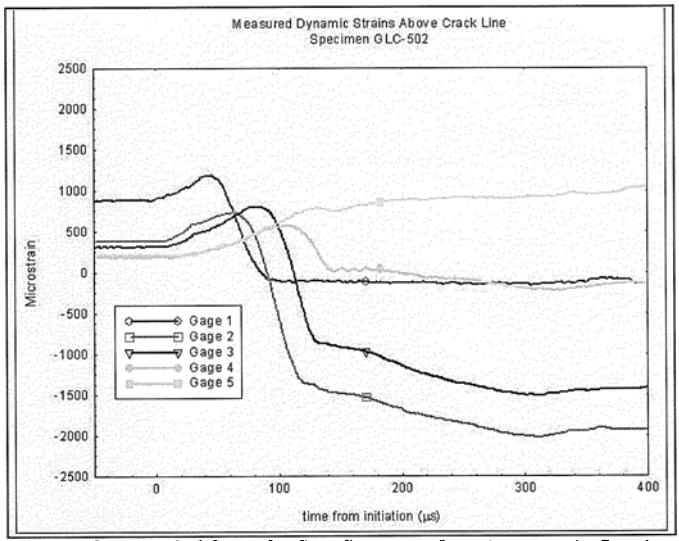


FIG. 9—*Strain signals recorded from the first five sets of strain gages in Specimen GLC-502.*

A summary of the available information from the crack arrest tests is presented in Table 3. At this point, only the arrest temperatures and arrested crack lengths were known, and it was not possible to determine the crack arrest fracture toughness.

TABLE 3—*Summary of results from crack arrest tests of HSLA-100 SE(T) specimens with thermal gradients.*

Specimen ID	a_0 (mm)	$T_{init.}$ (°C)	K_{init} (MPa-$m^{1/2}$)	a_f (mm)	T_{arrest} (°C)
GLC-501	39.4	−122	220	103	−44
GLC-502	37.9	−118	93	84.3	−62

Finite Element Analysis

Finite element analysis was used to model the crack arrest tests and to determine the dynamic and the crack arrest fracture toughness. The finite element code, Warp3D, was used to perform the analyses [14]. Plane strain and 3-D models of the specimen were used in this investigation. The plane strain models were for preliminary analyses to investigate the effect of various parameters, such as crack speed and elastic versus elastic-visco-plastic material behavior, on the results.

Isoparametric, 8-node bricks with a tri-linear displacement formulation and 2 × 2 × 2 integration were used for all analyses. These elements (the *l3disop* element in Warp3D) include support combined geometric and material nonlinear response. Plane strain analyses were performed by modeling the specimen with a single layer of elements with the out of plane displacements constrained.

The material constitutive behavior employed a von Mises yield criterion with isotropic hardening. A power-law, visco-plastic material model available in the Warp3D code [14] was used to characterize the strain-rate sensitivity of the steel. The relationship is:

$$\dot{\varepsilon}_{vp} = \frac{1}{D}\left[\left(\frac{q}{\sigma_e}\right)^m - 1\right] \tag{1}$$

where $\dot{\varepsilon}_{vp}$ is the strain rate, q is the rate dependent equivalent stress, σ_e is the inviscid equivalent uniaxial stress, and D and m are temperature independent, material specific constants determined from fitting the high-rate stress-strain curves. The temperature dependence of the visco-plastic response enters through the inviscid equivalent uniaxial stress, σ_e, which is a function of temperature. The parameters determined from fitting the HSLA-100 test results were D = 1 (mm/mm/s) and m = 125. The power-law exponent of 125 represents a relatively low sensitivity to strain rate. The power-law, visco-plastic material response was used for the elastic-plastic analyses. An isothermal, visco-plastic stress-strain curve, corresponding to the specimen temperature at the point of crack arrest was used. This was necessary because the current version of Warp3D does not support a temperature-dependent specification of the power-law, visco-plastic stress-strain curve. It was assumed that strain rate effects would be more significant than thermal effects on the stress-strain curves.

Crack growth was modeled by using a prescribed node-release technique wherein an equivalent reaction force replaced the displacement constraint at the crack tip and the reaction force was linearly relaxed to zero over a fixed number of time steps. This is a generation-mode analysis where the crack length versus time history is explicitly enforced as a known boundary condition.

The domain integral technique was used to calculate the dynamic J-integral averaged over the crack front. Under general dynamic loading, the local value of the J-integral at a point along the crack front is given by:

$$J(s) = \lim_{\Gamma \to 0} \int_{\Gamma} \left[(W + T) n_1 - P_{ji} \frac{\partial u_i}{\partial X_1} n_j \right] d\Gamma \tag{2}$$

where W is the stress-work density and T is the kinetic energy density per unit volume, n is the unit normal vector to Γ, P_{ji} is the nonsymmetric 1st Piola-Kirchoff stress tensor, u the displacement vector and X are the local coordinate directions, and s is the local point on the crack front [15].

The J-integral is calculated in the Warp3D code using a domain integral formulation of Eq 2 in which the contour integral is converted into a volume integral by means of a weight function [14]. The domain integral formulation calculates J using the expression:

$$\begin{aligned} J = & \int_{V_0}\left(P_{ji}\frac{\partial u_i}{\partial X_k}\frac{\partial q_k}{\partial X_j} - W\frac{\partial q_k}{\partial X_k}\right) dV_0 \\ & -\int_{V_0}\left(\frac{\partial W}{\partial X_k} - P_{ji}\frac{\partial^2 u_i}{\partial X_j \partial X_k}\right) q_k dV_0 \\ & -\int_{V_0}\left(T\frac{\partial q_k}{\partial X_k} - \rho\frac{\partial^2 u_i}{\partial t^2}\frac{\partial u_i}{\partial X_k}q_k + \rho\frac{\partial u_i}{\partial t}\frac{\partial^2 u_i}{\partial t \partial X_k}q_k\right) dV_0 \end{aligned} \tag{3}$$

where q_k is a component of the vector weight function in the k coordinate direction, and ρ is the material mass density. The domain integral formulation in Warp3D does not include the last term in the third integral of the expression above. This term is important for very high crack velocities but is expected to have a minimal contribution for the range of crack speeds considered in these analyses.

Computed J values were domain independent for analyses incorporating linear-elastic material models. This was not true for elastic-plastic analyses. Domains that pass through the plastic wake exhibit path dependence due to the nonproportional unloading in the plastic wake. Consequently, domains were specified to be remote from the crack tip so that they completely enclosed the plastic wake behind the advancing crack. J values calculated using remote domains were path independent for the linear and elastic-plastic analyses. A through-thickness average value of J was used in all of the results reported herein.

The J-integral was converted to an equivalent stress intensity using the relationship:

$$J = \mathcal{G} = \frac{K^2\left(1-\upsilon^2\right)}{E}A(\mathrm{v}) \tag{4}$$

where E is the elastic modulus, μ is Poisson's ratio, and $A(v)$ is a universal function of the crack velocity, v, given in [16] as

$$A(v) = \frac{v^2\alpha_d}{(1-\mathrm{v})c_s^2 D} \tag{5}$$

where $D = 4\alpha_d\alpha_s - (1+\alpha_s^2)^2$ and $\alpha_d = \sqrt{1-v^2/c_d^2}$, $\alpha_s = \sqrt{1-v^2/c_s^2}$ and c_d and c_s are the elastic dilatational and shear wave speeds, respectively. $A(v)$ goes to 1 as the crack velocity goes to zero and increases monotonically with crack speed.

In all of the results presented in this paper, the dynamic stress intensity factor is only computed at time steps corresponding to a complete increment of crack extension—that is, when restraint forces at the crack tip node have been completely relaxed to zero. Other investigations have reported an instantaneous reduction in J followed by monotonic increase in J as the node is progressively released and recommended using a J value averaged over the load-relaxation steps [17]. No such periodic response was noted in these analyses; however, the J values do exhibit considerable noise, especially for higher crack velocities. This is attributed to the acceleration term in the domain integral formulation that involves higher order derivatives of the displacements, which are affected by the numerical approximations inherent in the finite element method.

Preliminary analyses were performed using both plane strain and 3-D meshes to quantify the effects of element size along the crack plane, the number of unload steps per increment of crack growth, the modeling of the pin-loading, crack velocity, and material constitutive models on the specimen response.

The effect of element size was investigated by analyzing a series of linear elastic, 3-D models where the element size along the crack plane was varied from $0.004 \leq l/W \leq 0.017$, where l is the length of the element along the crack plane, which corresponds to the crack growth increment. The initial crack size was $a_0/W = 0.25$ with $W = 152$ mm and the thickness, $B = 25$ mm. A fixed remote displacement was specified to produce a load of 445 kN. The crack was extended 33 mm at a constant speed of 500 m/s and the crack tip reaction force was relaxed over 5 unload steps. There was no effect of element size on the calculated K_{ID} versus time over this range of element sizes.

The effect of the number of unload steps per increment of crack growth was investigated by comparing an analysis of an elastic-plastic, 3-D model with 5 and 100 unload steps per increment of crack growth. The crack speed was constant at 400 m/s, and the crack growth increment was $l/W = 0.004$. The difference between the calculated K_{ID} versus time for the two analyses was less than 1.5 %.

A series of plane strain models were analyzed to investigate the effect of remote boundary conditions on the specimen response. Both quasi-static and dynamic crack growth situations were investigated. The quasi-static analyses were performed to establish a baseline for evaluating the dynamic specimen response. The standard solution for the SE(T) specimen [18] does not take into account the pin hole and will not provide an accurate solution for K as the crack extends under fixed grip conditions. This is due to the effect of the remote specimen compliance due to the pinhole and to interactions between the loading pin and the specimen. The plane strain analyses showed that it was necessary to model the remote loading using a contact boundary condition at the pinhole. The normalized crack driving force is plotted versus crack extension for the Tada solution and for the finite element model assuming a contact boundary condition between a rigid pin and the specimen in Fig. 10. The Tada solution assumes a much stiffer specimen response than is the case when the specimen is loaded by a pin through a hole. Consequently, the Tada solution under predicts the increase in driving force with crack extension under fixed grip conditions. The finite element and the Tada solutions are in much better agreement under fixed load conditions because the specimen compliance at the hole does not affect the driving force. The contact boundary condition is also required for the dynamic case because the inertia of the specimen may cause the specimen to lose contact with the loading pin during the crack propagation event. A fixed displacement on the hole boundary would artificially restrict the specimen motion.

A series of plane strain analyses was performed to investigate the effect of crack velocity on the dynamic stress intensity and crack arrest behavior. The SE(T) specimen had an initial crack length, $a_0/W = 0.25$ with a remote applied displacement that produced a force of 1.3 MN and an initial stress intensity equal to 197 MPa-$m^{1/2}$. The element size along the crack plane was 0.635 mm (l/W = 0.004) and 5 unload steps were specified per increment of crack extension. The crack was extended a distance of 64 mm assuming a constant velocity of 500, 1000, and 1500 m/s and was abruptly arrested. This range of crack speeds is typical of those reported in the literature for brittle cleavage cracks in steel. The dynamic stress intensity as a function of time for each case is plotted in Fig. 11. Also plotted in the figure is the stress intensity assuming the quasi-static, fixed grip finite element solution for the case with crack speed of 1000 m/s.

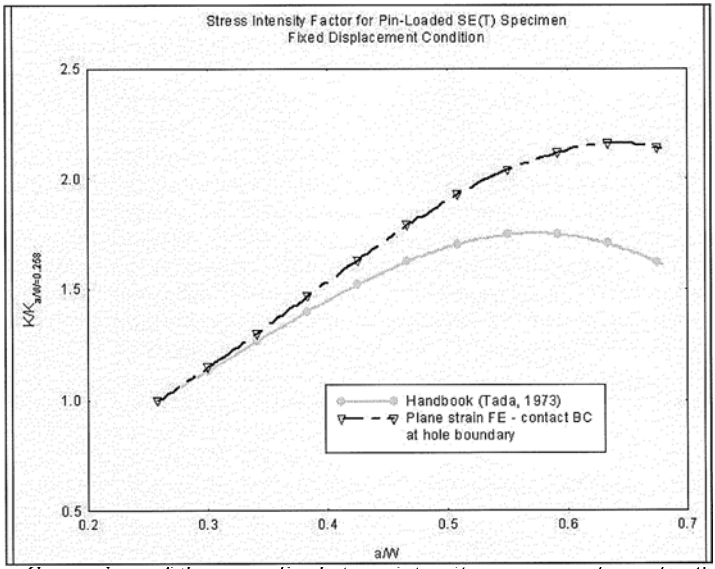


FIG. 10—*Comparison of the normalized stress intensity versus crack size for the handbook solution [18] and the finite element analysis with a contact boundary condition at the pin-hole interface.*

Some general observations can be made about the dynamic response of the SE(T) specimen. Immediately upon initiation, the stress intensity factor drops on the order of 10–45 %; the exact amount of reduction depends upon the crack speed. The reduction in the stress intensity is a result of stored elastic energy being converted into kinetic energy. Higher crack velocities lead to lower values for the crack driving force during dynamic crack propagation. As the crack propagates at the prescribed velocity, the driving force increases gradually but is well below the quasi-static, fixed grip solution. It is clear that a static analysis is of little use for predicting the dynamic response of the SE(T) specimen. Immediately after the last increment of crack growth corresponding to arrest, the stress intensity exhibits a step-like, rapid increase with some oscillation and then continues to rise more gradually as the specimen begins to ring as shown in Fig. 11. The stress intensity at crack arrest is slightly influenced by the assumed crack velocity.

The step increase in the driving force at crack arrest and the oscillations lead to considerable uncertainty in the determination of the crack arrest toughness and call into question the assumption of an abrupt arrest. If the arrest event is indeed as abrupt as assumed in these analyses, it is not clear which value of fracture toughness, that immediately prior to arrest or immediately after arrest, to designate as K_a. This is discussed further later in the paper.

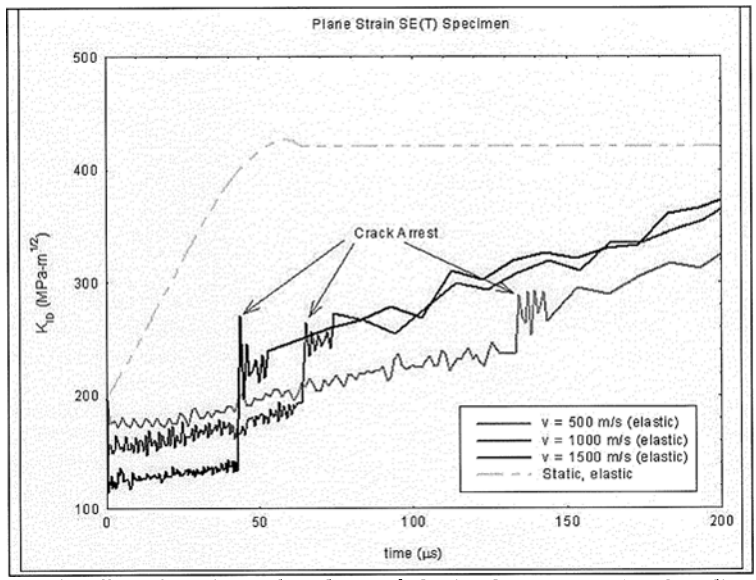


FIG. 11—*The effect of crack speed on the crack driving force versus time for a linear-elastic, plane strain analysis of the SE(T) specimen.*

The effect of plasticity on the crack driving force is illustrated in Fig. 12 for the case with an assumed crack speed of 1000 m/s. In general, the results are very similar to the linear elastic case. The visco-plastic material response tends to dampen out some of the calculated oscillations in the driving force but has very little effect on the magnitude of the crack arrest toughness. The greatest effect of plasticity in this instance occurs at initiation. There is considerable crack tip plasticity such that the plastic contribution to the driving force at initiation increases the magnitude of the driving force at initiation by about 8 % for the same initiation load. The initial crack tip plasticity does not influence the stored elastic energy in the specimen that is available to drive the crack and, within 20 μs after initiation, the driving force has dropped down to nearly the same level as in the elastic case. For the highest velocity considered, 1500 m/s, the reduction in crack driving force due to plasticity is more significant, around 10 %.

The analyses described above assumed that the crack speed dropped instantaneously from a constant velocity to zero. There is very little data in the literature on detailed experimental observations of the crack speed history of arresting cleavage cracks in steel. The crack speed history of a dynamic cleavage crack from a wide plate crack arrest test in a reactor pressure vessel steel showed a monotonically decreasing crack speed as the crack propagated into tougher material [19]. Other experimental results from dynamic fracture tests on polymers and high

strength steels provide evidence of constant velocity crack propagation as well as monotonically decreasing velocity with crack extension [20] [21]. Plastic deformation at the crack tip absorbs energy during the crack run event, and it is reasonable to expect that the loss of energy will be accompanied by a decrease in crack speed. The exact relationship between the energy dissipation due to plastic deformation and crack velocity is unclear.

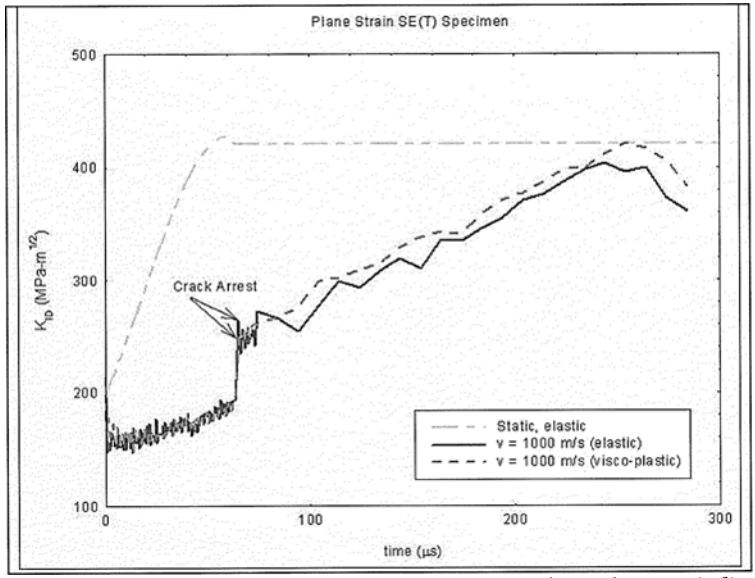


FIG. 12—*Comparison of the crack driving force versus time for a plane strain linear elastic and a visco-plastic finite element analysis with an assumed crack speed of 1000 m/s.*

The plane strain FE analyses above were repeated with the assumption that the crack speed was reduced by a factor of two over each of the last two increments of crack growth (0.625 mm per element) to see how this would affect the crack arrest toughness. The results are plotted in Fig. 13. The stress intensity increases rapidly as soon as the crack speed is reduced. Decelerating the crack causes the stress intensity to increase to the post arrest value over the last two increments of crack growth. This observation supports the idea that the correct value for the crack arrest toughness is the value of K just after arrest, even if the arrest is abrupt. The crack speed still has an effect on the crack arrest toughness and it is necessary to have an accurate means of determining the crack speed in order to determine the crack arrest toughness using the SE(T) specimen.

Validation of FE Analyses

A finite element analysis of a compact crack arrest specimen was performed as a validation of the modeling approach employed in this investigation. Experiments by Kalthoff et al. [20] employed the method of caustics to make direct experimental measurements of the dynamic stress intensity and crack speed in several crack arrest specimen geometries. The model material was a brittle epoxy resin, Araldite B. A transverse wedge loaded compact specimen was included

in his experiments and a linear elastic, plane strain finite model of the compact specimen was developed for analysis and comparison with the experimental results. The FE mesh modeled one half of the 250 × 250 × 10 mm specimen. The elements along the crack plane were 0.37 mm long (l/W = 0.0018) and crack growth was simulated by releasing the crack tip nodal forces over a sequence of five load steps. The crack speed was approximately constant at 200 m/s over the first 135 mm of growth and decreased to 70 m/s over the last 15 mm of growth, consistent with the measurements reported in [20].

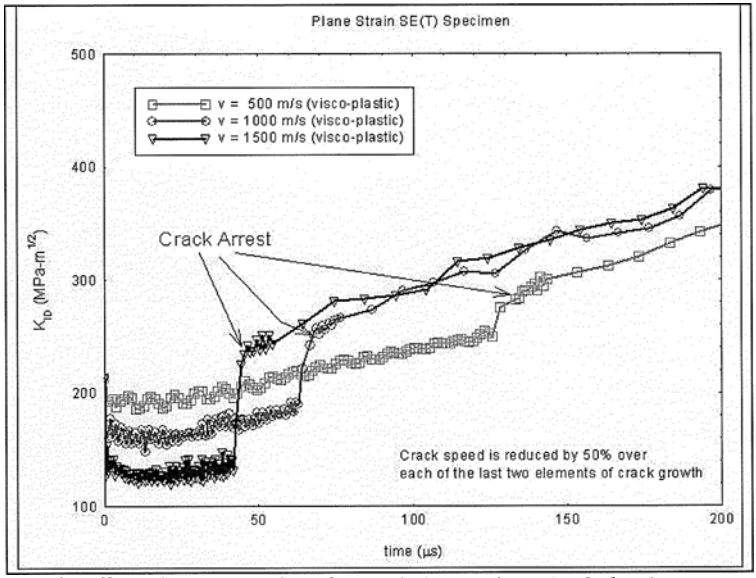


FIG. 13—*The effect of crack speed on the crack driving force (with deceleration over the last two increments of crack growth) for plane strain, visco-plastic finite element models of the SE(T) specimen.*

The original results from [20] are plotted in Fig. 14. The finite element results are plotted for comparison in Fig. 15. There is good qualitative agreement between the experimental results and the FE predictions. In both cases the dynamic stress intensity decreases below the static solution at initiation and subsequently crosses over above the static solution. At arrest, the static and dynamic solutions are in close agreement and after arrest the dynamic solution oscillates around the static solution. The FE solution does not exhibit as great a difference between the dynamic and static solutions as the experimental results just after initiation, and it also shows a greater difference between the static and dynamic solutions after they cross over. The overall agreement is fairly good and validates the FE approach used in this investigation.

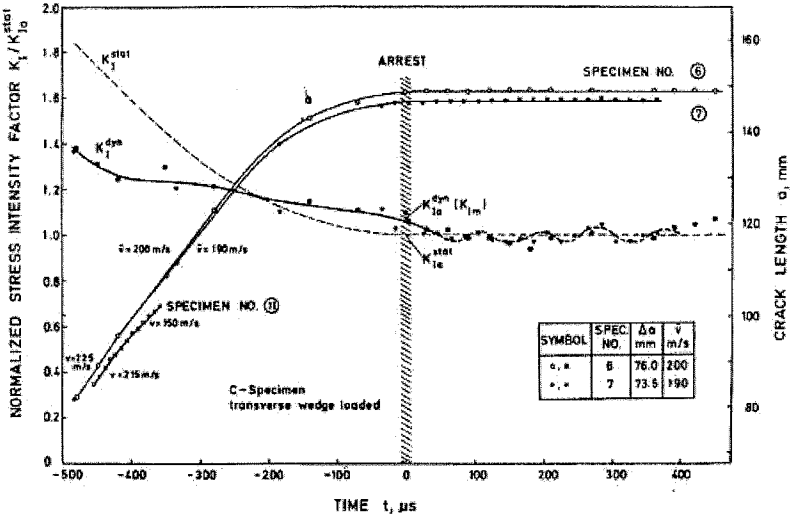


FIG. 14—*Normalized stress intensity and crack length versus time for a compact crack arrest specimen of a brittle polymer from [20].*

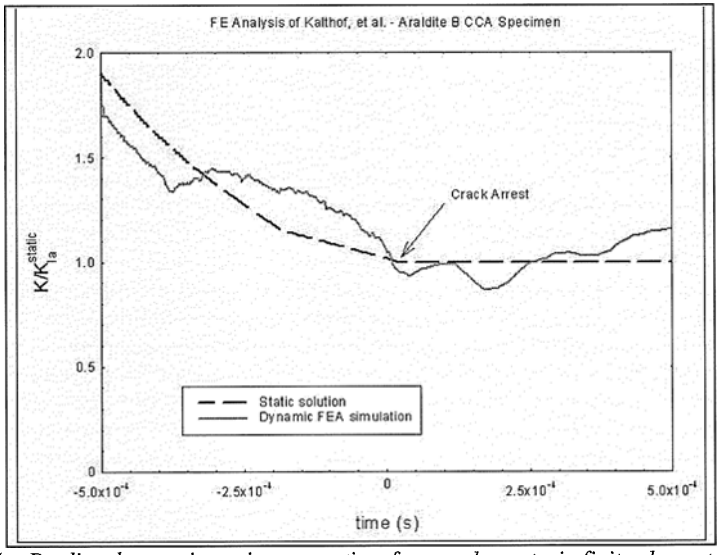


FIG. 15—*Predicted stress intensity versus time from a plane strain finite element analysis of a crack arrest experiment specimen with a brittle polymer from [20].*

FE Analysis of Crack Arrest Tests

A quarter-symmetric, three-dimensional finite element model of the actual SE(T) crack arrest specimens was developed to analyze the crack arrest tests. The model, shown in Fig. 16, had five layers of elements through the thickness and included side grooves. Elements along the crack plane had a length of 0.635 mm in the direction of crack growth ($l/W = 0.004$). The model had over 14 500 nodes and 11 000 elements. The thermal gradient was not explicitly modeled due to limitations of the FE code; instead, the specimen was assumed to be at a uniform temperature equal to the crack arrest temperature. The power-law, visco-plastic constitutive model for HSLA-100 described previously was used as the material model. The 2-D analyses presented earlier demonstrated that plasticity had little effect on the driving force, so ignoring the temperature dependence of the yield strength should introduce only small errors. The load was applied by specifying a fixed displacement of the rigid loading pin that produced the initiation force measured in the experiment. The pin displacement was held constant during the simulation and the contact condition at the pin was included in the analysis. Dynamic crack growth was modeled by prescribed release of the crack tip nodal reaction forces over a series of five time steps per element of crack advance. The crack speed was held constant during the crack propagation stage until the last two elements of crack growth, when the crack speed was reduced by 50 % over each element.

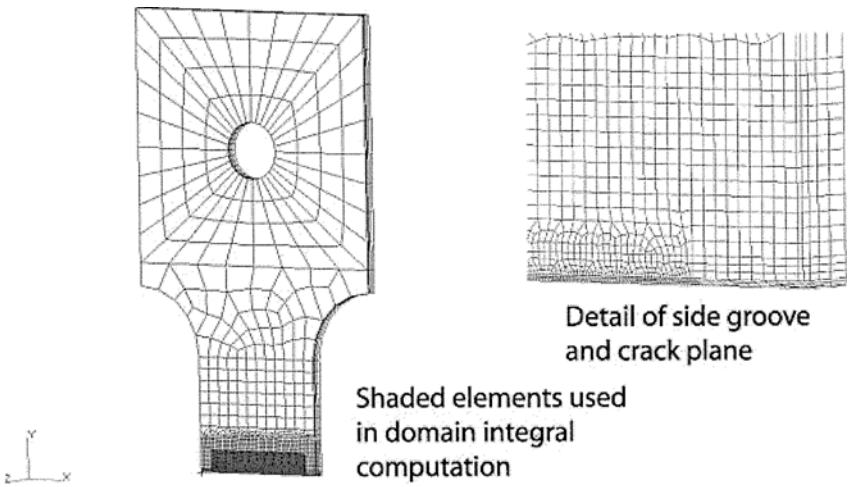


FIG. 16—*Quarter-symmetric, three-dimensional finite element mesh used in analysis of crack arrest tests of the SE(T) specimen.*

The selection of the particular crack speed for each experiment was based on the available experimental data from each test. For Specimen GLC-502, the initiation load was not known but local strain gage data were available to determine the proper boundary conditions. The initiation load prescribed in the FE analysis was selected by matching the peak strain reading from the single element strain gage nearest the crack tip with the FE results. The crack speed was selected

by comparing the FE predicted dynamic strain response with the experimentally measured strains over the complete run-arrest event. An initiation load of 598 kN and a crack speed of 360 m/s were ultimately selected for this specimen. The crack speed is slightly lower than the initial estimate based only on the strain peaks.

The initiation load was known to be 1.3 MN for Specimen GLC-501, but there were no strain data to determine the actual crack speed during this experiment. The crack speed had to be assumed and a value of 600 m/s was selected based on the crack speed versus driving force behavior of a reactor pressure vessel steel reported by Schwartz and Bass [22]. This crack speed corresponds to a similar stress intensity and temperature (relative to the T_o reference temperature) for the RPV steel compared to the HSLA-100. Based on the plane strain results presented earlier, the crack speed has a greater effect on the dynamic stress intensity factor than on the arrest toughness. The difference between the true crack speed in this test and the assumed value is expected to be relatively small, and small changes in the crack speed will have little effect on the calculated crack arrest toughness.

The predicted dynamic stress intensity versus time for Specimen GLC-502 is plotted in Fig. 17. The crack arrest toughness was calculated to be K_{IA} = 129 MPa-m$^{1/2}$ at a temperature of −62°C. The predicted local strain response is compared with the experimental strains in Fig. 18. There is excellent agreement between the predicted and measured response of the first three gages and good qualitative agreement for the next two gages. The general characteristics of the predicted strain response of Gages 4 and 5 match the experimental results but the exact magnitudes are slightly different. The close correspondence of the predicted and measured specimen response leads to a high confidence in the accuracy of the modeling.

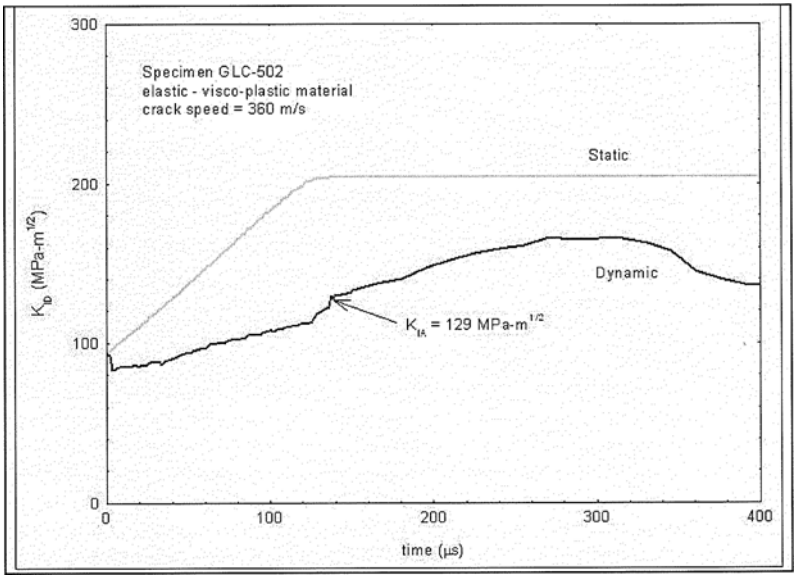


FIG. 17—*Finite element prediction of the stress intensity versus time for Specimen GLC-502 from a static and dynamic analysis.*

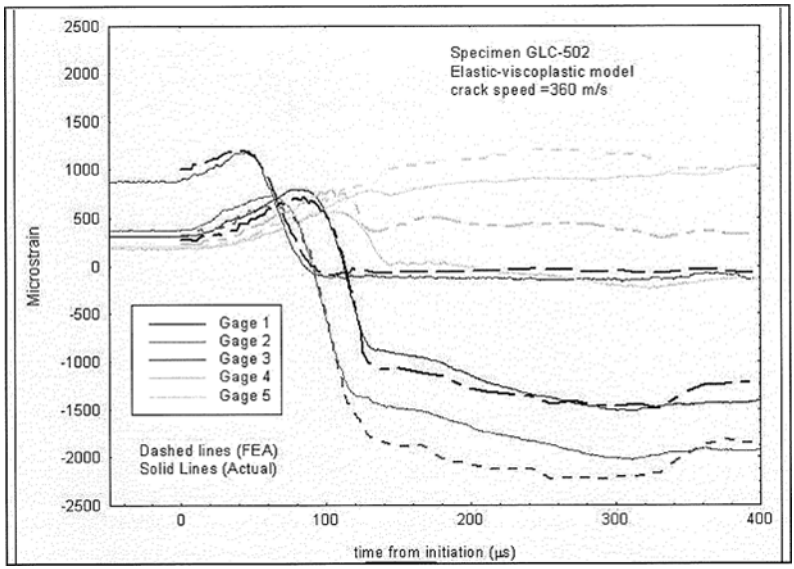


FIG. 18—*Comparison of predicted and measured strain response from gages located along the crack path for Specimen GLC-502.*

The predicted dynamic stress intensity versus time for Specimen GLC-501 is shown in Fig. 19. The crack arrest toughness was calculated to be K_{IA} = 285 MPa-m$^{1/2}$ at a temperature of – 44°C. The driving force continues to increase after crack arrest as the kinetic energy in the specimen is converted to strain energy and the plasticity accumulates at the arrested crack tip. Very soon after arrest, the driving force exceeds the static ductile initiation toughness for the HSLA-100, which is K_{JIc} = 290 MPa-m$^{1/2}$, and the arrested crack would be expected to begin tearing. In the actual test, the arrested cleavage crack did reinitiate in a ductile tearing mode after the initial crack arrest, consistent with the FE prediction. The ductile tearing response of the specimen was not modeled in this investigation. It is recognized that the dynamic ductile fracture toughness corresponding to the post-arrest crack tip-loading rate is expected to be higher that the static value—on the order of 10–20 %, but ductile tearing is still expected.

Discussion

The crack arrest fracture toughness measured in the SE(T) specimen is based on the value of the stress intensity immediately after crack arrest, K_{IA}, (within 1 μs) compared with the compact crack arrest specimen, which relies on the value of the stress intensity factor calculated a much longer time (1 ms) after arrest and is designated K_{Ia}. The stress intensity 1 ms after arrest in the compact specimen is a good approximation of the value at the instant of crack arrest, K_{IA}, but is not a useful parameter in the SE(T) specimen. Examination of the post-arrest behavior of the

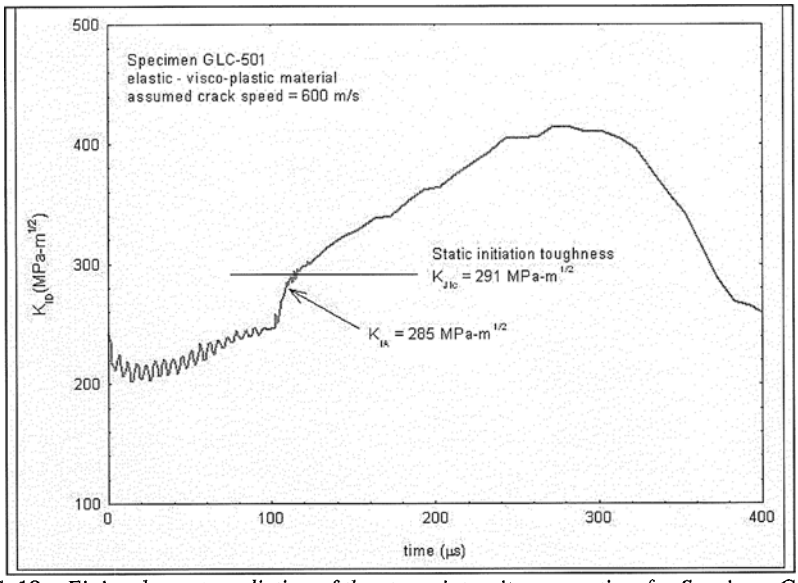


FIG. 19—*Finite element prediction of the stress intensity versus time for Specimen GLC-501 from a dynamic analysis with an assumed crack speed of 600 m/s.*

SE(T) specimen shows that there are considerable dynamic effects continuing in the SE(T) specimen that cause great variations in the stress intensity factor as the specimen rings down. The finite element results predict that there is a loss of contact between the specimen and the loading pin about 100 μs after crack arrest as a result of specimen inertia. Pin contact is subsequently re-established, but those details were not relevant to the dynamic crack propagation and arrest behavior.

Crack front curvature can be a problem in both the SE(T) and compact crack arrest specimens. For one of the tests, GLC-501, the arrested crack front had considerable curvature that was not modeled in the finite element analysis. The crack was assumed to advance with a uniform crack front and the arrested crack length was based on a nine-point average of the actual arrested crack front. A more detailed analysis of the effects of crack curvature on the stress intensity may provide additional insight on the mechanics of crack arrest but was outside the scope of the present investigation.

The visco-plastic material response was demonstrated to have little effect on the crack driving force calculations for the range of crack speeds encountered in these tests compared to a linear elastic material response. The main effect of the visco-plastic material model on the crack driving force was to dampen the numerical oscillations in the stress intensity factor. The plastic zone and plastic wake at the instant of crack arrest on the center-plane in Specimen GLC-501 is shown in Fig. 20. The crack tip plastic zone extends a considerable distance ahead of the crack tip (r/W = 0.1) along the crack plane and reaches a similar distance above the crack plane. The crack tip plastic zone expands rapidly after crack arrest as much of the remaining elastic and kinetic energy in the specimen is dissipated in plastic deformation. The effective strain rate

computed at a node just above the crack plane reached a peak of 10^4/s. The true peak strain rate may be an order of magnitude higher because this value was averaged over 5 time steps corresponding to one element of crack advance. Theoretical models of the strain rates accompanying rapid crack advance estimate strain rates on the order of 10^3–10^6 /s [23].

The analysis did not incorporate the effects of adiabatic heating in the modeling. Adiabatic heating may play an important role on the local crack tip plasticity by elevating the local temperature and partially offsetting increased strength due to the high strain rates. Based on the small effect of plasticity on the computed driving force for the crack speeds considered in these analyses, adiabatic heating is expected to have a similarly small effect on the driving force calculations.

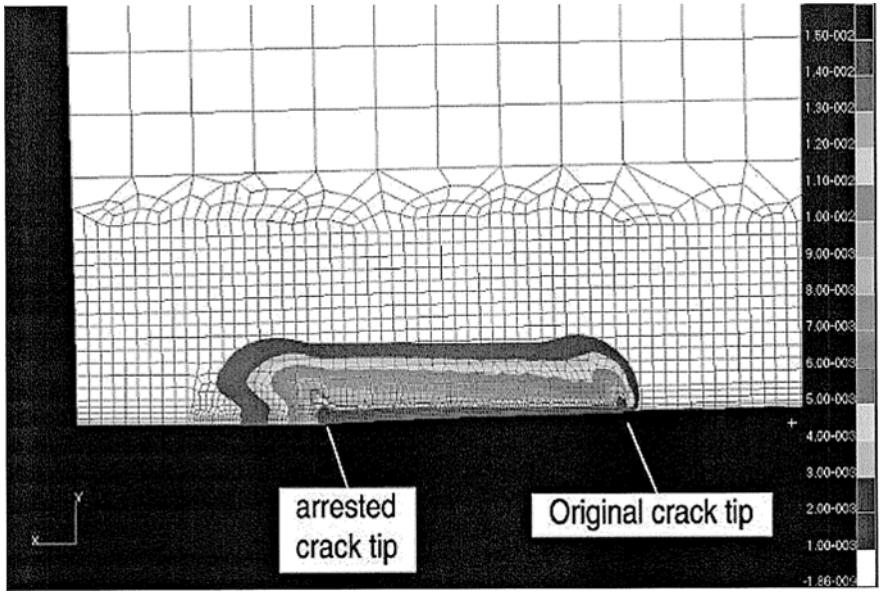


FIG. 20—*Contours of the effective plastic strains along the center plane of the SE(T) specimen at the instant of crack arrest for Specimen GLC-501. The initial plastic zone and the plastic wake accompanying crack growth are apparent.*

The SE(T) specimen is small enough that reflected stress waves can interact with the crack tip during the dynamic crack propagation phase of the test. The transit time for a longitudinal wave to reflect from the back edge of the specimen and return to the crack tip is approximately 38 μs. The run-arrest event for Specimen GLC-501 took about 112 μs, so there was time for several wave reflections from the back edge of the specimen. There was no distinct effect of the reflected stress waves on the crack driving force in Fig. 17. The time required for the first longitudinal wave to reflect from the loading pins and return to the crack tip was about 140 μs, which occurs after crack arrest. The reactions at the load pin did begin to drop at a time of 70 μs, corresponding to the arrival of the first stress waves. It is not clear if the stress waves

reflected from the back wall influence the crack arrest behavior of the specimen, but their effect on the driving force was included in the computation of the domain integral.

The crack arrest toughness was measured at only two temperatures in this investigation, but it is still possible to predict the crack arrest toughness-temperature behavior of HSLA-100 by employing the crack arrest master curve concept. Wallin has shown that the same master curve approach used to characterize the ductile-brittle transition for initiation fracture toughness, K_{Jc}, can be applied to the crack arrest fracture toughness [24]. The master curve equation used for initiation characterizes the crack arrest toughness with the use of a crack arrest reference temperature, T_{KIa}, replacing the standard reference temperature, T_o. The mean crack arrest fracture toughness is given by the expression:

$$K_{Ia} = 30 + 70\exp\left\{0.019\left(T - T_{KIa}\right)\right\} \tag{6}$$

where T_{KIa} is the temperature corresponding to a mean crack arrest toughness of 100 MPa-$m^{1/2}$. Furthermore, the scatter in the crack arrest toughness follows a log-normal distribution instead of a 3-parameter Weibull distribution, and there is no statistical size adjustment made to the data in the case of crack arrest.

A rough approximation of the crack arrest reference temperature for HSLA-100 was made from the two available data points using an equation based on the maximum likelihood approach from [5].

$$\sum_{i=1}^{n} \frac{\ln K_i \cdot \exp\left\{0.019\left[T_i - T_{KIa}\right]\right\}}{30 + 70 \cdot \exp\left\{0.019\left[T_i - T_{KIa}\right]\right\}} - \sum_{i=1}^{n} \frac{\ln\left(30 + 70 \cdot \exp\left\{0.019\left[T_i - T_{KIa}\right]\right\}\right) \cdot \exp\left\{0.019\left[T_i - T_{KIa}\right]\right\}}{30 + 70 \cdot \exp\left\{0.019\left[T_i - T_{KIa}\right]\right\}} = 0 \tag{7}$$

where K_i is the arrest toughness at T_i for the ith specimen and n is the number of specimens. The standard deviation, σ, on the distribution of K_{Ia} is given by [5]:

$$\sigma^2 = \frac{\sum_{i=1}^{n}\left\{\ln K_i - \ln\left(30 + 70 \cdot \exp\left\{0.019\left[T_i - T_{KIa}\right]\right\}\right)\right\}^2}{n} \tag{8}$$

Note that this equation is different from that specified in E 1921 because the data are assumed to follow a log-normal distribution instead of a normal distribution. The equation was solved iteratively for T_{KIa} yielding a result of $T_{KIa} = -97°C$ and $\sigma = 0.252$. No data censoring was used in estimating T_{KIa}. Since T_{KIa} was based on only two data points, the uncertainty in T_{KIa} is expected to be large, probably on the order of 15°C. The resulting crack arrest master curve and 5 % and 95 % tolerance bounds are plotted in Fig. 21 along with the initiation toughness master curve and the cleavage data initiation data points from Fig. 3. The shift in the master curve, $(T_{Kia}-T_o)$, was estimated to be 63°C for the HSLA-100 steel plate used in this investigation.

The results presented in this paper demonstrate that the SE(T) specimen is a viable specimen for studying the dynamic fracture and crack arrest behavior of ferritic alloys in the upper transition region. The test procedure and analysis are considerably more complex than that of the compact crack arrest specimen used in E 1221. There are several disadvantages to the SE(T) specimen compared with the compact crack arrest specimen: the specimen is larger, complex instrumentation and analysis of dynamic specimen response is required, a thermal gradient must be established and controlled, and the cost of testing is significantly higher. Specific validity criterion to demonstrate that the arrest toughness values are insensitive to the specimen geometry have not been addressed in this study. Nevertheless, the instrumented SE(T) specimen is a useful tool for studying dynamic crack propagation and arrest in the upper transition region.

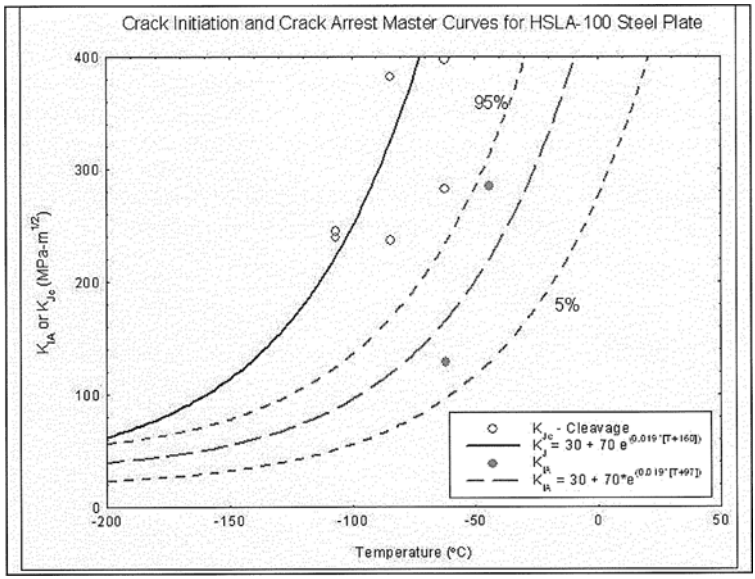


FIG. 21—*Crack initiation and crack arrest master curves for the HSLA-100 steel plate used in this investigation.*

Summary and Conclusions

A relatively small SE(T) specimen with an applied thermal gradient was shown to be a useful specimen for measuring the crack arrest fracture toughness of an HSLA steel plate in the ductile-brittle transition region. The SE(T) specimen exhibited considerably more dynamic effects on the crack driving force than the standard compact crack arrest specimen and required measurement of the crack length versus time coupled with a dynamic finite element analysis to calculate the crack arrest toughness. The effects of crack speed, visco-plastic material response, and other modeling parameters on the dynamic and crack arrest fracture toughness were characterized. There was excellent agreement between the transient strains predicted by the finite element model and the measured strain response from gages located along the crack path. The crack arrest reference temperature, T_{Kla}, was estimated to be –97°C and the shift in the reference

temperature between the static initiation and crack arrest master curves was estimated to be 63°C for the HSLA-100 steel plate used in this investigation.

Acknowledgments

The author would like to acknowledge the support of Mr. Gerard Mercier at the Naval Surface Warfare Center, Carderock Division in sponsoring this work and Prof. R. Dodds, Jr., Univeristy of Illinois, for valuable discussions on the modeling aspects of the investigation and the Warp3D software program.

References

[1] Crosley, P. B., Fourney, W. L., Hahn, G. T., Hoagland, R. G., Irwin, G. R., and Ripling, E. J., "Final Report on Cooperative Test Program on Crack Arrest Toughness Measurements," NUREG/CR-3261, U.S. Nuclear Regulatory Commission, Washington, D.C., April 1983.

[2] Barker, D. B., Chona, R., Fourney, W. L., and Irwin, G. R., "A Report on the Round-Robin Program Conducted to Evaluate the Proposed ASTM Standard Test Method for Determining the Plane Strain Crack Arrest Fracture Toughness, KIa, of Ferritic Materials," NUREG/CR-4996, U.S. Nuclear Regulatory Commission, Washington, D.C., January 1988.

[3] Pussegoda, L. N., Malik, L., and Morrison, J., "Measurement of Crack Arrest Fracture Toughness of a Ship Steel Plate," *Journal of Testing and Evaluation*, Vol. 26, No. 3, May 1998, pp. 187–197.

[4] Burch, I. A., Ritter, J. C., Saunders, D. S., Underwood, J. H., "Crack Arrest Fracture Toughness Testing of Naval Construction Steels," *Journal of Testing and Evaluation*, Vol. 26, No. 3, May 1998, pp. 269–276.

[5] Slater, S., et al., "An Energy Balance Approach to Crack Arrest," European Commission Report, EUR-20952EN, The European Commission, 2004.

[6] Crosley, P. B. and Ripling, E. J., "A Quality Control Test for Materials to Arrest Fast Running, Full Thickness Cracks," *Journal of Testing and Evaluation*, Vol. 18, 1990, pp. 396–400.

[7] Naus, D. J., et al., "Crack-Arrest Behavior in SEN Wide Plates of Quenched and Tempered A533 Grade B Steel Tested Under Nonisothermal Conditions," NUREG/CR-4930, U.S. Nuclear Regulatory Commission, Washington, D.C, August 1987.

[8] Naus, D. J., et al., "High-Temperature Crack-Arrest Behavior in 152-mm-Thick SEN Wide Plates of Quenched and Tempered A533 Grade B Class 1 Steel," NUREG/CR-5330, U.S. Nuclear Regulatory Commission, Washington, D.C., April 1989.

[9] Berger, J. R., Dally, J. W., deWitt, R., and Fields, R. J., "A Strain Gage Analysis of Fracture in Wide Plate Tests of Reactor Grade Steel," *Journal of Pressure Vessel Technology*, Transactions ASME, Vol. 115, November 1993, pp. 398–405.

[10] Czyryca, E. J., Link, R. E., Wong, R. J., Aylor, D. A., Montemarano, T. W., and Gudas, J. P., "Development and Certification of HSLA-100 Steel for Naval Ship Construction," *Naval Engineers Journal*, May 1990, pp. 63–82.

[11] Wilson, A. D., Hamburg, E. G., Colvin, D. J., Thompson, S. W., and Krauss, G., "Properties and Microstructures of Copper Precipitation Aged Plate Steels," *Proceedings of Microalloying 1988*, World Materials Congress, American Society for Metals, Metals Park, OH, September 1988.

[12] Dally, J. W. and Sanford, R. J., "Strain Gage Methods for Measuring the Opening Mode Stress Intensity Factor, KI," *Experimental Mechanics*, Vol. 27, No. 4, 1987, pp. 381–388.

[13] Berger, J. R., Dally, J. W., and Sanford, R. J., "Determining the Dynamic Stress Intensity Factor with Strain Gages Using a Crack Tip Locating Algorithm," *Engineering Fracture*

Mechanics, Vol. 36, No. 1, 1990, pp. 145–156.

[14] Gullerud, A. S., Koppenhoefer, K. C., Roy, A., and Dodds, R. H., Jr., "Warp3D: 3-D Dynamic Nonlinear Fracture Analysis of Solids Using Parallel Computers and Workstations," Report No. UILU- ENG-95-2012, University of Illinois, February 2004.

[15] Eshelby, J. D., "Energy Relations and the Energy Momentum Tensor in Continuum Mechanics," *Inelastic Behavior of Solids*, M. F. Kanninen, et al., Eds., McGraw- Hill, NY, 1970.

[16] Freund, L. B., *Dynamic Fracture Mechanics*, Cambridge University Press, 1990.

[17] Lo, C. Y. and Nakamura, T., "Computational Analysis of Dynamically Propagating Cracks in Axisymmetric Solids," *International Journal of Fracture*, Vol. 70, 1995, pp. 217–235.

[18] Tada, H., et al., *The Stress Analysis of Cracks Handbook,* Del Research Corporation, Lehigh, PA, 1973.

[19] Berger, J. R., Dally, J. W., deWitt, R., and Fields, R. J., "A Strain Gage Analysis of Fracture in Wide Plate Tests of Reactor Grade Steel," *Journal of Pressure Vessel Technology*, Transactions ASME, Vol. 115, November 1993, pp. 398–405.

[20] Kalthoff, J. F., Beinert, J., Winkler, S., and Klemm, W., "Experimental Analysis of Dynamic Effects in Different Crack Arrest Test Specimens," *Crack Arrest Methodology and Applications, ASTM STP 711*, G. T. Hahn and M. F. Kanninen, Eds., ASTM International, West Conshohocken, PA, 1980, pp. 109–127.

[21] Kobayashi, T. and Dally, J. W., "Dynamic Photoelastic Determination of the a(dot)-K Relation for 4340 Alloy Steel," *Crack Arrest Methodology and Applications, ASTM STP 711*, G. T. Hahn and M. F. Kanninen, Eds., ASTM International, West Conshohocken, PA, 1980, pp. 189–210.

[22] Schwartz, C. W. and Bass, B. R., "Crack Speed Relations Inferred from Large SEN Specimens of A533B Steel," *Engineering Fracture Mechanics*, Vol. 34, No. 5/6, 1989, pp. 1209–1223.

[23] Freund, L. B. and Hutchinson, J. W., "High Strain Rate Crack Growth in Rate-Dependent Solids," *Journal of the Mechanics and Physics of Solids*, Vol. 33, 1985, pp. 169–191.

[24] Wallin, K., "Application of the Master Curve Method to Crack Initiation and Crack Arrest," ASME Pressure Vessel and Piping Symposium, PVP-Vol. 393, American Society of Mechanical Engineers, August 1999, pp. 3–9.

Journal of ASTM International, Vol. 3, No. 6
Paper ID JAI100337
Available online at www.astm.org

Stephen M. Graham[1]

Application of the Normalization Method to Dynamic Fracture Toughness Testing of Alloy 718

ABSTRACT: The fracture toughness and tensile properties of Alloy 718 were measured at quasi-static and dynamic loading rates for two different heat treatments and two product forms. Two different methods for conducting the dynamic tests were investigated; one involving interrupted tests and the other utilizing a single impact. The interrupted test method used multiple impacts with displacement limits to enable measurement of crack lengths at intermediate points. The normalization method was used to generate tearing resistance curves for the dynamic tests following the guidelines in ASTM Standard Test Method for measurement of Fracture Toughness (E 1820). The analysis pointed out the importance of obtaining a good measurement of load, displacement, and crack length at the point of maximum displacement (the anchor point). As the amount of ductile crack extension increased, the uncertainty in the plasticity function fit also increased. Methods to improve the fit were investigated, including the addition of anchor points from multiple tests, and use of a tangency point to estimate initiation. The resulting curves are compared to ascertain the variability obtained from nominally identical specimens, and to evaluate the effect of loading rate on the plasticity function. The normalization tearing resistance curves are compared with curves generated from the interrupted tests using compliance measurements during unloads to determine crack extension. Good agreement was obtained between the two methods of measuring tearing resistance, thereby validating the normalization analysis. The tests showed that multiple impacts drive down the tearing resistance, which may be significant in applications where a dynamic event causes load fluctuation.

KEYWORDS: dynamic fracture toughness, Normalization method, Alloy 718

Introduction

Alloy 718 is a precipitation-hardenable nickel-chromium alloy composed of about 52 % nickel, 20 % iron, 18 % chromium, 5 % niobium, and 3 % molybdenum, along with lesser amounts of aluminum and titanium. This alloy is particularly attractive for many marine applications due to its corrosion resistance and high yield strength. However, fracture testing of this alloy has shown that its fracture toughness is very sensitive to the heat treatment and resulting microstructure [1–4]. In one particular study that conducted quasi-static tests on plate, bar, and forgings [2], fracture toughness values for a 954°C (1750°F) anneal heat treatment ranged from about 105 to 131 MPa$\sqrt{m}$, while for a 1093°C (2000°F) anneal they ranged from about 156 to 188 MPa$\sqrt{m}$. All of the tests in this study were conducted at quasi-static loading rates. There is no information in the open literature on the effect of loading rate on the fracture toughness of this alloy.

The objective of this test program was to measure the dynamic fracture toughness of Alloy 718 for forging and rod product forms in two different heat treatments and orientations. Specimen blanks cut from a rod and a forging were re-solution treated and aged according to AMS 5662, which uses a 968°C (1775°F) solution heat treatment and AMS 5664, which uses a 1066°C (1950°F) solution heat treatment. In total there were six groups of fracture toughness specimens and four groups of tensile specimens representing the two product forms, two heat treatments, and two orientations (forging only). Tests were conducted to characterize the effect of loading rate on fracture toughness and tensile properties at quasi-static and dynamic loading rates (maximum load in approximately 3 ms). All of the tensile tests and most of the fracture toughness tests were conducted at −2 °C (28°F).

Manuscript received March 31, 2005; accepted for publication April 13, 2006; published online May 2006. Presented at ASTM Symposium on Fatigue and Fracture Mechanics on 18–20 May 2005 in Reno, NV; R. E. Link and K. H. Nikbin, Guest Editors.
[1] Assistant Professor, United States Naval Academy, Annapolis, MD 21402.
Copyright © 2006 by ASTM International, 100 Barr Harbor Drive, PO Box C700, West Conshohocken, PA 19428-2959.

TABLE 1—*Summary of average tensile properties.*

Product/Heat Treatment	Loading Rate	Avg.Yield Strength MPa (ksi)	Avg.Ultimate Strength MPa (ksi)	Avg. Reduction of Area (%)	Avg. Percent Elongation (%)
Forging / AMS 5662	Quasi-Static	981(142.3)	1349(195.6)	15.6	10.9
	Intermediate[a]	1025(148.6)	1440(208.9)	23.1	11.8
	Dynamic	1071(155.4)	1464(212.3)	19.8	14.4
Forging/ AMS 5664	Quasi-Static	1225(177.7)	1385(200.9)	30.6	18.0
	Intermediate[a]	1311(190.2)	1458(211.5)	30.6	14.2
	Dynamic	1329(192.8)	1510(219.0)	31.0	15.6
Rod / AMS 5662	Quasi-Static	1144(165.9)	1427(207.0)	39.8	22.6
	Dynamic	1209(175.3)	1492(216.4)	41.5	20.4
Rod / AMS 5664	Quasi-Static	1125(163.2)	1367(198.3)	40.1	24.1
	Dynamic	1207(175.1)	1442(209.1)	41.9	20.6

[a]Results from single test.

Tensile Tests

Tensile tests were conducted at dynamic strain rates of about 2×10^7 $\mu\varepsilon/s$. At this rate, yielding occurred in about 0.4 ms. Limited tests were also conducted at intermediate (1.5×10^6 $\mu\varepsilon/s$) and quasi-static (60 $\mu\varepsilon/s$) loading rates to evaluate the effect of loading rate on yield strength.

The results of the tensile tests are presented in Table 1. Rate does not have a significant effect on tensile properties for this alloy at the temperature, and over the range of strain rates, investigated. There is about an 8 % increase in yield strength and a 9 % increase in ultimate strength as the strain rate is increased five orders of magnitude.

Fracture Toughness Tests

Fracture toughness tests were conducted at quasi-static and dynamic loading rates to investigate the effect of loading rate on fracture initiation toughness and tearing resistance. The quasi-static tests were conducted according to ASTM Standard Test Method for Measurement of Fracture Toughness (E 1820) in a closed loop servo-hydraulic test frame under computer control. The dynamic tests were conducted in a drop-tower following the recommendations of Annex A14 of E 1820, and the normalization analysis followed the guidelines in Annex A15. The specimens used in these tests were all 1T-C(T)s. Test temperature was either −2 °C (28°F) or 21°C (70°F).

Quasi-Static Fracture Toughness Tests

All of the AMS 5662 tests and three out of five AMS 5664 tests terminated by unstable fracture after some ductile crack growth. This was caused by a combination of decreasing tearing resistance and load train compliance. Representative load-displacement records for the four combinations of product and heat treatment are compared in Fig. 1. Relative fracture toughness can be inferred from the height and the area under the load-displacement curves. Based on this comparison, it is apparent that AMS 5664 gives higher fracture toughness for both product forms, which is consistent with the literature data [1], and that the rod has a higher toughness than the forging for both heat treatments.

Tearing resistance curves for the tests with significant ductile crack extension are shown in Fig. 2. The data from these tests were analyzed to determine J_{Ic} (Table 2). For the tests that terminated with instability it was not possible to identify the crack position at instability; consequently, it was not possible to conduct the validity checks on the final crack shape, crack extension, and accuracy of crack extension prediction. Comparison of the J_{Ic} values in Table 2 confirms that the rod has higher fracture toughness than the forging, and that AMS 5664 more than doubles the fracture toughness compared with AMS 5662.

Dynamic Fracture Toughness Tests

Test Procedure

The dynamic fracture initiation toughness, J_{Id}, is the value of crack driving force (in terms of the J-integral) where a pre-existing crack starts ductile growth under dynamic loading conditions. The primary

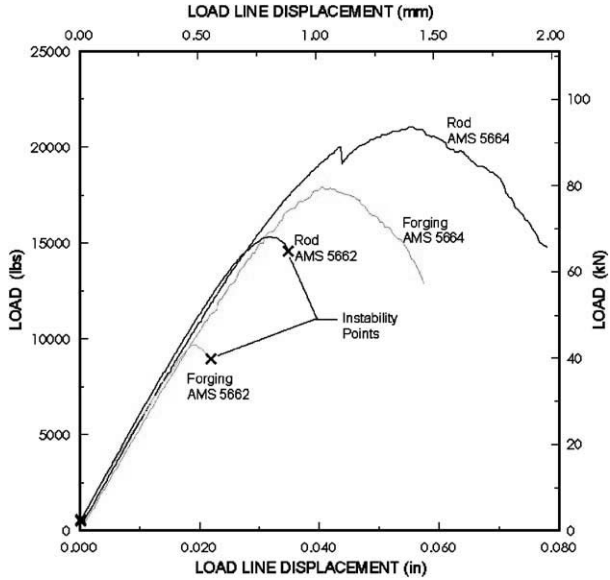


FIG. 1—*Representative load-displacement records for quasi-static fracture toughness tests (partial unloads have been removed).*

challenge in measuring J_{Id} is to measure crack extension in real time during a test. In a quasi-static test the specimen is partially unloaded at periodic intervals during the test to determine crack length using compliance. It is difficult to conduct partial unloadings during a dynamic test, and it is practically impossible at very high loading rates. Therefore, either the test must be interrupted, or the crack extension must be inferred from other measurements made during the test. Both of these techniques were utilized in this investigation.

All of the dynamic fracture toughness tests were conducted at −2 °C (28°F) in a drop tower in order to achieve loading rates of 1 to 3 ms to peak load. The loading fixture for a compact tension [C(T)] specimen is shown schematically in Fig. 3. For these tests, the cross-head of the drop tower was dropped from a height of 762 mm, which provided an impact velocity of 3.9 m/s. The moving cross-head of the loading fixture was attached to the lower clevis through vertical rods. The maximum deflection imparted to the specimen was controlled by placing gage-blocks between the moving and stationary cross-heads of the fixture. The blocks stopped the downward travel of the moving cross-head. The height of the blocks was chosen through trial and error to obtain the desired load-line deflection at the specimen; however, deflection could not be controlled precisely because of the compliance of the various parts in the load train.

Load was measured directly on the specimen using strain gages bonded on the upper and lower faces of the specimen. The specimen was calibrated to read load directly by applying a known static load approximately equal to the maximum final pre-cracking load. This is not the ideal way to calibrate because the maximum load in a test is well above the maximum load used in calibration. To improve the confidence in the direct specimen load measurements, load was also measured at the lower clevis of the test fixture for some of the tests. This alternate load measurement provided verification of the specimen loads up to the maximum load in the test. For the tests where this alternate load measurement was made, the specimen and clevis loads were within 3 %. The clevis load measurement was not used for data analysis because there was a time delay due to wave propagation effects that introduced complications into the data analysis. Load-line displacement was measured directly on the specimen using a capacitive displacement transducer mounted in the notch of the specimen, as shown in FIG. A14.5 of ASTM E 1820. Further information on the details of the instrumentation and test procedure are reported in Ref. [5].

As mentioned previously, two techniques were used to determine crack extension during the test. The

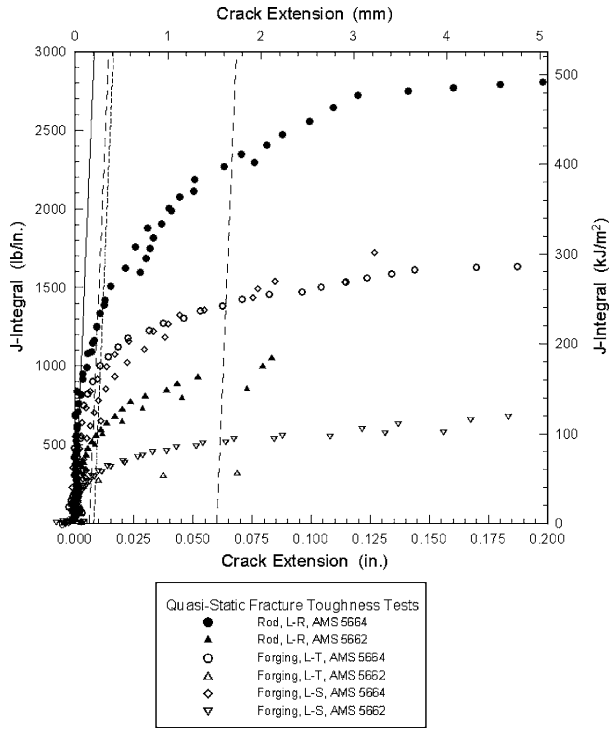


FIG. 2—*Tearing resistance curves for quasi-static fracture toughness tests.*

interrupted loading technique utilized repeated impacts of the same specimen with increasing deflections to create the equivalent of a dynamic test with unloadings. A typical record for a test with five impacts is shown in Fig. 4. It was difficult to accurately stop the cross-head, as is evidenced by the under-shot on impact #4. On the last impact significant crack growth occurred. The slopes of the unload and subsequent reloading were used to calculate crack extension using compliance. This will be discussed further in the section on data analysis. Not all tests had multiple impacts, although they all utilized displacement limits in an effort to control crack extension.

TABLE 2—*Results from quasi-static fracture toughness tests.*

Product Heat Treat	Orientation	Spec. ID	Temp. (°C)	J_{Ic} kJ/m^2 (lb/in.)	Valid ? (Y/N)	Stable Δa mm (in.)
Forging AMS	L-T	F1-4	-2	47.6 (272)	N[a,c]	1.75(0.069)
5662	L-S	F2-5	21	53.4 (305)	Y[c]	5.28(0.208)
	L-S	F2-7	21	57.3 (327)	Y[c]	5.56(0.219)
Rod AMS	L-R	R1-7	-2	91.8 (524)	N[b,c]	1.85(0.073)
5662	L-R	R2-8	21	102.3 (584)	Y[c]	2.11(0.083)
Forging AMS	L-T	XF1-1	-2	177.1(1,011)	Y	5.13(0.202)
5664	L-S	XF2-6	21	166.7 (952)	Y[c]	3.40(0.134)
	L-S	XF2-8	21	136.4 (779)	Y[c]	2.90(0.114)
Rod AMS	L-R	XR1-8	-2	240.5(1,373)	Y	5.03(0.198)
5664	L-R	XR3-2	21	242.0(1,382)	Y[c]	1.93(0.076)

[a]Fails requirements for number of data points and data spacing.

[b]Fails requirements on scatter in data.

[c]Test ended with crack instability. Final crack shape, crack extension, and crack extension prediction could not be checked. Test passed all other validity checks.

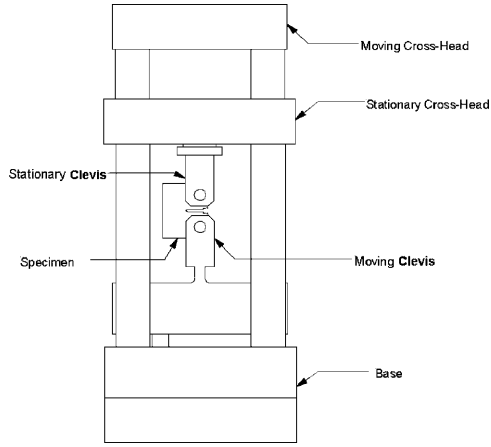


FIG. 3—*Test fixture for dynamic fracture toughness tests.*

The second technique utilized the normalization method to infer crack extension from measured load and load-line displacement. With this method it was not necessary to interrupt the test. The displacement stops for these tests were set with the objective of obtaining a small amount of stable crack extension without instability. Unfortunately, for the combinations of product form and heat treatments that exhibited low tearing resistance, it was not possible to avoid instability. The normalization method will be discussed further in the next section.

Data Analysis for Dynamic Tests—For the interrupted load tests, the unload from one impact and the reload from the subsequent impact were used to determine the compliance of the specimen at that point in the test. Compliance was then used to determine crack length. Crack extension was determined by measuring the pre-crack length after the test and subtracting that from the calculated crack lengths. The calculations to determine the *J-R* curve and J_{Id} were carried out using the procedures for quasi-static testing in E 1820, even though the complete unloading between each impact in an interrupted loading test

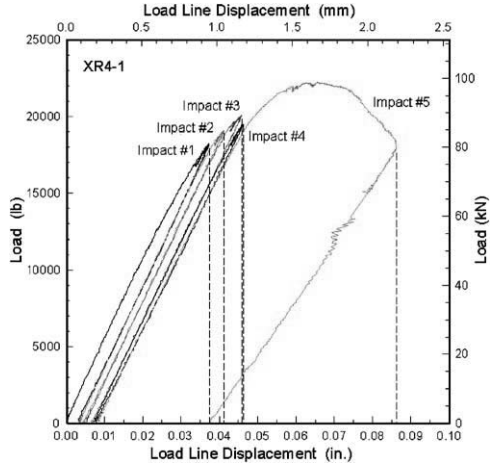


FIG. 4—*Typical load-displacement record for interrupted dynamic test. Vertical dashed lines show maximum deflection for each impact.*

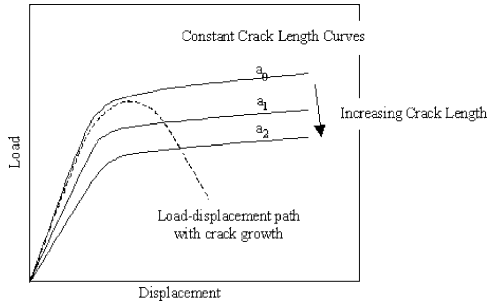


FIG. 5—*Illustration of crack length prediction using method of normalization.*

violates the limit on unloading in E 1820. When a specimen with a crack is unloaded completely, proportional loading is lost and the premise under which the *J*-integral was derived is violated. The partial unloadings in a quasi-static test also violate proportional loading; however, the effect is minimal as long as the amount of unloading is small.

Analysis of many of the dynamic tests was also conducted using the normalization method to extract crack extension from the load-displacement data. According to this method, the load for a particular specimen geometry can be expressed as a separable function of crack length and plastic displacement [6–18].

$$P(a, v_{pl}) = G\left(\frac{a}{W}\right) H\left(\frac{v_{pl}}{W}\right) \tag{1}$$

The geometry function, G, accounts for crack length and is different for each specimen type. The plasticity function, H, is a function of the material flow behavior (yield strength and strain hardening characteristics). The dependence on crack length can be removed by defining a normalized load.

$$P_N = \frac{P}{G} = H(v_{plN}) \tag{2}$$

v_{plN} is the normalized plastic displacement. The curve defined by H is a function of material flow properties and is independent of geometry and crack length. Load-displacement curves can be generated for fixed crack lengths using Eq 1 if the plasticity function and the geometry functions are known, as shown in Fig. 5. Any deviation of the load-displacement behavior in a test from the constant crack length curve is an indication of crack extension. The premise of this method is that the amount of deviation can be used to infer crack extension. At the point where the dashed curve crosses the curve for crack length a_1, the crack length is equal to a_1. The procedure in Annex A15 of E 1820 was followed in the normalization analysis, with the exception that an additional factor of 1.553 was added to the geometry function based on the early work of Donoso and Landes [14].

$$G = 1.553WB\left(\frac{W-a}{W}\right)^{\eta} \tag{3}$$

The exponent η comes from Annex A2 of E 1820 for a C(T) specimen. There are practical limits to the application of this method. For instance, crack growth must be preceded by some amount of plasticity. The method cannot be used when crack growth occurs with little or no plasticity because there is not enough data to accurately determine the plasticity function. The method also requires accurate measurement of the final load, deflection, and crack length, and that the crack extension in the test is not too large. This is because the plasticity function fit is highly dependent on the position of the anchor point (the point corresponding to the maximum deflection where load and crack length can be measured). The position of the anchor point is particularly sensitive to the final measured crack length. For tests that end in instability, it is preferable to use the point of instability as the anchor point. However, it is often impossible to determine the crack length at the point of instability, and the crack extension at arrest may be too large to accurately determine the plasticity function. In general, the larger the gap between the point of tangency

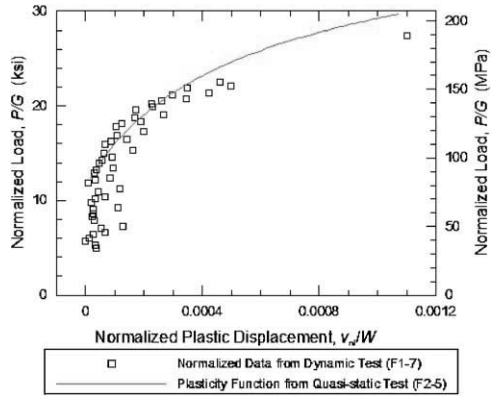


FIG. 6—*Normalized load-displacement data for dynamic test of F1-7 compared with plasticity function from quasi-static test of F2-5.*

and the anchor point, the less accurate the plasticity function will be.

In this study two approaches were used to improve the estimation of the plasticity function, particularly when the test ended in instability or when there was large crack extension. The first approach involved incorporating the anchor points from similar stable tests where crack extension was not too large and could be accurately measured. There is a limit to the effectiveness of this approach because the plasticity function will not necessarily be the same, even for two specimens that are identical in all outward respects. The second approach involved using the plasticity function from a quasi-static test to analyze a dynamic test. The plasticity function from a quasi-static test can be determined very accurately because the load, displacement, and crack length are known at each unload in the test. This approach is only valid when the flow properties are not sensitive to loading rate.

Results for Analysis of Dynamic Tests Using the Normalization Method—The dynamic tests of the AMS 5662 heat treat of the forging and the rod (F1-6, F1-7, and R1-9), ended with unstable crack growth after one or two impacts. Consequently, the crack length at instability could not be measured. This caused uncertainty in the location of the anchor point in the normalization analysis. Also, crack growth in these specimens occurred with very little plasticity (maximum v_{plN} 0.0011 to 0.0028), and it appeared that crack extension occurred well before maximum load. These two factors made it difficult to obtain the plasticity function from the dynamic data. These tests were analyzed using plasticity functions derived from the quasi-static unloading compliance data. The assumption was made that the plasticity function was not significantly affected by loading rate. This assumption was supported by the data, as evidenced by the good correlation between the quasi-static plasticity function for F2-5 and the normalized dynamic load-displacement data for F1-7 (see Fig. 6) and the fact that the tensile tests did not show a large rate effect. The results of the normalization analysis are summarized in Table 3 and the *J-R* curves are given in Fig. 7. Comparison with the results in Table 2 reveals that, for both product forms, the initiation toughness for the AMS 5662 heat treatment exhibited an increase with loading rate.

Crack growth in three out of five dynamic tests of the AMS 5664 forging specimens remained stable and there was enough plasticity that anchor points could be determined and plasticity functions could be obtained. The tests of specimens XF1-3 and XF1-8 went unstable on the last impact, thereby making it

TABLE 3—*Results from single or double-impact dynamic fracture toughness tests for AMS 5662 heat treatment at* −2 °C.

Product/ Heat Treat	Orientation	Specimen ID	J_{Id} kJ/m^2 (lb/in.)
Forging	L-T	F1-6	74.3 (424)
	L-T	F1-7	63.9 (365)
Rod	L-R	R1-9	114.5 (654)

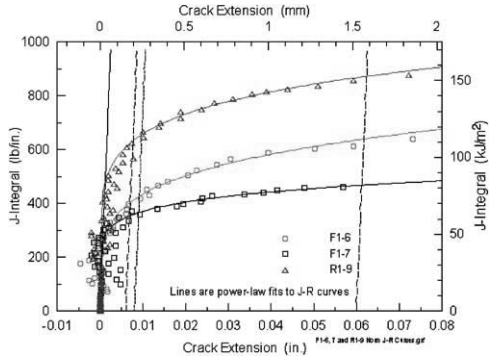


FIG. 7—*Dynamic J-R curves from normalization analysis of F1-6, F1-7, and R1-9.*

difficult to determine the anchor points. In an effort to improve the plasticity functions, the anchor points for the three stable tests (XF1-5, XF1-10, and XF2-1) were added to the normalized data for the unstable tests and plasticity function fits were performed using the E 1820 functional form for the plasticity function. This approach worked so well that these anchor points were also added to the stable test data to further improve the determination of the plasticity functions. The resulting plasticity functions are compared with each other, and with the quasi-static plasticity function, in Fig. 8. The *J-R* curves for these five specimens are compared with the quasi-static *J-R* curve in Fig. 9.

Crack growth in the three dynamic tests of the AMS 5664 rod specimens remained stable and there was enough plasticity that anchor points could be determined and plasticity functions could be obtained. Based on the success of using anchor points to supplement the normalized data and improve the plasticity functions for the previous forging tests, the same approach was used in the analysis of these rod tests. The resulting plasticity functions are compared with each other, and with the quasi-static plasticity function, in Fig. 10. The *J-R* curves for these five specimens are compared with the quasi-static *J-R* curve in Fig. 11.

The results from the normalization analysis of the dynamic tests are summarized in Table 4. Comparing these results with the quasi-static results in Table 2 reveals that there is no clear effect on rate on initiation toughness for the AMS 5664 heat treatment at −2 °C.

Results for Analysis of Dynamic Interrupted Load Tests Using Compliance

For the forging and rod specimens where it was possible to obtain multiple impacts, compliance was also used to determine crack extension and generate dynamic *J-R* curves. A typically multiple-impact test

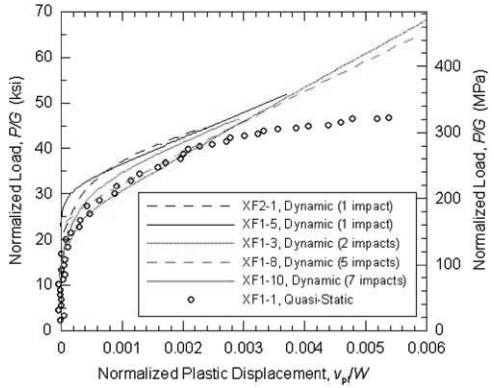


FIG. 8—*Comparison of plasticity functions for AMS 5664 forging tests (XF).*

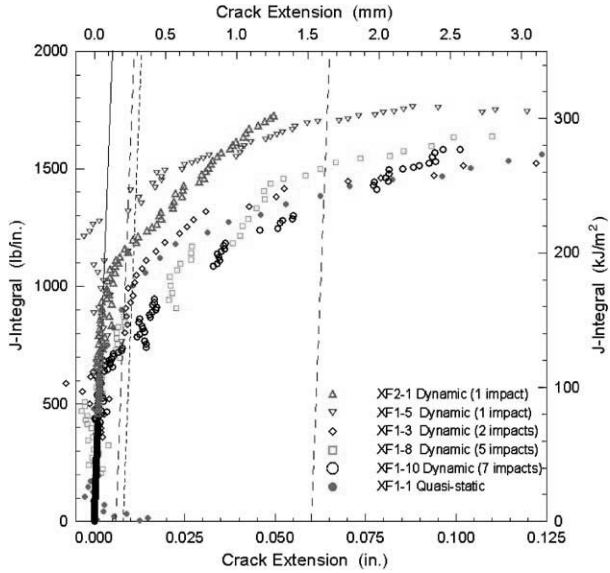


FIG. 9—*Comparison of quasi-static and dynamic J-R curves for forging with AMS 5664 heat treatment.*

record from the test of XF1-8 (Forging, AMS 5664) is shown in Fig. 12. The crack growth went unstable on the fifth impact, as evidenced by the large deflection and drop in load. The unload and subsequent reload after each impact were used to measure compliance and thereby determine crack extension. The resulting *J-R* curve is compared with the normalization *J-R* curve in Fig. 13. The same procedure was used to analyze the multi-impact tests of XF1-10, XR2-7, and XR4-1. The results for these tests are compared with the normalization *J-R* curves in Figs. 14–16 and the dynamic initiation toughnesses are compared in Table 5. The *J-R* curves from the compliance and normalization analyses compare pretty well for three of the four specimens. The exception is specimen XR4-1, where they agree pretty well in the initial part of the *J-R* curve, but then the normalization curve rises much higher than the trend implied by the compliance points at large crack extension. The high tearing resistance on the last impact is confirmed by the elevated load-displacement record after maximum load for this specimen. Apparently there were microstructural features in this specimen that led to higher tearing resistance.

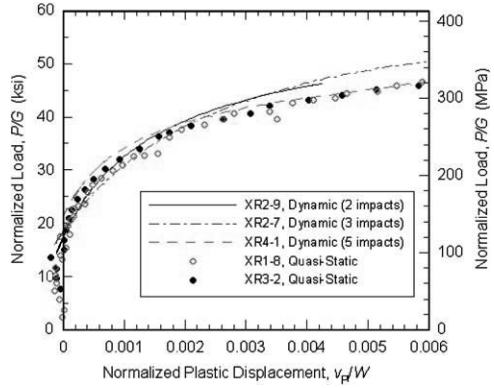


FIG. 10—*Comparison of plasticity functions for AMS 5664 rod tests (XR).*

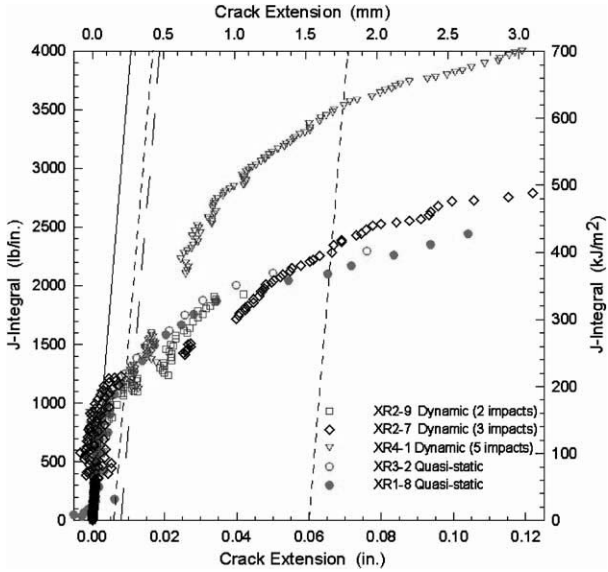


FIG. 11—*Comparison of quasi-static and dynamic J-R curves for rod with AMS 5664 heat treatment.*

Discussion

The fit of the plasticity function to the normalized load-displacement data is strongly influenced by the gap between the point of tangency and the anchor point. If the gap is large, the fitting function tends to take the

TABLE 4—*Results from dynamic fracture toughness tests for AMS 5664 heat treatment at −2°C.*

Product/ Heat Treat.	Orientation	Specimen ID	J_{Id} kJ/m^2(lb/in.)
Forging/ AMS	L-T	XF1-3	178(1017)
5664	L-T	XF1-5	241(1376)
	L-T	XF1-8	151 (860)
	L-T	XF1-10	135 (768)
	L-S	XF2-1	203(1158)
Rod/ AMS 5664	L-R	XR2-7	251(1433)
	L-R	XR2-9	206(1175)
	L-R	XR4-1	274(1567)

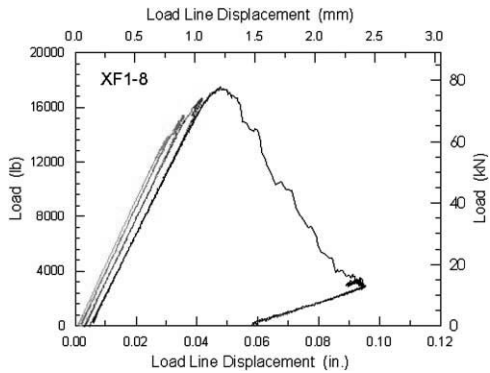


FIG. 12—*Load-displacement records for multi-impact test of XF1-8.*

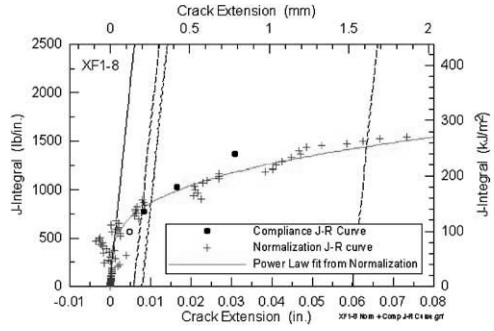


FIG. 13—*Comparison of compliance and normalization J-R curves for dynamic test of XF1-8.*

shortest route between the two points, thereby possibly depressing the plasticity function. An example of this is shown in Fig. 17. The net effect of this is to reduce crack extension and thereby raise the *J-R* curve. The resulting initiation toughness is then nonconservative. By conducting tests to different amounts of ductile crack extension, it is possible to obtain anchor points that fill in the gap. For the example shown, the additional anchor point at a normalized plastic displacement of about 0.004 reveals that the plasticity function should rise higher, and that crack growth started before the tangency point. Moving the tangency point back and adding the anchor points results in the higher plasticity function. The resulting *J-R* curve is considerably lower, as is the initiation toughness.

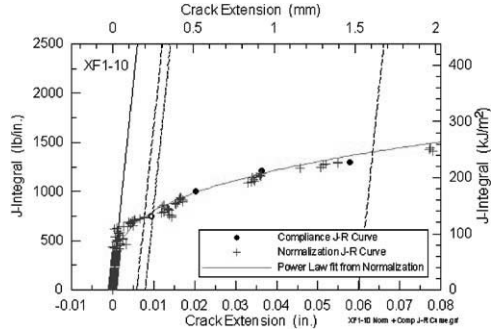


FIG. 14—*Comparison of compliance and normalization J-R curves for dynamic test of specimen XF1-10.*

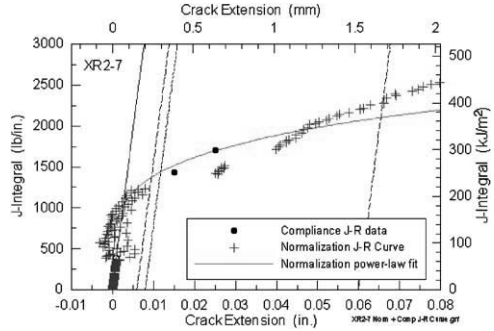


FIG. 15—*Comparison of compliance and normalization J-R curves for dynamic test of specimen XR2-7.*

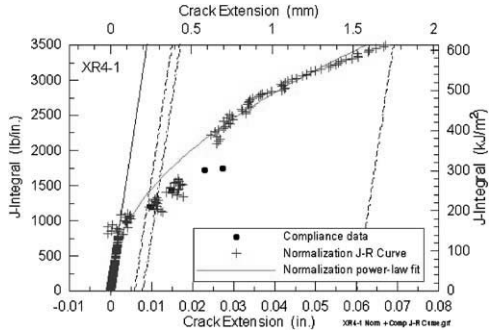


FIG. 16—*Comparison of compliance and normalization J-R curves for dynamic test of specimen XR4-1.*

The results from the dynamic tests show that there appears to be a depression of the tearing resistance curve due to damage induced by plastic work at the crack tip each time the specimen is completely unloaded. This can be seen by comparing *J-R* curves for the same heat treatment and product. Referring to the test results for the forging in Fig. 9, the two single-impact tests have the highest J-R curves. As the number of impacts increases, the tearing resistance decreases, particularly at low crack extension where the most damage is occurring. For the tests with five and seven impacts, the tearing resistance drops below the quasi-static curve for about the first 1.25 mm (0.050 in.) of crack extension. The final impact resulted in considerably larger crack extension, which allowed the crack to grow out of the damage zone from the previous impact and elevated the *J-R* curve, although not as high as the single-impact tests. Similar behavior can be seen in the test results for the rod, shown in Fig. 11, although the *J-R* curve for XR4-1 exhibits a considerably larger tearing resistance after the last impact than any of the other specimens. Once again note that the multiple impact *J-R* curves fall near or below the quasi-static curves right in the vicinity

TABLE 5—*Comparison of J_{Id} values from compliance and normalization for dynamic fracture toughness tests at −2 °C.*

Product/ Heat Treat	Orientation	Specimen ID	Compliance J_{Id} kJ/m² (lb/in.)	Normalization J_{Id} kJ/m² (lb/in.)
Forging, AMS	L-T	XF1-8	147 (838)	150 (860)
5664	L-T	XF1-10	150 (856)	135 (768)
Rod, AMS	L-R	XR2-7	229(1310)	251(1433)
5664	L-R	XR4-1	224(1281)	274(1567)

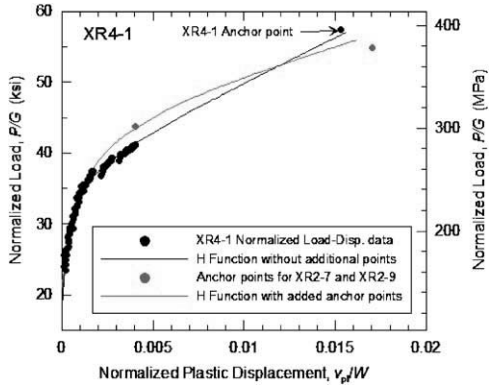


FIG. 17—*Influence of additional anchor points on plasticity function fit.*

of crack growth initiation. This has important implications for dynamic loading applications where there may be more than one load excursion during the dynamic event.

Conclusions

Alloy 718 is prone to unstable fracture under compliant loading conditions. This was particularly true for the AMS 5662 heat treatment, but also occurred to a lesser extent with AMS 5664. For the two product forms and heat treatments evaluated, the rod has higher fracture toughness than the forging, and AMS 5664 more than doubles the fracture toughness compared with AMS 5662. For both product forms the initiation toughness for the AMS 5662 heat treatment was elevated at high rates of loading. However, there was no clear effect of rate on initiation toughness for the AMS 5664 heat treatment at $-2\,^{\circ}\mathrm{C}$.

In the application of the Normalization method, care must be taken in determining the plasticity function. If there is a large gap before the anchor point, this can lead to under-estimating crack extension and over-estimating the initiation toughness. By conducting tests to different amounts of ductile crack extension, it is possible to obtain anchor points that fill in the gap and improve the crack extension estimates. In this study the *J-R* curves from compliance and normalization analyses compared pretty well, thereby lending confidence in this approach. The results from the multiple-impact dynamic tests showed that there is a depression of the tearing resistance curve due to damage induced by plastic work at the crack tip each time the specimen is completely unloaded. This has important implications for dynamic loading applications where there may be more than one load excursion during the dynamic event.

The results from this investigation confirm that heat treatment and the resulting microstructure have a significant effect on the fracture toughness and tearing resistance of Alloy 718. The higher temperature solution anneal exhibited superior fracture toughness for both product forms. Loading rate did not have a consistent effect on fracture toughness or tearing resistance. There was also no consistent effect of orientation on fracture properties for the forging.

References

[1] *Aerospace Structural Metals Handbook*, Volume 4, 1996 Edition, William F. Brown, Jr., Harold Mindlin and C. Y. Ho, Eds., CINDAS/USAF CRDA Handbooks Operation, Purdue University, Code 4103, p. 61.

[2] Mills, W. J., "The Effect of Heat Treatment on the Room Temperature and Elevated Temperature Fracture Toughness Response of Alloy 718," *ASME J. Eng. Mater. Technol.*, Vol. 102, 1980, pp. 118–126.

[3] Mills, W. J. and Blackburn, L. D., "Fracture Toughness Variations in Alloy 718," *ASME J. Eng. Mater. Technol.*, Vol. 110, 1988, pp. 286–293.

[4] Mills, W. J. and Blackburn, L. D., "Variations in Fracture Toughness for Alloy 718 Given a Modified Heat Treatment," *ASME J. Eng. Mater. Technol.*, Vol. 112, 1990, pp. 116–123.

[5] Graham, S. M., "Fracture Toughness of Alloy 718 Bar and Forging for ASDS Transit Latch Assembly," NSWCCD-TR-61-1999/06+CR, Naval Surface Warfare Center, Carderock Division, May 2003.

[6] Joyce, J. A., Ernst, H., and Paris, P. C., "Direct Evaluation of *J*-Resistance Curves from Load Displacement Records," *Fracture Mechanics: Twelfth Conference, ASTM STP 700*, ASTM International, West Conshohocken, PA, 1980, pp. 222–236.

[7] Paris, P. C., Ernst, H., and Turner, C. E., "A *J*-Integral Approach to Development of η-Factors," *Fracture Mechanics: Twelfth Conference, ASTM STP 700*, ASTM International, West Conshohocken, PA, 1980, pp. 338–351.

[8] Ernst, H. A., Paris, P. C., and Landes, J. D., "Estimations on *J*-Integral and Tearing Modulus *T* from a Single Specimen Test Record," *Fracture Mechanics: Thirteenth Conference, ASTM STP 743*, Richard Roberts, Ed., ASTM International, West Conshohocken, PA, 1981, pp. 476–502.

[9] Herrera, R. and Landes, J. D., "A Direct *J-R* Curve Analysis of Fracture Toughness Tests," *J. Test. Eval.*, Vol. 16, No. 5, 1988, pp. 427–449.

[10] Herrera, R. and Landes, J. D., "Direct *J-R* Curve Analysis: A Guide to the Methodology," *Fracture Mechanics: 21st Symposium, ASTM STP 1074*, J. P. Gudas, J. A. Joyce, and E. M. Hackett, Eds.,

ASTM International, West Conshohocken, PA, 1990, pp. 24–43.

[11] Zhou, Z., Lee, K., Herrera, R., and Landes, J. D., "Normalization: An Experimental Method for Developing *J-R* Curves," *Elastic-Plastic Fracture Test Methods: The User's Experience (2nd Volume), ASTM STP 1114*, J. A. Joyce, Ed., ASTM International, West Conshohocken, PA, 1991, pp. 42–56.

[12] Orange, T. W., "Method and Models for *R*-curve Instability Calculations," *Fracture Mechanics: 21st Symposium, ASTM STP 1074*, J. P. Gudas, J. A. Joyce, and E. M. Hackett, Eds., ASTM International, West Conshohocken, PA, 1990, pp. 545–559.

[13] Landes, J. D., Zhou, Z., Lee, K., and Herrera, R., "Normalization Method for Developing *J-R* Curves with the LMN Function," *J. Test. Eval.*, Vol. 19, No. 4, 1991, pp. 305–311.

[14] Donoso, J. R. and Landes, J. D., "Common Format for Developing Calibration Curves in Elastic-Plastic Fracture Mechanics," *Eng. Fract. Mech.*, Vol. 47, No. 5, 1994, pp. 619–628.

[15] Donoso, J. R. and Landes, J. D., "The Common Format Equation Approach for Developing Calibrations Functions for Two-Dimensional Fracture Specimens from Tensile Data," *Eng. Fract. Mech.*, Vol. 54, No. 4, 1996, pp. 499–512.

[16] Sharobeam, M. H. and Landes, J. D., "The Load Separation Criterion and Methodology in Ductile Fracture Mechanics," *Int. J. Fract. Mech.*, Vol. 47, 1991, pp. 81–104.

[17] Sharobeam, M. H. and Landes, J. D., "The Load Separation and η_{pl} Development in Precracked Specimen Test Records," *Int. J. Fract. Mech.*, Vol. 59, 1993, pp. 213–226.

[18] Ernst, H., Paris, P. C., Rossow, M., and Hutchinson, J. W., "Analysis of Load-Displacement Relationship to Determine *J-R* Curve and Tearing Instability Material Properties," *Fracture Mechanics, ASTM STP 677*, C. W. Smith, Ed., ASTM International, West Conshohocken, PA, 1979, pp. 581–599.

AUTHOR INDEX

A

Asakura, Toshiyuki, 234

B

Beretta, Stefano, 137
Biglari, Farid Reza, 469
Bjork, Timo, 343
Boyajian, David M., 407
Brooks, Craig L., 185
Bucher, Laurent, 168
Busso, E. P., 81

C

Calcaterra, Jeffrey Ronald, 174
Carboni, Michele, 137
Ceyhan, U., 23
Chona, Ravinder, 309
Chaouadi, Rachid, 374

D

Davies, C. M., 115, 321
Dean, D. W., 23
Diaz, Francisco A., 225
Dogan, B., 23
Dong, P., 206

F

Forman, R. G., 244
Forth, S. C., 244
Fukuda, Katsumi, 148

G

Geary, W., 457
Glancey, Christopher D., 158
Gomi, Kenji, 148
Govindaraj, Elumalai, 281
Graham, Stephen M., 445, 511

H

Hoeppner, David W., 271
Hong, J. K., 206
Hongo, H., 93

I

Ichinose, Kensuke, 148
Ilvonen, Reijo, 343
Ishihara, Kenichi, 234
Ishii, Hideyuki, 148

J

Jain, Nitesh, 309
Jin, Ohchang, 174
Jones, Kimerbli, 271
Joyce, J. A., 390
Joyce, P. J., 390

K

Kim, Seon-Jin, 71
Kim, Woo-Gon, 71
King, Peter J., 256
Kondo, Yoshiyuki, 195
Köster, Alain, 168
Kourmpetis, M., 321

L

Lawrence, Timothy O., 407
Leax, T. R., 425
Lee, Hyeong-Yeon, 54
Leis, Brian N., 357
L'Heureux, Brian P., 445
Link, Richard E., 485
Lucon, Enrico, 374

Copyright © 2008 by ASTM International www.astm.org

M

Madia, Maruo, 137
Mall, Shankar, 174
Marquis, Gary, 343
Mercier, Gerard P., 445
Meshii, Toshiyuki, 234
Mueller, F., 115

N

Newman, J. C., Jr., 244
Nikbin, Kamran M., 23, 43, 54, 81, 102, 115, 321, 469

O

O'Dowd, N. P., 81, 115, 321
Okuya, Kazuhiko, 195

P

Patterson, Eann A., 225
Pellikka, Veli, 343
Petroski, B., 23
Prost-Domasky, Scott A., 185

Q

Qu, Jie, 295

R

Rezaeinasab, Alireza, 469
Remy, L., 168
Roy, Ajit K., 281
Ryu, Woo-Seog, 71

S

Santacreu, Pierre-Olivier, 168
Sattarifar, Iradj, 469
Scibetta, Marc, 374
Shukla, Arun, 309
Stephens, Robert R., 158

T

Tabuchi, M., 93
Taniuchi, Kiyoshi, 148

V

Valliyil, Unnikrishnan, 281
Van Der Sluys, W. Alan, 256
van Walle, Eric, 374

W

Wang, Xin, 295
Wardle, G., 457
Wasmer, K., 102
Watanabe, T., 93
Webster, George A., 3, 102, 115

Y

Yates, John R., 225
Yatomi, Masataka, 43
Yi, Won, 71
Yokobori, A. T., Jr., 93
Yoon, Song-Nam, 71
Yoshida, Sanichiro, 148
Young, Bruce A., 256
Young, Nichole, 185

Z

Zhu, Xian-Kui, 357

SUBJECT INDEX

300M steel, 158

A

AISI 441, 158
Alloy 718, 511
Aluminum alloys, 174, 234, 271
ASTM E 647, 244
ASTM E 1457, 23, 115, 321
ASTM E 1820, 390, 511
ASTM E 1921, 445, 457
Austenitic stainless steel, 23, 71, 102, 115

B

Behavior model, 168
Biaxial loading, 295
Brittle crack initiation, 485
Brittle fracture, 343
BS 7910, 54

C

Carbon fiber reinforced polymer-concrete, 407
Carbon-manganese steel, 23, 43, 115
Carbon steel, 234
Charpy testing, 374, 445
Cleavage fracture, 445
Code of Practice, 23, 115
Compact tension specimen, 23, 43, 321
  miniature, 374
Constraint effects, 295, 357
Constraint factor, 137
Corrosion cracking, 281
Corrosion fatigue, 271
Crack arrest, 485
Crack closure, 115, 195, 244
Crack extension
  ductile, 309
  resistance, 457
Crack growth
  corrections, 390
  creep, 3, 23, 43, 71, 93, 102, 115, 321
  fatigue, 234, 244
  rate, 43, 71, 256
Crack initiation, 148
  creep, 23, 115
  high-temperature, 81
  Type IV, 93
Crack mouth opening displacement, 321
Crack propagation, 256
  dynamic, 469
Cracked tube, 256
Crack tip, 309
Creep, 43, 54, 81, 93
  deformation, 3
  ductility, 102
  structure, 93
Creep fracture parameter, 3, 23, 43, 102, 115, 321
Creep properties, uniaxial, 102
Creep stress relaxation rate, 54
CRETE, 23
Cyclic large strain, 195
Cyclic loading, 225, 407
Cyclic stress-strain diagram, 148
Cyclic temperature fluctuation, 225

D

Data scatter, 425
Defect shape,137
Differential thermography, 225
Double edge notch specimen, 321
Ductile fracture, 343, 374
Ductile tearing initiation, 374
Ductile-to-brittle transition, 457
Dynamic fracture, 485
Dynamic tear energies, 445

E

Earthquakes, 195
Edge crack, 185

Copyright © 2008 by ASTM International www.astm.org

Elastic-plastic-creep analysis, 43, 54
Elastic-plastic fracture, 321, 390
Elastic *T*-stress, 295
Embedded elliptical crack, 295
Elasto-viscoplastic behavior, 168
EN 1.4509, 168
Eta factor, 321

F

Failure assessment, 357
Fatigue crack , 225, 256
  growth, 244
  nucleation, 158
Fatigue damage, 148
Fatigue life, 158
Fatigue limit, 195
Fatigue strength, 147, 195
Fatigue thresholds, 137
Ferritic stainless steel, 168
Finite element analysis, 43, 81, 93, 185, 206, 321, 469, 485
  three-dimensional, 295
Fracture, 81, 407
  Type IV, 93
Fracture mechanics, 3, 23, 43, 115, 185, 234, 445, 485
  linear, 195
Fracture toughness, 357, 425, 445, 457
  dynamic, 485, 511
  measurement, 374
Fretting fatigue, 174, 185
Functionally graded materials, 309

G

Genetic algorithm, 234
Geometry effects, 390
Glass fiber reinforced polymer-concrete, 407

H

Heat affected zone, 93
High Cr heat resisting steel, 93
High strength low alloy steel, 445, 485
High temperature, 43
  redistribution of residual stresses, 54
  structural integrity assessment, 3
Holistic models, 185

I

Incubation period, 3
Inhomogeneities, 137
Isochromatics, 309

J

J-integral, 374, 390
J-Q theory, 357
J-R curve, 357, 374

K

Kitagawa diagram, 137

L

Least square fitting method, 71
Life prediction, 174
Lifetime assessment, 3
Linear elastic fracture mechanics, 256, 469
Loss of constraint, 374
Low cycle fatigue, 148
Lüder band, 148

M

Master Curve, 425, 457
Maximum energy release rate, 469
Mean value method, 71
Mesh-insensitive structural stress method, 206
Microcracks, 81
Micro-notches, 137
Microstructure, 271
Modified Gough's ellipse, 206
Monte Carlo simulation, 71

Multiaxial fatigue, 43, 206

N

Nickel base superalloy, 81
Node releasing, 469
Nondestructive evaluation, 158
Normalization method, 390, 511

O

Orange peel, 148
Overload, 54

P

Photo-emission, 225
Pipe, 43, 357
Pitting corrosion, 271
Plastic deformation, 195
Plastic zone, 225
Polytetrafluoroethylene, 390
Pop-in behavior, 390
Positron annihilation, 158
Potential, applied, 281
Potential drop, 256
Pre-crack, 195
Pressure vessel steels, 457
Pressurized water reactor, 256, 374, 425
Probabilistic methods, 71, 102
Process zone, 225

R

R6, 54
Reference stress, 43
Reference temperature, 445
Redistribution, 54
Residual stress, 3, 54
Resistance curve, 457

S

Scanning electron microscopy, 271
Seismic loading, 195
Sensitivity analysis, 54
Side grooves, 390
Simulation, 234
Single contoured cantilever beam, 407
Single crystal materials, 81
Single edge notched specimens, 321, 357, 485
Specimen geometry, 115, 256, 321
Static fracture mode, 234
Strain energy density, 469
Stress corrosion cracking testing, 281
Stress fields, asymptotic, 309
Stress intensity equation, 256
Stress intensity factors, 54, 295
  Mode I, 185
  threshold range, 234
Structural hollow section, 343
Structural integrity assessment, high temperature, 3
Structural stress parameter, 206
Surface condition, 148
Surface diffusion, 81
Surface roughness, 407

T

Thermoelasticity, 225
Thermomechanical fatigue, 168
Thermomechanical loading, 309
Titanium alloys, 174, 234
T-plate, 54
Transition curve shape, 457
Transition regime 425
Tubular T-joint, 54
Type IV fracture, 93

U

Uniaxial loading, 295

W

Welded joint, 3, 93, 195, 206, 343

Work hardening, 374

X

X80 steel, 357
X-joint, 343

Z

Zirconium alloy, 281

www.astm.org

Stock # STP1480
ISBN 978-0-8031-3406-5